## İÇİNDEKİLER / CONTENTS — Sayfa / Page

---

**Amaç/Objective**
Isı bilimi ve tekniğinin geliştirilmesini teşvik etmek, ısı bilimi ve tekniği alanında özgün, teorik, sayısal ve deneysel çalışmaların yayınlanmasına olanak sağlamaktır.
*To contribute to the improvement of thermal sciences and technology and publication of original, theoretical, numerical, and experimental studies in thermal sciences and technology.*

**İçerik/Content**
Isı bilimi ve tekniği alanındaki özgün ve derleme makaleler.
*Original and review articles in thermal sciences and technology.*

**Değerlendirme/Evaluation**
Dergi hakemli bir dergi olup, her bir makale konusunda uzman en az iki hakem tarafından değerlendirilir.
*Each article published in this journal is evaluated by at least two referees.*

# THE ANNUAL CO₂ EMISSIONS AND ENERGY COSTS OF DIFFERENT EXTERIOR WALL STRUCTURES IN RESIDENTIAL BUILDINGS IN TÜRKİYE

**Aynur UÇAR**
Firat University, Engineering Faculty, Department of Mechanical Engineering, 23279 Elazığ
aucar@firat.edu.tr, ORCID: 0000-0001-5973-3741

**Abstract:** Carbon dioxide emissions are one of the most important causes of global climate change. It is accepted in the world today that the world urgently needs to reduce carbon dioxide emissions in order to avoid the worst impacts of climate change. In this study, the optimum thickness of each insulation material is determined depending on the available costs and the total annual CO₂ emissions of insulation materials for building external walls with different structure in the selected cities from different climate regions of Turkey. The different wall types insulated with four different insulation materials are presented. The results indicate that the optimum insulation thickness varies from 2.5 to 13 cm and is different for each wall type and insulation material. The total annual CO2 emission per unit area of the wall varies between 3.32 and 10.32 kg CO₂/m² depending on the insulation material and wall type.
**Keywords:** CO₂ emissions; life cycle cost; Optimum insulation thickness; Eco-efficiency

## TÜRKİYE'DE KONUTLARDA FARKLI DIŞ DUVAR YAPILARININ YILLIK CO₂ EMİSYONLARI VE ENERJİ MALİYETLERİ

**Özet:** Karbondioksit emisyonları, küresel iklim değişikliğinin en önemli nedenlerinden biridir. İklim değişikliğinin en kötü etkilerinden kaçınmak için dünyanın acilen karbondioksit emisyonlarını azaltması gerektiği bugün dünyada kabul görmektedir. Bu çalışmada, her bir yalıtım malzemesinin optimum kalınlığı, Türkiye'nin farklı iklim bölgelerinden seçilen şehirlerde farklı yapıya sahip dış duvarlar için yalıtım malzemelerinin mevcut maliyetlerine ve yıllık toplam CO2 emisyonlarına bağlı olarak belirlenmiştir. Dört farklı yalıtım malzemesi ile yalıtılmış farklı duvar tipleri sunulmaktadır. Sonuçlar, optimum yalıtım kalınlığının 2.5 ile 13 cm arasında değiştiğini ve her duvar tipi ve yalıtım malzemesi için farklı olduğunu göstermektedir. Duvarın birim alanı başına yıllık toplam CO₂ emisyonu, yalıtım malzemesine ve duvar tipine bağlı olarak 3.32 ile 10.32 kg CO₂/m² arasında değişmektedir.
**Anahtar Kelimeler:** CO₂ emisyonları; Yaşam döngüsü maliyeti; Optimum yalıtım kalınlığı; Eko-verimlilik

## NOMENCLATURE

| | |
|---|---|
| $C_A$ | yearly energy cost ($/m² year) |
| $C_i$ | unit cost of insulation material ($/m³) |
| d | discount rate (%) |
| HDD | heating degree days (ºC-days) |
| $H_u$ | lower calorific value of fuel (J/kg) |
| i | inflation rate (%) |
| $k_{ins}$ | heat cond. coeff. of ins. material (W/m K) |
| N | lifetime (years) |
| $N_p$ | payback period (years) |
| $R_w$ | total thermal resistance of the wall (m² K/W) |
| S | savings ($/m²) |
| $T_b$ | base temperature (ºC) |
| $T_i$ | inside air temperature (ºC) |
| $T_o$ | average daily temperature (ºC) |
| U | total heat transfer coefficient (W/m² K) |
| q | annual heat loss from wall (W/m²) |
| $Q_H$ | annual heating load per unit area (kWh/m²) |
| $Q_C$ | annual cooling load per unit area (kWh/m²) |

## INTRODUCTION

Buildings play an important role in consumption of energy all over the world. The annual global CO₂ emissions generated by buildings are nearly 40%. The building operations are responsible from 28% of those total emissions annually, while building materials and construction (typically referred to as embodied carbon) are responsible for an additional 11% of those total emissions annually (Global ABC Global Status Report, 2018).

The recent works towards energy-saving design is not only in conditions of providing lower U-values, but also in the improving and use of natural and local insulation materials. In last years, the areas of thermal conservation in buildings are more concentrating on environmental properties. Measures to prevent environmental pollution are not only limited to energy savings (Stephan, Crawford and Myttenaere 2012). The optimum insulation thickness is determined by some researchers

(Nematchoua et al.2017; Kayfeci, Keçebas and Gedik 2013; Kurekci 2016; Çomaklı and Yüksel 2003; Dombaycı, Gölcü and Pancar 2006; Bolattürk 2006; Akan 2021).

The total $CO_2$ emissions of a building consist of operational and embodied emissions. Operational $CO_2$ emissions are emissions from the use of a building's heating and cooling system. Embodied carbon generally refers to the carbon dioxide ($CO_2$) emissions associated with the construction and material life throughout a building whole life span. Özel et al. (2015) determined the optimum insulation thickness using the environmental and life cycle cost analyses. They calculated the fuel consumption, the $CO_2$ emission and the environmental impacts of the system related to entransy loss. Gaarder et al. (2023) analyzed the influence of the energy emission factor and future climate change on the optimal insulation thickness. They used three independent models for case studies in Greenland and Norway. Jie et al. (2018) determined the optimum insulation thickness based on primary energy consumption, global cost and pollutant emissions and they analyzed four heat and cold sources for a case study. Akan and Akan (2022) determined $CO_2$ emissions based on the energy savings through the thermal insulation applied to the external walls of the buildings for eighty-one different zones using four diverse thermal insulation materials. They found that $CO_2$ emissions decreased by approximately 66-76% in the heating season and by 46-69% in the cooling season in buildings with thermal insulation. The environmental problems like global warming, acid rain, air pollution, urban sprawl, waste disposal, ozone layer depletion, water pollution, climate change affect all the human, animal and nation on world. The Life Cycle Assessment (LCA) methodology is used as a tool to assess potential environmental impacts of products along their life cycle. LCA is applied in many researches to evaluate the impact of different insulation materials (Braulio-Gonzalo 2017; Lazzarin, Busato and Castellotti 2008; Cabeza et al. 2014; Ferrández-García, Ibánez-Forés and Bovea 2016; Axaopoulos et al. 2019; Atmaca 2016; Huang et al. 2020).

As energy consumption in developing countries such as Turkey increase, environmental pollution and greenhouse gas emissions are increasing every year. Residential buildings are very important in reducing energy needs and greenhouse gas emissions. In this study, the optimum thickness of each insulation material is determined depending on the available costs and the total annual $CO_2$ emissions of insulation materials for residential building external walls with different structure in the selected different cities of Turkey. Firstly, the optimum value of Insulation thickness is determined by maximizing the net energy savings for heating, cooling and both heating and cooling found by the Life Cycle Costing (LCC) method. Secondly, the optimum insulation thickness is found by minimizing the total annual $CO_2$ emissions. In this study, the four wall types commonly used in Turkey were selected. The same

methodology can be repeated for other wall types and different climatic conditions.

## METHODOLOGY

The methodology is applied to residential building external walls with different structure as a case study by comparing four insulation materials. Methodological framework is presented in Fig.1.
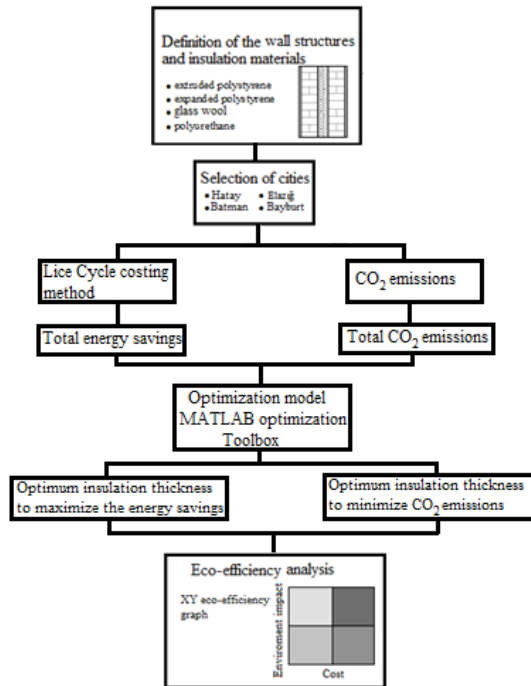


**Fig.1.** Methodological framework.

### Description of the building and wall structures

The gross area of studied building is about 140 m² per story, three stories, and two dwellings per story. Each dwelling unit has three bedrooms and a living room and a bathroom. Fig.2 presents the detailed floor plan of building.
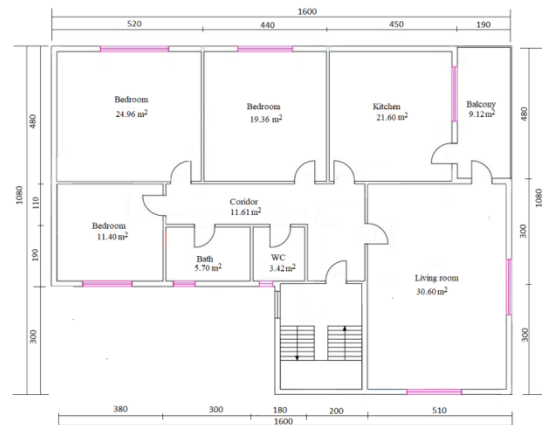


**Fig.2.** The floor plan of the studied building

The heat losses to environment from the external walls of buildings is occurred. Wall 1 consist of 2 cm inner plaster, 13 cm brick, insulation material and 2 cm

2

external plaster. Wall 2 is a sandwich wall which has a compound structure consisting of 2 cm inner plaster, 10 cm each of two brick layers and 2 cm external plaster. The materials used in Wall 3 are inner plaster, hollow concrete block, insulation and external plaster. In this wall configuration, the assumed total thickness for concrete is 20 cm, while the thickness for interior plaster is 2 cm and for exterior plaster is 2 cm. Wall 4 consist of

2 cm inner plaster, 30 cm CSEB (Compressed Stabilised Earth Block), insulation material and 2 cm external plaster. In this working, polyurethane (PU), extruded polystyrene (XPS), glass wool (GW) and expanded polystyrene (EPS) are selected as insulation materials. The physical properties of each material used in the wall structures are given in Table 1.

**Table 1.** Thermal characteristics of wall structures

| Wall type | Thickness (m) | Thermal conductivity (W/mK) | Resistance (m$^2$ K/W) | Insulation cost ($/m$^3$) | Cross-sectional views of the investigated external wall structures. |
|---|---|---|---|---|---|
| *Wall 1* 4-Interior plaster *(TS EN 998-1)* 3-Brick *(TS EN 771-1)* 2-Insulation 1-External plaster *(TS EN 998-1)* | 0.02 0.13 * 0.02 | 0.87 0.45 0.87 | 0.335 | | |
| *Wall 2* 4-Interior plaster 3-Brick 3-Brick 2-Insulation 1-External plaster | 0.02 0.10 0.10 * 0.02 | 0.87 0.45 0.45 0.87 | 0.490 | | |
| *Wall 3* 4-Interior plaster 5-Hollow concrete block *(TS EN 771-3)* 2-Insulation 1-External plaster | 0.02 0.20 * 0.02 | 0.87 0.60 0.87 | 0.379 | | |
| *Wall 4* 4-Interior plaster 6-CSEB 2-Insulation 1-External plaster | 0.02 0.30 * 0.02 | 0.87 0.88 0.87 | 0.387 | | |
| *Insulation Materials* Polyurethane *(TS EN 13165)* Extruded polystyrene *(TS EN 13164)* Expanded polystyrene *(TS EN 13163)* Glass wool *(TS EN 13167)* | * * * * | 0.024 0.031 0.039 0.040 | | 260 180 120 75 | |
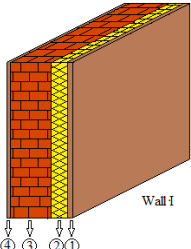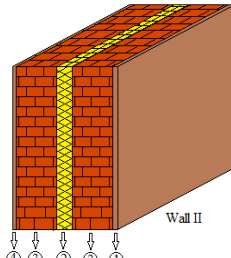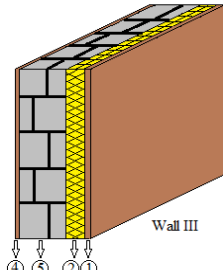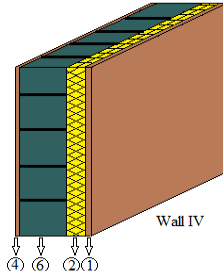
* The optimum thickness of insulation material which is found by the life cycle cost analysis

**Table 2.** The parameters used in calculations (Evin and Ucar, 2019)

| Parameter | Value | | | |
|---|---|---|---|---|
| *Cities* | *Hatay* | *Batman* | *Elazığ* | *Bayburt* |
| HDD | 1119 | 1823 | 2653 | 4149 |
| CDD | 614 | 763 | 337 | 8 |
| *Natural gas (Heating)* | | | | |
| $C_F$ | 0.332 $/m$^3$ | | | |
| $H_u$ | $34.526 \times 10^6$ J/m$^3$ | | | |
| $\eta_s$ | 0.90 | | | |
| $f_H$ | 0.181 kgCO$_2$/kWh | | | |
| *Electricity (Cooling)* | | | | |
| $C_e$ | 0.3496 $/kWh | | | |
| $f_C$ | 0.588 kgCO$_2$/kWh | | | |
| $f_{ins}$ (CO$_2$ emission factor of materials (kgCO$_2$/kg)) | | | | |
| *Polyurethane* | 3.75 | | | |
| *Extruded polystyrene* | 4.42 | | | |
| *Expanded polystyrene* | 2.35 | | | |
| *Glass wool* | 1.16 | | | |
| Brick | 0.246 | | | |
| Plaster | 0.23 | | | |
| Concrete | 0.170 | | | |
| CSEB | 51.5 | | | |
| Interest rate, i (TCMB, 2022) | 7.5% | | | |
| Inflation rate, d(TCMB, 2022) | 64% | | | |
| Lifetime, N | 10 | | | |
| $T_i$ | 20°C | | | |

**Climatic zones**

The degree-day method is one of the commonly used methods to estimate the amount of energy required for heating or cooling. The total number of annual heating and cooling degree-days (HDDs and CDDs) is calculated by

$$HDD = \sum_{days}(T_b - T_o)^+ \tag{1}$$

$$CDD = \sum_{days}(T_o - T_b)^+ \tag{2}$$

The plus sign above the parentheses indicates that only positive values are to be counted (Kaynakli 2012). In this study, the annual heating and cooling degree-days of studied cities are taken for base temperatures of 18 °C for heating and 22 °C for cooling. According to the updated code TS 825 Thermal Insulation Requirements for Buildings, Turkey is divided into five climatic zones in relation to their average temperature degree-days of heating (TS 825, 2013). Energy performance of the different types of buildings, the calculation method of annual heating energy demand, thermal transmittance "U" values for each region, which is defined by using the "degree day method" in TS-825, and the maximum heating demand values according to regions were described (Evin and Uçar, 2019). The heating and cooling degree-days of each region are different from each other due to their climatic characteristics. Heating degree-day values in the cities on the coast have lower values compared to cities in the eastern and inner regions.

In this study, Hatay from the coastal region and Batman from the southern region were selected. Elazig and Bayburt cities with different climatic characteristics of Turkey were selected from the eastern and inner regions and optimum values of insulation thickness were found. The annual heating degree-days of Hatay in the southernmost of Turkey is 1119, while degree-days of Bayburt in the north-east of Turkey is 4149. Batman is a Turkish province southeast of Anatolia and the annual heating degree-day of its is 1823. The annual heating degree-days of Elazığ is 2653. Table 2 shows the parameters used in calculations.

**Life Cycle Costing (LCC) method**

The heat transfer in building walls is realized by three mechanisms of heat transfer. Firstly, the solar radiation coming to the outside surface of the building wall is absorbed by wall surface and then, the heat transfer into the wall by conduction is occurred. The heat transfer between ambient air with the outside surface of wall and also between the inside surface of the wall with indoor air are occurred by convective.

Heat transfer rate from a unit area of building wall can be found as

$$q = U(T_i - T_o) \tag{3}$$

The annual heat rate from unit area can be determined using the degree days, as given by the following equation

$$q_H = 86400 \; HDD \; U \tag{4}$$

$$q_C = 86400 \; CDD \; U \tag{5}$$

The total heat transfer coefficient for an insulated wall can be written by

$$U = \frac{1}{1/h_i + R_w + x_{ins}/k_{ins} + 1/h_o} \tag{6}$$

where $x_{ins}$ is insulation material thickness (m) and $k_{ins}$ is heat conduction coefficient of insulation material (W/m K). $h_i$ is inner convective heat transfer coefficient (W/m$^2$K) and $h_o$ is outer convective heat transfer coefficient (W/m$^2$K). In this study, the convective heat transfer coefficient between inner and outer surface depending on speed and direction of the wind can be evaluated as follows (Axaopoulos et al., 2015)

$$h_i = 1.31\left(T_{s,i} - T_i\right)^{1/3} \tag{7}$$

$$h_{o,ww} = 1.53v + 1.43 \tag{8}$$

$$h_{o,lw} = 0.90v + 3.28 \tag{9}$$

where v is wind speed, $T_i$ is inside air temperature and $T_{s,i}$ is the inner surface temperature of wall. The wind speed and common direction data are received from examined weather stations in this working. It is accepted

4

that Eq. (8) is for the east, north and west facing wall surface, when Eq. (9) is for the south facing wall surface.

The surface temperatures of wall components are calculated as follows (Ucar, 2010)

$$T_{s,i} = T_i - \frac{1}{h_i} q \tag{10}$$

$$T_1 = T_{s,i} - \frac{l_1}{k_1} q \tag{11}$$

$$T_2 = T_1 - \frac{l_2}{k_2} q \tag{12}$$

$$T_n = T_{n-1} - \frac{l_n}{k_n} q \tag{13}$$

$$T_{s,o} = T_o - \frac{1}{h_o} q \tag{14}$$

The annual energy needs for heating and cooling can be calculated by (Evin and Ucar 2019);

$$E_H = \frac{86400\ U\ HDD}{H_u\ \eta_s} \tag{15}$$

$$E_C = \frac{86400\ U\ CDD}{COP} \tag{16}$$

where $\eta_s$ is efficiency of fuel and COP is coefficient of performance of the heat pump. In this working, the energy savings of each type of wall is calculated by using the life cycle cost (LCC) method. The annual heating and cooling energy cost of per unit area, $C_A$, is found by (Ucar and Balo, 2011)

$$C_{A,H} = \frac{86400\ U\ HDD\ C_F}{H_u\ \eta_s} \tag{17}$$

$$C_{A,C} = \frac{86400\ U\ CDD\ C_e}{COP} \tag{18}$$

where $C_F$ is cost of fuel ($/kg) and $C_e$ is cost of fuel ($/kWh). $P_1$ is the rate of energy savings obtained from fuel during the life cycle to the energy savings provided during the first year. $P_2$ is the rate of expenses during life cycle to first investment. This method facilitates economic analysis by collecting all the parameters in the economic analysis into $P_1$ and $P_2$. The $P_1$ and $P_2$ are determined by (Ertürk, 2016; Kumar et al., 2020)

$$P_1 = \frac{1}{(d-i)} \left[ 1 - \left( \frac{(1+i)}{(1+d)} \right)^N \right] \text{ if } i{\neq}d \tag{19}$$
and

$$P_1 = \frac{N}{(1+i)} \qquad \text{if } i{=}d$$

$$P_2 = 1 + P_1 M_S - R_v (1+d)^{-N} \tag{20}$$

where i is inflation rate, d is discount rate, N is lifetime, $M_s$ is the ratio of the annual maintenance and operation cost to the original first cost and $R_v$ is the ratio of the resale value to the first cost. Since there is no

maintenance and operating cost in the insulation application, the $P_2$ value is taken as 1.
The total insulation cost ($C_{ins}$) can be defined by

$$C_{ins} = C_i x_{ins} \tag{21}$$

Total heating and cooling costs are the total of the cost of insulation and the annual energy cost and they are determined as

$$C_H = C_{A,H} P_1 + P_2 C_i x_{ins} \tag{22}$$

$$C_C = C_{A,C} P_1 + P_2 C_i x_{ins} \tag{23}$$

The net energy savings for heating and cooling are determined as

$$S_H = \frac{86400\ HDD\ C_F}{\left( R_{wt} + \frac{x_{ins}}{k_{ins}} \right) H_u \eta_s} P_1 - P_2 C_i\ x_{ins} \tag{24}$$

$$S_C = \frac{86400\ CDD\ C_e}{\left( R_{wt} + \frac{x_{ins}}{k_{ins}} \right) COP} P_1 - P_2 C_i\ x_{ins} \tag{25}$$

$$S_T = \left( \frac{86400\ HDD\ C_F}{\left( R_{wt} + \frac{x_{ins}}{k_{ins}} \right) H_u \eta_s} + \frac{86400\ CDD\ C_e}{\left( R_{wt} + \frac{x_{ins}}{k_{ins}} \right) COP} \right) P_1 - P_2 C_i\ x_{ins} \tag{26}$$

The maximum value of the net energy savings for heating, cooling and both heating and cooling is the optimum value. In MATLAB optimization Toolbox, Eqs. (24)–(26) were taken as an objective function and the optimum thickness of insulation was found.

**CO$_2$ emissions and Eco-efficiency analysis**

In 2020, the largest share of CO$_2$ emissions in total greenhouse gas emissions was energy-related emissions with 70.2%, followed by agriculture with 14%, industrial processes and product use with 12.7%, and waste sector with 3.1% (Turkish Statistical Institute, 2020).

The annual total CO$_2$ emissions are divided into operational and embodied emissions. Operational CO$_2$ emissions are emissions from the use of the building's heating systems in winter and cooling systems in summer. The annual heating and cooling CO$_2$ emissions can be calculated by (Axaopoulos et al. 2019);

$$EM_{CO_2,H} = \frac{Q_H f_H}{\eta_s} \tag{27}$$

$$EM_{CO_2,C} = \frac{Q_C f_C}{COP} \tag{28}$$

where $f_H$ is CO$_2$ emission factor for thermal energy production from fuel (kgCO$_2$/kWh) and $f_C$ is CO$_2$ emission factor resulting from the electricity (kgCO$_2$/kWh). Annual embodied CO$_2$ emissions are emissions due to manufacture, transportation and installation procedures of the insulation material. The

annual embodied $CO_2$ emissions of insulation material can be defined by

$$EM_{ins} = \frac{\rho\, x_{ins}\, f_{ins}}{N} \qquad (29)$$

where $f_{ins}$ is $CO_2$ embodied emission factor of insulation material (kgCO$_2$/kg) and is given in Table 2. The total annual $CO_2$ emissions are calculated as,

$$EM_{tot} = EM_{CO_2,H} + EM_{CO_2,C} + EM_{ins} \qquad (30)$$

The optimum insulation thickness is calculated by minimize the total annual $CO_2$ emissions. Total annual $CO_2$ emissions from Eq. (30) is taken as objective function and the optimum thickness of insulation is obtained using MATLAB optimization Toolbox.

The products and processes are studied both economically and ecologically in eco-efficiency analysis. Eco-efficiency is often defined as a ratio between reduced environmental impact and increased production. (Ferrández-García et al. 2016).

**RESULTS AND DISCUSSION**

According to the life cycle cost analysis, the heating, cooling and total energy demands and costs for the studied building has been calculated with Eqs. (15)–(16) and Eqs. (22)–(23). Total heating demands of four wall types and insulation materials for four cities are shown in Fig. 4. Total energy demand of building in Bayburt is extremely high, while total energy demand of building for Hatay in hot region is the lowest. Total heating demand of the sandwich wall (Wall 2) insulated with glass wool (GW) is lowest compared to other wall types. The largest value of total heating load is found for the external wall (Wall1) insulated with Polyurethane (PU) at the optimum thickness.
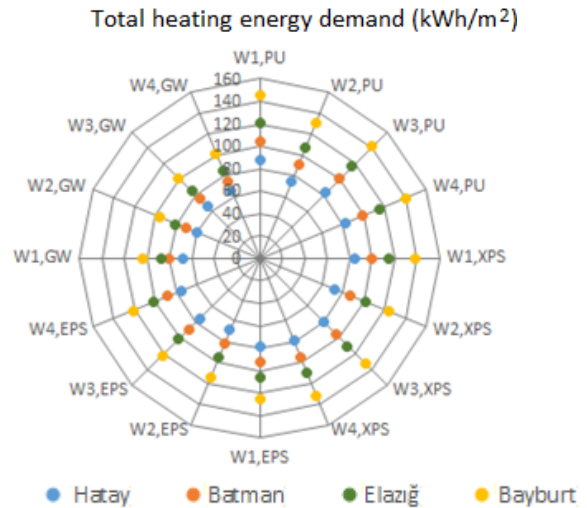


**Fig. 4.** Total heating energy demand of four wall types and insulation materials for four cities in Turkey.
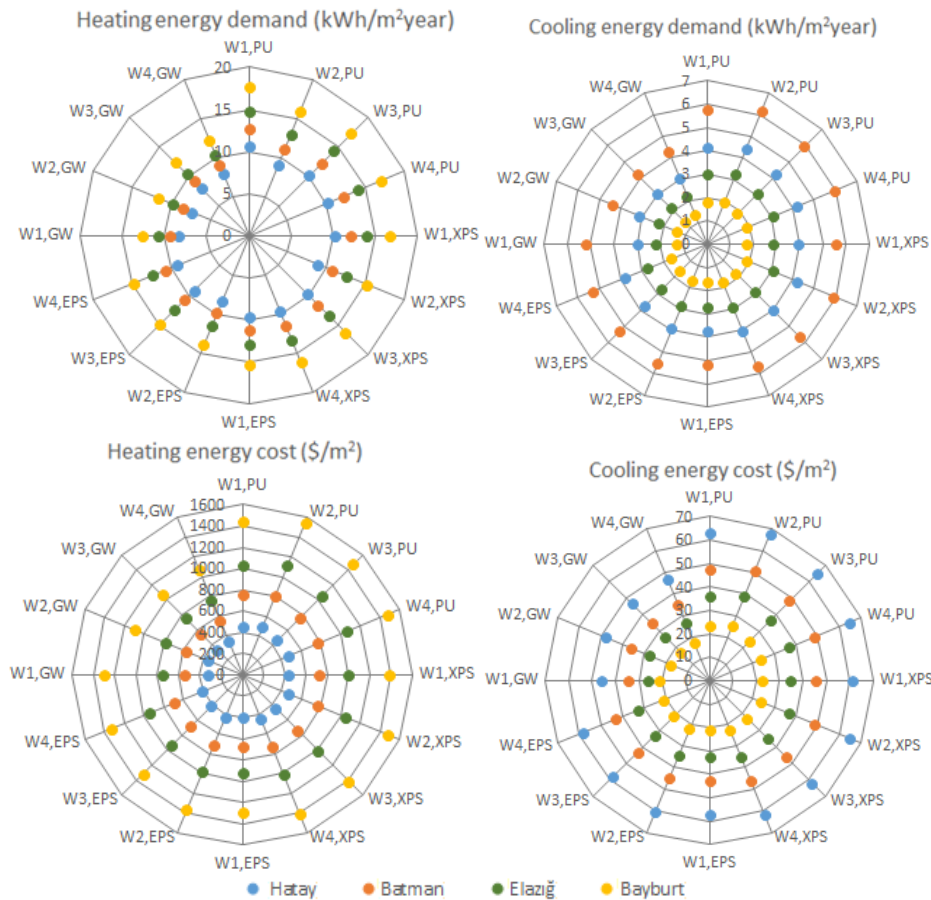


**Fig. 5.** Heating and cooling energy demand and cost of four wall types and insulation materials for selected cities.

6
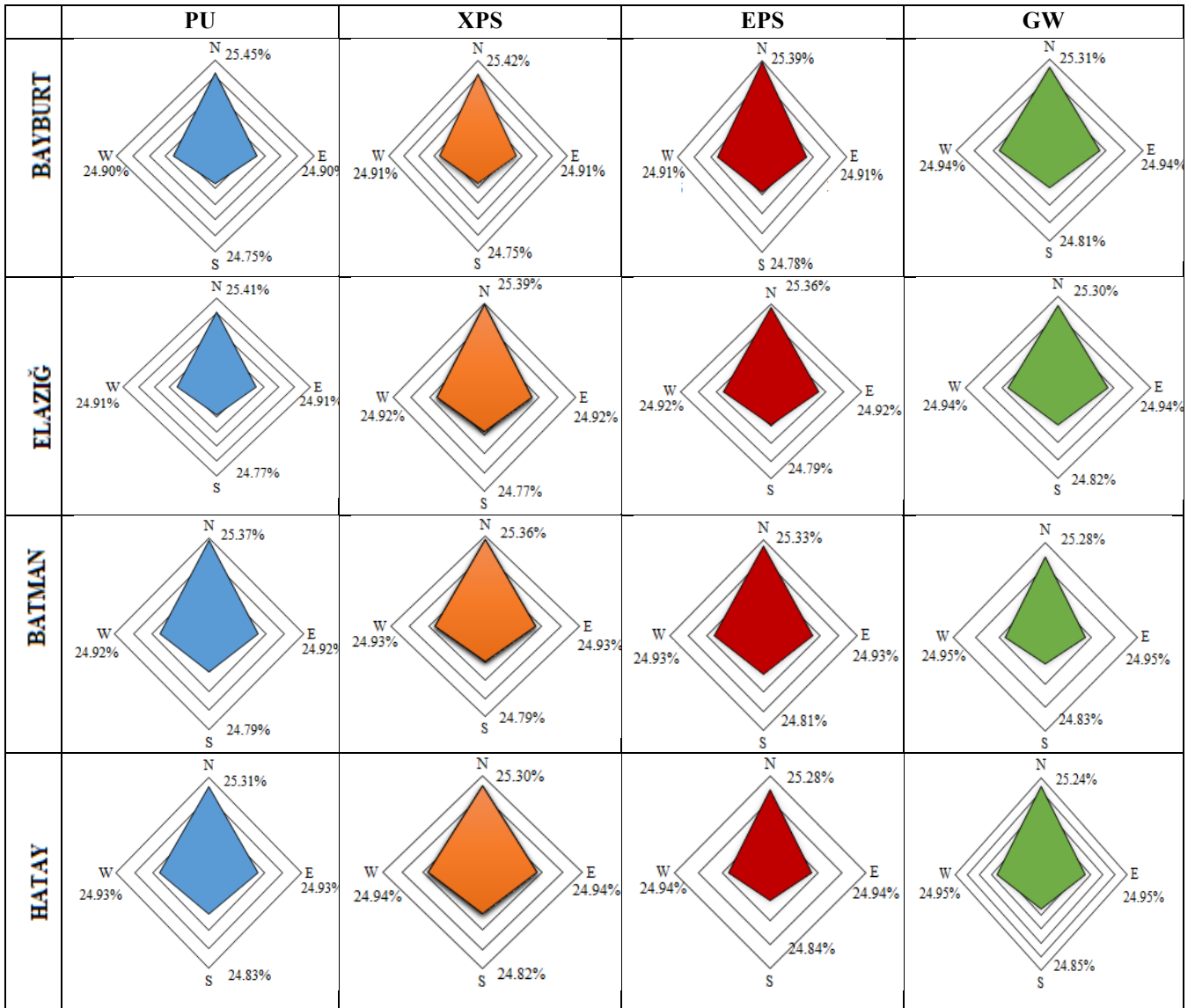
**Fig.6.** Each orientation percentage of the total heat transfer per unit area of external wall for different climatic conditions and insulation materials (for Wall 1)

Fig.5 shows the heating and cooling energy demand and cost found from the life cycle cost analysis for the studied building according to four cities by using natural gas as an energy source. The heating demand for the province of Bayburt (4149 ºC-days), located in the fourth degree day region of Turkey, is the highest among the three cities in the other regions. The total heating energy demand of building in Hatay is lowest, while cooling energy demand of building is the highest. The total energy costs of external walls insulated with glass wool (GW) has least among external walls insulated with other insulation materials. GW insulation material has the highest thermal conductivity coefficient among the selected insulation materials, but it also has the lowest cost.

Fig.6 shows the each orientation percentage of the total heat transfer per unit area of external wall for different climatic conditions and insulation materials (for Wall 1). The heating loss for north facing exterior surface of wall has highest percentage. The south facing exterior surface of wall has the lowest values according to other orientations for all climate conditions and wall structures, because this surface has the high solar heat gain.

Insulation thicknes versus $CO_2$ emissions for wall 1 type and Elazığ found are showed in Fig.7. The heat loss of external wall decreases with the insulation thickness increases. Therefore, the emissions resulting from the combustion of fuels will also decrease due to the reduction in annual fuel consumption. The total $CO_2$ emissions, achieved by adding these two values decreases with increase of insulation thickness until it reaches a minimum point and it increases again after a minimum value. This minimum point of total $CO_2$ emissions curve shows optimum insulation thickness.
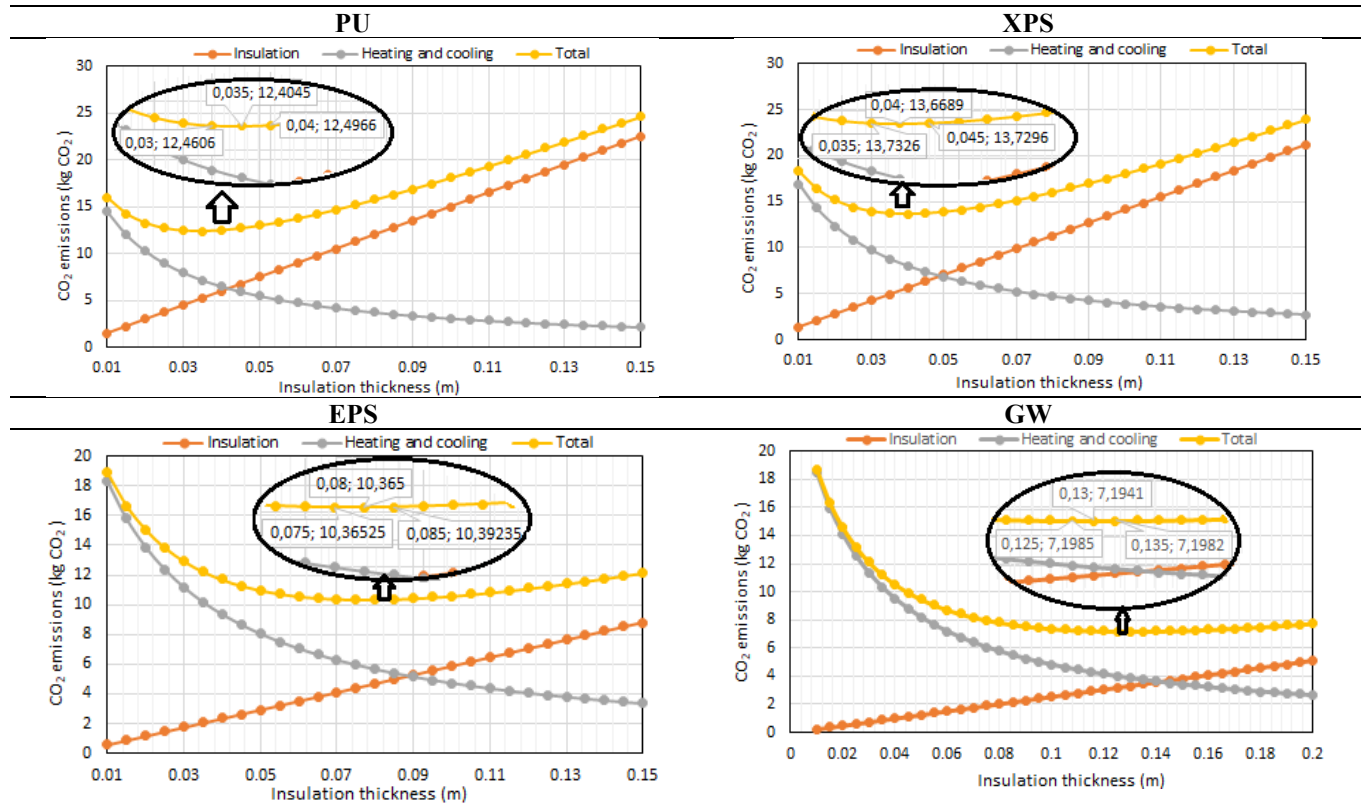
**Fig.7.** Insulation thicknes versus $CO_2$ emissions for four insulation materials and Elazığ (for wall 1 type)
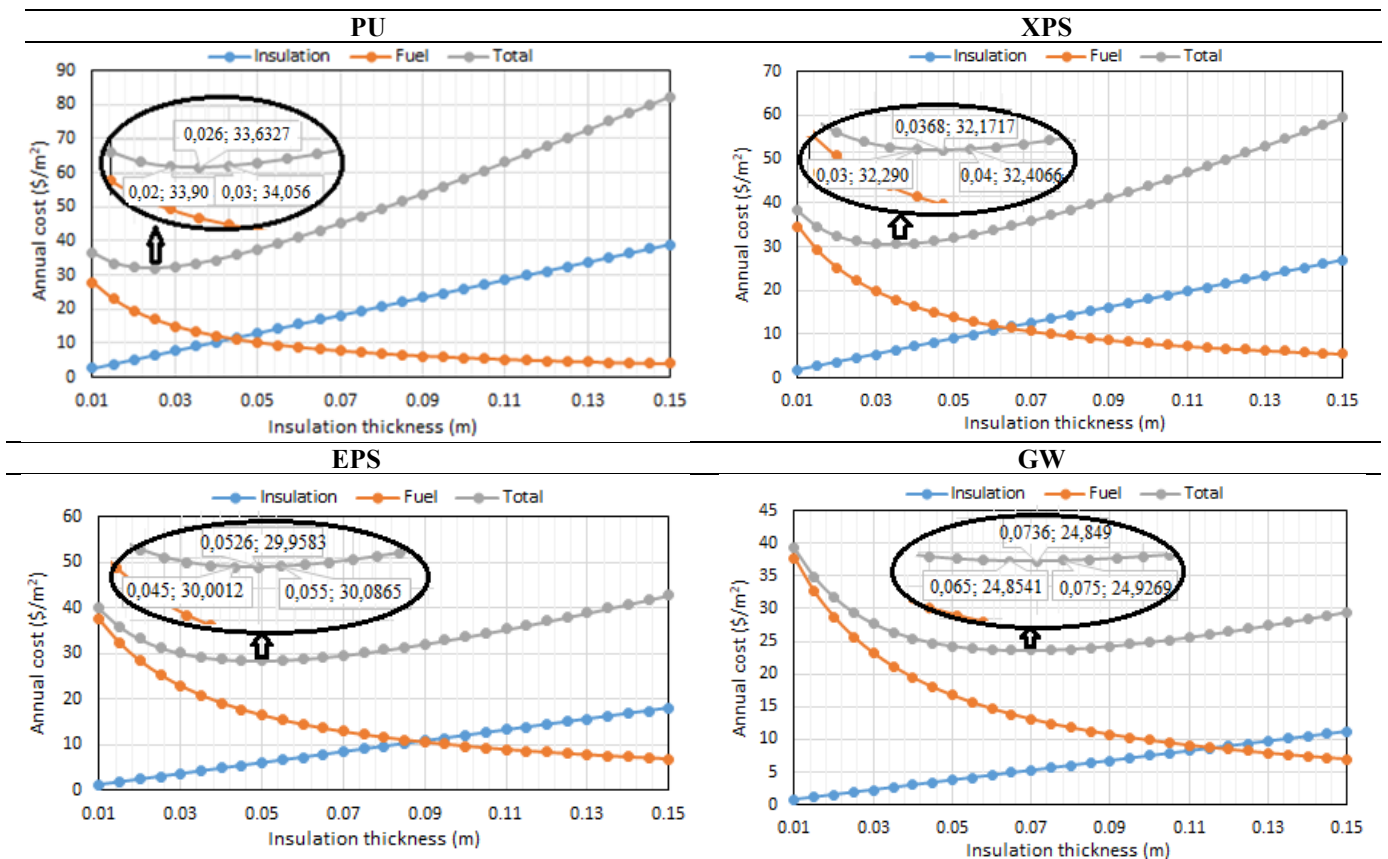


**Fig. 8**. Insulation thicknes versus annual cost heating and cooling for four insulation materials and Elazığ found using Life Cycle Cost (LCC) method (for wall 1 type)

The lowest value of $CO_2$ emission per unit area of wall insulated with GW insulation material were found as 7.19 kg $CO_2$ at optimum thickness (13 cm). the highest (13.67 kg $CO_2$) $CO_2$ emissions were obtained for the wall insulated with XPS insulation material at the optimum thickness (4 cm). Fig.8 shows the insulation thickness versus annual cost heating and cooling for four insulation materials and Elazığ found using Life Cycle Cost (LCC) method. The insulation cost increases linearly with insulation thickness, while operating costs corresponding to heating and cooling decreases. The optimum insulation thickness for external wall is minimum value of total cost which equals the summation of the insulation cost and operating cost.

The optimum insulation thickness for external wall insulated with PU has lowest value among other insulation materials. The optimum thickness for external wall insulated with XPS insulation material is 0.0368 m, whereas in case of insulation with EPS there is 0.0526 m. The optimal insulation thickness for external wall insulated with PU has lowest value among other insulation materials.

Fig. 9 shows the environmental impacts per unit area (Global warming, kg $CO_2$ eq.) of each construction material for the selected four wall types. In global warming potential (GWP) impact category, XPS insulation material has the highest GWP impact among the four insulation materials and the lowest impact belongs to GW which is 68% lower than XPS. The GWP of concrete (83.47 kg $CO_2/m^2$) used in wall 3 is quite high compared to materials used in the other external wall types. It is obtained that the $CO_2$ emissions of CSEB used in wall 4 is lowest than brick and concrete used in the other external wall types.
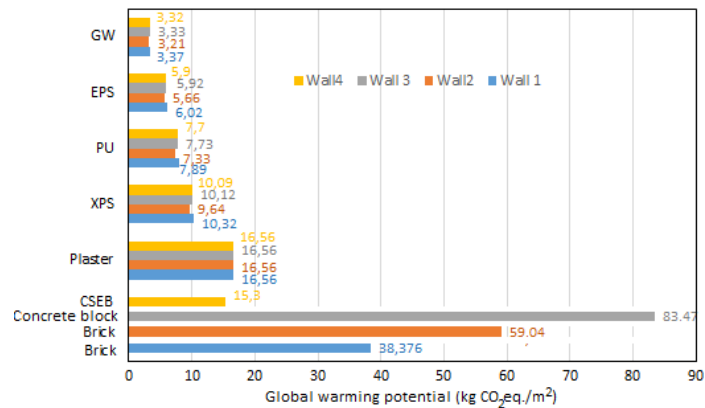


**Fig. 9.** The environmental impacts per unit area (GW, kg $CO_2$ eq.) of each construction material for the selected four wall types



Wall 1

Wall 2

Wall 3

Wall 4
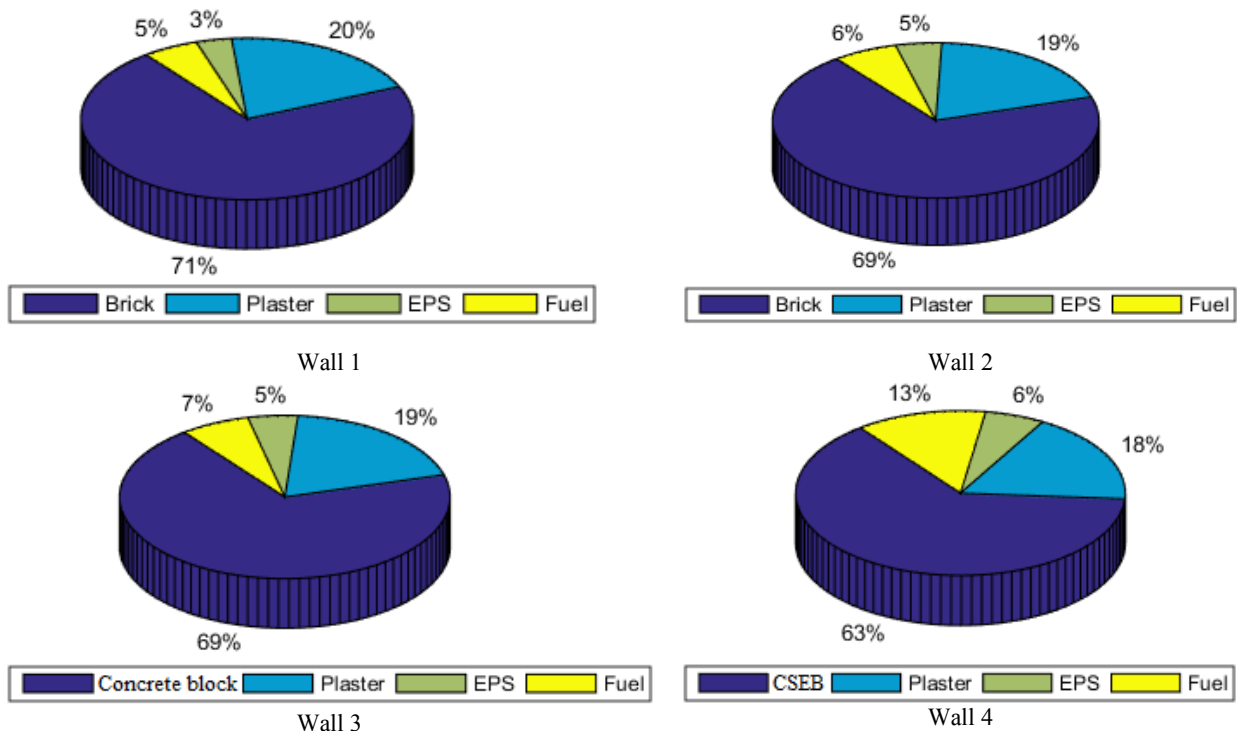
**Fig. 10.** Percentages of environmental impacts per unit area (Global warming, kg $CO_2$ eq.) each construction material for the selected four wall types

9

The percentages of environmental impacts per unit area (Global warming, kg $CO_2$ eq.) each construction material for the selected four wall types are shown Fig. 10. 69% of total GWP for wall 3 type belongs to hollow concrete block while 71% of total GWP for wall 1 type belongs to brick. While the highest $CO_2$ emission of natural gas which is used as an energy source is found for wall 4, the lowest $CO_2$ emission is obtained for wall 1. $CO_2$ emissions of EPS in the optimum thickness found using Life Cycle Cost (LCC) method present 3-6% of total $CO_2$ emissions for all wall types. Fig.11 shows the insulation thicknes versus annual cost and $CO_2$ emissions for selected cities. The difference between the optimum thicknesses of XPS insulation material found using these two method is 37-50% for the four selected cities. The optimum thickness of the insulation, where the total cost is minimum is 4.52 cm in Elazığ, while it is 2.6 cm in Hatay. The optimum thicknesses of insulation for minimum $CO_2$ emissions for Bayburt and Batman are 9.3 cm and 6.6 cm, respectively.
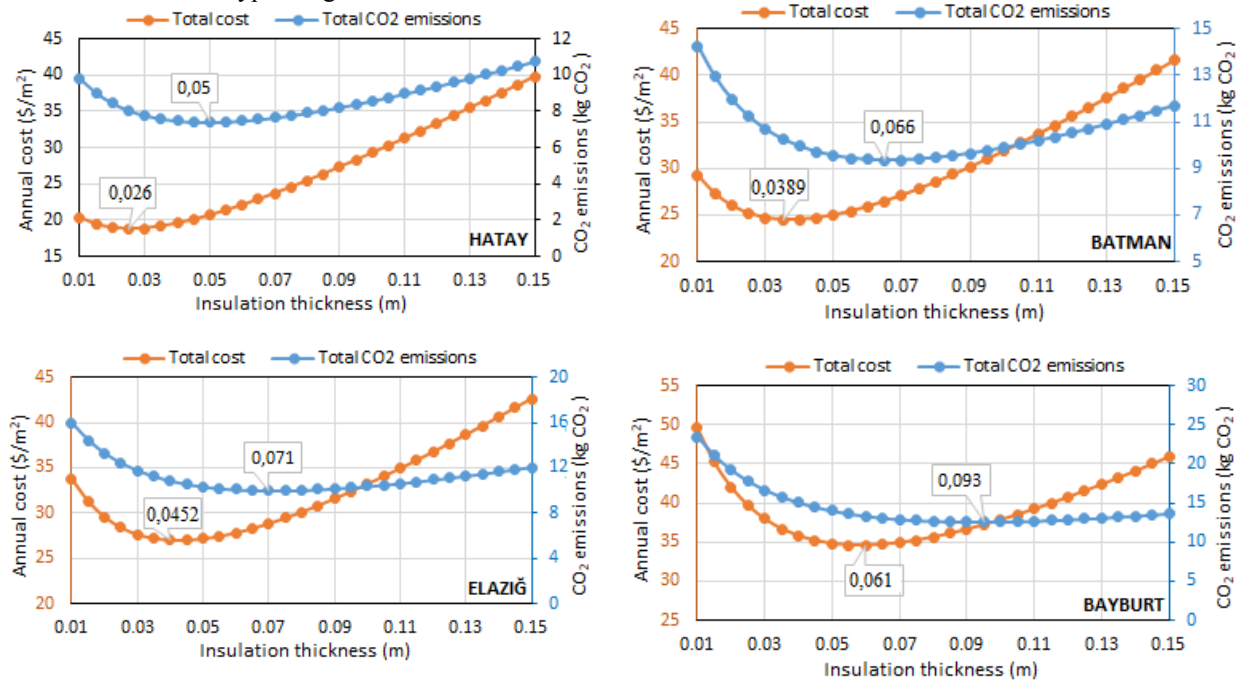


**Fig.11.** Insulation thicknes versus annual cost and $CO_2$ emissions for selected cities (for wall 1 type and XPS insulation material)

The environmental impacts per unit area (Global warming, kg $CO_2$ eq.) of the selected four cities and insulation materials is shown in Fig.12. It can see that $CO_2$ emissions of XPS insulation material are highest compared to the other insulation materials for four wall types and selected cities. The sandwich wall (wall 2) among all wall type studied displays greatest advantage with respect to the reduced $CO_2$ emissions per unit area of the wall.

The environmental impact assessments for selected four wall types and insulation materials are given in Fig.13. The four regions - Eco-Friendly, Stay Clear, Profiteering, and Eco-Efficient – are shown in each figure. Reduction in environmental impact and an increase in cost characterize this region. Despite the eco-friendly region, the Profiteering region is a region where there is a decrease in cost with the increase in global warming potential. While both the global warming potential and cost are the highest in Stay Clear region, they have the lowest values in the Eco-efficient region. Eco-efficient region displays contrasting features with the Stay Clear region. The external walls insulated with PU at the optimum thickness fall into the Eco-Efficient quadrant for the category global warming potential and the abiotic depletion of fossil resources. All constructions of the insulated external wall with glass wool positioned in region, which has low environmental impact and high cost.
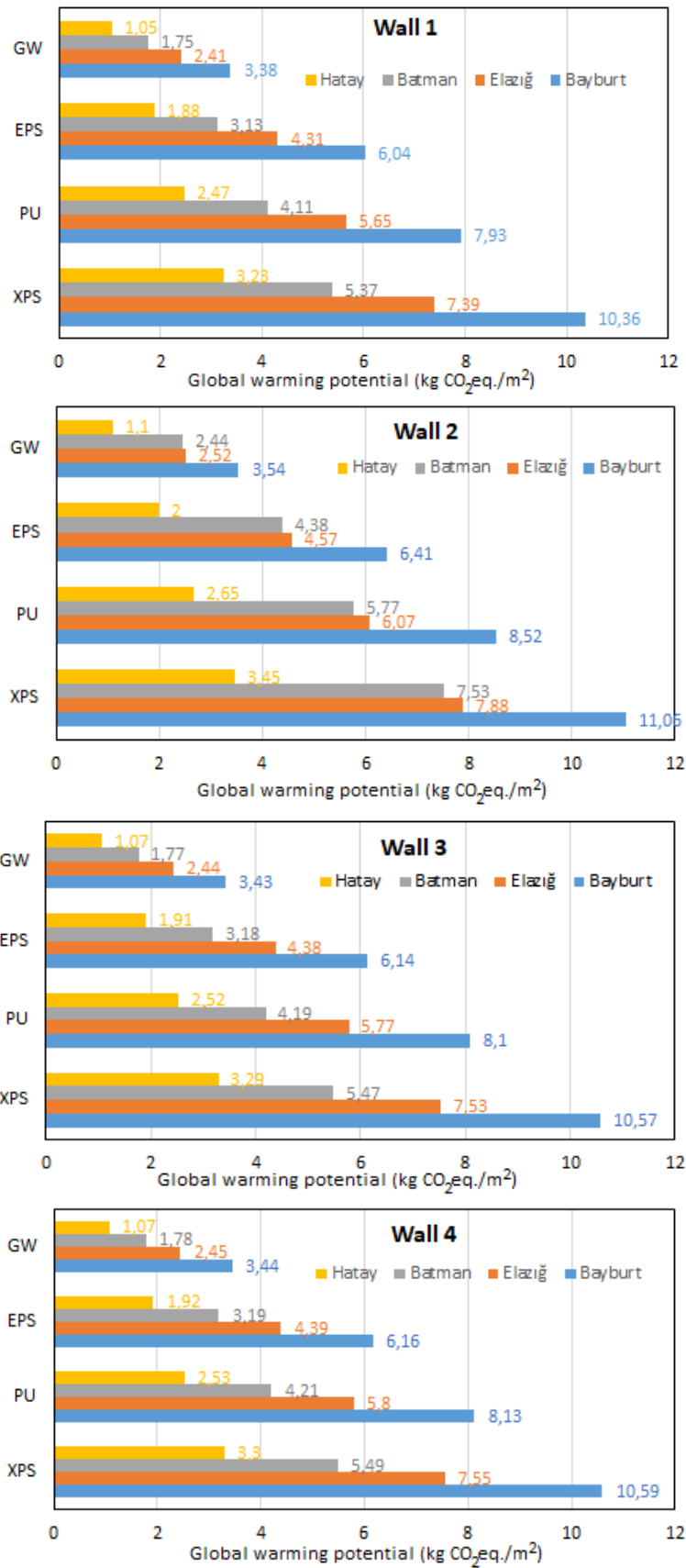
**Fig.12.** The environmental impacts per unit area (Global warming, kg $CO_2$ eq.) of the selected four cities and insulation materials
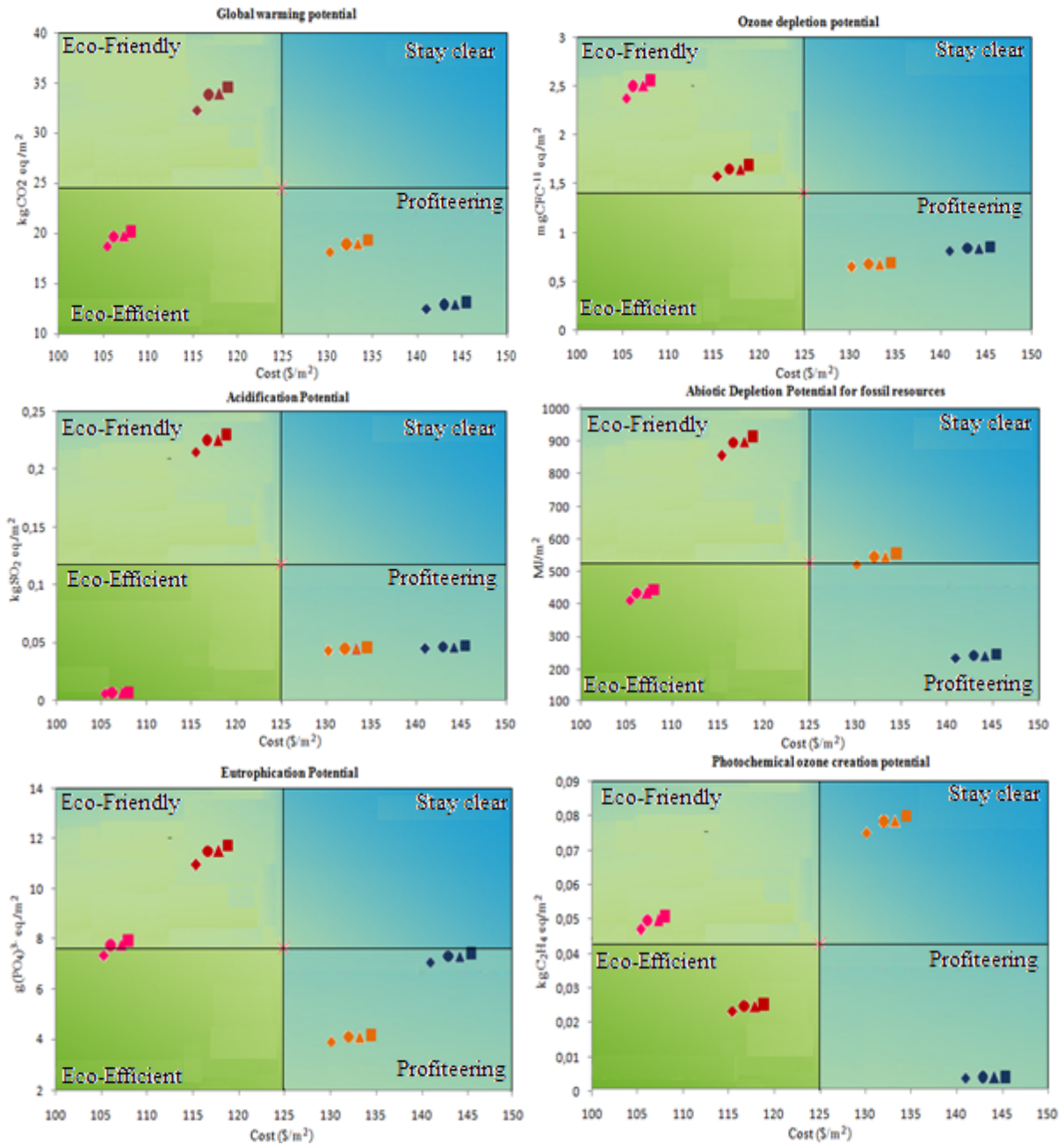
**Fig.13.** Eco-efficiency analysis results of selected four wall types and insulation materials
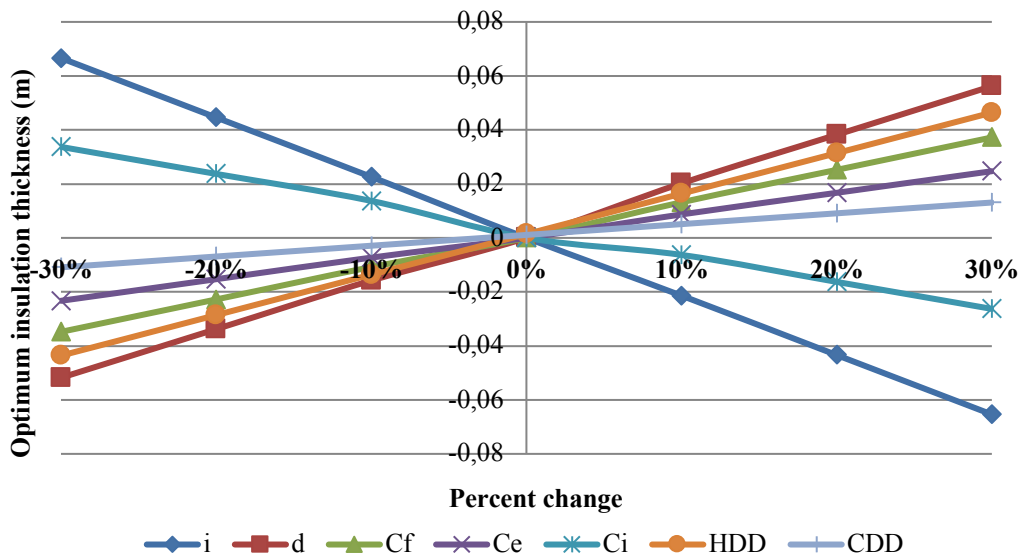
**Fig. 14.** A sensitivity analysis result of optimum insulation thickness for XPS insulation material and wall 1 type.

Fig. 14 shows a sensitivity analysis result of optimum insulation thickness for XPS insulation material and wall 1 type. It appears that the sensitivity degrees of increase in the interest rate, discount rate and heating degree-days the impacts on the optimum insulation thickness of wall are greater than other parameters.

## CONCLUSION

The optimum insulation thicknesses are calculated depending on the heating-cooling energy need and energy cost using Life Cycle Cost (LCC) method for external walls with different structure in the selected cities. In addition, the annual embodied $CO_2$ emissions of each building material are calculated for four wall types. It was presented from these results that The heating loss for north facing exterior surface of wall has highest percentage. The south facing exterior surface of wall has the lowest values according to other orientations for all wall structures and all climate conditions. The heating demand for the province of Bayburt, located in the fourth degree day region of Turkey, is the highest among the three cities in the other regions. The total energy costs of external walls insulated with glass wool (GW) has least among external walls insulated with other insulation materials.

The lowest value of $CO_2$ emission per unit area of wall insulated with GW insulation material were found as 7.19 kg $CO_2$ at optimum thickness (13 cm). The highest (13.67 kg $CO_2$) $CO_2$ emissions per unit area of wall were obtained for the wall insulated with XPS insulation material at the optimum thickness (4 cm). XPS insulation material has the highest global warming potential (GWP) impact among the four insulation materials and the lowest impact belongs to GW insulation material which is 68% lower than XPS. The GWP of concrete (83.47 kg $CO_2/m^2$) used in wall 3 is quite high compared to materials used in the other external wall types. The sandwich wall (wall 2) among all wall type studied

displays greatest advantage with respect to the decreased $CO_2$ emissions per unit area of the wall. In addition, the external walls insulated with PU at the optimum thickness are located in Eco-Efficient quadrant for the category global warming potential and the abiotic depletion of fossil resources.

This study was applied here in to four wall different and residential building, but the same methodology can be replicated to other kinds of buildings and to different climatic conditions. In addition, the results acquired in this study will be helpful guide the choice of insulation and wall type for building in different climates.

Carbon dioxide emissions are one of the most important causes of global climate change. It is accepted in the world today that the world urgently needs to reduce carbon dioxide emissions in order to avoid the worst impacts of climate change. The annual $CO_2$ emissions can be importantly reduced with the correct selection of wall type, insulation material and insulation thickness. Therefore, this study contributes to the fight against climate change caused by future carbon dioxide emissions.

## REFERENCES

Akan A. E., 2021, Determination and Modeling of Optimum Insulation Thickness for Thermal Insulation of Buildings in All City Centers of Turkey. *International Journal of Thermophysics,* 42:49

Akan, A. P. and Akan A. E., 2022, Modeling of $CO_2$ emissions via optimum insulation thickness of residential buildings, *Clean Technologies and Environmental Policy,* 24, 949–967

Atmaca, A., 2016, Life-cycle assessment and cost analysis of residential buildings in South East of Turkey: part 2—a case study, *Int. J. Life Cycle Assess,* 21, 925–942

Axaopoulos, I., Axaopoulos P., Gelegenis J. and Fylladitakis E.D., 2019, Optimum external wall insulation thickness considering the annual $CO_2$ emissions, *Journal of Building Physics,* 42, 527–544.

Axaopoulos I., Axaopoulos, P., Panayiotou, G., Kalogirou, S. and Gelegenis, J., 2015, Optimal economic thickness of various insulation materials for different orientations of external walls considering the wind characteristics, *Energy,* 90, 939-952.

Bolattürk, A., 2006, Determination of optimum insulation thickness for building walls with respect to various fuels and climate zones in Turkey. *Applied Thermal Engineering,* 26 (11), 1301–1309.

Braulio-Gonzalo, M. and Bovea, M. D., 2017, Department Environmental and cost performance of building's envelope insulation materials to reduce energy demand: Thickness optimization, *Energy and Buildings,* 150, 527–545.

Buyukalaca, O., Bulut H. and Yılmaz T., 2001, Analysis of variable-base heating and cooling degree days for Turkey, *Applied Energy,* 69, 269–283.

Cabeza, L.F., Rincón L., Vilariño V., Pérez G. and Castell A., 2014, Life cycle assessment (LCA) and life cycle energy analysis (LCEA) of buildings and the building sector: A review, *Renewable and Sustainable Energy Reviews,* 29, 394–416.

Çomaklı, K. and Yüksel B. 2003, Optimum insulation thickness of external walls for energy saving, *Applied Thermal Engineering,* 23 (4), 473–479.

Dombaycı, Ö.A., Gölcü M. and Pancar Y., 2006. Optimization of insulation thickness for external walls using different energy-source, *Applied Energy,* 83 (9), 921-928.

Ertürk M., 2016, Optimum insulation thicknesses of pipes with respect to different insulation materials, fuels and climate zones in Turkey, *Energy*, 113, 991-1003.

Evin D. and Ucar, A., 2019, Energy impact and eco-efficiency of the envelope insulation in residential buildings in Turkey, *Applied Thermal Engineering,* 154, 573–584.

Ferrández-García, A., Ibánez-Forés V. and Bovea M.D., 2016. Eco-efficiency analysis of the life cycle of interior partition walls: a comparison of alternative solutions, *J. Clean. Prod.,* 112, 649

Global ABC Global Status Report, EIA, 2018
Gaarder, J.E., Friis N.K., Larsen I.S., Time B., Møller E. B. and Kvande T., 2023, Optimization of thermal insulation thickness pertaining to embodied and operational GHG emissions in cold climates – Future and present cases, *Building and Environment,* 234, 110187

Huang, H., Zhou Y., Huang R., Wu H., Sun Y., Huang G. and Xu T., 2020, Optimum insulation thicknesses and energy conservation of building thermal insulation materials in Chinese zone of humid subtropical climate, *Sustainable Cities and Society,* 52, 101840.

Infation and interest rate values (2022). Data Accessed December 2022. https://www.tcmb.gov.tr/wps/wcm/connect/EN/TCMB+EN/Main+Menu/Statistics/Inflation+

Jie, P., Zhang F., Fang Z., Wang H. and Zhao Y, 2018, Optimizing the insulation thickness of walls and roofs of existing buildings based on primary energy consumption, global cost and pollutant emissions, *Energy,* 159, 1132–1147.

Kayfeci, M., Keçebas A. and Gedik E., 2013, Determination of optimum insulation thickness of external walls with two different methods in cooling applications, *Applied Thermal Engineering,* 50, 217-224.

Kaynakli, Ö., 2012, A review of the economical and optimum thermal insulation thickness for building applications, *Renewable and Sustainable Energy Reviews,* 16, 415–425

Kurekci, N. A., 2016, Determination of optimum insulation thickness for building walls by using heating and cooling degree-day values of all Turkey's provincial centers, *Energy and Buildings,* 118, 197–213.

Lazzarin, R. M., Busato F. and Castellotti F., 2008. Life cycle assessment and life cycle cost of buildings' insulation materials in Italy, *Int. J. of Low Carbon Technologies,* 3, 44-58.

Nematchoua, M. K., Ricciardi P., Reiter S. and Yvon A., 2017. A comparative study on optimum insulation thickness of walls and energy savings in equatorial and tropical climate, International *Journal of Sustainable Built Environment,* 6, 170-182.

Özel, G., Açıkkalp E., Görgün B., Yamık H. and Caner N., 2015, Optimum insulation thickness determination using the environmental and life cycle cost analyses based entransy approach*, Sustainable Energy Technologies and Assessments,* 11, 87-91.

Stephan, A., Crawford R.H. and Myttenaere K., 2012, Towards a comprehensive life cycle energy analysis framework for residential buildings, *Energy Building,* 55, 592–600.

Stocker, T.F., Qin D.G., Plattner K., Tignor M., Allen S. K., Boschung J., Nauels A., Xia Y., Bex V. and Midgley P.M., Climate Change 2013, The Physical Science Basis. Contribution of Working Group I to the Fifth Assessment Report of the Intergovernmental Panel on Climate Change, *Cambridge: Cambridge University Press.*

Ucar, A. and Balo, F. 2011, Determination of environmental impact and optimum thickness of insulation for building walls, *Environmental Progress & Sustainable Energy,* 30(1), 113–122.

Ucar, A., 2010, Thermoeconomic analysis method for optimization of insulation thickness for the four different climatic regions of Turkey, *Energy,* 35, 1854–186.

# ENERGY AND ENVIRONMENTAL ASSESSMENT OF CO₂ BOOSTER REFRIGERATION CYCLES WITH FLOODED EVAPORATORS AND PARALLEL COMPRESSOR FOR SUPERMARKETS IN TÜRKİYE

**Nagihan BİLİR SAĞ\*, Metehan IŞIK\*\***

\*Konya Teknik Üniversitesi Mühendislik ve Doğa Bilimleri Fakültesi Makina Mühendisliği Bölümü
42250 Selçuklu, Konya, nbilir@ktun.edu.tr ORCID: 0000-0001-8410-0268
\*\* Konya Teknik Üniversitesi Mühendislik ve Doğa Bilimleri Fakültesi Makina Mühendisliği Bölümü
42250 Selçuklu, Konya, misik@ktun.edu.tr ORCID: 0000-0002-0044-2701

**Abstract**: CO₂ booster refrigeration systems have higher energy efficiency and are more environmentally friendly. Therefore, the CO₂ booster refrigeration cycle with flooded evaporators and parallel compressors (BFP), BFP with mechanical subcooling (BFP-MSC), and BFP with evaporative cooling (BFP-EVC) are investigated for supermarkets in this study. For the first time in the literature, these systems are analyzed to present which system performs better in terms of energy and environmental performance for Türkiye. According to the results of the investigation, BFP-MSC has a better coefficient of performance (COP) values than BFP, with up to a 16.67% increase at equivalent dry bulb temperatures. Meanwhile, BFP-EVC has the lowest annual energy consumption (AEC) in each city, followed by BFP-MSC and then BFP. Annual savings obtained by BFP-EVC over BFP vary between 10.81% to 25.47%. Additionally, BFP-EVC offers more substantial savings in cities with lower humidity levels, as it was analyzed with respect to wet bulb temperatures.
**Keywords**: Booster systems, CO₂, Energetic analysis, Environmental analysis, Supermarket refrigeration.

# TÜRKİYE'DEKİ SÜPERMARKETLER İÇİN YAŞ EVAPORATÖRLÜ VE PARALEL KOMPRESÖRLÜ CO₂ BOOSTER SOĞUTMA ÇEVRİMLERİNİN ENERJİ VE ÇEVRE ANALİZİ

**Özet**: CO₂ booster soğutma sistemleri yüksek enerji verimliliğine sahip olup çevre dostudur. Bu nedenle, bu çalışmada süpermarketler için CO₂ akışkanlı yaş evaporatörlü ve paralel kompresörlü soğutma çevrimi (BFP), BFP'ye mekanik aşırı soğutma eklenen soğutma çevrimi (BFP-MSC) ve BFP'de buharlaşmalı soğutma kullanılan soğutma çevrimi (BFP-EVC) incelenmiştir. Bu sistemler analiz edilerek enerji ve çevre performansı açısından hangi sistemin daha iyi performans gösterdiği literatürde ilk kez Türkiye'deki süpermarketler için ortaya konulmuştur. Araştırma sonuçlara göre, BFP-MSC'nin aynı kuru termometre sıcaklıklarında BFP'ye göre %16.67'ye kadar daha yüksek soğutma performans katsayısına (COP) sahip olduğu belirlenmiştir. Bunun yanı sıra, her şehirde BFP-EVC, en düşük yıllık enerji tüketimine (AEC) sahiptir, onu BFP-MSC ve ardından BFP takip etmektedir. BFP-EVC'nin BFP'ye göre sağladığı yıllık tasarruf %10.81 ile %25.47 arasında değişmektedir. Ek olarak, BFP-EVC, yaş termometre sıcaklıklarına bağlı olarak analiz edildiği için, nem oranının düşük olduğu şehirlerde daha yüksek tasarruflar sağlamaktadır.
**Anahtar Kelimler**: Booster sistemleri, CO₂, Enerji analizi, Çevre analizi, Süpermarket soğutma.

## NOMENCLATURE

| | |
|---|---|
| 1, 2… | refrigerant state points |
| $\alpha$ | recycling factor |
| add | additional |
| AEC | annual energy consumption |
| amb | ambient |
| BFP | booster refrigeration cycle with flooded evaporators and parallel compressor |
| Comp | compressor |
| cond | condenser |
| COP | coefficient of performance |
| DBT | dry bulb temperature |
| EES | engineering equation solver |
| $\eta$ | overall compressor efficiency |
| EVC | evaporative cooling |
| FGBV | flash gas bypass valve |
| gc | gas cooler |
| GWP | global warming potential |
| h | specific enthalpy (kJ/kg) |
| HS | high stage |
| IHX | internal heat exchanger |
| LS | low stage |
| LT | low temperature |
| LVS | liquid/vapor separator |
| $\dot{m}$ | mass flow rate (kg/s) |
| MSC | mechanical subcooling |

MT      medium temperature
n       total operation time (years)
P       pressure (kPa)
PAR   parallel compressor
$\dot{Q}$      cooling capacity, heat rejection (kW)
R       ratio
RC    regional electricity conversion factor
SC    sub cooler
T       temperature (℃)
$\dot{W}$     energy consumption (kW)
WBT   wet bulb temperature
x       quality

## INTRODUCTION

The use of $CO_2$ as a refrigerant in supermarket refrigeration systems attracts attention with its thermophysical properties and nature-friendly behavior (Gullo et al., 2018). However, $CO_2$ refrigeration systems have some difficulties such as higher equipment costs because of $CO_2$'s high working pressures (Goetzler et al., 2014) and critical temperature of $CO_2$ which is 30.98 ℃ causing $CO_2$ systems to operate transcritical (heat rejection at supercritical zone). In the literature review, there are studies dealing with the use and improvement of $CO_2$ refrigeration systems both theoretically (Ersoy and Bilir, 2012; Ge et al., 2015; Gullo and Hafner, 2017; Mylona et al., 2017; Sarkar and Agrawal, 2010; Sawalha, 2008a, 2008b) and experimentally (Chesi et al., 2014; Fricke et al., 2016; Fritschi et al., 2017; Llopis, Sanz-Kock, et al., 2015; Nebot-Andrés et al., 2021). Alongside these studies focusing on the improvement of the systems, there are also city-based studies (Cui et al., 2020; Gullo et al., 2016; Işık, 2022; Karampour and Sawalha, 2018; Lata et al., 2021; Mitsopoulos et al., 2019; Sooben et al., 2019; Tsamos et al., 2017) to show the outcomes when they are used in supermarkets in daily operations.

The literature on $CO_2$ transcritical refrigeration systems encompasses a wide range of studies aimed at both understanding the key parameters influencing their performance and enhancing their overall efficiency. While some researchers have delved into understanding the aspects of these systems, others have focused on innovations to improve their functionality. Notably, modifications to the classical one-evaporator cycle have been explored, including the incorporation of auxiliary compressors, two-stage compressors, and internal heat exchangers. Additionally, researchers have examined the expansion process, exploring alternatives such as ejectors (Atmaca et al., 2018) or turbines (Bayrakçı et al., 2014). For instance, Bayrakçı et al. (2014) demonstrated that the utilization of a turbine can lead to a remarkable 10% increase in performance. However, a unique challenge arises in the context of supermarket refrigeration systems, where the need for two evaporator stages, catering to both fresh and frozen food sections, necessitates innovative solutions to adapt $CO_2$ refrigeration systems for optimal use in this specific application. This ongoing research strives to address the

complex demands of supermarket refrigeration while maximizing the benefits of $CO_2$ transcritical technology. According to studies in the literature, booster refrigeration systems come to the fore as they can meet the two temperature levels (low temperature and medium temperature) refrigeration needs of supermarkets in one single cycle with higher efficiency than traditional systems (European Commission, 2008; Mylona et al., 2017). Moreover, booster systems have lower annual energy consumption (AEC) when compared to R404A systems (Cui et al., 2020), which are frequently used in supermarket refrigeration (ICF Incorporated, 2020). This outcome has been presented in the literature by city-based studies by annual performance metrics for various climatic conditions. Several studies have highlighted the advantages of booster refrigeration systems over traditional R404A systems in terms of energy consumption. Mitsopoulos et al. (2019) have conducted research in Athens and found that some types of booster systems consumed less energy annually. Similarly, Gullo et al.'s (2016) study in cities like Valencia and Seville has yielded similar results, further emphasizing the superiority of booster systems in reducing energy consumption. Cui et al.'s (2020) examination of these refrigeration systems in five Chinese cities has revealed that energy savings were primarily observed in the coldest city, suggesting that booster systems may require further enhancements to optimize performance in warmer climates. These findings underscore the need for continued research and development to adapt booster systems for a wider range of environmental conditions.

The use of flooded evaporators has been presented in the literature as a method that increases energy savings for warmer climates. In the study of Karampour and Sawalha (2018), approximately 12% annual energy savings have been shown when both cooling level evaporators are flooded for Barcelona and Stockholm. Up to 155.1 MWh energy savings have been demonstrated for Indian context (Lata et al., 2021) and more than 10% annual energy efficiency ratio improvement over standard $CO_2$ booster refrigeration system have been shown for China by using flooded evaporators (Cui et al., 2020).

There are also studies considering the use of parallel compressors (Amaris et al., 2019; Caliskan and Ersoy, 2022; Dai et al., 2022), which is a step towards reducing the power consumed by the high-pressure compressor in booster refrigeration cycles. Besides Sacasas et al.'s (2022) study for Chile has shown that $CO_2$ booster systems with parallel compressors consume less energy than standard booster systems, similar results have been revealed for New Delhi, Seville, Phoenix, and Teheran (Purohit et al., 2017). Energy savings have also been obtained in Athens, London (Tsamos et al., 2017) and Chinese cities (Sun et al., 2020) with $CO_2$ booster systems with parallel compressor. Furthermore, the best annual energy efficiency ratios have been obtained for the $CO_2$ booster refrigeration cycle with flooded evaporators and parallel compressor (BFP) for all 5 cities considered in the study of Cui et al. (2020). Accordingly, the most energy savings have been achieved with the

BFP in Stockholm and Barcelona (Karampour and Sawalha, 2018) and 12 cities of Türkiye (Işık, 2022; Işık and Bilir Sağ, 2023). Although only medium temperature evaporator is flooded, the BFP has presented the lowest AEC for Rome, Valencia, and Seville (Gullo et al., 2016).

The application of mechanical subcooling as a modification to the booster systems has also been exhibited as advantageous in the literature. While Cui et al. (2020) have presented mechanical subcooling increases annual energy efficiency ratios for Chinese example, annual energy savings of 3% for Stockholm and 7.5% for Barcelona have been provided by mechanical subcooling in the standard $CO_2$ booster cycle (Karampour and Sawalha, 2018). In these two studies, the mechanical subcooling cycle used R290 as a refrigerant. In the study of Llopis et al. (2015) for one stage $CO_2$ refrigeration cycles, COP improvement percentages have shown almost the same according to different subcooling cycle refrigerants such as R290, R1270, R1234yf, R161, R512a, and R134a. To get rid of the negative effects of high ambient temperatures, an advantage can be provided for refrigeration systems by evaporative cooling (Lata and Gupta, 2020; Sooben et al., 2019). These systems are based on the evaporation of water to reduce the temperature of air, where the gas cooler/condenser releases heat. In the study of Lata et al. (2021), it has been shown that annual energy savings are achieved in the range of 120.2 MWh - 238.6 MWh for the standard $CO_2$ booster cycle with evaporative cooling, and in the range of 103.2 MWh - 205.9 MWh when evaporative cooling has been performed in the $CO_2$ booster refrigeration cycle with flooded evaporators.

According to recent studies, $CO_2$ booster systems are an energy-efficient and eco-friendly beneficial option, particularly for usage in supermarket refrigeration. This is especially significant in countries with many supermarkets, such as Türkiye. Türkiye is also dedicated to reducing $CO_2$ emissions in the future, emphasizing the importance of $CO_2$ booster systems. Additionally, due to the diverse climates of Türkiye's cities, it is essential to investigate $CO_2$ booster systems and their environmental effects in a variety of outdoor conditions. Therefore, three systems have been investigated in this study for the first time in the open literature, to the best of the authors' knowledge: the $CO_2$ booster refrigeration cycle with flooded evaporators and parallel compressors (BFP), the BFP with mechanical subcooling (BFP-MSC), and the BFP with evaporative cooling (BFP-EVC). The aim is to determine which of these systems performs better in terms of both energy efficiency and environmental effect across nine Türkiye cities.

**CO₂ BOOSTER REFRIGERATION CYCLE WITH FLOODED EVAPORATORS AND PARALLEL COMPRESSOR**

The schematic diagrams of systems examined in this study are given in this section with their P-h diagrams. The basis system in this study is the $CO_2$ booster refrigeration cycle with flooded evaporators and parallel

compressor (BFP) shown in Fig. 1. BFP was chosen as the main system as it has previously been shown the most energy saving system for supermarkets of Türkiye when compared to booster systems without flooded evaporators or parallel compressor (Işık and Bilir Sağ, 2023). The other two systems have modifications on that BFP basis.



(a)



(b)
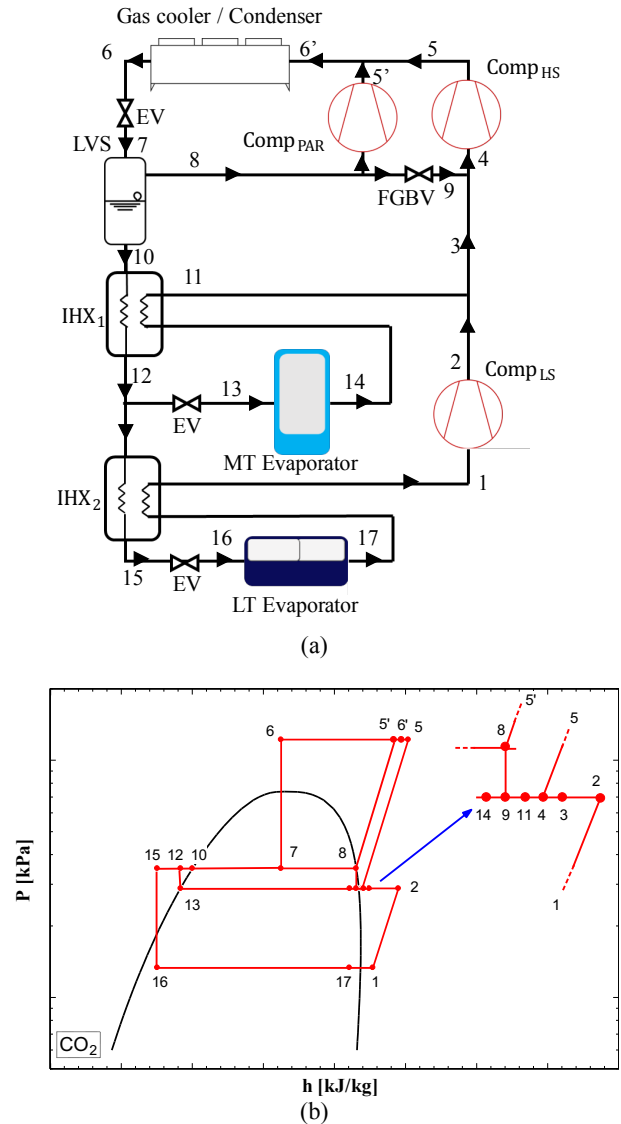
**Fig. 1.** The schematic (a) and P-h diagram (b) of the BFP.

In the BFP, $CO_2$ entering the gas cooler (condenser when it is a subcritical operation) rejects heat to the environment between points 5 and 6. The refrigerant is then throttled at the expansion valve (EV). The refrigerant, whose pressure and temperature are reduced, is divided as saturated liquid and saturated vapor at liquid-vapor separator (LVS). The saturated vapor of the separated refrigerant enters the flash gas bypass valve (FGBV) at point 8, while the saturated liquid proceeds to the internal heat exchangers (IHX) before the medium temperature (MT) and low temperature (LT) evaporators. In IHX 2, heat is transferred from saturated liquid $CO_2$ to saturated mixture $CO_2$ coming from MT evaporator. Similarly, in IHX 2, $CO_2$ coming from LT evaporator takes heat from compressed liquid $CO_2$ on the other side

of the heat exchanger. As a result, the quality of refrigerant entering the evaporators is decreased while the superheated vapor state of refrigerant is provided for compressors to operate appropriately.

The refrigerant taking heat from the frozen food cabinet between points 16 and 17 leaves the IHX 1 as superheated vapor at state 1 and is compressed in the low stage compressor ($Comp_{LS}$) to state 2. On the other hand, the fresh food cabinet is cooled by MT evaporator where refrigerant leaves the evaporator at state 14. It exits IHX 1 as state 11 and reaches state 3 by mixing with the refrigerant at state 2. The refrigerant at point 3 and the refrigerant exiting the FGBV at point 9 mix and enter the high stage compressor ($Comp_{HS}$) in the state point 4 to be compressed. Finally, the refrigerant enters the gas cooler, and the cycle continues.

When the parallel compressor is active, the refrigerant from the LVS does not enter the FGBV and is compressed in the parallel compressor ($Comp_{PAR}$). In this case, the $CO_2$ at state 3 enters $Comp_{HS}$ directly. The refrigerant comes out of the $Comp_{HS}$ and $Comp_{PAR}$ mix and enters the gas cooler to complete the cycle.

In this system, LVS and the use of FGBV equipment between points 8-9 are providing refrigerant to enter the evaporators with a high saturated liquid ratio and flooded evaporators provide lower quality and more wet surface for evaporators. Also, $Comp_{PAR}$ reduces the work done by $Comp_{HS}$.

Mechanical subcooling (MSC) and evaporative cooling (EVC) are the selected modifications to improve the BFP system. The schematic diagram and P-h diagram of BFP-MSC are demonstrated in Fig. 2 while Fig. 3 shows BFP-EVC's diagrams.

The integration of a mechanical subcooling cycle, positioned at the outlet of the gas cooler/condenser, plays a pivotal role in enhancing the performance of this refrigeration system. This innovative addition effectively reduces the quality of the refrigerant entering the liquid-vapor separator (LVS) by the transfer of heat from $CO_2$ to R290 in the subcooler (SC). Consequently, this reduction in refrigerant quality leads to decreased vapor mass flow rates at LVS and a subsequent reduction in the work done by the compressors. This improvement is crucial for achieving energy savings and enhancing the performance of the refrigeration system.

In the BFP-EVC system, a key strategy for reducing the temperature of the air involves employing evaporative cooling until it reaches the wet bulb temperature. This approach yields a significant advantage as the wet bulb temperature consistently registers lower values than the dry bulb temperature. Consequently, the BFP-EVC system exhibits lower power consumption compared to the BFP system operating at the same dry bulb temperature. Lower operating temperatures provide

lower inlet quality for LVS, leading to a reduction in the mass flow rates within the system.



(a)



(b)
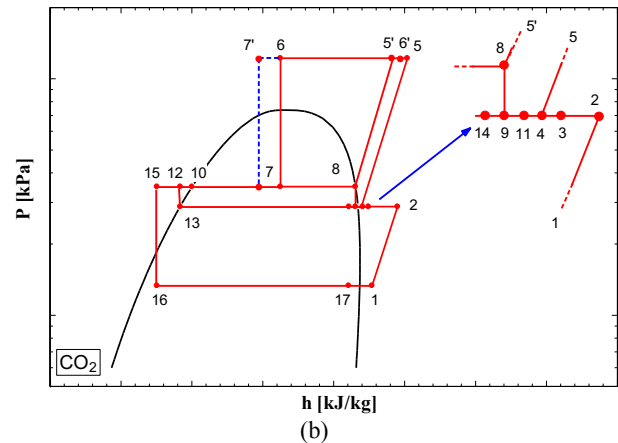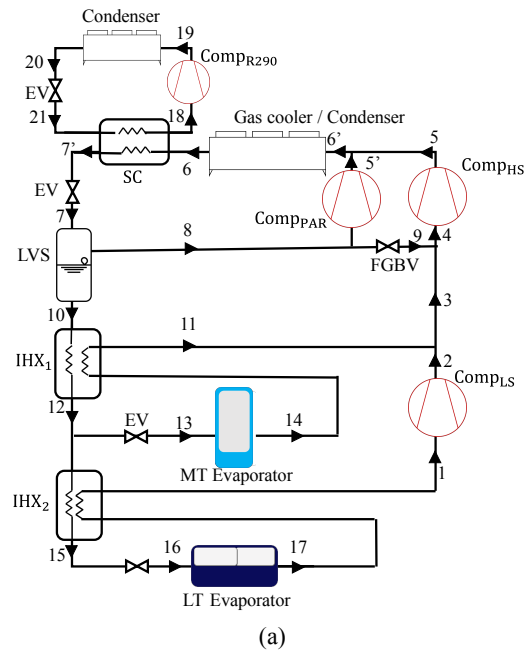
**Fig. 2.** a) Schematic diagram and b) P-h diagram of BFP-MSC.

## MATHEMATICAL MODELING

### Energy Analysis Model

For energy analysis, cities with different climates from different geographical regions of Türkiye are selected and the annual energy consumption (AEC) results of the systems in question are examined.

Ambient temperatures are divided as Subcritical 1, Subcritical 2, Transition, and Transcritical operating zones (Table 1) (Cui et al., 2020; Mitsopoulos et al., 2019). While subcritical operation occurs with saturation conditions, gas cooler pressure at transcritical operation zone has an optimum value (Kauf, 1999; Liao et al., 2000; Özgür et al., 2009) calculated by the Engineering Equation Solver (EES). Values for Transition zone are assumed to have a linear change between Subcritical 2 and Transcritical zones.

The cooling capacity of the low temperature (LT) evaporator for frozen foods is taken as 35 kW (Karampour and Sawalha, 2018) at -32 ℃ evaporator temperature, (Gullo et al., 2016) while the cooling capacity of the medium temperature (MT) evaporator to be used in the preservation of fresh foods is taken as 165 kW at -7 ℃ evaporator temperature (Cui et al., 2020) as this load is the average for Türkiye (Işık, 2022).

In the $CO_2$ booster refrigeration cycle with flooded evaporators, parallel compressor and mechanical subcooling (BFP-MSC), the temperature of the $CO_2$ leaving the gas cooler is reduced by the mechanical subcooling cycle. In this way, $CO_2$ releases heat, and the quality of the refrigerant entering the liquid vapor separator (LVS) is reduced. The activation of the parallel compressor starts when the ambient temperature is 14°C due to getting enough vapor for the auxiliary compressor (Mitsopoulos et al., 2019). The mechanical subcooling starts at the ambient temperature of 19°C (Cui et al., 2020). As a result of the reduction in quality of the refrigerant entering the LVS with subcooling, the parallel compressor goes out of its proper operating range and shuts down. Then it is activated again at 29 ℃ ambient temperature and operates together with mechanical subcooling as given in Table 2.

The assumptions done for the mathematical model are as follows:

- Heat losses and pressure drops in the heat exchangers and pipes are neglected.
- It is assumed that all expansion valves perform isenthalpic processes.
- The $CO_2$ flooded evaporator outlet vapor quality is accepted as 0.95 (Cui et al., 2020).
- Intermediate pressure is assumed to be 3500 kPa (Cui et al., 2020; Gullo et al., 2016; Tsamos et al., 2017).
- IHX effectiveness is taken 0.65 (Cui et al., 2020).
- R290 evaporator temperature is 10 ℃ with 10 ℃ superheat (Cui et al., 2020).
- R290 condenser temperature is 10 ℃ higher than the ambient temperature (Cui et al., 2020).
- Evaporative cooling occurs until saturation (ambient temperatures assumed as wet bulb temperatures)(Lata and Gupta, 2020).
- Additional work ($\dot{W}_{add}$)(fans etc.) is assumed 3% of the heat rejected from gas cooler/condenser (Cui et al., 2020).



(a)



(b)

**Fig. 3.** a) Schematic diagram and b) P-h diagram of BFP-EV

**Table 1.** Pressure and temperature values due to ambient temperature operating zones.

| Operating Zones | Ambient Temperature Ranges (℃) | Gas cooler outlet/condenser temperature (℃) | Gas cooler /condenser pressure (kPa) |
|---|---|---|---|
| Subcritical 1(Cui et al., 2020) | $T_{amb} < 2$ | 10 | $P_{sat}@10 ℃$ |
| Subcritical 2(Cui et al., 2020) | $2 \le T_{amb} < 14$ | $T_{amb} + 8$ | $P_{sat}@T_{cond}$ |
| Transition | $14 \le T_{amb} < 28$ | $0.642 T_{amb} + 13.007$ | $98.283 T_{amb} + 4627.03$ |
| Transcritical | $28 \le T_{amb}$ | $T_{amb} + 3$ | optimized |

**Table 2.** Activation temperatures of parallel compressor and mechanical subcooling for systems.

| Systems | Parallel Compressor | Mechanical Subcooling | Reference |
|---|---|---|---|
| BFP | $14 \le T_{amb}$ | - | (Mitsopoulos et al., 2019) |
| BFP-MSC | $14 \le T_{amb} < 18$ $29 \le T_{amb}$ | $19 \le T_{amb}$ | (Cui et al., 2020) |
| BFP-EVC | $14 \le T_{amb}$ | - | (Mitsopoulos et al., 2019) |

After determining all operating zones, operating conditions, and assumptions, COP and power consumption values are calculated as the following procedure explained below.

Conservation of mass and energy laws are applied at all calculations. Mass flow rates are determined as given below for LVS for all systems considered in this study:

$$\dot{m}_8 = \dot{m}_7 x_7 \tag{1}$$

$$\dot{m}_{10} = \dot{m}_7(1 - x_7) \tag{2}$$

$$\dot{m}_7 = \dot{m}_8 + \dot{m}_{10} \tag{3}$$

Heat exchanger energy balances are calculated by Eqn. (4) and Eqn. (5).

$$\dot{m}_{10}(h_{10} - h_{12}) = \dot{m}_{13}(h_{11} - h_{14}) \tag{4}$$

$$h_{12} - h_{15} = h_1 - h_{17} \tag{5}$$

Energy balances at mixing points are presented as:

$$\dot{m}_3 h_3 = \dot{m}_2 h_2 + \dot{m}_{11} h_{11} \tag{6}$$

$$\dot{m}_4 h_4 = \dot{m}_3 h_3 + \dot{m}_9 h_9 \tag{7}$$

$$\dot{m}_6 h_{6\prime} = \dot{m}_5 h_5 + \dot{m}_5 h_{5\prime} \tag{8}$$

In MSC cycle, the heat rejected by $CO_2$ is absorbed by R290 refrigerant within the subcooler. Energy balance of this process is given by Eqn. (10). The $CO_2$ is subcooled 10 °C after the gas cooler/condenser before entering LVS (Cui et al., 2020).

$$\dot{m}_{18}(h_{18} - h_{21}) = \dot{m}_{6\prime}(h_6 - h_{7\prime}) \tag{10}$$

MT and LT evaporator loads are calculated by the following equations.

$$\dot{Q}_{LT} = \dot{m}_{16} * (h_{17} - h_{16}) \tag{11}$$

$$\dot{Q}_{MT} = \dot{m}_{13} * (h_{14} - h_{13}) \tag{12}$$

The heat rejected from $CO_2$ gas cooler/condenser is calculated with Eqn. (13).

$$\dot{Q}_{gc/cond} = \dot{m}_{6\prime} * (h_{6\prime} - h_6) \tag{13}$$

Power consumption value of low stage compressor is calculated as given in Eqn. (14) as its overall efficiency is calculated by Eqn. (15) related with compression ratio. All overall efficiency correlations are taken from the study of Cui et al.(2020).

$$\dot{W}_{Comp_{LS}} = \frac{\dot{m}_1 * (h_{2,s} - h_1)}{\eta_{Comp_{LS}}} \tag{14}$$

$$\eta_{Comp_{LS}} = -0.0111 R_{P,LS}^2 + 0.0793 R_{P,LS} + 0.8030 \tag{15}$$

Similar to low stage, high stage compressor and parallel compressor's power consumptions are obtained as follows:

$$\dot{W}_{Comp_{HS}} = \frac{\dot{m}_5 * (h_{5,s} - h_4)}{\eta_{Comp_{HS}}} \tag{16}$$

$$\eta_{Comp_{HS}} = -0.01 R_{P,HS}^2 + 0.0468 R_{P,HS} + 0.6134 \tag{17}$$

$$\dot{W}_{Comp_{PAR}} = \frac{\dot{m}_{5\prime} * (h_{5\prime,s} - h_8)}{\eta_{Comp_{PAR}}} \tag{18}$$

$$\eta_{Comp_{PAR}} = -0.0102 R_{P,PAR}^2 + 0.0571 R_{P,PAR} + 0.5987 \tag{19}$$

Additionally, in the BFP-MSC, one more compressor consumes power (Eqn. (20,21)) in mechanical subcooling cycle.

$$\dot{W}_{Comp_{R290}} = \frac{\dot{m}_{18} * (h_{19,s} - h_{18})}{\eta_{Comp_{R290}}} \tag{20}$$

$$\eta_{Comp_{R290}} = -0.0866 R_{P,R290}^2 + 0.4521 R_{P,R290} + 0.0854 \tag{21}$$

Finally, COP value is calculated by Eqn. (22). When there is no mechanical subcooling, $\dot{W}_{Comp_{R290}}$ diminishes.

$$COP = \frac{\dot{Q}_{MT} + \dot{Q}_{LT}}{\dot{W}_{Comp_{LS}} + \dot{W}_{Comp_{HS}} + \dot{W}_{Comp_{PAR}} + \dot{W}_{Comp_{R290}} + \dot{W}_{add}} \tag{22}$$

Bin hour indicates the time spent at an ambient temperature for the period of consideration. Since hourly temperature data are obtained from the Turkish State Meteorological Service (2021) for the selected cities in the period of 2016-2020 for 5 years, bin hour values are divided by five. An annual average of the bin-hour data set is generated for dry bulb temperatures (DBT) (Fig. 4) and wet bulb temperatures (WBT) (Fig. 5). As can be seen from Fig. 4, Erzurum is the city with the lowest DBT while Mersin and Antalya attract attention with temperatures that do not fall into negative values. Diyarbakir, which has a significant amount of time at the highest temperatures, can also have values around -10 °C. In Istanbul and Samsun, on the other hand, it is seen that the hot and cold extreme points do not take long times in a year, but middle temperatures cover significant amount of time. In Fig. 5, it is seen that the cities with the highest WBT are the ones with high humidity such as Mersin, Antalya, İzmir, Samsun, and İstanbul. Diyarbakir, which has very high DBT bin-hour data, has much lower WBT values due to the dry air of the city. As a result of dry air, Erzurum, Ankara, and Konya also spend longer times in lower WBT than other cities.

According to the bin-hour data, the amount of the time spent at the cities in four operating zones in a year are given in Fig. 6. In each city, the periods spent in subcritical regions are longer at WBT than DBT. Transcritical operating time according to WBT is only 0.16% in Antalya and 0.02% in Mersin. However, in other cities, WBT are lower than 28 °C which is the first operating point for Transcritical zone.

## Environmental Analysis Model

Countries have targets to reduce $CO_2$ equivalent emissions due to international regulations (Goetzler et al., 2014). The emission values of the systems discussed in this paper should also be calculated to provide an overview to overcome the responsibilities of regulations, which Türkiye is also under obligation (Republic of Türkiye Ministry of Environment Urbanization and Climate Change, 2022).

Refrigeration systems contribute to these emissions directly due to leaks in the installation and indirectly through electricity consumption. The direct contribution depends on the total amount of refrigerant ($M_{charge}$), the recycling factor ($\alpha$), the leaks ($M_{leakage}$), and the global warming potential (GWP) of the fluid. Indirect contribution is calculated by annual energy consumption

(AEC), regional electricity conversion factor (RC) and total operation time (n). The values used in Eqn. (23,24) are given in Table 3.

$$\text{Direct Contribution} = \left(M_{leakage}n + M_{charge}(1-\alpha)\right)GWP \quad (23)$$

$$\text{Indirect contribution} = RC * AEC * n \quad (24)$$

**Table 3.** Parameter values in environmental analysis (Cui et al., 2020).

| Parameter | Value |
|---|---|
| $M_{charge}$ R290 (kg/kW) | 2 |
| $M_{charge}$ $CO_2$ (kg/kW) | LT:3;   MT:3 |
| $\alpha$ | 0.95 |
| RC (kg $CO_2$/kWh) | 0.997 |
| GWP $CO_2$ | 1 |
| GWP R290 | 3 |
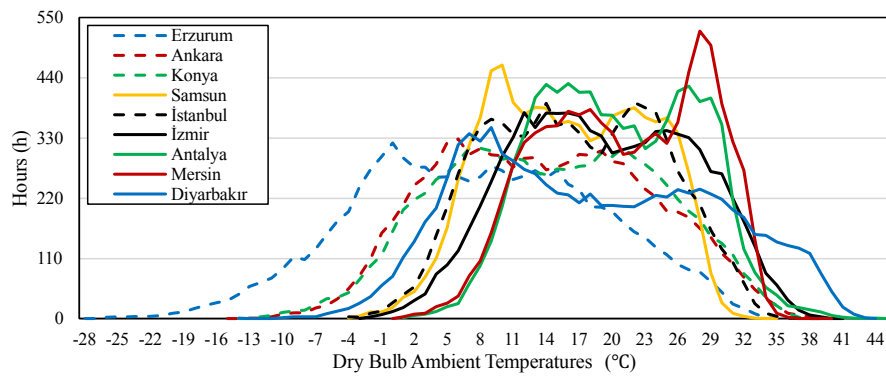


**Fig. 4.** Annual average DBT bin-hour values of the 9 selected cities.
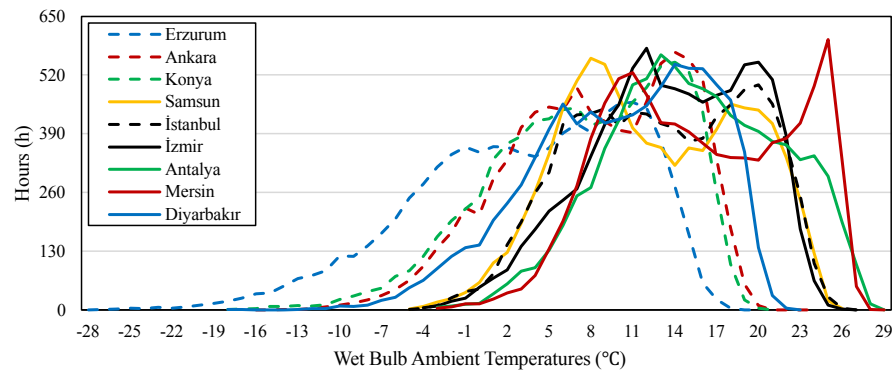


**Fig. 5.** Annual average WBT bin-hour values of the 9 selected cities.
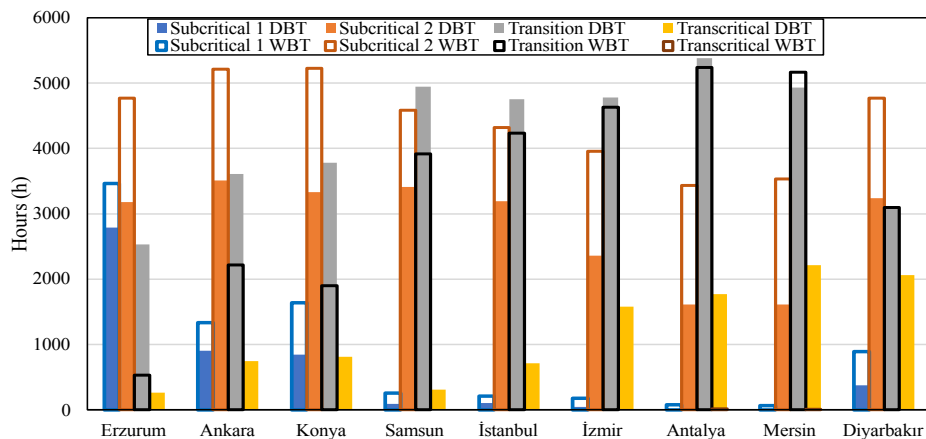


**Fig. 6.** Periods spent at operating zones in a year by each city.
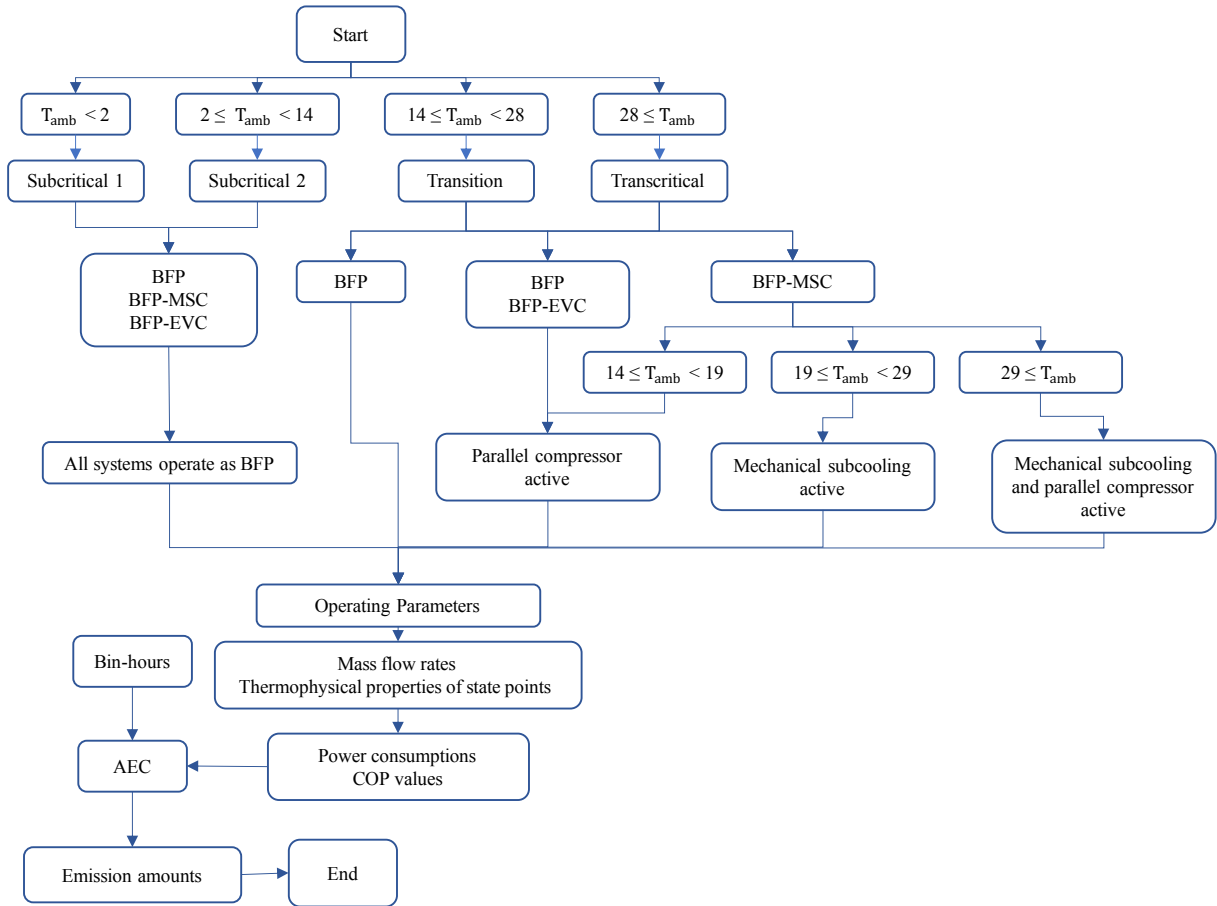
**Fig. 7.** Flow chart of analysis steps.

The flow chart of analyses is given in Fig. 7. Ambient temperatures at the flow chart should be considered as WBT for the BFP-EVC and DBT for others.

## RESULTS AND DISCUSSION

The energy and emission analysis results of the systems whose analysis steps and assumptions are defined before are given in this section. The COP and power consumption values of the systems in question are compared and the city-oriented energy consumption values on an annual basis are presented.

### Model Validation

The COP values obtained by the Engineering Equation Solver (EES) for the BFP (main system in the present study) were compared with the COP values extracted from the study of Cui et al. (2020) for the same system. Validation model was categorized into four distinct operating zones (the transcritical zone, transition zone, and two subcritical zones). Gas cooler/condenser outlet temperature and pressure values were determined according to the descriptions given in the reference paper (Cui et al., 2020).

In this validation model, the low-temperature (LT) load remained constant at 40 kW, while the medium-temperature (MT) load varies with ambient temperature. At 10°C, the MT load is 100 kW, and it linearly increases

to 130 kW as the ambient temperature rises to 20°C. Beyond that, when the ambient temperature reaches 40°C, the MT load reaches its peak at 250 kW. Furthermore, LT evaporator temperature of -27°C and MT evaporator temperature of -7°C were kept fixed throughout validation. The activation of the parallel compressor occurred at 15°C ambient temperature which is a crucial parameter in the system's operation. Additionally, intermediate pressure of 3500 kPa, heat exchanger effectiveness of 0.65, and evaporator outlet quality of 0.95 were applied in validation analysis due to the assumptions of the reference paper. In this paper, the same three parameters were employed as those utilized in the reference paper chosen for validation. The average difference in COP values between the present study and the reference study was determined to be 2.33%.
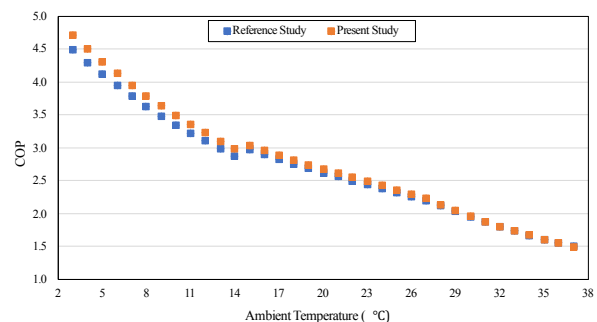


**Fig. 8.** COP comparison between the EES model and the study of Cui et al.(2020).

24

## Energy Analysis Results

It has been mentioned in Energy Analysis Model section that there is an optimum gas cooler pressure value that maximizes the COP value above the critical point for $CO_2$ refrigeration cycles. The change of gas cooler pressure and COP value for different ambient temperatures of $CO_2$ booster refrigeration cycles is demonstrated in Fig. 9. A peak point on lines where COP is maximum for a specific gas cooler pressure demonstrates the optimum gas cooler pressure fact. In this study, all gas cooler pressures were optimized for each ambient temperature considered.

Within the scope of this study, there were no WBT values over 29℃ available for selected Turkish cities. So, only BFP and BFP-MSC systems' COP values with respect to gas cooler pressure is presented in Fig. 9.

Fig. 10 provides valuable insights into the optimum gas cooler pressure values concerning ambient temperatures. One noteworthy observation from the data is that the optimum gas cooler pressures for the BFP consistently exceed those of the BFP-MSC across all ambient temperature conditions. It's important to note that higher gas cooler pressures can lead to increased energy consumption on compressors. This demonstrates that the utilization of mechanical subcooling enhances the performance of the BFP system. According to the meteorological data, the BFP-EVC system operates transcritical only at temperatures of 28 and 29 ℃. Consequently, the optimum gas cooler pressure for this specific operating range is not shown in Fig. 10.
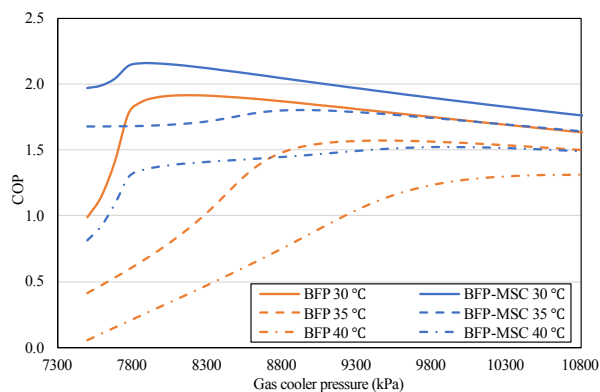


**Fig. 9.** Variation of COP of $CO_2$ booster refrigeration systems according to gas cooler pressure at different ambient temperatures.
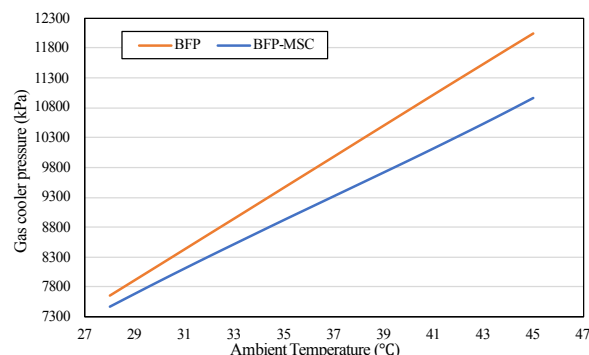


**Fig. 10.** Optimum gas cooler pressures with respect to ambient temperature.

Fig. 11 provides a representation of the distinct sections observed in mass flow rates, and these variations can be attributed to mechanical subcooling and the operation of parallel compressors, as indicated in Table 2. Once the parallel compressor comes into action, the HS compressor's mass flow rate is decreased to a specific value and stays constant. This reduces the work done by the HS compressor, thereby reducing total energy consumption. It becomes evident that any increase in energy consumption is primarily attributed to the influence and operation of the parallel compressor in the BFP at ambient temperatures over 14 ℃. This situation is also the same for the BFP-EVC for wet bulb temperatures over 14 ℃. Since the BFP and the BFP-EVC have equal mass flow rates with respect to ambient temperatures, the BFP-EVC's values were not displayed in Fig. 11 to simplify the plot. However, the ambient temperatures become wet bulb temperatures when the BFP-EVC is the system under consideration. Additionally, the mass flow rates of the LS compressor were not shown on Fig. 11 because they were constant at 0.1295 kg/s for each system under all ambient conditions.

Mass flow rates of parallel compressors are equal for BFP and BFP-MSC at 14 ℃ - 19 ℃ ambient temperature range. Above 19 ℃, parallel compressor of BFP-MSC is turned off until 29 ℃ due to the operation of mechanical subcooling. Over 29 ℃ ambient temperatures, mass flow rates of parallel compressors increase with respect to ambient temperature. Additionally, BFP-MSC's parallel compressor mass flow rate is lower than BFP's parallel compressor at all ambient temperatures above 29 ℃. The reason of it is the mechanical subcooling which reduces the quality of the refrigerant separated at LVS. Moreover, HS compressor's mass flow rate of BFP and BFP-MSC are equal except 19 ℃ - 29 ℃ ambient temperature range. In this temperature period, BFP-MSC system's parallel compressor is deactivated as it was previously mentioned. As a result, all the refrigerant is compressed at HS compressor at that period in BFP-MSC.
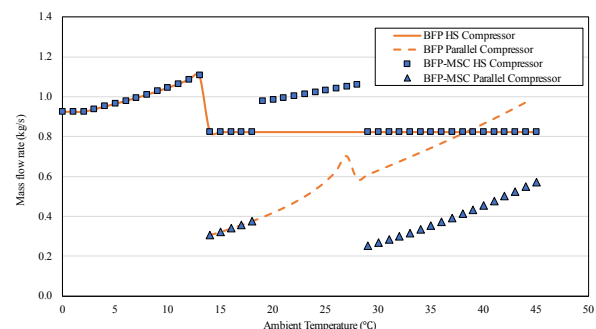


**Fig. 11.** Mass flow rates of HS Compressor and Parallel Compressor with respect to ambient temperature.

The variation of COP and power consumption according to the ambient temperatures for each cycle is given in Fig. 12. The performance of refrigeration systems is influenced by ambient temperature conditions. Research has consistently shown that the highest COP values are attained when the ambient temperature is at its lowest. In fact, under such conditions, the COP can reach

approximately 5. This emphasizes the efficiency of these systems when operating in colder climates. Conversely, as the ambient temperature rises, COP values exhibit a significant decline. At approximately 45 °C ambient temperature, the COP drops to around 1. These results align with the expected trends observed in the existing literature (Mitsopoulos et al., 2019). This inverse relationship between COP and ambient temperature highlights the critical importance of considering environmental factors in the design and operation of refrigeration systems, as well as the challenges of maintaining efficiency in warmer climates.

Since the parallel compressor is first activated at the ambient temperature of 14 °C, the COP of all systems are same below 14 °C. The COP value of the $CO_2$ booster refrigeration system with flooded evaporators and parallel compressor (BFP) are up to 14.29% lower than the BFP with mechanical subcooling (BFP-MSC) at temperatures above 19 °C. When examining the COP and power consumption values of the BFP with evaporative cooling (BFP-EVC) in Fig. 12, it should be noted that the temperature values for this system are the wet bulb temperatures (WBT). The highest WBT value is 29 °C for investigated cities according to the meteorological data.

According to the annual energy consumption (AEC) results shown in Fig. 13, the BFP-EVC has the lowest values in each city. It has energy savings over the BFP-MSC between 8.02%-20.89%, over the BFP between 10.81%-25.47% annually. Although energy savings are achieved with the BFP-MSC compared to the BFP, this gain remained between 1.78% and 5.79%. The higher energy savings occur for the BFP-EVC because it does not operate in the transcritical region (Fig. 6). The warm cities behave like a colder city due to evaporative cooling meanwhile further savings has emerged in cities with already lower dry bulb temperatures (DBT).
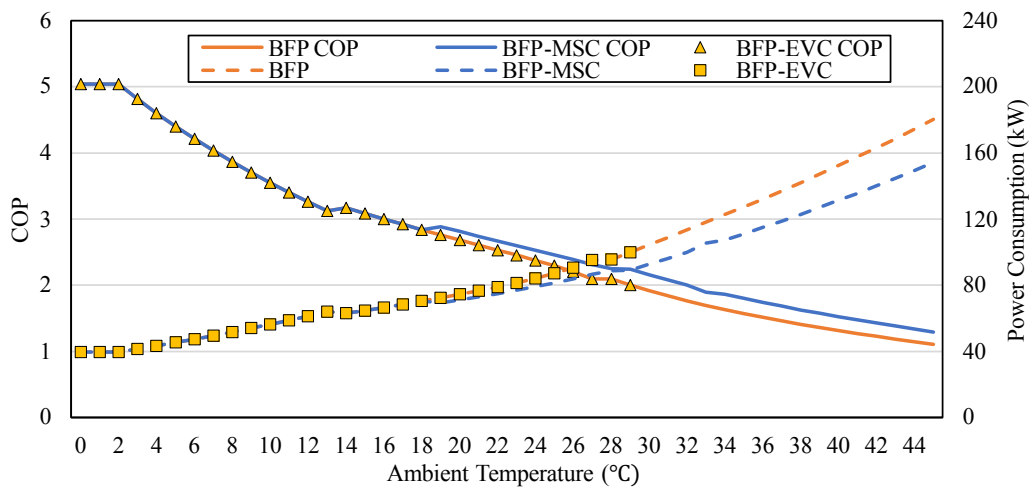


**Fig. 12.** COP and power consumption values with respect to ambient temperatures for systems included in this study.

When comparing results by cities, each system has the highest AEC in Mersin. Antalya, which has a similar climate to Mersin, has the second most AEC for all systems, while İzmir comes third after them. In İstanbul, Türkiye's most populated city, AEC values are 610.86 MWh for the BFP, 589.04 MWh for the BFP-MSC, and 541.01 MWh for the BFP-EVC. The lowest AEC is calculated in Erzurum.

Although the BFP-EVC is the system that consumes the least annual energy among all systems, the saving rate it provides compared to other systems differs a lot according to the cities. As seen in Fig. 14, the highest rate of savings is achieved in Diyarbakır with 25.47% and 20.89% according to the BFP and the BFP-MSC, respectively. Diyarbakır has high AEC values in systems without evaporative cooling with its high DBT. However, the humidity of this city is also low (Turkish State Meteorological Service, 2022). In this way, Diyarbakir stands out as a place where the difference between DBT and WBT is higher compared to other cities. This leads Diyarbakır to have 35.84-65.46 MWh more AEC than Samsun and İstanbul for the systems operating at DBT but 38.83-46.65 MWh lower AEC for the BFP-EVC with WBT. These results mirror those found in a study conducted in India (Lata and Gupta, 2020). The advantages of evaporative cooling are less pronounced in highly humid cities, with Ahmedabad showing a greater energy reduction compared to Chennai when employing evaporative cooling (Lata and Gupta, 2020).
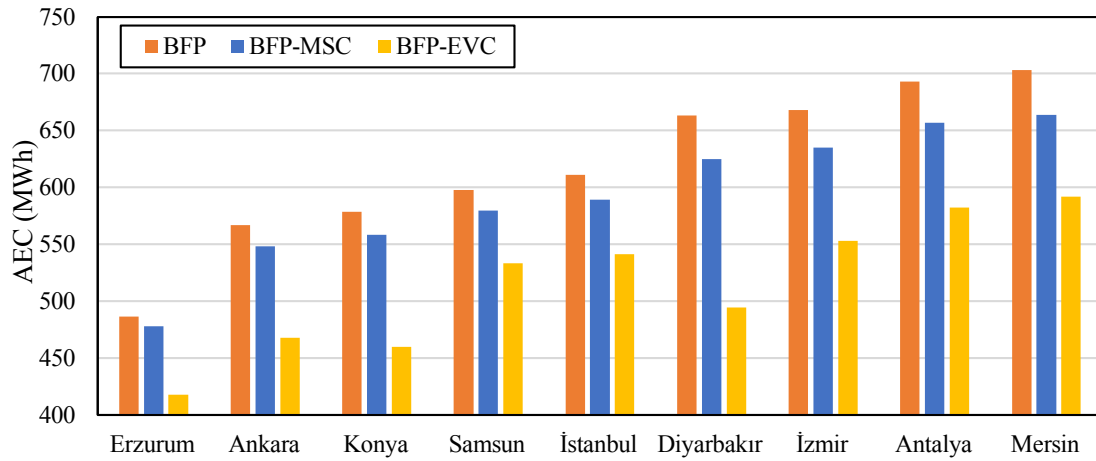
**Fig. 13.** AEC amounts of refrigeration systems examined according to cities
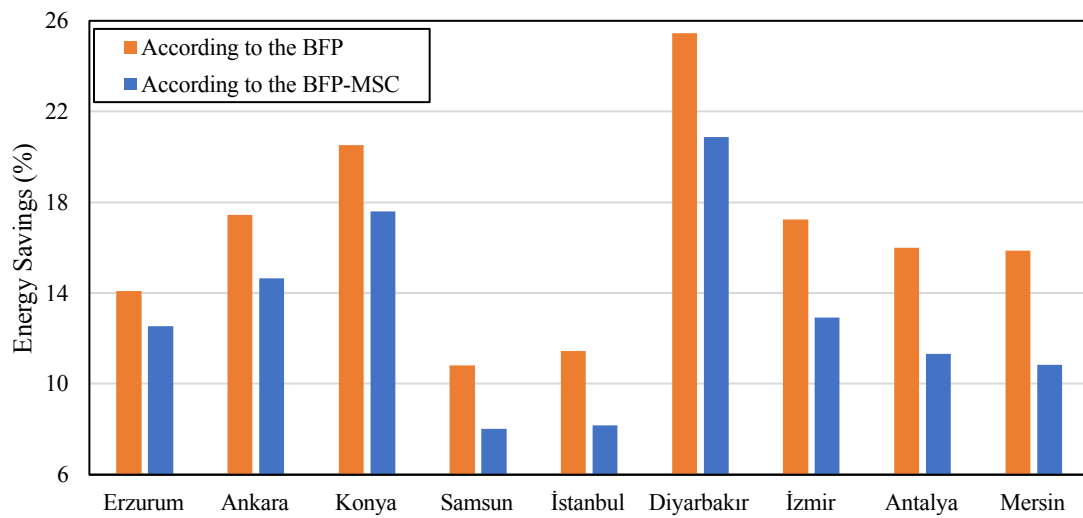


**Fig. 14.** Energy savings of the BFP-EVC over other systems in this study.
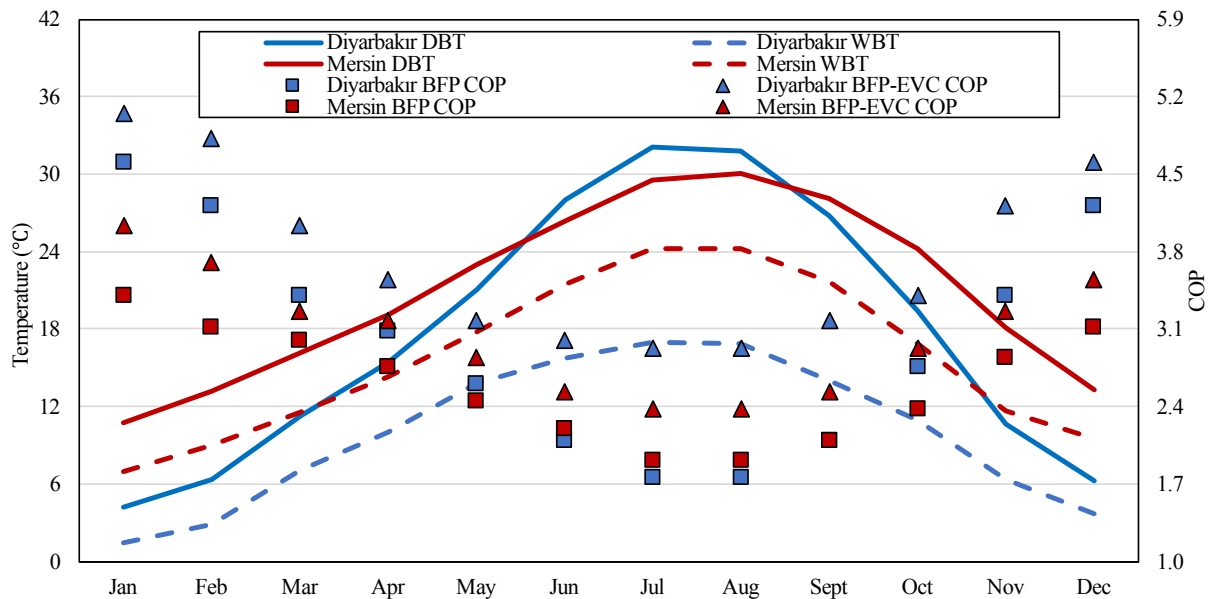


**Fig. 15.** Monthly average DBT, WBT, and COP values for Diyarbakır and Mersin.

Diyarbakır also has higher saving ratio with evaporative cooling in comparison to the Mediterranean cities Mersin, Antalya, and İzmir which have more humid air than Diyarbakır's. In Fig. 15, Mersin and Diyarbakır's monthly average temperature and COP values are exhibited. While Mersin's difference between DBT and WBT is similar throughout a year, this gap in Diyarbakır is increasing dramatically in summer. COP values for Diyarbakır's WBT are always higher than Mersin's. On the contrary, COP values for DBT are lower in Diyarbakır in June, July, and August.

Similarly, between Konya and Samsun, there is the AEC difference of 19.07 MWh for the BFP and 21.49 MWh for the BFP-MSC. However, the AEC difference for the BFP-EVC system is 73.21 MWh. This is because Samsun, located on the Black Sea coast, is a more humid city compared to Konya (Turkish State Meteorological Service, 2022) The difference between these two cities is also seen in Fig. 16 showing the annual duration of the COP values. Although it is clear in Fig. 16 that the WBT provides higher COP values for the BFP-EVC than other systems, it seems to have a similar time distribution pattern to the systems analyzed for DBT in Samsun. In Konya, it is seen in Fig. 16, the BFP-EVC not only has higher COP values compared to the other two systems, but also spends much more time at these COP values. A vertical line in both graphs occur since the COP value reaches its maximum and remains constant below 2°C. Konya's total bin-hour of maximum COP is also higher than Samsun's.
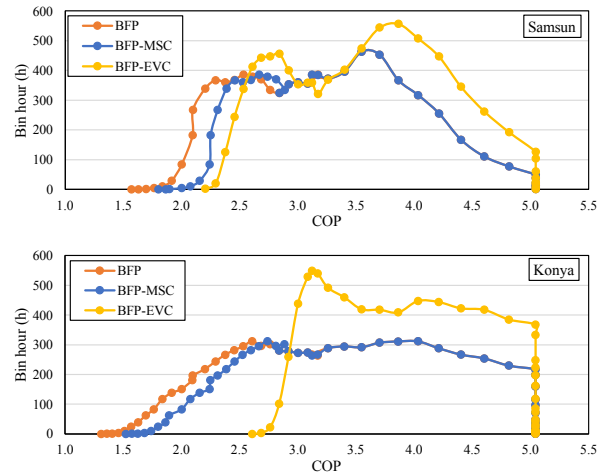


**Fig. 16.** Bin-hour for COP values for Samsun and Konya.

### Emission Analysis Results

Total equivalent $CO_2$ emission values of the investigated refrigeration systems are given in Fig. 17 for each city for 5 years due to the emission reduction targets of Türkiye between 2024 and 2029 (Republic of Türkiye Ministry of Environment Urbanization and Climate Change, 2022). According to the analysis results, the BFP-EVC has fewer emissions than the BFP between 322.13 tons and 842.05 tons for 5 years of operation time.
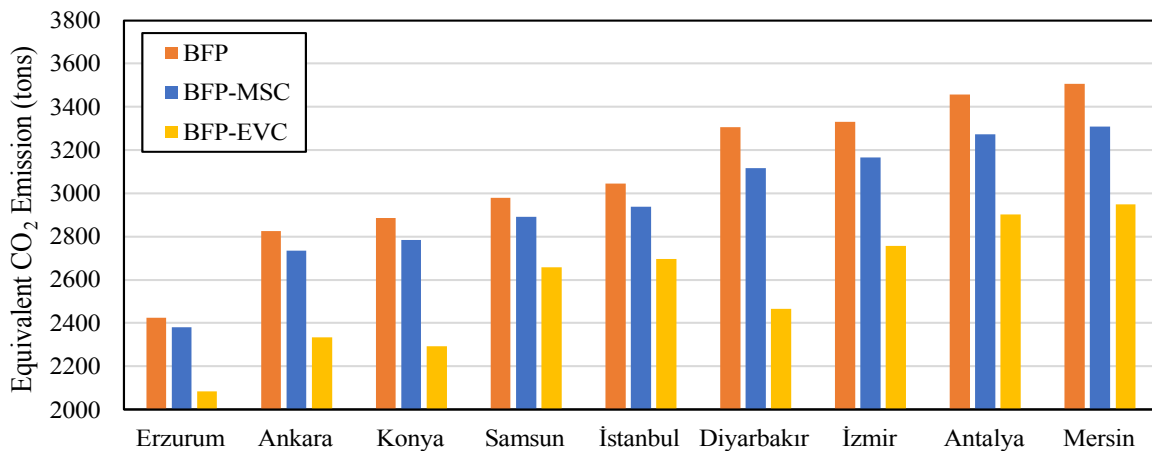


**Fig. 17.** $CO_2$ emission amounts of each refrigeration system by the city for 5 years.

$CO_2$ is used in all systems but only R290 is used in the mechanical subcooling cycle. Both these fluids have low global warming potential (GWP) values (Table 3). For this reason, the direct contribution of all refrigeration systems included in this study to the emission have a low share in the total (0.024%-0.033%).

As a result, the amount of emissions obtained is directly proportional to the annual energy consumptions (Fig. 13). So, the BFP-EVC's emission reduction ratios in comparison to the BFP are higher in low humidity cities as expected. These findings closely resemble those from a study conducted in China. In that study, cities with lower energy consumption also exhibited lower total

equivalent $CO_2$ emissions, reinforcing the relationship between energy efficiency and emissions reduction (Cui et al., 2020).

### CONCLUSION

Energetic and environmental analyses of the $CO_2$ booster refrigeration cycle with the flooded evaporators and parallel compressor (BFP), the $CO_2$ booster refrigeration system with the flooded evaporators, parallel compressor and mechanical subcooling (BFP-MSC) and the $CO_2$ booster refrigeration system with the flooded evaporators, parallel compressor and evaporative cooling

(BFP-EVC) were performed for nine cities in Türkiye for the first time in literature.

According to the results, these conclusions can be made:
- The primary factor contributing to energy savings is the reduction in mass flow rate achieved through the implementation of mechanical subcooling and a parallel compressor.
- COP of the $CO_2$ booster refrigeration systems increases at low ambient temperatures.
- COP of the BFP-MSC is up to 16.67% higher than the BFP for the same dry bulb temperatures.
- Annual energy consumption (AEC) of the BFP-EVC is the lowest for each city up to 25.47%.
- In comparison of AEC, the BFP-MSC and the BFP follow the BFP-EVC in each city, respectively.
- Evaporative cooling provides less energy saving ratio in cities with higher humidity.
- $CO_2$ emission amounts are directly proportional to the AEC due to the low GWP of $CO_2$ and R290.
- The highest AEC is obtained in Mersin and the lowest in Erzurum for all systems.
- According to the analysis results, it is recommended for all the cities to use the BFP-EVC.

## REFERENCES

Amaris, C., Tsamos, K. M., and Tassou, S. A., 2019, Analysis of an R744 typical booster configuration, an R744 parallel-compressor booster configuration and an R717/R744 cascade refrigeration system for retail food applications. Part 1: Thermodynamic analysis. *Energy Procedia,* 161, 259–267.
https://doi.org/10.1016/j.egypro.2019.02.090

Atmaca, A. U., Erek, A., Ekren, O., and Çoban, M. T., 2018, Thermodynamic Performance of the Transcritical Refrigeration Cycle with Ejector Expansion for R744, R170, and R41. *J. of Thermal Science and Technology,* 38, 111–127.

Bayrakçı, H. C., Özgür, A. E., and Alan, A., 2014, Çift Kademeli Transkritik R744 Soğutma Sistemlerinde Genleşme Türbini Kullanımının Termodinamik Analizi. *J. of Thermal Science and Technology,* 34, 91–97.

Caliskan, O., and Ersoy, H. K., 2022, Energy analysis and performance comparison of transcritical CO2 supermarket refrigeration cycles. The Journal of *Supercritical Fluids,* 189, 105698.
https://doi.org/10.1016/j.supflu.2022.105698

Chesi, A., Esposito, F., Ferrara, G., and Ferrari, L., 2014, Experimental analysis of R744 parallel compression cycle. *Applied Energy,* 135, 274–285.
https://doi.org/10.1016/j.apenergy.2014.08.087

Cui, Q., Gao, E., Zhang, Z., and Zhang, X., 2020, Preliminary study on the feasibility assessment of CO2 booster refrigeration systems for supermarket application in China: An energetic, economic, and environmental analysis. *Energy Conversion and Management*, 225.
https://doi.org/10.1016/j.enconman.2020.113422

Dai, B., Cao, Y., Liu, S., Ji, Y., Sun, Z., Xu, T., Zhang, P., and Nian, V., 2022, Annual energetic evaluation of multi-stage dedicated mechanical subcooling carbon dioxide supermarket refrigeration system in different climate regions of China using genetic algorithm. Journal of *Cleaner Production,* 333.
https://doi.org/10.1016/j.jclepro.2021.130119

Ersoy, H. K., and Bilir, N., 2012, Performance characteristics of ejector expander transcritical CO2 refrigeration cycle. *Proceedings of the Institution of Mechanical Engineers, Part A: Journal of Power and Energy,* 226(5), 623–635.
https://doi.org/10.1177/0957650912446547

European Commission, 2008, Development and demonstration of a prototype transcritical $CO_2$ refrigeration system Final Report.

Fricke, B., Zha, S., Sharma, V., Newel, J., and Sharma, V., 2016, Laboratory Evaluation of a Commercial $CO_2$ Booster Refrigeration System Laboratory Evaluation of a Commercial CO2 Booster Refrigeration System. *International Refrigeration and Air Conditioning Conference. Paper 1691.*
http://docs.lib.purdue.edu/iracc/1691

Fritschi, H., Tillenkamp, F., Löhrer, R., and Brügger, M., 2017, Efficiency increase in carbon dioxide refrigeration technology with parallel compression. International *Journal of Low-Carbon Technologies*, 12(2), 171–180.
https://doi.org/10.1093/ijlct/ctw002

Ge, Y. T., Tassou, S. A., Santosa, I. D., and Tsamos, K., 2015, Design optimisation of CO2 gas cooler/condenser in a refrigeration system. *Applied Energy*, 160, 973–981.
https://doi.org/10.1016/j.apenergy.2015.01.123

Goetzler, W., Sutherland, T., Rassi, M., and Burgos, J., 2014, Research and Development Roadmap for Next-Generation Low Global Warming Potential Refrigerants. www.osti.gov/home/

Gullo, P., Cortella, G., Minetto, S., and Polzot, A., 2016, Overfed evaporators and parallel compression in commercial R744 booster refrigeration systems - An assessment of energy benefits. *Refrigeration Science and Technology,* 261–268.
https://doi.org/10.18462/iir.gl.2016.1039

Gullo, P., and Hafner, A., 2017, Thermodynamic performance assessment of a CO2 supermarket refrigeration system with auxiliary compression economization by using advanced exergy analysis. *International Journal of Thermodynamics*, 20(4), 220–227. https://doi.org/10.5541/ijot.325883

Gullo, P., Hafner, A., and Banasiak, K., 2018, Transcritical R744 refrigeration systems for supermarket applications: Current status and future perspectives. In

*International Journal of Refrigeration,* 93, 269–310. https://doi.org/10.1016/j.ijrefrig.2018.07.001

ICF Incorporated, 2020, Supermarket Emission Reduction Analysis.

Işık, M., 2022, Thermodynamic Analysis of CO2 Booster Refrigeration Systems of Supermarket Applications for Türkiye [MSc Thesis]. Konya Technical University Graduate Education Institute.

Işık, M. and Bilir Sağ, N., 2023, Energetic, economic, and environmental analysis of CO2 booster refrigeration systems of supermarket application for Türkiye. *Sadhana*, 48, 275, https://doi.org/10.1007/s12046-023-02337-3

Karampour, M., and Sawalha, S., 2018, State-of-the-art integrated CO2 refrigeration system for supermarkets: A comparative analysis. *International Journal of Refrigeration*, 86, 239–257. https://doi.org/10.1016/j.ijrefrig.2017.11.006

Kauf, F., 1999, Determination of the optimum high pressure for transcritical CO2-refrigeration cycles. *International Journal of Thermal Sciences*, 38, 325–330.

Lata, M., and Gupta, D. K., 2020, Performance evaluation and comparative analysis of trans-critical CO2 booster refrigeration systems with modified evaporative cooled gas cooler for supermarket application in Indian context. *International Journal of Refrigeration*, 120, 248–259. https://doi.org/10.1016/j.ijrefrig.2020.08.004

Lata, M., Purohit, N., and Gupta, D. K., 2021, Techno-economic assessment of trans-critical CO2 booster system with modified evaporative cooling for supermarket application in Indian context. *Environmental Progress and Sustainable Energy*, 40(2). https://doi.org/10.1002/ep.13551

Liao, S. M., Zhao, T. S., and Jakobsen, A., 2000, A correlation of optimal heat rejection pressures in transcritical carbon dioxide cycles. *Applied Thermal Engineering*. www.elsevier.com/locate/apthermeng

Llopis, R., Cabello, R., Sánchez, D., and Torrella, E., 2015, Energy improvements of CO2 transcritical refrigeration cycles using dedicated mechanical subcooling. *International Journal of Refrigeration*, 55, 129–141. https://doi.org/10.1016/j.ijrefrig.2015.03.016

Llopis, R., Sanz-Kock, C., Cabello, R., Sánchez, D., and Torrella, E., 2015, Experimental evaluation of an internal heat exchanger in a CO2 subcritical refrigeration cycle with gas-cooler. *Applied Thermal Engineering*, 80, 31–41.https://doi.org/10.1016/j.applthermaleng.2015.01.040

Mitsopoulos, G., Syngounas, E., Tsimpoukis, D., Bellos, E., Tzivanidis, C., and Anagnostatos, S., 2019, Annual performance of a supermarket refrigeration system using different configurations with CO2 refrigerant. *Energy Conversion and Management: X*, 1. https://doi.org/10.1016/j.ecmx.2019.100006

Mylona, Z., Kolokotroni, M., Tsamos, K. M., and Tassou, S. A., 2017, Comparative analysis on the energy use and environmental impact of different refrigeration systems for frozen food supermarket application. *Energy Procedia*, 123, 121–130. https://doi.org/10.1016/j.egypro.2017.07.234

Nebot-Andrés, L., Sánchez, D., Calleja-Anta, D., Cabello, R., and Llopis, R., 2021, Experimental determination of the optimum intermediate and gas-cooler pressures of a commercial transcritical CO2 refrigeration plant with parallel compression. *Applied Thermal Engineering*, 189. https://doi.org/10.1016/j.applthermaleng.2021.116671

Özgür, A. E., Bayrakçı, H. C., and Akdağ, A. E., 2009, Kritik Nokta Üstü Çevrimli CO2 Soğutma Sistemlerinde Optimum Gaz Soğutucu Basıncı: Yeni Bir Korelasyon The Optimum Gas Cooler Pressure for Transcritical CO2 Refrigeration Cycle: a New Correlation. *J. of Thermal Science and Technology*, 29, 23–28.

Purohit, N., Gupta, D. K., and Dasgupta, M. S., 2017, Energetic and economic analysis of trans-critical CO2 booster system for refrigeration in warm climatic condition. *International Journal of Refrigeration,* 80, 182–196. https://doi.org/10.1016/j.ijrefrig.2017.04.023

Republic of Türkiye Ministry of Environment Urbanization and Climate Change, 2022, Montreal Protocol. https://iklim.csb.gov.tr/montreal-protokolu-i-4364

Sacasas, D., Vega, J., and Cuevas, C., 2022, An annual energetic evaluation of booster and parallel refrigeration systems with R744 in food retail supermarkets. A Chilean perspective. *International Journal of Refrigeration*, 133, 326–336. https://doi.org/10.1016/j.ijrefrig.2021.10.010

Sarkar, J., and Agrawal, N., 2010, Performance optimization of transcritical CO2 cycle with parallel compression economization. *International Journal of Thermal Sciences*, 49(5), 838–843. https://doi.org/10.1016/j.ijthermalsci.2009.12.001

Sawalha, S., 2008a, Theoretical evaluation of trans-critical CO2 systems in supermarket refrigeration. Part I: Modeling, simulation and optimization of two system solutions. *International Journal of Refrigeration*, 31(3), 516–524. https://doi.org/10.1016/j.ijrefrig.2007.05.017

Sawalha, S., 2008b, Theoretical evaluation of trans-critical CO2 systems in supermarket refrigeration. Part II: System modifications and comparisons of different solutions. *International Journal of Refrigeration*, 31(3), 525–534. https://doi.org/10.1016/j.ijrefrig.2007.05.018

Sooben, D., Purohit, N., Mohee, R., Meunier, F., and Dasgupta, M. S., 2019, R744 refrigeration as an alternative for the supermarket sector in small tropical island developing states: The case of Mauritius. *International Journal of Refrigeration*, 103, 264–273. https://doi.org/10.1016/j.ijrefrig.2019.03.034

Sun, Z., Li, J., Liang, Y., Sun, H., Liu, S., Yang, L., Wang, C., and Dai, B., 2020, Performance assessment of $CO_2$ supermarket refrigeration system in different climate zones of China. *Energy Conversion and Management*, 208. https://doi.org/10.1016/j.enconman.2020.112572

Tsamos, K. M., Ge, Y. T., Santosa, Id., Tassou, S. A., Bianchi, G., and Mylona, Z., 2017, Energy analysis of alternative $CO_2$ refrigeration system configurations for retail food applications in moderate and warm climates. *Energy Conversion and Management*, 150, 822–829. https://doi.org/10.1016/j.enconman.2017.03.020

Turkish State Meteorological Service, 2021, Meteorological Data.

Turkish State Meteorological Service, 2022, Climate Assessment of 2021. https://www.mgm.gov.tr

# DÖNEN PATLAMA MOTORLARINDAKİ OLUŞAN DALGA YAPISININ SAYISAL OLARAK İNCELENMESİ

**Osman KOCAASLAN\*, Kürşad Melih GÜLEREN\*\*,**
**Bayındır Hüseyin SARACOĞLU\*\*\*, Tolga YASA\*\*\*\***

*Selçuk Üniversitesi Huğlu Meslek Yüksekokulu, Makine ve Metal Teknolojileri Bölümü, 42700 Beyşehir, Konya, okocaaslan@selcuk.edu.tr, ORCID: 0000-0002-7848-6974
\*\*Eskişehir Osmangazi Üniversitesi, Mühendislik Mimarlık Fakültesi, Uçak Mühendisliği Bölümü, 26480 Batımeşelik, Eskişehir, kursadmelih.guleren@ogu.edu.tr, ORCID: 0000-0003-3464-7956
\*\*Von Karman Institute for Fluid Dynamics, Turbomachinery and Propulsion Department, 1640, Rhode-Saint-Genese, Belçika, saracog@vki.ac.be, ORCID: 0000-0002-3961-3555
\*\*\*\*Eskişehir Teknik Üniversitesi Mühendislik Fakültesi Makine Mühendisliği Bölümü 26555 Tepebaşı, Eskişehir, tyasa@eskisehir.edu.tr, ORCID: 0000-0002-7242-2507

**Özet:** Bu çalışmada dönen patlama motorundaki patlama dalgası yapısı ve itki performansı sayısal olarak incelenmiştir. Sayısal çalışmalar iki aşamada gerçekleştirilmiştir. İlk olarak deneysel ve sayısal verilerin yer aldığı referans çalışmaya yönelik doğrulama çalışmaları tamamlanmıştır. Deneysel çalışmalarda hidrojen 0.8 mm çapındaki 90 enjektörden, hava ise 0.4 mm genişliğindeki aralıktan patlama kanalına aktarılmaktadır. Referans sayısal çalışmada yer verildiği üzere tek basamaklı tersinmez hidrojen-hava mekanizması doğrulama çalışmalarında kullanılmıştır. Doğrulama analizleri sonrasında patlama dalgasının detaylı olarak incelenebilmesi için 19 basamaklı tersinmez hidrojen-hava reaksiyon mekanizması sayısal çalışmalara tanımlanmıştır. Sayısal çalışmalarda daimi olmayan yoğunluğa dayalı çözücü kullanılmıştır. İkinci aşamada patlama dalga yapısı ve dönen patlama motorunun itki performansı araştırılmıştır. Sonuç olarak patlama dalgasının 1.1 ms sonrasında kararlı yapıya ulaşabildiği belirlenmiştir. Değişen blokaj oranı nedeniyle t=1.1 ms öncesinde patlama dalgası yüksekliği sabit kalmamıştır. Kararlı patlama dalgası yüksekliğinin tek basamaklı ve 19 basamaklı çalışmalarında sırasıyla 29 mm ve 27 mm olduğu tespit edilmiştir. Patlama kanalı çıkışındaki itki dağılımının kararlı patlama dalgası ile neredeyse sabit olduğu belirlenmiş ve itki değerinde 678.7±2.3 N aralığında salınımların meydana geldiği gözlemlenmiştir.
**Anahtar Kelimeler:** Blokaj Oranı, Dönen Patlama Motoru, Hesaplamalı Akışkanlar Dinamiği, Patlama Dalgası

# NUMERICAL INVESTIGATION of WAVE STRUCTURE IN ROTATING DETONATION ENGINES

**Abstract:** In this study, the detonation wave structure and thrust performance of the rotating detonation engine were investigated numerically**.** Numerical studies are in two stages. First, validation studies were carried out according to the referenced study. Experimental and numerical studies are included in the reference study. In experimental studies, hydrogen is transferred from 90 injectors with a diameter of 0.8 mm, and the air is transferred to the detonation channel through a gap of 0.4 mm wide. As included in the reference numerical study, one-step irreversible hydrogen-air mechanism was used in validation studies. To examine the detonation wave in detail after the validation analysis, the 19-steps irreversible hydrogen-air reaction mechanism was defined in numerical studies. The transient density-based solver was used for numerical analyses. In the second stage, the detonation wave structure and the thrust performance of the rotating detonation engine were investigated. As a result, it was determined that the detonation wave could reach a stable structure after 1.1 ms. The detonation wave height was not constant due to the blockage ratio changing before t= 1.1 ms. The stable detonation wave height was found to be 29 mm and 27 mm in one-step and 19-steps reaction mechanism studies, respectively. When the thrust distribution at the exit of the detonation channel was examined, it was determined that it was almost constant with the stable detonation wave and it was observed that oscillations occurred in the range of 678.7±2.3 N in the thrust value.
**Keywords:** Blokage Ratio, Rotating Detonation Engine, Computational Fluid Dynamics, Detonation Wave

## SEMBOLLER

| | |
|---|---|
| A | Üstel faktor |
| b | Sıcaklık üssü |
| $c_{p,mix}$ | Karışım özgül ısı kapasitesi [J/kgK] |
| E | Toplam enerji [J] |
| $E_a$ | Karışım fraksiyonu [J] |
| *f* | Dalga frekansı [1/s] |
| F, G | Konvektif akı |
| $F_{(t)}$ | İtki [N] |
| $h_f^0$ | Standart şartlarda oluşum entalpisi [J/mol] |
| $h_{tot}$ | Patlama dalgası yüksekliği [mm] |
| $h_{tot,ave}$ | Ortalama patlama dalgası yüksekliği [mm] |
| H | Toplam entalpi [J] |
| $k_f$ | Reaksiyon hızı [1/s] |
| $Mw_k$ | K ürününün molekül ağırlığı [kg/kmol] |
| $\dot{m}$ | Kütlesel debi [kg/s] |
| $n_D$ | Dalga sayısı |
| p | Basınç [Pa] |
| $p_{back}$ | Geri basınç [Pa] |
| $p_{cj}$ | Chapman-Jouguet basıncı [Pa] |
| $p_{crt}$ | Kritik basınç [Pa] |
| $p_{det}$ | Patlama dalgası cephesi basıncı [Pa] |
| $p_w$ | Enjektör duvarına en yakın hücre basıncı [Pa] |
| $p_0$ | Toplam basınç [Pa] |
| Q | Konservatif değişkenler |
| R | Gaz sabiti [J/kg-K] |
| $\bar{R}$ | İdeal gaz sabiti [J/kmolK] |
| S | Kaynak terim |
| t | Zaman [s] |
| T | Sıcaklık [K] |
| $T_{cj}$ | Chapman-Jouguet sıcaklığı [K] |
| $T_0$ | Toplam sıcaklık [K] |
| $u,\vec{v}$ | Hız [m/s] |
| $U_D$ | Dalga hızı [m/s] |
| Y | Kütle fraksiyonu |
| P | Yoğunluk [kg/m³] |
| Γ | Özgül ısı oranı |

## KISALTMALAR

| | |
|---|---|
| İng. | İngilizcesi |
| DaPM | Darbeli patlama motorları |
| DoPM | Dönen patlama motorları |
| C-J | Chapman-Jouguet |

## GİRİŞ

Ticari ve savunma odaklı itki sistemlerinde daha yüksek performans ve termal verimlerin elde edilmesi motivasyonu patlama tabanlı motorlara yönelik ilginin artmasını sağlamıştır. Geleneksel havacılık itki sistemlerinde ses altı yanma (İng. deflegration) ile itki üretimi gerçekleştirilmektedir. İdeal Humprey ve Brayton çevrimlerine yönelik başlangıç sıcaklık ve basınç değerlerinin sırası ile 300 K ve 1 atm seçilerek gerçekleştirilen termodinamik analizler, termal verimin Humprey çevrimlerinde %9.8 oranında arttığını göstermiştir (Bigler *vd.*, 2017). Su vd. (2022) dönen patlama motoru beslemeli turbojet motorunun, turbofan motorlarına göre yakıt tüketimi ve itki kazanımlarını

analitik yöntemler ile incelemişlerdir. Orta ve yüksek basınç oranlarında yakıt tüketiminde %20 düşüşlerin elde edilebileceği belirlenmiştir.

Patlama (detonasyon) tabanlı motorlarda, şok dalgası ve kimyasal reaksiyon cephesinin oluşturduğu patlama dalgası cephesi sayesinde itki üretimi gerçekleşmektedir. Şok cephesi önüne gönderilen temiz yakıt-hava karışımının sıcaklık ve basıncı şok cephesi sayesinde ani olarak yükselmektedir. Bunun sonucu olarak hava-yakıt karışımı bölgesinde kimyasal reaksiyonlar başlamakta ve çok kısa sürelerde yüksek enerji salınımları gerçekleşmektedir. Bu enerji salınımı ise patlama dalgasının yayınımını desteklemektedir (Ma *vd.*, 2020; Zhang *vd.*, 2019).

Patlama-tabanlı motorlar genel olarak iki temel sınıf altında incelenmektedir; darbeli patlama motorları (DaPM) (İng. Pulse Detonation Engine) (Zheng *vd.*, 2020) ve dönen patlama motorlarıdır (DoPM) (İng. Rotating Detonation Engine) (Wang *vd.*, 2015; Ma *vd.*, 2018). Darbeli patlamalı motorlarda patlama dalgası (İng. detonation wave) doğrudan patlama dalgası oluşturma (İng. direct detonation initiation), ses altı yanmadan ses üstü yanmaya geçiş ve şokla patlama dalgası oluşturma yöntemleri (İng. shock initiated detonation) ile elde edilmektedir (Driscoll *vd.*, 2015; Alam *vd.*, 2019; Schauer *vd.*, 2015). Bu motorlar içten yanmalı motorlara benzer şekilde birbirini takip eden adımlar ile çalışır. Bu döngüsel çalışma şeklinin beş basamağı bulunmaktadır. Bunlar sırası ile doldurma, ateşleme, ses altı yanmadan ses üstü yanmaya geçiş, genişleme (İng. blow-down) ve soğutma olarak sıralanabilir. Sistemin sürekliliği için her döngüde yeniden ateşlemenin gerçekleşmesi gerekmektedir. Bunun yanında darbeli patlama motorlarında doldurma ve soğutma (İng. fill and purge) basamakları için zamana ihtiyaç duyulduğundan dolayı, bu sistemlerin çalışma frekansları sınırlıdır (Yi *vd.*, 2009).
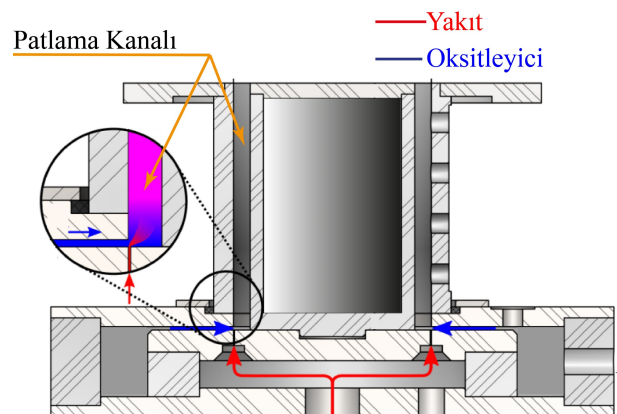


**Şekil 1.** Dönen patlama motoru şematik gösterimi (Bach *vd.*, 2021)

DoPM'larda şok tüpleri yerine Şekil 1'de görüldüğü üzere dairesel bir patlama kanalı bulunur. Bu kanala temiz yakıt-hava karışımı çevresel olarak belirli aralıklar ile yerleştirilen enjektörler tarafından beslenir. Bach *vd.* (2021) deneysel çalışmalarında kullanmış DoPM

konfigürasyonunda da görüldüğü üzere yakıt ve oksitleyici patlama kanalına ayrık kanallardan aktarılmaktadır. Yakıt ve oksitleyici patlama kanalında karıştırılarak, patlama dalgasının yayınımı için hazır hale getirilmektedir. Patlama cephesinde salınan enerji ile dönen patlama dalgasının (İng. rotating detonation wave) yayınımını sağlamaktadır (Lee, 2019). Bu sebeple bu tip motorlarda bir kez ateşlemenin gerçekleşmesi yeterlidir (Lu vd., 2014). Bu sayede, DaPM'daki tekrarlayan ve aralıklı itki üretimi yerine, DoPM'da sabit itki üretimi gerçekleştirilmektedir (Yi vd., 2009).

DoPM enjektör performansının motor performansı üzerine doğrudan bir etkisi vardır. Patlama cephesinin yüksek sıcaklık ve basınç koşullarında oluşu ve hareket hızının yüksek olması sebebi ile bu konudaki deneysel çalışmalar önemli kısıtlamalara sahiptir. Bu sebeple enjektör performansları çoğunlukla sayısal analiz çalışmaları ile belirlenmektedir. Dönen patlama motorlarında gerçek uygulamalarda her ne kadar yakıt, hava ile önceden karışmamış halde patlama kanalına salınsa da, sayısal analizlerde bu durum hem önceden karışmamış (İng. non-premixed) (Sun vd., 2019a; Prakash vd., 2020; Lietz vd., 2020; Zhao vd., 2020; Sun vd.,2019b; Vignat vd., 2024) hem de önceden karışmış (premixed) (Zhang vd., 2018; Zhang vd., 2019; Wu vd., 2014; Sun vd., 2018; Zhang vd., 2020; Xia vd, 2021) olarak modellenebilmektedir. Sun vd. (2019a) farklı hava kanalı genişliğinin (0.4, 1 ve 2 mm) DoPM patlama dalgası üzerine etkisini sayısal olarak incelemişlerdir. Düşük hava kanalı girişlerinde toplam kütlesel debinin artırılması sonrası iki patlama dalgalı moda geçiş gerçekleşmiştir. Hava kanalı genişliğinin artırılması enjeksiyon sürecinin gelişip güçlenmesini sağlamış ve yetersiz reaktanlar nedeniyle patlama dalgasının sönümlenmesine neden olmuştur. Sato ve Raman (2020) gerçekçi bir etilen tabanlı DoPM'nda patlama dalgasının temiz yakıt-hava cephesini sıkıştırmasına yönelik sayısal analizler yürütmüşlerdir. Strempfl vd. (2024) hidrojen-hava tabanlı DoPM'da karışımsız (tam ölçekli) ve karışımlı enjeksiyon yöntemi ile sayısal çalışmalar gerçekleştirmişlerdir ve enjeksiyon yöntemlerinin patlama dalgası özellikleri üzerine etkilerini incelemişlerdir. Zheng vd. (2020) patlama dalgasının yayınım karakteristiğini önceden karışmamış enjektör konfigürasyonunu dönen patlama motorlarında sayısal olarak incelemişlerdir. Patlama kanalında iki-dalga modu (eşdeğerlilik oranı 0.6, 0.8, 1.0 ve 1.4 tanımlandığında) ve tek-dalga modunun (eşdeğerlilik oranının 1.2'ye eşit olması durumunda) aktif olduğu belirlenmiştir. Yu vd. (2023) farklı dalga sayısı modlarında patlama kanalına yerleştirilen soğutma kanallarının patlama dalgası yapısı ve yayınımı üzerine etkisini incelemişlerdir. Yakıt ve oksitleyici karışımlı olarak patlama kanalına yönlendirilmiştir.

Patlama dalgası cephesi, yayınımı ve kararlılığının detaylı olarak incelenmesine yönelik sayısal analizlerde basitleştirmeler gerçekleştirilmektedir. Bu basitleştirme uygulamalarından bir tanesi de enjektör konfigürasyonları olmaksızın sayısal modelin oluşturulmasıdır. Önceden karışmış olarak patlama kanalına aktarılan yakıt-hava karışımışı için patlama kanalı girişinde değişken sınır koşulları tanımlanarak enjektörler mikro lüle dağılımı ile modellenmektedir. Bu yaklaşımda izantropik koşullar ile sınır şartları türetilmektedir. Zhang vd. (2018) dönen patlama motorlarında, patlama dalgalarının kararsızlığını incelemişlerdir. Yi vd. (2011) iki boyutlu sayısal analizler ile DoPM itki performansını araştırmışlardır. Gerçek bir DoPM enjektör aralıklarının da modellenebilmesi için mikro lüle yaklaşımına ek olarak enjektör duvar yüzeyleri oluşturulmuştur. Mikro lüle yaklaşımı ile sınır şartı hesaplanarak ayrık enjeksiyon modelinin patlama dalgası yapısı üzerine etkileri incelenmiştir (Chen vd., 2018). Yan vd. (2021) iki boyutlu olarak modellenmiş patlama kanalında farklı alan oranlarına sahip slot lüle enjeksiyonu ile patlama dalgası özelliklerindeki değişimleri sayısal olarak incelemişlerdir. Wang ve Weng (2022) keresone-hava tabanlı DoPM enjeksiyon koşullarının patlama dalgası yayınımına etkisine yönelik sayısal çalışmalar gerçekleştirmişlerdir. Mikro lüle enjeksiyon modelinin kullanıldığı sayısal çalışmalarda artan kerosen damlacık boyutu ve azalan enjeksiyon basıncının patlama dalgasının sönümlenmesine neden olduğu belirlenmiştir. Ladeinde vd. (2023) hidrojen-hava tabanlı DoPM'da patlama kanalını iki boyutlu modelleyerek patlama dalgası yayınımı süresince ısı akısı gelişimini sayısal olarak incelemişlerdir. Sayısal çalışmalarda mikro lüle enjeksiyon yöntemi ile yakıt-oksitleyici karışımı patlama kanalına yönlendirilmiştir.

Bu çalışmada DoPM'nun itki performansı ve patlama dalga yapısı araştırılmıştır. Sayısal çalışmalar iki basamakta gerçekleştirilmiştir. İlk olarak referans alınan DoPM'nun deneysel çalışmaları ile doğrulama çalışmaları tamamlanmıştır. Doğrulama analizlerinde mikro lüle yaklaşımı ile patlama kanalı iki boyutlu modellenerek sınır şartları oluşturulmuştur. İkinci basamakta ise patlama dalgasının detaylı irdelenebilmesi için 19 basamaklı tersinmez hidrojen-hava mekanizması kullanılmıştır (Ó Conaire vd., 2004). Sayısal analiz sonuçları ile patlama dalgasının zamanla gelişimi süresince eğik şok cephesinin gelişimi ve itki performansı üzerine etkisi irdelenmiştir.

## MATERYAL METOD

### Fiziksel Model ve Enjeksiyon Koşulları

Sayısal model Liu vd. (2012) çalışmalarında yer alan patlama kanalına göre uyarlanmıştır. Şekil 2'de verilen referans çalışma dönen patlama motoru konfigürasyonu patlama kanalı giriş ve çıkış çapları ve uzunluğu sırası ile 90, 100 ve 75 mm'dir. Yakıt eşit aralıklarda 0.8 mm çapında 90 enjektörden, hava ise 0.4 mm genişliğinde kanaldan patlama kanalına aktarılmaktadır.

Patlama kanalı uzunluğu ve orta çap değeri, patlama kanalı aralığından oldukça büyük olması nedeniyle literatürde yer alan çalışmalarda patlama kanalı akış hacmi iki boyutlu olarak oluşturulmaktadır (Lei vd.,

2020; Zhang *vd.*, 2018; Zhang *vd.*, 2020). Escobar *vd.* (2013) hidrojen-hava tabanlı DoPM'a yönelik patlama kanalı 2D ve 3D olarak modelleyerek sayısal çalışmalar gerçekleştirmişlerdir. 2D ve 3D sayısal çalışmalarında kullanılan hücre sayısı sırası ile 80000 ve 1000000'dur. Hücre sayısındaki yüksek fark ile birlikte 2D akış alanında eğrilik etkilerinin ihmal edilmesine rağmen 3D çalışmalara göre patlama dalgası hızında kayda değer bir değişimin (yaklaşık %4.7) meydana gelmediğini belirtmişlerdir. Bununla birlikte patlama dalgası yüksekliğindeki farkın da %1 olduğu ifade edilmiştir. Bu nedenle sayısal çalışmalarda, patlama kanalı iki boyutlu ve düzlemsel olarak modellenmiştir. Şekil 2'de görüldüğü üzere iki boyutlu akış alanının oluşturulmasında patlama kanalının orta çap değeri ($D_{mean}$) referans alınmıştır.



**Şekil 2.** Akış alanı ve sınır koşulları [Liu *vd.*, 2012]

Dönen patlama dalgası patlama kanalı içerisinde azimuthal doğrultuda (x doğrultusu) hareket etmektedir. Bu nedenle akış alanının sağ ve sol kenarları periyodik sınır olarak tanımlanmıştır. Temiz yakıt-hava karışımı önceden karışmış olarak modellenerek akış alanın alt yüzeyinden patlama kanalına giriş yapmaktadır. Yanma sonrası ürünler ise patlama kanalı çıkışından patlama kanalını terk etmektedir.

Giriş sınır koşuluna mikro lüle yaklaşımı kullanılarak kütle akısı tanımlaması gerçekleştirilmiştir. Mikro lüle yaklaşımında üç enjeksiyon modeli yer almaktadır (Yi vd., 2011). Enjeksiyon modellerinde enjektör duvarına yakın hücrenin basınç değeri ($p_w$) referans alınmaktadır. Tablo 1'de verilen enjeksiyon modellerinde $p_w$ değeri $P_0$ (enjeksiyon toplam basıncı) değerinden büyük ise patlama kanalına temiz yakıt-hava karışımı enjekte edilmemektedir. Eğer $p_0$ değeri $p_w$'den ve $p_w$ değeri $p_{cr}$'den (kritik basınç) büyük ise sırası ile ses altı ve ses üstü enjeksiyon gerçekleşmektedir.

**Tablo 1.** Enjeksiyon koşulları ve detayları (Liu *vd.*, 2012)

| Enjeksiyon Koşulu | u,T |
|---|---|
| $p_w \geq p_0$ (Enjeksiyon yoktur.) | N/A |
| $p_{cr} \leq p_w \leq p_0$ (Ses altı enjeksiyon) | $p = p_w$ $T = T_0 \left(\dfrac{p}{p_0}\right)^{\frac{\gamma-1}{\gamma}}$ $u = \sqrt{\dfrac{2\gamma}{\gamma-1} R T_0 \left[1 - \left(\dfrac{p}{p_0}\right)^{\frac{\gamma-1}{\gamma}}\right]}$ $p_{cr} = p_0 \left(\dfrac{2\gamma}{\gamma+1}\right)^{\frac{\gamma}{\gamma-1}}$ |
| $p_w \leq p_{cr}$ (Ses üstü enjeksiyon) | $p = p_{cr}$ $T = T_0 \left(\dfrac{p}{p_0}\right)^{\frac{\gamma-1}{\gamma}}$ $u = \sqrt{\dfrac{2\gamma}{\gamma-1} R T_0}$ |

Patlama kanalı çıkış sınır şartı olarak basınç tanımlanmıştır. Çıkış yüzeyinde dalga yansıması (İng. reflection) gerçekleşmesi halinde temiz yakıt-hava karışım katmanı etkilenmektedir. Patlama dalgası yüksekliğinin artışı patlama dalgasının şiddetini azaltırken, düşüşü ise patlama dalgasının şiddetini artırmaktadır. Bu durum, patlama cephesi ardındaki basınç dağılımının değişimine neden olmaktadır. Patlama dalgası yüksekliğindeki artış ve azalışlar patlama dalgasını kararsız kılmaktadır. Dalga yansıma koşulu için çıkış sınır şartı yanma sonrası ürünlerin patlama kanalını terk etme koşuluna bağlı olarak (ses altı ve ses üstü) tanımlanmıştır. Lokal değişken çıkış basıncının belirlenmesi için çıkış yüzeyine en yakın hücredeki basınç değeri ($p_{w,out}$) referans alınmıştır. Atık gazların hızı ses altı ise çıkış basıncı çevre basıncına ($p_\infty$=11 kPa) eşittir ve ses üstü ise Eş. (1)'de verilen

bağıntı ile lokal basınç değeri belirlenmiştir (Lei *vd.*, 2020).

$$p_{out} = (1 - 0.05)p_{w,out} + 0.05p_{\infty} \quad (1)$$

Değişken sınır şartlarının sayısal analizlere aktarılması UDF (User Defined Function) dosyaları ile gerçekleştirilmiştir. Giriş ve çıkış sınır şartları için hazırlanan UDF dosyaları Ansys/Fluent çok amaçlı yazılımına aktarılarak değişken sınır şartları tanımlanmıştır. UDF dosyaları ile giriş ve çıkış yüzeylerine en yakın hücrelerdeki lokal basınç değeri anlık olarak okunarak sınır şartları elde edilmiştir.

Sayısal analizlerde patlama dalgasının başlatılabilmesi için akış alanında küçük bir bölgede C-J basıncı ($p_{cj}$=1.565 MPa) ve sıcaklığı ($T_{cj}$=2940.85 K) tanımlanmıştır (Liu *vd.*,2012). Patlama dalgasının yayınımı için patlama kanalı önceden karışmış 0.1 MPa basınca ve 300 K sıcaklığa sahip stokiyometrik hidrojen-hava karışımı ile doldurulmuştur. Böylece patlama dalgasının kontrollü bir şekilde başlaması ve yayınımı sağlanmıştır.

**Korunum Denklemleri ve Sayısal Yöntem**

Patlama dalgasının yayınımı süresince viskozite, ısı iletimi ve kütle difüzyonu gibi taşınım özellikleri etkisi konveksiyon terimlerine göre daha düşüktür (Liu *vd.*, 2012). Ayrıca viskoz terimleri şok dalgasının ana özellikleri olan hızı, şiddeti vs. genellikle etkilemediği belirtilmektedir (Wu *vd.*, 2014). Bu nedenle taşınım özellikleri ihmal edilmiştir. Korunum denklemleri için, iki-boyutlu kimyasal reaksiyonlar nedeniyle Euler denklemleri kullanılmıştır (Yi *vd.*, 2011; Heidari *vd.*, 2011; Melguizo-Gavilanes *vd.*, 2011; Wang *vd.*, 2020). Korunum denklemlerinin gösterimi Eş. (2)'de verilmiştir (Yi *vd.*, 2011).

$$\frac{\partial \vec{Q}}{\partial t} + \frac{\partial \vec{F}}{\partial x} + \frac{\partial \vec{G}}{\partial y} = \vec{S} \quad (2)$$

$$Q = \begin{bmatrix} \rho \\ \rho u \\ \rho v \\ \rho E \\ \rho Y \end{bmatrix}, F = \begin{bmatrix} \rho u \\ \rho u^2 + p \\ \rho uv \\ \rho uH \\ \rho uY \end{bmatrix}, G = \begin{bmatrix} \rho v \\ \rho uv \\ \rho v^2 + p \\ \rho vH \\ \rho vY \end{bmatrix},$$

$$S = \begin{bmatrix} 0 \\ 0 \\ 0 \\ 0 \\ \dot{\omega} \end{bmatrix} \quad (3)$$

Eş. (3)'te verilen Q konservatif değişkenler, F ve G konvektif akı ve S ise kaynak terimdir. Y, $\dot{\omega}$, u, v ve w sırasıyla reaktanların kütle fraksiyonu, kütle üretim oranı ve hız bileşenleridir. Bütün ürünler için ideal gaz yaklaşımı kabul edilmiştir. Karışım yoğunluğu ve basıncı Eş. (4) ve Eş. (6)'te te verilen bağıntılar ile belirlenmiştir. Eş. (6)'da $\bar{R}$ ideal gaz sabiti ve $Mw_k$, k ürünün molekül ağırlığıdır. Toplam enerji denklemi Eş. (7)'de verilmiştir (Escobar *vd.*, 2013).

$$\rho = \sum_{k=1}^{N_s} \rho_k \quad (4)$$

$$\rho_k = \rho Y_k \quad (5)$$

$$p = \sum_{k=1}^{N_s} \rho_k \frac{\bar{R}}{Mw_k} \quad (6)$$

$$E = \int_{T_{ref}}^{T} c_{p,mix} dT + \sum_{k=1}^{Ns} Y_k h_f^0 (T_{ref}) + \frac{|\vec{v}|^2}{2} - \frac{p}{\rho} \quad (7)$$

Sayısal analizlerde zamana ve yoğunluğa dayalı çözücü kullanılmıştır. Viskoz olmayan akı vektörleri Roe-FDS modeli ile ayrıklaştırılmıştır. Gradyanların çözümlenmesi için en küçük kareler (least-square-cell) tabanlı yöntem kullanılmıştır. Hidrojen gibi patlayıcı yakıtların kimyasal reaksiyonları çok kısa sürelerde gerçekleşmektedir. Bu nedenle sayısal analizlere ikinci dereceden ayrıklaştırma tanımlanmıştır. Reaksiyon hızı sabitleri Arrhenius çözümlemesi ile elde edilmiştir. Eş. (8)'de verilen Arrhenius denkleminde $k_f$ reaksiyon hızı, $E_a$ aktivasyon enerjisi, R gaz sabiti ve T ise sıcaklıktır (Sun *vd.*, 2019a).

$$k_f = AT^b exp(-E_a/RT) \quad (8)$$

Döner patlama analizlerinde tek basamaklı (Shao *vd.*, 2010, Wu *vd.*, 2014; Schwer ve Kailasanath, 2011; Yi *vd.*, 2009) ve detaylı hidrojen/hava kimyasal reaksiyon mekanizmaları (Escobar *vd.*, 2013; Ettner *vd.*, 2014; Choi *vd.*, 2000; Sun *vd.*, 2019a) kullanılmaktadır. Kullanılan kimyasal reaksiyon mekanizmaları patlama dalgasının yayınımının modellenmesi için kritik öneme sahiptir. Bu nedenle sayısal çalışmalarda tek basamaklı ve 19 basamaklı tersinmez hidrojen/hava kimyasal reaksiyon mekanizması kullanılmıştır. Tek basamaklı reaksiyon mekanizmasında Ma *vd.* (2005) çalışmasında yer alan Arrhenius parametreleri tanımlanmıştır.

**BULGULAR**

**Çözüm Ağı Bağımsızlığı**

DoPM sayısal çalışmalarında dalganın yapısı ve yayınımı için uygun hücre yapısının türetilmesi gerekmektedir. Patlama dalgası yapısı ve kararsızlığının yakalanabilmesi için yarı-reaksiyon bölgesinde asgari 20 hücre oluşturulmalıdır (Yi *vd.*, 2011; Wescott *vd.*, 2004). Ayrıca hücre boyutlarının artırılması değişken sınır koşullarının kullanıldığı DoPM analizlerinde, yakıt-hava karışımının patlama kanalına aktarılmasını etkilemekte ve patlama dalgasının sönümlenmesine neden olmaktadır.

Çözüm ağından bağımsızlaştırma çalışmalarında çözüm ağlarında kullanılan en büyük hücre boyutları 0.125 mm, 0.25 mm, 0.5 mm, 0.75 ve 1 mm'dir. Kimyasal reaksiyonların çözüm ağından bağımsızlaştırma çalışmalarına eklenebilmesi için sayısal çalışmalar detaylı kimyasal reaksiyon mekanizması kullanılarak gerçekleştirilmiştir. Tablo 2'de sayısal çalışmalardan

elde edilen sonuçlar ve C-J değerlerine göre relatif farklılıklar verilmiştir. Detaylı kimyasal reaksiyon mekanizmasının kullanıldığı sayısal çalışmalarda tek dalga modunun hakim olduğu belirlenmiştir ve hücre boyutlarındaki artış ile kararlı patlama dalgası hızında da artışlar elde edilmiştir. Patlama dalgası hızı ve frekansı relatif farkının 0.5 mm hücre boyutlarında asgari düzeye indirgendiği tespit edilmiştir.

**Tablo 2.** Çözüm ağı hücre boyutlarına göre patlama dalgası özelliklerinin karşılaştırılması

| Hücre boyutu [mm] | $U_D$ [m/s] | $f$ [kHz] | $U_D$ Fark [%] |
|---|---|---|---|
| 0.125 | 1886 | 6.33 | 4.17 |
| 0.25 | 1949 | 6.53 | 1.00 |
| 0.5 | 1963 | 6.58 | 0.26 |
| 0.75 | N/A | N/A | N/A |
| 1.0 | N/A | N/A | N/A |
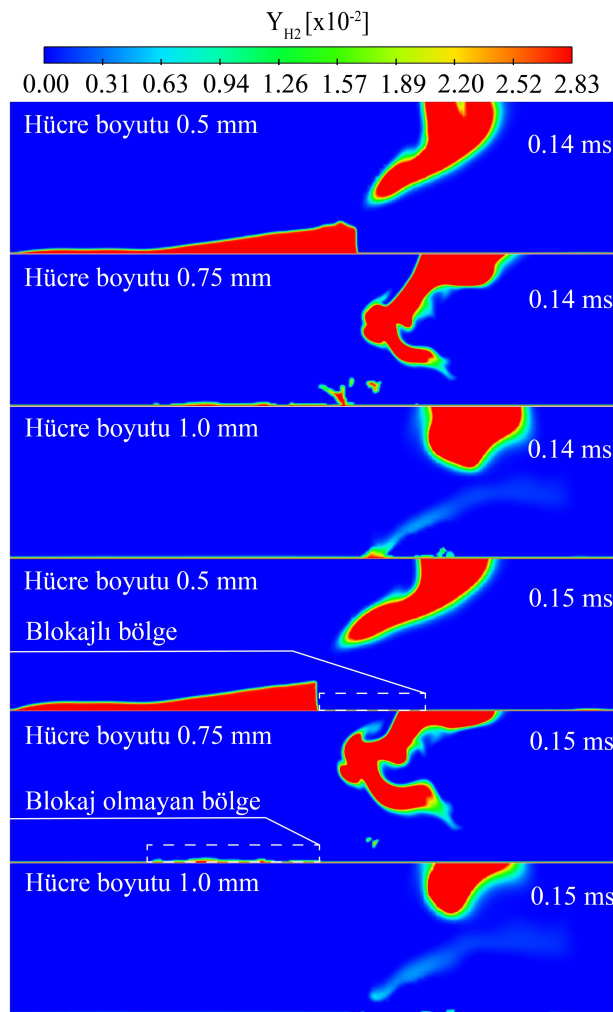


**Şekil 3.** Hücre boyutlarına göre anlık hidrojen kütle fraksiyon dağılımları

Şekil 3'te verilen hidrojen kütle fraksiyonu dağılımı incelendiğinde 0.75 mm ve 1.0 mm hücre boyutlarının kullanıldığı sayısal çalışmalarda patlama dalgasının t= 0.14 ms sonrasında ses altı yanma moduna geçiş yaptığı tespit edilmiştir. t= 0.15 ms anında 1.0 mm hücre boyutunun kullanıldığı sayısal çalışmada patlama kanalı girişi boyunca blokajın meydana geldiği görülmektedir. 0.75 mm hücre boyutunun kullanıldığı çalışmada daha

düşük blokaj oranına elde edilmesine rağmen patlama dalgası cephesinin temiz yakıt-oksitleyici katmanı ile etkileşiminin sonlanması yine ses altı yanma moduna geçişe neden olmuştur. 0.5 mm hücre boyutunun kullanıldığı sayısal çalışmada ise enjektör duvarındaki toplam blokaj oranının % 16 olduğu hesaplanmıştır ve patlama dalgasının yayınıma devam ettiği tespit edilmiştir. C-J değerine göre elde edilen doğruluk ve sayısal çözümleme gereksinimleri düşünüldüğünde sayısal çalışmalarda 0.5 mm hücre boyutlarının kullanılması gerekliliği sonucuna varılmıştır. Doğrulama çalışmalarında kullanılan toplam hücre sayısı 89550'dir.

**Doğrulama Çalışmaları**

Dönen patlama motorlarında patlama dalgası ile eğik şok cephesinin yayınımı söz konusudur. Ayrıca, patlama dalgası cephesinde kimyasal reaksiyon kapsamında yeniden oluşumlar ve bozulmalar çok kısa sürelerde meydana gelmektedir. Patlama dalgası cephesindeki yüksek sıcaklık ve basınç değerlerinin bu kısa sürede oluşması sayısal yöntemleri zorlayan ve hatalara yol açan bir unsur olarak karşımızda durmaktadır. Doğrulama analizlerinde Liu *vd.* (2012) çalışması referans alınmıştır. DoPM kapsamında yapılan sayısal analizlerde yaşanılan zorluklar nedeniyle referans sayısal çalışmada hidrojen/hava (bir basamaklı tersinmez) kimyasal reaksiyon mekanizması tercih edilmiştir.
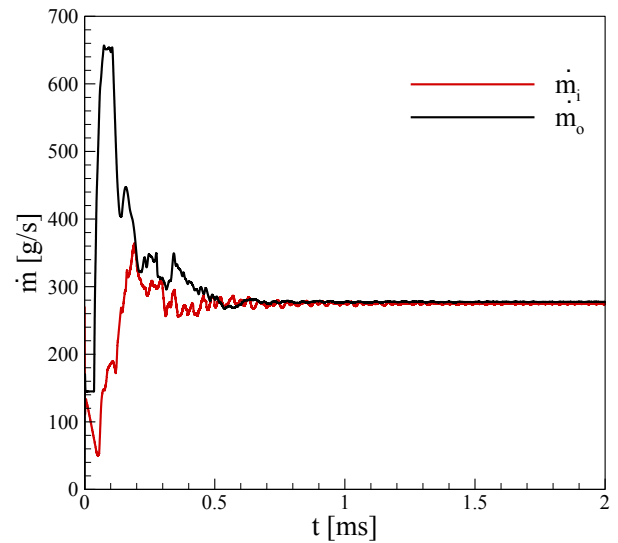


**Şekil 4.** Kütlesel debi değerinin zamanla gelişimi

Patlama dalgasının kararlı yapıya evrimi anına kadar patlama dalgası yüksekliği değerinde salınımlar meydana gelmektedir. Patlama dalgası yüksekliğindeki değişimler patlama dalgası şiddetini etkilemektedir. Dalga yüksekliğinin azalışı patlama dalgası şiddetini artırmaktadır. Bu durum patlama cephesi ve ardında daha yüksek basınç değerlerinin oluşmasına yol açmaktadır. Şekil 4'te verilen patlama kanalı girişindeki kütlesel debinin zamanla dağılımı incelendiğinde patlama kanalı girişindeki kütlesel debi ($\dot{m}_i$) değerinin ilk olarak 363.94 g/s değerine ani artış sergilediği ve sonrasında ise yine ani azalış ile 258.46 g/s değerine ulaştığı görülmektedir. Bu durum patlama dalgası ve ardındaki basınç değişimi

ile patlama kanalı girişinde meydana gelen blokaj oranındaki değişimi ortaya koymaktadır. Patlama dalgasının kararlı hale gelmesi (t=1.1 ms) sonrasında kütlesel debi değerinin neredeyse sabit olduğu görülmektedir. Referans çalışmada yer verilen deneysel çalışma kapsamında patlama kanalı girişindeki toplam kütlesel debi değerinin 272.7 g/s olduğu belirtilmiştir (Liu *vd.*, 2012). Bu değer doğrulama çalışmasında patlama dalgasının kararlı yapıya evrilmesi sonrası elde edilen ortalama kütlesel debi değeri olan 274.8 g/s değerine yakındır.

Patlama dalgası yayınımı konusunda patlama dalgasının hızı ve frekansı oldukça önemlidir. Kararlı bir dalga yapısında dalga hızı ve frekansı da neredeyse sabittir. Patlama dalgası frekansı Eş. (9)'da verilen bağıntı ile elde edilmiştir (Zheng *vd.*, 2020). Şekil 5'te verilen patlama dalgası hızı ve frekansı dağılımları incelendiğinde t=1.1 ms anına kadar büyük salınımların meydana geldiği görülmektedir. Patlama dalgası kararlı hale geldikten sonra dalga hızı ve frekansı değerlerinin periyodik salınımlar sergilediği belirlenmiştir. Kararlı patlama dalgasının ortalama hızı ve frekansı sırasıyla 1860 m/s ve 6.232 kHz'dir. Referans çalışmada yer verilen sayısal sonuçlarda ortalama dalga hızı ve frekansı değerlerinin sırası ile 1870.1 m/s ve 6.262 kHz'dir. Yapılan analizlerin bu açıdan da referans çalışma ile benzer sonuçlar aldığı söylenebilir.

$$f = \frac{n_D U_D}{\pi D} \qquad (9)$$
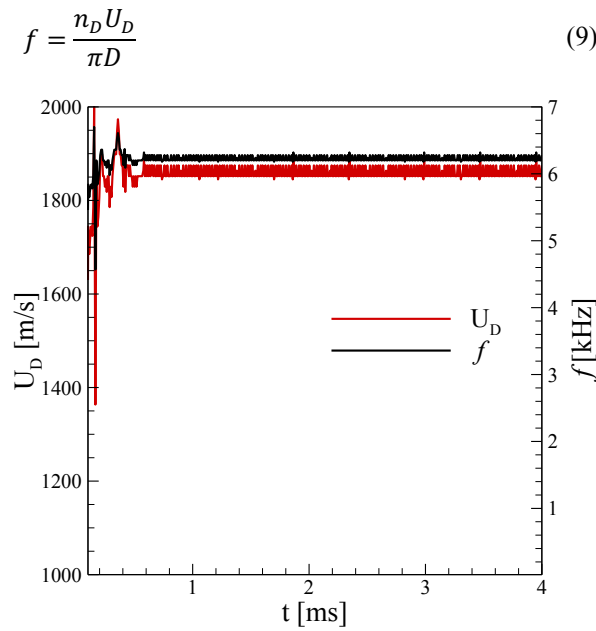


**Şekil 5.** Patlama dalgası hızı ve frekansı dağılımı

**Tablo 3.** Doğrulama çalışması sonuçları (Liu *vd.*,2012)

| Değişken | Sayısal Sonuçlar | Referans Çalışma | Teorik Değerler |
|---|---|---|---|
| $U_D$ [m/s] | 1860 | 1870.1 | 1968.12 |
| $f$ [kHZ] | 6.232 | 6.266 | 6.594 |
| $P_{det}$ [MPa] | 2.26 | 2.20 | N/A |
| $\dot{m}_{tot,inlet}$ [g/s] | 274.8 | 272.7 | N/A |

Doğrulama çalışması sonrasında kararlı patlama dalgasına yönelik elde edilen sonuçlar Tablo 3'te

verilmiştir. Doğrulama çalışmalarında kararlı patlama dalgası hızının teorik ve referans çalışma değerlerinin sırasıyla %94.5 ve %99.4'üne eşit olduğu hesaplanmıştır. Patlama dalgası cephesindeki basınç ($p_{det}$) değerinin doğrulama çalışmalarında 2.26 MPa'a ulaştığı görülmektedir. Patlama kanalı toplam kütlesel debi ve patlama dalgası cephesindeki basınç değerlerinin referans çalışmada belirtilen değerler arasındaki farkın sırası ile %0.7 ve %2.7 olduğu belirlenmiştir.

**Patlama Dalgası Yapısı**

Patlama dalgası cephesi kimyasal reaksiyon bölgesi ve şok dalgasını barındırmaktadır. Yüksek basınç ve sıcaklığın var olduğu bu bölgede meydana gelen enerji salınımı ile patlama dalgası cephesi yayınımı desteklenmektedir. Şekil 6'da bir basamaklı tersinmez kimyasal reaksiyon mekanizması kullanılarak gerçekleştirilen sayısal çalışmanın sonucu olarak patlama kanalındaki basınç ve sıcaklık dağılımları verilmiştir. Basınç ve sıcaklık dağılımları incelendiğinde akış yönünde eğik şok cephesinin meydana geldiği görülmektedir. Bunun yanı sıra sıcaklık dağılımları eğik şok cephesinin ardında yanma sonrası ürünlerin karışım bölgesini oluşturduğu belirlenmiştir.
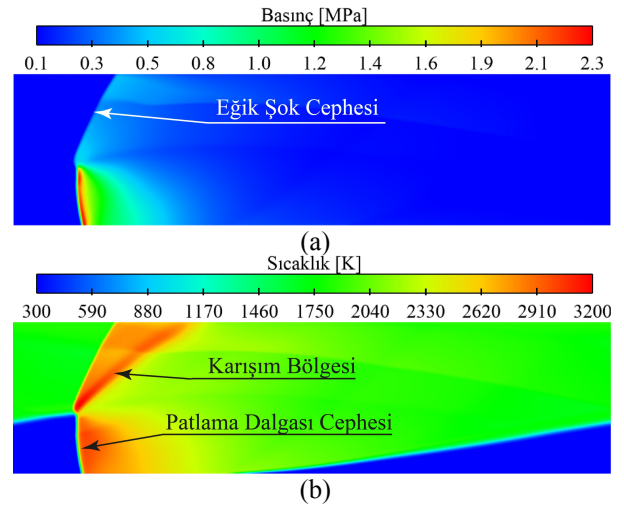


**Şekil 6.** t= 2ms anında patlama kanalında a) basınç ve b) sıcaklık dağılımı
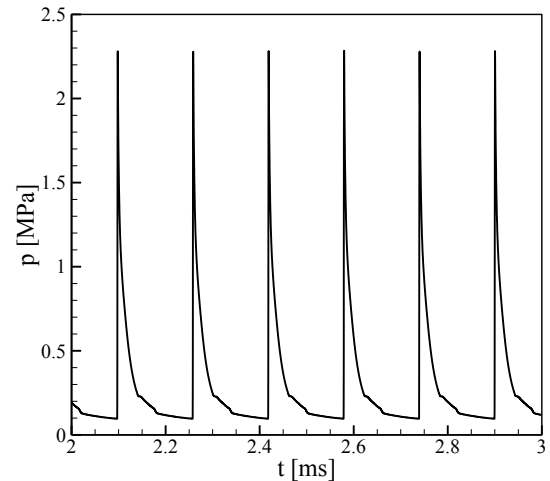


**Şekil 7.** t=2-3 ms aralığında patlama kanalında basınç gelişimi

Şekil 7'de verilen patlama kanalındaki basınç gelişimi incelendiğinde patlama dalgası cephesindeki basıncın 2.26 MPa değerine ulaştığı ve patlama dalgası ardında ise basınç, ani bir azalış sergileyerek 0.1 MPa değerine indiği görülmektedir. Patlama dalgasının kararlı hale evrilmesi ile periyodik değişimlerin meydana geldiği ve patlama cephesindeki basıncın her bir dalga turunda neredeyse sabit olduğu görülmektedir.



**Şekil 8.** Patlama kanalı girişi boyunca eksenel hız dağılımları

Patlama dalgası cephesinde ve ardında var olan yüksek basınç, temiz yakıt-hava girişini bloke etmektedir. Kararlı patlama dalgasına sahip dönen patlama motorlarında, temiz yakıt-hava karışımı patlama kanalında üçgensel bir bölge oluşturmaktadır ve patlama dalgası yüksekliği neredeyse sabittir. Patlama dalgası cephesi ve ardında var olan yüksek basınç dağılımı nedeniyle enjektör duvarında (patlama kanalı girişi) blokajlar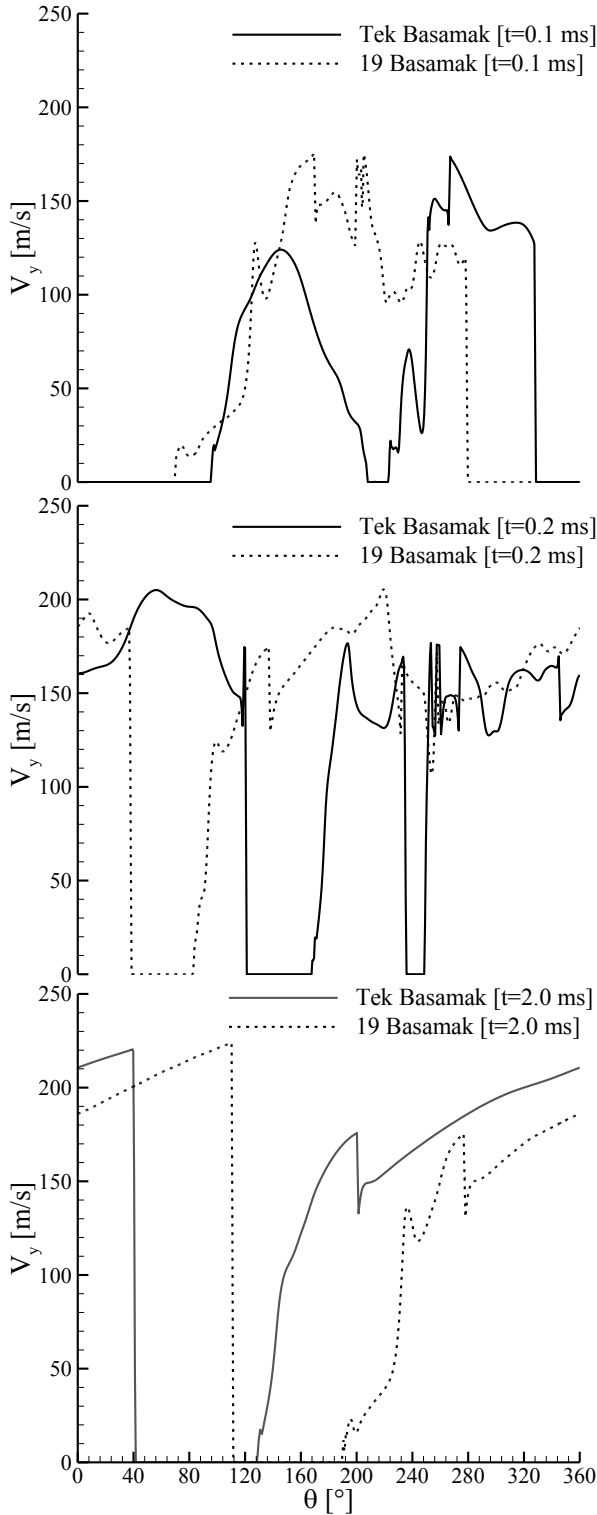 meydana gelmektedir. Bu durum temiz yakıt-hava karışımının patlama kanalına aktarımına engel olmaktadır. Şekil 8'de patlama kanalı girişindeki eksenel hız dağılımları verilmiştir. Patlama dalgasının geçişi anında enjektör duvarında görülen ters akışlar bu bölgelerde blokajın meydana geldiğini kanıtlamaktadır. Patlama dalgasının yayınımı süresince bu blokaj oranı değişkenlik göstermekle birlikte, patlama dalgasının kararlı hale gelmesinin ardından neredeyse sabit bir değere erişmektedir. Patlama dalgasının yayınımı süresince enjektör blokaj oranını üç farklı süreçte incelemek mümkündür. Patlama dalgasının ilk yayınımı süreci için t=0.1 ms, gelişim süreci için t=0.2 ve kararlı süreci için t=2.0 ms anı referans alınmıştır. Patlama dalgasının ilk yayınım zamanlarında 19 basamaklı ve 1 basamaklı tersinmez reaksiyonlar ile elde edilen sonuçlarda blokaj oranları sırası ile %41 ve %39'dur. Patlama dalgası cephesindeki basıncın patlama dalgası yayınımı süresince değişkenliği blokaj oranını da etkilemiş ve t=0.2 ms anında bu oranın sırası ile %12 ve %16'ya düşmesini sağlamıştır. Patlama dalgasının kararlı sürecinde blokaj oranlarının %21 ve %24 değerlerine ulaştığı tespit edilmiştir.

Patlama dalgasının yayınımı ve patlama dalgası yüksekliğinin değişim eğiliminin incelenebilmesi için patlama kanalındaki hidrojenin kütle fraksiyonu gradyanı dağılımı kullanılmıştır. Bu değişken temiz yakıt-hava bölgesini çevrelemekte ve patlama dalgası yüksekliğindeki değişimlerin incelenebilmesine olanak sağlamaktadır. Şekil 9'da patlama dalgası yayınımının ilk evrelerinde (t=0.1 ms) patlama dalgası yüksekliğinin ($h_{tot}$) yaklaşık 5 mm değerine kadar indiği görülmektedir. Bu durum patlama dalgası yüksekliğinin azalması ile patlama dalgası şiddetinin artmasını kanıtlamaktadır. Patlama dalgası şiddetindeki artış, patlama cephesi ve ardındaki basınç dağılımını da artırmakta ve var olan blokaj seviyesini de yükseltmektedir. Benzer eğilim, detaylı kimyasal reaksiyon mekanizması kullanıldığında da meydana gelmiştir. Detaylı kimyasal mekanizmanın kullanılması ile patlama dalgası yüksekliğinin t=0.1 ms anında yaklaşık 10 mm olduğu görülmektedir. Patlama dalgası yüksekliği sonraki turlarda artışlar göstererek kararlı haldeki ortalama dalga yüksekliği $h_{tot,ave}$=29 mm seviyesinin üzerine çıktığı belirlenmiştir. Tek basamaklı reaksiyon mekanizmasının kullanıldığı sayısal çalışmadaki patlama dalgası yüksekliğinin zamanla gelişimine benzer eğilimlerin detaylı kimyasal reaksiyon mekanizmasının kullanıldığı çalışmada da meydana geldiği tespit edilmiştir. Bir basamaklı reaksiyon mekanizmasının kullanıldığı çalışmadaki patlama dalgası yüksekliğinin detaylı kimyasal reaksiyon mekanizmasının kullanıldığı çalışmada dalga yüksekliğinden büyük olduğu görülmektedir. Kararlı

patlama dalgası yüksekliği bir basamaklı ve detaylı kimyasal reaksiyon mekanizması kullanıldığı çalışmalarda sırası ile 29 mm ve 27 mm'dir.



<div style="text-align:center">(a)      (b)</div>
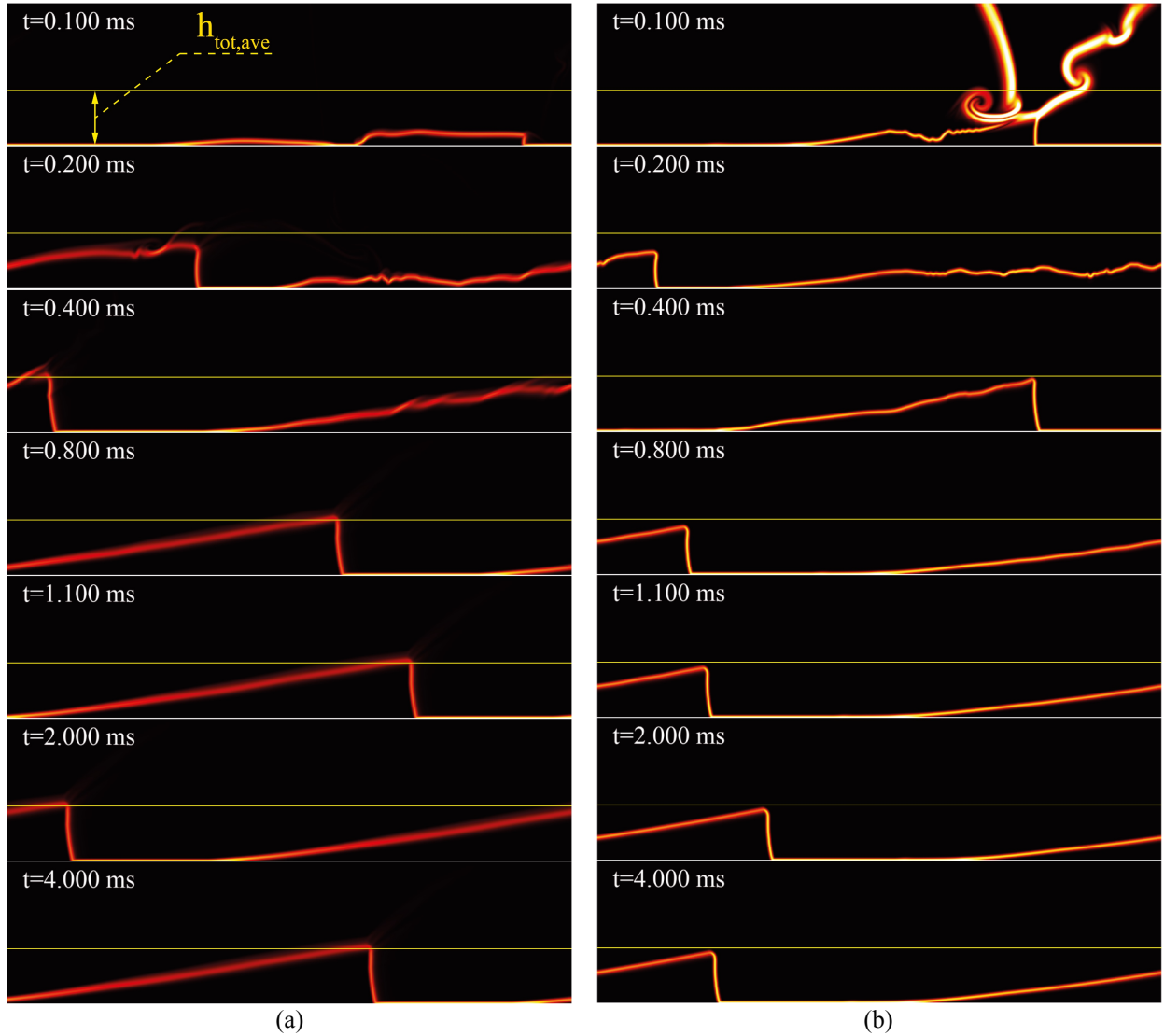
**Şekil 9.** Patlama kanalında hidrojen kütle fraksiyonu gradyanı dağılımı a) 1 basamaklı tersinmez ve b) 19 basamaklı tersinmez kimyasal reaksiyon mekanizması

### Döner Patlama Motoru Performansı

Sayısal çalışmalar sonrası patlama kanalı çıkışındaki itki dağılımının zamanla gelişimi Eş. (10)'da verilen bağıntı ile hesaplanmıştır (Sato ve Raman, 2020). Verilen bağıntıda "u" yüzey normali hızı, "$p_{back}$" ise geri basınç değerini ifade etmektedir.

$$F_{(t)} = \int\limits_{exit} \rho u^2 + (p - p_{back})dA_{exit} \qquad (10)$$

Şekil 10'da verilen itki dağılımı incelendiğinde, patlama dalgasının yüksekliğindeki değişimin eğik şok açısını etkilediği görülmektedir. Şekil 11'de verilen basınç gradyanı, patlama dalgası cephesi ve eğik şok cephesindeki değişimleri sergilemektedir. Patlama dalgasının ilk yayınım zamanlarında ortalama eğik şok açısının en yüksek seviyelere ulaştığı sonrasında ise ani

düşüş sergilediği görülmektedir. Ortalama eğik şok açısı t=0.1 ms anında 75°, t=0.2 ms anında ise 50° olduğu belirlenmiştir. Patlama dalgasının kararlı yapıya geçişi süresince eğik şok açısının yeniden artışların meydana geldiği görülmektedir. Patlama dalgası kararlı hale gelmesi ile ortalama eğik şok açısının 63° olduğu tespit edilmiştir.

Patlama kanalı çıkışı ve girişindeki toplam basınç oranları DoPM basınç kazanımını açıklar niteliktedir. Şekil 10'da verilen toplam basınç oranları incelendiğinde itki üretim dağılımına benzer bir eğilim söz konusudur. Patlama dalgası kararlı hale gelmeden önce yüksek salınımların meydana geldiği ve kararlı haldeki patlama dalgası sonrası toplam basınç oranlarının da sabit bir değere ulaştığı görülmektedir. Patlama dalgasının kararlı olması ile toplam basınç oranı değerinin 3.95±0.06 olduğu belirlenmiştir.
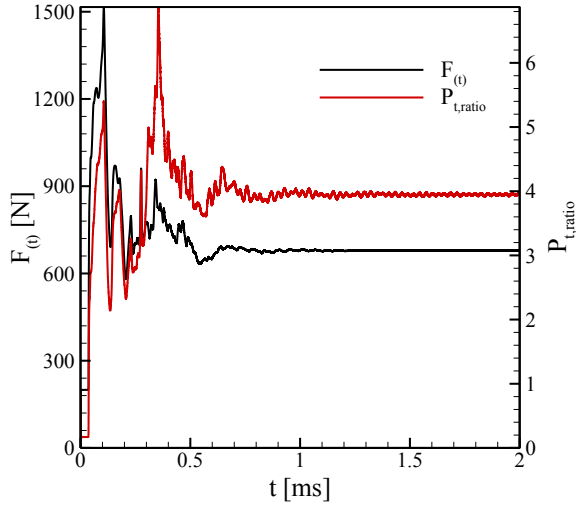
**Şekil 10.** İtki ve toplam basınç oranı dağılımı
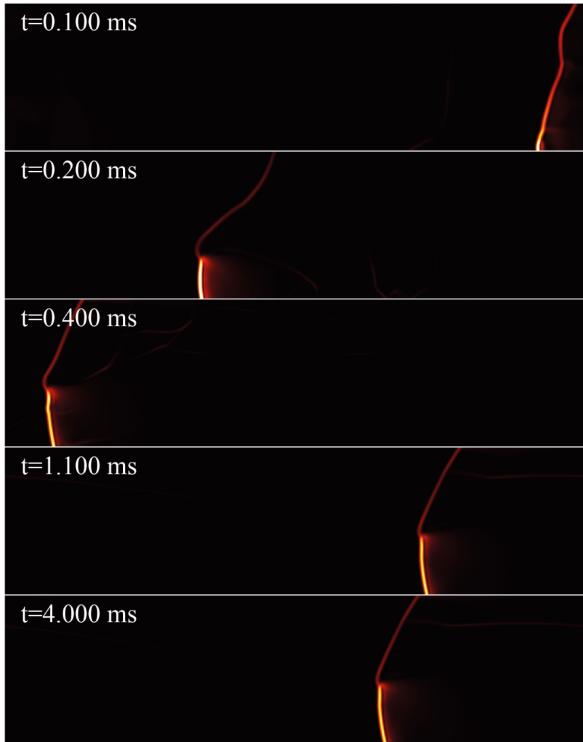


**Şekil 11.** Patlama dalgası ve eğik şok cephesinin zamana göre değişimi

Eğik şok cephesi ve patlama dalgasındaki değişimler, patlama kanalı çıkışındaki itki dağılımında salınımlara neden olmaktadır. Şekil 12'de tek basamaklı reaksiyon mekanizmasının kullanıldığı çalışmada patlama kanalı çıkışındaki basınç ve eksenel hız dağılımları verilmiştir. Eğik şok cephesi sonrası basınç ve eksenel hız değerlerinde ani artışların meydana geldiği görülmektedir. Ortalama eğik şok açısının artışı bu akış değişkenlerinin de artışına neden olmaktadır. Patlama dalgasının ilk yayınımı (t=0.1 ms), geçiş (t=0.2 ms) ve kararlı (t=4 ms) evrelerinde eğik şok cephesindeki basınç değerleri sırası ile 0.69 MPa, 0.31 MPa ve 0.42 MPa'dır. Belirtilen evrelerde eksenel hız dağılımlarının ise sırası ile 1140 m/s, 957 m/s ve 1068 m/s olduğu belirlenmiştir. Bu dağılımlar Şekil 10'da verilen patlama kanalı çıkışındaki itkinin zamanla

gelişim eğilimini de açıklayıcı niteliktedir ve kararlı dalga evresi (t=1.1 ms) sonrasında üretilen itki değerinin 678.7±2.3 N aralığında salınımlar yaptığı belirlenmiştir.
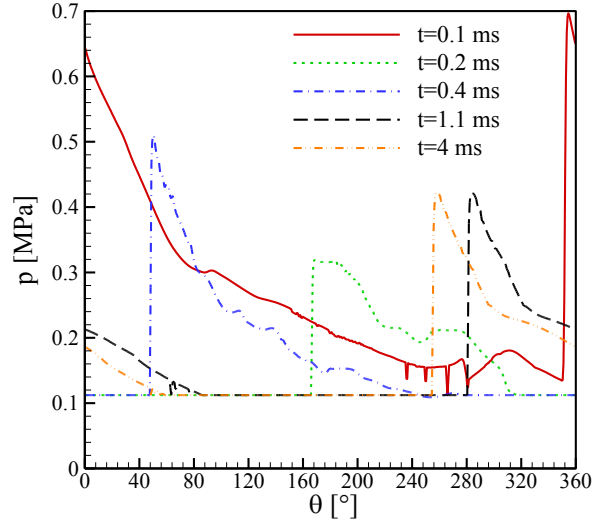


(a)
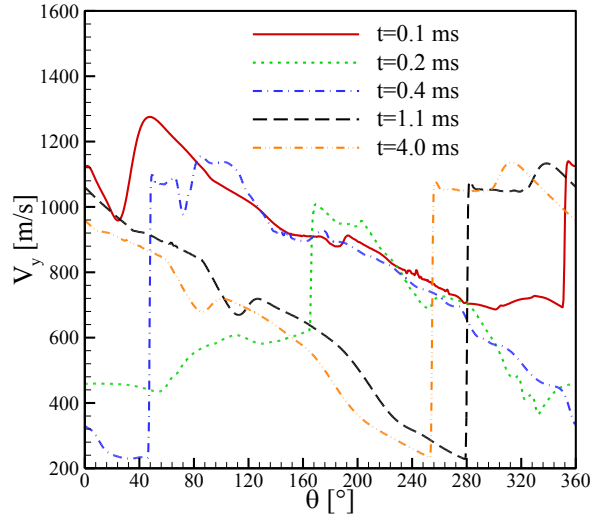


(b)

**Şekil 12.** Patlama kanalı çıkışında a) basınç ve b) eksenel hız dağılımı

Şekil 13'te tek basamaklı kimyasal reaksiyon mekanizmasının kullanıldığı çalışmada patlama kanalındaki Mach sayısı ve patlama kanalı çıkışında akış açısı dağılımı verilmiştir. Mach sayısı dağılımı incelendiğinde, eğik şok ve patlama dalgası cephesi sonrası akışın ses üstü olduğu görülmektedir. Patlama dalgası kararlı yapıya dönüşmesinin ardından patlama kanalı çıkışında ses üstü rejim bölgesi oranın %45'e ulaştığı belirlenmiştir.

Eş. (10)'da verilen itki bağıntısında da görüldüğü üzere patlama kanalı çıkışında momentum itki kazanımı patlama kanalı çıkışı normali hızı ($V_y$) ile elde edilebilmektedir. Şekil 13'te verilen akış açısı dağılımı incelendiğinde eğik şok cephesi sonrası akış açısı değerlerinde ani bir düşüşün gerçekleştiği görülmektedir. Eğik şok cephesi sonrası azimuthal

momentumun kısmen eksenel momentuma dönüştüğünü göstermektedir.
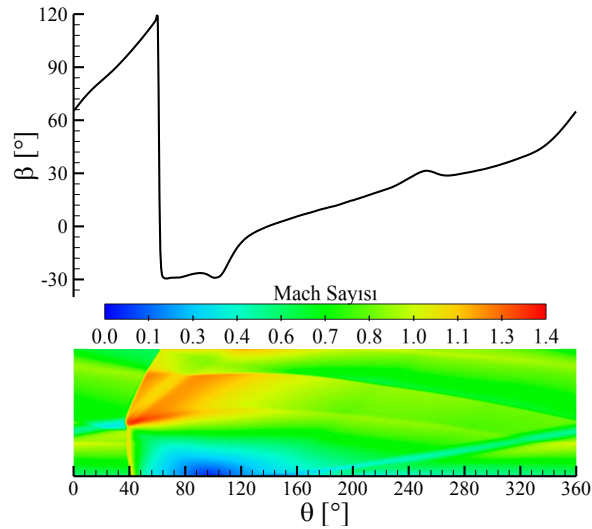


**Şekil 13.** t=2 ms anında Mach Sayısı ve patlama kanalı çıkışında akış açısı

### SONUÇLAR

Bu çalışmada DoPM'nun itki performansı ve patlama dalgası yapısı incelenmiştir. Sayısal çalışma iki aşamada gerçekleştirilmiştir. İlk olarak referans alınan çalışmaya yönelik doğrulama çalışmaları gerçekleştirilmiştir. Referans çalışmada yakıt ve oksitleyici olarak hidrojen-hava karışımı kullanılmıştır. Hidrojen 0.8 mm çapında 90 enjektör kanalından, hava ise 0.4 mm genişliğindeki kanaldan patlama kanalına yönlendirilmektedir. Doğrulama çalışmaları için referans çalışmada da belirtildiği üzere bir basamaklı tersinmez hidrojen-hava mekanizması kullanılmıştır. Dalga yapısının daha detaylı irdelenebilmesi için ikinci aşamada 19 basamaklı tersinmez hidrojen-hava kimyasal mekanizması tanımlanmıştır. Doğrulama çalışmaları sonrası patlama dalgasının kararlı hali ve öncesindeki yapısı ile DoPM'nun itki performansı incelenmiştir. Sayısal çalışmalardan elde edilen sonuçlar aşağıda sıralanmıştır.

- Kararlı haldeki patlama dalgası her bir periyodu ($t_{det}$) yaklaşık 0.159 ms tamamlamaktadır. Patlama dalgasının $t/t_{dej}$=6.892 sonrasında kararlı hale geldiği belirlenmiştir.
- Patlama dalgasının kararlı hale gelmesi ile patlama kanalı girişi ve çıkışındaki kütlesel debi değerleri neredeyse sabit değere ulaşmıştır. Referans deneysel çalışmada belirlenen kütlesel debi değeri ile sayısal çalışmalardan elde edilen kütlesel debi değeri arasında %0.7'lik bir fark olduğu belirlenmiştir.
- Referans sayısal çalışmada kararlı patlama dalgası cephesindeki basınç değerinin 2.2 MPa, sayısal çalışmada ise bu değerin 2.26 MPa olduğu belirlenmiştir. Patlama dalgası hızı incelendiğinde teorik ve referans çalışma değerlerinin sırası ile %94.5 ve % 99.4'üne eşit olduğu saptanmıştır.

- Doğrulama çalışmaları sonrası patlama dalgası yapısı irdelendiğinde kararlı patlama dalgası yüksekliğinin ve eğik şok açısının değişmediği gözlemlenmiştir. Kararlı patlama dalgası yüksekliği bir basamaklı ve detaylı kimyasal reaksiyon mekanizmalarında sırası ile 29 mm ve 27 mm olduğu belirlenmiştir.
- Patlama kanalındaki eksenel hız değerleri incelendiğinde patlama kanalı girişinde ters akışın meydana geldiği bölgeler tespit edilmiştir. Bu durum patlama kanalı cephesindeki ve ardındaki yüksek basınç dağılımları ile gerçekleşmektedir. Blokaj oranının patlama dalgasının kararlı yapıya ulaşmadan önce tek basamaklı ve detaylı kimyasal reaksiyon mekanizmasının kullanıldığı çalışmalarda sırası ile %41 ve %39'a yükselmiştir. Patlama dalgası kararlı hale gelmesi ile blokaj oranında bir değişimin meydana gelmediği ve sırası ile %21 ve %24' e eşit olduğu belirlenmiştir.
- Patlama kanalındaki Mach sayısı dağılımı incelendiğinde eğik şok ve patlama dalgası cephesi ardında akışın ses üstü olduğu tespit edilmiştir. Kararlı patlama dalgası elde edildiğinde patlama kanalı çıkışının %45'inin ses üstü rejime sahip olduğu belirlenmiştir.

### REFERANSLAR

Alam, N., Sharma, K. K., Pandey, K. M., 2019, Combustion characteristics of hydrogen-air mixture in pulse detonation engines, *Journal of Mechanical Science and Technology*, 33(5), 2451-2457, doi:10.1007/s12206-019-0442-7

Bach, E., Oliver Paschereit, C., Stathopoulos, P., Bohon, M. D., 2021, An empirical model for stagnation pressure gain in rotating detonation combustors, *Proceedings of the Combustion Institute*, 38(3), 3807-3814, doi.org/10.1016/j.proci.2020.07.071

Bigler, B. R., Paulson, E. J., Hargus, W. A., 2017, Idealized Efficiency Calculations for Rotating Detonation Engine Rocket Applications, *AIAA Propulsion and Energy Forum*, doi: 10.2514/6.2017-5011

Chen, Y., Liu, X., Wang J., 2018, Influences of Separate Injectors on Rotating Detonation Engines, *2018 Joint Propulsion Conference*, doi:10.2514/6.2018-4785

Choi, J. Y., Jeung, I. S., Yoon, Y., 2000, Computational Fluid Dynamics Algorithms for Unsteady Shock-

Induced Combustion, Part 1: Validation. *AIAA Journal*, 38(7), 1179–1187, doi:10.2514/2.1112

Driscoll, R., Stoddard, W., George, A. S., Gutmark E., 2015, Shock Transfer and Shock-Initiated Detonation in a Dual Pulse Detonation Engine/Crossover System, *AIAA Journal*, 53, 132–139, doi:10.2514/1.j053027

Escobar, S., Pakalapati, S. R., Celik, I., Ferguson, D. Strakey, P., 2013, Numerical Investigation of Rotating Detonation Combustion in Annular Chambers, *Volume 1A: Combustion, Fuels and Emissions*, doi:10.1115/gt2013-94918

Ettner, F., Vollmer, K. G., Sattelmayer, T., 2014, Numerical Simulation of the Deflagration-to-Detonation Transition in Inhomogeneous Mixtures, *Journal of Combustion*, 2014, 1–15, doi:10.1155/2014/686347

Heidari, A., Ferraris, S., Wen, J. X., Tam, V. H. Y., 2011, Numerical simulation of large scale hydrogen detonation, *International Journal of Hydrogen Energy*, 36, 2538–2544, doi:10.1016/j.ijhydene.2010.05.09

Ladeinde, F., Oh, H., Jacobs, S., 2023, Supersonic combustion heat flux in a rotating detonation engine, *Acta Astronautica*, 203, 226-245, doi.org/10.1016/j.actaastro.2022.11.044

Lee J. H. S., 2010, The detonation Phenomenon, Cambridge University Press.

Lei, Z., Yang, X., Ding, J., Weng, P., Wang, X., 2020, Performance of rotating detonation engine with stratified injection, *Journal of Zhejiang University-SCIENCE A*, 21, 734–744, doi:10.1631/jzus.a1900383

Lietz, C., Ross, M., Desai, Y., Hargus, W. A., 2020, Numerical investigation of operational performance in a methane-oxygen rotating detonation rocket engine, *AIAA Scitech 2020 Forum*, doi:10.2514/6.2020-0687

Liu, S.J., Lin, Z. Y., Liu, W. D., Lin, W., Sun, M.B., 2012, Experimental and three-dimensional numerical investigations on H2/air continuous rotating detonation wave, *Proceedings of the Institution of Mechanical Engineers, Part G: Journal of Aerospace Engineering*, 227, 326–341, doi:10.1177/0954410011433542

Lu, F. K., Braun, E. M., 2014, Rotating Detonation Wave Propulsion: Experimental Challenges, Modeling, and Engine Concepts, *Journal of Propulsion and Power*, 30, 1125–1142, doi:10.2514/1.b34802

Ma, F., Choi, J. Y., Yang, V., 2005, Thrust Chamber Dynamics and Propulsive Performance of Single-Tube Pulse Detonation Engines, *Journal of Propulsion and Power*, 21, 512–526, doi:10.2514/1.7393

Ma, J. Z., Luan, M. Y., Xia, Z. J., Wang, J. P., Zhang, S., Yao, S., Wang, B., 2020, Recent Progress, Development Trends, and Consideration of Continuous Detonation Engines, *AIAA Journal*, 58, 4976–5035, doi:10.2514/1.j058157

Ma, Z., Zhang, S., Luan, M., Yao, S., Xia Z., Wang, J., 2018, Experimental research on ignition, quenching, reinitiation and the stabilization process in rotating detonation engine, *International Journal of Hydrogen Energy*, doi:10.1016/j.ijhydene.2018.08.06

Melguizo-Gavilanes, J., Rezaeyan, N., Tian, M., Bauwens, L., 2011, Shock-induced ignition with single step Arrhenius kinetics, *International Journal of Hydrogen Energy*, 36, 2374–2380, doi:10.1016/j.ijhydene.2010.04.13

Ó Conaire, M., Curran, H. J., Simmie, J. M., Pitz ,W. J., Westbrook , C. K., 2004, A comprehensive modeling study of hydrogen oxidation, *International Journal of Chemical Kinetics*, 36, 603–622, doi:10.1002/kin.20036

Prakash, S., Raman, V., Lietz, C., Hargus, W. A., Schumaker, S. A., 2020, High Fidelity Simulations of a Methane-Oxygen Rotating Detonation Rocket Engine, *AIAA Scitech 2020 Forum*, doi:10.2514/6.2020-0689

Sato, T., Raman, V, 2020, Detonation Structure in Ethylene/Air-Based Non-Premixed Rotating Detonation Engine, *Journal of Propulsion and Power*, 36, 1–11, doi:10.2514/1.b37664

Shao, Y-T, Liu, M., Wang, JP., 2010, Numerical investigation of rotating detonation engine propulsive performance, *Combustion Science and Technology*, 182, 1586–1597, doi:10.1080/00102202.2010.497316

Schauer, F., Miser, C., Tucker, C., Bradley, R., Hokell, J., 2005, Detonation Initiation of Hydrocarbon-Air Mixtures in a Pulsed Detonation Engine, *43rd AIAA Aerospace Sciences Meeting and Exhibit*, doi:10.2514/6.2005-1343

Schwer, D., Kailasanath, K., 2011, Effect of Inlet on Fill Region and Performance of Rotating Detonation Engines, *47th AIAA/ASME/SAE/ASEE Joint Propulsion Conference & Exhibit*, doi:10.2514/6.2011-6044

Strempfl, P., Dounia, O., Laera, D., Poinsot, T., 2024, Effects of mixing assumptions and models for LES of Hydrogen-fueled Rotating Detonation Engines, *International Journal of Hydrogen Energy*, 62, 1-16, doi.org/10.1016/j.ijhydene.2024.03.033

Su, L., Wen, F., Wang, S., Wang, Z., 2022, Analysis of energy saving and thrust characteristics of rotating detonation turbine engine, *Aerospace Science and Technology*, 124, 107555, doi.org/10.1016/j.ast.2022.107555

Sun, J., Zhou, J., Liu, S., Lin, Z., Lin W., 2018, Plume flowfield and propulsive performance analysis of a rotating detonation engine, *Aerospace Science and Technology*, 81, 383-393, doi:10.1016/j.ast.2018.08.024

Sun, J., Zhou, J., Liu, S., Lin, Z., Lin, W., 2019a, Effects of air injection throat width on a non-premixed rotating detonation engine, *Acta Astronautica*, 159, 189–198, doi:10.1016/j.actaastro.2019.03.0

Sun, J., Zhou, J., Liu, S., Lin, Z., 2019b, Interaction between Rotating Detonation Wave Propagation and Reactant Mixing, *Acta Astronautica*, 164, 197-203, doi:10.1016/j.actaastro.2019.08.0

Vignat, G., Brouzet, D., Bonanni, M., Ihme, M., 2024, Analysis of weak secondary waves in a rotating detonation engine using large-eddy simulation and wavenumber-domain filtering, *Combustion and Flame*, 263, 113387, doi.org/10.1016/j.combustflame.2024.113387

Wang, C., Liu, W., Liu, S., Jiang, L., Lin, Z., 2015, Experimental verification of air-breathing continuous rotating detonation fueled by hydrogen, *International Journal of Hydrogen Energy*, 40, 9530–9538, doi:10.1016/j.ijhydene.2015.05.06

Wang, F., Weng, C., Wu, Y., Bai, Q., Zheng, Q., Xu H., 2020, Numerical research on kerosene/air rotating detonation engines under different injection total temperatures, *Aerospace Science and Technology*, 105899, doi:10.1016/j.ast.2020.105899

Wang, F., Weng, C., 2022, Numerical research on two-phase kerosene/air rotating detonation engines, *Acta Astronautica*, 192, 199-209, doi.org/10.1016/j.actaastro.2021.12.026.

Wescott, B. L., Stewart, D. S., Bdzil, J. B., 2004, On Self-Similarity of Detonation Diffraction, *Physics of Fluids*, 16, 373–384, doi:10.1063/1.1633552

Wu, D., Liu, Y., Liu, Y., Wang, J., 2014, Numerical investigations of the restabilization of hydrogen–air rotating detonation engines, *International Journal of Hydrogen Energy*, 39, 15803–15809, doi:10.1016/j.ijhydene.2014.07.15

Xia, Z.-J., Sheng, Z. H., Shen, D. W., Wang, J. P., 2021, Numerical investigation of pre-detonator in rotating detonation engine, *International Journal of Hydrogen Energy*, 46(61), 31428–31438, doi.org/10.1016/j.ijhydene.2021.07.013

Yan, C., Teng, H., Ng, H. D., 2021, Effects of slot injection on detonation wavelet characteristics in a rotating detonation engine, *Acta Astronautica*, 182, 274–285, doi.org/10.1016/j.actaastro.2021.02.010

Yi, T. H., Turangan, C., Lou, J., Wolanski, P., Kindracki, J., 2009, A Three-Dimensional Numerical Study of Rotational Detonation in an Annular Chamber, *47th AIAA Aerospace Sciences Meeting Including The New Horizons Forum and Aerospace Exposition*, doi:10.2514/6.2009-634

Yi, T. H., Lou, J., Turangan, C., Choi, J.Y., Wolanski P, 2011, Propulsive Performance of a Continuously Rotating Detonation Engine, *Journal of Propulsion and Power*, 27, 171–181, doi:10.2514/1.46686

Yu, J., Yao, S., Li, J., Li, J., Guo, C., Zhang, W., 2023, Numerical investigation of the rotating detonation engine with cat-ear-shaped film cooling holes under varying operating modes, *Aerospace Science and Technology*, 142, 108462, doi.org/10.1016/j.ast.2023.108642

Zhang, L. F., Zhang, S. J., Ma, Z., Luan, M. Y., Wang, J.P., 2019, Three-dimensional numerical study on rotating detonation engines using reactive Navier-Stokes equations, *Aerospace Science and Technology*, 93, 1-10, doi:10.1016/j.ast.2019.07.004

Zhao, M., Zhang, H., 2020, Large eddy simulation of non-reacting flow and mixing fields in a rotating detonation engine, *Fuel*, 280, 1-16, doi:10.1016/j.fuel.2020.118534

Zhang, S., Ma, J. Z., Wang, J., 2020, Theoretical and Numerical Investigation on Total Pressure Gain in Rotating Detonation Engine, *AIAA Journal*, 58, 1–12, doi:10.2514/1.j059259

Zhang, S., Yao, S., Luan, M., Zhang, L., Wang, J., 2018, Effects of injection conditions on the stability of rotating detonation waves, *Shock Waves*, 28, 1079-1087, doi:10.1007/s00193-018-0854-9

Zheng, H., Meng, Q., Zhao, N., Li, Z., Deng, F., 2020, Numerical investigation on H2/Air non-premixed rotating detonation engine under different equivalence ratios, *International Journal of Hydrogen Energy*, 45, 2289–2307, doi:10.1016/j.ijhydene.2019.11.01

# RÜZGAR ENERJİSİ GÜÇ YOĞUNLUĞU TAHMİNİNDE OPTİMUM WEİBULL OLASILIK DAĞILIM PARAMETRELERİNİN ELDE EDİLMESİ İÇİN İSTATİSTİK, MATEMATİK VE FİZİK TABANLI ALGORİTMALARIN KARŞILAŞTIRMALI ANALİZİ: LORAS VE FOÇA ÖRNEKLERİ

**Bayram KÖSE\*, Bekir Can TELKENAROĞLU\*\*, Bahar DEMİRTÜRK\*\*\***

\* İzmir Bakırçay Üniversitesi, Mühendislik ve Mimarlık Fakültesi, Elektrik Elektronik Mühendisliği,
İzmir, Türkiye, bayram.kose@bakircay.edu.tr https://orcid.org/0000-0003-0256-5921
\*\* İzmir Bakırçay Üniversitesi, Lisansüstü Eğitim Enstitüsü, Akıllı Sistemler Mühendisliği,
İzmir, Türkiye, 6016039@bakircay.edu.tr https://orcid.org/0000-0002-7085-6790
\*\*\*İzmir Bakırçay Üniversitesi, Mühendislik ve Mimarlık Fakültesi, Temel Bilimler Bölümü,
İzmir, Türkiye, bahar.demirturk@bakircay.edu.tr https://orcid.org/0000-0002-5911-5190

**Özet:** Bu çalışmada, genellikle elektrik enerjisi üretiminde tercih edilen rüzgar enerjisinin fizibilite ve verimlilik çalışmalarında kullanılan Weibull olasılık dağılım fonksiyonunun k ve c parametrelerinin, Isıl İşlem Algoritması(SA) ve Genelleştirilmiş İndirgenmiş Gradyan Algoritması(GRG) ile tahminlemesi yapılmıştır. Fonksiyon parametreleri ayrıca klasik sayısal yöntemlerden En Küçük Kareler Yöntemi(LMS), Justus Ampirik Moment Metodu(EMJ) ve Lysen Ampirik Moment(EML) Metodu ile tahmin edilmiştir. Sonuçlar kıyaslanırken belirlilik(determinasyon) katsayısı, hata kareleri ortalamasının karekökü(RMSE) ve ki-kare dağılımı($\chi^2$) kriterlerinden faydalanılmıştır. Tahminlenen şekil ve ölçek parametresiyle rüzgar hız frekans dağılımları hesaplanarak ölçüm sonuçları ile karşılaştırılmıştır. Sonuç olarak Genelleştirilmiş İndirgenmiş Gradyan Algoritmasının klasik sayısal yöntemlere göre Loras gözlem istasyonunda 0.0182 RMSE, 0.8473 belirlilik katsayısı, ve 0.0079 $\chi^2$ değeri ile, Foça gözlem istasyonunda da 0.0066 RMSE, 0.9793 belirlilik katsayısı, ve 0.0011 $\chi^2$ değeri ile daha iyi sonuçlar verdiği görülmüştür.
**Anahtar Kelimeler:** Yenilenebilir Enerji Kaynakları, Weibull dağılımı parametreleri, Isıl İşlem Algoritması, Genelleştirilmiş İndirgenmiş Gradyan Algoritması, Klasik Sayısal Yöntemler, Rüzgar Enerjisi Potansiyeli.

# COMPARATIVE ANALYSIS OF MATHEMATICS, STATISTICS AND PHYSICS BASED ALGORITHMS FOR OBTAINING OPTIMUM WEIBULL PROBABILITY DISTRIBUTION PARAMETERS FOR POWER DENSITY ESTIMATION IN WIND ENERGY: LORAS AND FOÇA EXAMPLES

**Abstract:** In this work, the k and c parameters of the Weibull probability distribution function, which is generally used in the feasibility and efficiency studies of wind energy and preferred in electrical energy production, were estimated by Simulated Annealing Algorithm (SA) and Generalized Reduced Gradient Algorithm (GRG). Function parameters were also estimated by classical numerical methods, Least Squares Method(LMS), Justus Empirical Moment Method(EMJ) and Lysen Empirical Moment Method(EML). When comparing the results, the coefficient of determination, the root mean square error (RMSE) and the chi-square distribution criteria($\chi^2$) were used. Wind speed frequency distributions were calculated with the estimated shape and scale parameter and compared with the measurement results. Consequently, better results can be seen from GRG algorithm than the classical numerical methods with coefficient of value of 0.0182 RMSE, determination of 0.8473, and the value $\chi^2$ of 0.0079 for Loras and with coefficient of value of 0.0066 RMSE, determination of 0.9793, and the value $\chi^2$ of 0.0011 for Foça.
**Keywords:** Renewable Energy Sources,Weibull distribution parameters, Simulated Annealing Algorithm, Generalized Reduced Gradient Algorithm, Classical Numerical Methods, Wind Energy Potential.

## GİRİŞ (INTRODUCTION)

Yenilenebilir enerji kaynakları, fosil yakıtların yakılmasının neden olduğu kirlilik ve iklim değişiklikleri başta olmak üzere insanlığın geleceğini sarsıcı bir şekilde etkileyebilecek olan çevresel sorunların minimize edilmesinde en önemli çözüm alternatiflerinden biri olarak görünmektedir (Hayli, 2001). Doğanın insanlığa sunmuş olduğu enerji kaynakları arasında hem çevresel kirlilik ve iklim üzerinde yıkıcı etkiler bırakmayan doğa dostu olması, hem de herhangi bir hammadde maliyetinin olmaması özellikleri rüzgarı oldukça yaygın kullanımı olan yenilenebilir enerji kaynağı haline dönüştürmüştür (Bayraktar ve Kaya, 2016).

Yaşamın ve üretim süreçlerinin enerjiye olan bağımlılıkları her geçen gün yeni enerji kaynakları arama girişimlerini hızlandırmaktadır (Çukurçayır ve Sağır, 2008). Bu girişimlerin doğal bir sonucu olarak özellikle son yıllarda enerji kaynaklarında önemli bir çeşitlenmenin ortaya çıktığı görülmektedir. Etkinlik, verimlilik ve karlılık ilkeleri çerçevesinde şekillenen ekonomik koşullar odağında ortaya çıkan çeşitlenmiş enerji kaynaklarının çevreye olan olumsuz etkilerinin yoğun olduğu gözlenmektedir. Bu durum enerji kaynaklarıyla çevresel faktörler arasında her geçen gün derinleşmekte olan bir uyumsuzluğun varlığına işaret etmekte ve hem mevcut çevresel krizlerin yıkıcı etkilerinin arttığına hem de farklı çevresel sorunların gelmekte olduğuna dair göstergeler sunmaktadır. Enerji ve çevre faktörleri uyuşmazlıkları temelindeki çatışmanın sonucu olarak ortaya çıkan ve çıkacak olan çevresel krizlerin yıkıcı etkilerinden kurtulma niyeti gelişmiş ve gelişmekte olan birçok ülkede temiz, ekonomik ve yeni fırsatlar sunabilme potansiyeline sahip yenilenebilir enerji kaynakları kullanımına olan ilgiyi her geçen gün arttırmaktadır. Bu artan ilgiye bağlı olarak önemli yenilenebilir enerji kaynaklarından biri olan rüzgar, dünyanın en yaygın yatırım ve kullanım alanı olan enerji kaynaklarından biri haline gelmiştir. Karadağ, enerji çevre ilişkisine kapsamlı bir şekilde yer vererek rüzgar enerjisinin ülkemiz için uygun bir kaynak olduğunu saptamıştır (Karadağ, 2009).

Rüzgarın diğer enerji kaynaklarından farklı olarak değişken ve aralıklı olması rüzgar temelli enerjinin üretilmesi ve kullanılması açısından oldukça önemlidir. Bunun yanında bir bölgede hakim olan rüzgarın karakteristik özelliklerinin belirlenmesi, üretilecek enerji üzerinde belirleyici olan diğer önemli bir faktördür. İfade edilen hususlar, rüzgar enerjisinin etkin ve verimli bir şekilde üretiminin sağlanmasına yönelik enerji potansiyelinin hesaplanmasında rüzgar hızı frekans dağılımının tahminlenmesini oldukça önemli hale getirmektedir. Bu önem temelinde rüzgar hızı frekans dağılımının tahminlenmesinde güvenilir ve doğru yöntemleri bulmaya yönelik çok sayıda araştırmanın yapılmış olduğu görülmektedir. Bu araştırmalar incelendiğinde, yaşam verilerinden hava durumu verilerine kadar birçok analizde yaygın olarak kullanılan Weibull dağılımının, rüzgar hız frekans dağılımının da doğru bir şekilde analiz edilmesinde yaygın olarak kullanılan istatistikteki modellerden birisi olduğunu göstermektedir.

Aslan ve Yaşar, rüzgar hızının enerji üretimi için düşük olduğu bir bölge olan Dumlupınar üniversitesi kampüsündeki düşük güçlü fakat yüksek kapasite faktörüne sahip türbin seçimi yaparak elektrik enerjisi üretimi üzerine bir çalışma yapmıştır. Yılmaz (2021), çalışmasında iki parametreli Weibull dağılımı ve Rayleigh dağılımının parametrelerinin, maksimum olabilirlik metodu (MLM) ile tahminlerini yapıp ele alınan bölgelerdeki rüzgar hızı verileri ile karşılaştırarak, gerçeğe en yakın sonuçları veren dağılım fonksiyonunun belirlenmesi problemini ele almıştır. Chen *vd.* (2021), Norveç Arktik bölgesindeki beş rüzgar parkının rüzgar

hızını modellemek için farklı olasılık yoğunluk fonksiyonları kullanarak, sayısal hava tahmin modellerinden ve ölçümlerden elde edilen rüzgar hızı verileri arasında bir karşılaştırma yapışmışlardır. Bu çalışmanın sonuçları, tek bir olasılık fonksiyonunun tüm senaryolarda daha iyi performans göstermediğini ortaya koymaktadır. Gülersoy ve Çetin (2010), Menemen bölgesinde rüzgar tribünleri için Rayleigh ve Weibull dağılımlarını kullanmıştır. Kaplan (2016), Rayleigh ve Weibull dağılımları kullanılarak Osmaniye bölgesinde rüzgar enerjisinin değerlendirilmesi üzerine çalışmıştır. Böylece yapılan diğer araştırmalar da göz önüne alındığında, rüzgar karakteristiği ve enerji potansiyelinin hesaplanmasında rüzgar hızı frekans dağılımının tahminlenmesinde olasılık yoğunluk fonksiyonlarından faydalanılması gerektiğine dair önemli bulgular sunmaktadır. Bilindiği üzere ilgili bölgedeki rüzgar hızları çeşitli aralıklarla sınıflandırılarak bir olasılık dağılımı fonksiyonu yardımıyla karakterize edilebilir. Bu durumda Weibull olasılık dağılımı, belirlenen bölgede bir ölçümün yapılmasında önemli bir ölçüm ve değerlendirme aracı olarak ön plana çıkmaktadır. İki parametreli Weibull olasılık dağılımı hem parametrelerin kolay belirlenebilmesi üstünlüğü hem de farklı bölgelerdeki doğruluk oranları nedeniyle pek çok alanda rüzgar karakteristik özelliklerinin tahminlenmesinde yararlanılan önemli bir yöntem haline gelmiştir.

Weibull olasılık dağılım fonksiyonu "k" şekil parametresi ve "c" ölçek parametresi ile karakterize edilen iki parametreli bir fonksiyondur. Weibull olasılık dağılımının rüzgar karakteristik özelliklerinin belirlenmesinde farklı sayısal tahmin metotları ve sezgisel optimizasyon algoritmalarının kullanıldığı ve farklı algoritmaların kullanımıyla rüzgar karakteristik özelliklerinin belirlenmesinde farklı ölçüm formlarının uygulanmasına gereksinim duyulduğu görülmektedir. Sayısal tahmin metotları yapısı, Weibull olasılık dağılım fonksiyonuna uygun olduğu için parametre tahminlenmesinde yaygın olarak kullanılmaktadır. En yaygın kullanılan tahmin metotlarının ise; Lysen Ampirik Moment Metodu, Justus Ampirik Moment Metodu, Grafik Metodu, Moment Metodu, Ampirik Metot, Güç Yoğunluğu Moment Metodu, Enerji Şekil Faktörü, Standart Sapma metotları oldukları görülmektedir (Jiang vd. 2017; Köse vd. 2021; Azad vd. 2014).

Sayısal tahmin metotlarının yanısıra sezgisel optimizasyon algoritmalarının da, Weibull olasılık dağılım fonksiyonu parametrelerini hesaplarken kullanılmaktadır. Sezgisel algoritmalar parametre tahminlenmesi hesaplanırken çözüme hızlı ulaşılması, güvenilirlik, esneklik, basit kod yazılımı ve kolay analiz edilmesi gibi üstünlükleri nedeniyle sıklıkla tercih edilmektedirler. Bu algoritmaların çoğu doğadaki sürü davranışlarından ilham alınarak bu sürü davranışlarının simüle edilmesiyle tasarlanmaktadır. Köse vd. 2018 yılında yaptığı çalışmada, Burr dağılımı ile rüzgar hızı yoğunluğunu tahmin etmek için yeni bir yaklaşım olarak en küçük kareler yöntemi kullanarak bir tahmin modeli tasarlamışlardır. Bu modeli doğrulamak için sekiz farklı

meteoroloji istasyonunun yıllık verileri analiz edilerek sonuçlar Weibull dağılım modeli ile karşılaştırılmıştır. Her iki modelin parametrelerini tahmin etmek için en küçük kareler yöntemi ve maksimum benzerlik kestirim yöntemi kullanılmıştır. Sonrasında Weibull olasılık dağılım fonksiyonu ile tek tepeli olmayan rüzgar hız verilerini modellemede kullanılan iki bileşenli karma Weibull dağılımı parametrelerini tahmin etmek üzere Yusufçuk Algoritmasını kullanmışlardır. Önerilen yöntemin performansını, meta-sezgisel optimizasyon algoritmalarından Genetik Algoritma ve Parçacık Sürüsü Optimizasyonu ile sayısal yöntemlerden Moment Yöntemi ve En Küçük Kareler Yöntemi ile karşılaştırarak değerlendirmişledir (Köse vd. 2023).

Yukarıda bahsedilen (Köse vd 2018; Köse vd. 2023) yayınlarda popülasyon tabanlı algoritmalar kullanılırken, bu çalışmamızda istatistik tabanlı en küçük kareler yöntemi ve moment metotlarının yanında, matematik tabanlı genelleştirilmiş indirgenmiş gradyan yöntemi ve fizik tabanlı ısıl işlem algoritmaları kullanılmıştır.

Bu doğrultuda bu çalışmada, iki parametreli Weibull dağılım fonksiyonunun parametre tahminlenmesinde En Küçük Kareler Yöntemi(LMS), Justus Ampirik Moment Metodu(EMJ), Lysen Ampirik Moment Metodu(EML), Isıl İşlem Algoritması(SA) (Isıl işlem algoritması metal malzemelerin katı halde sıcaklık değişmeleriyle bir ya da birbirine bağlı birkaç işlemle amaca uygun özellik değişimlerinin sağlanmasını simüle ederken kullanılan algoritmadır (Karaboğa, 2018)), Genelleştirilmiş İndirgenmiş Gradyan Algoritması(GRG) kullanılarak sonuçlar performans kriterleriyle karşılaştırılmış ve bunun üzerine rüzgar hız dağılımı ve Konya Loras dağı ile İzmir Foça potansiyel rüzgar enerjisi elde edilmesinde uygun bir yöntem olabileceği düşünülmüştür. Bu çalışmada gerçek saha verileri kullanılarak, istatistik tabanlı en küçük kareler yöntemi ve moment metotlarının yanında, matematik tabanlı genelleştirilmiş indirgenmiş gradyan yöntemi ve fizik tabanlı ısıl işlem algoritması kullanılmıştır. Çalışmada kullanılan genelleştirilmiş indirgenmiş gradyan yöntemi, yapılan literatür taraması sonucunda rüzgar enerjisi güç yoğunluğunda çok sık kullanılan bir yöntem olmadığından, diğer makalelere göre farklı bir kıyaslama olarak nitelendirilebilir. Ayrıca bu çalışmanın özgünlüğü istatistik, matematik ve fizik tabanlı algoritmaların birlikte kullanılarak sonuçların kıyaslanmasındadır.
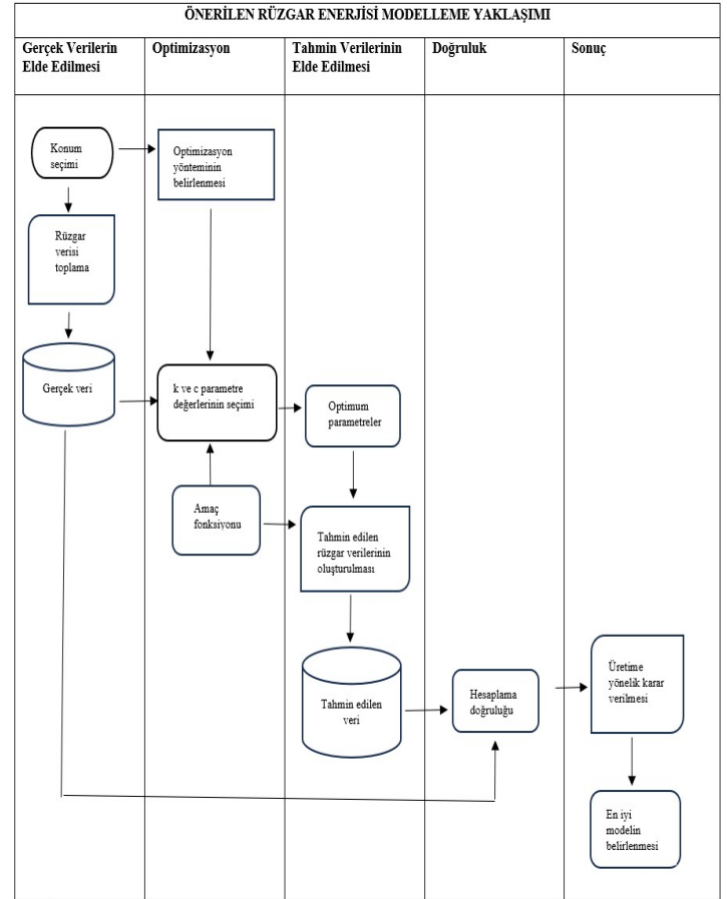


**Şekil 1. Önerilen Rüzgar Enerjisi Modelleme Yaklaşımı**

## MATERYALLER VE METOT (MATERIALS AND METHOD)

### Veriler (Data)

Bu çalışmada Konya Loras dağı ve İzmir Foça rüzgar hız ölçüm değerleri kullanılarak hesaplamalar yapılmıştır.
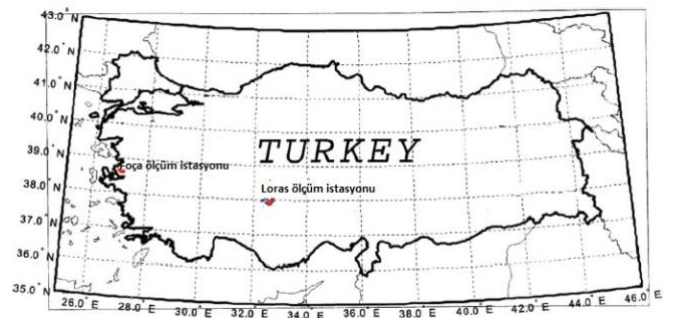


**Şekil 2.** Loras ve Foça Gözlem İstasyonlarının yeri (Köse vd. 2014)

Bölgedeki hakim rüzgar yönünü gösteren rüzgar gülü grafiği, on altı rüzgar sektörü belirtilerek **Şekil 3**' de gösterilmektedir.

Loras Rüzgar Gülü
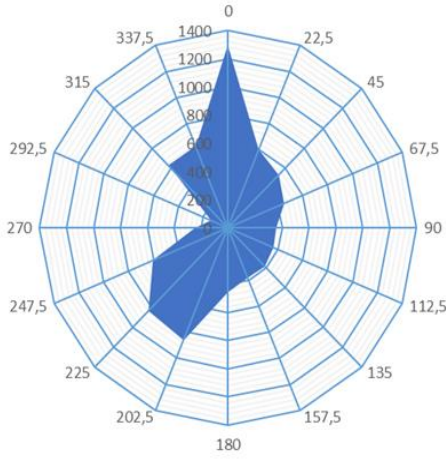
İzmir Foça Rüzgar Gülü
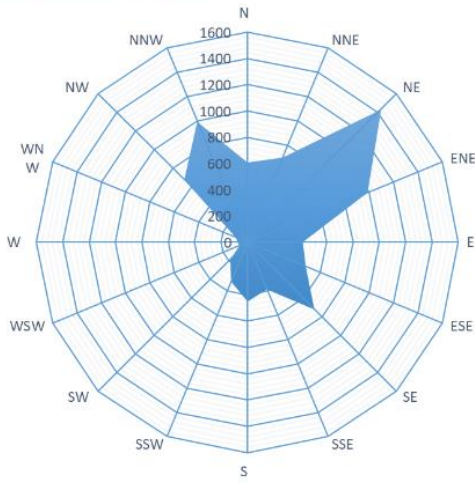
**Şekil 3.** Loras ve Foça Gözlem İstasyonu Rüzgar Gülü

**Tablo 1.** Loras ve Foça Gözlem İstasyonu Rüzgar İstasyonu Esme Yoğunluğu

| Hız sınıfı | LORAS Esme Yoğunluğu | FOÇA Esme Yoğunluğu |
|---|---|---|
| 0 | 0,0882 | 0,000931 |
| 1 | 0,0994 | 0,039213 |
| 2 | 0,1337 | 0,092972 |
| 3 | 0,1414 | 0,109262 |
| 4 | 0,1248 | 0,104724 |
| 5 | 0,0956 | 0,110193 |
| 6 | 0,0763 | 0,120084 |
| 7 | 0,0595 | 0,113219 |
| 8 | 0,0473 | 0,101350 |
| 9 | 0,034 | 0,065744 |
| 10 | 0,0262 | 0,046660 |
| 11 | 0,0215 | 0,032232 |
| 12 | 0,0155 | 0,025017 |
| 13 | 0,0124 | 0,016640 |
| 14 | 0,0082 | 0,009192 |
| 15 | 0,0062 | 0,006749 |
| 16 | 0,004 | 0,002909 |
| 17 | 0,0029 | 0,001164 |
| 18 | 0,0014 | 0,000931 |
| 19 | 0,0007 | 0,000349 |
| 20 | 0,0002 | 0,000233 |
| 21 | 0,0002 | 0,000116 |
| 22 | 0,0002 | 0,000116 |
| 23 | 0,0001 | 0 |
| 24 | 0,0001 | 0 |
| 25 | 0,0001 | 0 |
| Toplam | 1 | 1 |

Loras ve Foça Gözlem İstasyonlarındaki rüzgar hızı ölçümlerinin esme yoğunlukları **Tablo 1**'de verilmiştir (Köse vd. 2021). Konya Loras dağı rüzgar hız verileri incelendiğinde, rüzgarın ortalama hızı 4,552 m/s, bir yıllık hakim rüzgar yönü sıfır derece kuzey ve 202,5 derece güney batı yönü olarak saptanmıştır. İzmir Foça meteorolojik ölçüm istasyonu rüzgar hız ölçüm değerlerinin analizinde ortalama rüzgar hızı 6,15 m/s olarak, hakim rüzgar yönü 0 derece kuzey olmak üzere, 45 derece kuzey ve 330 derece kuzey batı yönü olarak tespit edilmiştir. Rüzgar potansiyeli hesaplamalarında kullanılmak üzere bir yıl içindeki saatlik rüzgar hızı verileri toplanmaktadır. Bir yılda alınması gerekli olan 8760 saatlik rüzgar hızı verisinden, 166 saatlik eksik rüzgar hızı verisi ile toplamda 8594 saatlik rüzgar hızı verisi üzerinden değerlendirme yapılmıştır.

Loras ve Foça rüzgar hız verilerinin tanımlayıcı istatistikleri Tablo 2'de verilmiştir. Loras rüzgar hız verilerinin tanımlayıcı istatistikleri; ortalama rüzgar hızından daha küçük değerlerin olduğu yere doğru çarpık olup, 1,44 basıklık katsayısı ile normal dağılıma göre biraz daha sivridir. Standart sapması 3,53 m/s olup, en büyük rüzgar hızı 25,96 m/s olarak kayıtlara geçmiştir. Tanımlayıcı istatistik verilerinden de anlaşılacağı üzere Foça rüzgar hız verilerinin; ortalama rüzgar hızından daha küçük değerlerin olduğu yere doğru çarpık olup, 0,27 basıklık katsayısı ile normal dağılıma göre biraz daha sivridir. Standart sapması 3,18 m/s olup, en büyük rüzgar hızı kaydı 21,9 m/s olarak kayıtlara geçmiştir.

**Tablo 2.** Tanımlayıcı İstatistikler Tablosu

| Tanımlayıcı İstatistik Verileri | Loras Tanımlayıcı İstatistik Verileri (10 dakikalık ortalama ölçümler) | Foça Tanımlayıcı İstatistik Verileri (Saatlik ortalama ölçümler) |
|---|---|---|
| Ortalama | 4,551589144 | 6,15459623 |
| Standart Hata | 0,015489232 | 0,034367716 |
| Ortanca | 3,782 | 5,9 |
| Standart Sapma | 3,539315031 | 3,186018848 |
| Örnek Varyansı | 12,52675089 | 10,1507161 |
| Basıklık | 1,445531814 | 0,276911107 |
| Çarpıklık | 1,139122863 | 0,638000799 |
| Aralık | 25,96 | 21,5 |
| En Büyük | 25,96 | 21,9 |
| En Küçük | 0 | 0,4 |
| Veri Sayısı | 52213 | 8594 |

Loras için bir yılda 10 ar dakikalık periyotla 52560 ölçüm alınması gerekirken bu çalışmada kaydedilen ölçüm sayısı 52213 olmuştur. Bu nedenle 10 ar dakikalık periyotta kaydedilen ölçümlerden 347 ölçüm eksik olup belirsizlik miktarı

$$(52560 - 52213)/52560 = 347/52560 = 0.0066$$

%0,66 olarak bulunmuştur. Bu da bu tür hesaplamalarda çok iyi sonuç olarak söylenebilir.

Meteorolojiden alınan verilere göre Foça için saatlik periyotlarla 8760 ölçüm alınması gerekirken bu çalışmada kaydedilen ölçüm sayısı 8594 olup 166 saatlik eksik ölçüm yapılmıştır. Bu da yaklaşık tüm ölçümler bazında

$$(8594 - 8760)/8760 = 0,0189$$

%1,89 belirsizlik miktarı bulunduğu anlamına gelir. Bu belirsizlik miktarı Loras gözlem istasyonunda yapılan ölçüme göre daha fazla olmasına rağmen, yapılan diğer çalışmalara göre kabul edilebilir bir oran olduğu söylenebilir.

**Weibull Olasılık Dağılım Fonksiyonu (Weibull Probability Distribution Function)**

Rüzgar enerjisi potansiyelinin belirlenmesinde seçilen bölgedeki rüzgar hız dağılımını doğru analiz etmek o bölgeye enerji tesisi kurmadan önce yapılması gereken en önemli adımdır. Rüzgar hızının değişken ve aralıklı olması sebebiyle istatistiksel yöntem tercih edilir. İki parametreli Weibull Olasılık Dağılım Fonksiyonu en güvenilir ve en doğru yöntemlerden biridir. Weibull olasılık dağılımına ait olasılık yoğunluk fonksiyonu Eş. (1)'de, kümülatif olasılık dağılım fonksiyonu Eş. (2)'de belirtilmiştir (Köse vd., 2018; Justus ve Mikhail, 1976).

$$f(v) = \frac{k}{c}\left(\frac{v}{c}\right)^{k-1} e^{\left[-\left(\frac{v}{c}\right)^k\right]} \tag{1}$$

$$F(v) = 1 - e^{\left[-\left(\frac{v}{c}\right)^k\right]} \tag{2}$$

**Parametre Tahmin Metodları (Parameter Estimation Methods)**

Rüzgar hızı karakterizasyonu için olasılık dağılım fonksiyonlarının parametrelerini tahmin etmek ve performans kıyası için yaygın olarak sayısal metotlardan; en küçük kareler metodu, Justus ampirik moment metodu ve Lysen ampirik moment metodu kullanılmaktadır. Ayrıca olasılık dağılım fonksiyonlarının parametrelerini tahmin etmek için bazı optimizasyon algoritmaları da kullanılmaktadır. Bu çalışmada sezgisel optimizasyon algoritmalarından Isıl İşlem Algoritması ve Genelleştirilmiş İndirgenmiş Gradyan Algoritmasından faydalanılarak Weibull Dağılım fonksiyonunun parametreleri tahmin edilmiştir.

**En Küçük Kareler Metodu (Least Square Method (LSM))**

Weibull olasılık dağılım fonksiyonunun $k$ ve $c$ parametreleri Eş. (3) ve Eş. (4) te şu şekilde verilir (Köse, 2018):

$$y_i = \ln\left(-\ln\left(1 - F(v_i)\right)\right)$$

$$k = \frac{n\sum_{i=1}^{n}(lnv_i)y_i - (\sum_{i=1}^{n}lnv_i)(\sum_{i=1}^{n}y_i)}{n\sum_{i=1}^{n}ln(v_i^2) - (\sum_{i=1}^{n}lnv_i)^2} \tag{3}$$

$$c = \exp\frac{k\sum_{i=1}^{n}lnv_i - \sum_{i=1}^{n}y_i}{nk} \tag{4}$$

**Justus Ampirik Moment Metodu (Empirical Moment Method of Justus(EMJ))**

Weibull olasılık dağılım fonksiyonundaki $k$ ve $c$ parametreleri sırasıyla Eş. (5), Eş. (6) kullanılarak hesaplanmıştır. Rüzgar hızının standart ortalama değeri $\bar{v}$, standart sapma değeri ise $\sigma$ ile ifade edilmiştir (Justus ve Mikhail, 1976; Abdulahad vd., 2016)

$$k = \left(\frac{\sigma}{\bar{v}}\right)^{-1.086} \tag{5}$$

$$c = \frac{\bar{v}}{\Gamma\left(1 + \frac{1}{k}\right)} \tag{6}$$

**Lysen Ampirik Moment Metodu (Empirical Moment Method of Lysen(EML))**

Weibull olasılık dağılım fonksiyonundaki $c$ parametresi Eş. (7) kullanılarak hesaplanmıştır. Rüzgar hızının standart ortalama değeri $\bar{v}$, $k$ parametresi ise Justus Ampirik Moment Metodu ile hesaplanan değer kullanılmıştır (Lysen, 1983).

$$c = \bar{v}\left(0.568 + \frac{0.433}{k}\right)^{-\frac{1}{k}}$$ (7)

## Isıl İşlem Optimizasyon Algoritması Metodu (Simulated Annealing Optimization Algorithm Method(SA))

Isıl işlem algoritması, fiziksel tavlamanın termodinamik sürecinde parçacıkların istatistiksel termodinamik kanunu baz alınarak oluşmuş bir algoritmadır. Amaç, parçacığı bir başlangıç durumundan mümkün olan en düşük enerjiye sahip bir duruma getirmektir. Başka bir deyişle, Isıl işlem algoritması fiziksel olarak üç bölümde incelenebilir.

1) Isıtma işlemi: Amacı, parçacıkların termal hareketini arttırmak ve onları denge konumundan saptırmaktır. Sıcaklık yeterince yüksek olduğunda, katı eriyerek sıvıya dönüşecek ve böylece sistemin üniform olmayan durumu ortadan kaldırılacaktır.

2) İzotermal süreç: Çevre ile ısı alışverişi yapan ve sıcaklığı sabit olan kapalı bir sistem için, sistem durumunun kendiliğinden değişimi, genellikle serbest enerjiyi azaltma yönündedir. Serbest enerji minimuma ulaştığında, sistem denge durumuna ulaşır.

3) Soğutma işlemi: Kristal yapı, parçacıkların termal hareketinin zayıflatılması ve sistemin enerjisinin düşürülmesiyle elde edilir.

Bunların arasında ısıtma işlemi, algoritmanın başlangıç sıcaklığına karşılık gelir. İzotermal süreç, algoritmanın geçiş sürecine karşılık gelir. Soğutma işlemi, kontrol parametrelerinin azalmasına karşılık gelir. Enerji değişimi amaç fonksiyonudur ve optimal çözüm en düşük enerji durumudur.

Isıl işlem algoritması birden fazla değişkene sahip fonksiyonun özellikle birçok yerel minimum değere sahip doğrusal olmayan fonksiyonların minimum değerlerinin bulunması için tasarlanmıştır. Bu algoritmada rassal olarak bir çözüm belirlenerek, bu çözüm üzerinde yapılan değişikliklerle yeni bir çözüm bulunur. Sonrasında bu işlemler tekrar eder. Yeni üretilen çözümler ile başlangıçtaki rassal çözüm kıyaslanarak hangisinin daha iyi olduğu araştırılır. Eğer yeni üretilen çözüm daha iyi ise en iyi çözüm olarak belirlenir.
Sıcaklık ısıl işlem algoritmasında başlangıçta belirlenmiş olan bir değer olup temelde en iyi sonuç bulunana kadar düşürülebilir. Bunun yanısıra sıcaklık değeri sıfırdan düşük olana kadar ya da algoritmanın çalıştırılması için belirlenen süre bitene kadar düşürülebilir (Köse, 2022; Wang, 2020).

**Tablo 3.** Isıl İşlem Algoritmasının Sözde Kodu

| | |
|---|---|
| 1: | SA kontrol parametreleri $T_0; T_{final}; L; c$ yi seç |
| 2: | Rastgele bir $X_0$ başlangıç çözümü seç |
| 3: | $X = X_0; T = T_0$ al, $f(X_0)$ değerini hesapla |
| 4: | While $T > T_{final}$ |
| 5: | Set $k = 1$ |
| 6: | While $k < L$ |
| 7: | $X$ in komşuluğunda yeni $X_{yeni}$ çözümünü üret |
| 8: | $\Delta f = f(X_{yeni}) - f(X)$ i hesapla |
| 9: | If $\Delta f < 0$ |
| 10: | $X = X_{yeni}$ |
| 11: | end if |
| 12: | else |
| 13: | $r \in (0,1)$ olacak biçimde rasgele $r$ sayısı üret |
| 14: | If $r < e^{\frac{-\Delta f}{T}}$ |
| 15: | $X = X_{yeni}$ , $k = k + 1$ |
| 16: | end if |
| 17: | end else |
| 18: | end while |
| 19: | Isıyı düşür: $T_1 = c*T_0$ ( c soğutma katsayısı=0.96) |
| 20: | end while |
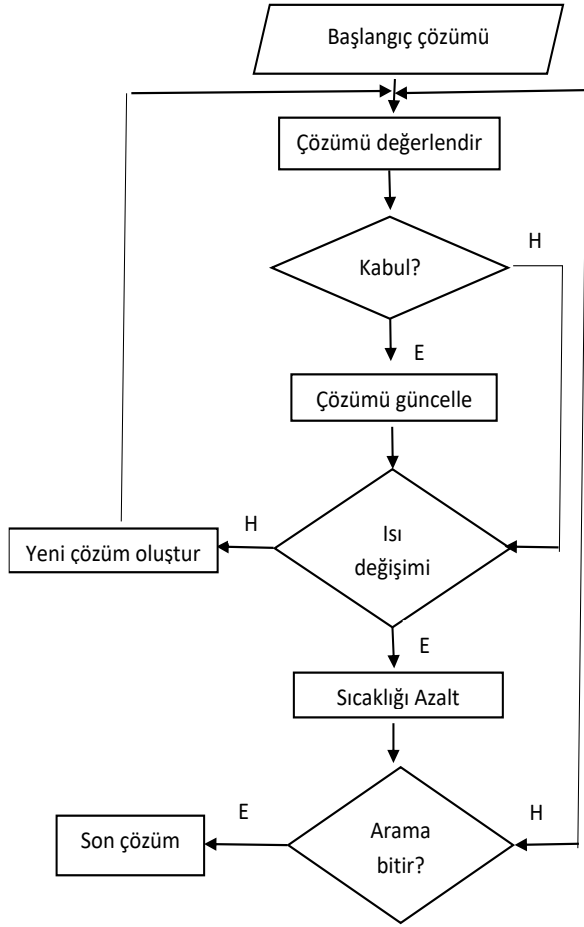
**Şekil 4.** Isıl İşlem Algoritması Akış Diyagramı (Köse vd., 2014)

## Genelleştirilmiş İndirgenmiş Gradyan Metodu (Generalized Reduced Gradient Method)

Kısıtlı optimizasyonun optimal olurlu yöntemlerinden, genelleştirilmiş indirgenmiş gradyan yöntemi, uygulamada önemli bir rol oynar ve teknolojik uygulamalarda hala yaygın olarak kullanılmaktadır (Brenan ve Hallman, 1995). Bu yöntemde esas olarak, bir yandan minimum yapılmak istenen $f$ nin içbükey olmadığı ve diğer yandan kısıtların genel olarak doğrusal olmadığı durumla ilgilenilmektedir (Abdelkrim, 2010).

Genelleştirilmiş indirgenmiş gradyan yöntemi, doğrusal optimizasyon yöntemlerini doğrusal olmayan durumlara genişletmeye çalışır. Bu yöntemler, öngörülen gradyan yöntemlerine yakın veya eşdeğerdir; sadece yöntemlerin sunumu genellikle farklıdır (Beck vd., 1983).

Genelleştirilmiş indirgenmiş gradyan metodu (GRG), yalnızca doğrusal kısıtlamalı problemlerin çözümü için sunulan indirenmiş gradyan yönteminin bir uzantısıdır (Gabriele ve Ragsdell, 1977). GRG metodunun detaylarını görmek için, $n$ tasarım değişkeni ve $m$ eşitlik kısıtı ile aşağıdaki nonlineer programlama problemi ele alınsın:

$Min \quad f(x)$

$Kısıtlar \quad g(x) = 0, \quad i = 1, 2, ..., m$

Tasarım değişkenleri $n - m$ bağımsız değişkenden oluşan $z$ ve $m$ bağımlı değişkenden oluşan $y$ olmak üzere bölümlere ayrılır. Bağımsız değişkenler, amaç fonksiyonunu iyileştirmek için, bağımlı değişkenler de bağlayıcı kısıtları karşılamak için kullanılacaktır. Mevcut gradyan vektörleri aşağıdaki şekilde bölümlere ayrılmak üzere

$$\nabla f(z)^T = \left[ \begin{array}{cccc} \dfrac{\partial f(x)}{\partial z_1} & \dfrac{\partial f(x)}{\partial z_2} & \cdots & \dfrac{\partial f(x)}{\partial z_{n-m}} \end{array} \right]$$

$$\nabla f(y)^T = \left[ \begin{array}{cccc} \dfrac{\partial f(x)}{\partial y_1} & \dfrac{\partial f(x)}{\partial y_2} & \cdots & \dfrac{\partial f(x)}{\partial y_m} \end{array} \right]$$

kısıtların kısmi türevlerinin bağımsız ve bağımlı matrisleri

$$\frac{\partial \psi}{\partial z} = \left[ \begin{array}{cccc} \frac{\partial g_1}{\partial z_1} & \frac{\partial g_1}{\partial z_2} & \cdots & \frac{\partial g_1}{\partial z_{n-m}} \\ \cdot & \cdot & \cdot & \cdot \\ \cdot & \cdot & \cdot & \cdot \\ \cdot & \cdot & \cdot & \cdot \\ \frac{\partial g_m}{\partial z_1} & \frac{\partial g_m}{\partial z_2} & \cdots & \frac{\partial g_m}{\partial z_{n-m}} \end{array} \right], \quad \frac{\partial \psi}{\partial y} = \left[ \begin{array}{cccc} \frac{\partial g_1}{\partial y_1} & \frac{\partial g_1}{\partial y_2} & \cdots & \frac{\partial g_1}{\partial y_m} \\ \cdot & \cdot & \cdot & \cdot \\ \cdot & \cdot & \cdot & \cdot \\ \cdot & \cdot & \cdot & \cdot \\ \frac{\partial g_m}{\partial y_1} & \frac{\partial g_m}{\partial y_2} & \cdots & \frac{\partial g_m}{\partial y_m} \end{array} \right]$$

biçiminde tanımlansın. Bu durumda amaç ve kısıtlardaki diferansiyel değişiklikler vektör formunda şu şekilde yazılabilir:

$$df = \nabla f(z)^T dz + \nabla f(y)^T dy$$

$$d\psi = \frac{\partial \psi}{\partial z} dz + \frac{\partial \psi}{\partial y} dy = 0$$

Buradan

$$dy = -\frac{\partial \psi}{\partial y}^{-1} \frac{\partial \psi}{\partial z} dz \qquad (8)$$

olur. Dolayısıyla

$$df = \nabla f(z)^T dz - \nabla f(y)^T \frac{\partial \psi}{\partial y}^{-1} \frac{\partial \psi}{\partial z} dz$$

olup, $\nabla f_R^T$ genelleştirilmiş indirgenmiş gradyan formülü

$$G_R = \nabla f_R^T = \nabla f(z)^T - \nabla f(y)^T \frac{\partial \psi}{\partial y}^{-1} \frac{\partial \psi}{\partial z} \qquad (9)$$

biçiminde elde edilir. İndirgenmiş gradyan, geometrik olarak $n$ boyutlu gradyanın tasarım değişkenleri tarafından tanımlanan $n - m$ boyutlu uygulanabilir optimal olurlu (feasible) bölgeye bir izdüşümü olarak tanımlanabilir. İndirgenmiş gradyan, etkin kısıtlara teğet olan en dik çıkışın yönüdür.

Bazen de ele alınan problemdeki kısıtlar aşağıdaki gibi hem eşitlik hem de eşitsizlik kısıtları olabilir.

$Min \quad f(x)$

$Kısıtlar \quad g(x) \le 0, \quad i = 1, ..., k$

$\qquad \qquad g_i(x) = 0, \quad i = k+1, ..., m$

GRG algoritmasının eşitlik ve eşitsizlikler ile verilen daha genel bu şekli biraz daha karmaşıktır. Çünkü GRG nin türetilmesi eşitlik kısıtlamalarına dayanır. Bu nedenle yapay (slack) değişkenler ekleyerek eşitsizlikler eşitliğe dönüştürülür. Buradaki GRG algoritması, aktif bir kısıtlama algoritmasıdır; arama yönünü belirlemek için yalnızca etkin eşitsizlik kısıtları kullanılır. Etkin olmayan kısıtlar, yalnızca bağlayıcı hale geldikleri veya ihlal edildikleri takdirde probleme dahil edilirler.

GRG algoritmasının adımları şu şekilde verilebilir:

**1.** Amaç fonksiyonunu ve mevcut noktadaki tüm kısıtları değerlendir.

**2.** Herhangi bir etkin eşitsizlik kısıtı için, yapay bir $s_i$ yapay değişkeni eklenir.

**3.** Değişkenler bağımsız değişkenler ve bağımlı değişkenler olarak ayrılır. Her etkin kısıt için bir bağımlı değişkene ihtiyaç vardır. Üst veya alt sınırındaki herhangi bir değişken, bağımsız bir değişken haline gelmelidir.

**4.** İndirgenmiş gradyanı hesaplamak için Eş. (9) kullanılır.

**5.** Bir arama yönü hesaplayın. İndirgenmiş gradyanın arama yönünü hesaplamak için herhangi bir yöntem kullanılabilir. Örneğin, Newton-Raphson (NR) yöntemi.

**6.** Bağımsız değişkenlerde bir satır araması yapılır. Her adım için, Eş. (8) da $dz$ ve $dy$ yerine $\nabla y$ ve $\nabla z$ kullanılarak bağımlı değişkenlerdeki karşılık gelen değerler bulunur.

**7.** Optimum çözüm aramasının her adımında, bağımlı değişkenleri belirlemek için Newton-Raphson (NR) yöntemini kullanarak ihlal edilen kısıtlar için kısıt sınırlarına geri dönülür. Bağımsız bir değişken sınırına ulaşırsa, onun sınırına eşitlenir. İndirgenmiş gradyanın hesaplamasında $\dfrac{\partial \psi^{-1}}{\partial y}$ matrisine sahip olduğumuz göz önüne alınsın. Burada Newton-Raphson iterasyonu

$$\Delta y = -\frac{\partial \psi^{-1}}{\partial y}(g-b) \ \text{ ile verilir.}$$

**8.** Optimum çözümü arama 4 yoldan biri ile sonlandırılabilir.

   **i.** Arama yönündeki minimum bulunur.
   **ii.** Bağımlı bir değişken üst veya alt sınırına ulaşır.
   **iii.** Önceden etkin olmayan bir kısıt etkin hale gelir.
   **iv.** NR yakınsamayı başaramazsa, NR yakınsayana kadar adım boyutu azaltılır.

**9.** Herhangi bir noktada 4. adımdaki indirgenmiş gradyan 0'a eşitse, Karush–Kuhn–Tucker koşulları karşılanır (Constrained Optimization 2).
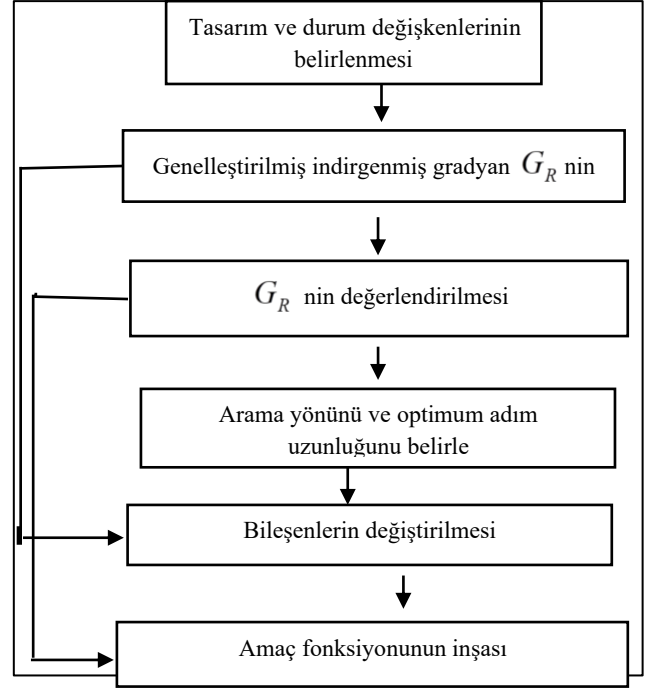


**Şekil 5.** Genelleştirilmiş indirgenmiş gradyan algoritmasının akış şeması (Kim ve Mun, 2021).

## GÜÇ YOĞUNLUĞU VE PERFORMANS ANALİZİ (POWER DENSITY AND PERFORMANCE ANALYSIS)

### Rüzgar Güç Yoğunluğu

Tesis için birim alan A ($m^2$), bölgedeki rüzgar hızı $v$ ve $\rho$ ($kg/m^3$) hava yoğunluğu olmak üzere, rüzgar güç yoğunluğu Eş. (10) ile tahmin edilebilir:

$$P_{w,d}(v) = \frac{1}{2}\rho A v^3 = \frac{1}{2}\rho v^3 \left( w/m^2 \right) \tag{10}$$

Weibull olasılık yoğunluk fonksiyonu ölçek parametresi $c$, şekil parametresi $k$ ve $\Gamma , \Gamma(t) = \displaystyle\int_0^\infty e^{-t}.t^{x-1}dt$ Gamma fonksiyonu olmak üzere, yerel rüzgar enerjisi kaynağının uygunluğu için, yıllık ortalama rüzgar güç yoğunluğu Eş. (11) ile hesaplanır (Köse vd., 2018).

$$P_{w,d} = \frac{1}{2}A\rho\int_0^{v\max} v^3 f(v)dv = \frac{1}{2}\rho c^3\Gamma\left(1+\frac{3}{k}\right) \tag{11}$$

Güç yoğunluğu açısından ölçüm yapılan sitenin rüzgar enerjisi sınıfları değerlendirme kriterleri Tablo 4'deki gibidir (Mostafaeipour vd., 2014).

**Tablo 4.** Rüzgar enerjisi sınıfları değerlendirme kriterleri

| Zayıf Kaynak | $(P_{w,d} < 100 W/m^2)$ |
|---|---|
| Normal Kaynak | $(100\ W/m^2 < P_{w,d} < 300 W/m^2)$ |
| İyi Kaynak | $(300 W/m^2 < P_{w,d} < 700 W/m^2)$ |
| Çok İyi Kaynak | $(P_{w,d} > 700 W/m^2)$ |

Elde edilen sonuç yukarıda verilen kritik değerlere göre sınıflandırılır ve yatırım kararı için bilgi üretilir.

## Amaç Fonksiyonunun Tanımlanması (Defining Objective Function)

Bu çalışmada, her iki gözlem istasyonunda ölçülen rüzgar hız olasılık değerleri ile Weibull olasılık dağılımı kullanılarak bulunan rüzgar hız olasılık değerleri arasındaki fark hatayı ifade etmekte olup

$$E(v, k, c) = \sum_{i=1}^{n} \left[ f_g(v_i) - f_w(v_i) \right]^2 \tag{12}$$

ile gösterilen amaç fonksiyonunda hata kareleri toplamının en aza indirilmesi hedeflenmektedir (Köse vd., 2018).

Eş. (12), Eş. (13), Eş. (14) ve Eş. (15) te $n$ toplam hız sınıfı sayısını, $f_g(v_i)$ gözlem istasyonunda ölçülen frekansları ve $f_w(v_i)$ Weibull dağılımı ile hesaplanan frekansları göstermektedir.

## Performans Kriterleri (Performance Criteria)

### Hata Kareleri Ortalamasının Karekökü (The Root Mean Square Error (RMSE))

Bu kriter tahminlemesi yapılan değerler ile deneysel veriler arasındaki gerçek sapmayı kıyaslamak maksadıyla kullanılır. Hata Kareleri Ortalamasının Karekökü kriteri Eş. (13) ile tanımlanmıştır.

$$HKOK(RMSE) = \sqrt{\frac{1}{n} \sum_{i=1}^{n} \left( f_g(v_i) - f_w(v_i) \right)^2} \tag{13}$$

Rüzgar hızının modellenmesinde kullanılacak doğru fonksiyon en küçük değere sahip en iyi rüzgar dağılımı fonksiyonudur (Abdulahad, 2016).

### Determinasyon (Belirlilik) Katsayısı (Determination Coefficient)

Determinasyon (Belirlilik) katsayısı tahminlemesi yapılan değerler ile deneysel veriler arasındaki yakınlığı kıyaslamak için kullanılan bir başka performans kriteri olup Eş. (14) ile tanımlanmıştır.

$$R^2 = 1 - \frac{\sum_{i=1}^{n} \left( f_g(v_i) - f_w(v_i) \right)^2}{\sum_{i=1}^{n} \left( f_g(v_i) - f_g(\bar{v}_i) \right)^2} \tag{14}$$

Burada $f_g(\bar{v}_i)$ Weibull ile tahminlemesi yapılan rüzgar dağılımının ortalamasını ifade eder (Azad, 2014).

### Ki-kare Dağılımı (Chi-square Distribution)

Bu kriter Eş. (15) ile tanımlanmıştır (Güngör, 2008).

$$\chi^2 = \frac{\sum_{i=1}^{n} \left( f_g(v_i) - f_w(v_i) \right)^2}{\sum_{i=1}^{n} f_g(v_i)} \tag{15}$$

## KARŞILAŞTIRMA VE ANALİZ (COMPARISION AND ANALYSIS)

Loras Gözlem İstasyonu verileri kullanılarak rüzgar hızlarının frekans dağılımının rüzgar karakteristiğini oluşturmak için klasik sayısal yöntemlerden En Küçük Kareler Yöntemi(LMS), Justus Ampirik Moment Metodu(EMJ) ve Lysen Ampirik Moment Metodu(EML) ile sezgisel optimizasyon algoritmalarından Isıl İşlem Optimizasyon Algoritması(SA) ve Genelleştirilmiş İndirgenmiş Gradyan Algoritması kullanılarak Weibull şekil(k) ve ölçek(c) parametreleri tahmin edilmiştir.

Loras gözlem istasyonu için, k şekil parametresi klasik sayısal metotlardan LMS ile 1,3711, EMJ ve EML ile 1,3115, c ölçek parametresi ise LMS ile 4,4747, EMJ ve EML ile 4,93-4,95 arasında yakın değerler bulunduğu gözlemlenmiştir. SA optimizasyon algoritması ve GRG algoritmasında ise k şekil parametresi 1,4048, c ölçek parametresi ise 5,40-5,75 arasında yakın değerler bulunarak parametrelerin klasik sayısal metotlardan daha büyük olduğu görülmüştür.

Foça gözlem istasyonu için, k şekil parametresi klasik sayısal metotlardan LMS ile 1,7919, EMJ ve EML ile 2,0166, c ölçek parametresi ise LMJ ile 6,1868, EMJ ve EML ile 6,89 a yakın değerler bulunduğu gözlemlenmiştir. SA ve GRG optimizasyon algoritmalarında ise k şekil parametresi 1.98 civarı olup, c ölçek parametresi ise 6,89-6,94 arasında bulunarak parametrelerin klasik sayısal metotlara çok yakın değerler olduğu görülmüştür.

**Tablo 5.** Loras ve Foça Rüzgar Hız Karakteristiği İçin Weibull Olasılık Dağılım Fonksiyonu Parametreleri

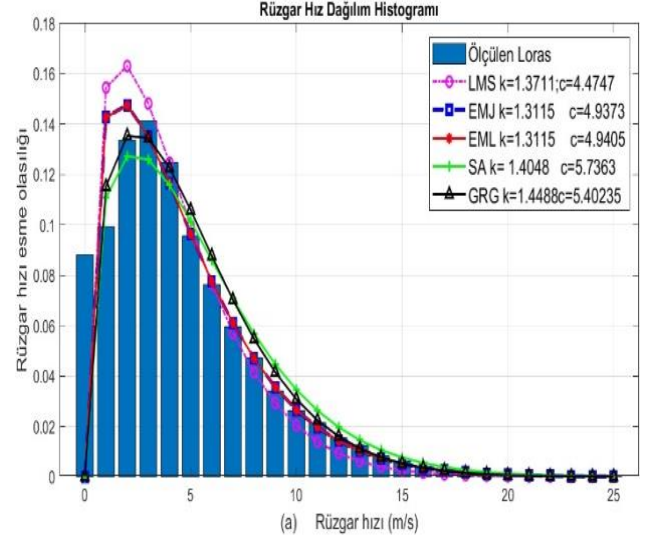| Parametre Tahmin Metotları | Loras Gözlem İstasyonu | | Foça Gözlem İstasyonu | |
|---|---|---|---|---|
| | k | c | k | c |
| LSM | 1.3711 | 4.4747 | 1.7919 | 6.1868 |
| EMJ | 1.3115 | 4.9373 | 2.0166 | 6.8901 |
| EML | 1.3115 | 4.9405 | 2.0166 | 6.8939 |
| SA | 1.4048 | 5.7363 | 1.9777 | 6.8948 |
| GRG | 1.4488 | 5.40235 | 1.9617 | 6.9359 |

**Tablo 6**'da LMS, EMJ, EML, SA ve GRG ile tahminlenen parametrelerin performans kriterlerine göre verdiği sonuçlar belirtilmiştir. Bu sonuçlar gözden geçirildiğinde, Loras Gözlem İstasyonu için GRG Algoritması 0,8473 sonucu ile klasik sayısal yöntemlere oranla optimal bir determinasyon katsayısı değeri vererek iyi bir performans sergilemiştir. Hata Kareleri Ortalamasının Karekökü performans kriteri incelendiğinde, GRG Algoritması Optimizasyon Metodu ile tahmin edilen parametrelerin klasik sayısal yöntem ile tahminlenen parametrelerin deneysel verilere göre daha az saptığı ve daha iyi sonuç verdiği görülmüştür. Ki-kare dağılımı performans kriteri incelendiğinde, yine GRG algoritması ile tahmin edilen parametrelerin klasik sayısal yöntemler ile tahminlenen parametrelere göre sıfıra daha yakın olması sebebiyle daha iyi netice verdiği görülmüştür.

Foça Gözlem İstasyonu için GRG Algoritması 0.9793 sonucu ile klasik sayısal yöntemlere oranla optimal bir determinasyon katsayısı değeri vererek iyi bir performans sergilemiştir. Hata Kareleri Ortalamasının Karekökü performans kriteri incelendiğinde, SA ve GRG Algoritmaları ile tahmin edilen parametrelerin klasik sayısal yöntem ile tahminlenen parametrelerin deneysel verilere göre daha az saptığı ve daha iyi sonuç verdiği görülmüştür. Ki-kare dağılımı performans kriteri incelendiğinde, tüm kullanılan yöntemlerin aynı sonucu verdiği görülmüştür.

**Tablo 6.** Weibull Olasılık Dağılım Fonksiyonu Parametreleri için Frekans Tahmini Performans Sonuçları

|  | Loras Gözlem İstasyonu | | | Foça Gözlem İstasyonu | | |
|---|---|---|---|---|---|---|
|  | RMSE | $R^2$ | $X^2$ | RMSE | $R^2$ | $X^2$ |
| LMS | 0.0215 | 0.7859 | 0.0118 | 0.0123 | 0.9268 | 0.0034 |
| EMJ | 0.0196 | 0.8223 | 0.0097 | 0.0068 | 0.9781 | 0.0011 |
| EML | 0.0196 | 0.8225 | 0.0096 | 0.0067 | 0.9781 | 0.0011 |
| SA | 0.0185 | 0.8424 | 0.0082 | 0.0066 | 0.9791 | 0.0011 |
| GRG | 0.0182 | 0.8473 | 0.0079 | 0.0066 | 0.9793 | 0.0011 |

Weibull Olasılık Dağılım Fonksiyonunun parametrelerini tahminlemede kullanılan klasik sayısal yöntemlerden LMS, EMJ ve EML ile optimizasyon algoritmalarından SA ve GRG algoritmaları kullanılarak, sırasıyla **Şekil 6(a)-6(b)**'de Loras ve Foça gözlem istasyonlarındaki esme yoğunlukları elde edilmiştir. Buna göre Weibull Olasılık Dağılım Fonksiyonu parametre tahmininde SA ve GRG algoritmalarının klasik sayısal yöntemlere göre daha iyi sonuç verdiği dolayısıyla daha başarılı yöntemler olduğu söylenebilir.



**Şekil 6(a).** Loras Gözlem İstasyonu Rüzgar Hız Dağılım Histogramı-Parametre Tahmin Yöntemleri ile bulunan frekanslar
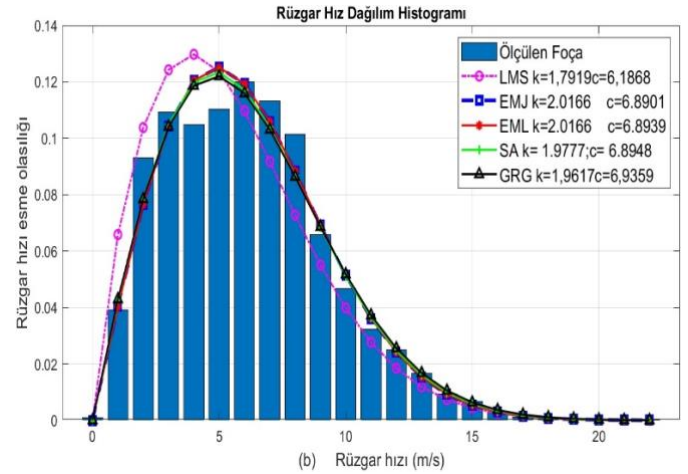


**Şekil 6(b).** Foça Gözlem İstasyonu Rüzgar Hız Dağılım Histogramı-Parametre Tahmin Yöntemleri ile bulunan frekanslar

**Tablo 7.** Gerçek ve LMS, EMJ, EML, SA ve GRG ile tahmini rüzgar güç yoğunluğu değerleri

|  | Loras Gözlem İstasyonu | Foça Gözlem İstasyonu |
|---|---|---|
| Geçek Güç Yoğunluğu | 225.5092 | 266.9153 |
| LMS | 131.2076 | 219.1995 |
| EMJ | 224.4751 | 263.8846 |
| EML | 224.9411 | 263.8846 |
| SA | 252.6022 | 269.8406 |
| GRG | 203.0299 | 277.0478 |

Tablo 7'ye göre Loras ve Foça gözlem istasyonlarındaki gerçek güç yoğunluğu verileri, Tablo 4'te verilen rüzgar enerjisi sınıfları değerlendirme kriterleri ile kıyaslandığında sırasıyla Loras gözlem istasyonu gerçek güç yoğunluğu $100w/m^2 < 226w/m^2 < 300w/m^2$ ve Foça gözlem istasyonu gerçek güç yoğunluğu $100w/m^2 < 267w/m^2 < 300w/m^2$ olduğundan bu bölgelere rüzgar tribünü kurmak için yatırım yapılması makul görülmektedir.

Ayrıca Tablo 7'ye göre Loras gözlem istasyonunda rüzgar güç tahmininde gerçeğe en yakın metodun EMJ olduğu, en uzak tahminin de LMS ile elde edildiği görülmektedir. Foça gözlem istasyonunda rüzgar güç tahmininde gerçeğe en yakın metodun EML olduğu, en uzak tahminin LMS ile elde edildiği görülmektedir.

**Tablo 8.** Rüzgar güç yoğunluğu değerlerindeki hata payları

| Rüzgar Güç Yoğunluğu Hata Payları | | |
|---|---|---|
| | **Loras Gözlem istasyonu** | **Foça Gözlem İstasyonu** |
| **LMS** | 0.4182 | 0.1788 |
| **EMJ** | 0.0046 | 0.0115 |
| **EML** | 0.0025 | 0.0098 |
| **SA** | 0.1073 | 0.0108 |
| **GRG** | 0.1107 | 0.0366 |

Tablo 8'e göre rüzgar güç yoğunluğu hata payları dikkate alındığında her iki gözlem istasyonu için klasik sayısal yöntemlerden EML metodunun en az hata payına sahip olduğu, GRG metodunun hata payının yüksek olduğu ve LMS metodunun da en fazla hata payına sahip olduğu görülmektedir.

**SONUÇ (CONCLUSION)**

Bu çalışmada, genellikle elektrik enerjisi üretiminde tercih edilen rüzgar enerjisinin fizibilite ve verimlilik çalışmalarında kullanılan Weibull Olasılık Dağılım Fonksiyonunun k ve c parametrelerinin tahminlenmesinde sezgisel algoritmalardan Isıl İşlem Algoritması (SA), Genelleştirilmiş İndirgenmiş Gradyan Algoritması (GRG) ve klasik sayısal yöntemlerden En Küçük Kareler Yöntemi(LMS), Justus Ampirik Moment Metodu(EMJ) ve Lysen Ampirik Moment Metodu(EML) kullanılmıştır. Ayrıca hata kareleri ortalamasının karekökü, belirlilik katsayısı ve ki-kare dağılımı performans kriteri kullanılarak parametre tahmin yöntemlerinin başarısı test edilmiştir.

Sonuç olarak, Weibull Olasılık Dağılım Fonksiyonu parametre tahminlenmesinde, eğri uyumu değerlendirilen hata performans kriterleri açısından klasik sayısal yöntemlere göre Loras gözlem istasyonu

için SA ve Foça gözlem istasyonu için GRG algoritmasının daha başarılı olduğu ve Eş. (11) ile hesaplanan gerçek rüzgar güç yoğunluğu verilerine göre de Loras gözlem istasyonu için en iyi sonuçların EMJ ve Foça Gözlem istasyonu için en iyi sonuçların EML metotları ile elde edildiği görülmektedir.

**KAYNAKLAR**

Abdelkrim, E.M. (2010). Two-phase generalized reduced gradient method for constrained global optimization. *J. Appl. Math*. 1-19.

Abdulahad, A. A., Saleh, M. A., & Mohammed, B. A. (2016). Analysis of wind speed and Estimation of Weibull Parameters by Three Numerical Methods in Al-Sulaimani Province. *Al-Mustansiriyah Journal of Science*, *27*(1).

Aslan, Y., & Yaşar, C. Dumlupınar Üniversitesi Kampüsündeki Rüzgar Enerjisinin Değerlendirilmesi İçin Örnek Bir Uygulama. chrome-extension://efaidnbmnnnibpcajpcglclefindmkaj/https://www.emo.org.tr/ekler/64939da0c6ae8ee_ek.pdf

Azad, A. K., Rasul, M. G., & Yusaf, T. (2014). Statistical diagnosis of the best Weibull methods for wind power assessment for agricultural applications. *Energies*, 7(5), 3056-3085.

Bayraktar, Y., & Kaya, H. İ. (2016). Yenilenebilir enerji politikaları ve rüzgâr enerjisi açısından bir karşılaştırma: Çin, Almanya ve Türkiye örneği. *Uluslararası Ekonomik Araştırmalar Dergisi*, *2*(4), 1-18.

Beck, P., Lasdon, L., and Engquist, M. (1983). A reduced gradient algorithm for nonlinear network problems. *ACM Transactions on Mathematical Software*, 9(1), 57–70.

Brenan, K.E., Hallman,W.P. (1995). A generalized reduced gradient algorithm for large-scale trajectory optimization problems. *Optim. Des. Control*, 19, 117–132.

Chen, H., Birkelund, Y., Anfinsen, S. N., Staupe-Delgado, R., & Yuan, F. (2021). Assessing probabilistic modelling for wind speed from numerical weather prediction model and observation in the Arctic. *Scientific Reports*, *11*(1), 1-11.

Çukurçayır, M. A., & Sağır, H. (2008). Enerji sorunu, çevre ve alternatif enerji kaynakları. *Selçuk Üniversitesi Sosyal Bilimler Enstitüsü Dergisi*, (20), 257-278.

Gabriele, G. A., & Ragsdell, K.M. (1977). The Generalized reduced gradient method: a reliable tool for optimal design, *ASME Journal of Engineering for Industry*, 99, 384-400.

Gülersoy, T., & Çetin, N. S. (2010). Menemen bölgesinde rüzgar türbinleri için Rayleigh ve Weibull

dağılımlarının kullanılması. *Politeknik Dergisi*, *13*(3), 209-213.

Güngör, M. (2008). Ki-kare testi üzerine. *Fırat Üniversitesi Doğu Araştırmaları Dergisi*, *7*(1), 84-89.

Hayli, S. (2001). Rüzgar enerjisinin önemi, Dünya'da ve Türkiye'deki durumu. *Fırat Üniversitesi Sosyal Bilimler Dergisi*, *11*(1), 1-26.

Jiang, H., Wang, J., Wu, J., & Geng, W. (2017). Comparison of numerical methods and metaheuristic optimization algorithms for estimating parameters for wind energy potential assessment in low wind regions. *Renewable and Sustainable Energy Reviews*, *69*, 1199-1217.

Justus, C. G., & Mikhail, A. (1976). Height variation of wind speed and wind distributions statistics. *Geophysical research letters*, *3*(5), 261-264.

Karaboğa, D. (2018). *Yapay Zeka Optimizasyon Algoritmaları*. Ankara: Nobel.

Karadağ, İ. H. (2009). *Yenilenebilir enerji kaynakları arasında rüzgar enerjisinin önemi ve rüzgar türbini tasarımı.* (Yüksek Lisans Tezi, Yıldız Teknik Üniversitesi Fen Bilimleri Enstitüsü)

Kaplan, Y. (2016). Rayleigh ve Weibull dağılımları kullanılarak Osmaniye bölgesinde rüzgar enerjisinin değerlendirilmesi. *Süleyman Demirel Üniversitesi Fen Bilimleri Enstitüsü Dergisi*, *20*(1), 62-71.

Kim D., Mun S. (2021). Development of an Interface Shear Strength Tester and a Model Predicting the Optimal Application Rate of Tack Coat. *Construction Materials*, 1(1), 22-38.

Köse, F., Aksoy, M. H., and Özgören, M. (2014). An Assessment of Wind Energy Potential to Meet Electricity Demand and Economic Feasibility in Konya, Turkey. *International Journal of Green Energy*, 1(6), 559-576.

Köse B., Düz M., Güneşer M. T., Recebli Z. (2018). Estimating Wind Energy Potential With Predicting Burr Lsm Parameters, A Different Approach. *Sigma Journal of Engineering and Natural Sciences,* 36(2): 389-404.

Köse, B. (2022). Optimizasyon Teknikleri Ders Notları. İzmir Bakırçay Üniversitesi.

Köse, B., Aygün, H. ve Pak, S. (2021) *"Rüzgar Enerjisinde Kullanılan Weibull Olasılık Dağılımı Parametrelerinin Tahminlenmesinde İstatistiksel Metotlar ve Optimizasyon Algoritmalarının Karşılaştırılması,"* Uluslararası Katılımlı 23. Isı Bilimi ve Tekniği Kongresi, Gaziantep.

Köse, B., Aygün, H., & Pak, Semih. (2023) Rüzgar hız dağılımı modelinin Yusufçuk algoritması ile parametre tahminlemesi. *Gazi Üniversitesi Mühendislik Mimarlık Fakültesi Dergisi*, *38*(3), 1747-1756.

Köse, B. (2023). Teknobilim-2023, Yapay Zeka ve Mühendislik, Isıl İşlem Algoritması, 46-60.

Lysen, E. H., 1983. Introduction to Wind Energy, 2nd edition, CWD-Consultancy Services Wind Energy Developing Countries.

Mostafaeipour A., Jadidi M., Mohammadi K., Sedaghat A. (2014). An analysis of wind energy potential and economic evaluation in Zahedan, Iran. *Renewable and Sustainable Energy Reviews,* 30, 641–650.

The Generalized Reduced Gradient (GRG) Algorithm, Constrained Optimization 2, https://apmonitor.com/me575/uploads/Main/chap8_constrained_opt_sqp_ip_grg_v2.pdf

Wang, Y., Li, Z., He, L. P., & Li, M. (2020). Parameters Estimation of Mixed Weibull Distribution Based on Nonlinear Least Square Method and Simulated Annealing Algorithm. In *2020 Global Reliability and Prognostics and Health Management, PHM-Shanghai*, 1-7, IEEE.

Yılmaz, M. (2021). Türkiye'nin Bölgesel Rüzgar Enerji Potansiyelinin Dağılım Fonksiyonları Kullanılarak Karşılaştırmalı Analizi (Yüksek Lisans Tezi). Bilecik Şeyh Edebali Üniversitesi.

# INVESTIGATION OF THE EFFECT OF OPERATING PARAMETERS ON NERNST VOLTAGE IN HYDROGEN-OXYGEN FUEL CELLS

**Muhittin BİLGİLİ**[*], **Yunus Emre GÖNÜLAÇAR**[**]

[*]Gazi University, Engineering Faculty, Mechanical Engineering Department,
06570, Maltepe, Ankara, bilgili@gazi.edu.tr, ORCID: 0000-0003-0692-8646
[**]Gazi University, Engineering Faculty, Mechanical Engineering Department,
06570, Maltepe, Ankara, yunusemre.gonulacar@gazi.edu.tr, ORCID: 0000-0002-1565-8564

**Abstract:** In hydrogen-oxygen fuel cells, operating parameters have an influence on the maximum expected open circuit (Nernst) voltage. Even though fuel cells have been the subject of many research, none of them have theoretically investigated the impact of various operating parameters, particularly concerning Nernst voltage and maximum thermodynamic efficiency. In this study, a computer program was developed to theoretically determine the effect of various operating parameters on the Nernst voltage in hydrogen-oxygen fuel cells. This computer program was developed in MATLAB to mathematically examine the effects of hydrogen and oxygen mole ratios, anode and cathode pressures, and operating temperatures on the maximum expected open circuit voltage. When calculating Nernst voltages and maximum thermodynamic efficiency for fuel cell reactions containing water as a by-product, the effects of higher heating value (HHV) and lower heating value (LHV) are also considered in the solutions. As a result, it was also concluded that temperature increase reduces the fuel cell Nernst voltage and maximum thermodynamic efficiency. Therefore, it was observed from the figures that the best conditions for the Nernst voltage occur when HHV is assumed, the temperature is 353 K, the mole ratios of hydrogen and oxygen are 1.0, the anode and cathode pressures are 5 atm and 6 atm, respectively. In terms of thermodynamic efficiency, it was determined that there was a maximum increase of 92.2% in the LHV assumption compared to the HHV assumption at the temperature of 1000 K, provided that other operating parameters were kept constant.
**Keywords:** Nernst voltage, Fuel cell, Thermodynamic efficiency, Hydrogen-oxygen.

## HİDROJEN-OKSİJEN YAKIT HÜCRELERİNDE ÇALIŞMA PARAMETRELERİNİN NERNST VOLTAJINA ETKİSİNİN İNCELENMESİ

**Özet:** Hidrojen-oksijen yakıt hücrelerinde çalışma parametrelerinin beklenen maksimum açık devre (Nernst) voltajı üzerinde etkisi vardır. Yakıt hücreleri birçok araştırmaya konu olmasına rağmen hiçbiri, özellikle Nernst voltajı ve maksimum termodinamik verimlilikle ilgili çeşitli çalışma parametrelerinin etkisini teorik olarak incelememiştir. Bu çalışmada, hidrojen-oksijen yakıt hücrelerinde çeşitli çalışma parametrelerinin Nernst voltajına etkisini teorik olarak belirlemek için bir bilgisayar programı geliştirilmiştir. Bu bilgisayar programı, hidrojen ve oksijen mol oranlarının, anot ve katot basınçlarının ve çalışma sıcaklıklarının beklenen maksimum açık devre voltajı üzerindeki etkilerini matematiksel olarak incelemek için MATLAB'da geliştirilmiştir. Yan ürün olarak su içeren yakıt hücresi reaksiyonları için Nernst voltajları ve maksimum termodinamik verim hesaplanırken, çözümlerde üst ısıl değeri (HHV) ve alt ısıl değerinin (LHV) etkileri de dikkate alınmaktadır. Sonuç olarak sıcaklık artışının yakıt hücresi Nernst voltajını ve maksimum termodinamik verimi azalttığı sonucuna varılmıştır. Dolayısıyla Nernst voltajı için en iyi koşulların HHV kabulünde, sıcaklığın 353 K, hidrojen ve oksijenin mol oranlarının 1,0, anot ve katot basınçlarının sırasıyla 5 atm ve 6 atm olduğu durumlarda oluştuğu, grafiklerden gözlemlenmiştir. Termodinamik verim açısından diğer çalışma parametrelerinin sabit tutulması koşuluyla 1000 K sıcaklıkta LHV varsayımında HHV varsayımına göre maksimum %92,2 oranında bir artış olduğu tespit edilmiştir.
**Anahtar Kelimeler:** Nernst voltajı, Yakıt hücresi, Termodinamik verim, Hidrojen-oksijen.

## NOMENCLATURE

| | | | |
|---|---|---|---|
| F | Faraday constant | $C_p$ | Specific heat [J/kg·K] |
| T | Temperature [K] | $R_u$ | Universal gas constant [J·K/mol] |
| a | Thermodynamic efficiency coefficient | $E^o$ | Reversible voltage [V] |

| $E^{oo}$ | Thermal voltage [V] |
| $\eta_{th}$ | Thermodynamic efficiency |

## INTRODUCTION

The energy need in the world is increasing day by day due to developing technology, increasing population and the search for continuous economic and industrial development (Cellek and Bilgili, 2021; Gonzatti and Farret, 2017; Hernández-Gómez et al., 2020). Today, the decrease in fossil energy sources such as oil and natural gas, which meet a large part of this need, and the increasing damage to the environment lead scientists to various alternative energy sources (Liu et al., 2023; Sadeghi et al., 2021; Wang et al., 2023). Due to the problems caused by fossil energy sources, there is an increasing interest in renewable energy in the world (Abouemara et al., 2024; Mitra et al., 2023; Riad et al., 2023). However, the need to store energy in the use of non-continuous alternative energy sources such as the sun and wind has brought the use of hydrogen energy to the agenda (Arıç et al., 2019). Since hydrogen is one of the most efficient, cleanest and lightest fuels, it is an alternative energy carrier (Hernández-Gómez et al., 2020). Fuel cells, which constitute the most weighty part of research on hydrogen energy, attract attention (Arıç et al., 2019).

Fuel cells are electrochemical devices that convert chemical energy into work in the form of electrical energy and heat, as shown in Figure 1 (Mitra et al., 2023; Wang et al., 2023; Zhao et al., 2023). Contrary to the harmful emissions resulting from the combustion of fossil fuels, only water is formed as a by-product as a result of the reactions occurring in fuel cells. For this reason, fuel cells are seen as an environmentally friendly power source (Cellek and Bilgili, 2021). In addition, these devices have advantages such as high efficiency, quiet operation, fuel flexibility and low maintenance requirements. Fuel cells are used in power plants, automobiles, laptop computers, mobile phones, etc. where power is required at different scales (Liu et al., 2023; Mitra et al., 2023).
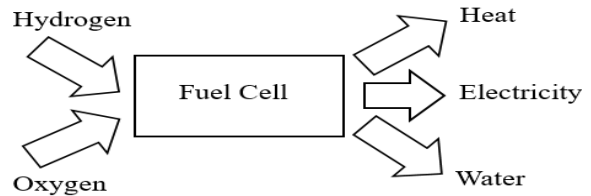


**Figure 1.** Simple $H_2/O_2$ fuel cell schematic impression

Determining the performance of a fuel cell depends on thermodynamic evaluation. Because a fuel cell is an electrochemical device that converts the chemical energy of a fuel and an oxidizing gas into electrical energy, predictions that can be made using thermodynamic equations are essential to understanding fuel cell performance. When a fuel cell is operating, some of the input is used to generate electrical energy, while some is converted into heat energy, depending on the type of fuel cell. Based on the first and second laws of thermodynamics, thermodynamic equations can be written to specify how energy can be transferred from one form to another (Khotseng, 2020).

Zhang et al. (2006) in their study on the PEM fuel cell, experimentally determined the open circuit voltage at 3 atm pressure and 6 different temperatures (between 23ºC and 120ºC). In their studies, it was stated that the open circuit voltage decreased with increasing temperature. Şefkat and Özel (2018) modeled a PEM fuel cell system with the help of MATLAB Simulink program. They concluded that the Nernst voltage increases with increasing hydrogen and oxygen pressures and decreases with increasing water pressure and temperature. (Sahli et al. (2017) examined the effect of various operating parameters on cell voltage and power density. As a result, they stated that the cell voltage and power density are proportional to the operating temperature and oxygen concentration, but inversely proportional to the supply pressure, fuel moisture and electrolyte thickness. In a similar study by Duncan et al. (2011) the dependence of open circuit voltage (OCV) and maximum power density on electrolyte thickness for solid oxide fuel cells (SOFCs) was investigated. As a result, it was emphasized that OCV decreases with decreasing electrolyte thickness and there is an optimum electrolyte thickness at which maximum power density occurs. Bo et al. (2009)

developed a thermodynamic model for the tubular SOFC stack and investigated the effects of various parameters on the SOFC system. They stated that the changes in current density, operating temperature, operating pressure, fuel utilization factor, air utilization factor and S/C ratio significantly affect the performance of SOFC and these parameters should be optimized for the best SOFC performance. Amadane et al. (2018) performed a PEM fuel cell model in MATLAB code and investigated the effect of temperature on PEMFC performance. As a result, they showed that the performance of the PEM fuel cell increases with temperature. In the study by Tu et al. (2020) the relationships between the reactions of methane on the nickel-based anode, fuel compositions, carbon deposition, electromotive force (EMF) and open circuit voltage (OCV) of SOFC were investigated. It was concluded that the temperature had different effects on the EMF and OCV values according to the fuel composition used. Matsui et al. (2005) emphasized that open circuit voltage in medium temperature solid oxide fuel cells (SOFCs) depends on electrode activity and electrolyte thickness, and overpotential at electrode/electrolyte interfaces affects OCV due to internal short circuit. In another study, Lyu et al. (2020) divided the voltage losses that cause the Nernst voltage drop in the hydrogen-oxygen fuel cell into three categories and said that the concentration loss does not cause the Nernst voltage loss.

The Nernst voltage is the starting point of the polarization curves that show the performance of fuel cells. Although there are many studies on fuel cells in the literature, there is no study that theoretically examines the effect of different operating parameters, especially on Nernst voltage and maximum thermodynamic efficiency. In this study, a MATLAB program was developed to theoretically examine the effect of various operating parameters on the Nernst voltage in hydrogen-oxygen fuel cells. The effects of cell temperature, hydrogen and oxygen mole ratios, anode and cathode pressures on the Nernst voltage were studied in detail theoretically. With the program developed in this context, the effect of each parameter on the Nernst voltage was calculated and the results were presented in graphics. In addition, analyzes were made considering both the lower heating value (LHV) and the higher heating value (HHV) of the fuel used. Maximum thermodynamic efficiency values for both heating value (LHV/HHV) assumptions were calculated at different operating temperatures. The results were compared by presenting them with graphics.

**FUEL CELL AND WORKING PRINCIPLE**

A fuel cell is an electrochemical device that converts chemical energy, typically from hydrogen, directly into electrical energy (Outeiro et al., 2008). The fuel cell is generally composed of an impermeable electrolyte, an anode and a cathode electrode in a permeable structure and in contact with both sides of the electrolyte. Electron flow occurs due to the potential difference formed as a result of the electrochemical reactions that occur when the gaseous fuel is sent to the anode part and the oxidizing gas to the cathode part. After the reactions take place, electrical energy is produced and external heat and pure water are formed. By connecting the fuel cells in series, more power output can be obtained than the power output from a single fuel cell. A basic representation for a single cell is given in Figure 2 (Işık, 2019).
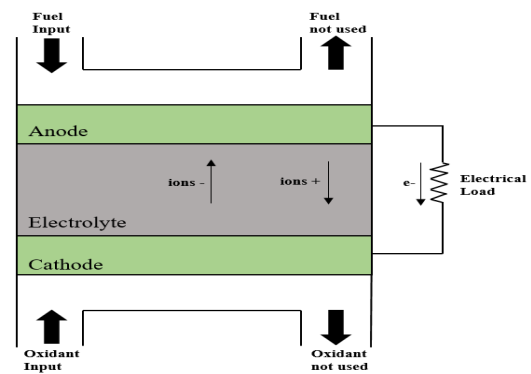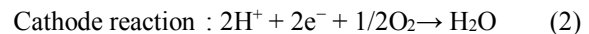


**Figure 2.** The basic structure of a fuel cell

Fuel cells are classified according to the choice of electrolyte, fuel and operating parameters. Hydrogen is the most used fuel for various fuel cells. It has high reactivity for anode reactions, can be produced chemically from a wide variety of fossil and renewable fuels as well as by electrolysis (Pachauri and Chauhan, 2015).

In a hydrogen fuel cell, electrochemical reactions occur simultaneously. The oxidation reaction of hydrogen occurs at the anode side, and the reduction reaction of oxygen occurs at the cathode side of fuel cell. These reactions take place at the anode, cathode and the total reaction are given in Equation (1), Equation (2), and Equation (3), respectively.

Anode reaction   : $H_2 \rightarrow 2H^+ + 2e^-$ (1)

Cathode reaction : $2H^+ + 2e^- + 1/2O_2 \rightarrow H_2O$ (2)

Total reaction     : $H_2 + 1/2O_2 \rightarrow H_2O$ (3)

When calculating thermodynamic voltages for reactions containing water as a product, the following defined Higher Heating Value (HHV) and Lower Heating Value (LHV) are selected:

• Higher Heating Value (HHV): It is assumed that all of the product water is in the liquid phase.
• Lower Heating Value (LHV): It is assumed that all of the product water is in the gas phase.

The difference between the two values is proportional to the latent heat of vaporization of the liquid. In practice, LHV is suitable for high temperature fuel cells, but the HHV value is also commonly used (Khotseng 2020).

## NERNST VOLTAGE THEORY

The open circuit voltage for an $H_2/O_2$ fuel cell is the maximum operating voltage (no current) and is determined by the chemical thermodynamics of the overall cell reaction. The Nernst equation provides a relationship between the reversible voltage ($E^o$) and the open circuit voltage for the cell reaction (Khotseng, 2020). The cell potential at equilibrium with the Nernst voltage is calculated by the Nernst equation.

The Nernst equation is a result of the equilibrium established at the electrode surfaces. A significant gradient can exist between the concentration of a species in the channel of a fuel cell and the electrode, especially under high-current-density conditions, which cannot be considered a true thermodynamic equilibrium situation anyway (Mench, 2008).

The Nernst equation for the hydrogen-oxygen fuel cell total reaction (Equation (3)) can be written as Equation (4). In this equation, the first term represents the reversible voltage, while the second term represents a term that depends on the thermodynamic efficiency coefficients and hence the pressure. The E(T, P) value (Nernst voltage) is calculated by adding these two terms.

$$E(T, P) = E^o(T) + \frac{R_u T}{nF} \ln \left[\frac{a_{H2}(a_{O2})^{\frac{1}{2}}}{a_{H2O}}\right] \qquad (4)$$

In Equation (4), $E^o(T)$ represents the reversible voltage, $R_u$ universal gas constant, T temperature, n the equivalent number of electrons per unit mole of the relevant species, F Faraday constant, a the thermodynamic efficiency coefficient for the reacting species. We can reduce Equation (4) to Equation (5) by assuming an ideal gas and changing the thermodynamic activity coefficients. The second term in Equation (5) is seen as a pressure-dependent term.

$$E(T,P) = E^o(T) + \frac{R_u T}{2F} \ln \left[\frac{(y_{H2}P_{anode}/P^o)(y_{O2}P_{cathode}/P^o)^{\frac{1}{2}}}{y_{H2O}P_{cathode}/ P_{sat}(T)}\right] \qquad (5)$$

where the reversible voltage ($E^o$) represents the maximum theoretical voltage that can be supplied by an open-circuit cell under standard pressure and temperature conditions (1 atm and 298 K). T represents temperature in [Kelvin], $R_u$ universal gas constant [J.K/mol], n represents the number of equivalent electrons per unit mole of the relevant species, F represents Faraday constant [C/equivalent e-]. Also, $y_{H2}$ and $y_{O2}$ are the mole ratios of hydrogen and oxygen, respectively, $P_{anode}$ and $P_{cathode}$ are the anode

and cathode pressures [atm], $P^o$ standard pressure [atm], and $P_{sat}$ saturation pressure (Nascimento et al., 2020).

The reversible voltage ($E^o$) can be determined as in Equation (6):

$$E^o(T) = \frac{-\Delta G^o(T)}{nF} = -\frac{\Delta H(T) - T\, \Delta S(T)}{nF} \qquad (6)$$

To calculate the reversible voltage value of the fuel cell at a certain temperature, it is necessary to determine both the enthalpy and the entropy change for the reacting species.

To determine the change in enthalpy of the reaction, we can use Equation (7) between the product and reactant states:

$$\Delta H_{P-R} = (\sum_{i=1}^{n} n_i h_i)_P - (\sum_{j=1}^{m} n_j h_j)_R \qquad (7)$$

where the index R represents the reactants, P products, n the number of moles of the species concerned, and h the specific enthalpy.

We can arrange Equation (7) for the reacting species as follows:

$$\Delta H_{P-R} = (h^o_{f,H_2O} + \int_{T_{ref}}^{T} c_{P,H_2O}(T)dT)H_2O -$$
$$\tfrac{1}{2}(h^o_{f,O_2} + \int_{T_{ref}}^{T} c_{P,O_2}(T)dT)O_2 - (h^o_{f,H_2} + \int_{T_{ref}}^{T} c_{P,H_2}(T)dT)H_2 \qquad (8)$$

where the specific heat functions can be directly integrated or the specific heat values can be considered constant at an average temperature. Assuming constant specific heat at average temperature, Equation (8) can be written as follows:

$$\Delta H = [h^o_{f,H_2O} + c_{P,H_2O,ave}(T - T_{ref})]H_2O - \tfrac{1}{2}[h^o_{f,O_2} + c_{P,O_2,ave}(T - T_{ref})]O_2 - [h^o_{f,H_2} + c_{P,H_2,ave}(T - T_{ref})]H_2 \qquad (9)$$

Enthalpies of formation ($h^o_f$) are available in thermodynamic reference books. Specific heat values for hydrogen, oxygen, and water can be found with the help of Equation (10), Equation (11) and Equation (12), respectively:

$$\frac{c_P(T)H_2}{R_u} = 3.057 + 2.677 \times 10^{-3}T - 5.810 \times 10^{-6}T^2 + 5.521 \times 10^{-9}T^3 - 1.812 \times 10^{-12}T^4 \qquad (10)$$

$$\frac{c_P(T)O_2}{R_u} = 3.626 - 1.878 \times 10^{-3}T + 7.055 \times 10^{-6}T^2 - 6.764 \times 10^{-9}T^3 + 2.156 \times 10^{-12}T^4 \qquad (11)$$

$$\frac{c_P(T)H_2O}{R_u} = 4.070 - 1.108 \times 10^{-3}T + 4.152 \times 10^{-6}T^2 - 2.964 \times 10^{-9}T^3 + 0.807 \times 10^{-12}T^4 \qquad (12)$$

Equation (13) can be used to determine the change in entropy:

$$\Delta S = (s^o_{f,H_2O} + \int_{T_{ref}}^{T} \frac{c_{P,H_2O}(T)dT}{T})H_2O - \frac{1}{2}(s^o_{f,O_2} + \int_{T_{ref}}^{T} \frac{c_{P,O_2}(T)dT}{T})O_2 - (s^o_{f,H_2} + \int_{T_{ref}}^{T} \frac{c_{P,H_2}(T)dT}{T})H_2 \tag{13}$$

Again, for the specific heat terms, their values can be obtained by integrating Equation (10), Equation (11) and Equation (12), but when solved with the assumption of constant specific heat at average temperature, the error is below 1%. Therefore, solutions are realized with constant specific heat assumption. The entropy of formation ($s^o_f$) at 1 atm pressure is available in thermodynamic reference books. The entropy change is obtained by the Equation (14) (Mench, 2008):

$$\Delta S = (s^o_{f,H_2O} + c_{P,H_2O,ave} \ln \frac{T}{T_{ref}})H_2O - \frac{1}{2}(s^o_{f,O_2} + c_{P,O_2,ave} \ln \frac{T}{T_{ref}})O_2 - (s^o_{f,H_2} + c_{P,H_2,ave} \ln \frac{T}{T_{ref}})H_2 \tag{14}$$

The effect of pressure on the Nernst voltage in Equation (5) is shown with P and can be calculated with the help of Equation (15):

$$P = \frac{R_u T}{2F} \ln \left[ \frac{(y_{H2}P_{anode}/P^o)(y_{O2}P_{cathode}/P^o)^{\frac{1}{2}}}{y_{H2O}P_{cathode}/P_{sat}(T)} \right] \tag{15}$$

The energy conversion process in a fuel cell must satisfy the first law of thermodynamics and ensure energy conservation. Since the purpose of a fuel cell is to convert chemical energy into electrical energy, the thermodynamic efficiency of a fuel cell can be written as in Equation (16):

$$\eta_{th} = \frac{actual\ electrical\ work}{maximum\ available\ work} \tag{16}$$

As shown in Equation (17), the ratio of reversible voltage ($E^o$) to thermal voltage ($E^{oo}$), in other words, the ratio of maximum electrical work to total available potential electrical work, represents the maximum possible thermodynamic efficiency:

$$\eta_{t,max} = \frac{E^o}{E^{oo}} = \frac{-\Delta G/nF}{-\Delta H/nF} = \frac{\Delta H - T\Delta S}{\Delta H} = 1 - \frac{T\Delta S}{\Delta H} \tag{17}$$

While calculating the maximum thermodynamic efficiency value in the study, Equation (17) was used. Therefore, the efficiency expression was obtained after calculating the entropy and enthalpy changes.

A computer program was written, which was developed in the light of the above-mentioned theory and primarily calculates the Nernst Voltage. In addition, maximum thermodynamic efficiency values were calculated at different temperatures. The flow chart of the working of the developed program is given in Figure 3. In the program, first of all, temperature, pressure, hydrogen/oxygen mole ratios, and determined heating value (lower/higher) of the fuel are used. Specific heat values are calculated for hydrogen, oxygen, and water for the species in the fuel cell's

overall reaction. Then, the reaction enthalpy and entropy changes are calculated for 41 different operating conditions. Nernst voltage and maximum thermodynamic efficiency values are obtained with the help of the developed program.
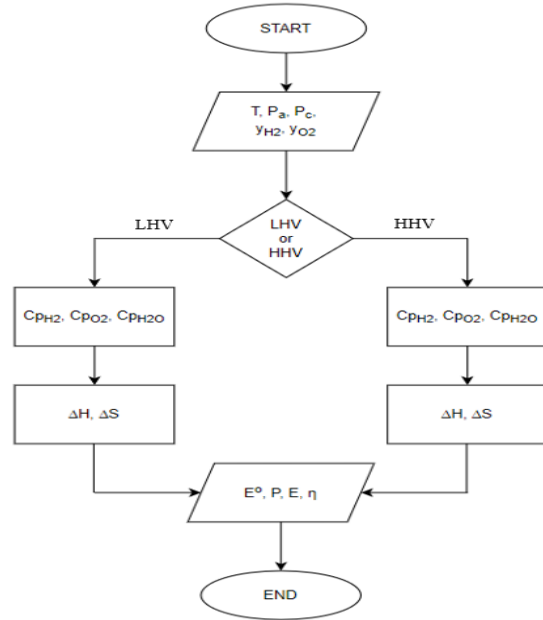


**Figure 3.** Flow chart of the developed program

**MATHEMATICAL ANALYSIS**

It is necessary to examine the Nernst voltage, which represents the voltage produced in the fuel cell, by taking into account the most important parameters affecting it. In this study, the effects of hydrogen mole ratio, oxygen mole ratio, operating temperature, anode and cathode pressures on the Nernst voltage were analyzed analytically. The thermodynamic equations written for the fuel cell were analyzed sequentially for the determined cases. In the numerical study, at a cell temperature of 353 K, the mole ratio of hydrogen ($y_{H_2}$) on the anode side is 0.8, the mole ratio of water vapor ($y_{H_2O}$) is 0.2, and the anode pressure ($P_a$) is 2 atm. On the cathode side, the mole ratio of oxygen ($y_{O_2}$) is 0.15, the mole ratio of water vapor ($y_{H_2O}$) is 0.1, the mole ratio of nitrogen ($y_{N_2}$) is 0.75 and the cathode pressure ($Pc$) is taken as 3 atm. These counted operating parameters were accepted as the reference case (Case-7) for future validation purposes and the Nernst voltage was calculated over this case. Then, the effect of each operating parameter such as temperature, anode and cathode pressure, hydrogen and oxygen mole ratios on the Nernst voltage was examined and compared with this reference case. The data for each case examined are given in Table 1.

**Table 1.** Different cases examined in the study

63

| Case | $y_{H_2}$ | $y_{O_2}$ | T [K] | $P_a$ [atm] | $P_c$ [atm] |
|------|-----------|-----------|-------|-------------|-------------|
| 1 | 0.5 | 0.15 | 353 | 2 | 3 |
| 2 | 0.55 | 0.15 | 353 | 2 | 3 |
| 3 | 0.60 | 0.15 | 353 | 2 | 3 |
| 4 | 0.65 | 0.15 | 353 | 2 | 3 |
| 5 | 0.70 | 0.15 | 353 | 2 | 3 |
| 6 | 0.75 | 0.15 | 353 | 2 | 3 |
| 7 | 0.80 | 0.15 | 353 | 2 | 3 |
| 8 | 0.85 | 0.15 | 353 | 2 | 3 |
| 9 | 0.90 | 0.15 | 353 | 2 | 3 |
| 10 | 0.95 | 0.15 | 353 | 2 | 3 |
| 11 | 1.00 | 0.15 | 353 | 2 | 3 |
| 12 | 0.80 | 0.21 | 353 | 2 | 3 |
| 13 | 0.80 | 0.25 | 353 | 2 | 3 |
| 14 | 0.80 | 0.35 | 353 | 2 | 3 |
| 15 | 0.80 | 0.45 | 353 | 2 | 3 |
| 16 | 0.80 | 0.55 | 353 | 2 | 3 |
| 17 | 0.80 | 0.65 | 353 | 2 | 3 |
| 18 | 0.80 | 0.75 | 353 | 2 | 3 |
| 19 | 0.80 | 0.85 | 353 | 2 | 3 |
| 20 | 0.80 | 0.95 | 353 | 2 | 3 |
| 21 | 0.80 | 1.00 | 353 | 2 | 3 |
| 22 | 0.80 | 0.15 | 400 | 2 | 3 |
| 23 | 0.80 | 0.15 | 500 | 2 | 3 |
| 24 | 0.80 | 0.15 | 600 | 2 | 3 |
| 25 | 0.80 | 0.15 | 700 | 2 | 3 |
| 26 | 0.80 | 0.15 | 800 | 2 | 3 |
| 27 | 0.80 | 0.15 | 900 | 2 | 3 |
| 28 | 0.80 | 0.15 | 1000 | 2 | 3 |
| 29 | 0.80 | 0.15 | 353 | 1 | 3 |
| 30 | 0.80 | 0.15 | 353 | 1.5 | 3 |
| 31 | 0.80 | 0.15 | 353 | 2.5 | 3 |
| 32 | 0.80 | 0.15 | 353 | 3 | 3 |
| 33 | 0.80 | 0.15 | 353 | 3.5 | 3 |
| 34 | 0.80 | 0.15 | 353 | 4 | 3 |
| 35 | 0.80 | 0.15 | 353 | 4.5 | 3 |
| 36 | 0.80 | 0.15 | 353 | 5 | 3 |
| 37 | 0.80 | 0.15 | 353 | 2 | 1 |
| 38 | 0.80 | 0.15 | 353 | 2 | 2 |
| 39 | 0.80 | 0.15 | 353 | 2 | 4 |
| 40 | 0.80 | 0.15 | 353 | 2 | 5 |
| 41 | 0.80 | 0.15 | 353 | 2 | 6 |

## Effect of Mole Ratios

It is known that the reactions in the fuel cell occur simultaneously at both the anode and the cathode. Therefore, the effect of both the hydrogen mole ratio at the anode and the oxygen mole ratio at the cathode on the voltage can be examined separately.

### Effect of oxygen mole ratio at the cathode on the Nernst voltage

Analyzes were made for different mole ratios of the oxygen gas at the cathode. Other parameters (pressure, temperature, hydrogen mole ratio) kept constant in the analyzes were taken from the reference case.
Numerical analyzes were performed at a cell temperature of 353 K. Numerical analyzes were performed for 11 different determined cathode oxygen mole ratios (0.15, 0.21, 0.25, 0.35, 0.45, 0.55, 0.65, 0.75, 0.85, 0.95 and 1.0). The effect of the oxygen mole ratio at the cathode on the Nernst voltage was numerically investigated and the change is given in Figure. 4.

When Figure 4 is examined, it is seen that the Nernst voltage increases with the increase in the mole ratio of $O_2$ in the cathode in both HHV and LHV cases, but this increase gradually decreases. For the LHV case, when the $O_2$ mole ratio is taken as 0.15, the Nernst voltage value is calculated as approximately 1.173 V. When the mole ratio of $O_2$ is taken as 1, that is, when the cathode is completely fed with pure oxygen, the Nernst voltage value is calculated as 1.187V. When these two values are compared, it is seen that there is an increase of 1.19% in the Nernst voltage. When the Nernst equation (Equation 5) is examined, it is seen that the mole ratio of oxygen is directly proportional to the Nernst voltage. Therefore, it is expected that the Nernst voltage will increase as the mole ratio of oxygen at the cathode increases. In some studies in the literature, it has been stated that Nernst voltage is directly proportional to the oxygen-mole ratio (Sahli et al., 2017).

For the HHV case, when the $O_2$ mole ratio is taken as 0.15, the Nernst voltage value is calculated as approximately 1.184 V, while the Nernst voltage value is calculated as 1.199 V when the $O_2$ mole ratio is taken as 1. When these two values are compared, it is seen that there is a 1.27% increase in Nernst voltage.

Ambient air is more preferred at the cathode because of the cost and storage problems caused by the use of pure oxygen in fuel cells. Therefore, the use of air is also analyzed. For this case ($O_2$ mole ratio 21%), the Nernst voltage was obtained as 1.175 V in the case of LHV and 1.186 V in the case of HHV.
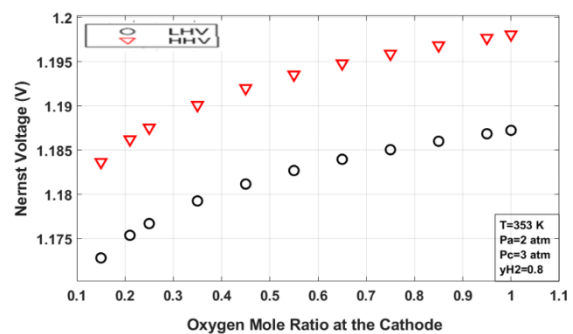


**Figure 4.** The Effect of Oxygen Mole Ratio at the Cathode to the Nernst Voltage

### Effect of mole ratio of hydrogen at the anode on Nernst voltage

Analyzes were made for different mole ratios of hydrogen gas at the anode. Other parameters (pressure, temperature, oxygen mole ratio) kept constant in the analyzes were taken from the reference situation. The mole ratio of $H_2$ was repeated with increasing values such as 0.50, 0.55, 0.60, 0.65, 0.70, 0.75, 0.80, 0.85, 0.90, 0.95 and 1.00. The effect of the hydrogen mole

ratio at the anode on the Nernst voltage is given in Figure 5.

It is seen that the Nernst voltage increases almost linearly for increasing hydrogen mole ratio in both HHV and LHV cases in Figure 5. For LHV assumption when the mole ratio of $H_2$ is taken as 0.50, the Nernst voltage value is calculated as approximately 1.166 V. When the mole ratio of $H_2$ is taken as 1, the Nernst voltage value is calculated as 1.176 V. As the mole ratio of $H_2$ in the anode side is increased from 50% to 100%, it has been observed that there is an increase of 0.86% in the Nernst voltage value. As explained in the previous section, considering the Nernst equation, it is seen that the hydrogen mole ratio at the anode affects the Nernst voltage directly. Since the hydrogen concentration in the fuel flow is high, a higher Nernst voltage is obtained (Mench, 2008; Pachauri and Chauhan, 2015).

For HHV assumption, when the mole ratio of $H_2$ is taken as 0.50, the Nernst voltage value is calculated as approximately 1.177 V. When the mole ratio of $H_2$ is taken as 1, the Nernst voltage value is calculated as 1.187 V. When these two values are compared, it is seen that there is an increase of 0.85% in the Nernst voltage.
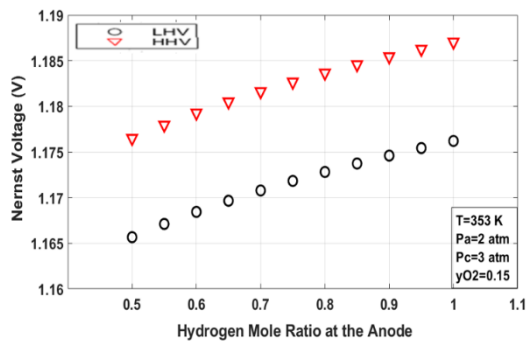


**Figure 5.** The effect of hydrogen mole ratio at the anode on the Nernst voltage

## Pressure Effect

Different anode and cathode pressure values were determined in the computer program. The partial pressure of hydrogen can be calculated by multiplying the determined anode pressure with the mole ratio of hydrogen. The partial pressure of oxygen can be calculated by multiplying the determined cathode pressure with the mole ratio of oxygen.
It can be seen in Equation 5 that the partial pressures of hydrogen ($P_{H_2} = y_{H_2} \times P_{anode}$) and oxygen ($P_{O_2} = y_{O_2} \times P_{cathode}$) gases, and therefore the anode and cathode pressures, affect the Nernst voltage. In the numerical analysis, nine different anode pressures and six different cathode pressures are selected and solved. Effects of these pressures on the Nernst voltage are given separately following sections.
### Effect of anode pressure

The effect of anode pressure on Nernst voltage is shown in Figure 6. The anode pressure was taken at different values such as 1, 1.5, 2, 2.5, 3, 3.5, 4, 4.5, and 5 atm, and its effect on the Nernst voltage was examined. As seen in Figure 6, the Nernst voltage increases with the increase of anode pressure for both the HHV case and the LHV case, but this increase gradually decreases. There are other studies in the literature stating that increasing pressure positively affects fuel cell Nernst voltage (Arıç et al., 2019; Lyu et al., 2020; Nascimento et al., 2020).

In the case of LHV, the Nernst voltage value obtained as 1.162 V at 1 atm pressure increased to 1.187 V at 5 atm pressure. Accordingly, it is seen that there is an increase of approximately 2.15% in the Nernst voltage value as the anode pressure rises from 1 to 5 atm.

In the case of HHV, the Nernst voltage value obtained as 1.173 V at 1 atm pressure increased to 1.198 V at 5 atm pressure. Therefore, as the anode pressure increased from 1 to 5 atm, there was an increase of approximately 2.13% in the Nernst voltage value.
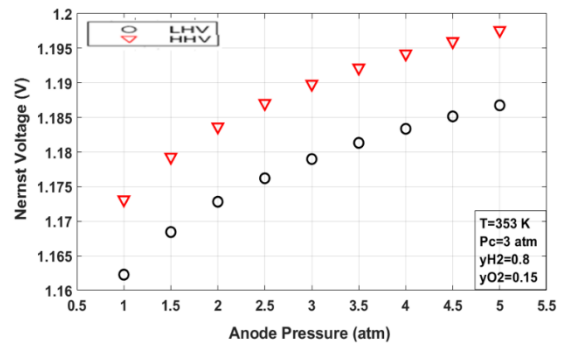


**Figure 6.** Effect of anode pressure on Nernst voltage

### Effect of cathode pressure

The effect of cathode pressure on Nernst voltage is shown in Figure 7. The cathode pressure was taken at different values such as 1, 2, 3, 4, 5 and 6 atm, and its effect on the Nernst voltage was investigated. It is seen that the increase in cathode pressure positively affects the Nernst voltage for both the HHV and the LHV assumptions (Figure 7). The increase in pressure has some beneficial effects on fuel cell performance due to higher reactant partial pressure, gas solubility, and mass transfer values. In addition, electrolyte losses due to evaporation are reduced at high operating pressures. System efficiency tends to increase with increasing pressure (Çavuşoğlu, 2006).

In the case of LHV, increasing the cathode pressure from 1 to 6 atm increased the Nernst voltage value from 1.164 V to 1.178 V. When these two values are compared, it is seen that there is an increase of approximately 1.2% in the Nernst voltage. In the case of HHV, increasing the cathode pressure from 1 to 6

atm increased the Nernst voltage value from 1.175 V to 1.189 V. Considering these two values, it is understood that there is an increase of approximately 1.19% in the Nernst voltage.

In summary, when the cathode pressure increased from 1 to 6 atm, the Nernst voltage increased by about 1.2% for both LHV and HHV cases.
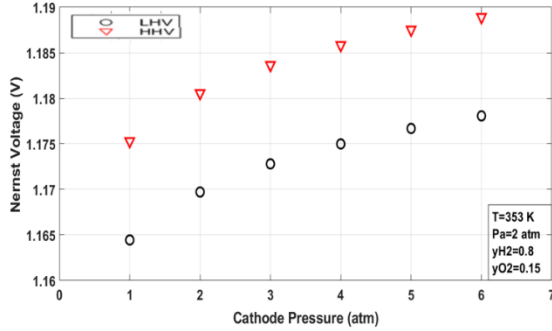


**Figure 7.** Effect of cathode pressure on Nernst voltage

**Temperature Effect**

Thermodynamic analyzes were carried out at different operating temperatures to see the effect of temperature, which is another important parameter for Nernst voltage. The findings obtained for the Nernst voltage and the maximum thermodynamic efficiency of the fuel cell in both the LHV case and the HHV case are explained in detail below.

**Effect of LHV and HHV values on Nernst voltage**

The Nernst voltage was calculated one by one using the LHV and HHV assumptions for different temperature values. The variation of the calculated Nernst voltage values with different temperature values is shown in Figure 8. The solutions were first started at 353 K and continued at increasing temperature values such as 400, 500, 600, 700, 800, 900, and 1000 K. As a result of the analysis, it was seen that the temperature increase caused a decrease on the fuel cell Nernst voltage. Since the entropy change of the $H_2/O_2$ reaction is negative, the Nernst voltage of $H_2/O_2$ fuel cells decreases with an increase in temperature of 0.84 mV/°C (Çavuşoğlu 2006). There are other studies in the literature where it is observed that the fuel cell Nernst voltage decreases with increasing temperature (Arıç et al., 2019; Lyu et al., 2020; Outeiro et al., 2008; Riad et al., 2023; Sahli et al., 2017; Şefkat and Özel, 2018).

The Nernst voltage values decreased more rapidly when the analyzes with HHV assumption were compared with those with LHV. For the LHV case, the Nernst voltage value was obtained as 1.173 V at 353 K and 1.003 V at 1000 K. Nernst voltage decreased by approximately 14.49% as the temperature increased from 353 K to 1000 K. For the HHV case, the Nernst

voltage value at 353 K was obtained as 1.184 V. In the case where the temperature was 1000 K, the Nernst voltage value was 0.616 V. The temperature increase from 353 K to 1000 K resulted in a 47.97% decrease in the Nernst voltage. Therefore, the decrease in Nernst voltage was much greater in the HHV case compared to the LHV case.
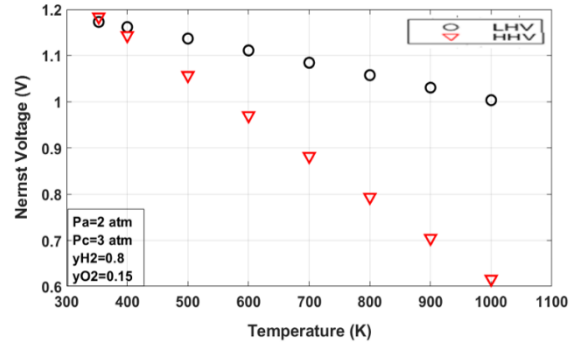


**Figure 8.** Variation of Nernst voltage with temperature for LHV and HHV status

**Effect of LHV and HHV values on maximum thermodynamic efficiency**

Maximum thermodynamic efficiencies were calculated one by one using LHV and HHV cases for different temperature values. The variation of the calculated efficiency values with different temperatures is shown in Figure 9. It is seen that the maximum thermodynamic efficiency of the fuel cell decreases with increasing temperature. This decrease is considered as a correct change in terms of fuel cell thermodynamics. When the electrochemical reaction occurring in the hydrogen fuel cell is examined in terms of the equilibrium equation, the total number of moles of the reactants is greater than the products. This means that the reaction entropy change (ΔS) value is less than zero. This result shows that the maximum thermodynamics efficiency decreases with increasing temperature for hydrogen fuel cells (Tu et al., 2020).

It is understood that the thermodynamic efficiency values decrease more rapidly in the HHV assumption compared to the LHV assumption, and the efficiency is higher in the LHV assumption under the same conditions. The maximum thermodynamic efficiency value for the LHV case was obtained as 0.933 at 353 K and 0.778 at 1000 K. As the temperature increased from 353 K to 1000 K, there was a decrease of approximately 16.61% in efficiency.

For the HHV case, the maximum thermodynamic efficiency value at 353 K was obtained as 0.797. In the case where the temperature was 1000 K, the efficiency value was 0.405. An increase in temperature from 353 K to 1000 K resulted in a decrease of approximately 49.18% in efficiency. Therefore, when the temperature increased from 353 K to 1000 K, there was a 16.61% decrease in the maximum thermodynamic efficiency in

the LHV case, while the decrease in the maximum thermodynamic efficiency was 49.18% in the HHV case.
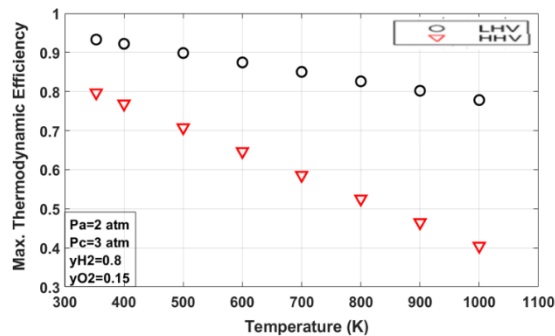


**Figure 9.** Effect of temperature on maximum thermodynamic efficiency for LHV and HHV assumption

## CONCLUSIONS

In this study, the effects of different operating parameters on Nernst voltage and maximum thermodynamic efficiency were numerically investigated using the developed computer program. The findings obtained as a result of the analyzes are given below.

1) It was observed that the Nernst voltage increased with the increase in the mole ratio of $O_2$ in the cathode, but the amount of increase gradually decreased. When the mole ratio of $O_2$ in the cathode was increased from 15% to 100%, the Nernst voltage value increased by 1.19%.

2) It was found that the Nernst voltage also increased linearly for increasing hydrogen mole ratio on the anode side. As the mole ratio of $H_2$ in the anode was increased from 50% to 100%, the Nernst voltage value increased by 0.86%.

3) Nernst voltage values also increased with the increase of anode pressure. As the anode pressure rises from 1 to 5 atm the Nernst voltage value increased approximately 2.15% and 2.13% for LHV and HHV assumption, respectively.

4) It has been observed that the increase in the cathode pressure has a positive effect on the Nernst voltage. In both the LHV and HHV assumption, the Nernst voltage increased by about 1.2% as the cathode pressure increased from 1 to 6 atm.

5) Increasing the operating temperature caused a decrease in both the fuel cell Nernst voltage and the maximum thermodynamic efficiency.

6) In the case of LHV, the decrease rate of Nernst voltage with the increase in temperature from 353K to 1000K was obtained as 14.5%, while in the case of HHV, this decrease rate was obtained as approximately 48%. The decrease in Nernst voltage was much greater in the HHV case compared to the LHV case.

7) When the temperature increased from 353 K to 1000 K, there was a 16.6% decrease in the maximum thermodynamic efficiency in the LHV case, while the decrease in the maximum thermodynamic efficiency was 49.2% in the HHV case.

The Nernst voltage, which is seen as the starting point of fuel cell polarization curves, has been numerically calculated according to different operating parameters. By calculating this voltage value, the effects of different operating parameters were examined. The results obtained from this study may be informative for researchers considering various applications of fuel cells in the future. Additionally, different operating parameters and fuel cell types can be considered for future research.

## REFERENCES

Abouemara K., Shahbaz M., Boulfrad S., Mckay G., and Al-ansari T., 2024, Design of an Integrated System That Combines the Steam Gasification of Plastic Waste and a Solid Oxide Fuel Cell for Sustainable Power Generation, *Energy Conversion and Management: X*, 21, 100524, doi: 10.1016/j.ecmx.2024.100524.

Amadane Y., Mounir H., Elmarjani A., and Ayad G., 2018, Modeling the Temperature Effect on PEM Fuel Cell Performance, *Eleven International Conference on Thermal Engineering: Theory and Applications*, Doha, Qatar.

Arıç, T., Bilgili M., and Özsunar A., 2019, Numerical Analysis of Two Units PEM Fuel Cell Stack Tugay, *Gazi University Journal of Science Part C: Design and Technology,* 7(4), 999–1011, doi: 10.29109/gujsc.623951.

Bo C., Yuan C., Zhao X., Wu C. B., and Li M. Q., 2009, Parametric Analysis of Solid Oxide Fuel Cell, *Clean Technologies and Environmental Policy,* 11, 391–99, doi: 10.1007/s10098-009-0197-4.

Çavuşoğlu A., 2006, *Fuel Cells and Their Applications*, M.Sc. Thesis, Uludağ University, Bursa, Turkey.

Cellek M., and Bilgili M., 2021, Investigation of the Effect of Stoichiometry Ratio on Two-Cell PEM Fuel Cell Stack Performance, *Gazi University Journal of Science Part C: Design and Technology,* 9(1), 134–47, doi: 10.29109/gujsc.799620.

Duncan K. L., Lee K., and Wachsman E. D., 2011, Dependence of Open-Circuit Potential and Power

Density on Electrolyte Thickness in Solid Oxide Fuel Cells with Mixed Conducting Electrolytes, *Journal of Power Sources,* 196(5), 2445–51, doi: 10.1016/j.jpowsour.2010.10.034.

Gonzatti F., and Farret F. A., 2017, Mathematical and Experimental Basis to Model Energy Storage Systems Composed of Electrolyzer, Metal Hydrides and Fuel Cells, *Energy Conversion and Management,* 132, 241–50, doi: 10.1016/j.enconman.2016.11.035.

Hernández-Gómez Á., Ramirez V., and Guilbert D., 2020, Investigation of PEM Electrolyzer Modeling: Electrical Domain, Efficiency, and Specific Energy Consumption, *International Journal of Hydrogen Energy,* 45(29), 14625–39, doi: 10.1016/j.ijhydene.2020.03.195.

Işık R., 2019, *Numerical and Experimental Investigation of the Effect of Flow Type on Performance and Temperature Distribution in Solid Oxide Fuel Cell,* M.Sc. Thesis, Ömer Halisdemir University, Niğde, Turkey.

Khotseng L., 2020, *Thermodynamics and Energy Engineering* (First Ed.), IntechOpen, London, United Kingdom, 3-19.

Liu Y., Tu Z., and Hwa S., 2023, Water Management and Performance Enhancement in a Proton Exchange Membrane Fuel Cell System Using Optimized Gas Recirculation Devices, *Energy,* 279, 128029, doi: 10.1016/j.energy.2023.128029.

Lyu J., Kudiiarov V., and Lider A., 2020, Corrections of Voltage Loss in Hydrogen-Oxygen Fuel Cells, *Batteries,* 6(9), 1-8, doi: 10.3390/batteries6010009.

Matsui T., Kosaka T., Inaba M., Mineshige A., and Ogumi Z., 2005, Effects of Mixed Conduction on the Open-Circuit Voltage of Intermediate-Temperature SOFCs Based on Sm-Doped Ceria Electrolytes, *Solid State Ionics*, 176(7–8), 663–68, doi: 10.1016/j.ssi.2004.10.010.

Mench M., 2008, *Fuel Cell Engines*, John Wiley & Sons, New Jersey, ABD.

Mitra U., Arya A., and Gupta S., 2023, A Comprehensive and Comparative Review on Parameter Estimation Methods for Modelling Proton Exchange Membrane Fuel Cell, *Fuel,* 335, 127080, doi: 10.1016/j.fuel.2022.127080.

Nascimento A. L., Yahyaoui I., Fardin J. F., Encarnação L. F., and Tadeo F., 2020, Modeling and Experimental Validation of a PEM Fuel Cell in Steady and Transient Regimes Using PSCAD/EMTDC Software, *International Journal of Hydrogen Energy,* 45(55), 30870–81, doi:

10.1016/j.ijhydene.2020.04.184.

Outeiro M. T., Chibante R., Carvalho A. S., and de Almeida A. T., 2008, A Parameter Optimized Model of a Proton Exchange Membrane Fuel Cell Including Temperature Effects, *Journal of Power Sources,* 185(2), 952–60, doi: 10.1016/j.jpowsour.2008.08.019.

Pachauri R. K., and Chauhan Y. K., 2015, A Study, Analysis and Power Management Schemes for Fuel Cells, *Renewable and Sustainable Energy Reviews,* 43, 1301–19, doi: 10.1016/j.rser.2014.11.098.

Riad, A. J., Hasanien H. M., Turky R. A., and Yakout A. H., 2023, Identifying the PEM Fuel Cell Parameters Using Artificial Rabbits Optimization Algorithm, *Sustainability,* 15(4625), 1–17.

Sadeghi M., Jafari M., Hajimolana Y. S., Woudstra T., and Aravind P. V., 2021, Size and Exergy Assessment of Solid Oxide Fuel Cell-Based H 2 -Fed Power Generation System with Alternative Electrolytes : A Comparative Study, *Energy, Conversion and Management* 228, 113681, doi: 10.1016/j.enconman.2020.113681.

Sahli Y., Zitouni B., and Ben-Moussa H., 2017, Solid Oxide Fuel Cell Thermodynamic Study, *Çankaya University Journal of Science and Engineering,* 14(2), 134–51.

Şefkat G., and Özel M. A., 2018, Simulink Model and Analysis of PEM Fuel Cell, *Uludağ University Journal of The Faculty of Engineering,* 23(2), 351–66, doi: 10.17482/uumfd.400337.

Tu B., Wen H., Yin Y., Zhang F., Su X., Cui D., and Cheng M., 2020, Thermodynamic Analysis and Experimental Study of Electrode Reactions and Open Circuit Voltages for Methane-Fuelled SOFC, *International Journal of Hydrogen Energy,* 45(58), 34069–79, doi: 10.1016/j.ijhydene.2020.09.088.

Wang Y., Wu K., Zhao H., Li J., Sheng X., Yin Y., Du Q., Zu B., Han L., and Jiao K., 2023, Degradation Prediction of Proton Exchange Membrane Fuel Cell Stack Using Semi-Empirical and Data-Driven Methods, *Energy and AI,* 11, 100205, doi: 10.1016/j.egyai.2022.100205.

Zhang J., Tang Y., Song C., Zhang J., and Wang H., 2006, PEM Fuel Cell Open Circuit Voltage (OCV) in the Temperature Range of 23 °C to 120 °C, *Journal of Power Sources,* 163(1), 532–37, doi: 10.1016/j.jpowsour.2006.09.026.

Zhao L., Hong J., Yuan H., Ming P., Wei X., and Dai H., 2023, Dynamic Inconsistent Analysis and Diagnosis of Abnormal Cells within a High-Power Fuel Cell Stack, *Electrochimica Acta,* 464, 142897.

**Muhittin Bilgili** received his B.Sc. degree of Mechanical Engineering from Gazi University in 2000, Ankara. He completed his M.Sc. and Ph.D. studies at Gazi University in 2003 and 2011, respectively. During his Ph.D. study, he worked as researcher at ENEA in Italy. He also worked as a postdoctoral reseacher at (Institute for Energy and Transport) Cleaner Energy Unit of European Commission in Petten, The Netherlands between 2012 and 2013. His research is about fuel cell modelling and simulation, hydrogen energy, hydrogen storage methods, heat transfer, and thermodynamics.

**Yunus Emre Gönülaçar** received his B.Sc. degree from Bursa Uludağ University, Department of Mechanical Engineering in 2015. He completed his M.Sc. studies at Batman University in 2018 and continues his Ph.D. studies at Gazi University. He is research assistant at Gazi University.

# COMBINED FORCED AND NATURAL CONVECTION FROM A SINGLE TRIANGULAR CYLINDER

**Zerrin Sert**[*]

[*] Eskişehir Osmangazi University, School of Engineering and Architecture, Mechanical Engineering Department, 26480, Eskişehir/TURKEY, zbocu@ogu.edu.tr, ORCID: 0000-0001-6934-5443

**Abstract:** Unsteady laminar confined and unconfined fluid flow and mixed (forced and free) convection heat transfer around equilateral triangular cylinders are investigated numerically. The computation model is a two-dimensional domain with blockage ratios of BR=0.5, 0.25, 0.2, 0.1, 0.05, and 0.0333, with the Reynolds numbers ranging from 100 to 200. The working fluid is water (Pr = 7). The effects of aiding and opposing thermal buoyancy are incorporated into the Navier-Stokes equations using the Boussinesq approximation. The Richardson number, which is a relative measure of free convection, is varied in the range $-2 \leq Ri \leq 2$. The governing equations are solved by using the Finite Volume Method with a second-order upwind scheme used for differencing of the convection terms, and the SIMPLE algorithm is used for the velocity-pressure coupling. A discussion of the effect of the blockage ratio on the mean drag, mean rms lift coefficients, the Strouhal number, and the mean Nusselt number is also presented. The iso-vorticity contours and dimensionless temperature field are generated to interpret and understand the underlying physical mechanisms. The results reveal that, in addition to the Richardson and Reynolds numbers, the blockage rate is effective in the vortex distribution in the channel. It has been determined that the vortices formed behind the cylinder spread to the channel with a decreasing blockage rate. Especially at high Reynolds numbers, both the drag coefficient and the mean Nusselt number are significantly affected by the blockage ratio. For Ri=0, the drag coefficients for BR=0.25 in comparison to the BR=0.05 case are about 9% and 29% larger for Re= 100 and 200, respectively. For BR<0.1, two-column vortex formation at the back of the cylinder gave way to single vortexes in the aiding thermal buoyancy condition (Ri=2) compared to Ri=0 and -2. Also, useful correlations for flow characteristics and heat transfer are derived using the computed data.

**Keywords:** Heat transfer, Confined flow, Mixed convection, Equilateral triangle cylinder, Correlations.

# TEK ÜÇGEN SİLİNDİRDEN TÜMLEŞİK ZORLANMIŞ VE DOĞAL TAŞINIM

**Özet:** Eşkenar üçgen silindir etrafında kararsız laminer sınırlı/sınırsız akışkan akışı ve tümleşik (doğal ve zorlanmış) taşınımla ısı transferi sayısal olarak incelenmiştir. Sayısal model, BR=0.5, 0.25, 0.2, 0.1, 0.05 ve 0.0333 blokaj oranlarına ve Reynolds sayılarının 100 ile 200 arasında değiştiği iki boyutlu bir alandır. Çalışma akışkanı sudur (Pr=7). Termal kaldırma kuvvetininin destek olma ve buna karşı çıkma etkileri, Boussinesq yaklaşımı kullanılarak Navier-Stokes denklemlerine dahil edilmiştir. Doğal taşınımın göreceli bir ölçüsü olan Richardson sayısı 2≥Ri≥-2 aralığında değişmiştir. Yönetici denklemler, taşınım terimlerinin ayrıklaştırılması için second order upwind şeması ile Sonlu Hacim Yöntemi kullanılarak çözülmüş ve hız-basınç bağlantısı için SIMPLE algoritması kullanılmıştır. Blokaj oranının ortalama sürükleme katsayısı, ortalama rms kaldırma katsayısı, Strouhal sayısı ve ortalama Nusselt sayısı üzerindeki etkisine ilişkin elde edilen sonuçlar çalışmada sunulmuştur. Eş girdap ve boyutsuz eş sıcaklık eğrileri altta yatan fiziksel mekanizmaları yorumlamak ve anlamak için oluşturulmuştur. Sonuçlar Richardson ve Reynolds sayılarına ek olarak blokaj oranının kanalda girdap dağılımında etkili olduğunu ortaya koymaktadır. Azalan blokaj oranı ile silindir arkasında oluşan girdapların kanala yayıldığı tespit edilmiştir. Özellikle yüksek Reynolds sayılarında hem sürükleme katsayısı hem de ortalama Nusselt sayısı blokaj oranından önemli ölçüde etkilendiği görülmüştür. Ri=0'da BR=0.25 için sürükleme katsayısı BR=0.05 durumuyla karşılaştırıldığında Re=100 ve 200'de sırasıyla yaklaşık %9 ve %29 daha yüksek çıkmıştır. BR<0.1 için Ri=0 ve -2'ye kıyasla termal kuvveti destekleyici durumda (Ri=2) kanal arkası çift girdap oluşumu yerini tekli girdaplara bırakmıştır. Ayrıca akış özellikleri ve ısı transferi için faydalı korelasyonlar, elde edilen veriler kullanılarak türetilmiştir.

**Anahtar Kelimeler:** Isı transferi, Sınırlı akış, Tümleşik taşınım, Eşkenar üçgen silindir, Korelasyonlar.

## INTRODUCTION

The eddy shedding phenomenon behind the cylinder has been extensively studied by the fluid dynamics community because of its importance in engineering applications. Contrary to numerous publications on circular cylinders, it is only recently that research has been conducted on the forced flow over cylinders of different cross-sections (circular (Lupi, 2013; Laidoudi and Bouzit, 2018; Patel and Chhabra, 2019; Barati et al., 2022), square (Mahir and Altaç, 2019; Arif and Hasan, 2020; Sharma and Dutta, 2022), semicircular, elliptic (Zhang et al., 2020; Hyun and SikYoon, 2022; Salimipour and Yazdani, 2022), and trapezoidal). Although non-circular cylinders play a dominant role in many technical applications, there is very limited information in the literature on mixed (natural and force) convection heat transfer and flow over or from non-circular cylinders. Triangular cylinders can be used in different applications such as in the novel designs of heat exchangers (Tiwari and Chhabra, 2014), finned heat removal devices utilized as sinks in electronic cooling applications (Tiwari and Chhabra, 2014), polymer engineering applications (Laidoudi and Bouzit, 2018), and continuous thermal treatment of foodstuffs (Laidoudi and Bouzit, 2018), etc.

The 2-D numerical simulations of laminar flow around a triangular cylinder placed in free-stream (unconfined flow) were examined by De and Dalal (2006), Dulhani and Dalal (2015). Zeitoun et al. (2010) analyzed forced convection from a triangular cross-section in an unconfined channel for Re=1.3-2×10⁵. They found that the stream flows smoothly past the body with no separation at Re = 1.38 for their study. Zeitoun et al. (2011) examined 2-D laminar forced convection heat transfer around the horizontal triangular cylinder in the unconfined channel for Re≤200 and Pr=0.71. They considered two configurations of the triangular cylinders: one when the vertex of the triangle faces the flow and the other when the base of the triangle faces the flow. They found the critical Reynolds number for both vertex-facing and the base-facing flows to be 38.03 and 34.7, respectively. Dhiman and Shyman (2011) examined the effects of Reynolds number on the heat transfer characteristics of a long (heated) equilateral triangular cylinder in the unconfined cross-flow regime for 50≤Re ≤150 and Pr=0.71. The fluid flow and mixed heat transfer around a triangular cylinder placed in an unconfined channel were examined numerically by Chatterjee and Mondal (2015). Their numerical simulations for combinations of Reynolds (Re=10-100), and Richardson (Ri=0-1) numbers are carried out for Pr=0.71. They reported that the amplitude of oscillation of the global flow and heat transfer quantities increased drastically, resulting from rapid mixing behind the obstacle. Altaç et al. (2019) investigated mixed convection heat transfer and fluid flow over a long horizontal equilateral triangular cylinder in an unconfined channel. Their simulation variables, Reynolds and Richardson numbers, are varied in the range $10 \leq Re \leq 200$ and $0 \leq Ri \leq 10$.

Çelik and Altaç (2023) numerically investigated unsteady heat and fluid flow over a triangular cylinder with rounded corners. They considered a 2-D laminar regime ($50 \leq Re \leq 250$), two fluids (air and water), corner rounding, and cylinder orientation on the heat and flow characteristics. They reported that the mean Nusselt number (local heat transfer coefficient) for Pr = 0.7 and 7 is markedly influenced by the flow conditions and geometric orientations rather than corner rounding. However, in this study, the confined channel was handled, and the effects of the blockage ratio on heat transfer were examined.

The heat transfer and flow past a triangular cylinder in horizontal channels of $1/12 \leq BR \leq 1/3$ were numerically investigated by De and Dalal (2007) for $80 \leq Re \leq 200$. Srikanth et al. (2010) investigated the fluid flow and heat transfer across a long equilateral triangular cylinder placed in a confined channel for Re=1-80, Pr=0.71, and a blockage ratio of 0.25. They reported that the mean Nusselt number and the wake length increased with the increasing Reynolds number, and the average drag coefficient decreased with the increasing Reynolds number. Shademani et al. (2013) analyzed viscous and incompressible flow over an equilateral triangular obstacle placed in a confined horizontal channel (BR=0.05). They found the critical value of the Reynolds number (Re ≤ 38.03). In reference (De and Dalal, 2007; Srikanth et al., 2010; Shademani et al., 2013), studies were performed for pure forced convection in the confined channel. Abbasi et al. (2001) examined the flow and heat transfer from a heated triangular cylinder in a 2D horizontal confined channel for Pr = 0.71, Grashof number (0≤Gr≤1.5×10⁴), and $20 \leq Re \leq 250$. Hassab et al. (2013) examined experimentally laminar mixed convection heat transfer from an isothermal horizontal triangular cylinder for Grashof numbers ranging from 26.32×10⁴ to 213.46×10⁴, Reynolds numbers ranging from 75.3 to 1251.6, and the attack angles from 0° to 180°. They concluded that whereas convection heat transfer increased with the angle of attack, conduction heat transfer remained constant with the Reynolds number. Additionally, they noted that for a given Reynolds number, the Nusselt number decreased as the airflow's attack angle increased. Rasool et al. (2015) examined the effects of mixed (natural and force) convection from a confined equilateral triangular cylinder placed centrally at an axis of a horizontal channel with a blockage ratio of 25% for Pr=0.71, Re=1-150, and Ri=0-2. Varma et al. (2015) studied mixed convective flow and heat transfer characteristics past a triangular cylinder placed symmetrically in a vertical channel with the blockage ratios BR=1/3, 1/4, and 1/6 for Re = 100 and −1≤Ri≤1. Dhiman (2016) studied the flow and heat transfer around a long equilateral triangular placed in a horizontal channel with a blockage ratio range of 0.1 to 0.5 for Re= 1-80. Zhu et al. (2020) numerically investigated the fluid flow around trapezoidal cylinders with various base length ratios in the confined channel (BR=0.05) for Re=150. They examined typical attack angles and the different base length ratios. Moreover, some information on the flow around a triangular

cylinder in the turbulent flow regime is presented in the literature. The considered problems have been solved both experimentally (Peng et al., 2008; Srigrarom and Koh, 2008; Akbari et al., 2021) and numerically (El-Wahed et al., 1993; Camarri et al. 2006; Chattopadhyay, 2007; Ali et al., 2011). Yagmur et al. (2017) examined experimentally and numerically the flow structures around an equilateral triangular cylinder using the Particle Image Velocimetry (PIV) technique and the Large Eddy Simulation (LES) turbulence model. Numerical analyses were examined at three different Reynolds numbers (Re=$2.9\times10^3$, $5.8\times10^3$, and $1.16\times10^4$) to obtain the changes in the Strouhal numbers and drag coefficients. They found that the Strouhal numbers were nearly St=0.22 for PIV and LES at all Reynolds numbers, and it could be inferred that these values were independent of the Reynolds number.

The literature review shows that mixed (buoyant and forced) convection heat transfer and fluid flow over triangular cylinders have received very little attention; however, the results on forced convection have shown that the use of triangular cylinders increases heat transfer compared to circular and square cylinders (Bovand et al., 2015). The purpose of this research is to computationally investigate the effects of aiding and opposing thermal buoyancy on heat transfer and fluid flow from triangular cylinders in a confined and/or unconfined upward cross-flow. The numerical simulation results have been obtained for $100 \leq \mathrm{Re} \leq 200$ and for blockage ratios of BR= 0.5, 0.25, 0.2, 0.1, 0.05, and 0.0333. Water (Pr = 7) is the working fluid, and the Richardson number range examined is $-2 \leq \mathrm{Ri} \leq 2$. This study is especially unique in that it examines the effect of blockage ratio as well as aiding and opposing buoyant forces.

## PHYSICAL PROBLEM AND MATHEMATICAL MODEL

A schematic of the two-dimensional computational domain with a triangular cylinder embedded in it is shown in Fig. 1. The working fluid is water (Pr=7). The equilateral triangular cylinder of side length $D$ is located at a distance of 15$D$ from the channel entrance, and the overall length of the channel is constant at 50$D$ in all cases. The heat transfer and flow simulations are carried out for blockage ratios (BR=$D/H$) of 0.5, 0.25, 0.2, 0.1, 0.05, and 0.0333. Furthermore, the channel width in the unconfined channel is $H$=70$D$.

In the two-dimensional flow of an incompressible fluid subjected to buoyant forces, the dimensionless governing equations can be expressed by for (Mahir and Altaç, 2019),

Continuity equation:

$$\nabla \cdot \mathbf{u} = 0 \qquad (1)$$

Momentum equations:

$$\frac{\partial \mathbf{u}}{\partial \tau} + \mathbf{u} \cdot \nabla \mathbf{u} = -\nabla P + \frac{1}{\mathrm{Re}} \nabla^2 \mathbf{u} - \mathbf{g}\, Ri\, \Theta \qquad (2)$$

Energy equation:

$$\frac{\partial \Theta}{\partial \tau} + \mathbf{u} \cdot \nabla \Theta = \frac{1}{\mathrm{Re}\,\mathrm{Pr}} \nabla^2 \Theta \qquad (3)$$
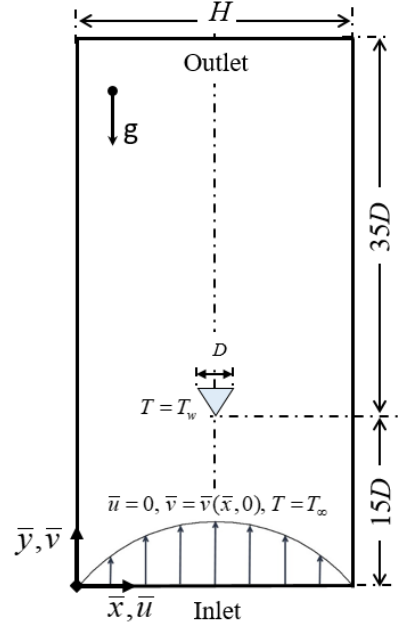


**Figure 1.** The schematic (dimensional) view of the applied geometry and computational domain.

where $\mathbf{u}$ is the dimensionless fluid velocity non-dimensionalized as $(\bar{u},\bar{v})/U_\infty$, $\tau$ is the dimensionless time defined as $\tau = U_\infty t/D$, $t$ is time, $x$ and $y$ are the dimensionless coordinate variables in Cartesian coordinates non-dimensionalized as $(\bar{x},\bar{y})/D$, $P$ is the pressure non dimensionalized by $\bar{P}/\rho U_\infty^2$, $\rho$ is density of fluid, $\mathbf{g}$ is the dimensionless gravity defined by $(0,-1)^T$, $\Theta$ is the dimensionless temperature defined as $\Theta = (T-T_\infty)/(T_w - T_\infty)$, $T$ is temperature, $T_w$ and $T_\infty$ are cylinder wall temperature and fluid inlet (or free stream) temperatures, respectively.

The boundary conditions used in the simulations are set as follows:

At the inlet:

For confined channel flows: The parabolic velocity profile defined by $u(x,0)$=0, $v(x,0) = 9\mathrm{BR} \cdot x(1 - x \cdot \mathrm{BR})$ for $1/70 \leq \mathrm{BR} \leq 1/2$, and $\Theta(x,0) = \Theta_\infty = 0$.

For unconfined channel flows: The fluid velocity and dimensionless temperature at the channel entrance are set $u(x,0) = 0$, $v(x,0) = 1$, and $\Theta(x,0) = \Theta_\infty = 0$.

On the left and right boundaries:

For confined channels: $u = 0$, $v = 0$, $\dfrac{\partial \Theta}{\partial y} = 0$

For unconfined channels: $u = 0$, $v = 1$, $\Theta_\infty = 0$

On the equilateral triangular cylinder walls:

$u = 0$, $v = 0$, $\Theta_w = 1$

<u>At the outlet:</u> $\dfrac{\partial u}{\partial x} = \dfrac{\partial v}{\partial x} = \dfrac{\partial \Theta}{\partial x} = 0$

An equilateral triangular cylinder is positioned along the centerline of the computational domain, and it is maintained at a constant isothermal temperature $\left( \Theta_w = 1 \right)$.

The Boussinesq approximation is used to simulate the effect of aiding and opposing buoyant forces. The Richardson number defined as $\mathrm{Ri} = \mathrm{Gr} / \mathrm{Re}^2$ is varied in the range $-2 \leq \mathrm{Ri} \leq 2$. The mixed-convection configurations corresponding to the positive and negative values of the Richardson number, respectively, are assisting and opposing flow situations. In the heated cylinder ($\Theta_w > 0$), the buoyancy force assists forced convection (i.e., forced and free convection directions are upwards), while for a cooled cylinder case ($\Theta_w < 0$) the free convection is downwards in a direction that opposes the upwards forced convection.

The Reynolds, Grashof, and Prandtl numbers are defined as follows:

$$\mathrm{Re} = \frac{\bar{U} D}{\nu}, \; \mathrm{Gr} = \frac{g \beta \left| T_w - T_\infty \right| D^3}{\nu^2}, \; \mathrm{Pr} = \frac{\nu}{\alpha} \qquad (4)$$

where $\bar{U}$ is the mean velocity of the fluid at the channel inlet, $\nu$ is the kinematic viscosity, $\beta$ is the thermal expansion coefficient, and α is the thermal diffusivity of the fluid. The side length $D$ of the equilateral triangular cylinder is used to non-dimensionalize all geometrical lengths. The Reynolds numbers range from 100 to 200.

The mean Nusselt number over the whole cylinder surface is evaluated as follows:

$$\mathrm{Nu} = \frac{hD}{k} = \frac{1}{A_s} \int\limits_{A_s} \mathrm{Nu}_s \, dA_s \qquad (5)$$

where $h$ is the mean heat transfer coefficient, $k$ is the thermal conductivity of the fluid, $A_s$ is the cylinder wall surface area, $\mathrm{Nu}_s = -(\partial \Theta / \partial n)_s$ is the local Nusselt number computed as the dimensionless temperature gradient in the normal dimensionless direction ($n$) to the

cylinder wall, and $s$ represents the circulation distance along the perimeter of the triangular cylinder.

The drag and lift coefficients are defined as:

$$C_D = \frac{2F_D}{\rho D U_\infty^2}, \quad C_L = \frac{2F_L}{\rho D U_\infty^2} \qquad (6)$$

where $F_D$ and $F_L$ are the drag and lift forces. The Strouhal number is defined as $St = fD / \bar{U}$ where $\bar{U}$ is the mean inlet velocity and $f$ is the vortex shedding frequency.

## NUMERICAL VALIDATION AND VERIFICATION

Numerical simulations in this study are carried out using the commercially available software ANSYS-Fluent®, where the continuity, momentum, and energy equations, Eqs. (1)-(3), are numerically solved by employing the finite volume method. The SIMPLE algorithm is used to solve the governing equations, and the second-order upwind differencing scheme is applied to discretize the equations. The convergence criterion for residuals is set to $10^{-5}$.

The computational domain (unconfined channel, $70D \times 50D$) is meshed with non-uniform meshing using triangular elements (Gambit®). To determine the finest mesh, four alternative mesh structures with a wide range of nodes are used. G1, G2, G3, and G4 were established as grid alternatives. Table 1 shows the effects of the grid sensitivity on the cylinder surface mean Nusselt number (Nu), the mean drag coefficient ($C_{D,mean}$), and the Strouhal number for Re=100, Ri=0, Pr=0.7, and BR=0.1. The growth rate for the size of the triangular elements was 15% stretched out to the boundaries of the computational domain for G3. Moreover, an adaption procedure to the computation domain near the cylinder was employed. Due to yielding relative errors of 0.15% and 1.12%, respectively, for the mean Nusselt and $C_{D,mean}$ numbers, the G3 grid structure was selected for conducting numerical simulations of this study. Figure 2 shows a typical grid structure (G3) near the equilateral triangle.
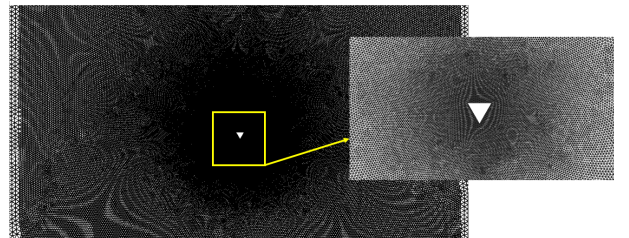


**Figure 2.** The grid structure of near the equilateral triangle.

The time step size in transient analysis also affects the accuracy of the numerical simulation. For this reason, the time step size is also varied to determine the optimum time step. The effect of varying the time step on the Nu, $C_{D,mean}$, and St is presented in Table 2 for the case of

Re=100, Ri=0, Pr=0.7, and BR=0.1. As a result, for subsequent simulations, the time step was chosen to be $\Delta\tau = 0.05$.

**Table 1.** The grid sensitivity for Re=100, Ri=0, Pr=0.7 and BR=0.1.

|  | G1 | G2 | G3 | G4 |
|---|---|---|---|---|
| Nodes Number | 25952 | 57492 | 102986 | 410300 |
| Cells Number | 51082 | 113752 | 204328 | 817312 |
| Nu | 7.155 | 7.109 | 7.097 | 7.086 |
| $C_{D,mean}$ | 0.858 | 0.878 | 0.886 | 0.896 |
| St | 0.3175 | 0.3125 | 0.3125 | 0.3125 |

According to the literature, a 2-D confined channel (BR=0.333) with an equilateral triangular cylinder is investigated at Ri=0 and Pr=0.7. The velocity at the inlet of this case is uniform. Table 3 depicts a comparison of the heat transfer and flow parameters for Re=100 and 150 with those available in the literature.

**Table 2.** The effects of time step size on heat and flow parameters for Re=100, Ri=0, Pr=0.7, and BR=0.1.

| Time Step Size | Nu | $C_{D,mean}$ | St |
|---|---|---|---|
| 0.1 | 7.129 | 0.892 | 0.3223 |
| 0.075 | 7.109 | 0.888 | 0.3125 |
| 0.05 | 7.097 | 0.886 | 0.3125 |
| 0.025 | 7.091 | 0.886 | 0.3149 |

The comparison of the current pure convective computations reveals a good agreement in the cases of confined flow. The results for the mean drag coefficient, Nusselt and Strouhal numbers are quite consistent with those in the literature. Some minor discrepancies can be attributed to the selection of the size of the computational domain, gridding and near wall meshing strategies adopted, the time step size, differencing schemes employed to transient and convective terms, and so on.

**Table 3.** Verification of mean Nusselt number and flow quantities with the available literature values for different Re numbers.

|  |  | Nu | Relative Error % | $C_{D,mean}$ | Relative Error % | St | Relative Error % |
|---|---|---|---|---|---|---|---|
| Re=100 | Present | 5.626 |  | 1.722 |  | 0.1953 |  |
|  | Chatterjee and Mondal (2015) | 5.6932 | 1.19 | 1.7546 | 1.89 | 0.1926 | 1.38 |
|  | Dhiman and Shyam (2011) | 5.5843 | 0.74 | 1.7316 | 0.56 | 0.1916 | 1.89 |
|  | De and Dalal (2007) |  |  | 1.7607 | 2.25 | 0.1982 | 1.48 |
|  | Zeitoun et al. (2011) | 5.557 | 1.23 |  |  |  |  |
|  | Dalal et al. (2008) | 5.67 | 0.78 |  |  |  |  |
| Re=150 | Present | 7.175 |  | 1.874 |  | 0.2148 |  |
|  | Chatterjee and Mondal (2015) | 7.1534 | 0.30 | 1.9037 | 1.58 | 0.2029 | 5.54 |
|  | Dhiman and Shyam (2011) | 7.0447 | 1.82 | 1.8937 | 1.05 | 0.2041 | 4.98 |
|  | De and Dalal (2007) |  |  | 1.875 | 0.05 | 0.2015 | 6.19 |
|  | Zeitoun et al. (2011) | 7.246 | 0.99 |  |  |  |  |
|  | Dalal et al. (2008) | 7.31 | 1.88 |  |  |  |  |

Errors in quantity $f$ evaluated as $f\% = (f_{present} - f_{literature})/f_{present} \times 100$.

**Table 4.** Validation of Nu, CD,mean, and St with the available literature values for Re=100 and 150.

|  |  | Nu | Relative Error % | $C_{D,mean}$ | Relative Error % | St | Relative Error % |
|---|---|---|---|---|---|---|---|
| Re=100 | Present | 5.576 |  | 1.662 |  | 0.2051 |  |
|  | Rasool et al. (2015) | 5.589 | 0.23 | 1.7 | 2.29 | 0.2036 | 0.73 |
|  | Srikanth et al. (2010) | 5.562 | 0.25 | 1.671 | 0.54 | 0.2004 | 2.29 |
| Re=150 | Present | 7.2 |  | 1.935 |  | 0.2344 |  |
|  | Rasool et al. (2015) | 7.161 | 0.54 | 2 | 3.36 | 0.2247 | 4.14 |
|  | Srikanth et al. (2010) | 7.127 | 1.01 | 1.934 | 0.05 | 0.2212 | 5.63 |

Errors in quantity $f$ evaluated as $f\% = (f_{present} - f_{literature})/f_{present} \times 100$.

In Table 4, the mean Nusselt number, mean drag coefficient, and Strouhal number results of the validation study are presented for a blockage ratio of BR=0.25 in Re=100 and 150. The velocity profile of the inlet is parabolic in this comparative study. This numerical investigation also depicts a good agreement. The minor variations in the results of Tables 3 and 4 can be explained by the size of the computational domain, meshing type and strategy, selection of convergence criteria, and so on.

## RESULTS AND DISCUSSION

The effect of blockage ratio on the flow field and heat transfer in confined (BR=0.5, 0.25, 0.2, 0.1, 0.05, and 0.0333) and unconfined (BR=0.0143) channels where the fluid is water (Pr=7) is examined for Re=100, 150, and 200 and the Richardson number ranging from $-2 \leq Ri \leq 2$.

**Investigation of the characteristics of flow and dimensionless temperature patterns**

Seven cases of blockage ratios (BR=0.5, 0.25, 0.2, 0.1, 0.05, and 0.0333) and unconfined flow (BR=0.0143) are examined to observe their effects on the flow and heat transfer parameters. The iso-vorticity contours are presented in black lines whereas the the dimensionless temperature field is plotted only in brown color contours for temperatures above $\Theta \geq 0.1$) for a better depiction of cold and hot regions. The figures are intended to give an idea of how the flow evolves. The iso-vorticity contour labels (which scale differently for each case) condensed near the cylinder make the figures incomprehensible. However, the legend for the dimensionless temperature is the same for all cases and it is provided in Fig. 3 only to save printing space (Fig. 3 is cited for the legends in the other figures).

For BR=0.5, the iso-vorticities contours (black lines) superimposed on the dimensionless temperature field for Ri=-2, 0, 2, and Re=100 and 200 are shown in Fig. 3. The case of Ri=0 corresponds to pure forced convection from the cylinders. The vortex is regular at Re=100 and interacts with the boundary layer on the channel walls. In particular, when Ri=2, these vortex forms are seen to be more erratic. The assisting flow—natural and forced convection—being in the same direction weakened the vortex structure at a low Reynolds number. It is seen from Fig. 3 that the wake structure for Re=100 is significantly different from that for Re=200. The reason for the difference in this flow structure is the increasing inertia force with the increase in the Reynolds number. In Re=200, the dimensionless temperature field and iso-vorticity contours for all Ri numbers have shown similar characteristics, and in all cases, tightly-packed iso-vortices along the channel.

The instantaneous iso-vorticity contours and the dimensionless temperature field for BR=0.2, Ri=-2, 0, 2, and Re=100 and 200 obtained from the computations are given in Fig. 4. It is seen that the vortices do not interact

with the boundary layer on the channel walls. Compared to Fig. 3, the reduction in the blocking ratio (widening the channel) leads to a larger vortex shedding period.
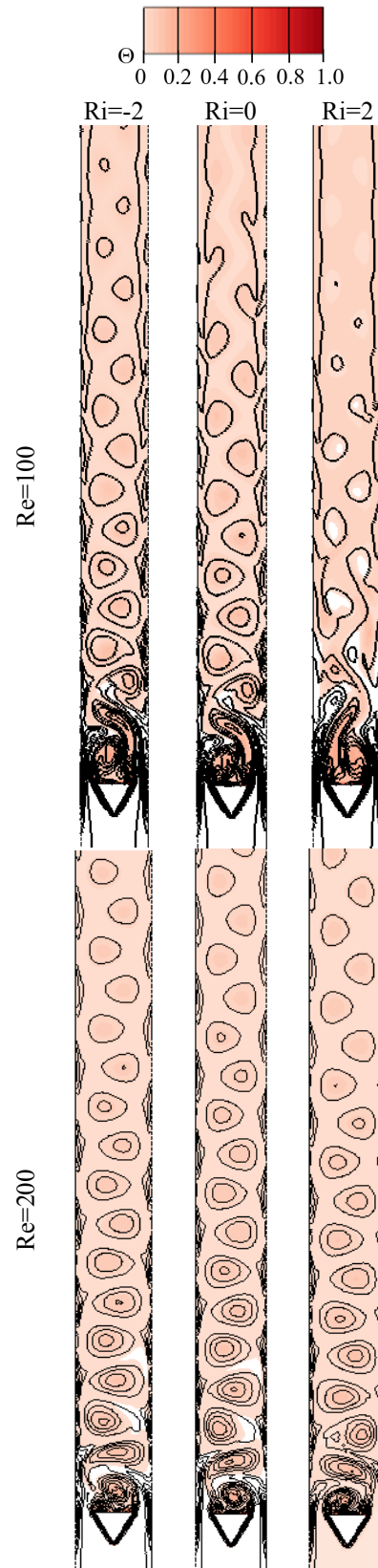


**Figure 3.** The iso-vorticity contours (black lines) superimposed with the dimensionless temperature field with different Ri and Re numbers for BR=0.5.

In the downstream area, the single-row closed vortex is formed behind the triangular cylinder. These iso-vortices are uniform and periodic in each case. In addition, the dimensionless temperature field near the cylinder walls is stacked very close to the walls, indicating that the temperature gradient is large.
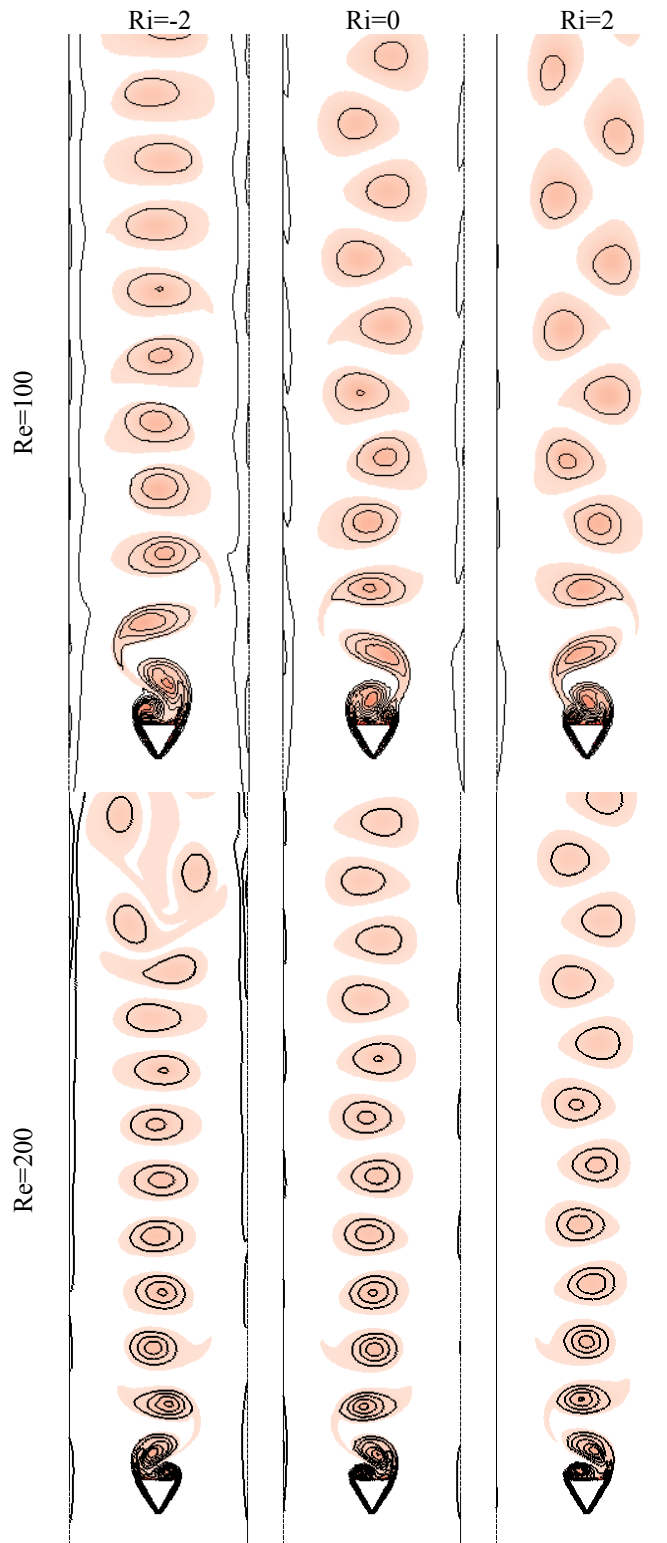


**Figure 4.** The iso-vorticity contours (black lines) superimposed with the dimensionless temperature field with different Ri and Re numbers for BR=0.2.

The variation of instantaneous iso-vorticity contours superimposed on the dimensionless temperature field for BR=0.1, Ri= -2, 0, 2, and Re=100 and 200 is shown in Fig. 5. In the Ri=-2 case, the vortices separated on the cylinder surface form two separate vortex columns after a certain distance, about *6D*, at both Re numbers. With increasing flow velocity at Re=200, two separate vortices occur closer to the cylinder (≈*4D*). At Ri=0 and Re=100, the double rows of round vortices formed behind the cylinder stretch out and tend to converge in the downstream direction. At Re=200, the double-column vortex structure is disrupted to form a single vortex structure in the downstream region. In the case of Ri=0 and Re=200, it is noted that the flow separation moves closer to the back of the cylinder. Natural convection, in the direction supporting forced convection, at Re=200 and Ri=2, the vortices behind the cylinder converged towards the center of the channel at about *7D*, yielding a single vortex column. In addition, the period of the vortices is slightly higher than that for Ri=-2 due to aiding natural convection.
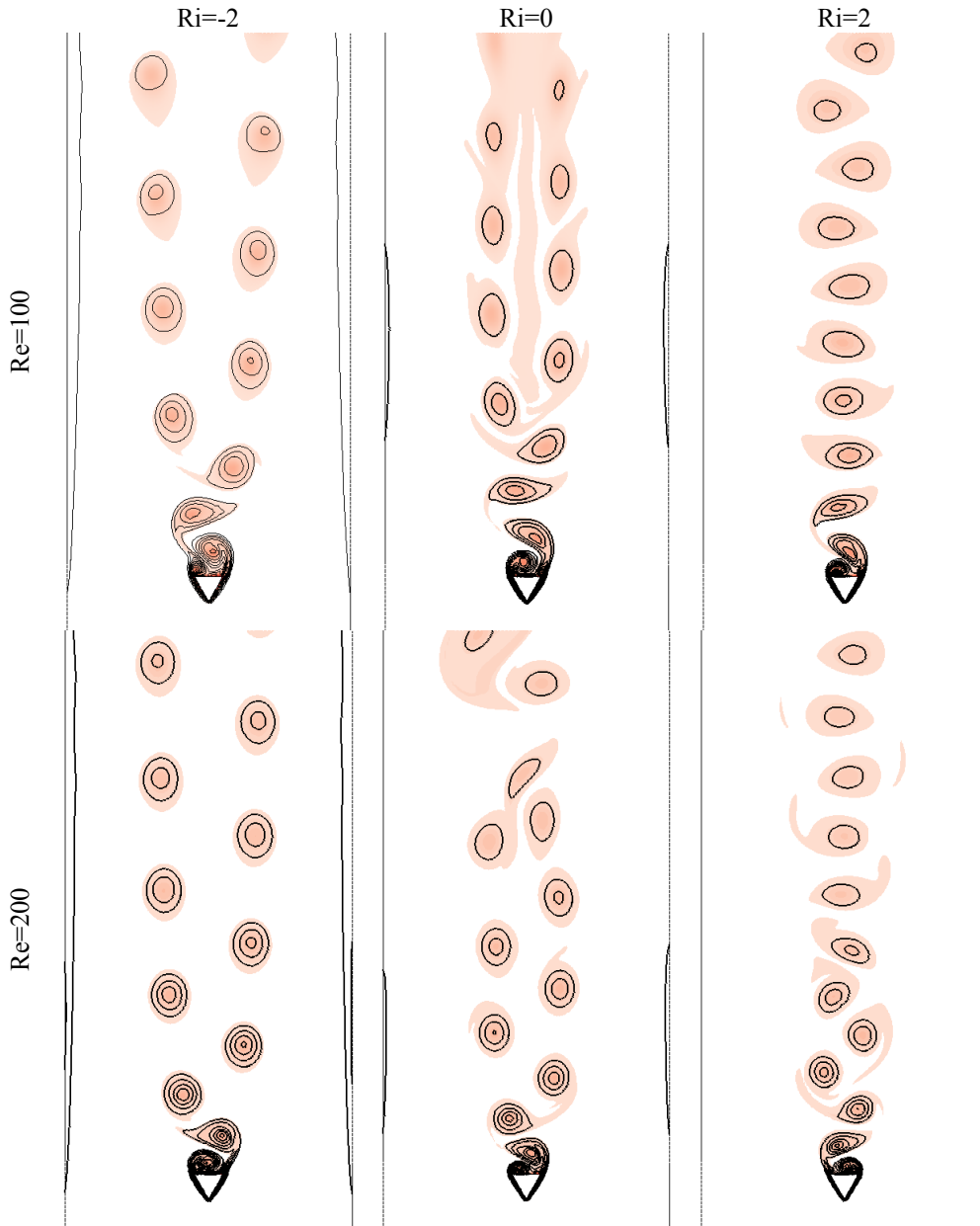


**Figure 5.** The variation of instantaneous iso-vorticity contours superimposed on the dimensionless temperature field (same legend as that of Figure 3) with different Ri and Re numbers for BR=0.1.

The variation of instantaneous iso-vorticity contours superimposed on the dimensionless temperature field for BR=0.033, Ri=-2, 0, 2, and Re=100 and 200 is illustrated in Fig. 6. For BR=0.033, the cylinder was away from the channel walls (H=30D), therefore vortex formation is not effected by the walls in all Re and Ri cases. Therefore, the channel walls are not shown in Fig. 6.

With the increasing Re number in Ri=-2, two separate vortices are formed behind the cylinder closer to the cylinder. Because of the downwards buoyancy force, the natural convection has a greater effect on the flow. Since the inertia force increases with Re = 200, the vortex shedding behind the cylinder is previously separated.

Initially, two distinct vortex columns are formed at about 11D distance behind the cylinder at Ri=0 and Re=100. However, the vortex columns stretch out as they tend to approach each other. At Re=200 and Ri=0, the vortices formed a non-uniform vortex trace. This situation is similar for Re=200.

Figure 7 illustrates the instantaneous iso-vorticity contours superimposed on the dimensionless temperature field in the unconfined channel (BR=0.0143) for Re=100, 200, and Ri=-2, 0, 2. For an unconfined channel and opposing buoyant flow (Ri=-2), it is seen that the wake behind the cylinder does not interact with the side walls, and the the dimensionless temperature field and iso-vorticities are able to spread out wider as it travels downwards along the channel. In both Reynolds cases, the formation of two vortices behind the cylinders is evident, and the two-column vortex structure is formed and maintained.

In pure forced convection (Ri=0), the formation of a two-column vortex street behind the cylinder dissolves further in the downstream region. Especially in Re = 200, the vortices in the left and right columns merge and turn into a single vortex street in the further downstream region. In Re=100, the two column vortex streets approach the channel center.

For the aiding buoyant flow case (Ri=2), a single von Karman vortex street appears instead of the two-column street for both Re cases. In Re=200, each vortex is lined up one after the other, whereas in Re=100, a single vortex column tends to diverge into two columns at about 14D. In addition, while the boundary layer formed around the cylinder at the same Reynolds numbers is thicker at Ri=-2, the boundary layer becomes thinner with increasing Ri numbers due to the direction of the fluid flow. As the first boundary layer separation takes place at about a 4D distance behind the cylinder for Ri=-2, this distance is 1D for Ri=2.

Consequently, the period of vortex shedding from an equilateral triangle cylinder decreases with increasing the Richardson number.
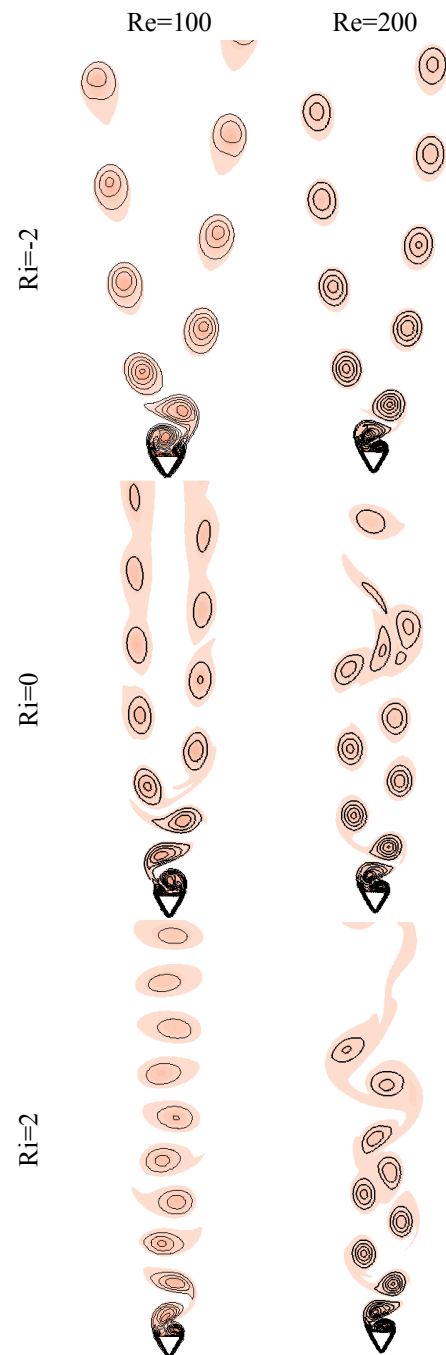


**Figure 6.** Variation instantaneous iso-vorticity contours superimposed on the dimensionless temperature field (same legend with that of Figure 3) with different Ri and Re numbers for BR=0.033.

**Investigation of the flow and heat transfer coefficients**

In Fig. 8, the variation of the average drag coefficient on the triangular cylinder with the blockage ratio and Richardson number is presented for Re=100 and 200. For all Reynolds and Richardson numbers, the average drag coefficient is the largest for BR=0.5 and the lowest in unconfined case. It is noted here that the average velocity at the center of the cylinder in the unconfined channel is 1 m/s, while the velocity at the center of the channel in the confined channel is 1.5 m/s. This causes the mean drag coefficient in the unconfined channel to be lower.
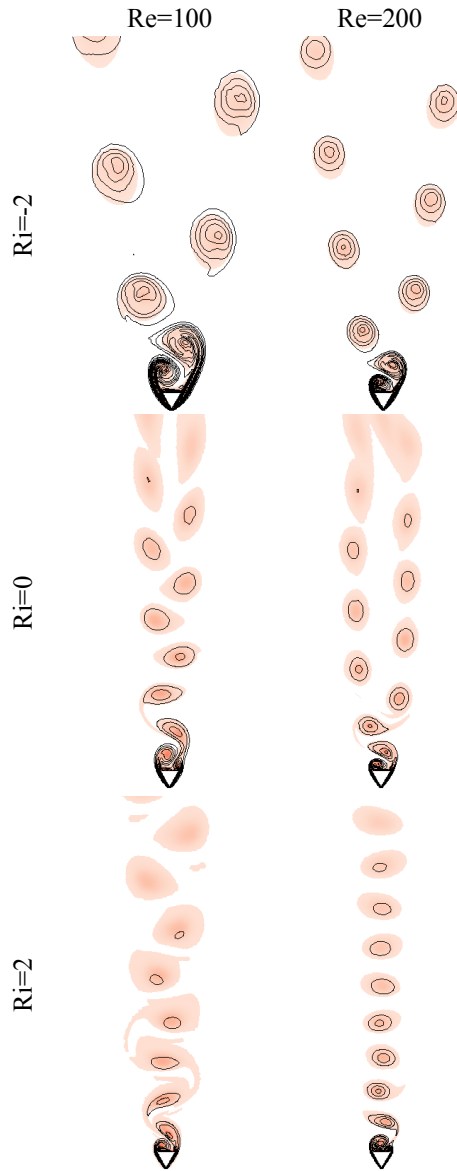
**Figure 7.** Variation instantaneous iso-vorticity contours superimposed on the dimensionless temperature field (same legend with that of Figure 3) with different Ri and Re numbers for the unconfined channel.

At Re=100, the mean $C_D$ coefficient is close at all blocking ratios except for BR=0.5 and unconfined cases. The sudden decrease in the $C_D$ coefficient at Re=100 and Ri=2 is attributed to the increasing effect of buoyancy, leading to a weakening of the vortex shedding (see Fig. 3). At Re=200, the mean $C_D$ coefficient increases linearly with increasing Ri number and BR. Since the Richardson number gives the relative importance of buoyancy, the effect of buoyant flow becomes more pronounced, resulting in an increase in drag. In addition, the change in $C_D$ with respect to the blockage ratio is more evident, especially at high Re numbers. For example: At Ri=-2, the drag coefficients of BR=0.25—with respect to the BR = 0.05 case—are about 36% and 61% larger for Re= 100 and 200, respectively. At Ri=2, the drag coefficients of BR=0.25–with respect to the BR=0.05 case–are about 5% and 17% larger for Re= 100 and 200, respectively. Teixeira et al. (2018) reported that the structural design application is important for the evaluation of design in

external convective flows. According to the results obtained in this study, the blockage ratio is an important parameter in mixed heat transfer. The fluid undergoes convective acceleration in the region between the walls and the cylinder. For an increasing blockage ratio, the velocity gradient in the channel near the cylinder walls increases which, in turn, results in an increase in the viscous force acting on the cylinder and causes the drag coefficient to increase and delay the boundary layer separation.
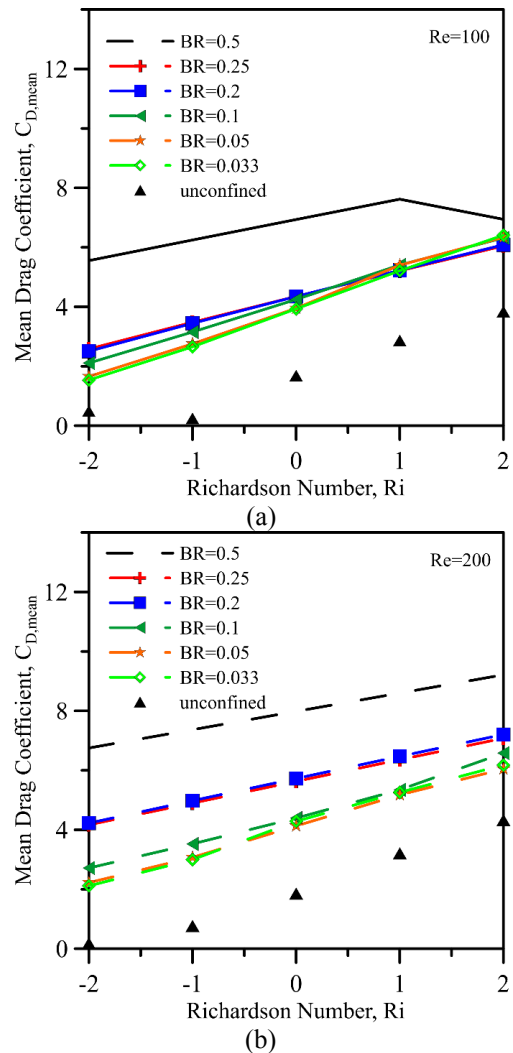


**Figure 8.** Variation of mean drag coefficient with (a) Re=100 and (b) Re=200 at various Richardson numbers and the blockage ratio.

The effect of Richardson number on $C_{L,rms}$ of various BR values is shown in Fig. 9 for Re=100 and 200. For both cases, the variation of $C_{L,rms}$ with Richardson number exhibits similar behavior, which increases with increasing Reynolds number. This outcome is attributed to the flow pattern in the downstream region. We also note that $C_{L,rms}$ also increases with increasing BR. At large BR ratios, the smaller the spacing between the channel walls, the stronger vortices that form behind the cylinder, resulting in a larger amplitude oscillation of the lift coefficient.
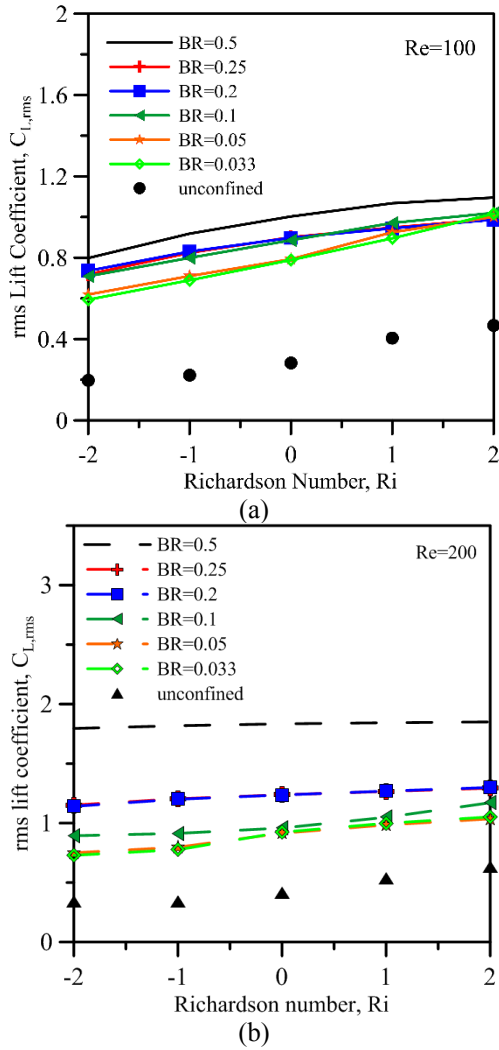
**Figure 9.** Variation of rms lift coefficient with (a) Re=100 and (b) Re=200 at various Richardson numbers and the blockage ratio.

Figure 10 shows the effect of the BR over the Strouhal number for Re=100 and 200. In the presence of a block effect, the St number varied in the range of about 0.22-0.47. On the other hand, in the unconfined channel, the St number is around 0.1-0.25. As can be seen from the vortex structure and the dimensionless temperature field in this study, the shedding of vortices develops behind the triangular cylinder. While the Strouhal number takes its maximum value in the narrowest channel configuration, it becomes minimum in unconfined flow cases. In unconfined channels, the vortices are formed as a result of the interaction of the inertial and buoyant forces. In this case, too, the effect of increasing the Richardson number (i.e., buoyancy) shows a significant change in the Strouhal number. As Sharma and Eswaran (2005) noted, the aiding flow (Ri>0) accelerates both the cylinder's boundary layers and the iso-vorticity shedding process, while opposing flow (Ri<0) slows it down and inhibits the shedding process. As a result, the Strouhal number also increases approximately linearly with the Richardson number for unconfined channels. However, the variation of the Strouhal number with the variation of the Richardson number in confined channels is relatively less compared to the unconfined channel. At Re=200, the

St numbers are higher than Re=100. In addition, it is observed that the St numbers are very close to each other at BR=0.05 and BR=0.033 values in both Re numbers, where the blocking rate is small.
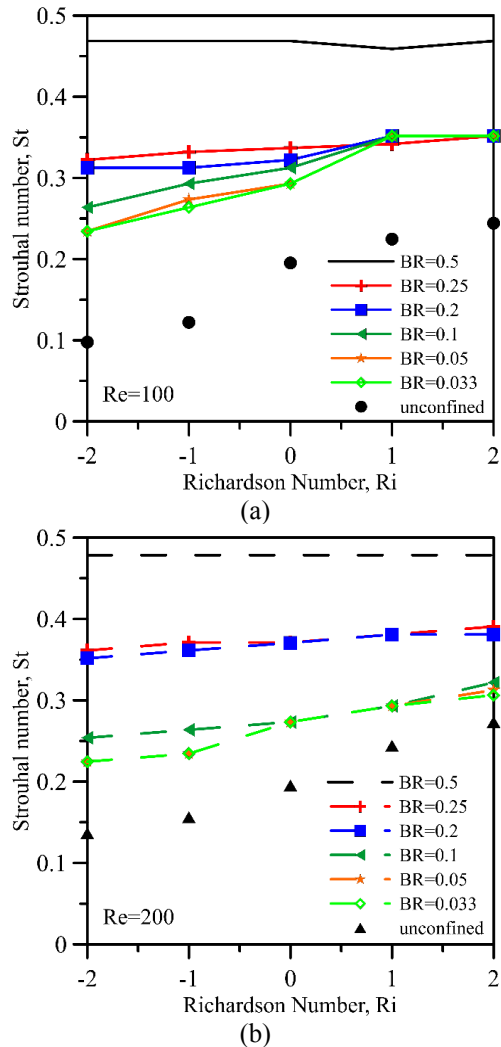




**Figure 10.** Variation of Strouhal number with (a) Re=100 and (b) Re=200 at various Richardson numbers and the blockage ratio.

Figure 11 shows the mean Nusselt number variations with the Richardson number and the blockage ratio for Re=100 and Re=200. A mean Nusselt number represents the heat transfer through a fluid layer as a result of convection relative to conduction across the same fluid layer. It is a dimensionless number usually derived from experimental or analytical and/or numerical studies, and it is often used in thermal engineering design calculations to estimate the convective heat transfer rates. The mean Nusselt number increases with an increase in the Reynolds number, as usual for all blockage ratios. Furthermore, the increase in the Nusselt number with the blocking rate is more pronounced at Re=200. For example, for Re=100, the mean Nusselt number for the case of BR=0.1 with respect to BR=0.033 depicts an increase of 4.67%, 3.35% and 3.86% for Ri=-2, 0 and 2, respectively. But in the case of BR=0.1 with respect to BR=0.033, the increase in the mean Nusselt number for Re=200 is 13%, 13.48% and 16.32% for Ri=-2, 0, and 2,

respectively. This is because, similar to the study done by Gandikota et al. (2010), as the blockage ratio increases, the shedding frequency of vortices increases, which in turn increases he heat transfer rate.
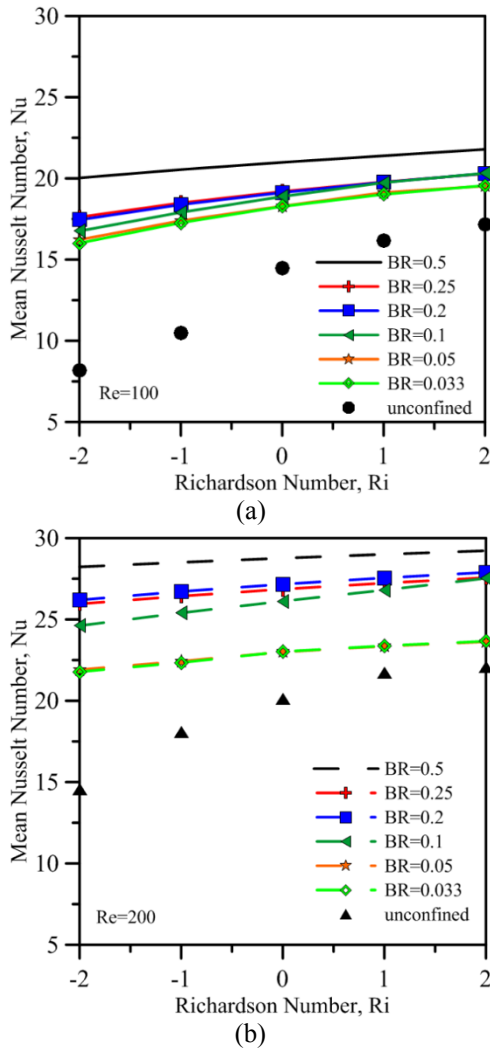


Figure 11. Comparison of the mean Nusselt number for different Richardson number and the blockage ratio at Re=100 (a) and Re=200 (b).

Note that the mean Nusselt number increases with increasing Richardson number due to the fact that the forced convection aids the natural convection transfer for Ri>0 and the forced convection constraints the natural convection transfer for Ri<0. In the unconfined channel case, higher Re and Ri numbers, which increase the effects of both buoyancy and inertia forces, result in a significant increase in the mean Nu number. For an unconfined channels, the average slope of the lines is 2.25 and 2.7 for Re=100 and 200, respectively. On the other hand, for BR=0.1, the average slope of the lines is 0.89 and 0.73 for Re=100 and 200, respectively. This shows that the Richardson number is a more important parameter for unconfined channel.

When the boundary layer around the cylinder is examined for the unconfined channel, we see that the boundary layer developed over the cylinder is thicker for Ri=-2, while the boundary layer formed around the cylinder decreases with the increase in the Ri number (see Fig. 7). As the temperature gradient increases, heat transfer also increases. In BR=0.5, the boundary layer around the cylinder is almost the same for all Ri numbers (see Fig. 3). Thus, it proves that the mean Nusselt number has not changed with Ri numbers.

The cases with maximum and minimum heat transfer rates are observed in BR=0.5 and unconfined flow cases, respectively. The local Nusselt number variations for these cases are depicted in Figure 12. The local Nusselt numbers ($Nu_s$) are plotted clockwise (0-1-2-3) in the direction along the periphery of the cylinders. In each case, the local Nusselt numbers reach their maximums at corners 1 and 2. The fluid, which encounters the fluid at the front corner (0-3), moves along the cylinder's side walls: 0-1 and 3-2. The local Nusselt number on these lateral walls (0-1 and 3-2) continues to increase towards the corners at 1 and 2. Since the system is symmetrical, the local Nusselt values between 0-1 and 3-2 are also symmetrical. The back (vertical) (from 1 to 2), on the other hand, is exposed to the slow-moving fluid, leading to a relatively slow moving vortex region, smaller temperature gradients, and local Nusselt number variations.

The local Nusselt number variation also changes with the Richardson number in both Reynolds numbers for the unconfined case. In the case of BR=0.5, it is observed that the local Nusselt number does not change significantly with the Richardson number in both cases where the inertia forces increased. The similarity and closeness of the local Nusselt number (seen in Figure 12) support the similarity of the boundary layers.

**Correlations for flow characteristics and heat transfer**

To the best of our knowledge, no correlation has been found in the literature for flow and heat transfer characteristics by combining the blocking ratio with the Reynolds and Richardson numbers. In this study, the drag/lift coefficients, Strouhal number, and mean Nusselt number for the range of 100≤Re≤200, -2≤Ri≤2 have been computed for BR=0.5, 0.25, 0.2, 0.1, 0.05, 0.033, and 0.0143 (unconfined). Using the computed (observed) data, correlations for the mean drag and mean rms lift coefficients, Strouhal number, and mean Nusselt number have been developed.
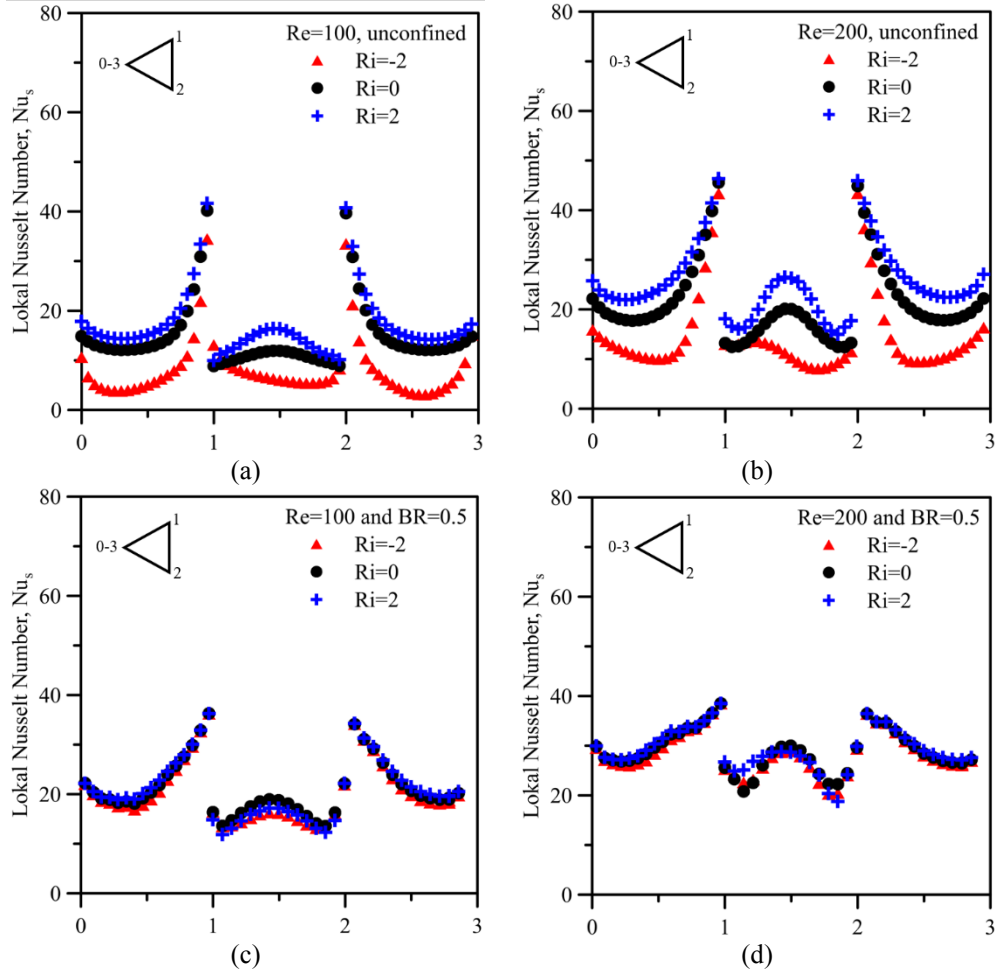
**Figure. 12.** Variation of time-averaged local Nusselt Number for a) Re=100 and unconfined channel, b) Re=200 and unconfined channel, c) Re=100 and BR=0.5, d) Re=200 and BR=0.5.

The mean computed drag coefficient over the equilateral-triangle cylinder surface area was compiled and used to obtain a non-linear regression. The mean drag coefficient correlation derived (prediction) is as follows:

$$C_{D,mean} = 3.3326\,\mathrm{Re}^{0.22}\left(-0.2074 + 0.091\mathrm{Ri} + \mathrm{BR}^{0.182}\right)$$
$$r^2 = 0.9804 \tag{7}$$
$$100 \le \mathrm{Re} \le 200, -2 \le \mathrm{Ri} \le 2, 0.5 \le \mathrm{BR} \le 0.0143$$

We note that the r-squared value for the correlation is excellent. The mean drag coefficient increases with increasing blockage ratio, Reynolds, and Richardson numbers. According to the Eq. 7, the most dominant term is the Ri number. The plots of predicted (computed) data versus observed (computed) data provide both qualitative and quantitative information about how the curve fits. The consistency and model bias are described by the slope (*m*) and intercept (*b*) of the Predicted-Observed (PO) line, $C_{D,observed} = b + mC_{D,predicted}$, respectively. The resulting PO plot should be exactly aligned on the diagonal (i.e., *y*=*Y* line with rms=0) for identical observations/predictions. Similarly, data points that are near the diagonal line (normally, rms≠0) suggest that the entire data is reasonably well suited. All the drag coefficient PO data was additionally fitted to a linear

curve, yielding the following results: $-0.000147831 + 0.999972x$. The linear relationship between $C_{D,observed}$ and $C_{D,predicted}$ is validated by the slope of *m*=0.999972 (approaching unity). Any deviation of the slope from unity indicates a relative scaling factor between the two sets. A non-zero intercept indicates that the population is shifted by a constant offset relative to the other. The intercept of the correlation is very small (*b*=-0.0001478), so the model bias is negligible.

Similarly, using nonlinear regression, developed correlations for other flow characteristic properties, $C_{L,rms}$ and St, are presented as follows:

$$C_{L,rms} = 0.0456\,\mathrm{Re}^{0.5}\,e^{\left(1+0.0531\mathrm{Ri}+0.01955\mathrm{Ri}^2\right)}\mathrm{BR}^{0.2324}$$
$$r^2 = 0.9582 \tag{8}$$
$$100 \le \mathrm{Re} \le 200, -2 \le \mathrm{Ri} \le 2, 0.5 \le \mathrm{BR} \le 0.0143$$

$$\mathrm{St} = 0.354\,\mathrm{Re}^{0.027}\left(0.396 + 0.047\mathrm{Ri} + \mathrm{BR}^{0.443}\right)$$
$$r^2 = 0.9903 \tag{9}$$
$$100 \le \mathrm{Re} \le 200, -2 \le \mathrm{Ri} \le 2, 0.5 \le \mathrm{BR} \le 0.0143$$

The lift rms coefficient changes drastically with the Reynolds and Richardson numbers, and the Strouhal number also varies greatly with the blockage ratio. For these correlations, all rms lift coefficient and St numbers PO data are also fitted to linear curves, which yielded $C_{L,rms,observed} = -0.01195 + 1.01164 C_{L,rms,predicted}$ and $St_{observed} = 0.0001279 + 0.999626 St_{predicted}$, respectively.

Early experimental studies involving forced flows for the flow characteristics and the Nusselt numbers were usually expressed (due to the nonlinear nature of flow and transfer) by a simple power-law model where the Re number was the main independent variable; that is, $Nu = C Re^n Pr^m$ (Bergman et al., 2018). To determine the variation with the Richardson number, the graph of $Nu_{mixed} / Nu_{forced}$ ratio is examined. The plot of this ratio reveals the magnitude and behavior of the deviations from that of the forced convection due to natural convection effects (i.e., Ri number). The effect of BR was also observed in the same manner, and the general form of a correlation was assumed to be in the form $C Re^n f(Ri, BR)$, where $f(Ri, BR)$ is a function determined by visual inspection of $Nu_{mixed} / Nu_{forced}$ ratio and trial-and-error that minimized the sum of squares and maximizes $r^2$. It has been observed that the Nusselt number varies linearly with the Richardson number while exponentially with the BR ratio. This strategy has been employed in the literature to determine

the effect of parameters other than Reynolds and Prandtl numbers (Chen et al., 1986; Lin et al., 1990; Altaç and Altun, 2014; Dalkilic et al., 2019).

Using a nonlinear regression model that minimizes the sum of the squares of the errors for the mean Nusselt numbers collected from the cylinder surface area leads to

$$Nu = 2.858 Re^{0.449} \left(1 + 0.0356 Ri\right) BR^{0.092}$$
$$r^2 = 0.99603 \tag{10}$$
$$100 \leq Re \leq 200, -2 \leq Ri \leq 2, 0.5 \leq BR \leq 0.0143$$

To assess the accuracy of the correlation, the Nusselt number obtained by the proposed correlation against the Nusselt number calculated by numerical simulation. The linear curve for the Nusselt number is $Nu_{observed} = -0.25642 + 1.01149 Nu_{predicted}$. The model is consistent since the slope is very close to 1 (i.e., 45 degree inclination), and the intercept is -0.25642, which is a very small deviation, considering the average value of the mean Nusselt number is 21.6701. Figure 13 depicts visually the Predicted-Observed plots of correlations for (a) the mean drag coefficient, (b) rms lift coefficient, (c) Strouhal number, (d) Nusselt number. It should be noted that the data for all the Nusselt and Strouhal numbers and the mean drag coefficient spread well around the best curves fit, which is supported with r-squared values of greater than 0.98.
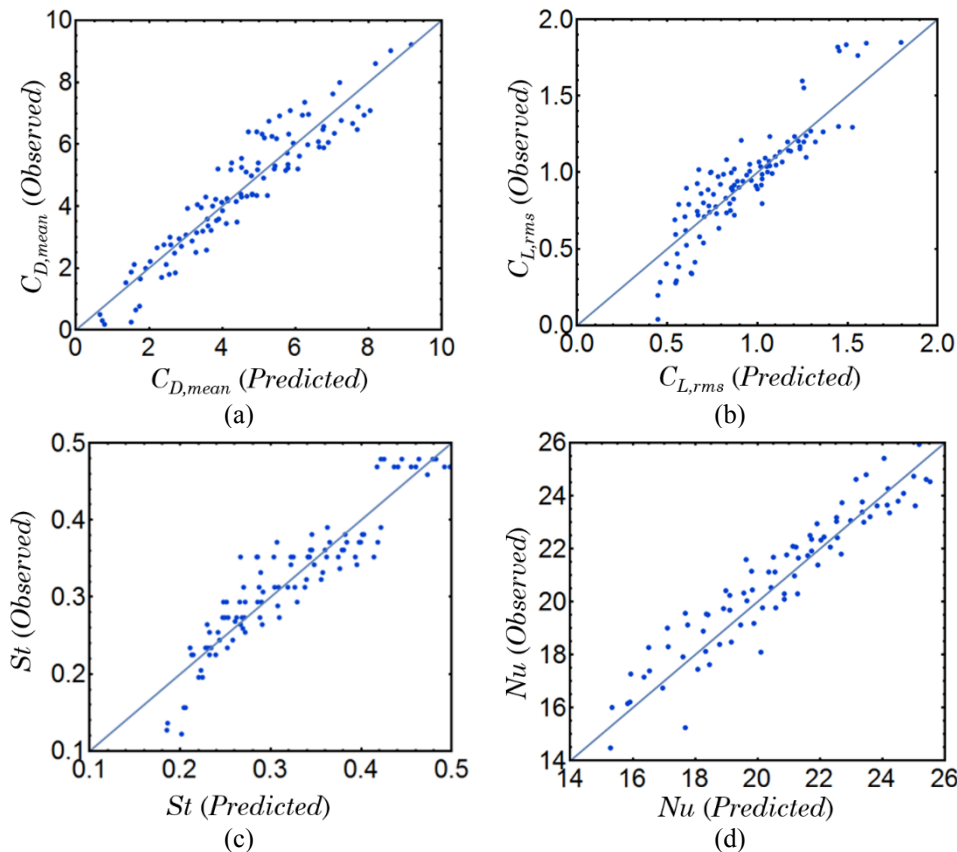


**Figure 13.** The Predicted-Observed plots of correlations for (a) the mean drag coefficient, (b) rms lift coefficient, (c) Strouhal number, (d) Nusselt number.

**CONCLUSION**

In this study, two-dimensional mixed heat transfer (transient forced convection and natural convention) and fluid flow over equilateral triangular cylinders in confined and unconfined channels are performed numerically. Three dimensionless parameters (Blockage Ratio, Reynolds, and Richardson numbers) implemented in the new correlations considered the influence of mixed convective heat transfer (i.e., Nu) and flow (i.e., $C_{D,mean}$, $C_{L,rms}$, and St). Five Richardson numbers (Ri=-2, -1, 0, 1, and 2), three Reynolds numbers (Re=100, 150, and 200), and seven blockage ratios (BR=0.5, 0.25, 0.2, 0.1, 0.05, 0.0333 for confined channels and 1/70 for unconfined channels) are investigated. The results obtained from this study are summarized below.

- When the blockage ratio increases, the boundary layer of the channel wall and the vortex behind the cylinder interact in the downstream region. Thus, the vortices formed behind the cylinder at the decreasing blockage ratio can be spread to the channel.
- With decreasing blockage ratios, a two-column vortex was observed at Ri=0 and Ri=-2. A single vortex form is formed when natural convection supports forced convection (Ri=2). This is due to the fact that the boundary layer around the triangular cylinder is thinner compared to Ri=0 and Ri=-2.
- In the presence of a strong buoyant forces, the flow field is significantly altered. The density difference causes hot fluid to be discharged into the near wake region, increasing the mass moving underneath the cylinder and affecting the flow field. While examining the iso-vorticity contours and the dimensionless temperature field for the unconfined channel, it is seen that the frequency of the vortices increases with the increasing Richardson number due to aiding natural convection.
- In all Reynolds and Richardson numbers, the drag coefficient and the mean Nu number are the lowest in the case of the unconfined channel and the highest in the severely confined BR=0.5 case. In addition, at high Reynolds numbers, both the drag coefficient and the mean Nu number are affected largely by the blockage ratio. For Ri=0, the drag coefficients of BR=0.25–with respect to the BR=0.05 case–are about 9% and 29% larger for Re= 100 and 200, respectively.
- Any flow characteristic's rms value serves as a gauge for fluctuations in that specific flow characteristic. However, the Reynolds and Richardson numbers for which the Re-Ri domain for the lift coefficient was created also influence these oscillations. The $C_{L,rms}$ value tends to increase as the Reynolds and Richardson numbers increase. However, the $C_{L,rms}$ value is more affected by the change in the BR. At high BR ratios, stronger vortices develop behind the cylinder due to the narrower channel wall spacing, which leads to a lift coefficient oscillation with a bigger amplitude. However, in cases where BR is high, $C_{L,rms}$ does not change much with the change in the Richardson number due to the dominance of inertia forces at high Reynolds numbers. At BR=0.5, the $C_{L,rms}$ of Ri=2 relative to Ri=-2 are greater than 37.283% and 3.067% at Re=100 and 200, respectively.

- The mean Nusselt increases with Re number and BR, as well as Ri number, due to buoyancy-induced effects of the flow field. The mean Nusselt number of BR=0.5 and Ri=-2 is about 2.5-2 times that of the unconfined channel and R=-2, and the mean Nusselt number of BR=0.5 and Ri=2 is about 1.22-1.15 times that of the unconfined channel and Ri=2.
- For small blockage rates, the Strouhal number increases with increasing Ri number, whereas it is almost the same with increasing Ri number for BR=0.5. The minimum value of the Strouhal number is obtained at an unconfined channel, and the maximum value is obtained at BR=0.5.
- As demonstrated, the correlations developed by nonlinear regressions achieve good prediction capability for mixed convection heat transfer and fluid flow from a triangular cylinder in a vertical channel.

**NOMENCLATURE**

| | |
|---|---|
| $A$ | surface area [m²] |
| BR | blockage ratio defined as $D/H$ [-] |
| C | coefficient |
| $D$ | side lenght of equilateral triangular cylinder [m] |
| F | force [N] |
| $g$ | acceleration of gravity |
| **g** | dimensionless gravity |
| Gr | Grashof number [-] |
| $H$ | channel width [m] |
| $h$ | mean heat transfer coefficient [W/m²·K] |
| $k$ | thermal conductivity [W/m·K] |
| Nu | mean Nusselt number [-] |
| $\bar{P}$ | pressure [N/m²] |
| $P$ | dimensionless velocity components [-] |
| Pr | Prandtl number [-] |
| Ri | Richardson number [-] |
| Re | Reynolds number [-] |
| $T$ | temperature [K] |
| $t$ | time |
| $\bar{u}, \bar{v}$ | velocity components [m/s] |
| $u, v$ | dimensionless velocity components [-] |
| $\bar{U}$ | mean velocity components [m/s] |

| $\overline{x}, \overline{y}$ | cartesian coordinate system [m] |
| $x, y$ | dimensionless cartesian coordinates [-] |

*Greek Symbol*

| $\alpha$ | thermal diffusivity [m²/s] |
| β | thermal expansion coefficient [K⁻¹] |
| μ | dynamic viscosity [N·s/m²] |
| $\upsilon$ | kinematic viscosity [m²/s] |
| ρ | density [kg/m³] |
| Θ | dimensionless temperature [-] |
| $\tau$ | dimensionless time [-] |

*Subscripts*

| D | drag |
| L | lift |
| w | wall |
| ∞ | free stream property |

## References

Abbassi, H., Turki, S., and Nasrallah, S. B., 2001, Mixed convection in a plane channel with a built-in triangular prism, *Numerical Heat Transfer, Part A: Applications: An International Journal of Computation and Methodology* 39: 307–320.

Akbari, M., Lavasani, A. M. and Naseri, A., 2021, Experimental investigation of the heat transfer for non-circular tubes in a turbulent air cross flow, *Experimental Heat Transfer* 34 (6): 531-530.

Altaç Z. and Altun, Ö., 2014, Hydrodynamically and thermally developing laminar flow in spiral coil tubes, *International Journal of Thermal Sciences* 77: 96-107.

Altaç, Z., Sert Z., Mahir, N., and Timuralp, Ç., 2019, Mixed convection heat transfer from a triangular cylinder subjected to upward cross flow, *International Journal of Thermal Sciences* 137: 75-85.

Ali, M., Zeitoun, O., and Nuhait, A., 2011, Forced convection heat transfer over horizontal triangular cylinder in cross flow, *International Journal of Thermal Sciences* 50: 106–114.

Arif, M. R. and Hasan, N., 2020, Large-scale heating effects on global parameters for flow past a square cylinder at different cylinder inclinations, *International Journal of Heat and Mass Transfer* 161: 120237.

Barati, E., Biabani, M. and Zarkak, M. R., 2022, Numerical investigation on vortex-induced vibration energy harvesting of a heated circular cylinder with various cross-sections. *International Communications in Heat and Mass Transfer* 132: 105888.

Bergman, T. L., Lavine, A. S. and Incropera, F. P., and DeWitt, D. P., 2018, Fundamentals of Heat and Mass Transfer, Wiley (WileyPLUS Products); 8th edition, Table 7.7, page 447.)

Bovand, M., Rashidi, S., Esfahani, J.A., 2015, Enhancement of heat transfer by nanofluids and orientations of the equilateral triangular obstacle, *Energy Conversion and Management* 97: 212-223.

Camarri, S., Salvetti, M. V., and Buresti, G., 2006, Large-eddy simulation of the flow around a triangular prism with moderate aspect ratio, *Journal of Wind Engineering and Industrial Aerodynamics* 94: 309-322.

Chatterjee, D., and Mondal, B., 2015, Mixed convection heat transfer from an equilateral triangular cylinder in cross flow at low Reynolds numbers, *Heat Transfer Engineering* 36 (1): 123–133.

Chattopadhyay, H., 2007, Augmentation of heat transfer in a channel using a triangular prism, *International Journal of Thermal Sciences* 46: 501-505.

Chen T. S., Armaly, B. F., Ramachandran, N., Correlations for laminar mixed convection flows on vertical, inclined, and horizontal flat plates, *Journal of Heat Transfer*, 108, 835-840.

Çelik, Z., Altaç, Z., 2023, Numerical investigation of two-dimensional unsteady flow and heat transfer from rounded equilateral isothermal triangular cylinders in cross flow, *Ocean Engineering* 269: 113468.

Dalal, A., Eswaran, V., and Biswas, G., 2008, A finite-volume method for Navier-Stokes equations on unstructured meshes, *Numerical Heat Transfer, Part B: Fundamentals* 54 (3): 238–259.

Dalkilic, A. S., Çebi, A., Celen, A., 2019, Numerical analyses on the prediction of Nusselt numbers for upward and downward flows of water in a smooth pipe: effects of buoyancy and property variations, *Journal of Thermal Engineering*, 5 (3): 166-180.

De, A. K., and Dalal, A., 2006, Numerical simulation of unconfined flow past a triangular cylinder, *International Journal for Numerical Methods in Fluids* 52 (7): 801–821.

De, A. K., and Dalal, A., 2007, Numerical study of laminar forced convection fluid flow and heat transfer from a triangular cylinder placed in a channel, *ASME Journal of Heat Transfer* 129: 646–656.

Dhimana, A., and Shyam, R., 2011, Unsteady heat transfer from an equilateral triangular cylinder in the unconfined flow regime, *ISRN Mechanical Engineering* 932738: 1–13.

Dhiman, A. K., 2016, Flow and heat transfer phenomena around an equilateral triangular bluff body: effect of wall confinement, *Heat Transfer - Asian Research* 45: 608–630.

Dulhani, J. P., and Dalal, A., 2015, Flow past an equilateral triangular bluff obstacle: computational study of the effect of thermal buoyancy on flow physics and heat transfer, *Numerical Heat Transfer, Part A: Applications: An International Journal of Computation and Methodology* 67: 476–495.

El-Wahed, A. K., Johnson, M. W., and Sproston, J. L., 1993, Numerical study of vortex shedding from different shaped bluff bodies, *Flow Measurement and Instrumentation* 4: 233-240.

FLUENT 6.3.26 User's Guide, Fluent Inc., Lebanon, NH, 2007.

GAMBIT 2.2 User's Guide, Fluent Inc., Lebanon, NH, 2004.

Gandikota, G., Amiroudine, S., Chatterjee, D., and Biswas, G., 2010, The effect of aiding/opposing buoyancy on two dimensional laminar flow across a circular cylinder, *Numerical Heat Transfer, Part A: Applications: An International Journal of Computation and Methodology* 58: 385-402.

Hassab, M. A., Teamah, M. A., El-Maghlany, W. M., and Kandil, M. A., 2013, Experimental study for a mixed convection heat transfer from an isothermal horizontal triangular cylinder, *International Journal of Engineering Sciences* 6: 210–225.

Hyun, S., and SikYoon, N. H., 2022, Effect of the wavy geometric disturbance on the flow over elliptic cylinders with different aspect ratios, *Ocean Engineering* 243: 110287.

Laidoudi, H. and Bouzi, M., 2018, The effects of aiding and opposing thermal buoyancy on the downward flow around a confined circular cylinder, *Periodica Polytechnica Mechanical Engineering* 62 (1): 42-50.

Lin, H. T., Yu, W. S., Chen, C. C., 1990, Comprehensive correlations for laminar mixed convection on vertical and horizontal flat plates, *Wärme - und Stoffübertragung*, 25, 353-359.

Lupi, F., 2013, A new aerodynamic phenomenon and its effects on the design of ultra-high cylindrical towers, Chapter 3. Flow around circular cylinders: state of the art, *Ph.D. Thesis* University of Florence. (https://flore.unifi.it/retrieve/handle/2158/829166/

Mahir, N. and Altaç, Z., 2019, Numerical investigation of flow and combined natural-forced convection from an isothermal square cylinder in crossflow, *International Journal of Heat and Fluid Flow* 75: 103-121.

Patel, S. A. and Chhabra, R. P., 2019, Buoyancy-assisted flow of yield stress fluids past a cylinder: Effect of shape and channel confinement, *Applied Mathematical Modelling* 75: 892-915.

Peng, J., Fu, X. and Chen, Y., 2008, Experimental investigations of Strouhal number for flows past dual triangulate bluff bodies, *Flow Measurement and Instrumentation* 19: 350-357.

Rasool, T., Dhiman, A. and Parveez, M., 2015, Cross-buoyancy mixed convection around a confined triangular bluff body, *Numerical Heat Transfer, Part A: Applications: An International Journal of Computation and Methodology* 67: 454–475.

Salimipour, E., and Yazdani, S., 2022, Study on the fluid flow and heat transfer characteristics of a horizontal elliptical cylinder under thermal buoyancy effect, *International Journal of Heat and Mass Transfer* 192: 122948.

Shademani, R., Ghadimi, P., Zamanian, R. and Dashtimanesh, A., 2013, Assessment of air flow over an equilateral triangular obstacle in a horizontal channel using FVM, *Journal of Mathematical Sciences and Applications* 1: 12-16.

Sharma, A., and Eswaran, V., 2005, Effect of channel-confinement and aiding/opposing buoyancy on the two-dimensional laminar flow and heat transfer across a square cylinder, *International Journal of Heat and Mass Transfer* 48 (25-26): 5310-5322.

Sharma, K. R. and Dutta, S., 2022, Flow over a square cylinder at intermediate Reynolds numbers, *Journal of Fluids Engineering* 144 (12): 121303.

Srigrarom, S. and Koh, A. K. G., 2008, Flow field of self-excited rotationally oscillating equilateral triangular cylinder, *Journal of Fluids and Structures* 24: 750-755.

Srikanth, S., Dhiman, A. K. and Bijjam, S., 2010, Confined flow and heat transfer across a triangular cylinder in a channel, *International Journal of Thermal Sciences* 49: 2191–2200.

Teixeira, F. B., Lorenzini, G., Errera, M. R., Rocha, L. A. O., Isoldi, L. A., and dos Santos, E. D., 2018, Constructal Design of triangular arrangements of square bluff bodies under forced convective turbulent flows, *International Journal of Heat and Mass Transfer* 126: 521-535.

Tiwari, A. K., and Chhabra, R. P., 2014, Effect of Orientation on the Steady Laminar Free Convection Heat Transfer in Power-Law Fluids from a Heated Triangular Cylinder, *Numerical Heat Transfer, Part A: Applications* 65 (8): 780-801.

Varma, N., Dulhani, J. P., Dalal, A., Sarkar, S., and Ganguly, S., 2015, Effect of channel confinement on mixed convective flow past an equilateral triangular cylinder, *ASME Journal of Heat Transfer* 121013: 1-7.

Yagmur, S., Dogan, S., Aksoy, M. H., Goktepeli, I., and Ozgoren, M., 2017, Comparison of flow characteristics around an equilateral triangular cylinder via PIV and Large Eddy Simulation methods, *Flow Measurement and Instrumentation* 55: 23-36.

Zeitoun, O., Ali, M., and Nuhait, A., 2010, Numerical study of forced convection around heated horizontal triangular ducts, *Heat Transfer* 68: 201-212.

Zeitoun, O., Ali, M., and Nuhait, A., 2011, Convective heat transfer around a triangular cylinder in an air cross flow, *International Journal of Thermal Sciences* 50 (9): 1685-1697.

Zhang, N., Rong, L. W., Dong, K. J., and Zeng, Q. D., 2020, Fluid flow and heat transfer characteristics over a superelliptic cylinder at incidence, *Powder Technology* 360: 193-208.

Zhu, H., Tang, T., Zhou, T., Liu, H., and Zhong. J., 2020, Flow structures around trapezoidal cylinders and their hydrodynamic characteristics: Effects of the base length ratio and attack angle, *Physics of Fluids* 32: 1036061-22.

Zerrin SERT is an assistant professor at Eskişehir Osmangazi University. She received her M.Sc. and Ph.D. in mechanical engineering from Eskişehir Osmangazi University, Turkey. Her research area is CFD, forced convection, aerodynamics, radiation, and heat transfer.

# FARKLI GÖZENEKLİLİK VE AÇI DEĞERLERİNE SAHİP GEÇİRGEN AYIRICI PLAKA İLE DAİRESEL BİR SİLİNDİRİN AKIŞ KONTROLÜ

**Serdar ŞAHİN\*, Tahir DURHASAN\*\*, Engin PINAR\*\*\*, Hüseyin AKILLI\*\*\*\***

\* Çukurova Üni., Makine Müh. Böl., Adana, Türkiye serdarsa@gmail.com, https://orcid.org/0000-0002-6451-3329
\*\* Adana Alparslan Türkeş Bilim ve Teknoloji Üniversitesi, Havacılık ve Uzay Bilimleri Fakültesi, Havacılık ve Uzay Mühendisliği Bölümü, Adana, Türkiye, tdurhasan@atu.edu.tr https://orcid.org/0000-0001-5212-9170
\*\*\* Çukurova Üni., Makine Müh. Böl., Adana, Türkiye epinar@cu.edu.tr, https://orcid.org/0000-0002-7484-8616
\*\*\*\* Çukurova Üni., Makine Müh. Böl., Adana, Türkiye hakilli@cu.edu.tr, https://orcid.org/0000-0002-5240-8441

**Özet:** Titreşim ve akustik gürültü veya rezonans gibi iz akışının olumsuz etkilerini ortadan kaldırmak için batık gövdelerin akış kontrolü kapsamlı bir şekilde incelenmiştir. Isı eşanjör boruları, enerji nakil hatları, egzoz bacaları, köprüler, radyo teleskoplar, enerji hatları, açık deniz sondaj kuleleri vb. birçok mühendislik uygulamalarında kullanılan, silindir gövdenin iz akışını kontrol etmek için çeşitli art iz konumuna geçirgen bir ayırıcı plaka yerleştirilmiştir. Tüm deneyler, Çukurova Üniversitesi Akışkanlar Mekaniği Laboratuvarı'ndaki büyük ölçekli bir kapalı devre su kanalında, PIV kullanılarak, silindir çapına (D) bağlı olarak Re=5000'de gerçekleştirilmiştir. Dört farklı ayırıcı plaka açısı (θ =0°; 15°; 30°; 45°), üç farklı gözeneklilik (ε=0.30; 0.50; 0.70) incelenmiştir. Ayırıcı plakaların geçirgenliği (ε) plaka üzerindeki toplam delik alanının, plaka toplam alanına oranı olarak belirlenmiştir. Tüm değişkenler silindir çapına (D) bölünerek boyutsuzlaştırılmış ve * indisi ile gösterilmiştir. Ayırıcı plaka uzunluğu da deney sırasında ls\*=1 olarak sabit tutulmuştur. Ayırıcı plaka ile silindir arasındaki mesafe, ayırıcı plakanın art iz eksenine göre açısı değişken olduğundan sabit değildir. Bunun üstesinden gelebilmek için silindir ile ayırıcı plaka dönme ekseni arasındaki mesafe ele alınmış ve ** indisi ile gösterilmiştir. Ayırıcı plaka orta noktası ile silindir (lg\*\*) arasındaki boşluk, deneyler boyunca lg\*\*=1.5 olarak sabit tutulmuştur. Plakalar döndürüldüğünde akışa paralel kesit azalmakta, bu da sınır tabakalar arasındaki etkileşimi artırmaktadır. Geçirgen ayırıcı plakalar, silindir etrafındaki akışta oluşan sınır tabakaların etkileşimini engellediğinden, sınır katmanların etkileşiminin arttığı ardıl bölgelerde geçirgen ayırıcı plakaların etkisi artmaktadır. Böylece dalgalanmalar azalmakta ve silindirin akış aşağında daha kararlı bir iz akışı oluşmaktadır. Ayırıcı plaka açısının artmasıyla çevrinti oluşumunun geciktiği gözlenmiştir. Bu çalışmada ayırıcı plaka açısının etkisi ve plaka geçirgenliğinin etkisi net bir şekilde gözlemlenmiştir.

**Anahtar Kelimeler:** PIV, Akış Kontrol, Silindir, Ayırıcı plaka, Geçirgen plaka

# FLOW CONTROL OF A CIRCULAR CYLINDER BY PERMEABLE SPLITTER PLATE WITH DIFFERENT POROSITIES AND ANGLE VALUES

**Abstract:** Flow control of bluff bodies has been studied extensively to eliminate adverse effects of wake flow such as vibration and acoustic noise or resonance. The circular cylinder has been studied as the bluff body since it is basic geometry and has been used in engineering applications such as heat exchanger tubes, power transmission lines, chimney stacks, bridges, radio telescopes, power lines, offshore drilling rigs etc. In this study, a permeable splitter plate was located at various downstream locations to control the wake flow of the cylinder. All experiments were carried out in a large-scale closed-loop water channel in the Fluid Mechanics Laboratory at Cukurova University. PIV was used to measure the instantaneous velocity vector field in the wake region of the cylinder at Reynolds number Re=5000, which is based on the cylinder diameter, D. Four different splitter plate angle values (θ =0°; 15°; 30°; 45°), three different porosity values (ε=0.30; 0.50; 0.70) were investigated. The porosity (ε) of the separator plates is defined as the ratio of the total hole area to the plate surface area. All lengths are nondimensionalized by dividing by the cylinder diameter and shown with the * index. The splitter plate length kept to constant during the experiment as ls\*=1. The distance between the leading edge of the splitter plate and the cylinder (lg\*) is variable due to the rotation of the separator plate at certain angles in the flow direction. To overcome this, the distance between the splitter plate rotation axis and the cylinder was taken as a parameter and shown with the \*\*. The gap between splitter plate midpoint and cylinder (lg\*\*) kept to constant during the experiments as lg\*\*=1.5. When the plates are rotated, the cross-section parallel to the flow decreases, which increases the interaction between the boundary layers. Since the permeable separator plates prevent the interaction of the boundary layers formed in the flow around the cylinder, the effect of the permeable separator plates increases in the downstream regions where the interaction of the boundary layers increases. Thus, the fluctuations are reduced, and a more stabilized trail flow occurs downstream of the cylinder. It was observed that the vortex

formation was delayed with the increase of the separator plate angle. In this study, the effect of the separator plate angle and the effect of the plate permeability were clearly observed.

**Key Words:** PIV, Flow Control, Cylinder, Separator plate, Permeable plate

## GİRİŞ (INTRODUCTION)

Batmış bir cisim etrafındaki sabit bir akış periyodik çevrinti dökülmesine neden olur. Meydana gelen çevrinti dökülmesi, cisim üzerindeki sürüklenme kuvvetlerini artmasına sebep olur ve akışa dik yönde oluşan periyodik kuvvetler, cisim üzerinde istenmeyen zorlanmalara sebep olur. Bu zorlanmalar enerji nakil hatları, baca bacaları, köprüler, binalar, radyo teleskopları, açık deniz sondaj kuleleri, su altı boru hatları, deniz kabloları vb. gibi birçok mühendislik uygulamasında istenen veya istenmeyen titreşimlere, akustik gürültüye, rezonansa ve yorulmaya sebep olabilir. Mühendislik uygulamalarında olumlu veya olumsuz etkilerinden ötürü, art izi bölgesindeki akış davranışını kontrol etmek önemlidir. Akış kontrol yöntemleri pasif akış kontrol yöntemleri ve aktif akış kontrol yöntemleri olarak iki ana dal altında incelenebilir. Pasif akış kontrol yöntemleri batmış cismin geometrisini değiştirme (Favier, vd., 2009) ve/veya ilave kontrol hacimleri (A. Roshko 1952) kullanımıyla sınırlıdır. Aktif kontrol yöntemlerin de ise elektromanyetik kontrol (Weier, vd., 1998), döner salınımı (Guilmineau 2002), ısıtma (Lecordier vd. 1991), akustik uyarılar (Blevins 1985), plazma aktüatörleri (Tabatabaeian 2015) gibi yöntemlerle akışa ilave enerji verilir. Kontrol yaklaşımı ise akış geri bildirimi yapılmayan açık çevrim veya akıştan anlık geri bildirimin yapıldığı ve buna göre değişkenlerin ayarlandığı kapalı çevrim olabilir.
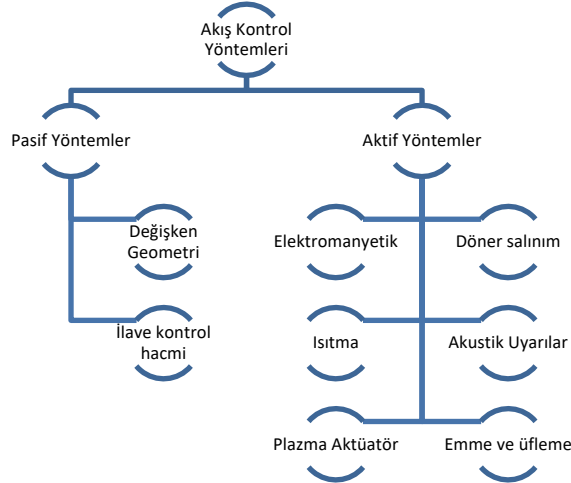


**Şekil 1.** Akış kontrol yöntemleri

Akış kontrolü için ayırıcı plaka kullanımı ilave kontrol hacmi ile kontrol yöntemlerinden biridir. Plaka yukarı akış, aşağı akış veya hem yukarı hem de aşağı akış bölgelerine yerleştirilebilir. Plakanın esnek (Teksin ve Yayla 2016) veya katı (Sahin vd., 2021) olabildiği uygulamalarda plaka uzunluğu ve plaka ile incelenen cisim arasındaki mesafe temel değişkenler olmakla birlikte, duruma göre plaka katılığı (Zhou vd. 2019), plaka geçirgenliği (Cardell 1993) ve plaka konumu (Gao,

vd., 2020) gibi değişkenler, farklı Reynolds akış değerlerine sahip durumlar için sürükleme katsayısı (Cd), çevrinti dökülme sıklığı (St), Reynolds gerilmeleri, türbülans kinetik enerji seviyeleri gibi veriler kullanılarak değerlendirilmiştir. **Şekil 1** de akış kontrol yöntemleri gösterilmiştir.

Ayırıcı plakalar ile akış kontrolü üzerine çalışan araştırmacıların öncüllerinden Roshko (A. Roshko 1952), (A. Roshko 1954), periyodik saçılmanın serbest girdap katmanları arasındaki iletişime bağımlılığını göstermek için bir dizi çalışma yaptı (Re=14500). Silindirin art izi merkez düzlemine yerleştirdiği ayırıcı plaka uzunluğu 5d'ye ulaştığında (d, silindirin çapıdır), girdap dökülmesinin tamamen ortadan kalktığını ve basınç direnci önemli ölçüde azaldığını gözlemledi. Ayırıcı plakanın uzunluğu 1d olup silindire bağlandığında dökülme frekansını çok değiştirmediğini ancak silindir ile plaka arasında boşluk bırakıldığında dökülme frekansının azaldığını ve taban basıncının arttığını bulmuştur. (**Şekil 2**). Aralık 3.85d'ye ulaşıldığında, dökülme frekansı minimuma inmiş ve taban basıncı maksimuma çıkmıştır. Burada Roshko, boşluğu silindir yüzeyi ile ayırıcı plakanın arka tarafı arasındaki mesafe olarak vermektedir.
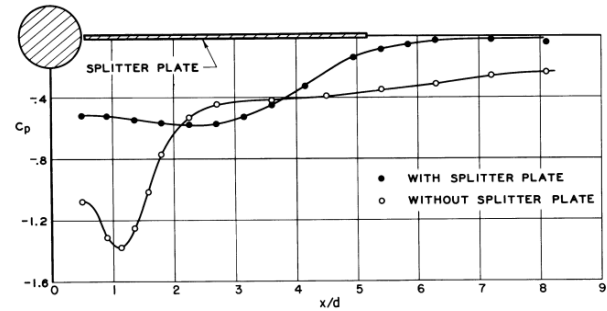


**Şekil 2**. Ayırıcı plakalı ve ayırıcı plakasız iz merkez hattı üzerindeki basınç. Re:14500 (A. Roshko 1954)

Cardell (Cardell 1993) $2.5 \; 10^3 \leq Re \leq 1.8 \; 10^4$ Reynolds sayısı aralığında düzgün bir akışta dairesel bir silindirin art izi bölgesine farklı geçirgenlikte ayırıcı plakalar yerleştirerek bir dizi deney gerçekleştirmiştir. Ayırıcı plaka olarak ince tellerden oluşturulan plakalar kullanmıştır ve plakaların geçirgenliği ile plakaların katılığı arasında basınç düşüşüne bağlı olarak bir ilişki belirlemiştir. Kwon ve Choi (Kwon 1996) ayırıcı plaka uzunluğu, Reynolds sayısıyla orantılı olan kritik uzunluktan daha büyük olduğunda , silindirin arkasındaki girdap saçılımının tamamen ortadan kalktığını buldular. Belirli bir Reynolds sayısı için sürüklenmeyi en aza indirmek için 1<l/d <2 arasında bir optimum uzunluk olduğunu tespit ettiler. Hwang ve diğerleri (Jong-Yeon Hwang 2003) silindir art iz bölgesine yerleştirilmiş, silindir çapıyla aynı uzunluğa sahip bir ayırıcı plakanın akış kaynaklı kuvvetlere etkisini sayısal olarak incelemiştir. Ayırıcı plaka ile silindir arasındaki mesafenin ayırıcı plaka çapına oranı G/D=2.6 olduğunda, Girdap dökülmesini sönümlenmesi, sürükleme kuvvetini ve kaldırma kuvvetlerinin dalgalanmasını önemli ölçüde azaldığını bulmuşlardır. Akıllı ve ark. (Huseyin Akilli

2005) (Akilli vd., 2005), sığ akışta silindir arkasına yerleştirilen ayırıcı plakaların kalınlık çap oranı (T/D) ve silindir ayırıcı plaka arası mesafe oranının (G/D) girdap dalgalanmasına etkisini Re=5000 'de incelemişler ve G/D=1.75 olduğunda akıştaki Reynolds gerilmesinin 8.5 kat azaldığını tespit etmişlerdir. Matsumoto ve ark. (Matsumoto vd. 2008) rüzgâr tünelinde, silindir art iz bölgesine yerleştirdikleri %60-%70 geçirgenlikli ayırıcı plakalar vasıtasıyla girdap dökülmesinin %10 civarında azaltılabileceğini gösterdiler. Xiao ve diğerleri (Xiao 2011) D kesitli silindirin art iz bölgesine yerleştirilmiş NACA0012 folyosunun hidrodinamik performansı üzerine bir dizi sayısal çalışma yaptı ve dalgalı folyonun silindir sürükleme ve kaldırma genliği üzerindeki etkilerinin, dalgalanma oranının yanı sıra boşluk oranına da önemli ölçüde bağlı olduğunu bulmuşlardır.



**Şekil 3.** Deneysel düzenleme (Matsumoto, ve diğerleri 2008)



**Şekil 4.** Deneysel düzenleme (Xiao 2011)

Özgören (Ozgoren 2006) çalışmasında 550 ≤ Re ≤ 3400 aralığında, kare ve dairesel silindir art iz bölgesindeki akışı incelemiştir. Kesitlere ve kesit yerleşimine bağlı olarak Strouhal sayılarındaki değişimleri tespit etmiş ve literatürdeki değerlerle uyumluluğunu göstermiş, Beklendiği gibi Reynolds sayısının artışı ile birlikte çevrinti oluşumu mesafesinin azaldığını belirmiştir. Özgören ve arkadaşları (Ozgoren vd. 2011) bir başka çalışmalarında ise Re=5000 ve Re=10000 de silindir ve kürenin art iz bölgesindeki akış özelliklerini incelemişlerdir. Küre art iz bölgesinde küçük ölçekli çevrintilerin daha baskın olduğunu ve silindirden farklı olarak, küre için 3 boyutlu akış sebebiyle ayrılma tabakları boyunca TKE'nin en yüksek değerinin iki noktada görüldüğünü ifade etmişlerdir. Ghadimi ve ark. (Ghadimi vd. 2013) Re=200 için farklı uzunluk ve konuma sahip ayırıcıların dairesel bir silindirin ses basıncı düzeyine etkilerini araştırmışlar. Ayırıcıların frekans üzerinde herhangi bir etkisinin olmadığını bulmuşlardır. Kaldırma kuvveti salınımının. Ayırıcılar

çift formda kullanıldığında ve merkez çizgisinden yarım silindir yarıçapı uzaklıkta bir konuma yerleştirildiğinde, kaldırma kuvveti salınımı yaklaşık %99.6 oranında azalır ve ses basıncı seviyesi (SPL) yaklaşık %15.4 oranında artar (durum 8). Son olarak, bir ayırıcı aynı belirlenen konuma yerleştirildiğinde, SPL %6.4 oranında azalır ve kaldırma kuvveti salınımı da %90.5 oranında bir azalma sergiler (durum 7).

| Case | Length of splitter (m) | Vertical position of splitter from the center of cylinder (m) | Shape |
|---|---|---|---|
| 1 | - | - | |
| 2 | 0.1 | 0 | |
| 3 | 0.075 | 0 | |
| 4 | 0.05 | 0 | |
| 5 | 0.025 | 0 | |
| 6 | 0.1 | 0.025 | |
| 7 | 0.1 | 0.05 | |
| 8 | 0.1 | 0.025 | |

**Şekil 5.** Plaka yerleşimleri (Ghadimi, ve diğerleri 2013)

Bao ve Tao (Bao ve Tao 2013) sayısal olarak laminer akış rejimi (Re=20-160) dahilinde olan, arka yüzeye simetrik olarak tutturulmuş çift plakalar tarafından dairesel bir silindirin art iz akış bölgesini incelemişlerdir. ($40^0 \leq \theta \leq 50^0$) için, Re=160'ta sürüklenme değerlerinde %13'e varan düşüş tespit etmişlerdir; bu, aynı plaka uzunluğundaki tek ayırıcı plakanın neredeyse iki katıdır.



**Şekil 6.** Deneysel düzenleme (Bao ve Tao 2013)

Reza-zadeh (Reza-zadeh 2013) silindir etrafındaki sıvı akışını kontrol etmek için tel plakalı elektrotları ve ayırıcı plakayı aynı anda uyguladı. Ayırma plakasının açısı $5^0$ derecelik artışlarla $0^0$ ila $45^0$ arasında değişir. Bu düzenlemeye bağlı olarak korona rüzgâr etkisinin nasıl değiştiğini gözlemlediler.

Lee ve You (Lee ve You 2013) ayırıcı plakanın uzunluğunu ve rijitliğini değiştirerek, esnek bir ayırıcı plakaya sahip dairesel bir silindir art iz akışını incelemişlerdir. Bir ayırıcı plakanın esnekliğinin, plakanın salınımını arttırırken, silindir yüzeyine etki eden sürükleme ve kaldırma kuvvetlerini olumsuz yönde modüle ettiğini buldular. Oruç ve diğerleri (Oruc vd. 2013) yan yana iki silindir arasına uzunluğu L ($1 \leq L/D \leq 5$) olan bir ayırıcı plaka yerleştirerek art iz bölgesindeki akışı incelediler. $L/D \geq 3$ için ayırıcı plakanın varlığıyla izdeki sapmanın ve dolayısıyla izdeki iki durumluğun önemli ölçüde önlendiğini, bunun da yaklaşık olarak aynı girdap saçılımı büyüklük sırasına sahip iki iyi simetrik,

kararlı iz ile sonuçlandığını bulmuşlardır. Teksin ve Yayla (Teksin ve Yayla 2016) parçacık Görüntülü Hız Ölçümü (PIV) kullanarak Re=2500 için silindir art iz bölgesine farklı uzunlukta elastik ayırıcı plakalar yerleştirmişler ve L/D=2.5 için girdap özgün değerlerindeki düşüşün en yüksek seviyeye çıktığını ve L/D=>2.5 için bu düşüşün neredeyse sabit kaldığını tespit etmişlerdir.
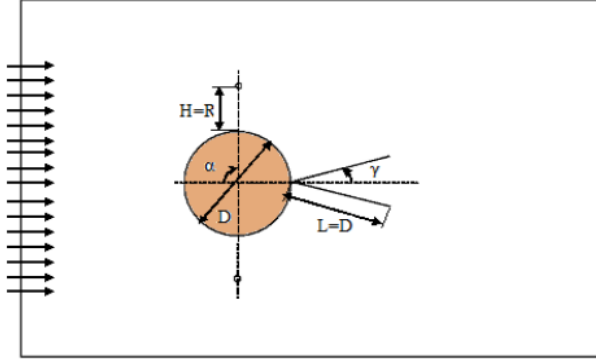


**Şekil 7**. Deneysel düzenleme (Reza-zadeh 2013)
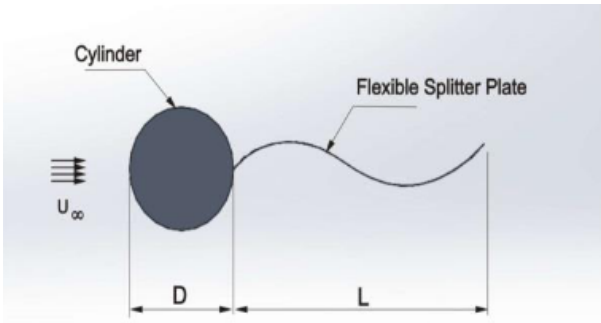


**Şekil 8**. Deney yerleşimi (Teksin ve Yayla 2016)

Sahin ve arkadaşları (Sahin vd., 2021) Re=5000 için, silindir art iz bölgesinde farklı konumlara yerleştirdikleri, farklı geçirgenliklere sahip ayırıcı plakaların akış özniteliklerine etkisini incelemişler, özniteliklerdeki en yüksek düşüş için plaka geçirgenliği artıkça plaka ile silindir arasındaki mesafenin artması gerektiğini tespit etmişlerdir.

Bu makalenin amacı, iki boyutlu Parçacık Görüntülü Hız Ölçümü (PIV) teknikleri kullanılarak, farklı gözenekliliğe sahip ve akış yönünde çeşitli konumlarda bulunan ayırıcı plakalar kullanılarak silindirin arkasındaki kararsız akış yapısının pasif kontrolünü araştırmaktır. Hesaplama alanı, sınır koşulları ve kullanılan yöntembilimi Bölüm 2'de anlatılmakta, ardından Bölüm 3'te deney sonuçları ve irdelemeler verilmiş, bulunan sonuçlar Bölüm 4'te sunulmuştur.

## DENEYSEL METOT (EXPERIMENTAL METHOD)

Bu çalışmada, düşey konumda bulunan dairesel bir silindirin art izi bölgesindeki akış davranışı deneysel olarak incelenmiştir. Tüm deneysel çalışmalar, Çukurova üniversitesinin 8000 mm uzunluğunda, 1000 mm genişliğinde ve 750 mm derinliğindeki su kanalında,

Dantec PIV sistemi kullanılarak gerçekleştirilmiştir. Deneyler esnasında ve su yüksekliği 0.45m (hw) ye sabitlenmiş olup tüm deneyler Re=5000 de yapılmıştır.

Bu çalışmada seçilen Reynolds sayısı (Re=5000) gibi kritik altı Reynolds sayılarına sahip akışlar ters basınç gradyanları ve türbülansa geçiş süreci etkisi ile akış kararlı bir rejimde değildir. Kritik altı akışlarda, küt cisim etrafındaki daimî olmayan akış yapıları mühendislik açısından birçok belirsizliğe yol açmaktadır ve dikkatle incelenmelidir. Düşük Reynolds sayılarını gerçek dünya akış yapılarına uyarlamak, deneysel kurulum ile gerçek sistem arasında geometrik, kinematik ve dinamik benzerliklerin korunmasını gerektirir. Geometrik benzerlik, ölçeklenmiş deneysel kurulumun gerçek dünya uygulamasının fiziksel geometrisini doğru bir şekilde temsil etmesini sağlar. Kinematik benzerlik, model ve gerçek sistem arasında akış hızlarını ve ivmeleri eşleştirmeye odaklanır. Dinamik benzerlik, model üzerinde etkili olan kuvvetlerin gerçek uygulamadaki kuvvetlere orantılı olmasını sağlar, böylece genel akış davranışı korunur.

$$Re = \frac{U_\infty . D}{\vartheta} \tag{1}$$

1 numaralı denklemde Re Reynolds sayısı, $U_\infty$=0.0837m/s serbest akış hızı, D silindir çapı, $\vartheta = 1.00401E-06$ 20 °C de suyun kinematik viskozitesidir. Dantec PIV Sistemi, akış alanı aydınlatması için her biri maksimum 120 mJ enerji çıkışlı, 532 nm dalga boyuna sahip iki Nd-YAG darbeli lazer kaynağı kullanmaktadır. Su, çapı 12 μm, yoğunluğu 1100kg/m³ olan, nötr olarak yüzer, gümüş kaplı küresel cam parçacıklar ile tohumlanmış, akış alanını tarayan yaklaşık 1.5mm kalınlığındaki lazer tabakası tarafından aydınlatılarak akışkan hareketi gözlemlenmiştir. Parçacıkların Stokes sayısı 1.83x10⁻³ civarında hesaplanmıştır ve bu değer, deneylerde parçacıkların akış çizgilerini tam olarak takip ettiğini göstermektedir (Raffel vd., 2007) (Gozmen vd., 2013). Kullanılan üstü açık dikdörtgen kesitli su kanalı için Froude sayısı denklem 2 de verilmiştir.

$$Fr = \frac{U_\infty .}{\sqrt{(g.h_w)}} \tag{2}$$

2 numaralı denkleme göre Froude sayısı 0.042 hesaplanmış olup kritik Froude sayısı (1) den çok düşük olmasından ötürü akış serbest yüzeyinin etkisi göz ardı edilmiştir. Tüm deneyler, Nikon AF micro 60 f/2.8D lens ile donatılmış CCD kamera kullanılarak, 1600x1200 piksel çözünürlük ve 60 mm odak uzaklıklı lens ile görüntülenmiştir. Deneyler iki set olarak gerçekleştirilmiş olup, her iki set de 1000 anlık görüntü içerir. Görüntü işlemede 7227 (99x73) hız vektörünü kapsayan 32x32 piksel dikdörtgen etkili sorgulama pencereleri kullanılmıştır. Sorgulama sürecinde, Nyquist kriterini karşılamak için %50'lik bir örtüşme kullanılmıştır. Westerweel (Westerweel 1993), Adrian (Adrian 1991) ve Raffel (Raffel vd., 2007) PIV yönteminde kullanılan matematiksel ve fiziksel yaklaşımları çalışmalarında detaylı olarak anlatmışlardır.

Westerweel (Westerweel 1993) PIV yönteminde, lazer tarafından aydınlatılacak taneciklerin rastlantısal dağılımı, hız hesaplarının yapıldığı alanın boyutu, ölçüm ve görüntüleme aygıtlarının hassasiyeti gibi sebeplerden dolayı, taneciklerin hız ölçümlerinde %2 oranında yaklaşık belirsizlik olduğunu hesaplamıştır. Bu çalışmada da benzer bir yaklaşım yapıldığı için, yapılan deneylerde derinlik ortalamalı hıza göre hızdaki belirsizlik yaklaşık %2 olarak kabul edilmiştir. Deney düzeneğinin şematik gösterimleri **Şekil 9**, **Şekil 10** ve **Şekil 11**'de verilmiştir.
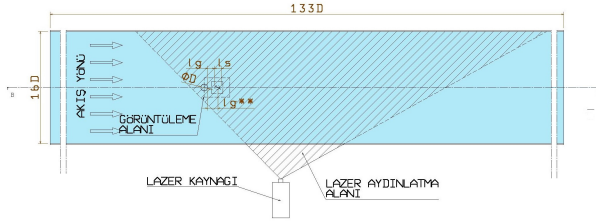


**Şekil 9**. Deney düzeneği üstten bakış
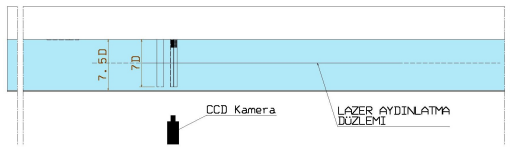


**Şekil 10**. Deney düzeneği B-B kesiti
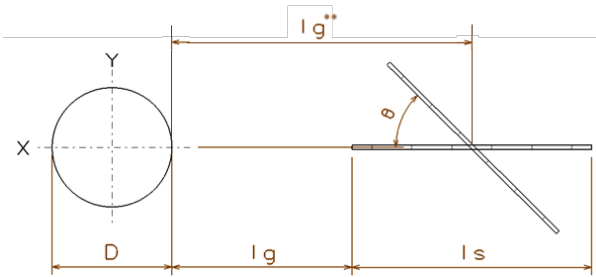


**Şekil 11**. Deney değişkenleri

Silindir art izi bölgesinde, farklı konumlara yerleştirilen, farklı geçirgenliklere sahip bir akış ayırıcı plaka vasıtasıyla, art izi bölgesindeki akış niteliklerindeki değişimler gözlemlenmiştir. Delikli ayırıcı plakalar $t=8\times10^{-4}$m kalınlığında paslanmaz çelik saçtan imal edilmiştir. Plaka üzerindeki $d=2.5\times10^{-3}$m çapındaki delikler lazerde kesilmiştir. Ayırıcı plakaların geçirgenliği ($\varepsilon$) toplam delik alanının, plaka yüzey alanını oranı olarak tanımlanmıştır. (**Şekil 12**)
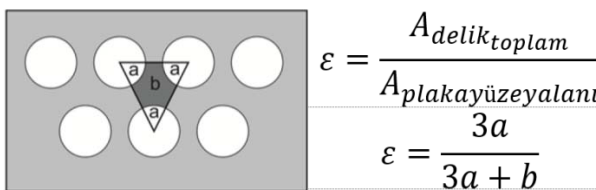


**Şekil 12**. Plaka geçirgenlik tanımı

Deneylerde kullanılan silindir çapı (D) 60 mm'dir. Silindir (h) yüksekliği 7D'dir. Dört farklı ayırıcı plaka açısı değeri ($\theta$=0°; 15°; 30°; 45°) ve üç farklı gözeneklilik

değeri ($\varepsilon$=0.30; 0.50; 0.70) incelenmiş ve ayırıcı plaka uzunluğu (ls*) ve ayırıcı plaka orta noktası ile silindir (lg**) arasındaki boşluk, deneyler sırasında ls*=1 ve lg**=1.5 olarak sabit tutulmuştur.

$$ls^* = \frac{ls}{D} \tag{2}$$

$$lg^* = \frac{lg}{D} \tag{3}$$

$$lg^{**} = lg^* + ls^*/2 \tag{4}$$

## DENEYSEL SONUÇLAR VE İRDELEME

Farklı geçirgenlik ve açısal konumlamalar için akış yönündeki farklı kesitlerdeki Reynolds Gerilme profilleri, |u'u'|, **Şekil 13**, **Şekil 14**, **Şekil 15** ve **Şekil 16**'de verilmiştir. Şekillerde, her sütun farklı açısal konumu ve her satır kesit konumunu göstermektedir. Her hücrede |u'u'|, plakasız silindir ve art izi akış bölgesine farklı geçirgenlikte plakalar yerleştirilmiş silindirler için yapılan ölçümlerle oluşturulmuş, akış yönündeki Reynolds gerilme profilleri verilmiştir. Silindirin akışta oluşturduğu kayma tabakaları büyük bir hız gradyanına yol açar. Hız gradyanındaki tepe noktaları en yüksek |u'u'| değerlerini temsil eder. Bundan ötürü elde edilen Reynolds gerilme profilleri, silindir kayma tabakasına benzer bir davranış göstermektedir. Akış yönünde ilerleyen (x/D) kesit konumlarında, çevrinti dökülmesi ve kuyruk çevrintilerinin artışından ötürü, tepe noktaları akış yönünde büyümektedir.

Her hücrede |v'v'|, plakasız silindir ve art izi akış bölgesine farklı geçirgenlikte plakalar yerleştirilmiş silindirler için yapılan ölçümlerle oluşturulmuş, akışa dik yöndeki Reynolds gerilme profilleri verilmiştir. Akış yönünde ilerleyen (x/D) kesit konumlarında, çevrinti dökülmesi ve kuyruk çevrintilerinin artışından ötürü, |v'v'| tepe noktaları akış yönünde büyümektedir.

Tüm açısal yönelimler ve tüm geçirgenlik değerleri için |u'u'|'nun ulaştığı en büyük değerde, plakasız silindire göre düşüş olduğunu görülmektedir. Özellikle x/D=1.5 ve x/D=2 kesitlerinde |u'u'|'nun tepe değerlerindeki düşüş daha açık olarak gözlemlenmektedir. x/D=2.5 ve x/D=3 kesitlerinde çevrinti çalkalanması ve kuyruk çevrintilerinin etkisiyle profiller birbirine yaklaşmaktadır. $\varepsilon = 0.3$ geçirgenlik değeri, düşük geçirgenlik değeri sebebiyle, tabakalar arasındaki karışmayı önlemekte bu da genel olarak |u'u'| değerlerinin daha düşük olmasını sağlamaktadır. Açısal yönelim artıkça akış simetrisi bozulmakta, 30° ve 45°'lik yönelimler için ise bu bozulma daha açık bir şekilde görülebilmektedir. |u'u'| tepe değerlerindeki en büyük düşüş, 45°'lik yönelimli plaka ve x/D=2 kesitinde, $\varepsilon = 0.3$ geçirgenliği için sağlanmaktadır.

93

**Şekil 13**. Θ=0° ve Θ=15° açı yönelimlerine sahip farklı geçirgenlik değerlerindeki plakalar için 0.5≤x/D<1.5 kesitlerinde oluşan akış yönünde Reynolds gerilimi profilleri.
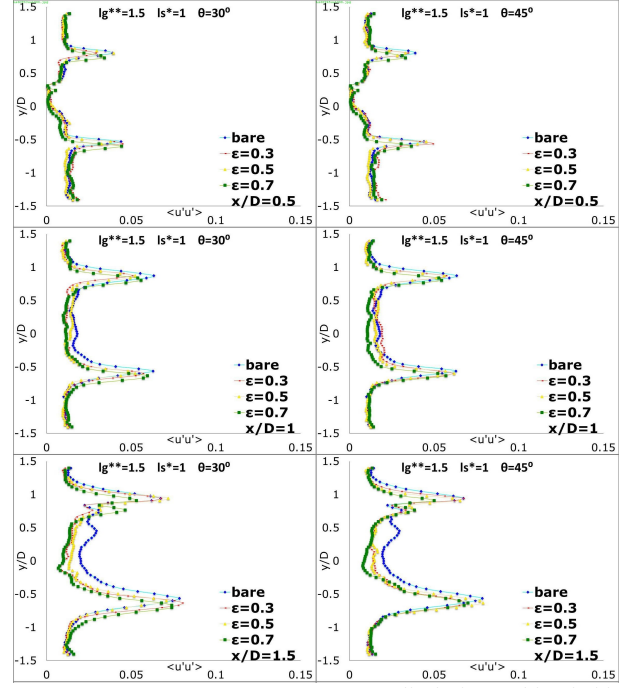


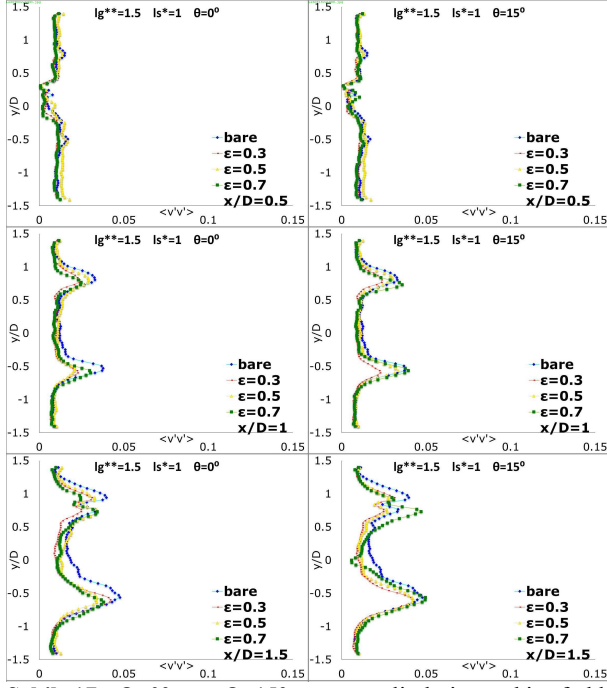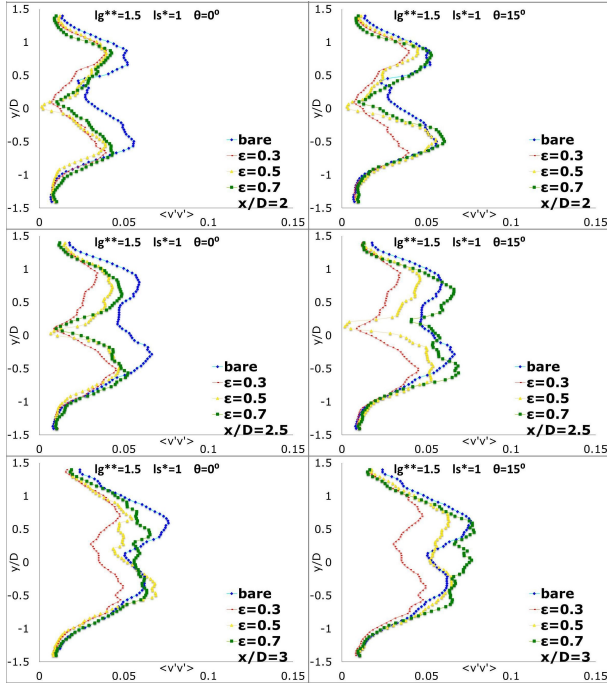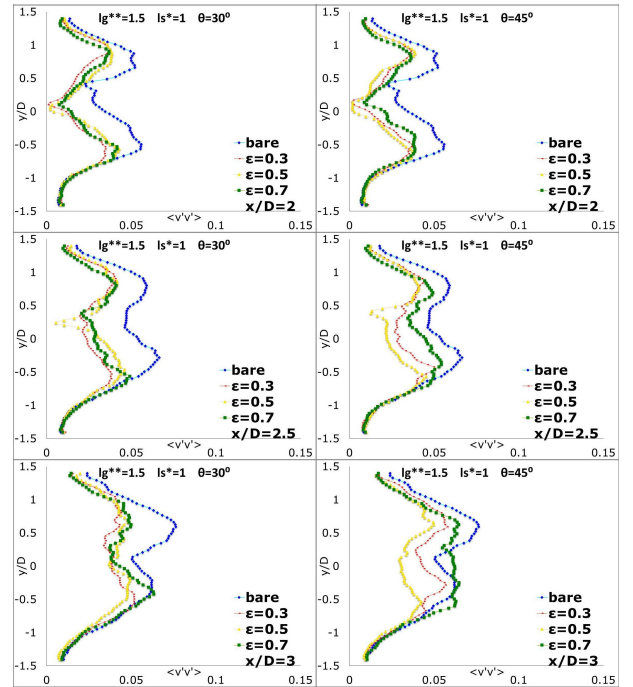**Şekil 15**. Θ=30° ve Θ=45° açı yönelimlerine sahip farklı geçirgenlik değerlerindeki plakalar için 0.5≤x/D≤1.5 kesitlerinde oluşan akış yönünde Reynolds gerilimi profilleri.
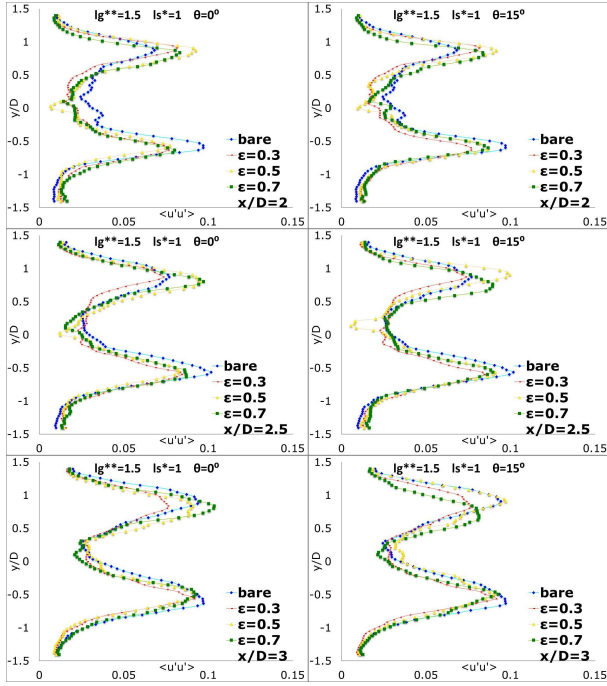


**Şekil 14**. Θ=0° ve Θ=15° açı yönelimlerine sahip farklı geçirgenlik değerlerindeki plakalar için 2≤x/D≤3 kesitlerinde oluşan akış yönünde Reynolds gerilimi profilleri



**Şekil 16**. Θ=30° ve Θ=45° açı yönelimlerine sahip farklı geçirgenlik değerlerindeki plakalar için 2≤x/D≤3 kesitlerinde oluşan akış yönünde Reynolds gerilimi profilleri

**Şekil 17**, **Şekil 18**, **Şekil 19** ve **Şekil 20**, silindir art izi akış bölgesine farklı açısal yönelim ve farklı geçirgenliklere sahip plakaların yerleştirildiği durumlar için, farklı kesitlerdeki, akışa dik yönde oluşan Reynolds gerilim, |v'v'|, profillerini göstermektedir. Şekillerde, her sütun farklı açısal konumu ve her satır kesit konumunu göstermektedir.

**Şekil 17**. Ɵ=0° ve Ɵ=15° açı yönelimlerine sahip farklı geçirgenlik değerlerindeki plakalar için 0.5≤x/D<1.5 kesitlerinde oluşan akış yönüne dik Reynolds gerilimi profilleri.



**Şekil 18**. Ɵ=0° ve Ɵ=15° açı yönelimlerine sahip farklı geçirgenlik değerlerindeki plakalar için 2≤x/D≤3 kesitlerinde oluşan akış yönüne dik Reynolds gerilimi profilleri.

Tüm açısal yönelimler ve tüm geçirgenlik değerleri için |v'v'|'nin ulaştığı en büyük değerde, plakasız silindire göre düşüş olduğunu görülmektedir. Özellikle x/D=1.5 ve x/D=2 kesitlerinde |v'v'|'nin tepe değerlerindeki düşüş daha açık olarak gözlemlenmektedir. x/D=2.5 ve x/D=3 kesitlerinde çevrinti çalkalanması ve kuyruk çevrintilerinin etkisiyle profiller birbirine yaklaşmaktadır. ε=0.3 geçirgenlik değeri, düşük geçirgenlik değeri sebebiyle, tabakalar arasındaki karışmayı önlemekte bu da genel olarak |v'v'|

değerlerinin daha düşük olmasını sağlamaktadır. Açısal yönelim artıkça akış simetrisi bozulmakta, 30° ve 45°'lik yönelimler için ise bu bozulma daha açık bir şekilde görülebilmektedir.
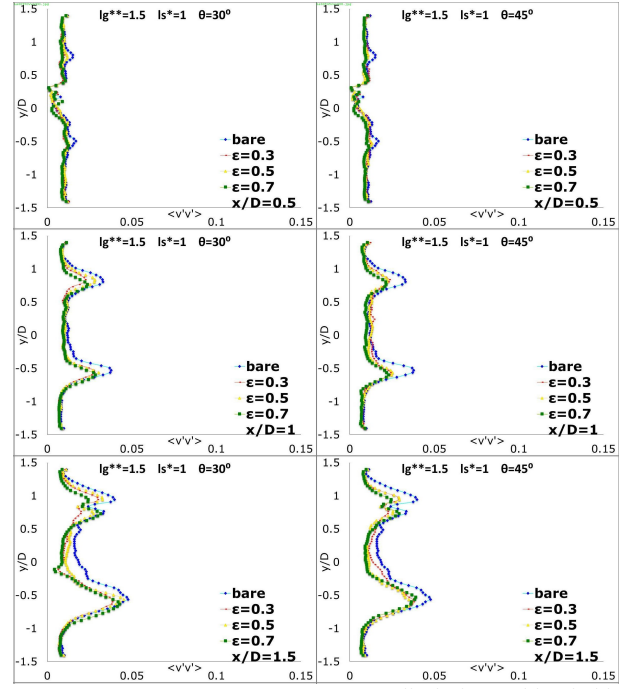


**Şekil 19**. Ɵ=30° ve Ɵ=45° açı yönelimlerine sahip farklı geçirgenlik değerlerindeki plakalar için 0.5≤x/D<1.5 kesitlerinde oluşan akış yönüne dik Reynolds gerilimi profilleri.



**Şekil 20**. Ɵ=30° ve Ɵ=45° açı yönelimlerine sahip farklı geçirgenlik değerlerindeki plakalar için 2≤x/D≤3 kesitlerinde oluşan akış yönüne dik Reynolds gerilimi profilleri.

|v'v'| tepe değerlerindeki en büyük düşüş, 45°'lik yönelimli plaka ve x/D=2 kesitinde, ε=0.3 geçirgenliği için sağlanmaktadır. Tüm durumlar için, art izi bölgesindeki zaman ortalamalı normalize çevrinti

dağılımı **Şekil 23**'de verilmiştir. Negatif işaretli çevrinti büyüklükleri saat yönünde dönüşü gösterir. Silindirin her iki tarafında kayma tabakaları oluşur ve bunların mukavemeti aşağı yönde azalır. Arkasında plaka olmayan silindir ile yapılan deneylerde, kayma tabakasındaki girdabın büyüklüğü-12.1'e ulaşmaktadır. Art izi bölgesine plaka yerleştirilmiş durumlarda, ε=0.3 geçirgenlik değeri için, 0°, 15°, 30°, ve 45° derecelik yönelimlerde oluşan en büyük çevrinti değerleri sırasıyla %-1, %-3, %-2 ve %-2 oranlarında düşmüştür. Art izi akış bölgesine plaka yerleştirilmiş durumlarda, ε=0.5 geçirgenlik değeri için, 0°, 15°, 30° ve 45° derecelik yönelimlerde oluşan en büyük çevrinti değerleri sırasıyla %-4, %-3, %-3 ve %-2 oranlarında düşmüştür. Art izi akış bölgesine plaka yerleştirilmiş durumlarda, ε=0.7 geçirgenlik değeri için, 0°, 15°, 30° ve 45° derecelik yönelimlerde oluşan en büyük çevrinti değerleri sırasıyla %-9, %-3, %-9 ve %-6 oranlarında düşmüştür. İz bölgesindeki geçirgen ayırıcı plaka kesme tabakalarının etkileşimlerini engellediğinden, kayma tabakalarının direncinin azaldığı açıktır. Artan gözeneklilik ile ayırıcı plaka etkinliği artmaktadır.

Silindir art iz bölgesine konuşlandırılmış farklı geçirgenlikli ve farklı yönelimli plakalar için Reynolds kayma gerilmesinin, yalnız silindir olması durumuna göre değişimi **Şekil 21** de verilmiştir. Yalnız silindir olması durumunda, silindir art iz bölgesindeki Reynolds kayma gerilmesinin en yüksek değeri 0.05 olarak bulunmuştur.
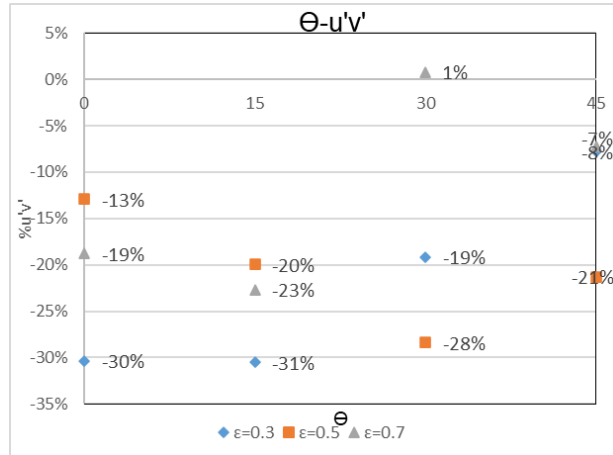


**Şekil 21**. Farklı geçirgenlikteki plakalar için plaka yöneliminin en büyük Reynolds kayma gerilmesi değerine etkisinin, plakasız silindire göre mukayesesi

Ayırıcı plakaların akış iziyle aynı doğrultuda yerleştirildiği durumda, tabakalar arasındaki etkileşimin en düşük olduğu ε=0.3 geçirgenlik değeri için, 0º, 15º, 30º ve 45º derecelik açısal yönelimlerde, Reynolds gerilme değerinin ulaştığı en yüksek değerde sırasıyla %30, %31, %19 ve %8'lik düşüşler görülmüştür. ε=0.5 geçirgenlik değeri için, 0º,15º, 30º ve 45º derecelik açısal yönelimlerde, Reynolds gerilme değerinin ulaştığı en yüksek değerde sırasıyla %13, %20, %28 ve %21'lik düşüşler görülmüştür. ε=0.7 geçirgenlik değeri için, 0º, 15º, 30º ve 45º derecelik açısal yönelimlerde, Reynolds

gerilme değerinin ulaştığı en yüksek değerde sırasıyla %19, %23, %1 ve %7'lik düşüşler görülmüştür.
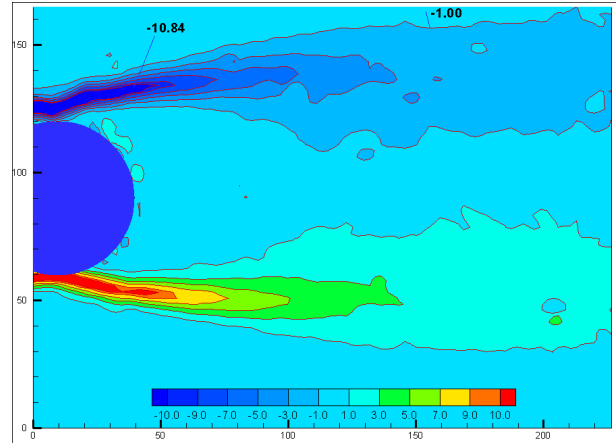


**Şekil 22**. Arka plakasız silindir için yakın iz bölgesinde çevrinti dağılımları.

15º'lik açılı konumlandırma için, Reynolds gerilmesi tepe değerlerindeki düşüş, tüm geçirgenlikler için en yüksek değerlerine ulaşmış ve geçirgenlik ve açısal konumlandırma değerlerindeki artışla birlikte Reynolds gerilme değerinin tepe noktasındaki düşüş, artan etkileşimle birlikte azalmıştır. Reynolds kayma geriliminin belirli bir oranda azalması, kayma katmanlarının etkileşiminin delikli ayırıcı plaka tarafından zayıflatıldığını ve dolayısıyla çevrinti şiddetinin düştüğü şeklinde değerlendirilebilir. Özkan ve diğerleri (Ozkan vd. 2017), temel silindire göre türbülans istatistiklerinin azaldığı durumlarda sürüklenme direnç katsayısının da düştüğünü göstermiştir. Dolayısıyla Reynolds kayma gerilmesindeki bu azalma, silindirin direnç katsayısının azalması olarak ta değerlendirilebilir. Arka plakasız silindi için yakın iz çevrinti dağılımları **Şekil 22**'de, tüm test durumları için yakın iz bölgesinde çevrinti dağılımları **Şekil 23**'de verilmiştir.

Yüksek Reynolds sayılarında, basınç ve hız dağılımın periyodik olarak değişmesinden ötürü art izi bölgesinde türbülans oluşumları görülür. Diğer bir deyişle, bu bölgedeki akışta, akışkanın hızı ve akış yönü sürekli değişir. Boyutsuz türbülans kinetik enerjisi (TKE), türbülansın yoğunluğunun bir ölçüsüdür ve Chen tarafından belirtildiği gibi art izi bölgesindeki akış özellikleri için bir değerlendirme göstergesi olarak kullanılabilir (Chen vd., 2014) (Pinar vd., 2015). 2D-PIV ölçümleriyle yakalanan iki boyutlu hız alanları sayesinde ortalama TKE yaklaşık olarak 5 numaralı formülle hesaplanır.

$$TKE = \frac{3}{4} \frac{\overline{(u')^2} + \overline{(v')^2}}{U^2} \qquad (5)$$

Bu formülde $u'$ akış yönündeki hız değişimlerini, $v'$ akış yönüne dik yöndeki hız değişimlerini gösterir. Bu çalışmada da TKE art izi bölgesindeki akış kontrolünde değerlendirme parametresi olarak seçilmiştir. Farklı geçirgenliklere sahip ayırıcı plakaların, silindir art izi bölgesindeki akış yapısına etkisini belirlemek için bir dizi PIV çözümlemesi yapılmıştır.

Tüm test durumları için yakın iz bölgesindeki akış çizgileri **Şekil 24** de verilmiştir. **Şekil 24** de sütunlar sırasıyla 0.3, 0.5 ve 0.7 plaka geçirgenliklerini, satırlar ise sırasıyla 0°, 15°, 30° ve 45° açısal plaka yönelimleri için akış çizgilerini göstermektedir. Yapılan deneylerde, türbülans kinetik enerjisinin tepe değerleri ile türbülans kinetik enerjisinin tepe değerinin oluşum noktaları, ayırıcı plaka kullanılmayan, çıplak silindir durumundaki değerlerle karşılaştırılmıştır. **Şekil 25**, **Şekil 26**, **Şekil 27** ve **Şekil 28** da silindir art iz bölgesine yerleştirilen farklı geçirgenlikli plakalar kullanılarak yapılan deneylerde, akış yönündeki farklı kesitlerde yapılan ölçümlerden elde edilen türbülans kinetik enerji (TKE) profilleri, plakasız yapılan ölçümlerle birlikte verilmiştir. Şekillerde her sütun farklı açısal yönelimi, her satır ise farklı kesit konumlarını belirtmektedir. Kesit konumu, silindir çapına bölünerek boyutsuz hale getirilmiştir. Silindir merkezi koordinat merkezidir. Profillerdeki tepe noktaları, en yüksek türbülans kinetik enerji değerlerinin, silindirin alt ve üst akış ayrılma hattı boyunca oluştuğunu göstermektedir. Plakasız silindir grafikleri incelendiğinde, beklendiği gibi art izi bölgesindeki TKE değerleri akış yönünde büyük ölçekli çevrinti dalgalanmaları sebebiyle artış göstermektedir X/D=0.5 kesiti silindirin arka teğetine denk gelmesinden ötürü, herhangi bir açıyla yönelmiş ayırıcı plakaların türbülans kinetik enerji profilleri üzerinde fark edilir bir etkisi gözlemlenmemiştir.
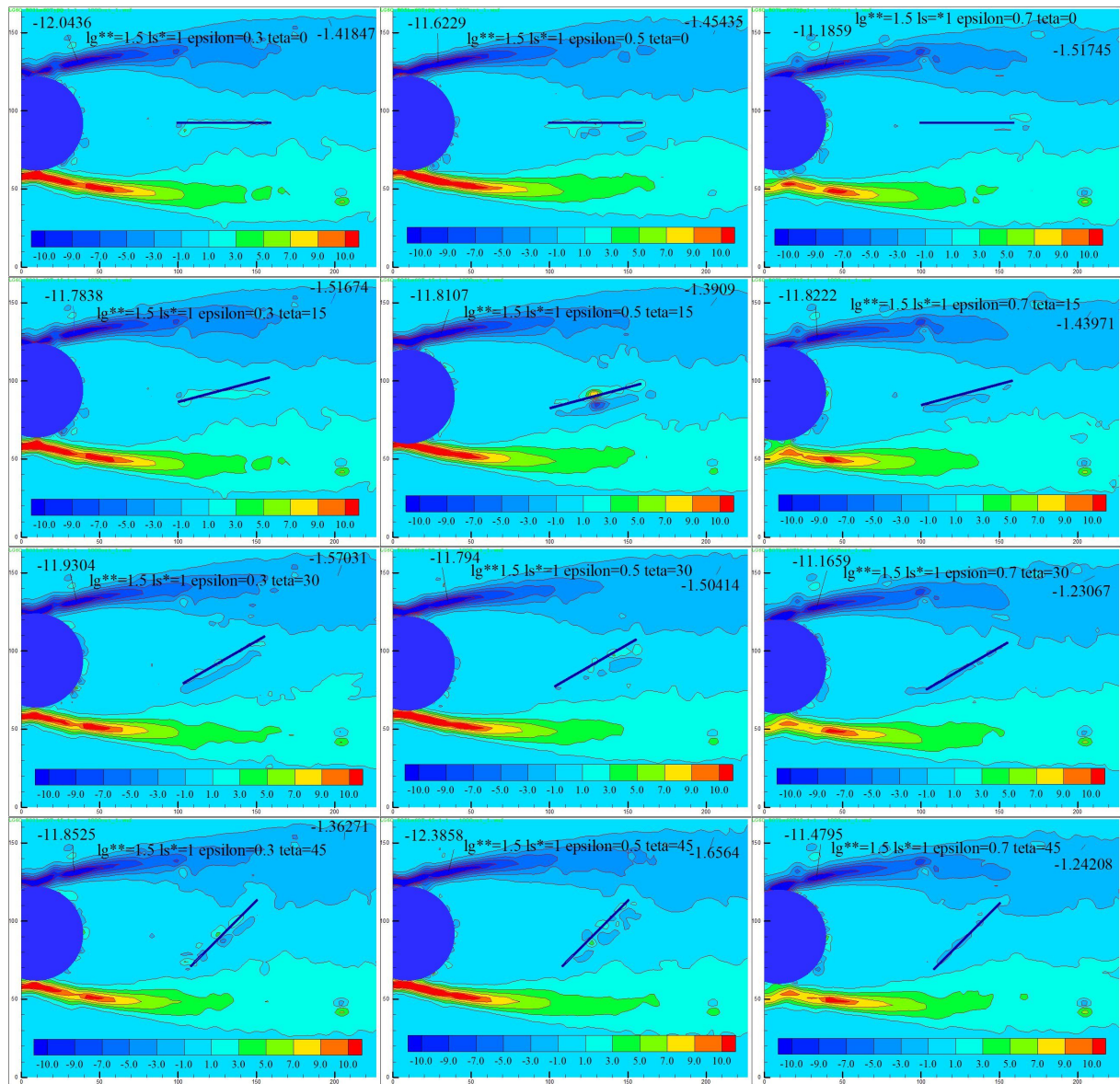


**Şekil 23**.Tüm test durumları için yakın iz bölgesinde çevrinti dağılımları

Bu durum tüm plaka geçirgenlikleri için aynıdır. X/D=1 kesitiyle beraber ayırıcı plakaların etkisi görülmeye başlanmakta ve art izi bölgesindeki TKE değerlerinde, plakasız akışa göre düşüş görülmektedir. Tüm geçirgenlikler için bu düşüş geçerli olmakla birlikte, farklı geçirgenlikteki plakaların çok yakın sonuçlar vermesi sebebiyle, X/D=1 kesiti için geçirgenliğin TKE üzerindeki etkisi gözlemlenememiştir. X/D=1.5 ve sonrasındaki kesitlerde ayırıcı plakaların, türbülans kinetik enerji profilleri üzerindeki etkisi daha açık görülmeye başlanmaktadır. X/D=2.5 ve X/D=3 kesitlerinde akış içindeki etkileşimin artmasından ötürü, özellikle yüksek geçirgenlikli ayırıcı plakaların etkisinde azalma

gözlemlenmektedir. Plakalar döndürüldüğünde, plakaların akışa paralel kesiti azalmaktadır bu durum ayrıcı plaka uzunluğunun, silindir çapına eşit olmasından ötürü sınır tabakalar arasındaki etkileşimi artırmakta buda açıdan dolayı oluşan akışa dik yöndeki kesitten gelen faydayı sıfırlamaktadır. Geçirgen ayırıcı plakalar, silindir etrafındaki akışta oluşan sınır tabakalarının etkileşimini engellediği için, sınır tabakaların etkileşiminin artığı daha geri konumdaki kesitlerde geçirgen ayırıcı plakaların etkisi artmaktadır. Böylece, akış yönünde ve enine dalgalanmalar azalmakta ve silindirin aşağı akışında daha stabilize bir iz akışı meydana gelmektedir. Geçirgenlik artıkça, etkileşimde artığı için en yüksek sönümlemeyi, neredeyse tüm açı ve kesit değerlerinde $\varepsilon = 0.3$ için sağlamaktadır. Farklı açılardaki plakaların etkisi, plakalar henüz sınır tabakalarla yeterli temasa geçemediği için belirsizdir. Tüm kesit değerleri, iki defa alınan ölçümlerin ortalaması alınarak oluşturulmuştur.
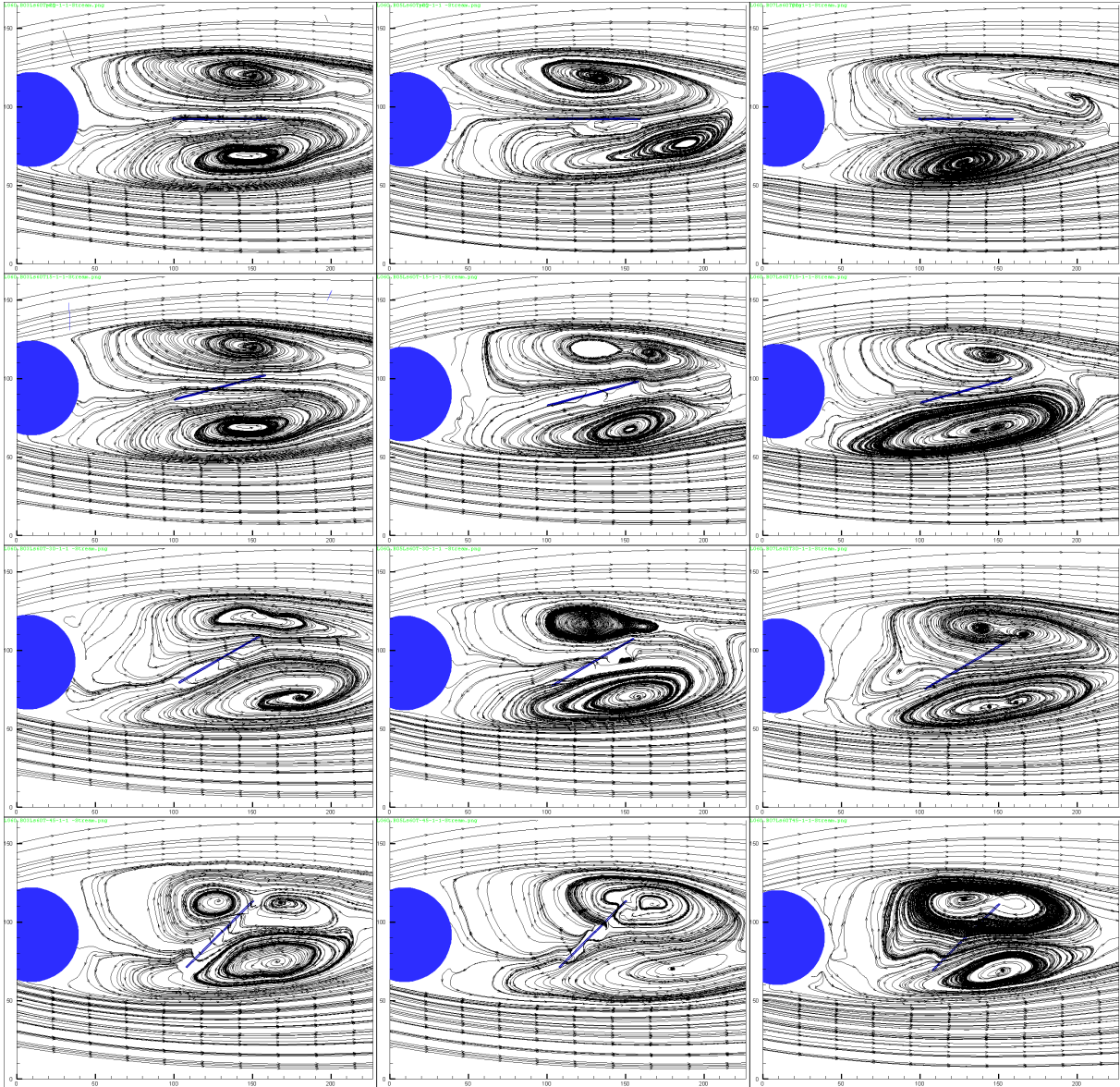


**Şekil 24**. Tüm test durumları için yakın iz bölgesinde akış çizgileri

**Şekil 25**. Θ=0° ve Θ=15° açı yönelimlerine sahip farklı geçirgenlik değerlerindeki plakalar için silindir ardıl bölgesindeki 0.5≤x/D<1.5 kesitlerinde oluşan TKE profilleri.
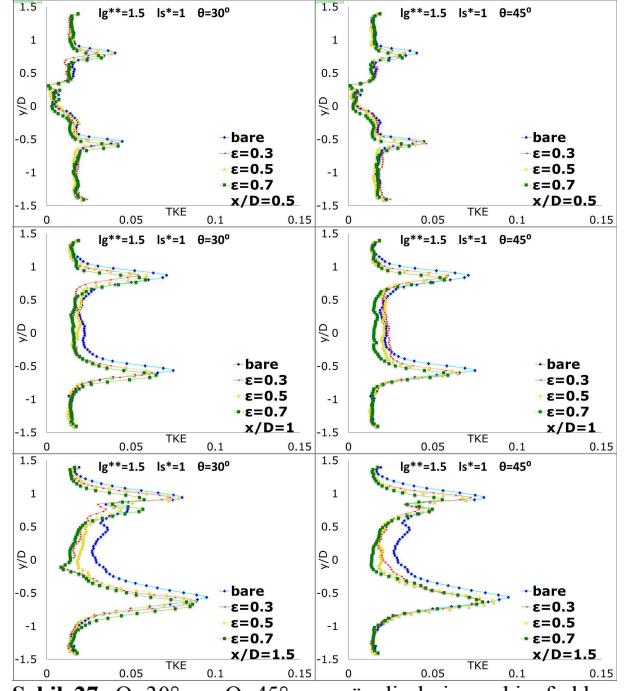


**Şekil 27**. Θ=30° ve Θ=45° açı yönelimlerine sahip farklı geçirgenlik değerlerindeki plakalar için silindir ardıl bölgesindeki 0.5≤x/D<1.5 kesitlerinde oluşan TKE profilleri.
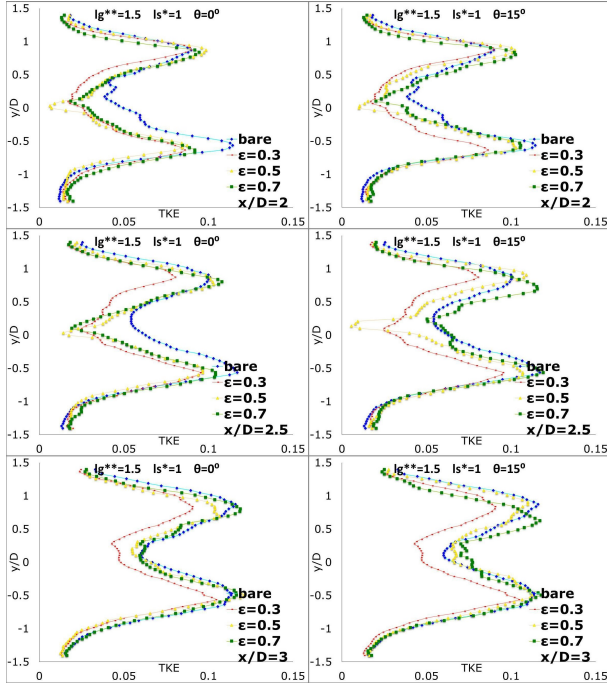


**Şekil 26**. Θ=0° ve Θ=15° açı yönelimlerine sahip farklı geçirgenlik değerlerindeki plakalar için silindir ardıl bölgesindeki 2≤x/D≤3 kesitlerinde oluşan TKE profilleri.
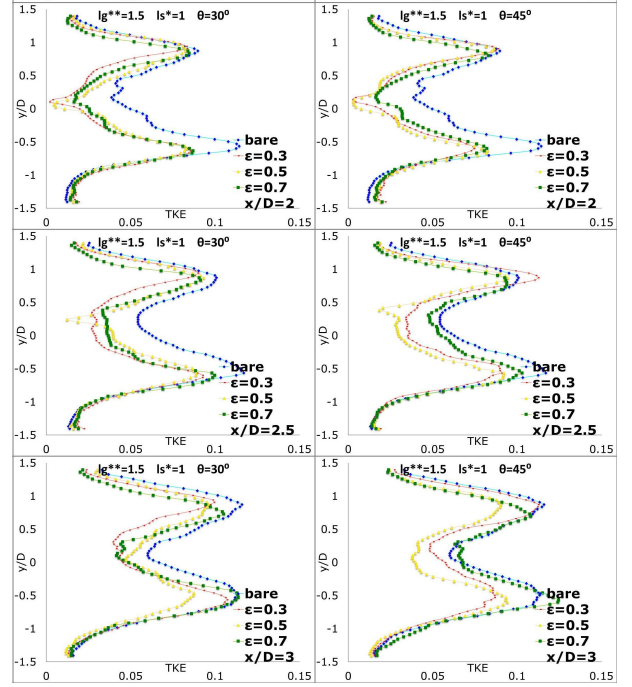


**Şekil 28**. Θ=30° ve Θ=45° açı yönelimlerine sahip farklı geçirgenlik değerlerindeki plakalar için silindir ardıl bölgesindeki 2≤x/D≤3 kesitlerinde oluşan TKE profilleri.

**Şekil 29** tüm açısal yönelimler ve tüm geçirgenlik değerleri için türbülans kinetik enerjisinin ulaştığı en büyük değerde, plakasız silindire göre ne kadar düşüş olduğunu göstermektedir. Oluşan en büyük TKE değerleri, $\varepsilon = 0.3$ geçirgenlik değeri ve 0°, 15°, 30° ve 45° açısal plaka yönelimleri için sırasıyla %16, %20, %14 ve %20 oranlarında düşüş göstermiştir. $\varepsilon = 0.3$ Geçirgenlikli ayırıcı plaka, 30° açısal yönelim haricinde tüm diğer ayırıcı plakalar göre daha iyi sonuç vermiştir.

TKE'nin en büyük konuma ulaştığı noktalar ise 0° ve 30° açısal yönelimler için %2 ve %4 oranlarında silindire doğru yaklaşmıştır (**Şekil 30**). Oluşan en büyük TKE değerleri, $\varepsilon = 0.5$ geçirgenlik değeri ve 0°, 15°, 30° ve 45° açısal plaka yönelimleri için sırasıyla %5, %13, %25 ve %18 oranlarında düşüş göstermiştir. TKE'nin en büyük konuma ulaştığı noktalar ise 0°, 15°, 30° ve 45° açısal yönelimler için %9, %2, %6 ve %3 oranlarında silindire doğru yaklaşmıştır. Oluşan en büyük TKE değerleri, $\varepsilon = 0.7$ geçirgenlik değeri ve 0°,

15°, 30° ve 45° açısal plaka yönelimleri için sırasıyla %12, %2, %20 ve %16 oranlarında düşüş göstermiştir. TKE'nin en büyük konuma ulaştığı noktalar ise 0°, 15°, 30° ve 45°'lik açısal yönelimler için %2, %4, %11 ve %0 oranlarında silindire doğru yaklaşmıştır.
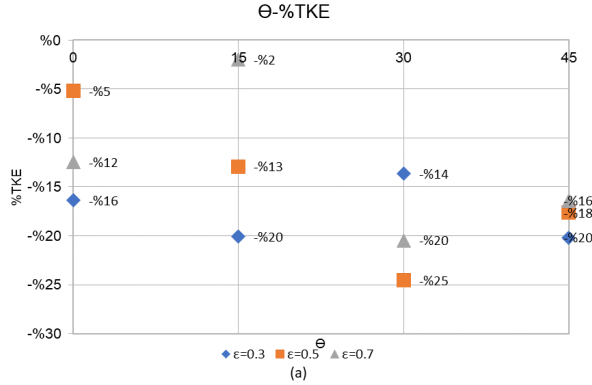


**Şekil 29**. Farklı geçirgenlikteki plakalar için plaka yöneliminin en büyük TKE değerine etkisinin, plakasız silindire göre mukayesesi
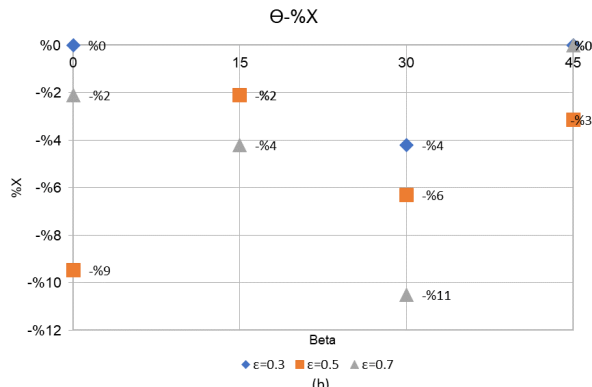


**Şekil 30**. Farklı geçirgenlikteki plakalar için plaka yöneliminin en büyük TKE değerine oluştuğu konuma etkisinin, plakasız silindire göre mukayesesi

## SONUÇ

Farklı gözeneklere sahip ayırıcı plakaların, çıplak bir silindirin iz bölgesindeki akış yapılarına etkisini belirlemek için TKE tepe değerleri ve bu değerlerin oluşum noktaları karşılaştırılmıştır. Dört farklı ayırıcı plaka açısı değeri (θ =0°; 15°; 30°; 45°) ve üç farklı gözeneklilik değeri (ε=0.3; 0.5; 0.7) incelenmiş ve ayırıcı plaka uzunluğu (ls*) ve ayırıcı plaka orta noktası ile silindir arasındaki boşluk (lg**) deneyler boyunca ls*=1 ve lg**=1.5 olarak sabit tutulmuştur. PIV ölçümlerinden elde edilen sonuçlar şu şekildedir:

- Ayırıcı plakanın geçirgenliği ve açısal konumu girdap dökülmesini azaltmak için etkili değişkenlerdir.
- Plakalar döndürüldüğünde, akışa paralel kesit azalmakta, bu da sınır katmanları arasındaki etkileşimi arttırmaktadır.
- Geçirgen ayırıcı plakalar, silindir etrafındaki akışta oluşan sınır katmanlarının etkileşimini engellediğinden, sınır katmanlarının etkileşiminin

arttığı art izi akış bölgelerinde geçirgen ayırıcı plakaların etkisi artmaktadır. Böylece, dalgalanmalar azalmakta ve silindirin aşağı yönünde daha stabilize bir iz akışı meydana gelmektedir.

- Ayırıcı plaka açısının artmasıyla çevrinti oluşumunun geciktiği gözlenmiştir. ε =0.5 ve θ=30º derece için akış kontrolü sağlanır. TKE'nin tepe büyüklüğünün konumu %6 oranında silindir merkezine yaklaşmış, TKE'nin tepe büyüklüğü %25'e kadar azaltılmıştır. Aynı açı ve geçirgenlik değeri için Reynolds kayma gerilmesi %28 oranında azalmıştır. Bir başka akış kontrol noktası ise ε =0.3 ve θ=15º derece için sağlanmıştır. Bu açı ve geçirgenlik değerleri için TKE'nin ulaştığı en yüksek değer %20 oranında, Reynolds kayma gerilmesinin tepe değeri ise %31 oranında azalmıştır.

Türbülans istatistiklerindeki belirli bir azalma (TKE, |u'u'|, |v'v'| ve |u'v'|), kesme tabakaları arasındaki etkileşimin delikli ayırıcı plaka tarafından zayıflatıldığını gösterir. Bu nedenle, çevrinti saçılım kontrolünün ayırıcı plakalar vasıtasıyla sağlandığı sonucuna varılabilir. Bu araştırmada ayırıcı plaka açısının etkisi ve plaka geçirgenliğinin etkisi açıkça gözlemlenmiştir.

## İSİMLENDİRME

D       Silindir çapı [m]

$\theta$       Ayırıcı plakanın akış yönüyle yaptığı açı

$\varepsilon$       Ayırıcı plaka geçirgenliği

Re       Reynolds sayısı $[Re = \frac{U_\infty \cdot D}{\vartheta}]$

ls*       Boyutsuzlaştırılmış ayırıcı plaka uzunluğu

lg*       Boyutsuzlaştırılmış ayırıcı plaka silindir arası mesafe

lg**       Boyutsuzlaştırılmış ayırıcı plaka dönme ekseni ile silindir arası mesafe

U       Akış hızı [m/s]

$\vartheta$       Akışkanın kinematik viskozitesi [m²/s]

$\rho$       Akışkan yoğunluğu [kg/m³]

u'u'       Akış yönünde Reynolds normal gerilmesi

u'v'       Reynolds kayma gerilmesi

Vrms       akışa dik yöndeki çevrinti yoğunluğu

v'v'       akışa dik yönde Reynolds normal gerilmesi

TKE       Türbülans kinetik enerjisi $[TKE = \frac{3}{4}\frac{\overline{(u')^2}+\overline{(v')^2}}{U^2}]$

Urms       Akış yönünde çevrinti yoğunluğu

$u'$       Akış yönündeki hız değişimi

$v'$       Akış yönüne dik yöndeki hız değişimi

g       Yerçekimi ivmesi [m/s²]

hw       Serbest su yüksekliği [m]

fr       Froude sayısı $[Fr = \frac{U_\infty \cdot}{\sqrt{(g.h_w)}}]$

**KAYNAKÇA**

Adrian, Ronald J. 1991. «Particle-Imaging Techniques for Experimental Fluid Mechanics.» *Annual Review of Fluid Mechanics*, 261-304. doi:https://doi.org/10.1146/annurev.fl.23.010191.001401.

Bao, Y., ve J. Tao. 2013. «The passive control of wake flow behind a circular cylinder by parallel dual plates.» *Journal of Fluids and Structures*, 201-219. doi:https://doi.org/10.1016/j.jfluidstructs.2012.11.002.

Blevins, R. D. 1985. «The effect of sound on vortex shedding from cylinders.» *J. of Fluid Mech.*, 217-237. doi:https://doi.org/10.1017/S0022112085002890.

Cardell, G. S. 1993. *Flow Past a Circular Cylinder with a Permeable Wake Splitter Plate. Dissertation (Ph.D.)*. California Institute of Technology. doi:10.7907/25C5-1150.

Chen, WL., H Li, ve H. Hu. 2014. «An experimental study on a suction flow control method to reduce the unsteadiness of the wind loads acting on a circular cylinder.» doi:https://doi.org/10.1007/s00348-014-1707-7.

Favier, J., A. Dauptain, D. Basso, ve A. Bottaro. 2009. «Passive separation control using a self-adaptive hairy coating.» *J Fluid Mech*, 451-483. doi:10.1017/S0022112009006119.

Gao, Dong-Lai, Guan-Bin Chen, Ye-Wei Huang, Wen-Li Chen, ve Hui Li. 2020. «Flow characteristics of a fixed circular cylinder with an upstream splitter plate: On the plate-length sensitivity.» *Experimental Thermal and Fluid Science*. doi:https://doi.org/10.1016/j.expthermflusci.2020.110135.

Ghadimi, Parviz, Saman Kermani, Sabra Razughi, ve Rahim Zamanian. 2013. «Aerodynamic and Acoustical Analysis of Flow around a Circular Cylinder in a Channel and Parametric Study on the Effects of a Splitter Plate on the Generated Vibration and Noise.» *Applied Mathematics and Physics*, 1-5. doi:https://doi.org/10.12691/amp-1-1-1.

Gozmen, Bengi, Huseyin Akilli, and Besir Sahin. 2013. "Passive control of circular cylinder wake in shallow flow." *Measurement* (46): 1125-1136. doi:http://dx.doi.org/10.1016/j.measurement.2012.11.008.

Guilmineau, P. Q. E. 2002. «A numerical simulation of vortex shedding from an oscillating circular cylinder.» *J. Fluid Struct.*, 773-794. doi:https://doi.org/10.1006/jfls.2002.0449.

Huseyin Akilli, Besir Sahin, N. Filiz Tumen,. 2005. «Suppression of vortex shedding of circular cylinder in shallow water by a splitter plate.» *Flow Measurement and Instrumentation*, 211-219. doi:https://doi.org/10.1016/j.flowmeasinst.2005.04.004.

Jong-Yeon Hwang, Kyung-Soo Yang, Seung-Han Sun. 2003. «Reduction of flow-induced forces on a circular cylinder using a detached splitter plate.» *Physics of Fluids*, 1 8: 2433-2436. doi:https://doi.org/10.1063/1.1583733.

Kwon, K., & Choi, H. 1996. «Control of laminar vortex shedding behind a circular cylinder using splitter plates.» *Physics of Fluids*, 479-486. doi:https://doi.org/10.1063/1.868801.

Lecordier, J. C., L. Hamma, ve P. Parantheon. 1991. «The control vortex shedding behind heated cylinders at low Reynolds numbers.» *Exp. in Fluids*, 224-229. doi:https://doi.org/10.1007/BF00190392.

Lee, Jinmo, ve Donghyun You. 2013. «Study of vortex-shedding-induced vibration of a flexible splitter plate behind a cylinder.» *Physics of Fluids*. doi:https://doi.org/10.1063/1.4819346.

Matsumoto, Masaru, Michio Hashimoto, Tomomi Yagi, Tomoyuki Nakase, ve Kouji Maeta. 2008. «Steady Galloping/Unsteady Galloping And Vortex-Induced Vibration Of Bluff Bodies Associated With Mitigation Of Karman Vortex Shedding.» *BBAA VI International Colloquium on:Bluff Bodies Aerodynamics & Applications*. Milano.

Oruc, V., M. Akar, Akilli, H. A., ve B. Sahin. 2013. «Suppression of asymmetric flow behavior downstream of two side-by-side circular cylinders with a splitter plate in shallow water.» *Measurement: Journal of the International Measurement Confederation*, 442-455. doi:https://doi.org/10.1016/j.measurement.2012.07.020.

Ozgoren, Muammer. 2006. «Flow structure in the downstream of square and circular cylinders.» *Flow Measurement and Instrumentation*, 225-235. doi:https://doi.org/10.1016/j.flowmeasinst.2005.11.005.

Ozgoren, Muammer, Engin Pinar, Besir Sahin, ve Huseyin Akilli. 2011. «Comparison of flow structures in the downstream region of a cylinder and sphere.» *International Journal of Heat and Fluid Flow*, 1138-1146. doi:https://doi.org/10.1016/j.ijheatfluidflow.2011.08.003.

Ozkan, G.M., E Firat, ve H. Akilli. 2017. «Control of vortex shedding using a screen attached on the separation point of a circular cylinder and its effect on

drag.» *J. Fluids Eng. Transactions ASME*, July. doi:https://doi.org/10.1115/1.4036186.

Pinar, Engin, Gokturk M. Ozkan, Tahir Durhasan, Muhammed M. Aksoy, ve Besir Sahin Huseyin Akilli. 2015. «Flow structure around perforated cylinders in shallow water.» *Journal of Fluids and Structures*, 52-63.
doi:https://doi.org/10.1016/j.jfluidstructs.2015.01.017.

Raffel, M., Christian Willert, Steve Wereley, ve Juergen. Kompenhans. 2007. *Particle Image Velocimetry*. Springer.

Reza-zadeh, S. 2013. «Investigation of fluid flow around a cylinder with EHD actuation on inclined plates behind the cylinder.» *In Proceedings of the 2013 International Conference on Applied Mathematics and Computational Methods in Engineering.*, 212-217.

Roshko, A. 1954. «On the drag and shedding frequency of two-dimensional bluff bodies.» *NACA Technical Note 3169*, 1-30. doi:https://doi.org/10.1.1.477.979.

Roshko, Anatol. 1952. *On the development of turbulent wakes from vortex streets. Dissertation (Ph.D.),*. California Institute of Technology. doi:10.7907/4WDN-9807.

Sahin, Serdar, Tahir Durhasan, Engin Pinar, ve Huseyin Akilli. 2021. «Experimental study on passive flow control of circular cylinder via perforated splitter plate.» *Wind and Structures*, 613-621. doi:10.12989/WAS.2021.32.6.613.

Tabatabaeian, S., Mirzaei, M., Sadighzadeh, A., Damideh, V., & Shadaram, A. 2015. «Experimental Study of the Flow Field around a Circular Cylinder Using Plasma Actuators.» *J. Applied Fluid Mechanics*, 291-299.
doi:https://doi.org/10.18869/acadpub.jafm.67.221.21459.

Teksin, S., ve S. Yayla. 2016. «Effects of Flexible Splitter Plate in the Wake of a Cylindrical Body.» *Journal of Applied Fluid Mechanics*, 3053-3059. doi:10.29252/jafm.09.06.25564.

Weier, T., G. Gerbeth, G. Mutschke, E. Platacis, ve O. Lielausis. 1998. «Experiments on cylinder wake stabilization in an electrolyte solution by means of electromagnetic forced localized on the cylinder surface.» *Exp. Therm Fluid Sci.*, 84-91. doi:https://doi.org/10.1016/S0894-1777(97)10008-5.

Westerweel, J. 1993. *Digital particle image velocimetry: Theory and application, PhD Thessis.* Delft University Press.

Xiao, Q., Sun, K., Liu, H., & Hu, J. 2011. «Computational study on near wake interaction between undulation body and a D-section cylinder.»

*Ocean Engineering*, 3: 673-683. doi:https://doi.org/10.1016/j.oceaneng.2010.12.017.

Zhou, X., J. Wang, ve Y. Hu. 2019. «Experimental investigation on the flow around a circular cylinder with upstream splitter plate.» *J Vis (Tokyo)*, 683-695. doi:10.1007/s12650-019-00560-x.

# OUTDOOR DEGRADATION ANALYSES OF SIX DIFFERENT AGED PHOTOVOLTAIC MODULE TECHNOLOGIES UNDER THE ARID-STEPPE CLIMATE CONDITION

**Zeynep CANTÜRK[1,2,*], Talat ÖZDEN[3,2], Bulent G. AKINOGLU[1,2,4]**

[1] Department of Physics, Middle East Technical University, Ankara 06800, Turkey
[2] ODTU-GÜNAM, Middle East Technical University, Ankara 06800, Turkey
[3] Department of Electrical and Electronics Engineering, Gumuşhane University, Gumuşhane 29100, Turkey
[4] Earth System Science Program, Middle East Technical University, Ankara 06531, Turkey
0000-0003-2833-1832, 0000-0002-0781-2904, 0000-0003-1987-6937

**Abstract:** Outdoor tests of photovoltaics module are crucial both for marketing and for research and technological developments. The electric generation performance and their degradation rates and lifetime are also related to different climatic conditions of the regions. In this work, the outdoor tests are carried out for six different photovoltaic (PV) modules under Arid-steppe Climate condition of Ankara, Türkiye. Their degradation rates are calculated by using linear regression (LR) and year on year (YOY) methods. The comparison between LR and YOY are carried out and with the other performed studies of different regions of world. In addition, it is investigated that how effective the climatic conditions on daily degradation rates. The results obtained are as follows: Mono-Si and Hetero-junction Silicon (HIT) cell modules degradation rates of 0.71/1.56 %/year and 0.84 %/year are respectively obtained by LR method and 0.57/0.90 %/year and 0.85%/year are respectively by YOY method. The degradation rates for Cupper Indium Selenide (CIS), Cupper Indium Gallium Selenide (CIGS) and microcrystalline Silicon/Amorphous Silicon (μc-Si/a-Si) modules have 1.73/1.49 %/year, 11.55/9.52 %/year and 1.48 %/year for LR method and 1.28/1.12 %/year, 9.94/9.53 %/year and 0.99 %/year for YOY method are obtained respectively. It is also obtained for the Polycrystalline Silicon Modules as 1.20/1.86 %/year degradation rates by LR method and 0.79/1.88 %/year degradation rates by YOY method.
**Keywords:** Photovoltaic modules, Long-term outdoor testing, Degradation rates, Linear regression degradation method, year on year degradation method

## INTRODUCTION

Utilization of renewable energy and especially solar energy has grown worldwide over the past decade as governments consider the increasing global warming and the supply of fossil fuels is declining (Grübler, Jefferson, and Nakićenović 1996). The Solar PV modules are one of the most important systems of generating electricity by renewable energy. Their properties are related with the PV module performances of electrical energy generation and also to their length of life time. Environmental and climate conditions are also effective for the lifetime of PV modules. Consequently, the degradation rates of PV modules are important property to identify their life time to be supplied for PV modules by the manufacturers, which is very important to make economic plan for solar energy power plant (Annigoni et al. 2019; Tsanakas, Ha, and Buerhop 2016) (Micheli et al. 2022).

Degradation rates of PV modules can be calculated by two different steps to reach overall degradation. The first one includes only PV module degradation using the measures of the energy generated by the module. The second is the degradation coming from system equipment loss such as the maximum power point tracking (MPPT),

cables and/or invertor (Ozden et al. 2015). The overall degradation rate is together with the system and PV modules degradations.

Ishii et al (Ishii, Takashima, and Otani 2011) tested 14 different modules under moderate climate conditions for 4 years. The results of degradation rates are between 0.64 %/year and 0.92 %/year for mono-crystalline silicon modules while 0.4 %/year for poly-crystalline silicon modules within the same time interval. Besides, the obtained degradation rate for amorphous silicon modules is higher than 1.45 %/year.

Makrides et al (Makrides et al. 2010) studied on 11 solar modules under the Mediterranean climate in Cyprus region for the period June 2006 – June 2009 including 5 kind modules which are mono-crystalline, poly-crystalline, amorphous silicon, Cadmium Telluride (CdTe), and Cupper Indium Gallium Selenide (CIGS). They found that the first-year degradation rates are in range 2.12 %/year and 4.73 %/year, for mono-crystalline modules, changes between 1.47 %/year and 2.40 %/year for poly-crystalline, 0.26 %/year for CIGS modules, 0.32

%/year for CdTe Modules and 0.23 %/year for amorphous silicon modules.

Bogdanski et al. (Bogdanski et al. 2010) studied on the influence of the climate conditions on the solar modules in four different regions. The climates are warm moderate climate (Cologne, Germany), tropical climate (Serpong, Indonesia), cold high mountain climate (Zugspitze, Germany) and arid climatic conditions (Sede Boqer, Israel). They outline that the climate is very effective on the degradation rates. The highest degradation rate belongs cold high mountain climate due to high snowfall and wind stress. Because of high temperature and irradiation, in the desert and tropical climate, higher degradation is observed. In Israel and Indonesia, the contamination with sand were observed and this situation results in high decrease of the generated energy. All modules analyzed in the all-climate condition showed less than 1 %/year degradation although the mountain climate data.

Quansah et al. (Quansah and Adaramola 2018) studied using 29 crystalline solar modules at six different locations in Ghana. They found that the degradation rates in a range from 0.8 %/year to 6.5 %/year. In addition to I-V investigations, they observed some mechanical degradation such as broken glass, delimitation, yellowing encapsulates materials and bubbles.

Savvakis et al. (Savvakis and Tsoutsos 2015) work out a grid-connected system having 2.18 kWp micro crystalline and based amorphous silicon (μc-Si / a-Si) thin-film modules. The systems located in island of Crete in Mediterranean for two years and the authors used monthly average data. Their study included the module temperature to clarify the outdoor PV operating temperatures. This group found the performance ratio of 85.1 % with efficiency of about 7.25 %.

Tabatabaei et al. (Tabatabaei, Formolo, and Treur 2017) studied on the degradation rates of 23 PV modules installed on a roof of a family house in Netherlands. The time interval of the data obtained is from May 2013 to January 2017 and PV panels installed in the same location and with the same orientation are compared with respect to each other. They set the data to Seasonal and Trend decomposition using LOESS technique. Locally estimated scatterplot smoothing (LOESS) is a nonparametric method. This method is used for smoothing a series of data where no assumptions have been made about underlying structure of the data set. According to this study, panels at the same location and orientation have the same degradation rates and the average degradation rate of modules in this system is 0.92 %/year.

Limmanee et al. (Limmanee et al. 2017) presented a study about degradation rates analysis of 73 different PV modules of 4 different module types: multi c-Si, heterojunction Si, thin film Si and CIGS on Thailand Science Park with 4 years data from 2012 to 2016. According to this study, performance rates of thin film Si

modules are having low efficiencies and they degraded seriously. Except that these modules, the degradation rates of other modules are in a range between 0.3 %/year and 1.9 %/year.

Solís-Alemán et al. (Solís-Alemán et al. 2019) in Spain studied on degradation rates of four different thin film solar module; a-Si, a-Si/μc-Si, CdTe and CIGS with a five-and-a-half-year and a six-and-a-half-year periods, respectively) by using classical seasonal decomposition technics and year-on-year statistical technics and they found ~1.3 %/year of average degradation rates.

Singh et al. (Singh et al. 2020) presented a study in 2020 about field analysis of three different PV system technologies. Analysis included monthly average performance rates, weather corrected performance rate series resistance and effective peak power of HIT, poly-crystalline and a-Si solar modules of three years data. Also, degradation rates were calculated by using three methods which were linear regression, classical seasonal decomposition (CSD), and locally weighted scatterplot smoothing (LOESS) via performance rate and normalized efficiency. The degradation rates were found as 1.24 %/year, 1.16 %/year and 1.16 %/year for a-Si modules, 0.14 %/year, 0.56 %/year and 0.11 %/year for HIT modules and 1.50 %/year, 0.82 %/year and 1.46 %/year for poly-Si modules using linear regression, CSD and LOESS analysis respectively. The average efficiency is found to be 5.17 % for a-Si, 15.40 % for HIT and 10.78% of poly-Si modules.

Frick et al. (Frick et al. 2020), at 2020, presented a unified methodology to calculate degradation rate of PV systems accurately and prove this calculation is location dependent. The PV systems were installed at different climatic locations by using different c-Si PV modules to compare long term degradation rates. After 7 years, the degradation rate results showed convergence between time series analytical methods applied and degradation results from the indoor standardized procedures. Hence the multi crystalline silicon systems at the warm climatic locations had more degradation rate in comparison with the system in moderate climatic location. They obtained in between 0.1%/year to 0.4%/year degradation rates of the modules.

Dhimish at al. (Dhimish and Alrashidi 2020) presented a study on degradation rates using 10 years of data (from 2008 to 2017) in U.K. and Australia. The degradation rates are changing from 1.05 %/year to 1.16 %/year and from 1.35 %/year to 1.46 %/year for the system in the U.K and Australia respectively. In Australia, because of rapidly changing ambient temperature and nonuniform irradiance, multiple faulty bypass diodes were found while, in U.K., damaged diodes were not observed. Also, performance rate of PV systems was calculated as 88.81 % and 86.35 % in U.K and Australia, respectively.

Dag at al.(Dag and Buker 2020), in 2020, studied on the degradation rates and performance characteristic of poly-crystalline and hetero-junction with intrinsic thin layer PV modules for half and two years. They installed the system on a roof, in the region of Central Anatolia

(Konya). In this study, they consider also the temperature, and the calculation of degradation rates were carried out by corrected performance rates. The results are lower than 0.1 %/year for thin film and within a range of 0.67 %/year and 0.83 %/year poly- crystalline. Kurtz and Jordan from National Renewable Energy Laboratory (NREL) (Jordan and Kurtz 2013), made an extensive analysis of degradation rates of PV modules and systems by using the results of outdoor measurements of five different types of modules and systems. To analyze degradation rates of PV modules, 2000 reported degradation rates in last 40 years before 2012 were worked out. The gaining value of average degradation rate for a-Si PV systems installed before the year 2000 was around 1.8 %/year, and after the year 2000 the average rate was about 1 %/year. For CdTe thin film PV systems, however, their reported values of average degradation rates were about 2 %/year for pre-2000 and about 0.6 %/year for post-2000. Finally, for Mono-Si arrays, the reported values were 0.7 %/year and 0.6 %/year for pre- and post-2000, respectively.

Daher et al. (Hassan Daher, Gaillard, and Ménézo 2022) presented a study on performance degradation of solar PV power plant in Djibouti whose climate is desert maritime over five years operation and the degradation rates was considered using Photovoltaics for Utility Scale Applications (PVUSA) regression analysis and PR analysis based on 1-min intervals data. The degradation rates were found 0.96 ± 0.37%/year and 1.01 ± 0.38%/year respectively for the DC and the AC parts of the PV solar system. For PVUSA under PTC conditions: 0.057 ± 0.68%/year for DC power and 0.085 ±

same climatic conditions of central Anatolia were analyzed with 44 months data. As a result of this study, the degradation rates are 0.4%/year, 1.88%/year and 10.60 %/year for Mono-Si, a-Si and CdTe thin film modules, respectively. The yearly average efficiencies of these modules are 11.86%, 6.49% and 5.30%, respectively (Ozden et al. 2017).

In this paper, 10 modules are performance tested in Middle Anatolia climate conditions for nine years in six different module groups, which are cupper indium selenide (CIS-1 & 2), cupper indium gallium selenide (CIGS-1 & 2), tandem cell (μc-Si / a-Si), mono-crystalline (Mono-Si-1 & 2) and heterojunction with intrinsic thin layer (HIT), poly- crystalline (Poly-Si-1 & 2), Their degradation rates are calculated by using Year-On-Year (YOY) Method and Linear Regression (LR). The results obtained are discussed and these two methods are compared to each other and to some other studies in different regions by the researchers.

## MATERIAL AND METHODS

### Test Site

This study includes the outdoor testing in middle Anatolia, Ankara-Turkey (latitude 39.9° N, longitude 32.8° E), nine years data obtained from solar modules on the roof of METU Physics Building; Figure 1. The climate of Ankara is cold semi-arid (Hasselbrink et al. 2013; Köppen, Volken, and Brönnimann 2011; Peel, Finlayson, and McMahon 2007). The average monthly



**Figure 1**: METU-GUNAM Outdoor Test Facilities (39.894204, 32.781977)

0.68%/year for AC power. Also Daher et al. (Daher et al. 2023)release a study at 2023 given an information about degradation rates of different area for different module technologies. According to this study, the degradation rates are in range between 0.03 % /year (Singapore, c-Si) and 6.5 %/year (Ghana, m-Si and p-Si). In addition to these studies, at the same location with this study Özden at al. (Ozden et al. 2015) studied on two system arrays with an μc-Si/a-Si and a CdTe thin film arrays and they found that the degradation rates are 0.39 %/year and 6.98%/year. Özden at al. (Ozden, Akinoglu, and Turan 2017) also studied the PV system performances and analyzed the degradation rates and performance ratios for three years. The systems consist of a mono-Si, an a-Si thin film and a CdTe thin film array. The degradation rates of these systems were 0.40 %/year, 1.88 %/year and 10.60 %/year for mono-Si, a-Si thin film and CdTe systems, respectively. Three different systems under the

temperature is about 12 ºC with maximum and minimum values of around 41 ºC and -25 ºC for the months July and August, and January, respectively. In the recent 90 years' average value of precipitation depth are 387 mm The modules have been connected separately to a multi-tracer that is a testing system of it. This system continuously measures the performances of modules, and the modules are individually controlled and operated at their peak power during daylight hours. The output data and several input data (like ambient temperature, tilted and horizontal irradiance and module temperatures) were automatically measured and logged in every 10 minutes.

### Test Modules

The modules are in operation for nine years within the time interval of 2012-2021. They are connected to a data logging system which extracts the energy at maximum

**Table 1** Tested PV Modules Specifications

| Module Type | $P_{MAX}$ [W] | $V_{OC}$ [V] | $I_{SC}$ [A] | $V_{MPP}$ [V] | $I_{MPP}$ [A] | Area [$m^2$] | Testing Period Started | Testing Period Ended |
|---|---|---|---|---|---|---|---|---|
| CIS 1 | 130 | 59.5 | 3.28 | 44.9 | 2.90 | 1.05 | Oct, 2014 | Jun, 2021 |
| CIS 2 | 130 | 59.5 | 3.28 | 44.9 | 2.90 | 1.05 | Oct, 2014 | Jun, 2021 |
| CIGS 1 | 75 | 72.36 | 1.6 | 54.02 | 1.4 | 0.70 | Jan, 2013 | Sep, 2018 |
| CIGS 2 | 75.5 | 74.10 | 1.6 | 56.71 | 1.3 | 0.70 | Jun, 2012 | Sep, 2018 |
| µc-Si / a-Si | 128 | 59.8 | 3.45 | 45.4 | 2.82 | 1.40 | Apr, 2012 | Jun, 2021 |
| Mono-Si 1 | 160 | 43.7 | 5.06 | 35.3 | 4.58 | 1.28 | Aug, 2012 | Jun, 2021 |
| Mono-Si 2 | 160 | 43.7 | 5.06 | 35.3 | 4.58 | 1.28 | Apr, 2012 | Jun, 2021 |
| HIT | 230 | 42.3 | 7.22 | 34.3 | 6.71 | 1.39 | Apr, 2012 | continue |
| Poly-Si 1 | 240 | 36.6 | 8.70 | 30.2 | 7.96 | 1.63 | Apr, 2012 | Jun, 2021 |
| Poly-Si 2 | 130 | 21.7 | 8.18 | 17.8 | 7.30 | 1.02 | May, 2012 | Jun, 2021 |

power point (MPP) with a properly adjustable load. The elements of our testing system can be seen in Figure 1 and the specifications of all types of ten tested modules are tabulated in Table 1.

**Data**

For the years 2012-2016, we used the data taken by Türkiye State Meteorological Service (TSMS) where the station is located at some 20 km away from our testing site of PV modules (Anon n.d.). After that time, for the years 2016 to 2021, plane-of-modules irradiance was measured by a Kipp&Zonnen high precision secondary standard Pyranometer. The accuracy of the procedure for using data from the first four years was presented by Ozden (Akinoglu, Karaveli, and Özden 2017; Ozden et al. 2017) and Akinoglu (Akinoglu et al. 2017) The data we obtained from TSMS was horizontal global solar irradiation. To estimate the hourly global solar irradiation on tilted PV modules the anisotropic model of HDKR (Reindl, Beckman, and Duffie 1990) and later modified by Reindl et al. (Reindl et al. 1990)), entitled by in the book by Duffie and Beckman (Duffie and Beckman 2013). The equation used is given below:

$$I_t = (I_b + I_d A_i)_b + I_d(1 - A_i)\left(\frac{1+cos\beta}{2}\right)\left[1 + f sin^3\left(\frac{\beta}{2}\right)\right] + I\rho_g\left(\frac{1-cos\beta}{2}\right) \quad (1)$$

In this equation, $I_t$ represents the hourly total irradiation incident to the module surface. $I_b$ represents direct beam, $I_d$ represents diffuse radiation from Sun. $\beta$ is the tilt angle of the PV modules, which is between module and horizontal surface and $\rho_g$ is a constant value that represents the coefficient of reflectance of ground. According to Liu et all (Liu and Jordan 1963), the average value of $\rho_g$ is taken as 0.20 for all months during which the ground is free of snow (Ineichen, Guisan, and Perez 1990).

The output, that is the yield of the PV modules, are measured by multi-tracer in every 10-minutes interval.

Because of the failure of some device's due to hard weather conditions, some small amount of data could not be obtained. To overcome this problem, data was normalized and non-computational data filtering is applied. In this calculation, data were filtered if solar irradiation coming to the plane of solar PV module was larger than 50 Watthour/$m^2$. Hence, after this process hourly, daily and monthly yields can be obtained. Also, for monthly calculation, some minor deficiencies were normalized but the greater deficiencies of the data in a month were accepted as "Outliers". The monthly yield data for modules resulted due to the input measured accurately for last one year (from January 2020 to December 2020) is presented in Figure 2. The yields of the modules clearly follow the seasonal variation of the input while also reflects the proper outputs that corresponds to the technology of the module.

**Linear Regression Degradation Methodology**

To calculate the degradation rates, firstly, the performance ratio ($R_p$) of modules are needed. $R_p$ is the ratio of the final energy yield of the solar module ($Y_f$) to the reference yield ($Y_r$), as shown in Eq. 2 (IEC 61724 1998; Ozden et al. 2017) .

$$R_p = \frac{Y_f}{Y_r} = \frac{E_{out}/E_{STC}}{E_{in}/G_{STC}} \quad (2)$$

The first method used for calculating degradation rates is the simple linear regression (LR) method. This method is a simple linear regression analysis applied to the monthly time series of the performance parameter which is the performance ratio (Rp). By using the linear fitting of graphs to time series versus monthly performance ratios data set of each PV module and obtain an equation of the form as shown in the Eq. 3
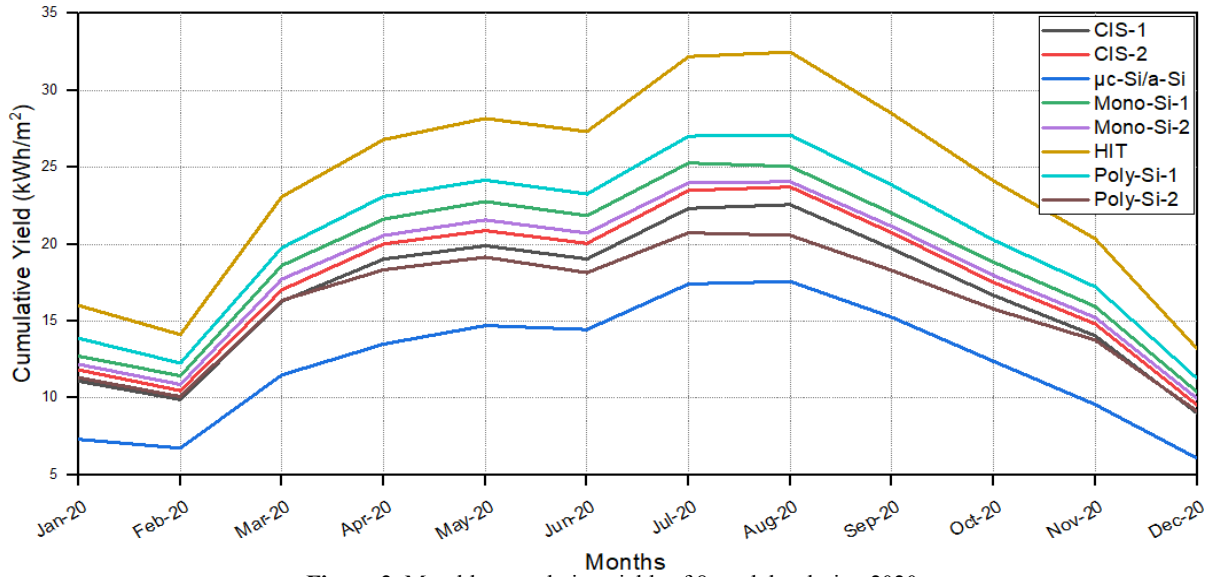
$$y = mx + n \quad (3)$$

**Figure 2**: Monthly cumulative yields of 8 modules during 2020

Thus, the below equation 4, for the percent degradation rate can be expressed using the regression parameters $m$ and $n$ given in Eq. 3. Also, $N$ is the number of the months of outdoor operation.

$$R_d = \left[ \frac{n - y(N)}{n} \times \frac{12}{N} \right] \times 100 \qquad (4)$$

**Year on Year (YOY) Methodology**

The other method used in this study was year-on-year (YOY) degradation method. Firstly, daily performance rates are calculated. Afterwards, daily degradation rates are calculated for each operation time, Eq. 5. At this equation, $j$ represents $j^{th}$ month and $i$ represents $i^{th}$ day and as mentioned in previous section, $R_{p,daily}$ is daily performance ratio and $R_{d,daily}$ is daily degradation rates of modules.

$$R_{d,daily,ji} = \frac{R_{p,daily(j+6)i} - R_{p,daily,(j-6)i}}{R_{p,daily,(j-6)i}} \times 100 \qquad (5)$$

The final annual degradation ratio is accepted as the median value of the distributions of degradations after the frequency of degradations are plotted.

**RESULTS AND DISCUSSION**

**Linear Regression Degradation**

Figure 3 gives the time series of the monthly outdoor performance ratios for the module groups of (a) thin film, (b) monocrystalline and HIT and (c) polycrystalline. The trend lines are also drawn, and the regression equations are presented in the legend boxes. The linear regression expressions are used to obtain degradation rates of the modules as mentioned in section "Linear Regression Degradation Methodology" and with Eqn. (4) (Ozden et al. 2017). We should note again that the efficiencies before April 2016 were computed using the solar

irradiation data taken from TSMS located at around 20 km away from GÜNAM's test facility.

As can be observed from Figure 3-a, CIS-1 & 2 and μc-Si/a-Si modules have similar performance ratios. Also, their degradation rates are close to each other. CIS-1 & 2 have 1.73 %/year and 1.49 %/year respectively while μc-Si/a-Si has 1.48 %/year annual degradation. The performance of the CIGS modules seems rather having manufacturing problem, one started rather with reasonable performance but degrades rapidly (CIGS 1) while the other starts with unexpectedly low performance value (CIGS 2). However, we calculated and presented the degradation rates for CIGS and the results are 11.55 %/year and 9.52 %/year, respectively.

Figure 3-b is the same time series for the two Mono-Si modules and one HIT module. The performance ratios of Mono-Si-1 and HIT modules are too close to each other while the performance rate of Mono-Si-2 module is a little higher than two other modules. On the other hand, the degradation of Mono-Si-2 module is 1.56 %/year and higher than Mono-Si-1 and HIT modules. The annual degradations rates are for Mono-Si and HIT 0.71 %/year and 0.82 %/year respectively. That is, Mono-Si-2 degrades faster than HIT and Mono-Si-1 as shown in the results. In the literature, according to Table-2, HIT modules showed lower degradation (Ozden et al. 2020). Although Mono-Si-1 and Mono-Si-2 modules are the same brand, some processes of making module such as cells, encapsulation material, lamination are different each other. So according to this study, Mono-Si-2 shows higher degradation rate.

As Poly-Si modules are shown at Figure 3-c, at the start of testing, two modules have the same performance ratio. However, the performance of Poly-Si-2 modules decreased faster than Poly-Si-1 in the test duration. Nevertheless, there is not too much difference among the degradation of these two modules. Poly-Si-1 has 1.20 %/year degradations and Poly-Si-2 has 1.86 %/year.
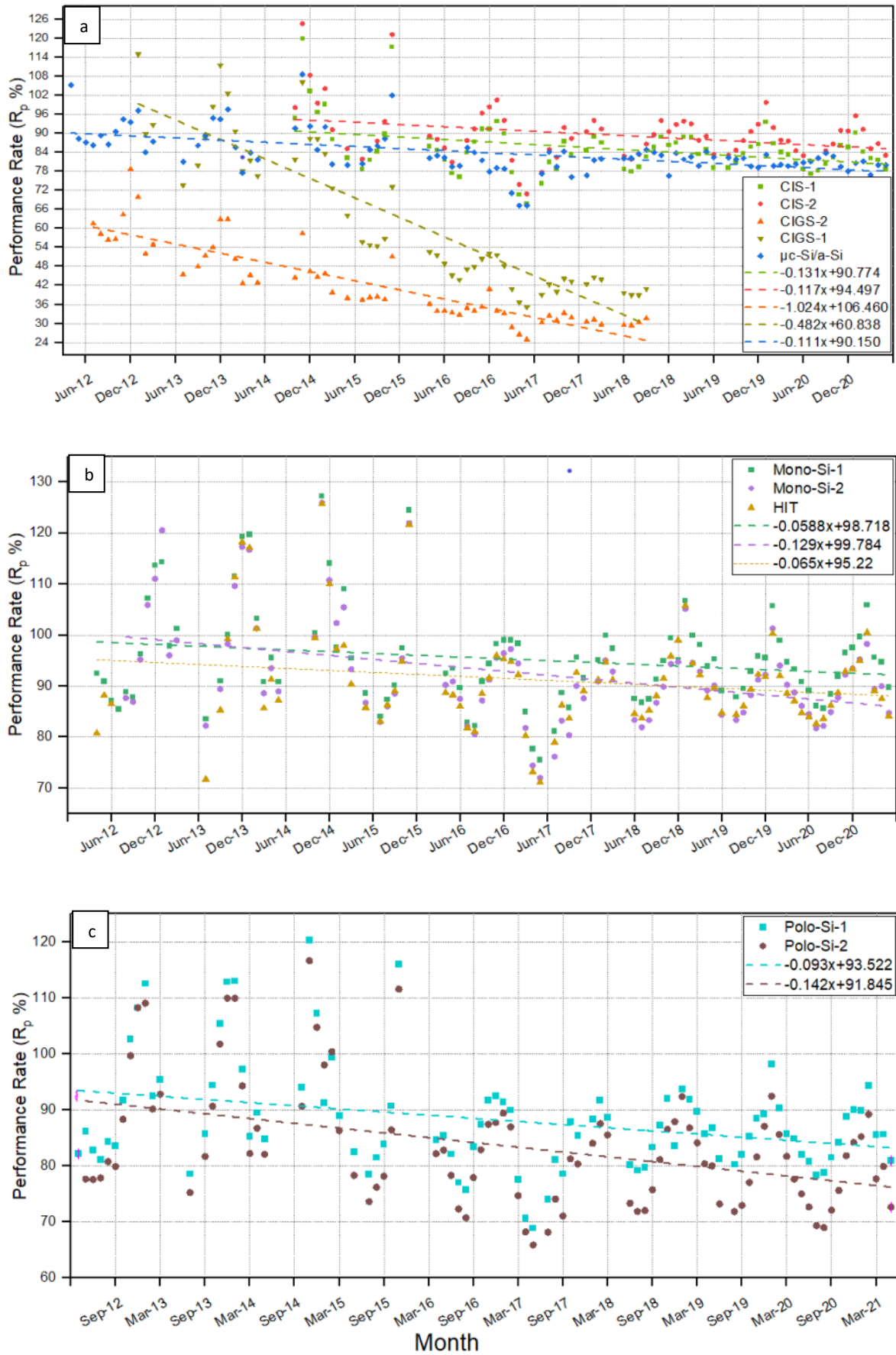
**Figure 3**: Monthly performance ratios of (a) Thin film, (b) Mono-Si and (c) Poly-Si module groups over the nine years
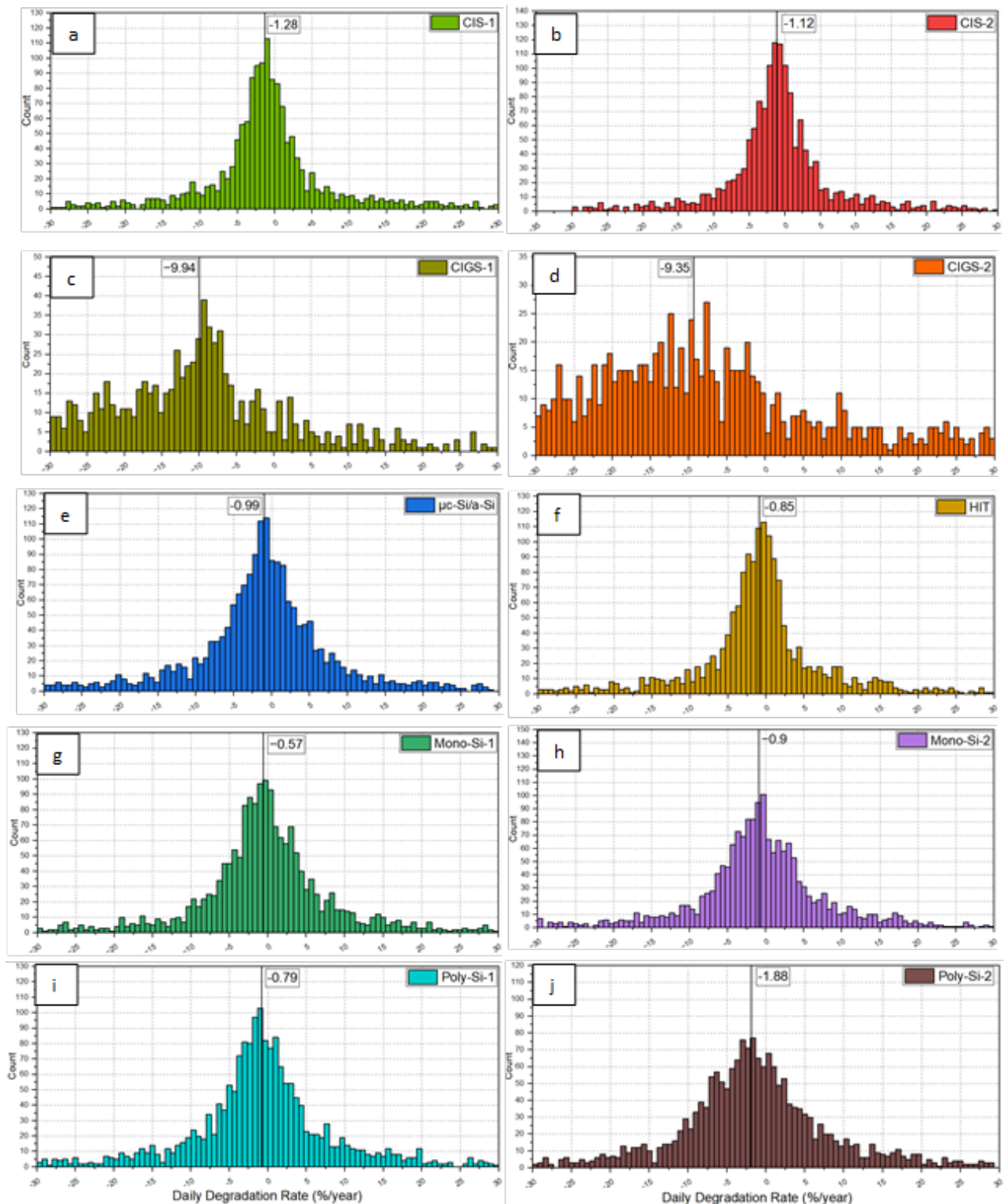
**Figure 4**: YOY Degradation Rate of PV Modules: (a) CIS-1, (b) CIS-2, (c) CIGS-1, (d) CIGS-2, (e) µc-Si/a-Si, (f) HIT, (g) Mono-Si-1, (h) Mono-Si-2, (i) Poly-Si-1, (j) Poly-Si2

**Year on Year Degradation Method**

For YOY degradation method, daily performance rates were calculated, and the annual degradation of PV module were calculated for each day during outdoor test process. At Figure 4, daily degradation rates are shown for each module separately. The median values of daily degradation data sets are also shown on this graph. In Figure 4-a and 4-b, CIS-1 & 2 modules demonstrate

similar results. CIS-1 has 1.28 %/year and CIS-2 has 1.12 %/year degradation. Also, the distributions of degradations data set of CIS-1 & 2 are close to each other. When we look at the CIGS-1 & 2 modules as given in Figure 4-c and 4-d, they have a wide range distribution. Because of reasons aforementioned at the LR section, these modules demonstrate high degradation and according to results, these degradation rates increase in time. While CIGS-1 has 9.94 %/year degradation, the

ratio of degradation of CIGS-2 is 9.35 %/year. In Figure 4-e, the distribution of data set of µc-Si/a-Si module accumulate ± 10 %/year daily degradation and its annual YOY degradation is 0.99%/year. µc-Si/a-Si modules is the best module in terms of degradation, among the thin film modules in our test area.

In Figure 4-f, HIT modules degradations data set are shown and the degradation of this module is annually 0.85 %/year, and it is not observed that the distribution accumulation of degradation is spread. Mono-Si-1 &2 have similar degradation distribution and their degradations are 0.57 %/year and 0.9 %/year annually respectively as shown at Figure 4g and 4-h. Poly-Si-1&2 is not different from Mono-Si Modules. In Figure 4i and 4-j, daily degradation distribution of data sets of Poly-Si-1 & 2 are shown and they degraded 0.79 %/year and 1.88 %/year annually. Poly-Si-1 much less degraded than Poly-Si-2.

**Comparisons of YOY and LR**

At the Table 2, annual degradation rates and process time of outdoor test of ten different modules are shown. The degradation rates are in the range of 1.88%/year and 0.71 %/year except CIGS 1 & 2. CIGS-1 & 2 modules were problematic and their degradation rates higher than expected. They were uninstalled in September 2018 and they could be tested roughly 6-year operation. Moreover, CIS-1 & 2 was installed October 2014 and their operation time is seven years.

The comparisons of these two methods and the literature are also shown at the Table 2. According to these results, the degradations are close to each other but there are some differences between the YOY and LR.

LR method show higher degradation rates than YOY method expect HIT and Poly-Si-2 but the differences are too small. If the LR Degradation method is used instead of YOY, the degradations values could be observed higher. On the other hand, the degradation rates found in As shown in figure 5, CIS-1 & 2, also CIGS-1 & 2 showed lower performance in the lower temperature over the years while higher temperatures did not show any effect on performance ratios. µc-Si/a-Si module performance ratio did not show any effect on performance ratios both lower and higher temperature. The group of monosilicone modules were not affected by temperature. Polysilicone modules have been affected by higher temperature. While ambient temperature increased, performance ratios decreased.

The wind speed annual average value is 0.9 km/h according to our data in the module's location. We can say that is not an area gets a lot of wind and the effect of the wind on modules has been not observed.

**CONCLUSION**

In this study, we tried to calculate degradation rates of ten different PV modules by using two different methods. Firstly, data getting the setup were adjusted to calculate by making needed filtering and normalizations. After that, performance ratios of modules are calculated, and degradations rates are found based on performance rates. Performance ratio of modules were compared with each other. According to these results Mono-Si-1 module shows better results in terms of degradation rates.

**Table 2:** Comparison of YOY and LR Degradation values of PV Modules

| Module | This Study | | | Literature | |
|---|---|---|---|---|---|
| | Test Time (Month) | LR (%/year) | YOY (%/year) | LR (%/year) | YOY (%/year) |
| **CIS** | 80 | 1.73 / 1.49 | 1.28 / 1.12 | 2.34 (Silvestre et al. 2016) 1.04 (Ozden et al. 2020) | ---- |
| **CIGS** | 69/75 | 11.55 / 9.52 | 9.94 / 9.35 | 0.17(Makrides et al. 2010) | 0.96 (Jordan and Kurtz 2013) 0.46 (Solís-Alemán et al. 2019) |
| **µc-Si/a-Si** | 110 | 1.48 | 0.99 | 1.45(Ishii et al. 2011) 0.23(Makrides et al. 2010) 3.67~3.76(Solís-Alemán et al. 2019) 1.73 (Silvestre et al. 2016) 2.28 (Ozden et al. 2020) | 0.87(Jordan and Kurtz 2013) 0.53 (Solís-Alemán et al. 2019) |
| **Mono-Si** | 110 | 0.71 / 1.56 | 0.57 / 0.90 | 0.78 (Ishii et al. 2011) 0.10 (Makrides et al. 2010) | 0.36 (Jordan and Kurtz 2013) |
| **HIT** | 110 | 0.84 | 0.85 | 0.26~0.63(Singh et al. 2020) 0.109 (Dag and Buker 2020) | ---- |
| **Poly-Si** | 110 | 1.20 / 1.86 | 0.79 / 1.88 | 0.40 (Ishii et al. 2011) 0.67 (Dag and Buker 2020) | 0.64 (Jordan and Kurtz 2013) |
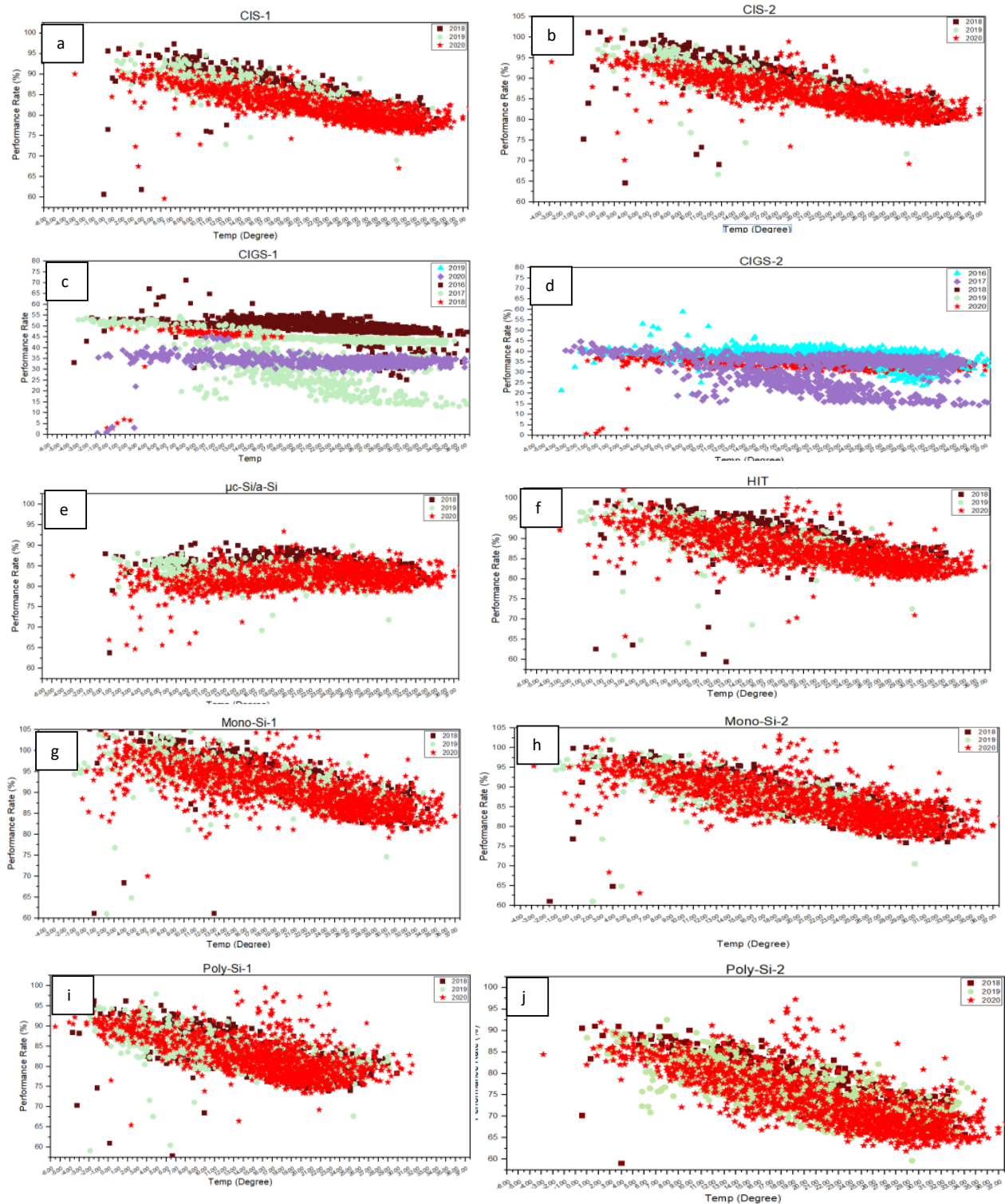
**Figure 5:** Temperature vs performance rates graphs according to years with: (a) CIS-1, (b) CIS-2, (c) CIGS-1, (d) CIGS-2, (e) µc-Si/a-Si, (f) HIT, (g) Mono-Si-1, (h) Mono-Si-2, (i) Poly-Si-1, (j) Poly-Si2

his study for both methods are in the range of values at the literatures except HIT and CIGS. HIT results for YOY and LR method are the same in this study but, in the literature degradation for HIT modules are lower for LR method.

**The effect of weather conditions on performance rates**

In this study the effect of weather condition on performance rate has been investigated such as humidity and ambient temperature. As shown in the appendix, humidity vs performance ratios graph there are not any effect or changes modules performance rates. However, ambient temperature shows different effect on different module technologies.

111

Although this module was working nine years, its performance decreased only 0.71 %/year in LR and 0.57 %/year YOY annually. Mono-Si-2 module shows 1.56 %/year and 0.90 %/year degradation according to LR and YOY method respectively. HIT module degraded 0.84 %/year for LR method and 0.85 %/year for YOY method. Overall Mono-Crystalline group (Mono-Si 1&2 and HIT) performed well. On the other hand, Poly-Si Group and thin film group except CIGS 1&2, show a similar performance. The degradation ratios of Poly-Si 1&2 are 1.20 /1.86 % /year according to LR method, 0.79/1.88 %/year according to YOY method. CIS 1&2 modules show a degradation amount of 1.73 %/year and 1.49 %/year according to LR method, 1.28 %/year and 1.12 %/year according to YOY method respectively. The degradation ratio of μc-Si/a-Si module 1.48 %/year and 0.99 %/year for LR method and YOY method respectively. CIGS 1&2 were problematic PV modules and they performed badly. Their degradation was highest with 10 %/year average. In conclusion, YOY method shows lower degradation rates compare to LR method. Used method in the calculation of degradation rates has a crucial impact.

## REFERENCES

Akinoglu, B. G., A. B. Karaveli, and T. Özden. 2017. "Evaluation and Comparisons of the Models to Calculate Solar Irradiation on Inclined Solar Panels for Ankara." *33rd European Photovoltaic Solar Energy Conference and Exhibition* (November):2501–4. doi: 10.4229/EUPVSEC20172017-6BV.3.24.

Annigoni, Eleonora, Alessandro Virtuani, Mauro Caccivio, Gabi Friesen, Domenico Chianese, and Christophe Ballif. 2019. "35 Years of Photovoltaics: Analysis of the TISO-10-KW Solar Plant, Lessons Learnt in Safety and Performance—Part 2." *Progress in Photovoltaics: Research and Applications* 27(9):760–78. doi: 10.1002/PIP.3146.

Anon. n.d. "Meteoroloji Genel Müdürlüğü." Retrieved December 27, 2022 (https://mgm.gov.tr/veridegerlendirme/il-ve-ilceler-istatistik.aspx?k=A&amp;m=ANKARA).

Bogdanski, N., W. Herrmann, F. Reil, M. Köhl, K. A. Weiss, and M. Heck. 2010. "Results of 3 Years' PV Module Weathering in Various Open-Air Climates." *Https://Doi.Org/10.1117/12.859807* 7773:165–72. doi: 10.1117/12.859807.

Dag, H. I., and M. S. Buker. 2020. "Performance Evaluation and Degradation Assessment of Crystalline Silicon Based Photovoltaic Rooftop Technologies under Outdoor Conditions." *Renewable Energy* 156:1292–1300. doi: 10.1016/J.RENENE.2019.11.141.

Daher, Daha Hassan, Mohammadreza Aghaei, David A. Quansah, Muyiwa S. Adaramola, Parviz Parvin, and Christophe Ménézo. 2023. "Multi-Pronged Degradation Analysis of a Photovoltaic Power Plant after 9.5 Years of Operation under Hot Desert Climatic Conditions."

*Progress in Photovoltaics: Research and Applications* 31(9):888–907. doi: 10.1002/pip.3694.

Dhimish, Mahmoud, and Abdullah Alrashidi. 2020. "Photovoltaic Degradation Rate Affected by Different Weather Conditions: A Case Study Based on PV Systems in the UK and Australia." *Electronics 2020, Vol. 9, Page 650* 9(4):650. doi: 10.3390/ELECTRONICS9040650.

Duffie, John A., and William A. Beckman. 2013. *Solar Engineering of Thermal Processes, 4th Edition | Wiley.*

Frick, Alexander, George Makrides, Markus Schubert, Matthias Schlecht, and George E. Georghiou. 2020. "Degradation Rate Location Dependency of Photovoltaic Systems." *Energies 2020, Vol. 13, Page 6751* 13(24):6751. doi: 10.3390/EN13246751.

Grübler, Arnulf, Michael Jefferson, and Nebojša Nakićenović. 1996. "Global Energy Perspectives: A Summary of the Joint Study by the International Institute for Applied Systems Analysis and World Energy Council." *Technological Forecasting and Social Change* 51(3):237–64. doi: 10.1016/0040-1625(95)00251-0.

Hassan Daher, Daha, Léon Gaillard, and Christophe Ménézo. 2022. "Experimental Assessment of Long-Term Performance Degradation for a PV Power Plant Operating in a Desert Maritime Climate." *Renewable Energy* 187:44–55. doi: 10.1016/J.RENENE.2022.01.056.

Hasselbrink, Ernest, Mike Anderson, Zoe Defreitas, Mark Mikofski, Yu Chen Shen, Sander Caldwell, Akira Terao, David Kavulak, Zach Campeau, and David Degraaff. 2013. "Validation of the PVLife Model Using 3 Million Module-Years of Live Site Data." *Conference Record of the IEEE Photovoltaic Specialists Conference* 7–12. doi: 10.1109/PVSC.2013.6744087.

IEC 61724. 1998. *Photovoltaic System Performance Monitoring-Guidelines for Measurement, Data Exchange and Analysis.*

Ineichen, Pierre, Olivier Guisan, and Richard Perez. 1990. "Ground-Reflected Radiation and Albedo." *Solar Energy* 44(4):207–14. doi: 10.1016/0038-092X(90)90149-7.

Ishii, Tetsuyuki, Takumi Takashima, and Kenji Otani. 2011. "Long-Term Performance Degradation of Various Kinds of Photovoltaic Modules under Moderate Climatic Conditions." *Progress in Photovoltaics: Research and Applications* 19(2):170–79. doi: 10.1002/PIP.1005.

Jordan, D. C., and S. R. Kurtz. 2013. "Photovoltaic Degradation Rates—an Analytical Review." *Progress in Photovoltaics: Research and Applications* 21(1):12–29. doi: 10.1002/PIP.1182.

Köppen, Wladimir, Esther Volken, and Stefan Brönnimann. 2011. "The Thermal Zones of the Earth According to the Duration of Hot, Moderate and Cold Periods and to the Impact of Heat on the Organic World."

*Meteorologische Zeitschrift* 20(3):351–60. doi: 10.1127/0941-2948/2011/105.

Limmanee, Amornrat, Sasiwimon Songtrai, Nuttakarn Udomdachanut, Songpakit Kaewniyompanit, Yukinobu Sato, Masaki Nakaishi, Songkiate Kittisontirak, Kobsak Sriprapha, and Yukitaka Sakamoto. 2017. "Degradation Analysis of Photovoltaic Modules under Tropical Climatic Conditions and Its Impacts on LCOE." *Renewable Energy* 102:199–204. doi: 10.1016/J.RENENE.2016.10.052.

Liu, Benjamin Y. H., and Richard C. Jordan. 1963. "The Long-Term Average Performance of Flat-Plate Solar-Energy Collectors: With Design Data for the U.S., Its Outlying Possessions and Canada." *Solar Energy* 7(2):53–74. doi: 10.1016/0038-092X(63)90006-9.

Makrides, George, Bastian Zinsser, George E. Georghiou, Markus Schubert, and Jürgen H. Werner. 2010. "Degradation of Different Photovoltaic Technologies under Field Conditions." *Conference Record of the IEEE Photovoltaic Specialists Conference* 2332–37. doi: 10.1109/PVSC.2010.5614439.

Micheli, Leonardo, Marios Theristis, Diego L. Talavera, Gustavo Nofuentes, Joshua S. Stein, Florencia Almonacid, and Eduardo F. Fernández. 2022. "The Economic Value of Photovoltaic Performance Loss Mitigation in Electricity Spot Markets." *Renewable Energy* 199:486–97. doi: 10.1016/J.RENENE.2022.08.149.

Ozden, Talat, Bulent G. Akinoglu, and Rasit Turan. 2017. "Long Term Outdoor Performances of Three Different On-Grid PV Arrays in Central Anatolia – An Extended Analysis." *Renewable Energy* 101:182–95. doi: 10.1016/J.RENENE.2016.08.045.

Ozden, Talat, Ensar Mesut Ozgun, Bedirhan Keles, and Bulent G. Akinoglu. 2020. "Nine Years Long Term Performance and Degradation Assessment of Two On-Grid PV Systems." in *2020 2nd International Conference on Photovoltaic Science and Technologies, PVCon 2020.* Institute of Electrical and Electronics Engineers Inc.

Ozden, Talat, Ugur Yardim, Bulent G. Akinoglu, and Rasit Turan. 2015. "Outdoor Efficiency Analyses and Comparison of On-Grid CdTe and Mc-Si/a-Si Thin-Film PV Systems for Three Years in Ankara – Turkey." *Physica Status Solidi (c)* 12(9–11):1283–87. doi: 10.1002/PSSC.201510077.

Peel, M. C., B. L. Finlayson, and T. A. McMahon. 2007. "Updated World Map of the Köppen-Geiger Climate Classification." *Hydrology and Earth System Sciences* 11(5):1633–44. doi: 10.5194/HESS-11-1633-2007.

Quansah, David A., and Muyiwa S. Adaramola. 2018. "Comparative Study of Performance Degradation in Poly- and Mono-Crystalline-Si Solar PV Modules Deployed in Different Applications." *International Journal of Hydrogen Energy* 43(6):3092–3109. doi: 10.1016/J.IJHYDENE.2017.12.156.

Reindl, D. T., W. A. Beckman, and J. A. Duffie. 1990. "Evaluation of Hourly Tilted Surface Radiation Models." *Solar Energy* 45(1):9–17. doi: 10.1016/0038-092X(90)90061-G.

Savvakis, Nikolaos, and Theocharis Tsoutsos. 2015. "Performance Assessment of a Thin Film Photovoltaic System under Actual Mediterranean Climate Conditions in the Island of Crete." *Energy* 90:1435–55. doi: 10.1016/J.ENERGY.2015.06.098.

Silvestre, Santiago, Sofiane Kichou, Letizia Guglielminotti, Gustavo Nofuentes, and Miguel Alonso-Abella. 2016. "Degradation Analysis of Thin Film Photovoltaic Modules under Outdoor Long Term Exposure in Spanish Continental Climate Conditions." *Solar Energy* 139:599–607. doi: 10.1016/J.SOLENER.2016.10.030.

Singh, Rashmi, Madhu Sharma, Rahul Rawat, and Chandan Banerjee. 2020. "Field Analysis of Three Different Silicon-Based Technologies in Composite Climate Condition – Part II – Seasonal Assessment and Performance Degradation Rates Using Statistical Tools." *Renewable Energy* 147:2102–17. doi: 10.1016/J.RENENE.2019.10.015.

Solís-Alemán, Ernesto M., Juan de la Casa, Irene Romero-Fiances, José Pedro Silva, and Gustavo Nofuentes. 2019. "A Study on the Degradation Rates and the Linearity of the Performance Decline of Various Thin Film PV Technologies." *Solar Energy* 188:813–24. doi: 10.1016/J.SOLENER.2019.06.067.

Tabatabaei, Seyed Amin, Daniel Formolo, and Jan Treur. 2017. "Analysis of Performance Degradation of Domestic Monocrystalline Photovoltaic Systems for a Real-World Case." *Energy Procedia* 128:121–29. doi: 10.1016/J.EGYPRO.2017.09.025.

Tsanakas, John A., Long Ha, and Claudia Buerhop. 2016. "Faults and Infrared Thermographic Diagnosis in Operating C-Si Photovoltaic Modules: A Review of Research and Future Challenges." *Renewable and Sustainable Energy Reviews* 62:695–709. doi: 10.1016/j.rser.2016.04.079.
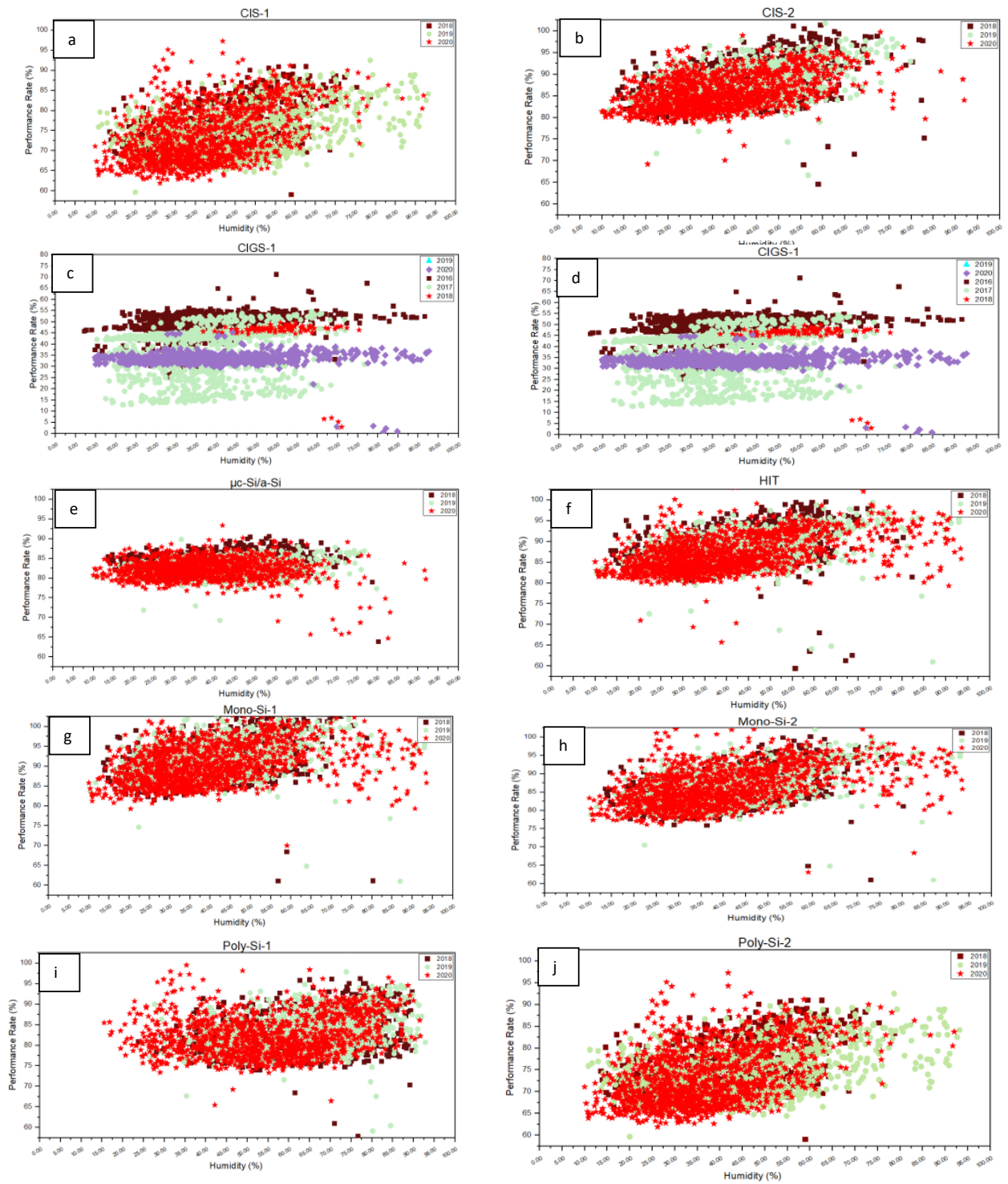
**APPENDIX 2**

| Years | Annual wind speed (km/h) |
|-------|--------------------------|
| 2016  | 0.99                     |
| 2017  | 0.94                     |
| 2018  | 0.83                     |
| 2019  | 0.79                     |
| 2020  | 0.83                     |
| 2021  | 0.77                     |

# Numerical optimization and experimental investigation of renewable diethyl ether-fueled off-road CI engines for sustainable transportation

**M. Gowthama Krishnan\*, R. Praveen\*\*, V. Pugalendhi\*\*\*, S. Ram S\*\*\*\***
\*Department of Mechanical Engineering, Sri Sivasubramaniya Nadar College of Engineering,
Chennai – 603 110, Tamil Nadu, India, gowthamakrishnanm@ssn.edu.in, ORCID: 0000-0002-8742-2112
\*\*Department of Robotics and Automation, Karpaga Vinayaga College of Engineering and Technology,
Chengalpattu – 603 308, Tamil Nadu, India, praveenrajendran5@gmail.com, ORCID: 0000-0002-8832-9665
\*\*\*Department of Mechanical Engineering, Tagore Engineering College,
Chennai – 600 127, Tamil Nadu, India, pugalmit@gmail.com, ORCID: 0009-0001-3659-8505
\*\*\*\*School of Mechanical Engineering, Sathyabama Institute of Science and Technology,
Chennai – 600 119, Tamil Nadu, India, ramprakashnec@gmail.com, ORCID: 0000-0002-7969-2155

**Abstract:** Cleaner energy generation on light-duty off-road diesel engines is one of the objectives of this study, which utilizes renewable diethyl ether (DEE) as a replacement for diesel to minimize the reliance on fossil diesel fuel. In an air-cooled single-cylinder diesel engine, various DEE mixes of 5, 10, 15, 20 and 25% were attempted and evaluated under varying loads (0, 25, 50, 75 and 100%) in an effort to enhance the performance and emission characteristics of agriculture diesel engines and lower the environmental effect of harmful emissions. The injection pressure was optimized using computational fluid dynamics (CFD), and performance and emission outcomes were optimized through response surface methodology (RSM) techniques. The experimental results found that brake thermal efficiency and specific fuel consumption were enhanced for a higher proportion of DEE blends under increasing loads. In addition, increasing the engine load decreased CO emissions while increasing carbon dioxide ($CO_2$), hydrocarbon (HC), and nitrogen oxide (NOx) emissions. Reduced CO, NOx, and HC emissions and increased $CO_2$ were realized in the blended fuel samples compared to those of pure diesel fuel at increasing DEE percentages. In summary, the utilization of a 15% DEE blend and the optimization of the injection pressure to 210 bar resulted in a notable improvement of 10% in thermal efficiency and a decrease in emissions by 5% when compared to other parameters.
**Keywords:** Diesel engine, diethyl ether, performance, emission, NOx, CFD

## Sürdürülebilir ulaşım için yenilenebilir dietil eter yakıtlı arazi dışı CI motorlarının sayısal optimizasyonu ve deneysel incelenmesi

**Özet:** Fosil dizel yakıtına bağımlılığı en aza indirmek için dizel yerine yenilenebilir dietil eter (DEE) kullanan bu çalışmanın amaçlarından biri, hafif hizmet arazi dizel motorlarında daha temiz enerji üretimidir. Hava soğutmalı tek silindirli bir dizel motorda, %5, 10, 15, 20 ve 25'lik çeşitli DEE karışımları denenmiş ve değişen yükler altında (%0, 25, 50, 75 ve 100) değerlendirilmiştir. Tarımsal dizel motorların performans ve emisyon özelliklerini azaltarak zararlı emisyonların çevresel etkisini azaltır. Enjeksiyon basıncı, hesaplamalı akışkanlar dinamiği (CFD) kullanılarak optimize edildi ve performans ve emisyon sonuçları, yanıt yüzeyi metodolojisi (RSM) teknikleri aracılığıyla optimize edildi. Deney sonuçları, artan yükler altında daha yüksek oranda DEE karışımı için fren termal verimliliğinin ve spesifik yakıt tüketiminin arttığını buldu. Ayrıca motor yükünün arttırılması CO emisyonlarını azaltırken karbondioksit (CO2), hidrokarbon (HC) ve nitrojen oksit (NOx) emisyonlarını artırdı. Artan DEE yüzdelerinde, saf dizel yakıtla karşılaştırıldığında, harmanlanmış yakıt örneklerinde CO, NOx ve HC emisyonlarında azalma ve CO2 artışı elde edildi. Özetle, %15 DEE karışımının kullanılması ve enjeksiyon basıncının 210 bar'a optimizasyonu, diğer parametrelerle karşılaştırıldığında termal verimlilikte %10'luk kayda değer bir iyileşme ve emisyonlarda %5'lik bir azalma ile sonuçlandı.
**Anahtar Kelimeler:** Dizel motor, dietil eter, performans, emisyon, NOx, CFD

## Nomenclature

BTE-Brake thermal efficiency
BSFC -brake specific fuel consumption
$CO_2$- Carbon dioxide
CO-Carbon monoxide
CI-Compression Ignition
CFD-Computational fluid dynamics
DEE- Diethyl ether
HC- Hydrocarbon
ICEs -Internal combustion engines
NOx- Nitrogen oxide
RSM - Response surface methodology
SI-Spark Ignition
WHO- World Health Organization
0% DEE- 100% diesel and 0% diethyl ether
5% DEE- 95% diesel and 5% diethyl ether
10% DEE-90% diesel and 10% diethyl ether
15% DEE-85% diesel and 15% diethyl ether
20% DEE-80% diesel and 20% diethyl ether
25% DEE-75% diesel and 25% diethyl ether

## INTRODUCTION

Internal combustion engines (ICEs) are significant prime movers expected to play a significant role in the transportation industry for the foreseeable future. IC engines rely heavily on fossil fuels for power. Heavy reliance on fossil fuels boosted both greenhouse gas emissions and fuel demand. In addition, high industrial and transportation demands are driving up the price of and scarcity of fossil fuels. To minimize fossil fuel utilization for IC engines in the near future, they must use cleaner and alternative fuels. Consequently, the necessity for alternative fuels and their quality enhancement should be explored (Martin et al. 2020). Furthermore, according to the WHO reports, nine out of the ten most polluted cities in the world are in India. By 2024, the nation anticipated reducing air pollution levels by 20 to 30% in 100 major cities (Cristian 2018).

Two of the largest markets for petroleum products are the transportation industry and the farming or agriculture sector. Conventional fossil-based diesel fuel is widely used to power diesel engines in the automobile and agricultural sectors. The necessity of a diesel engine is higher since the thermal efficiency, fuel economy, and endurance limit are higher than gasoline engines. As a result, diesel engines are widely adopted in transport, electricity power generation, and heavy industrial machinery and agriculture sectors. In India's agricultural industry, diesel fuel tractors, farm equipment, and irrigation pump set depend on diesel fuel (Agarwal, Avinash Kumar and Krishn Chandra 2022a; 2022b). However, the increased usage of diesel fuel contributes to harmful high soot and NOx emissions because of the fuel-rich zones from fuel spray and high combustion temperatures from the high compression ratio

(Emaish et al. 2021). However, further efforts will be needed to reduce harmful pollution from diesel combustion processes by decreasing nitrogen oxides and particulate matter emissions.

Emission control strategies and enhancing the fuel characteristics like fuel volatility, diminishing the fuel's aromatic and sulfur content, and augmenting the cetane number could be better options to mitigate these emissions. From these points of view, exploring potential alternate fuel sources is typically beneficial, i.e., using oxygenated renewable additives (Mofijur et al. 2015). There is widespread availability of different oxygenated sources; among them, biodiesel, alcohols and ethers are prominent oxygenated fuel sources. Alcohols such as ethanol, methanol, butanol, pentanol, and ethers such as dimethyl, diethyl, dibutyl, and dimethyl carbonate (Praveen et al 2014a; 2014b; Sezer, Ismet 2019; Gainey et al 2021) have been investigated by several studies as oxygenated additives in diesel, biodiesel, and diesel-biodiesel blends (Negi, Himani and Raj Kumar Singh 2020).

Alcohol is primarily used in SI engines due to its superior octane rating, and these days alcohol is also considered a blended fuel for diesel engines (Goktas et al. 2021). However, the usage of alcohol in diesel engines suffers from cold starting issues, and lower calorific values of alcohol affect the performance of the engine. In addition, ethanol and methanol as a binary and ternary blend for diesel cause immiscibility (above 10 % by volume), hygroscopic and phase separation problems under higher alcohol proportion (Nanthagopal et al. 2020).

In this context, ethers are another oxygenated option in which among different ethers the DEE is a renewable oxygenated additive or fuel produced from ethanol using a dehydration process (Jawre et al. 2016; Dinesha et al. 2019). DEE offers numerous desirable characteristics for diesel-powered engines as an alternate fuel, i.e., high oxygen content (21.6%), enhanced miscibility, reasonable energy density, high cetane number, non-corrosive, increased flammability limits and low auto-ignition temperature (Agarwal et al. 2022). Furthermore, the greater H/C ratio and fewer C-C bonds of DEE as a diesel fuel addition resulted in less soot production (Nanthagopal et al. 2019).

Gorski and Przedlacki (2014) analyzed the physicochemical properties of diesel fuel containing DEE. They noticed that blends were stable at temperatures below 0°C, that the cold filter pour point decreased, and that the miscibility of the blend was improved throughout a range of temperatures. In addition, fuel injectors were not affected by the modest reduction in lubricity. However, the viscosity decreases, and if the blend is tested above 20% by volume, it creates vapour locks and deteriorates performance. As well, Iranmanesh et al. (2008) reported

that DEE as an additive (2,5 and 10% volume) in diesel fuel improved the viscosity, cetane number, flash point and fuel volatility.

Ibrahim (2016) tested a single-cylinder diesel engine with 5, 10 and 15% DEE blends and found that 15% DEE improved the brake thermal efficiency by 7.2% and abridged the BSFC by 6.7% in comparison to diesel fuel. However, the combustion stability was slightly affected when the blends were more than 20%. In another study, Subramanian et al. (2002) investigated DEE (5,10 and 15% by weight) together with water-diesel emulsion and reported improved performance and lower NOx, smoke and increased HC and CO emissions. Ismet Sezer (2018) reviewed the effect of DEE on NOx emissions and reported that adding DEE to diesel and biodiesel blends reduces the NOx emissions owing to the higher cetane number and latent vaporization, and lower heating value.

Similarly, Lee and Kim (2017) studied the maximum concentration of DEE (10, 25 and 50%) in diesel fuel, compared the results with diesel fuel, and found lower CO, HC, and particular emissions. However, DEE blends suffered from higher NOx emissions because of reduced ignition delay and inborn oxygen content. Rakopoulos et al. (2013) investigated the combustion behaviour of diethyl ether in diesel fuel. They reported no cyclic variations, i.e., stable operation of engine operated with DEE blends up to 24% relative to diesel fuel. Moreover, the maximum pressure rate was lower (~ 3 bar/deg), whereas it is ~4.3 bar/degree for diesel fuel at a rated (5.37 bar BMEP) load.

Researchers also tested diethyl ether as an additive for diesel-biodiesel blended fuels. Ali et al. (2016) showed that DEE as an additive (2, 4, 6 and 8% by volume) for diesel-biodiesel blends (B30) deteriorated the heating value of B30 and increased the cyclic variability at increased DEE proportion. Carvalho et al. (2020) found that the addition of 5% DEE in ternary blends of diesel-ethanol-biodiesel under different loads (8, 16 and 24 kW) increased the HC emissions and decreased the NOx and smoke emissions at all loads. In an investigation on DEE (Ibrahim 2018), 5% of DEE in a diesel-biodiesel blend showed improved BTE and BSFC; however, the performance (efficiency and fuel consumption) was affected when the DEE blend increased to 10% owing to the latent heat of vaporization and lower calorific value of DEE. Prabakaran et al. (2022) reported that for diesel-biodiesel-DEE blends under all load conditions (0 to 100%), the NOx emissions were increased by 11.6, 16.2 and 18.7% at increased DEE content (5,7.5 and 10% by volume). The increased oxygen content of DEE and biodiesel in ternary blends was the primary reason for NOx formation. A similar increase in NOx emission was reported by Reddy et al. (2022) for DEE-biodiesel blends. However, other emissions (HC, CO and smoke) were decreased with improved performance due to better oxidation and combustion. Similar reduction in HC and CO was also reported in the studies of different biodiesel fuel with DEE blends (Rami Reddy et al. 2022; Dinesha et al. 2019).

Literature indicates that biodiesel blends and ternary blends of diesel-DEE-biodiesel reported higher NOx emissions at rated loads. In addition, the alcohols as a diesel blend suffered from phase separation problems at increased alcohol concentration. Hence, oxygenated DEE is chosen as an alternative fuel in this work. Literature is scarce on the combined effects of diethyl ether-diesel and response surface approaches on the performance and emissions of a compression ignition engine. The novelty of this work comprises a numerical and experimental approach to identifying the optimum usage of renewable diethyl ether across distinct load circumstances of agricultural diesel engines in order to reduce diesel utilization and $CO_2$ emission and enhance performance and other emission characteristics. Consequently, the objective of the study is to examine the optimal injection pressure for tested DEE blends of 0 to 25% using CFD and investigate the different DEE blends in diesel fuel operating under diverse loads of 0 to 100%. Finally, the performance and emission outcomes of DEE blends are compared with conventional diesel fuel.

**MATERIALS and METHOD**

**CFD modelling**

Controlling the fuel injection conditions is one way to influence the combustion parameters. This study employs computational fluid dynamics (CFD) to investigate the combination of diesel and oxygenated fuel on spray properties under high-pressure fuel injection. Cross-sectioned model dimensions of the injector and closed chamber are shown in Figure 1. The injector had six orifice holes of 0.04 mm diameter with an equal spacing of 60 degrees. The injection pressure was varied between 200, 205, and 210 bars, while the ambient pressure and temperature were kept constant at 1 atm and 305K. The mixture of 75% diesel and 25% diethyl ether blend fuel was considered for all simulation trials. Table 1 describes the properties and boundary conditions of the chamber and injector. The properties of diesel-diethyl ether blends are given in Table 2. The spray characteristics of diesel-diethyl ether blends were studied using CFD. This includes spray angle, penetration length, and air-fuel mixture parameters such as pressure, velocity and viscosity patterns.
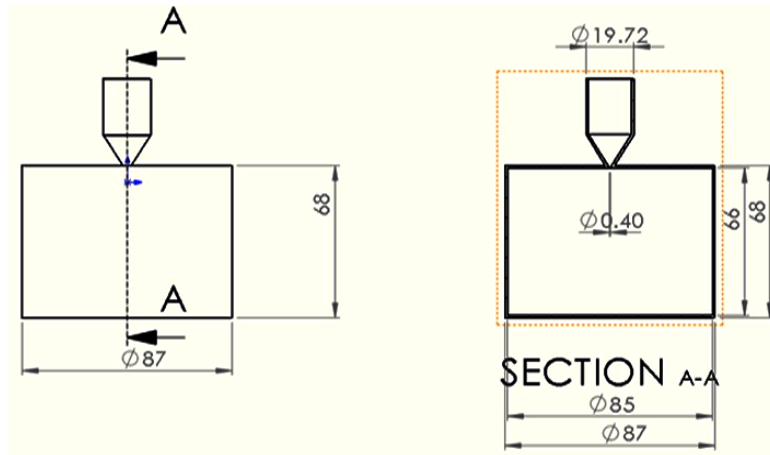
**Figure 1.** Dimensional cross-section of the CFD model: Cylindrical chamber and fuel injector

**Table 1.** Properties and boundary conditions of cylindrical chamber and injector

| Material Specification | Aluminium |
|---|---|
| Ambient pressure | 1 bar |
| Ambient temperature | 305K |
| Injection pressure | 200 bar, 205 bar 210 bar |
| Boundary condition | |
| (i) Inlet | fuel injector |
| (ii) Boundary | wall |
| (iii)Interior | Compressed air |

**Table 2.** Fuel properties of diesel and diethyl ether (DEE)

| Fuel Properties | Diesel | Diethyl ether |
|---|---|---|
| Density at 20ºC (kg/m³) | 820 | 713.4 |
| Boiling point (°C) | 240-360 | 34.6 |
| Latent Heat of vaporization (kJ/kg) | 250-290 | 376 |
| Flash point (°C) | 52-96 | -45 |
| Auto ignition temperature (°C) | 260 | 160 |
| Calorific Value at 20ºC (MJ/kg) | 44.9 | 33.892 |
| Stoichiometric A/F ratio | 14.4 | 11.2 |
| Octane number | - | 92 |
| Cetane number | 50 | 125 |
| Kinematic Viscosity (cS) | 0.223 | 0.224 |

**Experimental test facilities and methods**

Experimentation was conducted using a single-cylinder, air-cooled research engine. The maximum power output of the test engine is 4.4 kW at a constant speed of 1,500 rpm. Table 3 details the test engine's specifications. Figure 2 depicts a pictorial representation of the research engine. An electrical dynamometer was used to apply load by varying the field current. To monitor airflow, a manometer connected to a large tank was attached to the engine. Using a burette and stopwatch, the flow rate of fuel was measured volumetrically. A crank angle encoder (365C Indi Advanced) manufactured by AVL is installed on the camshaft of the engine. The test apparatus is outfitted with AVL software to generate an operational performance measurement.

**Table 3.** Specification of research engine

| Engine type | Four stroke diesel engine |
|---|---|
| Bore | 87.5 mm |
| Stroke | 110 mm |
| Swept volume | 661.5 cc |
| Injection timing | 23º b TDC |
| Nozzle opening pressure | 220 bar |
| Rated output | 4.4 kW |
| Rated speed | 1500 rpm |
| Compression ratio | 17.5:1 |

Initially, conventional diesel fuel was used to obtain baseline data under fixed speeds and different load conditions (25–100%). Secondly, the diesel fuel was blended with oxygenated diethyl ether diesel. The amount of oxygenated diethyl ether in diesel was then varied between 5, 10, 15, 20, and 25%. Based on CFD analysis, the optimal injection pressure was determined. Then the prepared blends were tested, and their performance and emission parameters were investigated and compared with those of baseline diesel fuel. The Bridge five gas exhaust emissions analyzer was used to measure exhaust pollutants such as carbon monoxide (CO), carbon dioxide ($CO_2$), nitrogen oxides (NOx), hydrocarbons (HC), and oxygen ($O_2$).

**Table 4.** Accuracy and error (%) of measuring instruments

| Parameters | Accuracy | Error (%) |
|---|---|---|
| CO | $\pm$ 0.01% | $\pm$ 0.1 |
| $CO_2$ | $\pm$ 0.3 % | $\pm$ 1.5 |
| HC | $\pm$ 8 ppm | $\pm$ 0.2 |
| NOx | $\pm$ 5 ppm | $\pm$ 0.1 |

An investigation of the experimental setup's uncertainty was required to reduce error and confirm the experiment's accuracy. Hence, the uncertainty analysis was performed for all the tested conditions and were calculated based on the equation (1) given below.

$$\Delta U = \sqrt{\left\{\left(\frac{\partial U}{\partial x_1}\Delta x_1\right)^2 + \left(\frac{\partial U}{\partial x_2}\Delta x_2\right)^2 + \left(\frac{\partial U}{\partial x_3}\Delta x_3\right)^2 + \cdots + \left(\frac{\partial U}{\partial x_n}\Delta x_n\right)^2\right\}}$$ (1)

Where, U denoted the overall uncertainty. $x_1, x_2, x_3 \ldots x_n$ are independent variables and $\Delta x_1, \Delta x_2, \Delta x_{n1}$ are the errors. Table. 4 represent an accuracy and error percentage of measuring instruments and Table. 5 represent the overall uncertainties.

**Table 5.** Overall percentage of uncertainty

| Parameters | Uncertainty (%) |
|---|---|
| Shaft power | 0.83 |
| Fuel consumption | 0.31 |
| BTE | 1.05 |
| BSFC | 0.95 |
| CO | 1.23 |
| HC | 1.35 |
| $CO_2$ | 1.12 |
| $NO_x$ | 0.80 |

**Results and discussion**

This section explains the spray characteristics, performance, and emission parameters of diesel and oxygenated blended fuel (i.e., diethyl ether) in varying amounts.

**Numerical spray characteristics**

The numerical spray characteristics such as pressure, velocity, viscosity, spray cone length and spray cone angle of diesel and diethyl ether blends are discussed in this section.

The change in pressure, velocity, and viscosity distribution of diesel and DEE blends at varied fuel injection pressures (i.e., 200, 205, and 210 bar) are shown in Figures 3–5. In the case of fuel injection pressures of 200 and 205, a partial amount of vaporization and atomization of fuel occurred. But when fuel was injected at 210, the pressure was spread evenly across the cylindrical chamber, and the fuel was completely atomized. This is depicted in Figures 3 (a-c). The change in velocity distribution of fuel injection pressures of 200, 205, and 210 bars is shown in Figures 4 (a–c). Upon increasing the injection pressure, the velocity distribution of fuel decreases. When the injection pressure was low and there was some semi-liquid fuel, the peak velocity of the spray gathered in the middle portion. Figures 5 (a-c) depict the variation in the viscosity pattern of diesel-diethyl ether fuel blends at various injection pressures. In the case of low injection pressure (200 bar), the viscosity of fuel was higher compared to high injection pressure (210 bar). The spray cone length and cone angle were similar in all cases. However, the uniform distribution of fuel in a cylindrical chamber with a swirl flow pattern was achieved in the case of 210 bar injection pressure, and this phenomenon was absent in the case of 200 and 205 bar injection pressure. Based on these observations, it shows clear evidence that the complete vaporization, atomization, and uniform distribution of fuel blends were achieved in the case of 210 bar injection pressure. Hence, this optimized injection pressure was considered for all the experimental test trials.

**Performance Characteristics**

The performance characteristics like BTE, BSFC, mechanical efficiency and exhaust gas temperature of diesel and DEE blends are discussed in this section.

The variations in BTE of diesel and DEE blends under diverse loads are shown in Figure 6. The BTE rises as the engine load rises because, with increasing load levels, the fuel required to match is higher to meet the operating load and effective power produced is higher results in increased BTE. From Figure 6, it can be observed that for all load levels, increasing the DEE concentration from 5 to 25% in diesel fuel improved the BTE. This is because the inclusion of DEE increased combustion efficiency due to the inherent oxygen content and higher cetane number (Agarwal et al. 2022a), hence increasing the BTE of diesel-DEE blends.
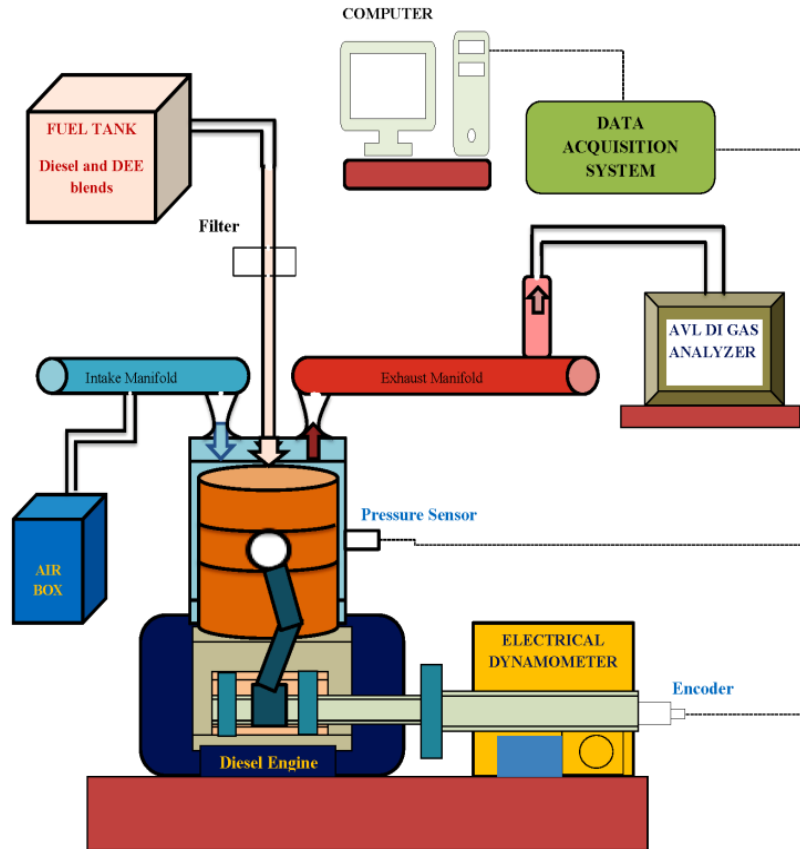
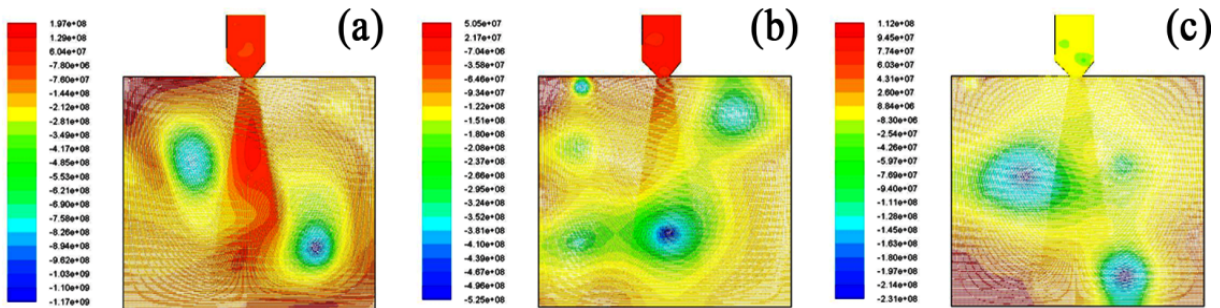**Figure 2.** Schematic of research engine test setup



**Figure 3.** Change in pressure distribution of diesel-diethyl ether fuel blends at varied injector pressure
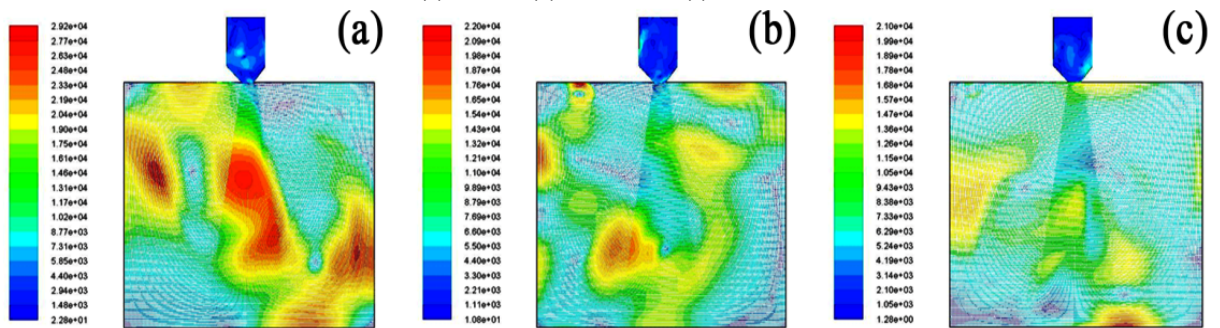(a) 200 bar (b) 205 bar and (c) 210 bar



**Figure 4.** Change in velocity distribution of diesel-diethyl ether fuel blends at varied injector pressure
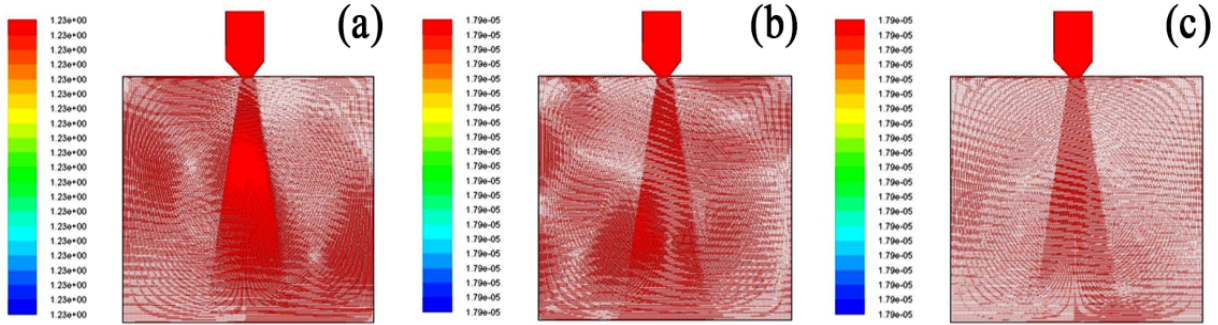(a) 200 bar (b) 205 bar and (c) 210 bar

**Figure 5.** Change in viscosity distribution of diesel-diethyl ether fuel blends at varied injector pressure (a) 200 bar (b) 205 bar and (c) 210 bar

Furthermore, the interfacial tension between two or more interacting immiscible liquids helped fuel atomization, improving diesel combustion. Among the tested fuels, the maximum BTE is observed for 25% DEE at 75 and 100% rated loads. This is because, at increased DEE concentration, the higher volatile characteristics and reduced viscosity of DEE improve air-fuel mixing, which promotes combustion and facilitates an increase in BTE (Ibrahim 2016).
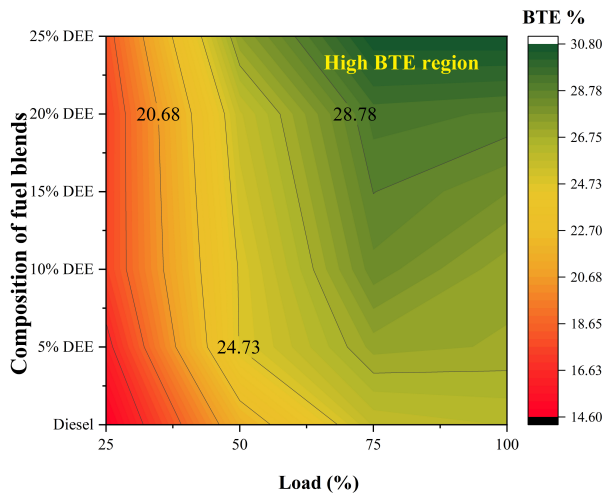


**Figure 6.** Comparison of BTE of diesel and DEE blends

The variations in brake specific fuel consumption (BSFC) of diesel and DEE blends under varied loads are shown in

Figure 7. From Figure 7, it can be seen that the increasing DEE proportion decreases the BSFC compared to pure diesel fuel for all load points. Therefore, the drop in BSFC with increasing load could be attributable to the greater availability of fuel oxygen.
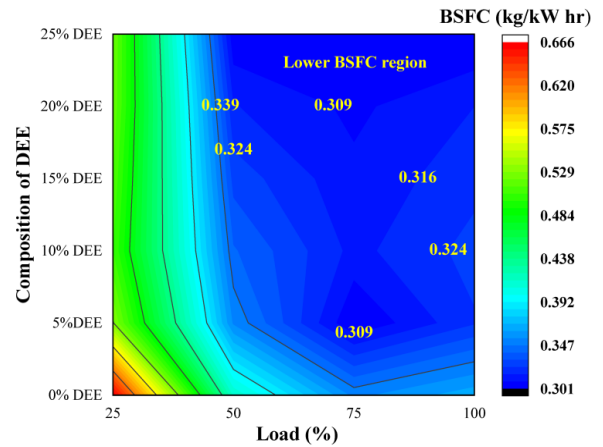


**Figure 7.** Comparison of BSFC of diesel and DEE blends

Figure 8 represents the improvement scale of mechanical efficiency of DEE blends under different loads. It is observed from Figure 8 that the increase in the proportion of DEE from 0 to 25% in diesel improved the mechanical efficiency under all loads. It could be due to the inherent oxygen content of DEE that promotes combustion and increases power output.

| Load (%) | Diesel | 5% DEE | 10% DEE | 15% DEE | 20% DEE | 25% DEE |
|---|---|---|---|---|---|---|
| 25 | 20.74 | 24 | 24.96 | 25.13 | 25.3 | 26.1 |
| 50 | 41.86 | 44 | 44.97 | 44.925 | 44.88 | 45.12 |
| 75 | 57.28 | 61.7 | 60.77 | 61.45 | 62.13 | 63.11 |
| 100 | 69.98 | 75.52 | 75.91 | 76.03 | 76.15 | 77.23 |

**Improvement Scale**

**Figure 8.** Comparison of mechanical efficiency of diesel and DEE blends
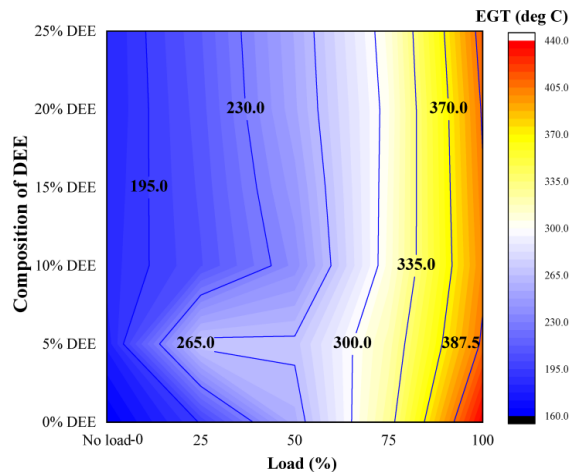
**Figure 9.** Comparison of EGT of diesel and DEE blends

Figure 9 depicts the variation in exhaust gas temperature (EGT) of DEE blends under different loads. From Figure 9, it is observed that the EGT of the diethyl ether blend is lesser than the conventional diesel under medium to high loads (50 to100%). This reduction in exhaust gas temperature of DEE blends could be accredited to the presence of lower calorific value fuel of DEE than diesel fuel.

**Emission Characteristics**

This section discusses the effect of DEE addition in diesel fuel and its various engine exhaust emission parameters like carbon monoxide, carbon dioxide, oxides of nitrogen, and hydrocarbon.

CO emissions in diesel engines are mainly due to inefficient fuel combustion in an oxygen-deficient environment. Figure 10 depicts the variation in Carbon Monoxide (CO) emissions of DEE blends under different loads. Figure 10 shows that CO emissions were decreased with a rise in engine load level. This is because low combustion temperature at load loads contributes to higher CO emissions. However, the scenario is different at high load conditions because the in-cylinder environment is high enough to oxidize carbon monoxide, resulting in reduced CO level than low load conditions.

It can be seen from Figure 10 that CO emissions were lower for increased DEE concentration from 5 to 15% at all load conditions. The inherent oxygen content of DEE promotes CO oxidation, resulting in lower CO emissions compared to conventional diesel fuel. However, Fig.10 shows that CO emissions are elevated at lower loads for all DEE blends compared to high loads. This could be accredited to the latent heat of evaporation of DEE producing a cooling effect that affects the oxidation process resulting in a considerable increase in CO emissions. The fuel-bound oxygen in DEE blends is offset by the latent heat of vaporization of DEE fuel (Sezer 2019). Overall, 10% DEE

exhibits lower CO levels among tested blends at all load conditions.
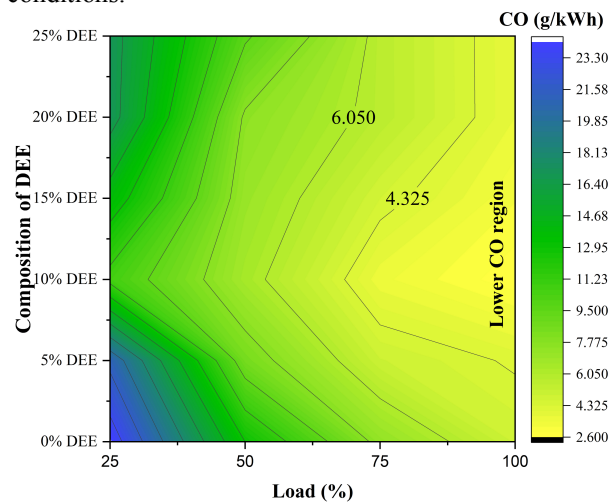


**Figure 10.** Comparison of CO emissions of DEE blends and diesel under different loads

In general, HC emissions from diesel engines are influenced by fuel-air mixing and the physical properties of the fuel. During diesel engine combustion, HC emission mainly forms due to partial or un-burnt fuel. This could be due to flame quenching near cylinder walls, over mixing or under mixing of air-fuel mixtures. Figure 11 represents the variation in hydrocarbon (HC) emissions of DEE blends under different loads. It can be seen from Figure 11 that HC emissions were decreased for all the tested DEE blends compared to diesel fuel up to part loads and identical values and slight variations at high loads. It could be attributed to the cetane number of DEE, which is higher than diesel, resulting in shorter ignition delay and contributing to enhanced combustion (Agarwal et al. 2022).

Furthermore, the oxygen content of DEE oxidizes the HC leading to a lower HC level. Increasing the DEE concentration in diesel fuel decreases the HC up to 10% and then increases at 15 to 25% DEE. Because the higher concentration of DEE produces a cooling effect which affects the HC oxidation. Similar studies (Agarwal et al. 2022a; Dinesha et al. 2019; Iranmanesh et al. 2008 and Lee and Tae 2017) in the literature also reported higher HC with increased DEE. Overall, 10% DEE exhibits a lower HC level among tested blends at all load conditions.
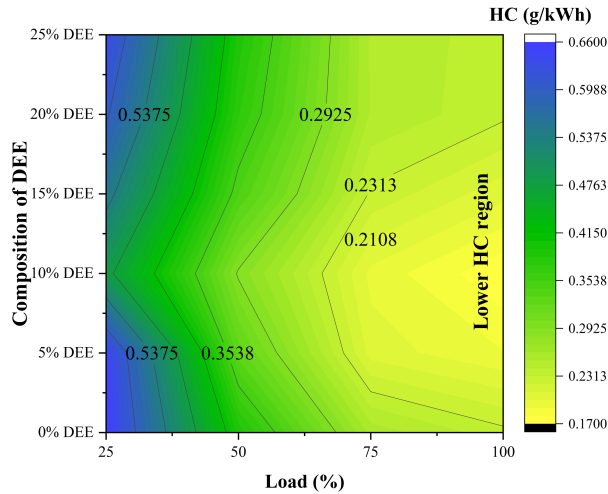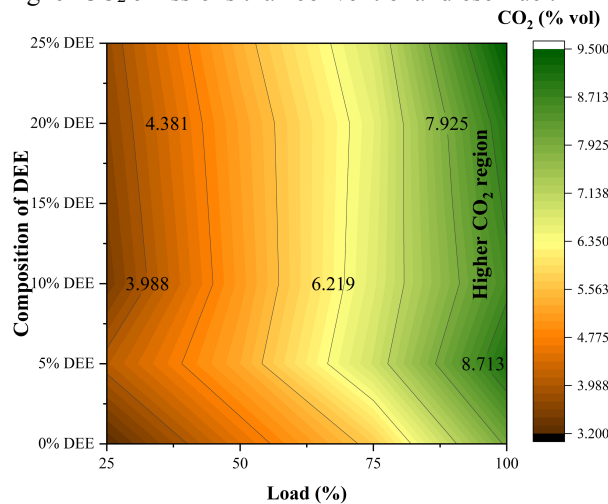
**Figure 11.** Comparison of HC emission of DEE blends and diesel under different loads

Generally, the more fuel the engine burns, the more carbon dioxide is emitted into the atmosphere. Figure 12 depicts the variation in carbon dioxide ($CO_2$) emissions of DEE blends under different loads. Figure 12 shows that $CO_2$ emissions increased with the increase in engine load from no load to full load conditions. Since better in-cylinder environment temperature occurs at elevated loads, enhanced combustion causes greater $CO_2$ level than lower load levels. As the $CO_2$ level increases, there is a betterment of combustion. Figure 12 indicates that $CO_2$ emissions were more significant for all the DEE blends (5 to 15%) under all load conditions because the fuel-bound oxygen of DEE contributes to more efficient combustion, resulting in higher $CO_2$ emissions than conventional diesel fuel.



**Figure 12.** Comparison of $CO_2$ emission of DEE blends and diesel under different loads

In general, NOx formation in diesel engines is influenced by the duration of combustion, oxygen availability, temperature, pressure and increased compression ratios. In the diesel engine, combustion occurs at higher temperatures, causing nitrogen in the air to react with oxygen to form NOx emissions. Furthermore, the spray characteristics, oxygen concentration and adiabatic temperature of fuel blends influenced the exhaust NOx emissions.
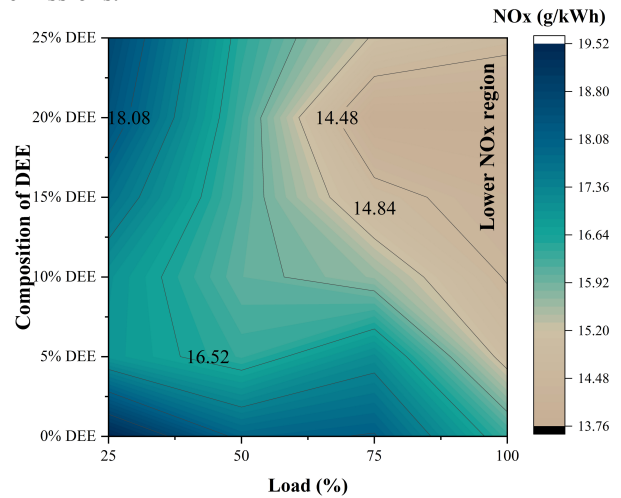


**Figure 13.** Comparison of $NO_x$ emission of DEE blends and diesel under different loads

NOx emission variations of DEE blends under different loads are shown in Figure 13. In general, the thermal NOx effect at increasing loads increasing the combustion temperature led to increased NOx formation level. However, From Figure 13, it is observed that increasing the load from 0 to 100% load decreases the NOx emissions. This could be due to lower NOx emissions per unit brake power output than lower loads. Figure 13 shows that under all load levels, NOx emission of DEE blends is decreased with an increase in blend level from 0 to 15%, and it is also lower than baseline diesel fuel. This could be accredited to the addition of DEE to diesel fuel in which diethyl ether diminishes the combustion temperature since the latent heat of vaporization of DEE is higher than diesel which is beneficial in reducing the combustion temperature. This decreasing NOx trend with increased DEE concentration was corroborated with similar diesel-DEE blend studies (Agarwal et al. 2022a; Sezer 2018; Ibrahim 2018; Firew et al. 2016).

**Response surface methodology (RSM) method**

In general, there will be a greater number of experiments carried out in order to validate the reproducibility and accuracy of the findings. To reduce the number of experiments, an attempt was made to predict engine performance (BTE, BSFC, and mechanical efficiency) and exhaust gas emissions (CO, HC, and NOx) as a function of percentage of engine load and percentage of DEE blends using response surface methodology. Using this method, 3D surface plots (Figures 14 and 15) between the aforementioned variables were created with a fit efficiency between 96% and 100%.
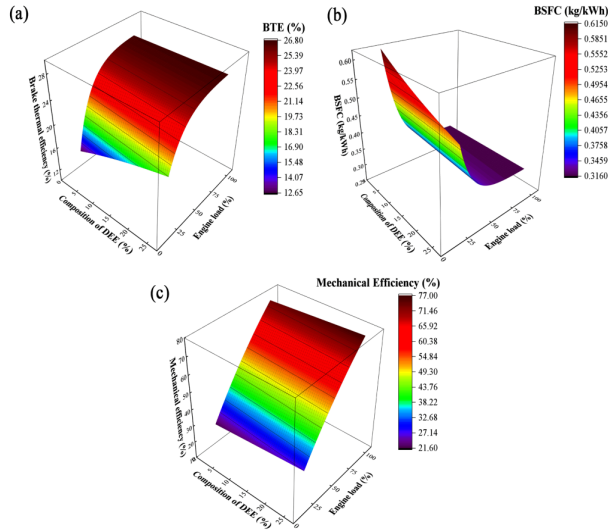
**Figure 14.** Response surface plots of performance characteristics of DEE blends (a) BTE (b) BSFC and (c) Mechanical efficiency

From Figure 14, it is clearly indicated that BTE and mechanical efficiency were higher and BSEC was lower when an engine runs with 25% DEE blends at peak load conditions compared to neat diesel. Similarly, exhaust gas emissions (CO, HC, and NOx) were lower compared to neat diesel, as shown in Figure 15. An optimized injection pressure of 210 bar and 15% DEE blends show a significant rise in engine performance as well as reduced emissions.
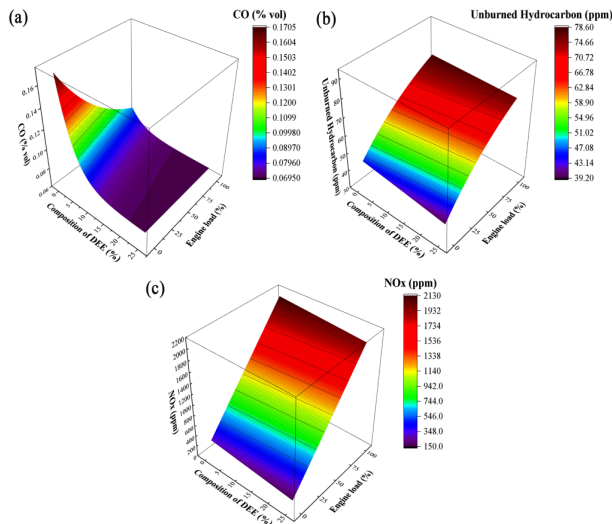


**Figure 15.** Response surface plots of emission characteristics of DEE blends (a) CO (b) HC and (c) NOx

A polynomial 2D exponential fit equation was generated using the fit surface, and the same is given in Eq. 2. The surface equation was used to predict engine performance (BTE, BSFC, and mechanical efficiency) and exhaust gas emissions (CO, HC, and NOx) for different engine loads (%) and DEE blend compositions (%). Using this

expression, one can determine the engine parameters with respect to the engine load (%) and composition of DEE blends.

$$Z = Z_o + \left\{ B \left( \exp\left(\tfrac{-X}{C}\right)\right) \left( \exp\left(\tfrac{-Y}{D}\right)\right)\right\} \qquad (2)$$

**Percentage variations comparison of DEE blends with baseline diesel**

The Percentage variations of Performance and emissions of DEE blends compared to pure diesel fuel, as given in Table 6. BTE is highest at a 25% DEE for all loads, having 25.9% improvement 25.9% over pure Diesel fuel. When employing 20% DEE at varied loads, NOx shows a reduction of up to 24% than diesel. DEE at 10% shows significant reduction of HC and CO among other blends across loads. Reduced by a maximum of 26.9% at 100% for HC and 64.8% at 25% load for CO.

**Table 6.** Percentage variations of Performance and emissions of DEE blends compared to pure diesel fuel (-) denotes percentage decrement

| Performance & emission parameters | Load (%) | Fuel blends | | | | |
|---|---|---|---|---|---|---|
| | | 5% DEE | 10% DEE | 15% DEE | 20% DEE | 25% DEE |
| BTE (%) | 25 | 10.7 | 19.9 | 19.6 | 19.3 | 23.7 |
| | 50 | 13.8 | 14.1 | 16.0 | 17.9 | 25.9 |
| | 75 | 5.5 | 9.7 | 11.5 | 13.4 | 19.1 |
| | 100 | 3.6 | 4.3 | 7.8 | 11.3 | 18.0 |
| NOx (g/kWh) | 25 | -13.1 | -12.7 | -9.2 | -5.7 | -4.2 |
| | 50 | -8.7 | -10.5 | -9.9 | -9.2 | -8.2 |
| | 75 | -5.3 | -13.6 | -18.8 | -24.0 | -16.4 |
| | 100 | -8.3 | -11.7 | -13.5 | -15.4 | -10.3 |
| HC (g/kWh) | 25 | -1.5 | -26.1 | -16.4 | -8.3 | -3.6 |
| | 50 | -16.1 | -25.9 | -12.2 | -4.0 | 0.0 |
| | 75 | -20.0 | -23.5 | -11.2 | -3.0 | -3.2 |
| | 100 | -18.7 | -26.9 | -13.1 | -0.4 | 0.5 |
| CO (g/kWh) | 25 | -30.3 | -64.8 | -54.2 | -43.6 | -43.6 |
| | 50 | -34.1 | -49.9 | -45.7 | -41.6 | -25.0 |
| | 75 | -32.6 | -51.5 | -36.9 | -22.4 | -22.5 |
| | 100 | -12.9 | -45.0 | -33.8 | -22.5 | -22.7 |

**Conclusions**

This study evaluated an air-cooled agricultural diesel engine with various DEE-to-diesel mixtures. The conclusions can be summarized as follows:

- The 210-bar injection pressure was found to be optimal for the DEE blends.
- The higher proportion of DEE blends under increasing loads enhanced the brake thermal efficiency and specific fuel consumption

compared to diesel fuel. The maximum BTE was noted for the 25% DEE blends at rated loads.

- Increasing DEE blends improved the mechanical efficiency at all load levels.
- For all load levels, all the DEE percentages lowered CO, NOx, and HC emissions compared to pure diesel fuel. Expect the HC emission of 25% DEE blend.
- By increasing the DEE blend in diesel fuel by up to 20%, NOx and CO emissions are reduced. In contrast, HC lowers the DEE blend up to 15%.
- Among the assessed mixtures, when evaluating the balance between brake thermal efficiency (BTE) and emissions, the use of a 15% DEE blend and optimizing the injection pressure to 210 bar led to a significant 10% enhancement in thermal efficiency and a 5% reduction in emissions.

## References

Agarwal, Avinash Kumar, & Krishn Chandra. (2022). Di-ethyl ether-diesel blends fuelled off-road tractor engine: Part-I: Technical feasibility. *Fuel,* 308: 121972. https://doi.org/10.1016/j.fuel.2021.121972.

Agarwal, Avinash Kumar, Hardikk Valera, & Nirendra Nath Mustafi. (2022). Di-ethyl ether- diesel blends fuelled off-road tractor engine: Part-II: Unregulated and particulate emission characteristics. *Fuel,* 308: 121973. https://doi.org/10.1016/j.fuel.2021.121973.

Ali, Obed M., Rizalman Mamat, Haji Hassan Masjuki, & Abdul Adam Abdullah. (2016). Analysis of blended fuel properties and cycle-to-cycle variation in a diesel engine with a diethyl ether additive. *Energy Conversion and Management,* 108: 511-519. https://doi.org/10.1016/j.enconman.2015.11.035.

Carvalho, Márcio, Felipe Torres, Vitor Ferreira, Júlio Silva, Jorge Martins, & Ednildo Torres. (2020). Effects of diethyl ether introduction in emissions and performance of a diesel engine fueled with biodiesel-ethanol blends. *Energies,* 13(15): 3787. https://doi.org/10.3390/en13153787.

Dinesha, P., Shiva Kumar, & Marc A. Rosen. (2019). Combined effects of water emulsion and diethyl ether additive on combustion performance and emissions of a compression ignition engine using biodiesel blends. *Energy,* 179: 928-937. https://doi.org/10.1016/j.energy.2019.05.071.

Dinesha, P., Shiva Kumar, & Marc A. Rosen. (2019). Combined effects of water emulsion and diethyl ether additive on combustion performance and emissions of a compression ignition engine using biodiesel blends.

*Energy,* 179: 928-937. https://doi.org/10.1016/j.energy.2019.05.071.

Emaish, Haitham, Khamael M. Abualnaja, Essam E. Kandil, & Nader R. Abdelsalam. (2021). Evaluation of the performance and gas emissions of a tractor diesel engine using blended fuel diesel and biodiesel to determine the best loading stages. *Scientific Reports,* 11(1): 9811. https://doi.org/10.1038/s41598-021-89287-0.

Firew, Deresse, N. Ramesh Babu, & Mukesh Didwania. (2016). The performance evaluation of diethyl-ether (DEE) additive with diesel blends using diesel engine test rig. *International Journal of Scientific & Engineering Research,* 7(6): 23-29.

Gainey, Brian, & Benjamin Lawler. (2021). The role of alcohol biofuels in advanced combustion: An analysis. *Fuel,* 283: 118915. https://doi.org/10.1016/j.fuel.2020.118915.

Göktaş, Meltem, Mustafa Kemal Balki, Cenk Sayin, & Mustafa Canakci. (2021). An evaluation of the use of alcohol fuels in SI engines in terms of performance, emission and combustion characteristics: A review. *Fuel,* 286:119425. https://doi.org/10.1016/j.fuel.2020.119425.

Górski, Krzysztof, & Marcin Przedlacki. (2014). Evaluation of the influence of diethyl ether (DEE) addition on selected physicochemical properties of diesel oil and ignition delay period. *Energy & Fuels,* 28(4): 2608-2616. https://doi.org/10.1021/ef4025036.

Nanthagopal, K., B. Ashok, Raghuram Srivatsava Garnepudi, Kavalipurapu Raghu Tarun, & B. Dhinesh. (2019). Investigation on diethyl ether as an additive with Calophyllum Inophyllum biodiesel for CI engine application. *Energy Conversion and Management,* 179: 104-113. https://doi.org/10.1016/j.enconman.2018.10.064.

Huse, Cristian. (2018). Fuel choice and fuel demand elasticities in markets with flex-fuel vehicles. *Nature Energy,* 3(7): 582-588. https://doi.org/10.1038/s41560-018-0175-3.

Ibrahim, Amr. (2016). Investigating the effect of using diethyl ether as a fuel additive on diesel engine performance and combustion. *Applied Thermal Engineering,* 107: 853-862. https://doi.org/10.1016/j.applthermaleng.2016.07.061.

Ibrahim, Amr. (2018). An experimental study on using diethyl ether in a diesel engine operated with diesel-biodiesel fuel blend. *Engineering science and technology, an international journal,* 21(5): 1024-1033. https://doi.org/10.1016/j.jestch.2018.07.004.

Iranmanesh, Masoud, J. P. Subrahmanyam, & M. K. G. Babu. (2008). Potential of Diethyl ether as supplementary fuel to improve combustion and emission characteristics of diesel engines. F*uel,* 1: 7. https://doi.org/10.4271/2008-28-0044.

Jawre, Sandip S., Amit Bhagat, Sachin M. Moghe, & Vikram A. Pakhale. (2016). Diethyl ether as additive and its effect on diesel engine performance-a review. *Global Research and Development Journal for Engineering,* 1(5): 27-31.

Lee, Seokhwan, & Tae Young Kim. (2017). Performance and emission characteristics of a DI diesel engine operated with diesel/DEE blended fuel. *Applied Thermal Engineering,* 121: 454-461. https://doi.org/10.1016/J.APPLTHERMALENG.2017.04.112.

Mofijur, M., M. G. Rasul, J. Hyde, & M. M. K. Bhuyia. (2015). Role of biofuels on IC engines emission reduction. *Energy Procedia,* 75: 886-892. https://doi.org/10.1016/j.egypro.2015.07.211.

Nanthagopal, K., R. Susanth Kishna, A. E. Atabani, H. Ala'a, Gopalakrishnan Kumar, & B. Ashok. (2020). A compressive review on the effects of alcohols and nanoparticles as an oxygenated enhancer in compression ignition engine. *Energy Conversion and Management* 203:112244.
https://doi.org/10.1016/j.enconman.2019.112244.

Negi, Himani, & Raj Kumar Singh. (2020). A review on lignin utilization in petroleum exploration, petroleum products formulation, bio-fuel production, and oil spill clean-up. *Biomass Conversion and Biorefinery,* 1-12. https://doi.org/10.1007/s13399-020-01126-w.

Prabakaran, Rajendran, G. Manikandan, P. Somasundaram, Poongavanam Ganesh Kumar, Mohammad Salman, C. Jegadheesan, & Sung Chul Kim. (2022). Feasibility of tea tree oil blended with diethyl ether and diesel as fuel for diesel engine. *Case Studies in Thermal Engineering,* 31: 101819. https://doi.org/10.1016/j.csite.2022.101819.

Praveen, R, & Natarajan, S. (2014). Experimental study of selective catalytic reduction system on CI engine fuelled with diesel-ethanol blend for NOx reduction with injections of urea solutions. *International Journal of Engineering and Technology*, 975(4024): 895-904.

Praveen, R & Vivek, S. (2014). Experimental study on macroscopic spray characteristics in a direct injection diesel engine. *International Journal of Applied Engineering Research*, 9(22): 7633-7637.

Rakopoulos, D. C., C. D. Rakopoulos, E. G. Giakoumis, & A. M. Dimaratos. (2013). Studying combustion and cyclic irregularity of diethyl ether as supplement fuel in diesel engine. *Fuel,* 109: 325-335. https://doi.org/10.1016/j.fuel.2013.01.012.

Rami Reddy, S., G. Murali, & V. Dhana Raju. (2022). "Assessment of diethyl ether as a fuel additive on the diverse characteristics of diesel engine powered with waste mango seed biodiesel blend. *International Journal of Ambient Energy,* 43(1): 3365-3376. https://doi.org/10.1080/01430750.2020.1824944.

Sezer, İsmet. (2018). A review study on the using of diethyl ether in diesel engines: Effects on NOx emissions. *International Journal of Automotive Engineering and Technologies,* 7(4): 164-183.

Sezer, İsmet. (2019). A review study on the using of diethyl ether in diesel engines: Effects on CO emissions. *International Journal of Automotive Science and Technology,* 3(1): 6-20. https://doi.org/10.30939/ijastech..507799.

Subramanian, K. A., & A. Ramesh. (2002). Use of diethyl ether along with water-diesel emulsion in a DI diesel engine. *SAE Transactions,* 1361-1367.

Unglert, Martin, Dieter Bockey, Christine Bofinger, Bert Buchholz, Georg Fisch, Rolf Luther, Martin Mueller et al. (2020). Action areas and the need for research in biofuels. *Fuel,* 268 : 117227. https://doi.org/10.1016/j.fuel.2020.117227.

# EXPERIMENTAL STUDY OF DELAYING THE STALL OF THE NACA 0020 AIRFOIL USING A SYNTHETIC JET ACTUATOR ARRAY WITH DIFFERENT ORIFICE GEOMETRIES

**Esra TÜREN\*, Hakan YAVUZ\***
**\*** Çukurova University Engineering Faculty, Mechanical Engineering Department 01330, Adana, TURKEY
essraturen@gmail.com,  ORCID: 0000-0002-2863-6444
hyavuz@cu.edu.tr,  ORCID:  0000-0002-6166-0921

**Abstract:** An experimental study on the effect of active flow control using a synthetic jet mechanism on stall delay for the NACA 0020 airfoil is conducted. The experiments are carried out at an open-suction type wind tunnel at Reynolds number $5 \times 10^4$. In the presented experimental study, aerodynamic force measurements of the airfoil with having different orifice geometries (cylindrical, rectangular, sinusoidal, v-type, inclined rectangular) are examined by using a speaker type actuator in synthetic jet mechanism. It is observed that all different orifice geometries are effective in delaying the stall angle of NACA 0020 airfoil. However, it is observed that the inclined rectangular type of synthetic jet geometry is the most advantageous in delaying the stall of the airfoil. The effects of geometric parameters of the actuator on lift and drag coefficient of the NACA0020 airfoil are investigated. Experimental results show that among the all-orifice geometries the rectangular orifice geometry is the most effective in increasing lift coefficient of the airfoil. It is observed that there is a maximum decrease in drag at 10° where the stall occurs. In addition, the decrease in drag is observed after 10° in rectangular, v-type and inclined rectangular orifice geometries.
**Keywords:** Active flow control, synthetic jet, NACA0020 airfoil, drag and lift coefficient, stall shifting

## FARKLI DELİK GEOMETRİSİNE SAHİP SENTETİK JET AKTÜATÖR DİZİSİ KULLANARAK NACA 0020 HAVA FOLYOSUNUN DURUŞUNUN GECİKTİRİLMESİNE YÖNELİK DENEYSEL ÇALIŞMA

**Özet:** NACA 0020 kanat profili üzerinde sentetik jet mekanizması için aktif akış kontrolünün stall gecikmesi üzerindeki etkisi hakkında deneysel bir çalışma gerçekleştirilmiştir. Deneyler 5x104 Reynolds sayısında açık emişli tip rüzgar tünelinde gerçekleştirilmiştir. Sunulan deneysel çalışmada, sentetik jet mekanizmasında hoparlör tipi bir aktüatör kullanılarak farklı orifis geometrilerine (silindirik, dikdörtgen, sinüzoidal, v-tipi, eğimli dikdörtgen) sahip kanadın aerodinamik kuvvet ölçümleri incelenmiştir. Tüm farklı orifis geometrilerinin NACA 0020 kanadının stall açısını geciktirmede etkili olduğu gözlemlenmiştir. Ancak eğimli dikdörtgen tip sentetik jet geometrisinin kanadın stall açısını geciktirmede en avantajlı olduğu gözlemlenmiştir. Aktüatörün geometrik parametrelerinin NACA0020 kanadının kaldırma ve sürükleme katsayısı üzerindeki etkileri araştırılmıştır. Deneysel sonuçlar, tüm delikli geometriler arasında dikdörtgen delikli geometrinin kanadın kaldırma katsayısını arttırmak için en etkili olduğunu göstermektedir. Stall' un meydana geldiği 10°'de sürüklemede maksimum azalma olduğu gözlemlenmiştir. Ayrıca dikdörtgen, v-tipi ve eğimli dikdörtgen orifis geometrilerinde 10°'den sonra sürüklemede azalma olduğu gözlenmiştir.
**Anahtar Kelimeler:** Aktif akış kontrolü, sentetik jet, NACA0020 kanat profili, sürükleme ve kaldırma katsayısı, durma kayması

## NOMENCLATURE

$F_L$    Lift force
$F_D$    Drag force
$C_D$    Drag coefficient
$C_L$    Lift coefficient
D    Diameter of the cylinder [mm]
$\rho$    Fluid density [kg/m³]
$\mu$    Fluid dynamic viscosity [kg/(m.s)]
Re    Reynolds number [$=U_0\rho D/\mu$]
$U_0$    Free stream velocity [m/s]
A    Airfoil area [mm²]

f    Excitation frequency [kHz]

## INTRODUCTION

Throughout history, people have experimented with the dream of flying through the air. With the beginning of human flight in the 18th century, many researchers tried to increase the lift force and reduce the drag force by making changes to the aircraft's structure and configuration, aiming to improve the aerodynamic performance of the system Therefore, the flow control applications are used to delay or prevent undesirable situations occurring in the flow. The aerodynamic flow control is initially defined by Gad-el-Hak (2000) as a method of appropriately changing the natural shape or character of a desired section of a flow field. The flow control methods cause changes in many factors such as increase in lift, decrease in drag, delaying flow separation etc. contributing to its aerodynamic performance.

Mainly, the flow control methods are classified as active and passive methods (Genç et al. 2012; Joshi and Gujarathi, 2016). The active or passive flow control methods aim to change the flow field on an aerodynamic body by using various techniques (Traub et al. 2004). The passive control technique is a method that does not require any external power. For example, vortex generators, roughness, hump, groove and tip blade type airfoil modification are defined as passive flow control methods. Since passive flow control methods do not utilize an external power, they cannot adjust the components that change according to variable flow conditions, such as different angles of attack and Reynolds numbers, under desired conditions. The active flow control techniques are methods that require an additional power source. The active flow controllers have many advantages in terms of increasing efficiency in obtaining data at the right time and reducing power consumption of control systems. The biggest advantage compared to passive flow control methods is that they can adjust actuators according to the changing variables in the desired conditions. The piezoelectric, acoustic (loudspeaker) and piston-cylinder mechanisms are used as actuators in synthetic jet, which is one of the active flow control applications. Mallinson et al. (2004), a piezoelectric diaphragm and a speaker created using a piston-cylinder mechanism as the moving surface were investigated. Frequency and amplitude variation types of actuators such as piston cylinder, speaker and piezoelectric diaphragm have generally been created for such purposes. In the piston-cylinder mechanism, the frequency is lower and the amplitude is larger. However, in piezoelectric diaphragms the frequency is high and the amplitude is very low. The advantage of the speaker is about its fast response time and controllability as a synthetic jet mechanism, which is preferred in flow control applications. Zhao et al. (2016) investigated experimentally using speakers as actuators in synthetic jet arrays. As a result of this experimental study, it is seen that synthetic jet arrays are effective in delaying the flow separation. It is also observed that it contributes to delaying the airfoil stalling. Pulsed jet is an unstable type

of a jet. Because they need an additional flow source and produce instantaneous high velocity in the exit gap. Pulsed jets can be created as fast-acting solenoid valves, high-speed rotary sounder valves or structures with rotating cavities (Critten et al, 2001). Fibre composite materials occur by changing the shape of airfoil. It contributes to improving aerodynamic performance in different flight conditions. However, the morphing aircraft wings created with fibre composite materials always have disadvantages in terms of cost, complexity or weight (Barbarino et al., 2011) In their study, Ahuja and Burrin (1984) used it to control the flow of signal generation in a given Reynolds number and angle of attack for specific frequency generation in an audio source connected to an amplifier. The synthetic jets, which are one of the active flow control methods, attract the attention of researchers because of their wide application area. The Synthetic jet mechanisms are used for many different purposes such as heat transfer (Youmin et al. 2014), mixing vessels (Qingfeng et al. 2013), cooling of electronic devices (Chaudhari et al. 2010), separation control in aircraft wings (Gillarranz et al. 2005), (Holman et al. 2003), increase in lift (Kim a Kim, 2009), reduction in friction force (He et al. 2001), boundary layer control (You and Moin. 2008) and stall control (Yen and Ahmed 2012). An important advantage of the synthetic jet mechanism is that it has a simple working principle in which the liquid is sucked and blown by the forward and backward movement of the cavity diaphragm in an open pipe or channel. In the periodic flow movement that occurs here, the fluid forms a vortex ring in the cavity during blowing. This vortex ring spreads outward at its own speed. During suction, this liquid is drawn back into the cavity. By repeating this periodic motion, synthetic jets are formed.

Studies of synthetic jet mechanisms began in the 1950s with the study of acoustic flow by Ingard and Labate (1950). Later, as synthetic jet studies became more widespread as studies in this field expanded in the late 20th century. Smith and Glezer (1998) carried out extensive studies on this subject and introduced the term 'Synthetic Jet' to the literature. After the 21st century, numerical and experimental studies on the structures of synthetic jets have become widespread (Trávníček 2005). The use of loudspeakers in synthetic jets is preferred because it is easy to integrate into the system and has a short response time. The synthetic jet mechanism is affected by the actuator, its geometric form and related fluid parameters (Hong, 2020). Zhang et al., (2015) numerically examined the frequency variation of the actuator parameters of the synthetic jet mechanism. In the models created in their study, it was observed that the heat transfer has increased with the increase in the frequency. Feero et al. (2015) examined the effect of jet structure in the orifice of a change in the diaphragm cavity. In this study, the performance of cylindrical, conical and curvilinear contraction structures in the cavity structure of the diaphragm was investigated. As a result of the study, it was observed that the cavity oscillation had the best performance in the curvilinear cavity. Although the synthetic jet mechanism is relatively

new active flow control method, it has been observed that it is an effective method in many areas such as flow separation around the wing, shifting the stall angle, and increase in lift and decrease in drag. In a study by Seifert et al. (1996), a synthetic jet mechanism, which is one of the active flow control applications, was used for the NACA 0015 airfoil. In this study, it reported that synthetic jet mechanism was effective in delaying the stall. Hassan (2006) numerically investigated the stall control in a two-actuated jet array used in the airfoil. As a result of the study, it is determined that when the existing two-point hybrid active flow control strategy is used instead of a single point at a certain angle of attack of the airfoil in the jet array, the improvement post-stall lift-drag ratio. Amitay et al. (2001) investigated flow separation using synthetic jet actuators on a symmetrical airfoil. It has been observed that the momentum required to recombine the separated air decreases as the actuator approaches the separation point. Zhang and Zhong (2009) observed flow control in water by creating a series of circular synthetic jet structures in the airfoil. In their study, a laser-induced fluorescence was used for flow visualization. It has been determined that in separated flow, flow separation occurs in two or three high flow velocity lines.

Collins and Zelenevitz (1975) studied the Reynols number between 25000 and 53000 using a synthetic jet mechanism in an airfoil. A loudspeaker was placed on the surface of the airfoil. The experiments were performed by generating a constant sound wave until partial bonding occurred. As a result of the experiments, it was observed that the lift greatly increased as the amplitude value of the acoustic stimulation increased. Zaman and McKinzie (1991) studied the acoustic effect in a two-dimensional airfoil with Reynolds number between 25 000 and 100 000. The Smoke wire flow visualization and hot-wire anemometry were used to support the experimental setup. In addition, in this study, frequency variation was investigated by keeping the excitation amplitude constant. In the experimental results, it is observed that there is an increase in the $C_L$ lift coefficient. Yarusevych et al. (2003) studied acoustic excitation in a NACA 0025 airfoil at Reynolds numbers 57 000, 100 000 and 150 000 and at three different angles of attack (0, 5 and 10 degrees). In the study, a hot wire anemometer was used for velocity measurements. As a result of the experiment, it was observed that the optimum frequency and amplitude values of acoustic stimulation varied depending on the Reynolds number and attack angles. Guaqing et al. (2016) experimentally investigated the NACA 0025 airfoil on the airfoil using the synthetic jet mechanism from the active flow control method. In this study, they examined the effect on synthetic jet locations. In addition, the effect of the angle change in the synthetic jet inlet was investigated. As a result, jets located close to the front of the airfoil were more advantageous in delaying the stall. In addition, it has been determined that the performance of jet arrays in flow control application is more effective than single actuator performances. Moreover, it has been observed that the aerodynamic performance of the lifting force has been improved.

In this study, one of the active flow control applications is used to examine the flow control effects of Reynolds number 50 000 on the NACA 0020 airfoil in a synthetic jet mechanism using a loudspeaker as an actuator. In addition, in this study, it is aimed to investigate the contribution of the flow control around the airfoil of the orifice jet geometries named in five different structures as cylindrical, rectangular, sinusoidal, V-type and inclined rectangular. The experimental study is carried out in an open suction wind tunnel. It is aimed that different orifice jet geometries can shifting the stall angle formed on the airfoil and contribute to aerodynamic properties such as improvements in drag, lift force and stall.

## EXPERIMENTAL SETUP

### Airfoil Model and Synthetic Jet Design

In this study, 40 mm loudspeakers are used as the synthetic jet mechanism as shown in Figure 1. In this experimental study, five different models are selected to examine the effects of the jet structures in different orifice geometries of the synthetic jet mechanism. The orifice models of the synthetic jet mechanism are determined as circular, rectangular, sinusoidal, V-type and inclined rectangular. The circular (Lee et al. 2012 and Zhao et al. 2016) and rectangular (Abdou et al. 2006) orifices are used in the literature. In addition, three new different geometries are also used as namely as sinusoidal, V-type and inclined rectangular to control the flow around the airfoil. Figure 2 shows orifice geometries in different geometries. When Guoqing et al. (2016) examined the position of the synthetic jet mechanism in their study; maximum lift coefficient and stall were observed when it was close to the leading edge. In this study, considering the airfoil and the dimensions of the speaker, it is positioned at approximately %21 of the chord as the closest position to the leading edge.
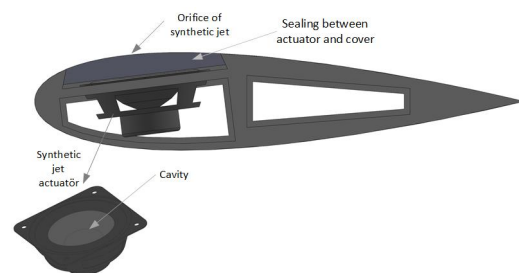


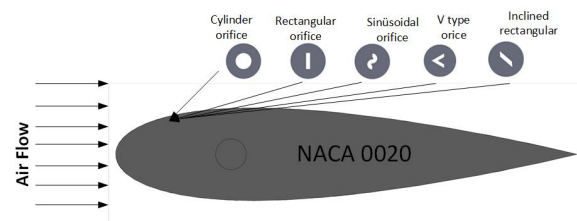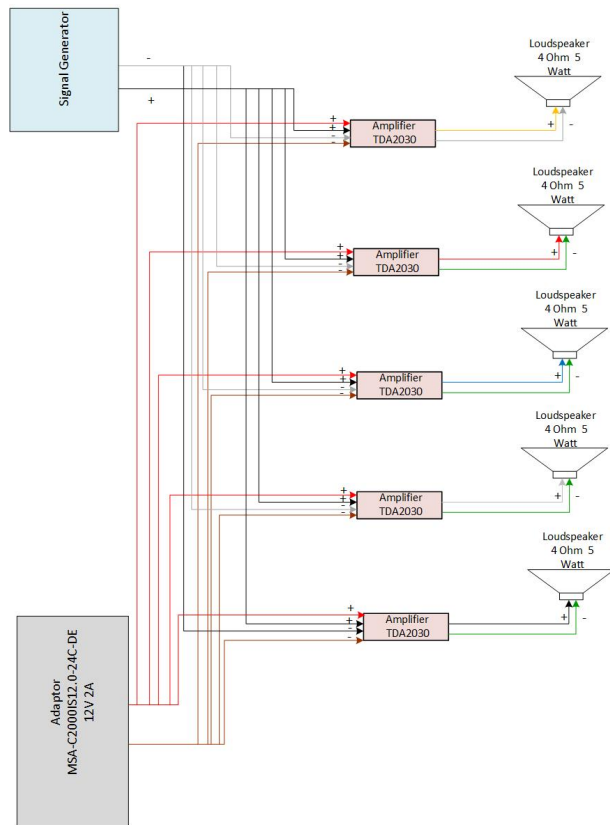**Figure 1.** Assembly of the jet actuator in the airfoil model

**Figure 2.** Design of 5 different orifice geometric models in a synthetic jet actuator



**a.**



**b.**                                    **c.**

**Figure 3**. The loudspeaker used as the actuator in the synthetic jet mechanism **a.** Systematic wiring diagram **b.** Connection equipment in the experimental setup **c.** Illustration of each connection of the speaker actuator

In the study of Paula et al. (2017), NACA0012, NACA0020 and NACA0030 airfoils were examined at low Reynolds number (MAV and UAV operating conditions). As a result of the study, it was seen that although the profile drag increases as the wing thickness increases in airfoil design, thicker airfoils are more suitable in terms of maximum lift values. In the light of this study, the selection of the NACA 0020 airfoil model was also made by taking into account the dimensions of the actuator, the assembly of the actuator arrays and the location of the actuators at low Reynolds number (MAV and UAV operating conditions). NACA 0020 airfoil model is designed with a span length of 300 mm and a chord length of 150 mm. In design of the wind, five 40 mm-long speakers, are used as synthetic jet actuator

array, are placed on the airfoil profile at equal intervals. Figure 3a shows the loudspeaker electrical connection diagram. Figure 3b shows the connection of the system to the computer and the Arduino. In Figure 3c, each connection of the loudspeaker actuator is numbered. In Figure 3c, all green, and white cables were connected to the "-" output of each amplifier for speaker connection in connections 1, 2, 3, 4, and 5, respectively. Black, white, blue, red and yellow 22 AWG cables were connected to the "+" output respectively. Connection cable number 6 is brown coloured to the "-" output of the adapter, and a red cable is connected to the "+" output. Arduino Uno is used as the signal driver in the speaker connection circuit. The circuit is completed by connecting a grey cable to the GND input at connection number 7 and a white cable to pin number 10. In order to prevent the amplifiers from overheating, a 12V 2A fan has been added to the system. Finally, the operating frequency of the experiment (Türen and Yavuz, 2023) is created at 2, 4 and 8 Hz, with a constant pulse width of 1%.

The NACA 0020 airfoil is selected, taking into account the size of the actuator and the placement of the actuator arrays in the airfoil model. The NACA 0020 airfoil is designed by taking the chord length as 150 mm and the span length as 300 mm. The first design of the NACA 0020 aircraft wing is modelled in the Computer Aided Design (CAD) software, as seen in Figure 4.
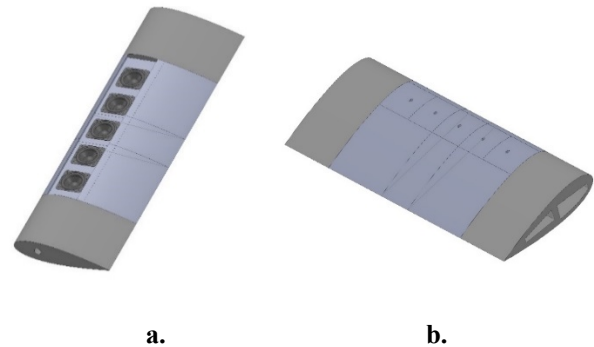


**a.**                                    **b.**

**Figure 4. a.** Loudspeaker placement image of NACA 0020 airfoil in CAD software **b.** Image of top cover designs of NACA 0020 airfoil in CAD software

Then, the parts of the designed airfoil profile are produced by using a Three-Dimensional Printer (3D printer). There are parts of the airfoil as seen in Figure 5. After the airfoil model is produced on a 3D printer, its surface is first sanded with P320 sandpaper. Then, polyester body filler is applied to the model surface and the airfoil is mounted. The model surface is finally sanded smooth with P2000 sandpaper. Finally, the smoothness is achieved by painting the model. Table 1 shows the parameters of the airfoil in the experiment and the loudspeaker used as a synthetic jet actuator.
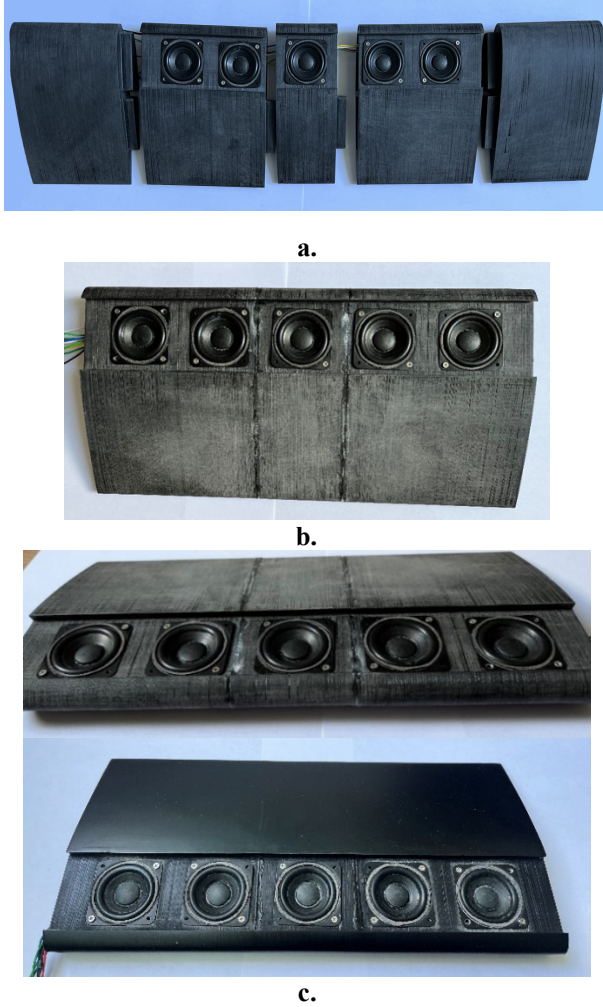
**Figure 5.** NACA 0020 airfoil a. Pre-assembly view of loudspeakers and cables b. Assembled top view c. Assembled side view and airfoil assembly image without slides

**Table 1.** Parameters of airfoil and jet actuator

| PARAMETERS | VALUE |
|---|---|
| **Chord x Span (mm)** | 150 x 300 |
| **Width x lenght of jet orifice (mm)** | 0.5 x 2 |
| **Size of jet actuator (mm³)** | 40 x 40 x 18 |
| **Resistance of actuator (Ω)** | 4 |
| **Rated power of actuators (W)** | 5 |

## Wind Tunnel

The experiments are carried out in the wind tunnel located in the Aerodynamics Research Laboratory of Niğde Ömer Halisdemir University, Department of Mechanical Engineering. This wind tunnel is an open suction type wind tunnel with the test section having a cross section of 570 mm x 570 mm and a length of 1000 mm. The experiments on flow control around the NACA 0020 airfoil are carried out in a wind tunnel at a Reynolds number of 50000 and a free stream speed of 6.2 m/s.

Starting from the entrance of the test area in the wind tunnel, speed scanning is carried out in horizontal and vertical directions using a hot wire anemometer (Dantec Multichannel CTA and 55P11 probe). Turbulence intensity is found to be around 0.5% in the region outside the boundary layer region where uniform velocity distributions are obtained. The experimental setup of the wind tunnel is shown in Figure 6. NACA 0020 The chord length and span length of the airfoil are defined as 150 and 500 mm, respectively. Two end plates are used and their diameter is chosen as 300 mm. The wing profile is mounted in the wind tunnel section made of Plexiglas material.
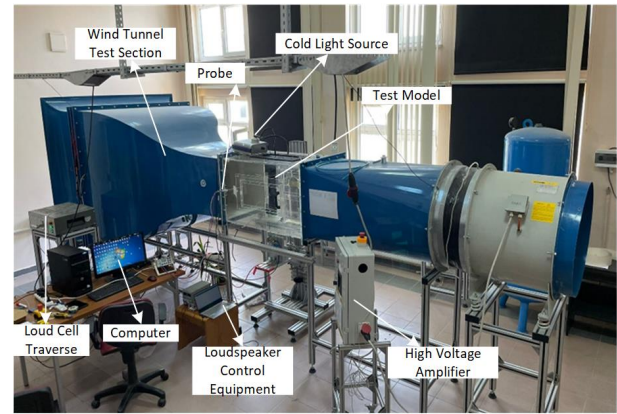


**Figure 6.** Wind tunnel experimental setup

In the 3D printer, the main body of the airfoil model is produced from PLA+ filament with 1.75 mm diameter. In addition, end plates made of Plexiglas material is added to the two ends of the airfoil model and the whole model is assembled. As seen in Figure 7, the airfoil is placed vertically on the test setup in the wind tunnel.

**Force Measurement**

ATI Gamma model six-axis load force is used to measure the drag and lift force of the test model. It is mounted on a computer-controlled rotating unit to measure the angle of attack of the test model. Measurements are taken at a sampling frequency of 300 Hz and the average of every 100 measurements is taken to record 3 measurements per second. The measurements lasted 25 seconds and 2500 data are taken for each experiment. These experiments are repeated twice in each experimental session. Angle of attacks for the force measurement is varied between 0° and 18° with an increment of 1°. Uncertainty for the force measurement is calculated to be lower than ±3%. The experiments are repeated and hence the error rate is minimized. To determine the net forces acting on the airfoil, the connection plates between the end plates, retaining rod and model are subtracted from the total force. Considering the interface effect, the forces acting on the retaining rod and the lower end plate are measured together. The test model, consisting of the upper end plates, the airfoil model and the connecting elements between the model, the bottom end plate and the retaining rod, is prepared and mounted in the test section of the wind tunnel. As a result of these measurements, the force

acting on the lower end plate is calculated. The force acting on the bottom end plate is also considered as the force acting on the upper end plate. As a result of these experimental studies, the net force acting on the airfoil is determined based on the interface effect. These experimental steps are repeated for all angles of attack. Lift force was defined as

$$F_L = \frac{1}{2}\rho . U_0^2 A . C_L \tag{1}$$

$\rho$ is the density of the fluid flowing in the tunnel, $U_0$ is the free stream velocity of the fluid flowing in the tunnel, A is the upper airfoil area, $C_L$ is the lift coefficient. Drag force is defined as,

$$F_D = \frac{1}{2}\rho . U_0^2 A . C_D \tag{2}$$

$\rho$ is the density of the fluid flowing in the tunnel, $U_0$ is the free stream velocity of the fluid flowing in the tunnel, A is the area, $C_L$ is the drag coefficient.



**Figure 7.** The vertical view of the airfoil in the wind tunnel

**EXPERIMENTAL RESULT**

In this study, the effect of drag and lift force of 5 synthetic jet actuators placed linearly along the NACA 0020 aircraft wing is examined. Aerodynamic force measurements are made at 50000 Reynolds number (with ±4% uncertainty). Mueller (1999) described MAVs and UAVs as being compatible with flow conditions in this Reynolds number range. The operating frequency applied in the experiment is examined at 2, 4 and 8 Hz using a total of 5 loudspeakers of 4 ohms and 5 Watts. Jet outlets with 2 mm orifice lengths are examined in cylindrical, rectangular, sinusoidal, v-type and inclined rectangles. As reported by Türen and Yavuz (2023), as a result of the experiments conducted at 4 Hz with a fixed pulse width ratio of 1%, flow structures with different orifice geometries are formed at the best flow jet exits. As reported by Genç et all. (2016), the force measurement are measured at 2 ° intervals. Post-stop measurements are made in 1° increments to obtain the

necessary data. In this study, in force measurement experiments, lift and drag coefficients are measured at 50000 Reynolds number, between 0°-18° angle of attack, with a 1° measurement interval. Force measurements are made with the loudspeaker on and the loudspeaker off. In these experiments, lift and drag coefficients in different jet geometries and their effects on stall characteristics are investigated by using the loudspeaker as an actuator. The lift ($C_L$) and drag ($C_D$) coefficients are calculated and plotted for the attack angle α of the airfoil. In Figure 8, the lift and drag forces on the NACA 0020 airfoil are measured when the loudspeakers are turned off. To provide a reference for comparison, the loudspeaker off condition is defined as basic model. In this case, the repose angle of the NACA 0020 airfoil is approximately 10 degrees. The 10° angle of repose in measurements made with the speaker turned off also supports the baseline measurements in the study of Ethiraj and Pillai (2021). In Figure 8, when the speaker is off, the $C_L$ value is 1.068.

Figure 8, a delay in shifting stall is observed in all synthetic jet orifice models except the inclined rectangular orifice model with linear and spaced synthetic jet actuators. The main reason for this appears to be due to the activated synthetic jet actuator, actuator position and orifice jet structures. The maximum lift coefficient and stall angle shift are observed when close to the leading edge (Guoqing et al., 2016).

In the first step of the presented study, the cylinder orifice model placed in the synthetic jet actuator is activated. It is observed that the increase in the best lift coefficient in the Cylinder orifice synthetic jet actuator occurred at 4 Hz frequency, compared to the loudspeaker actuator off condition, by 8%. In the cylinder orifice, there is an increase in the lift coefficient at frequencies of 2 and 4 Hz, but it is observed that it started to decrease again after the frequency of 8 Hz. The reason for this is that after a certain frequency increase, it causes a loss in lift coefficient due to distortions in the vortex structures that occur at the orifice jet exit. The cylinder orifice is shifted stall angle from 10° to approximately 13° in the synthetic jet actuator array. This means that despite a low increase in the lift coefficient in the cylinder orifice structure, a significant change in the shifted stall angle is observed. In Figure 8b, as the operating frequency increases in the Rectangular orifice synthetic jet actuator, the lift coefficient increases. As a result, a better improvement (about 17%) in the buoyancy coefficient is observed with increasing frequency compared to the cylinder orifice model. This seems to be due to the effect of vortex structures formed at the cylinder and rectangular orifice jet exit. Wang et al. (2017) observed that the vortex area of the rectangular orifice is larger compared to the cylindrical orifice shape. Additionally, a 3° shift in the stall angle was observed in the rectangular orifice synthetic jet actuator array. In the V-type orifice synthetic jet actuator, the coefficient of lift force increases linearly with the stall angle. In Figure 8c, as the operating frequency increased, the lift coefficient increased and it is observed that there is an improvement in the best lift

force (approximately 17%) at 8 Hz. A decrease in the lift coefficient is observed compared to the rectangular orifice. The main reason for this is due to the angular structure of the model, distortions occur in the jet structures formed at the orifice exit. It has been observed that these deteriorations lead to a decrease in the lift coefficient and the angle of stall. In this orifice structure, the stall angle creates a 2° translation. In Figure 8d, a 16% improvement is observed at the highest lift coefficient and 10° angle of attack at 2 Hz operating frequency in the sinusoidal orifice synthetic jet actuator. While the stall angle is only shifted by 1° at 2 Hz, a shift of 4° at 4 Hz and 5° at 8 Hz are observed with increasing frequency. Although the maximum lift force decreased at 4 and 8 Hz, the aircraft wing does not enter the stall immediately after the stall angle and the lift coefficient remains at 1.18 levels. It appears that the lift coefficient curve is horizontal at 4 and 8 Hz and then stalls, due to the disruption of the 'laminar separation bubble' formation on the suction surface of the airfoil at low Reynolds numbers by the synthetic jet actuator. In Figure 8e, it is observed that as the operating frequency increases, the lift force coefficient increases and there is an improvement in the best lift force (about 12%) at 4 Hz.

Although there is an increase in the lift coefficient of the Inclined rectangular orifice model compared to the cylinder orifice model, a smaller improvement (about 12%) is observed compared to the other orifice structure. In this orifice model, similar to the sinusoidal geometric structure, the lift coefficient remained constant for a while before stalling and then stalled. In the Inclined rectangular orifice synthetic jet model, it is observed that there is a translation of 4° at 2 and 4 Hz and 5° at 8 Hz. It has been observed that the synthetic jet mechanism is effective in shifting the stall angle in 5 different synthetic jet orifice models. Guoqing et al. (2016) supports the study that the synthetic jet mechanism created using a speaker jet array is effective in analysing the stall control effects of the airfoil. Thus, with the presented study, higher lift coefficient effects are observed and separation is taken under control.

In the NACA 0020 airfoil, in Figure 9, firstly, when the loudspeaker actuator is closed in the synthetic jet mechanism, the drag coefficient ($C_D$) increases with the angle of attack. It is observed that the $C_D$ of the NACA 0020 airfoil increased by up to 10 degrees, except for the cylinder orifice model. However, after the stall angle, the drag coefficient gradually increases in all orifice structures. As seen in Figure 11, 4 Hz operating frequency is more effective than 2 Hz operating frequency in reducing the drag coefficient. However, at the 8 Hz operating frequency, it causes irregular fluctuations. The main reason for this is the fluctuations in the flow structures formed in orifice jet models. Especially in inclined rectangular models, unstable fluctuations in the drag coefficient are quite high at 8 Hz operating frequency. This causes a negative effect on the wing. Additionally, in rectangular, V type, inclined rectangular orifice models, it is observed that 2 Hz operating frequency is more effective in pre-stall situations, but 4 Hz operating frequency is more effective after stopping. Among the orifice models in the synthetic jet mechanism, the minimum improvement, called the reduction in drag coefficient, is at 8° angle of attack (about 20%) at 2 Hz of the cylindrical model, while the maximum improvement is sinusoidal at 4 Hz at 8° angle of attack (about 80%) and inclined rectangle at 8 Hz.
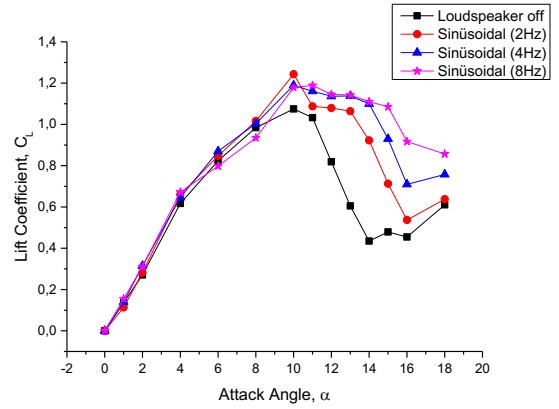


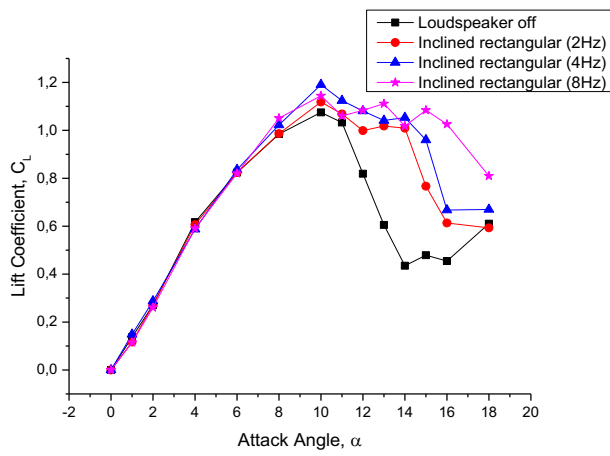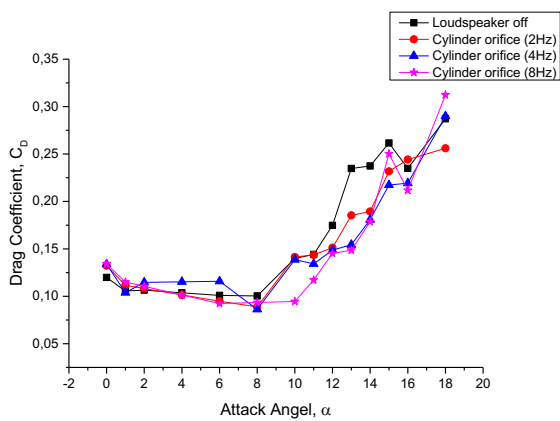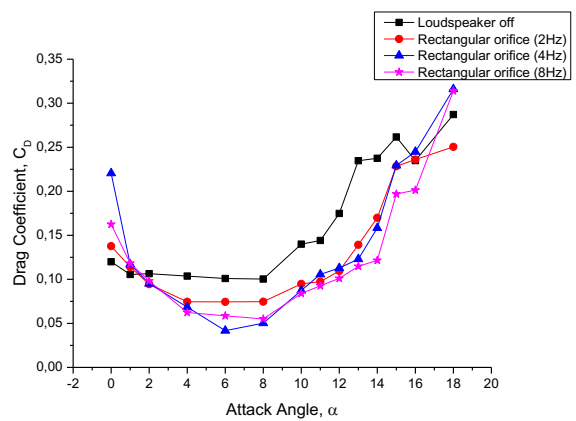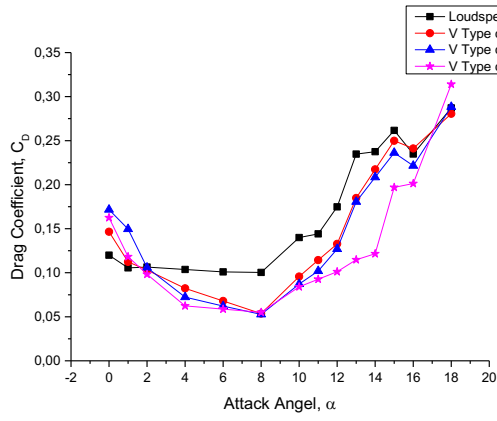**a.**



**b.**
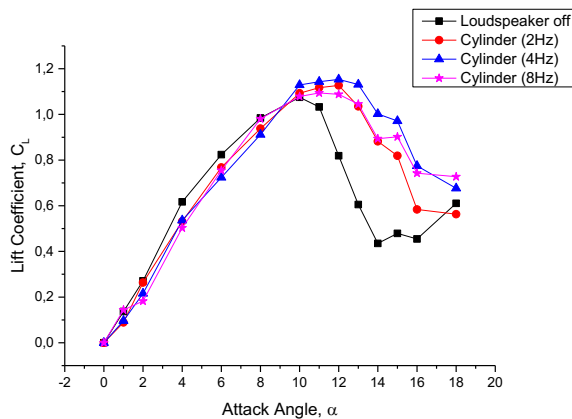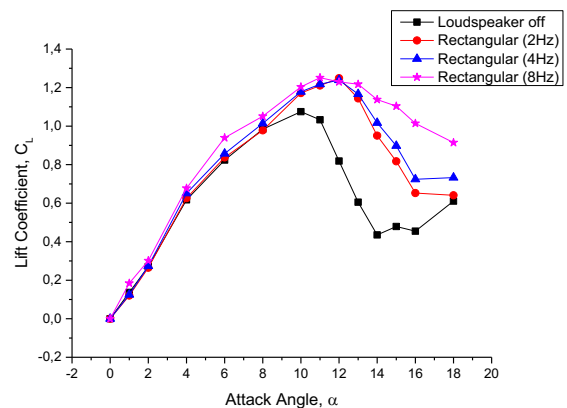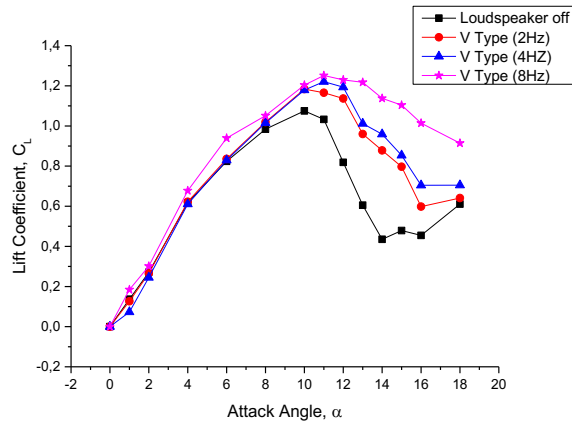
**Figure 8.** Lift coefficient of the NACA 0020 airfoil synthetic jets at Reynolds number 50 000 **a.** cylinder **b.** Rectangle **c.** Sinusoidal **d.** V type **e.** Inclined rectangular
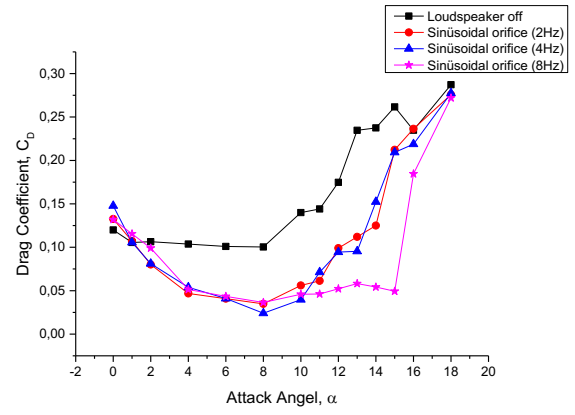


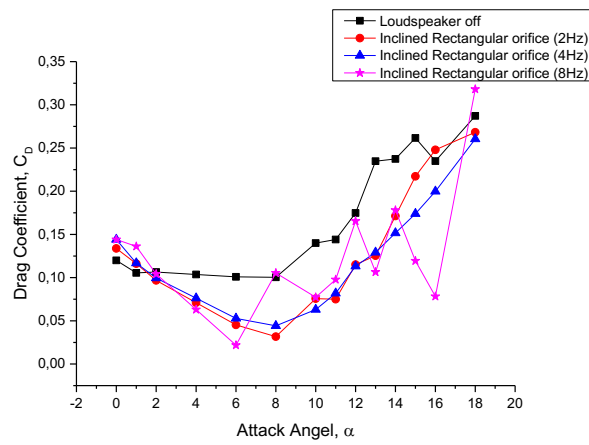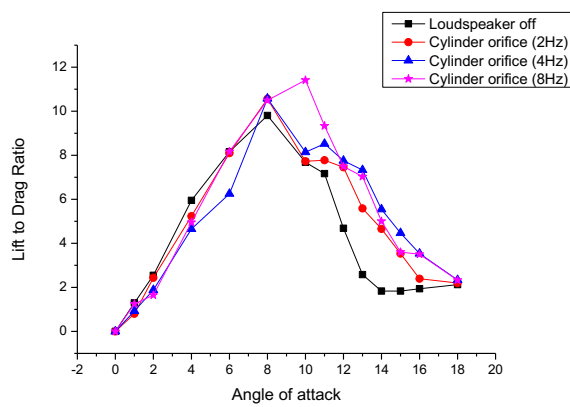136

**Figure 9.** Drag coefficient of the NACA 0020 airfoil synthetic jets at Reynolds number 50 000 **a.** cylinder **b.** Rectangle **c.** Sinusoidal **d.** V type **e.** Inclined rectangular
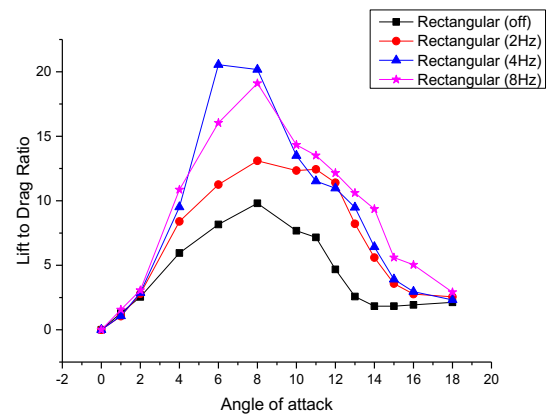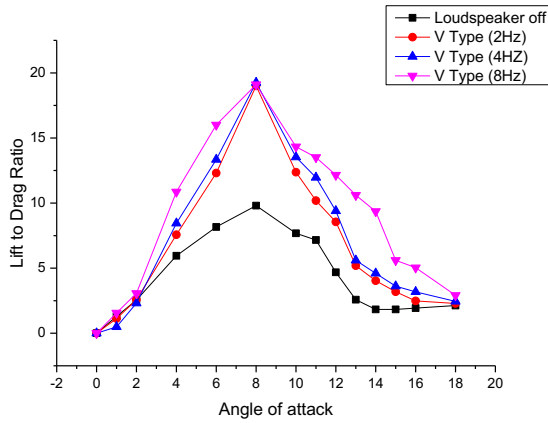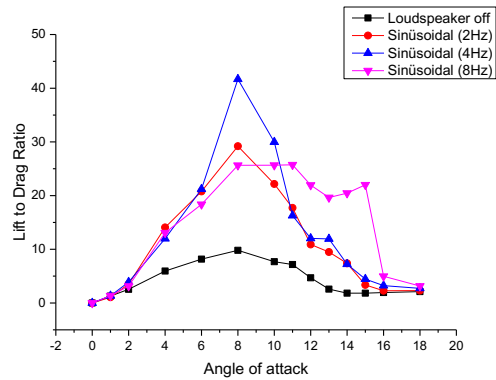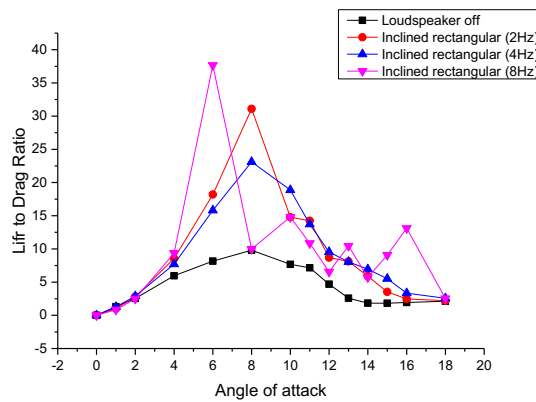
**c.**       **d.**



**e.**

**Figure 10.** Lift to drag of the NACA 0020 airfoil synthetic jets at Reynolds number 50 000 **a.** cylinder **b.** Rectangle **c.** Sinusoidal **d.** V type **e.** Inclined rectangular

Mueller (1999) observed that the lift and drag coefficient of a smooth airfoil can vary significantly in the range of 10000 to 100000 Reynolds numbers. In the light of these observations, it is observed in our study that the flow in the different orifice synthetic jet mechanism causes shifting in stall, increase in lift coefficient and decrease in drag coefficient.

In this study, it was observed that the different orifice models presented in Figure 9 play a critical role in reducing the drag coefficient. In Figure 10, in the lift-drag ratio graphs of 5 different orifice models in the synthetic jet mechanism, improvements are observed for all models when compared to the basic model with the loudspeaker off. As a result of this study, when the aerodynamic forces are analyzed and interpreted together, different orifice structures have shorter take-off distances and fuel consumption is saved for the same journey. When comparing the loudspeaker off model of

the NACA 0020 airfoil with other orifice models, the flight range is extended with improvements in the lift-drag ratio in the aerodynamic design.

To demonstrate the reliability of the lift coefficient at low Reynolds number (Dajun and Takafumi, 2018), the fluctuation of the lift coefficient in a randomly selected time interval is seen in Figure 11. It can be seen that there is a stable fluctuation structure when the loudspeaker is off and the wavelength increases slightly after the stall angle. When orifice models are tested with frequencies of 2, 4 and 8 Hz, it is observed that wavelengths increase with increasing frequency and wavelength frequency increases. Additionally, when the graphs are compared with the lift coefficient graph, it is observed that the periodic oscillation increases after the stall angle in each of them, and these oscillations and the lift coefficient ($C_L$) fluctuation are directly related to each other.
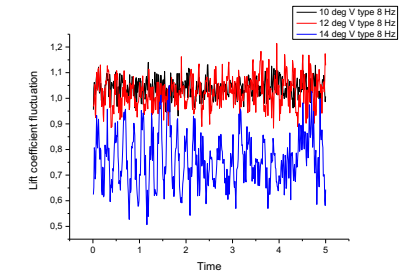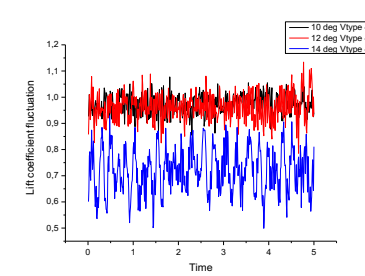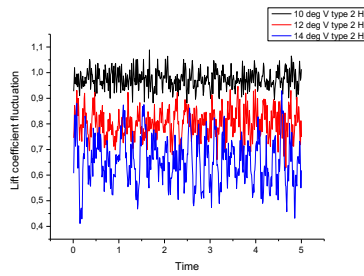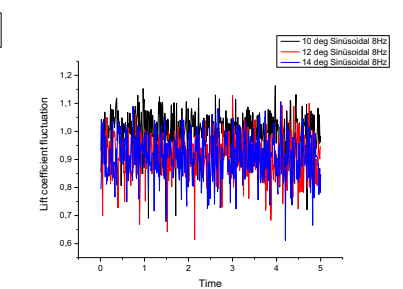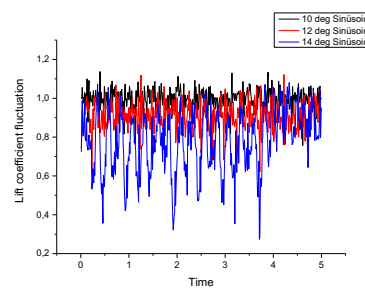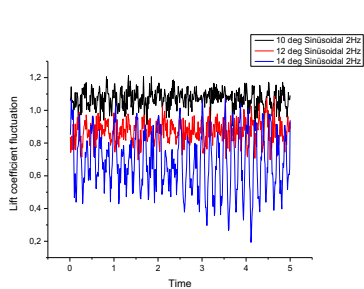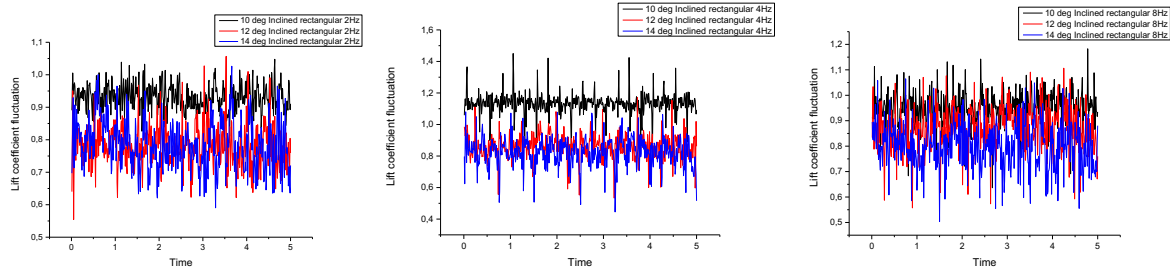
a.



b.



c.



d.



e.

139
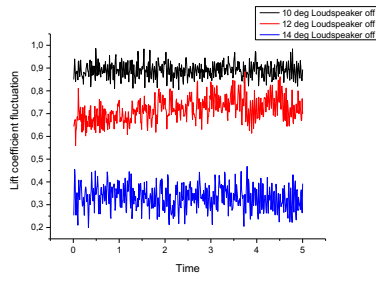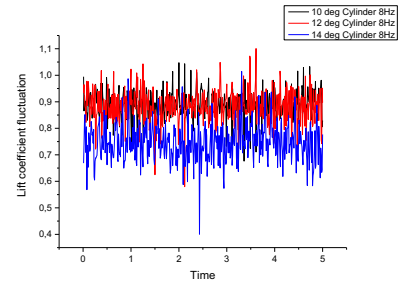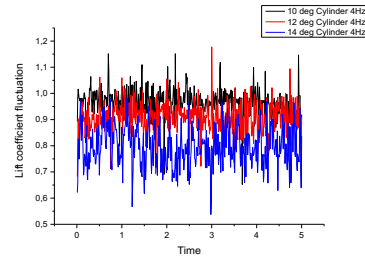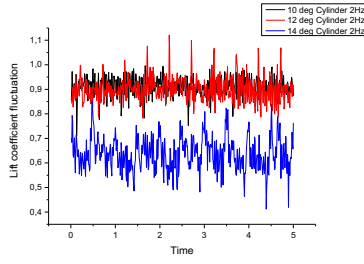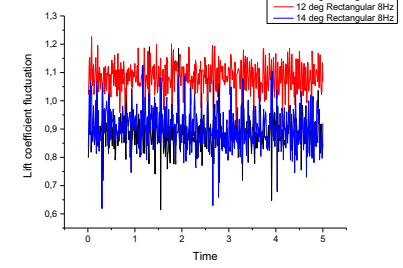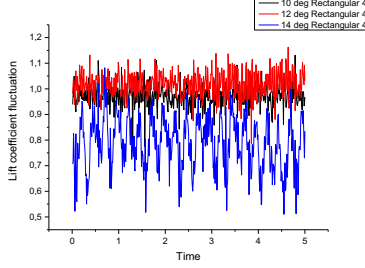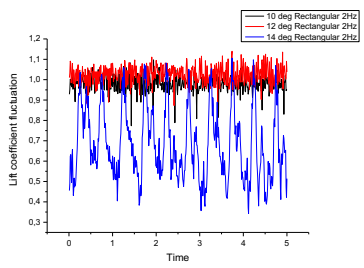
**Figure 11.** Fluctuating lift coefficient of the NACA 0020 airfoil in closed synthetic jets at Reynolds number 50 000 **a.** Loudspeaker off **b.** Cylinder 2, 4, and 8 Hz **c.** Rectangular 2, 4, and 8 Hz **d.** V type 2, 4, and 8 Hz **e.** Sinusoidal 2, 4, and 8 Hz **f.** Inclined rectangular

## CONCLUSIONS

The main objective of this study is to investigate the effects of different orifice geometries on shifting the stall angle in the synthetic jet mechanism. In addition, the effects of different orifice geometries on the airfoils lift coefficient and drag properties are investigated by varying the angle of attack. Based on the presented experimental data, some significant results obtained are as follows:

It has been observed that the use of synthetic jet for flow control has a potential for enhancing the aerodynamic performance. It has been noted that synthetic jet mechanisms based on different orifice geometries have delayed the stall with geometry based differing performance levels.

The orifice geometry, which is most effective in shifting the stall angle, shifted the inclined sinusoidal orifice stall from $10^0$ to $14^0$ in 4 Hz and from $10^0$ to $15^0$ in 8 Hz. In addition, it is observed that the stall angles are shifted from $10^0$ to $13^0$ for cylinder, rectangular, and from $10^0$ to $12^0$ for V-type orifice structures and from $10^0$ to $11^0$ for inclined rectangular. According to the results of these experiments, different orifice models have found to be effective in shifting the stall angle.

When the different orifice geometries in the NACA 0020 airfoil are examined, an improvement of approximately 17% in the lift coefficient is observed at 8 Hz and $11^0$ angles of attack for the rectangular and V-type orifice models.

In the NACA 0020 airfoil, when stalling occurred, an 80% decrease in the drag coefficient is observed at its maximum value at 8 Hz for the rectangular and sinusoidal models at an angle of attack of 8 degrees, and an outstanding improvement in the drag coefficient is observed. In 8 Hz operation in the inclined rectangular orifice structure, irregularity occurred in the drag coefficient. As a result, this irregularity in the drag force that occurs as the frequency increases has a negative effect on the airfoil.

The study presents results regarding its contribution to the improvements in aerodynamic performance of synthetic jet mechanisms for different orifice geometries on the NACA 0020 airfoil. It contributes to aerodynamic performance by increasing the lift force by approximately 17% and the decrease of drag force by up to 80%. These results contribute to the literature on aerodynamic performance improvements of airfoils in the rapidly developing aircraft industry.

140

## REFERENCES

Andou S. And Ziada S., 2006, Spanwise Characteristics of High-Aspect-Ratio Synthetic jets, *AIAA JOURNAL,* 44(7), 1516-1523

Ahuja K.K. and Burrin R. H., 1984, Control of flow separation by sound, *9 th Aeroacustics Conf. Amerikan Institute of Aeronautics and Astronautics*, Williamsburg, VA

Amitay M., Smith D. R., Kibens V., Parekh D. E., Glazer A., 2001, Aerodynamic flow control over an unconventional airfoil using synthetic jet actuators, *AIAA Journal*, 39(3), 361-370

Babarino S., Bilgen O., Ajaj R. M., Friswell M. I., Inman D. J., 2011, A review of morphing aircraft, *Journal of Intelligent Material Systems and Structures,* 22(9)

Chaudhari M., Bhalchandra P., Agrawal A., 2010, Heat transfer characteristics of synthetic jet impingement cooling, *International Journal of Heat and Mass Transfer,* 53(5–6), 1057-1069

Collins F. G. and Zelenevitz, J., 1975, Influence of sound upon separated flow over wings, *AIAA JOURNAL.* 13(3), 408-410

Crittenden, T., Glezer, A., Funk, R., Parekh, D. 2001, Combustion-driven jet actuators for flow control, *15th AIAA Computational Fluid Dynamics Conference,* Anaheim, California, 2001-2768

Dajun L. and Takafumi N., 2018 Numerical analysis on the oscillation of stall cells over a NACA 0012 aerofoil, *Computers and Fluids,* 175, 246-259

Ethiraj L., Pillai N.S., 2021, Effect of trailling-edge modification over aerodynamic characteristics of NACA 0020 airfoil. *Wind and Structures,* 33(6), 463-470

Feero M. A., Lavoie P. and Sullivan P. E., 2015, Influence of cavity shape on synthetic jet performance, *Sensors and Actuators A: Physical*, 233,1-10

Gad-el-Hak M., 2000, *Flow Control*. by Mohamed Gad-el-Hak, pp. 442. ISBN 0521770068. Cambridge, UK: Cambridge University Press, August

Genç M. S., Karasu İ., Açıkel H. H., 2012, An experimental study on aerodynamics of NACA 2415 aerofoil at low Re numbers., *Experimental Thermal and Fluid Science*, 39, 252-264

Gillarranz J. L., Traub L.W., Rediniotis O. K., 2005, A new class of synthetic jet actuators-Part II: Application to flow separation control, *Journal of Fluids Engineering* 127(2): 377-387

Guoqing Z., Qijun Z., Yunsong G., Xi C., 2016, Experimental investigations for parametric effects of dual synthetic jets on delaying stall of a thick airfoil. *Chinese Journal of Aeronautic,* 29(2): 346-357

Hassan A.A., 2006, A two -point active flow control strategy for improved airfoil stall/post stall aerodynamics. *AIAA JOURNAL.*, AIAA-2006-0099

He Y. Y., Cary A. W., Peters D. A., 2001, Parametric and dynamic modeling for synthetic jet control of a post-stall airfoil. Reno/ NV 39th *AIAA Aerospace Science Meeting and Exhibit*, 8-11 January 2001, 0733

Holman R., Galles Q., Carroll., Cattafesta L., 2003, Interaction of adjacent synthetic jet in an airfoil separation control application, *33rd AIAA Fluid Dynamics Conference and Exhibit,* 23-26 June 2003, 2003-3709

Hong, M.H., Cheng, S.Y., Zhong S., 2020, Effect of Geometric Parameters on Synthetic Jet: A review. *Physics of Fluids* 32, 031301

Ingard, U. and Labate, S., 1950, Acoustic Circulation Effects and the Nonlinear Impedance of Orifices. *Journal of the Acoustical Society of America,* 22(2), 211–218

Joshi S. N., Gujarathi Y. S., 2016, A Review on Active and Passive Flow Control Techniques, *International Journal on Recent Technologies in Mechanical and Electrical Engineering,* 3(4)

Kim S. H., Kim C., 2009, Separation control on NACA 23012 using synthetic jet, *Aerospace Science Technology*, 13,172-182

Lee B, Kim M, Lee J, Kim C., 2012, Separation control characteristics of synthetic jets with circular exit array. *AIAA Flow Control Conference*, New Orleans, AIAA-2012-3050

Mohsen J., 2011, *Laminar separation buble: Its structure, dynamics and control*. Charmers University. of Tecnology. Gothenburg, Sweeden

Mallinson S.G., Reizes J.A., Hong G., Westbury P.S., 2004, Analysis of hot-wire anemometry data obtained in a synthetic jet flow. *Experimental Thermal and Fluid Science* 28, 265–272

Mueller T. J., 1999*, Aerodynamic Measurements at Low Reynolds Numbers for Fixed Wing Micro-Air Vehicles. Development and Operation of UAVs for Military and Civil Applications*, Hessert Center for Aerospace Research, University of Notre Dame, 8.1-8.32

Paula A. A., Kleine V. G., Porto F. M., 2017, The Thickness Effect on Symmetrical Airfoil Flow Characteristics at low Reynolds number, *55th AIAA Aerospace Sciences Meeting,* 2017-1422

Qingfeng X. and Zhong S., 2013, Liquids mixing enhanced by multiple synthetic jet pairs at low Reynolds numbers, *Chemical Engineering Science*, 102, 10-23

Seifert A., Darabi A., Wyganski I., 1996, Delay of airfoil stall by periodic excitation, *Journal of Aircraft*, 33(4), 691–698

Smith B. L., and Glezer A., 1998, The Formation and Evolution of Synthetic Jets. *Physics of Fluids* 10 (9): 2281–2297

Traub L., Miller A. and Rediniotis O., 2004, Effect of Synthetic jets of actuation on a ramping NACA 0015 airfol, Journal of Aircraft,41(5), 1153-1162

Trávníček Z., Vogel J., Vít T., Maršík F., 2005, Flow field and mass transfer experimental and numerical studies of a synthetic impinging jet. *In: Proc. 4th International Conference on Heat Transfer, Fluid Mechanics and Thermodynamics (HEFAT2005)*, Cairo, Egypt, No. ZT4

Türen E., & Yavuz H., 2023, Schlieren imaging investigation of flow fields in synthetic jets generated by different orifice geometries with varying aspect ratios, *Journal of Visualization*, 26(4), 851-874.

Wang L., Feng L.H., Wang J.-J., Li T., 2017, Parameter influence on the evolution of low-aspect-ratio rectangular synthetic jets, Journal of. Visualization, 21, 105

Yarusevych, S., Kawall, J. G., and Sullivan, P. E., 2003, Effect of acoustic excitation on airfoil performance at low Reynolds numbers, *AIAA JOURNAL*. 41(8),1599-1601

Yen J., Ahmed N. A., 2012, Parametric study of dynamic stall flow field with synthetic jet actuation, *Journal of Fluids Engineering*, 134, 071106(1-8)

You D., Moin P., 2008, Active control of flow separation over an airfoil using synthetic jets, *Journal of Fluids and Structures*, 24,1349-1357

Youmin Y., Simon T W., Zhang M., Yeom T., North M. T., Cui T., 2014, Enhancing heat transfer in air-cooled heat sinks using piezoelectrically-driven agitators and synthetic jets. *International Journal of Heat and Mass Transfer*, 68, 184-193

Zaman K. B. M.Q., and McKinzie D. J., 1991, Control of laminar separation over airfoil by acoustic axcition. *AIAA JOURNAL*, 29(7), 1075-1083

Zhang S., Zhong S., 2009, Experimental investigation of flow separation control using an array of synthetic jets. 39th *AIAA Fluid Dynamics Conference*, San Antonio, Texas, 22 25 June

Zhang D., Yang K., Cheng Q.H., Gao J., 2015, Numerical investigation of heat transfer performance of synthetic jet impingement onto dimpled/protrusioned surface. *Thermal Science* 19 (1), 221-229

Zhao G., Zhao Q., Yunsong G., Xi C., 2016, Experimental investigations for parametric effects of dual synthetic jets on delaying stall of a thick airfoil. *Chinese Journal of Aeronautics*, 29(2), 346-357

**Authors**

**Esra TÜREN,** received her B.Sc. degree and M.Sc. degree in Mechanical Engineering from Süleyman Demirel University, Isparta, Turkey in 2013 and 2015, respectively. She is currently a PhD student at Çukurova University. Her research interests for flow control and flow control applications.

**Hakan YAVUZ**, received his B.Sc. degree in mechanical engineering from Gazi University, Ankara, Turkey and the M.Sc. and Ph.D. degrees in mechatronics engineering from the Lancaster University,Lancaster, U.K., respectively. His current research interests include active flow control, robotic systems, development of intelligent control, design and development of mechatronic systems, renewable energy systems, modeling and analysis of engineering systems, input shaping for residual vibration elimination, and wave energy converters and related control applications.

# ANALYSIS OF AUGMENTATION IN PERFORMANCE OF PV MODULE INTEGRATED WITH FINNED PCM BY THREE-DIMENSIONAL TRANSIENT NUMERICAL SIMULATION

**K.S. UNNIKRISHNAN\*, Sumanth Babu PATHIPATI\*\*, Rohinikumar BANDARU\*\*\***

\* National Institute of Technology Calicut, Department of Mechanical Engineering,
673601 Kozhikode, India, kgsunnikrishnan@gmail.com ORCID: 0000-0002-2231-5391
\*\* National Institute of Technology Calicut, Department of Mechanical Engineering,
673601 Kozhikode, India, sumanth3a6@gmail.com ORCID: 0009-0002-3033-5349
\*\*\* National Institute of Technology Calicut, Department of Mechanical Engineering,
673601 Kozhikode, India, rohinikumar@nitc.ac.in ORCID: 0000-0002-3975-3996

**Abstract**: The overall performance of PV-PCM integrated with rectangular straight fins is analysed by three-dimensional transient numerical simulations. The influence of fin lengths, number of fins ($n$), and inclination ($\theta$) of the system is investigated and compared with the PV-only system, and an optimal system configuration is then identified. Finite element analysis is used to conduct the simulations using COMSOL *Multiphysics* 6.0. The PV front surface is subjected to a constant flux of 1000 W/m$^2$ for 180 min, and the PCM employed is RT25HC. The results indicate that the average PV temperature tends to drop with increasing inclination and fin length, thereby enhancing the PV efficiency, with maximum improvement attained for the full fin case for a given inclination and number of fins. Compared to the PV-only system, the highest PV temperature reduction and PV efficiency enhancement are 59.65 °C and 45.1%, respectively, for the horizontal system of full-length fins with a number of fins equal to 6. The full-fin PV-PCM system with 6 fins and 45° inclination gives the highest instantaneous power output of 14.16 W. The melting rate of PCM is strongly related to the heat transfer rate inside PCM, and the lowest melting time is obtained for the 8-finned PV-PCM system with $\theta$ = 45°. The peak velocity magnitude for all systems with different fin lengths is also examined to analyse the extent of convection levels within PCM.
**Keywords**: Transient numerical simulations, Number of fins, Inclination angle, PV efficiency, Melting rate

## ÜÇ BOYUTLU GEÇİCİ SAYISAL SİMÜLASYON İLE KANATLI PCM İLE ENTEGRE PV MODÜLÜN PERFORMANSINDAKİ ARTIŞIN ANALİZİ

**Özet**: Dikdörtgen düz kanatlarla entegre edilmiş PV-PCM'nin genel performansı, üç boyutlu geçici sayısal simülasyonlarla analiz edilir. Sistemin kanat uzunluklarının, kanat sayısının ($n$) ve eğiminin ($\theta$) etkisi araştırılır ve yalnızca PV sistemiyle karşılaştırılır ve daha sonra optimum sistem konfigürasyonu tanımlanır. Simülasyonları COMSOL *Multiphysics* 6.0 kullanarak gerçekleştirmek için sonlu elemanlar analizi kullanıldı. PV'nin ön yüzeyi 180 dakika boyunca 1000 W/m$^2$ 'lik sabit bir akışa maruz bırakılır ve kullanılan PCM, RT25HC'dir. Sonuçlar, ortalama PV sıcaklığının artan eğim ve kanat uzunluğuyla birlikte düşme eğiliminde olduğunu, dolayısıyla PV verimliliğinin arttığını ve belirli bir eğim ve kanat sayısı için tam kanat durumunda maksimum iyileştirmenin elde edildiğini göstermektedir. Yalnızca PV sistemiyle karşılaştırıldığında, kanat sayısı 6'ya eşit olan tam uzunlukta kanatlardan oluşan yatay sistem için en yüksek PV sıcaklık düşüşü ve PV verimlilik artışı sırasıyla 59,65 °C ve %45,1'dir. -6 kanatlı ve 45° eğimli PCM sistemi, 14,16 W ile en yüksek anlık güç çıkışını verir. PCM'nin erime hızı, PCM içindeki ısı aktarım hızıyla güçlü bir şekilde ilişkilidir ve en düşük erime süresi, 8 kanatlı PV- için elde edilir. $\theta$ = 45° olan PCM sistemi. Farklı kanat uzunluklarına sahip tüm sistemler için tepe hız büyüklüğü de PCM içindeki konveksiyon seviyelerinin kapsamını analiz etmek için incelenir.
**Anahtar Kelimeler**: Geçici rejim sayısal simülasyonlar, Kanat sayısı, Eğim açısı, PV verimliliği, Erime hızı.

## NOMENCLATURE

| | |
|---|---|
| $A$ | Upper surface of the PV panel [m$^2$] |
| $B$ | Liquid fraction |
| $\beta$ | Volume expansion coefficient [K$^{-1}$] |
| $c_P$ | Heat capacity [J/ kg.K] |
| $\Delta T$ | Phase change zone [°C] |

| | |
|---|---|
| $\eta$ | Efficiency [%] |
| $G_T$ | Solar irradiation [W/m$^2$] |
| $\gamma$ | Temperature coefficient of PV material [K$^{-1}$] |
| $g$ | Acceleration due to gravity [m/s$^2$] |
| h | heat transfer coefficient [W/m2 .K] |
| $k$ | Thermal conductivity [W/m.K] |
| $L_c$ | Characteristic length [m] |

| $L_h$ | Latent heat [J/kg] |
| $\mu$ | Dynamic viscosity [Pa s] |
| $v$ | Kinematic viscosity [m²/s] |
| $P$ | Pressure [Pa] |
| $Q_g$ | Heat generation per unit volume [W/m³] |
| $Ra$ | Rayleigh number |
| $Re$ | Reynolds number |
| $\rho$ | Density [kg/m³] |
| $T$ | Temperature [°C] |
| $T_m$ | Melting temperature [°C] |
| $t$ | Time [s] |
| $\theta$ | Inclination angle (°) |

## INTRODUCTION

Growing global power demand, rising fossil fuel prices, and global warming worries have accelerated the idea of a swift transition to renewable energy supply, particularly in the last two decades (Azarpour et al., 2013). The most abundant renewable energy source on earth is solar energy. Installing photovoltaic (PV) on the roofs of houses can reduce reliance on the electrical grid and lead to net-zero energy (Cuce and Cuce, 2014). Over the years, various methods have been developed to increase the efficiency of solar power generation and make it a more cost-effective technology (Mohanraj et al., 2016). The effectiveness of photovoltaic solar cells diminishes with the rise in their temperature, according to the experiments done by Radziemska (Hui Dai and Wei-Min Ma, 2002). The drop in open-circuit cell voltage is the primary source of the decrease in conversion efficiency of the cell, and hence, PV cells must be cooled to work efficiently during peak sunshine hours (Kaldellis et al., 2014). The commercially available PV module has 12% to 18% electric conversion efficiency. The excess solar radiation falling on the PV is converted to thermal energy, which raises the solar modules' working temperature (Agrawal and Tiwari, 2010; Dubey et al., 2013). To combat the impacts of high cell temperatures and keep the cell's operating temperature within an acceptable range, effective cooling mechanisms must be used to remove excess thermal energy by heat transfer from the cells (Ali, 2020; Bilen and Erdoğan, 2023). PCM with a proper melting temperature can be used to maintain the temperature of the PV module within the required temperature range, allowing it to achieve high efficiency. PCM provides the added benefit of storing thermal energy as compared to other passive techniques of thermal regulation (Da et al., 2023). The PCMs used are mostly organic types with very low thermal conductivity, so enhancement techniques such as the inclusion of fins are adopted for effective thermal regulation of PV (Kazem et al., 2023).

Bria et al. (2023) numerically investigated the utilisation of a PV-PCM cooling system as a means to minimise the adverse impact of temperature on the efficiency of PV with six different PCM thicknesses. The optimal PCM thickness for achieving maximum power output is found to be 0.06 m. Chibani et al. (2023) examined the integration of fins composed of different materials and explored the effects of the inclination angle of the panel. Cuce et al. (2011) studied a passively cooled silicon solar cell with a heat sink and observed a significant energy and exergy efficiency increase. The power conversion of PV increased by 13% at a solar radiation of 800 W/m². Experimental and numerical analyses were done by Park et al. (2014) to study the performance of a vertical PV-PCM, and the results showed that the power output rose by 1.0 to 1.5% compared to the conventional PV module.

The thermal management of a building with a concentrated PV–PCM system was investigated by Sharma et al. (2016), and a maximum improvement in electrical efficiency of 6.8% was reported for the incident radiation flux of 1200W/m². A transient numerical investigation of the PV-PCM system was conducted by Kant et al. (2016) by using RT35HC as PCM, and a maximum temperature reduction of 58.5 °C was found. It was reported that the increased wind speed and inclination resulted in a reduced PV panel temperature. The effects of employing several PCMs of different thicknesses and outside working conditions on PV-PCM performance were analysed by Nouira and Sammouda (2018). The results showed that the power output of PV increases with low dust deposition, increased PCM thickness, high wind speed, and low wind azimuth angle. Metwally et al. (2021) combined RT25 PCM with PV panels and found that efficiency increased by 2.5% in summer and 3.5% in normal weather.

The integration of two PCMs (PCM27 and PCM31) through an alternative tubular shape enclosure on PV was experimentally studied by Savvakis et al. (2020), and the results showed a temperature decrease of 6.4 and 7.5 °C, respectively, for PCM27 and PCM31 compared to the PV only system. Kumar et al. (2020) studied the impact of integrating PCM on the thermal behaviour and electrical performance of the panel to examine the system's behaviour. The use of PCM could lower the panel temperature by an average of 4.4 °C and boost efficiency by 2.2%. The influence of tilt angle on the melting of PCM-based heat sink and its potential usage for passive cooling of PV was examined by Abdulmunem et al. (2021). The findings demonstrated that when the tilt angle of the system increases from 0° to 90°, the PV temperature decreases from 0.4% to 12%. Akshayveer et al. (2021) explored a new bifacial PV–PCM system, which significantly increases PV electric output by about 74% compared to the PV-PCM system. According to Variji et al. (2022), incorporating metal foam with a porosity of 0.9 led to a 6.8% increase in average PV temperature and a 9.8% improvement in electrical efficiency compared to the PV-PCM system.

The impact of convection with RT27 PCM on the heat transfer rate from the PV panel in a finned PV-PCM system was investigated theoretically and experimentally by Huang et al. (2011), and they found that PCM with internal fins resulted in a reduction in the PV temperature up to 12 °C. Khanna et al. (2018) compared the performances of PV, PV-PCM, and Finned-PV-PCM systems using modelling and simulation and inferred that the PV module could be kept cooler by reducing the distance between fins, but reducing spacing below 25 cm does not improve the performance. Singh et al. (2020) proposed a mathematical model for a finned PV-PCM system. The effects of wind azimuths, ambient temperature, phase change temperature, and FPCM confinement dimensions were studied. The results showed that for 5 cm deep FPCM confinement, the power enhancement period increases from 6.1 h to 7.3 h when the wind azimuth varies from 75° to 0°. The impact of various structures of fins on the thermal performance of finned PV-PCM system oriented at various inclinations was quantitatively examined by Groulx et al. (2020) using a two-dimensional numerical study. Full fin and front fin configurations were found to be the most effective. Khanna et al. (2019) conducted a study to optimise a finned PV-PCM system for power augmentation under various operating conditions such as wind speed, azimuth angle, outdoor temperature, phase transition point, fin spacing, and fin width. A power generation of 143 W/m$^2$ was obtained for the system with a fin width of 4 mm, as compared to 125 W/m$^2$ for PV-only system.

The impact of fins in a rectangular enclosure of solid-liquid PCM on heat transfer was investigated numerically by Biwole et al. (2018). The results revealed that increasing the number of fins decreases the front surface temperature as well as the regulation period and speeds up the latent energy stored in the PCM. Emam and Ahmed (2018) computationally simulated a PV-PCM system with heat sinks in four different configurations based on the number and position of cavities and showed that a five-parallel cavity configuration significantly reduces solar cell temperature. Yıldız et al. (2020) explored the heat transfer inside a PCM container, which can serve as a typical model for PV/PCM systems, numerically, taking into account varied aspect ratios and types of fins. When the aspect ratio equals 1, the natural convection rate inside PCM is at its highest. Johnston et al. (2021) carried out a combined computational and experimental analysis to determine how orientation impacts the performance of a heat sink in a PV-PCM system and how fin height influences the heat sink's ability. Power output rose by 11.3 % and 15.3 % for PV integrated with 20 mm and 100 mm heat sinks, respectively, compared to standalone PV.

Klemm et al. (2017) numerically investigated the passive cooling of the system consisting of PCM with metallic fibre architectures using the COMSOL *Multiphysics* and found that the peak panel temperature was reduced by around 20 K compared to the PV alone system. Duan (2021) examined the utilisation of porous PV-PCM systems with various inclinations numerically as well as experimentally and concluded that the inclination has little effect on the porous PCM system when the porosity is minimal. Based on numerical simulation, Mahdi et al. (2021) showed that the employment of multiple PCMs in a particular position may improve in liquid fraction and thermal regulation period by 18% and 33%, respectively. Additionally, combining several PCMs with acceptable thermophysical properties at lower inclinations can further reduce the PV temperature. Sasidharan and Bandaru (2022) conducted an analysis by numerical simulation of a nano-enhanced PCM (PV-NEPCM) system with mass concentrations of 1%, 3%, and 5% and compared its performance with that of a conventional PV-PCM system. It was found that NEPCM performs better at lower inclinations with a temperature drop of the PV module as 1.26 °C for horizontal orientation PV-PCM system.

From the literature, it can be concluded that the integration of PCM with a PV module is an effective way of thermal regulation of the module when PCM is incorporated with proper thermal conductivity enhancers like fins, metallic fibres and nanoparticles. It is also worth noting that practically most of the previous numerical studies related to finned PV-PCM systems have started with the assumption of the two-dimensional domain without considering the variation of temperature and velocity of PCM in the *z*-axis and almost all deal with its thermal performance. To this end, the novelty of the present work is that, here, a three-dimensional transient numerical model has been developed for finned PV-PCM systems to study the effect of PCM and fins on the thermal performance of the system and the electrical performance of the PV module. Modelling finned PV-PCM systems in three dimensions for numerical analysis offers several important advantages and provides a more realistic representation of the system's behaviour compared to two-dimensional models. Key reasons for the importance of 3D modelling are (1) Accurate representation of complex geometries, accounting for variations in shape, size, and positioning of components such as fins. This is critical for capturing the interactions and flow patterns within the system; (2) Realistic boundary conditions that account for heat transfer from all directions essential for capturing natural convection and radiation heat transfer, which can vary significantly with spatial positioning, and (3) it is essential for analyzing the fluid flow pathways. This includes understanding the velocity distribution and pressure variations within the system. Accurate fluid flow analysis is critical for assessing heat transfer rates and efficiency.

The main objective of this paper is to propose a three-dimensional mathematical model of the domain and investigate the performance of PV module integrated with finned PCM system by numerical simulation at

different inclinations ($\theta$), number of fins and fin lengths. Rectangular-shaped straight fins are considered in the system. The influence of the number of fins ($n$) and the inclination angle is also examined. Simulation results are then compared with that of the only system. An optimum finned PV-PCM system is then proposed based on maximum temperature reduction, efficiency enhancement and maximum power output. The effect of fin length on the PV temperature, electrical efficiency, PV electrical output, melting time and convection velocity magnitude is also investigated. While increasing the number of fins, the thickness of the fin is so adjusted that the mass of PCM is kept constant for all the finned PV-PCM configurations. In all, five finned PV-PCM systems are considered with the number of fins ($n$) = 0 (no fin), 2, 4, 6 and 8, with three different fin lengths at four different inclination angles $\theta$ = 0°, 15°, 30°, and 45°. So a total of 60 finned PV-PCM geometries are considered for the present work. The reliability of the model is authenticated by using validation with the available and established experimental data.

## METHODOLOGY

### Physical Model

The three-dimensional representation of the physical geometry of the finned PV-PCM system on which the present investigations are carried out is shown in Fig. 1. The system consists of a PCM-based heat sink within the aluminium plates, which is mounted on the bottom side of the polycrystalline PV module. Table 1 represents the geometry and properties of different layers of PV module. The PCM used in the system is RT25HC, which is commercially available, and its thermophysical properties are specified in Table 2. The ambient temperature is kept constant at 20 °C; therefore, selecting RT25HC with a melting point of 26.6 °C as PCM is appropriate. The system's inclination ($\theta$) is the angle it makes with the horizontal plane. The depth of the PCM layer is taken as 20 mm. The top surface of the PV module is subjected to incident solar radiation. The top and bottom surfaces are exposed to a combined convective-radiative environment.

Internal longitudinal parallel aluminium fins are provided inside the PCM domain of the system. Different physical configurations of the finned PV-PCM system are established with different lengths and numbers of fins. Different lengths of the fins considered are $\delta$, $3\delta/4$ and $\delta/2$, where $\delta$ is the depth of the PCM in the system, which is normal to the plane of the PV module. The thickness of the fin is so varied in such a way that whatever the number of fins in the system, the volume of the fin remains constant. This is achieved by reducing the fin thickness as the number of fins increases. The thickness of the fin and spacing between the fins for different finned PV-PCM systems are shown in Table 3. Every physical configuration of the system will be operated at different tilt angles.

Different operational configurations of the system are established with the variation of the fin arrangement in the system as well as variation of the inclination angle of the system, and this leads to simulating the performance of different configurations of the system and to investigate the effect of fins and inclination of the system on the performance of PV module.
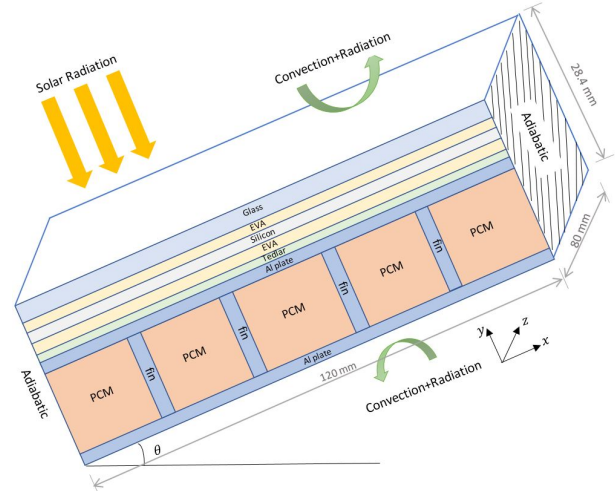


**Figure 1.** Schematic diagram of three-dimensional finned PV-PCM system.

**Table 1.** Properties and geometry of PV materials and aluminium (Khanna et al., 2019)

| Layer | Thickness (m) | $\rho$ (kg/m$^3$) | $k$ (W/m.K) | $c_p$ (J/kg K) |
|---|---|---|---|---|
| Glass | 0.003 | 3000 | 1.8 | 500 |
| EVA | 0.0005 | 960 | 0.35 | 2080 |
| Silicon | 0.0003 | 2330 | 147 | 678 |
| Tedlar | 0.0001 | 1200 | 0.2 | 1250 |
| Aluminium | 0.002 | 2675 | 211 | 903 |

**Table 2.** Properties of RT25HC (Khanna et al., 2018)

| | |
|---|---|
| Thickness (mm) | 20 |
| $\rho$ (kg/m$^3$) | 785/749 |
| $k$ (W/m.K) | 0.19/0.18 |
| $c_p$ (J/kg K) | 1800/2400 |
| $L_h$ (kJ/kg) | 232 |
| $\mu$ (Pa s) | 0.001798 |
| $T_m$ (°C) | 26.6 |

**Table 3.** Details of finned structure with varying number of fins

| Number of fins | Fin thickness (mm) | Fin spacing (mm) |
|---|---|---|
| 2 | 4 | 40 |
| 4 | 2 | 24 |
| 6 | 1.33 | 20 |
| 8 | 1 | 15 |

### Governing Differential Equations

Governing differential equations of the problem domain and applicable boundary and initial conditions need to be specified to define the problem. Specifying

the governing differential equations leads to modelling the system mathematically. The assumptions used for the mathematical modelling of the system are:

- Incoming solar flux on the PV module is uniformly distributed at an instant.
- Materials of different layers of PV module are considered homogeneous and isotropic.
- Flow of the PCM is considered as Newtonian, laminar, incompressible and unsteady.
- Effect of viscous dissipation is neglected.
- Thermal contact resistances between different layers of the system are neglected.
- Radiation effect inside PCM is neglected.
- Dust and rain effects are neglected.
- Resistive losses in the PV module are neglected.

The unsteady heat conduction equation is invoked for describing the temperature distribution of different layers of PV module and aluminium plates in the system, and it is (Khanna et al., 2018)

$$\rho c_p \frac{\partial T}{\partial t} = k \left( \frac{\partial^2 T}{\partial x^2} + \frac{\partial^2 T}{\partial y^2} + \frac{\partial^2 T}{\partial z^2} \right) + \dot{Q}_g \tag{1}$$

$\dot{Q}_g$ is the rate of heat generation per unit volume in the silicon layer it is to be considered as zero for aluminium layers since they are not involved with heat generation. It can be expressed as

$$\dot{Q}_g = \left[ 1 - \eta_{PV} \right] (\tau\alpha) \, G_T \, A_{si} / V_{si} \tag{2}$$

where $(\tau\alpha)$ is the effective transmissivity-absorbtivity coefficient, and $G_T$ is the solar irradiation in W/m². The efficiency of the solar cell is represented by $\eta_{PV}$ which is defined as (Kaplani and Kaplanis, 2014)

$$\eta_{PV} = 20 \left[ 1 - 0.005 \left( T_{PV} - 25°C \right) + 0.085 \ln \left( G_T / 1000 \right) \right] \tag{3}$$

Modelling of the PCM was done by a modified specific heat capacity method. The governing equations for the PCM, as a fluid coupled with buoyant volumetric force, can be formulated based on the assumptions as:

continuity: $\quad \dfrac{\partial u}{\partial x} + \dfrac{\partial v}{\partial y} + \dfrac{\partial w}{\partial z} = 0 \tag{4}$

x-momentum:

$$\rho \left( \frac{\partial u}{\partial t} + u \frac{\partial u}{\partial x} + v \frac{\partial u}{\partial y} + w \frac{\partial u}{\partial z} \right) = -\frac{\partial P}{\partial x} +$$
$$\mu \left( \frac{\partial^2 u}{\partial x^2} + \frac{\partial^2 u}{\partial y^2} + \frac{\partial^2 u}{\partial z^2} \right) + \rho g_x \beta \left( T - T_m \right) - A(T) u \tag{5}$$

y-momentum:

$$\rho \left( \frac{\partial v}{\partial t} + u \frac{\partial v}{\partial x} + v \frac{\partial v}{\partial y} + w \frac{\partial v}{\partial z} \right) = -\frac{\partial P}{\partial y} +$$
$$\mu \left( \frac{\partial^2 v}{\partial x^2} + \frac{\partial^2 v}{\partial y^2} + + \frac{\partial^2 w}{\partial z^2} \right) + \rho g_y \beta \left( T - T_m \right) - A(T) v \tag{6}$$

z-momentum:

$$\rho \left( \frac{\partial w}{\partial t} + u \frac{\partial w}{\partial x} + v \frac{\partial w}{\partial y} + w \frac{\partial w}{\partial z} \right) = -\frac{\partial P}{\partial z} +$$
$$\mu \left( \frac{\partial^2 w}{\partial x^2} + \frac{\partial^2 w}{\partial y^2} + + \frac{\partial^2 w}{\partial z^2} \right) + \rho g_z \left( T - T_m \right) - A(T) w \tag{7}$$

thermal energy:

$$\rho c_p \frac{\partial T}{\partial t} = \frac{\partial}{\partial x} \left( k \frac{\partial T}{\partial x} - \rho c_p u T \right) + \frac{\partial}{\partial y} \left( k \frac{\partial T}{\partial y} - \rho c_p v T \right)$$
$$+ \frac{\partial}{\partial z} \left( k \frac{\partial T}{\partial z} - \rho c_p w T \right) \tag{8}$$

For the solid phase of the PCM, the effect of velocity components in Eqn. (8) becomes zero. The third term on the RHS of momentum equations is the buoyant force which is volumetric in nature, and it results in motion in the melted PCM due to variation in density. The secondary volumetric force is represented by the last term in the RHS of momentum equations, and it is included to help the solver to arrive at the PCM velocities equal to 0 in the solid phase quickly. The porosity operator is derived from the Carmen-Kozeny equation for porous media, which is represented by $A(T)$ (Brent et al., 1988), and it is,

$$A(T) = \frac{C_m \left( 1 - B(T) \right)^2}{B(T)^3 + \psi} \tag{9}$$

The value of $C_m$ specifies how quickly the velocity is decreased to zero when the PCM is in the solid state, and it is determined by the morphology of the PCM. The value of $C_m$ is generally taken as $10^5$ for organic PCM (Khanna et al., 2017). The denominator was added with a very small computational constant $\psi$ to prevent division by zero. In effect, the initial large value of $A(T)$ swamps out all the terms in the governing equations and effectively forces velocity to reach zero in completely solid elements. The validity of the Carman-Kozeny equation in modelling the flow mushy zone was shown experimentally by Poirier (1987).

The viscosity of the PCM can be modified as

$$\mu(T) = \mu_l \left( 1 + A(T) \right) \tag{10}$$

It ensures the usage of very high and very low viscosities in the regions of PCM that are below the solidus temperature, $(T_m - \Delta T / 2)$, and above the liquidus temperature $(T_m + \Delta T / 2)$, respectively.

The density and thermal conductivity of the PCM can be modelled as (Khanna et al., 2017)

$$\rho_{pcm}(T) = \rho_s + (\rho_l - \rho_s) B(T) \qquad (11)$$

$$k_{pcm}(T) = k_s + (k_l - k_s) B(T) \qquad (12)$$

where $B(T)$ is the liquid fraction which characterises the phase change, and it can be defined as (Balavinayagam et al., 2021)(Khanna et al., 2017)

$$B(T) = \begin{cases} 0 & \text{if } T < (T_m - \Delta T/2) \\ (T - T_m + \Delta T)/(2\Delta T) & \text{if } (T_m - \Delta T/2) \leq T \leq (T_m + \Delta T/2) \\ 1 & \text{if } T > (T_m + \Delta T/2) \end{cases} \quad (13)$$

The modified specific heat capacity of the PCM is (Unnikrishnan et al., 2023)

$$c_{p,pcm}(T) = c_{ps} + (c_{pl} - c_{ps}) B(T) + L_h D(T) \qquad (14)$$

and

$$D(T) = \frac{e^{\frac{-(T-T_m)^2}{(\Delta T/4)^2}}}{\sqrt{\pi (\Delta T/4)^2}} \qquad (15)$$

where $D(T)$ is a smoothed Dirac delta function, with a value of zero everywhere except in the transition zone of the PCM. This function is used to disperse PCM's latent heat evenly around the melting temperature in the transition region.

**Boundary and Initial Conditions**

The top and bottom surfaces of the system are subjected to combined convection and radiation heat transfer. A solar irradiation $G_T$ is uniformly applied on the front surface of the PV module as input.

The boundary condition on the top surface of the system is:

$$k_g \left( \frac{\partial T}{\partial y} \right) = (h_{free} + h_{forced})(T_{amb} - T_g) + \alpha_g G_T + \varepsilon_g \sigma (T_{amb}^4 - T_g^4) \qquad (16)$$

The boundary condition on the bottom surface of the system is:

$$k_{al} \left( \frac{\partial T}{\partial y} \right) = (h_{free} + h_{forced})(T_{al} - T_{amb}) + \varepsilon_{al} \sigma (T_{al}^4 - T_{amb}^4) \qquad (17)$$

where $h_{free}$ and $h_{forced}$ are the free and forced convection heat transfer coefficients, respectively,

which are defined as (Kaplani and Kaplanis, 2014; Khanna et al., 2017)

$$h_{free} = \begin{cases} \frac{k_a}{L_c} \left[ 0.68 + \frac{0.67 (Ra_L \sin\theta)^{0.25}}{\left(1 + \left(\frac{0.492 k_a}{\mu c_p}\right)^{9/16}\right)^{4/9}} \right] & \text{if } Ra_L \leq 10^9 \\ \frac{k_a}{L_c} \left[ 0.825 + \frac{0.387 (Ra_L \sin\theta)^{1/6}}{\left(1 + \left(\frac{0.492 k_a}{\mu c_p}\right)^{9/16}\right)^{8/27}} \right]^2 & \text{if } Ra_L > 10^9 \end{cases}$$

$$(18)$$

where $Ra_L$ is the Rayleigh number, which is defined as (Incropera and Dewitt, 1985)

$$Ra_L = \frac{g(1/T_f)(T - T_a) L_c^3}{\nu \alpha} \qquad (19)$$

with $\alpha$ and $\nu$ as thermal and momentum diffusivities of air, respectively, at the film temperature (Fujii and Imura, 1972).

$$h_{forced} = \begin{cases} \frac{2k \left(0.332 Re_L^{\frac{1}{2}} Pr^{\frac{1}{3}}\right)}{L_c} & \text{if } Re_L \leq 5\times10^5 \\ \frac{2k Pr^{\frac{1}{3}} \left(0.037 Re_L^{0.8} - 871\right)}{L_c} & \text{if } Re_L > 5\times10^5 \end{cases} \quad (20)$$

with $Re_L$ and $L_c$ as Reynolds number and characteristic length, respectively.

The side walls of the system are insulated, and hence, the boundary conditions at the side walls are:

$$\left( \frac{\partial T}{\partial x} \right) = 0 \qquad (21)$$

front and rear side walls: $\left( \dfrac{\partial T}{\partial z} \right) = 0 \qquad (22)$

No slip condition at six boundary surfaces of the PCM in the system leads to the boundary condition at all the surfaces.

$$u = v = w = 0 \qquad (23)$$

At all the interfaces in the system, the boundary condition is applicable, and it can be defined as

$$k_r \left( \frac{\partial T_r}{\partial y} \right) = k_s \left( \frac{\partial T_s}{\partial y} \right) \tag{24}$$

where $r$ and $s$ represent the materials of two different layers on either side of the interface in the system.

Initial Conditions:

$$At \ t = 0, \ u \ = \ v \ = \ w \ = \ 0 \tag{25}$$

$$At \ t = 0, \ T = T_i = 20 \ ^\circ C \tag{26}$$

The value of $G$ and other inputs required to carry out the simulation are specified in Table. 4.

**Table 4.** Inputs to simulation

| Parameter | Value |
|---|---|
| PCM thickness (mm) | 20 |
| $\beta$ (K$^{-1}$) | $9.1 \times 10^{-4}$ |
| $T_a$ (°C) | 20 |
| $G_T$ (W/m$^2$) | 1000 |
| $(\tau\alpha)$ | 0.9 |
| $\Delta T$ (°C) | 2 |

## NUMERICAL PROCEDURE and VALIDATION of THE MODEL

The simulation of all the configurations of the system considered in the present work is carried out using COMSOL *Multiphysics* 6.0. Easy linking and solution of partial differential equations related to different fields of physics are possible by the COMSOL *Multiphysics* software based on the finite element approach. The coupled problem of heat transfer and fluid flow (laminar) in melted PCM is modelled using continuity, momentum equations with Boussinesq approximation and energy equations by employing the conservation principles and solved using COMSOL software. The three-dimensional geometry of the PV-PCM system is developed using the geometry module of the COMSOL interface, and appropriate materials with dimensions and thermophysical properties are attached to each PV-PCM layer and fins. Different configurations of PV-PCM system geometries considered in the present work are established, and the same is shown in Fig. 2 when they are operating at 15° inclination. Aspects of physics involved in the development of the present mathematical model are heat transfer in solids (PV, solid PCM fins and aluminium), heat transfer in fluids (liquid PCM) and laminar fluid flow (liquid PCM), which replicate heat transfer and buoyancy-driven fluid flow along with phase transition. Material properties of the PCM and variables and functions involved in the mathematical model of the PCM are defined to establish the PCM domain in the PV-PCM system.

The COMSOL Multiphysics® provides an automated process of meshing the geometry of the model. The default physics-controlled mesh sequence setting is invoked for the meshing of the field's geometry. The physics-controlled meshing process examines the physics to determine the size attributes and operations needed to create a mesh that is suited to the task. The tetrahedral mesh is used in the three-dimensional domain of the present system. Under the physics-controlled mesh sequence type, the different mesh settings from *coarse* to *extra fine* are chosen for conducting grid independence study, as shown in Fig. 3. The study shows that going from *fine* to *extra fine* yields no significant change in the PV temperature, therefore, *fine* mesh is selected as the preferred mesh option. There are 176822 domain elements, 45698 boundary elements, and 2308 edge elements in the final mesh. Fig. 4 shows the mesh that was created for the system with eight fins at 30° inclination.

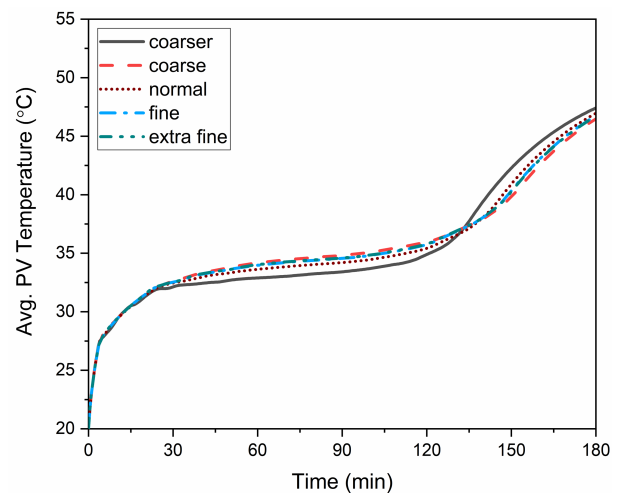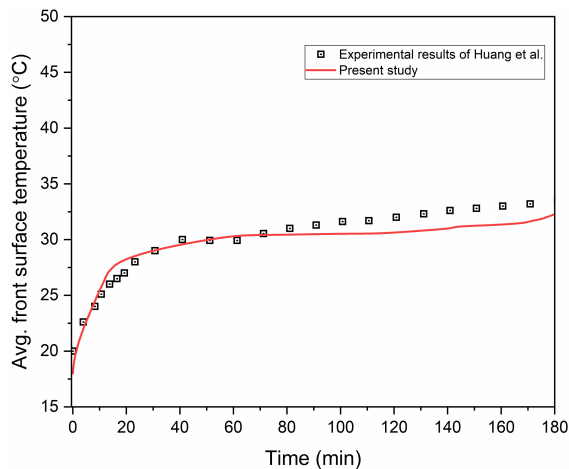**Figure 2.** PV-PCM system configurations with different numbers of fins at 15° inclination.



**Figure 3.** Grid Independence study.

Most time-dependent problems like the current one in COMSOL *Multiphysics* are solved by default using an adaptive time-stepping technique. The solver will adjust the appropriate time-step size to maintain the chosen *Relative Tolerance* of 0.001. Lowering the relative tolerance to smaller values results in smaller time steps, thereby improving solution accuracy and reducing solving time. Here, the initial time-step size is set to 0.001 sec, and the maximum time step that can be taken is set to one second. The solver will automatically adjust the time-step size as needed to address any fast variations in the solution during the solution procedure. The implicit Backward Differentiation Formula (*BDF*) with an order of accuracy equal to 2 is utilised as the time-stepping approach.

**Figure 4.** Generated mesh.

The current model is validated by comparing the simulation predictions with the experimental results of Huang et al. (2011) for the thermal performance of a PV-PCM system with internal fins. The fins are provided in the PCM domain with 24 mm spacing, and the top surface of the PV-PCM system is exposed to a constant flux of 750 W/m$^2$ with an initial temperature of 19°C. RT27 is used PCM in the system for validation purpose. The measurements of the PV-PCM system are 0.132 m × 0.04 m × 0.3 m. The experimental average temperature of the finned PV-PCM system is compared with the simulated values, as shown in Fig. 5. It can be inferred from the comparison that the simulated predictions are found to be in



reasonable agreement with the experimental results.

**Figure 5.** Validation of the model.

## SIMULATION OF THE SYSTEM

The performance of PV module in different configurations of PV-only systems, PV-PCM systems (no fins) and finned PV-PCM systems considered in the present work are numerically simulated. The effect of including the PCM and fins in the system on the performance of the PV module was analysed by comparing it with the performance of the only system at different inclinations. The numbers of fins considered for the study are no fin, 2, 4, 6 and 8, and different inclinations of the system considered are 0°, 15°, 30 and 45°. All the configurations of the system systems under the study are subjected to constant solar radiation flux throughout the duration of the

simulation, considered with an ambient temperature. The area of the PV module is 120 mm×60 mm. Fins having lengths of 10 mm (half fin), 15 mm (three-quarter fin) and 20 mm (full fin) are considered in the PCM in different systems. The average PV temperature profiles, temperature contours, and PV efficiency variation are simulated for all the PV-PCM and finned PV-PCM systems and compared with the conventional PV-only system. The time-dependent study is carried out for all the configurations.

## RESULTS AND DISCUSSION

The investigations were carried out for different configurations of finned PV-PCM systems with the inclusion of longitudinal fin with multiple numbers of fins and lengths at various inclinations, and the effect of fins and PCM on the performance of the PV module was explored.

### For PV-only Case

Fig. 6 depicts the temporal evolution of average PV temperature and PV efficiency of standard PV alone systems at various orientations. The temperature rises rapidly with time, reaching an almost steady-state temperature of 88.7 °C and 65.4 °C for 0° and 45° inclinations, respectively, in almost 45 min, as shown in Fig. 6 (a). External natural and forced convection, along with radiation, are the sources of cooling. The PV temperature decreases because of the increased external natural convection heat transfer rate with an inclination angle. The lowest PV temperature is observed for the system with a 45° inclination. The efficiency of the PV module follows the opposite trend compared to PV temperature, and PV efficiency rises as the inclination rises, as shown in Fig. 6 (b).

### For Finned PV-PCM

Fig. 7 shows the time-dependent variation of average PV temperature of all PV-PCM system (no fin) configurations and finned PV-PCM system configurations with different fin lengths of 10 mm, 15 mm and 20 mm at different inclinations. The average PV temperature decreases with the increasing inclination of the system, with the lowest PV temperature recorded at an inclination of 45°. When the PV-PCM system is in horizontal orientation ($\theta = 0°$), the presence of the buoyant forces is negligible, and convection currents within the melted PCM of the system hardly exist. As a result, conduction is the primary mode of heat transfer within the PCM, resulting in thermal stratification. Due to this, the rate of heat transfer involved through PCM is less, which leads to the maximum PV temperature for horizontal systems than systems at other inclinations. There is a significant presence of buoyant force, which is volumetric in nature and thus, the existence of convection currents in the melted PCM for sloped PV-PCM systems. Convection heat transfer becomes the major heat transfer mode within the melted PCM due

to this increased intensity of buoyant volumetric force. So, natural convection heat transfer plays a vital role, which affects the melting rate of PCM. The direction of the gravitational force vector is highly important in this scenario. The intensity of the convection heat transfer rate so developed increases with increasing inclination, thereby enhancing the rate of heat transfer from the PV module and lowering the temperature of the module. Hence, it is critical to look into how the inclination of the overall system affects the thermal processes that occur within it.

It is evident for PV-PCM systems from Fig. 7 that the solid PCM first receives heat, resulting in a sharp increase in time-dependent temperature initially due to sensible heating. After that, the melting process of PCM begins and continues until the solid PCM becomes liquid. Within the melting zone, the PCM temperature rises slightly. Whatever heat is transferred from the PV module is used by PCM to satisfy its latent heat requirement for undergoing a phase change. The time interval required from the commencement of the phase change process to its completion is the actual period of thermal regulation. Heat transfer to the PCM after the phase change process leads to sensible heating of the liquid PCM, which causes the steep temperature rise. This behaviour can be observed for all PV-PCM systems irrespective of its inclination.

However, the poor thermal conductivity of paraffin PCMs creates a hurdle for the higher heat extraction from the PV module to the PCM in the system. The heat transfer rate is lower for sensible heating of the solid PCM because as the layer thickness increases, conduction is the only heat transfer mode through the solid PCM at any inclination of the system. The thermal resistance of the PCM is too high for the required phase transformation rate because of its low thermal conductivity. Natural convection can form in the liquid PCM layer due to a temperature difference between the heated boundary and the solid section of the PCM, complicating the physical scenario. The system's geometry and PCM thickness determine the extent of natural convection and its contribution to overall heat transfer. Aluminium Fins were included in the system to overcome the low thermal conductivity of the paraffin PCM in the present work. Low density and high thermal conductivity of aluminium compared to many other metals results in a significantly lighter thermal energy storage device. The inclusion of fins in the PV-PCM system transforms the system into a finned PV-PCM system. Fins of multiple numbers and different heights are used to establish different finned systems. This leads to a considerable reduction of the operating temperature of the PV module in the finned PV-PCM systems with different numbers of fins and fin lengths considered at any inclination compared to the PV-PCM system, as shown in Fig. 7. The presence of fins within the PCM enhances the heat transfer rate from the PV module to PCM and improves the module's performance in the finned PV-PCM systems at all inclinations. A steep increase in temperature of the module during sensible heating of the PCM in the solid and liquid phases and a slight increase in temperature of the module during the phase change process of the PCM are also seen in all the configurations of the finned PV-PCM systems. It is worth noting that the temperature trends converge in the end, indicating that the entire PCM has melted. The presence of fins accelerates all the thermal processes, and the thermal regulation happens at a lower temperature compared to the unfinned cases.

The fin heights of 10 mm, 15 mm and 20 mm are selected and distributed evenly over the PCM domain. Fins are used in PCM to increase the heat transfer surface area. The liquid PCM will have more thermal contact with the heat transfer surface when fins are introduced into the system, and thermal resistance to heat transfer will be lowered consequently. The heat transfer rate from PV to PCM and inside the PCM is greatly improved by the presence of fins because more area is accessible for heat transfer. As a result, the PV temperature drops, increasing its energy conversion performance.
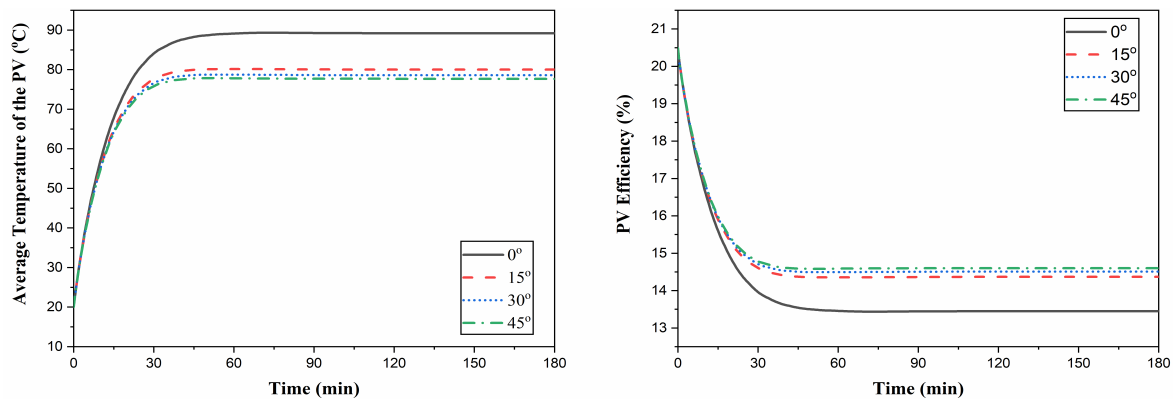


**Figure 6.** Variations of (a) average PV temperature and (b) PV efficiency with time for different inclinations of PV-only system.

From Fig. 7, it is evident that for the systems with fin lengths of 10 mm and 15 mm, the temperature is lowest initially for finned PV-PCM system with 8 fins up to 50 min for 10 mm fin systems and 80 min for 15 mm fin systems and then, the system with 6 fins shows the lowest temperature for all the angles except for the system with 10 mm fins at 0° case. The system with 2 fins shows the lowest average PV temperature after 50 min at 0° inclination with 10 mm fins. For the 20 mm fin length case (full fin), the lowest average PV temperature is obtained for the finned PV-PCM system with 6 fins for all the angles. When comparing different lengths of fins, systems with 20 mm fin lengths are found to be better systems with the lowest PV temperature. It is also clear that the relative temperature decreases with an increase in the inclinations of the systems. Considering the fin lengths, the number of fins and inclinations, the optimum system, i.e., one with the lowest PV temperature, is found for the PV-PCM PCM system with 6 fins at an inclination angle of 45°.
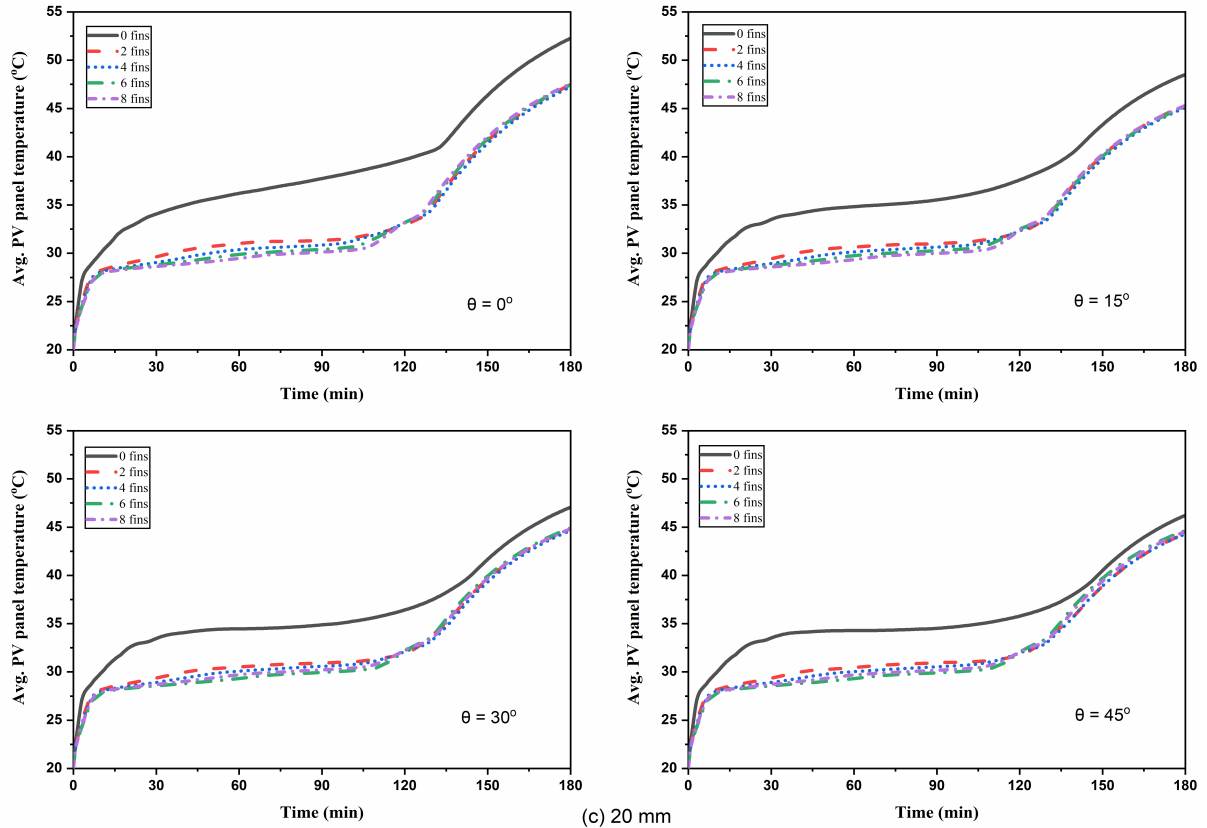


b) 15 mm

152
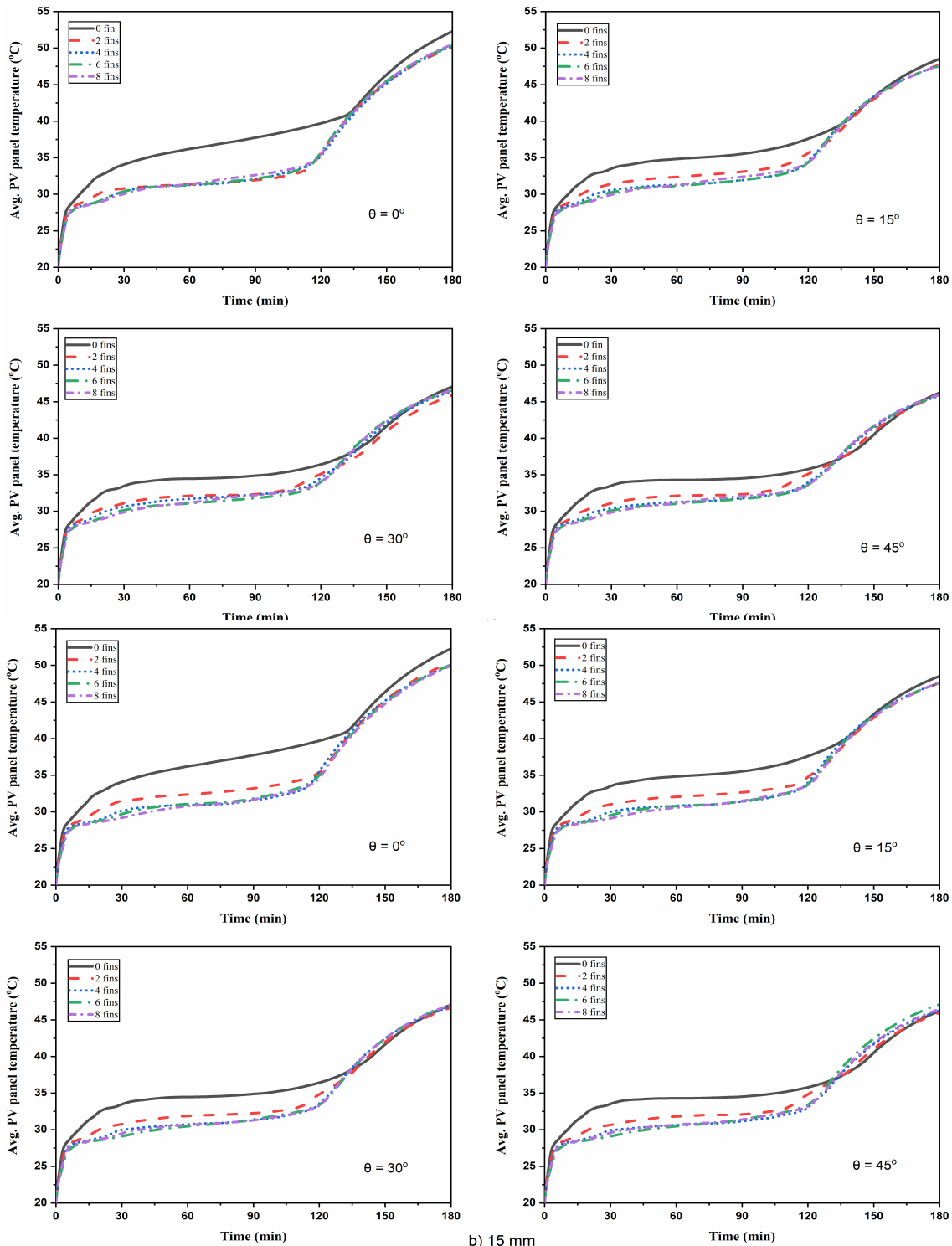
**Figure 7.** Variation of the mean temperature of the module with time for PV-PCM and finned PV-PCM systems with fin lengths (a) 10 mm, (b) 15 mm and (c) 20 mm at different inclinations.

The temperature contours of PV-PCM system (no fin) and finned PV-PCM (fin length of 20 mm) systems with the number of fins of 2, 4, 6 and 8 for the inclinations of 0°, 15°, 30°, and 45° at different instants are shown in Fig. 8 (a) - (e). The figures indicate that the temperature front for the horizontal system with the inclination of 0° orientation travels uniformly downwards with the progress of time for PV-PCM and finned PV-PCM systems. In the presence of fins for finned PV-PCM systems, the temperature front travels faster compared to the PV-PCM system due to the enhanced heat transfer rate to the PCM. The temperature front movement in inclined systems is non-uniform due to the presence of a buoyancy effect within the melted PCM. As solar radiation falls on the PV panel's front surface, the temperature rises, and heat transfer from the PV panel to the PCM begins. In its solid phase, the PCM absorbs and stores energy in the form of sensible heat as its temperature rises.

Storage of energy in the form of latent heat in PCM commences when the temperature of a solid PCM approaches the transition temperature. The temperature profile in inclined systems is non-uniform because of the existence of melted PCM's buoyancy effect by virtue of convection currents present in it. At first, pure conduction dominates the heat transfer process in PCM. The temperature front remains about parallel during the initial conduction-dominated melting process. As time progresses in the interaction between the module and PCM, the temperature front moves closer to the bottom. With time, the motion of the liquid PCM will be detected in the upper right portion of the melt zone, followed by a nearly immobile liquid PCM below it. Both conduction and convection heat transfer modes dominate the melting process in such a transition state. In the upper portion of the PCM liquid zone (dominated by convection), the temperature profile curves sharply, followed by a front parallel to the left wall in the lower half of the liquid region (conduction-dominated). The height of the convection-dominated zone increases with time throughout the transition phase. The convection-dominated zone of the transition regime will fill the whole domain of the PCM. The spontaneous circulation of liquid PCM distinguishes this regime. At a certain point in time, the upper part of the curved melting front makes contact with the right vertical wall. In the liquid phase, convection is the predominant route of heat transfer, while in the solid phase, conduction is the primary mode of heat transfer. After completing the melting process, the melted PCM absorbs energy from the PV module in sensible heat, and its temperature rises. During sensible heating, the heated liquid PCM near the upper aluminium plate flows downwards and circulates throughout the container. The inclusion of fins reduces PV temperature significantly, as shown by the contour plots, by virtue of improved heat transfer rate from the module to PCM in the system.
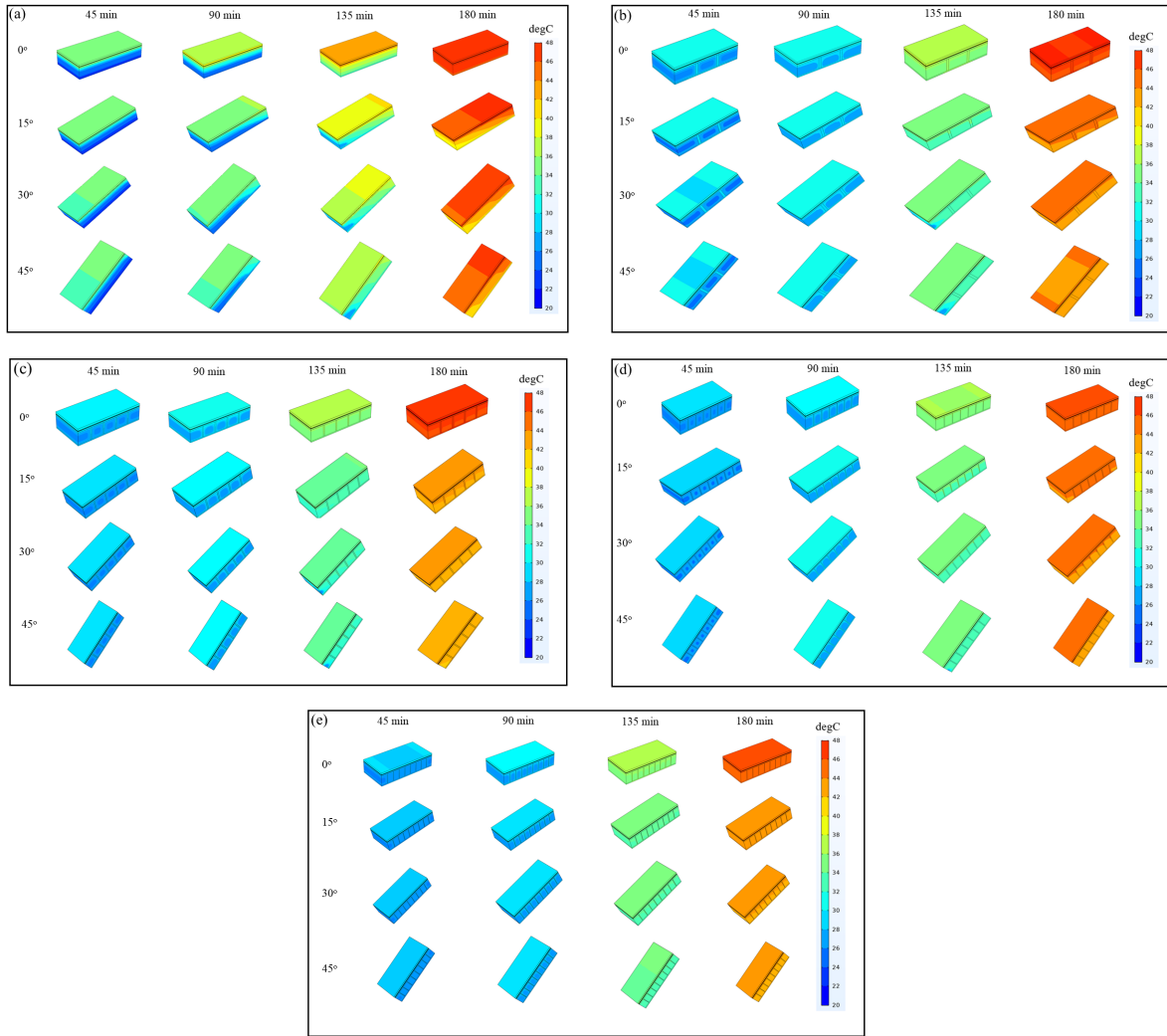
153

**Figure 8.** Temperature profiles and liquid PCM movement at various inclinations in different systems: (a) No fin (PV-PCM), (b) 2 fin, (c) 4 fin, (d) 6 fin and (e) 8 fin at different instants.

The trend of efficiency of the PV module is opposite to its temperature, and the same is explained with Eqn. (3). For mono and polycrystalline PV cells, an increase in operating temperature causes a decrease in open-circuit voltage, fill factor and power output, with an increase in short circuit current, which ultimately results in the loss of electrical efficiency of the module and irreversible damage to the PV cell materials. PV module works better at lower temperatures, as shown in Fig. 9. (a)-(c) At the system's inclinations, 45° and 0°, the highest and lowest efficiency trends are reported, respectively, for PV-PCM and finned PV-PCM systems of fin lengths 10 mm, 15 mm and 20 mm. The efficiency of the PV module is highest at 45° inclination for the finned PV-PCM system with 6 fins, as the PV temperature is lowest for this case.
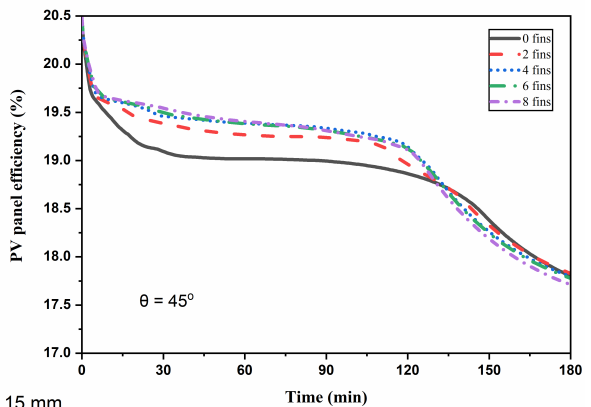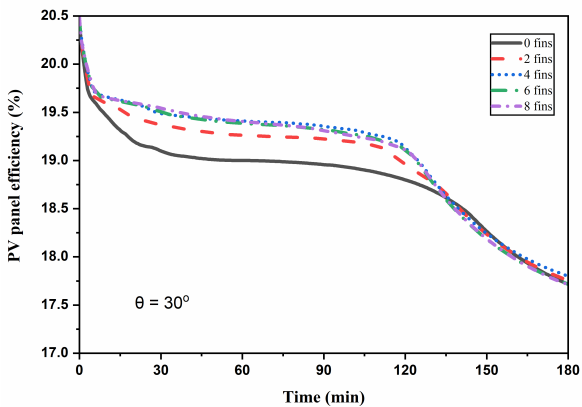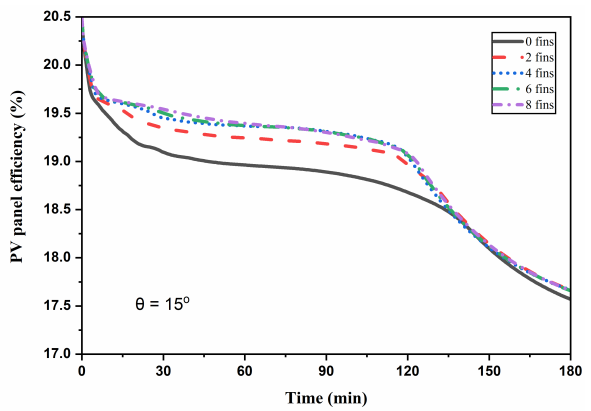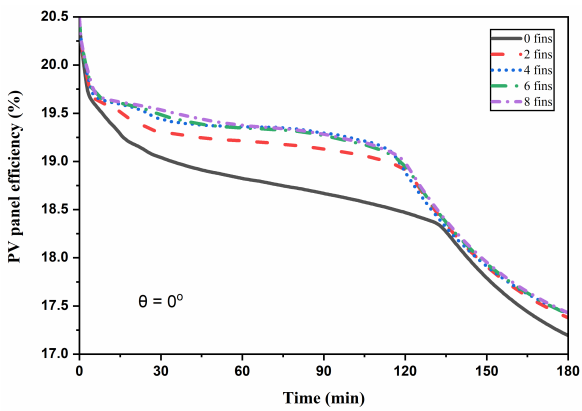
Trends of mean PV temperature and electrical efficiency of PV-PCM systems without any fins are compared with corresponding PV-only systems for each system's inclination. The maximum reduction in mean temperature and enhancement in the electrical efficiency of the module in the PV-PCM system over PV only system at each inclination is shown in Fig. 10.

The maximum PV temperature reduction of 53.4 °C, 45.58 °C, 44.4 °C, and 43.63 °C are achieved with PV-PCM systems at inclinations of 0°, 15°, 30°, and 45°, respectively. Maximum and minimum relative enhancement in electrical efficiency is obtained as 39.6% and 30.45% for PV-PCM systems at the inclinations of 0° and 45°, respectively.

Trends of mean PV temperature and electrical efficiency of PV-PCM systems without any fins are compared with corresponding PV-only systems for each system's inclination. The maximum reduction in mean temperature and enhancement in the electrical efficiency of the module in the PV-PCM system over PV only system at each inclination is shown in Fig. 10. The maximum PV temperature reduction of 53.4 °C, 45.58 °C, 44.4 °C, and 43.63 °C are achieved with PV-PCM systems at inclinations of 0°, 15°, 30°, and 45°, respectively. Maximum and minimum relative enhancement in electrical efficiency is obtained as 39.6% and 30.45% for PV-PCM systems at the inclinations of 0° and 45°, respectively.
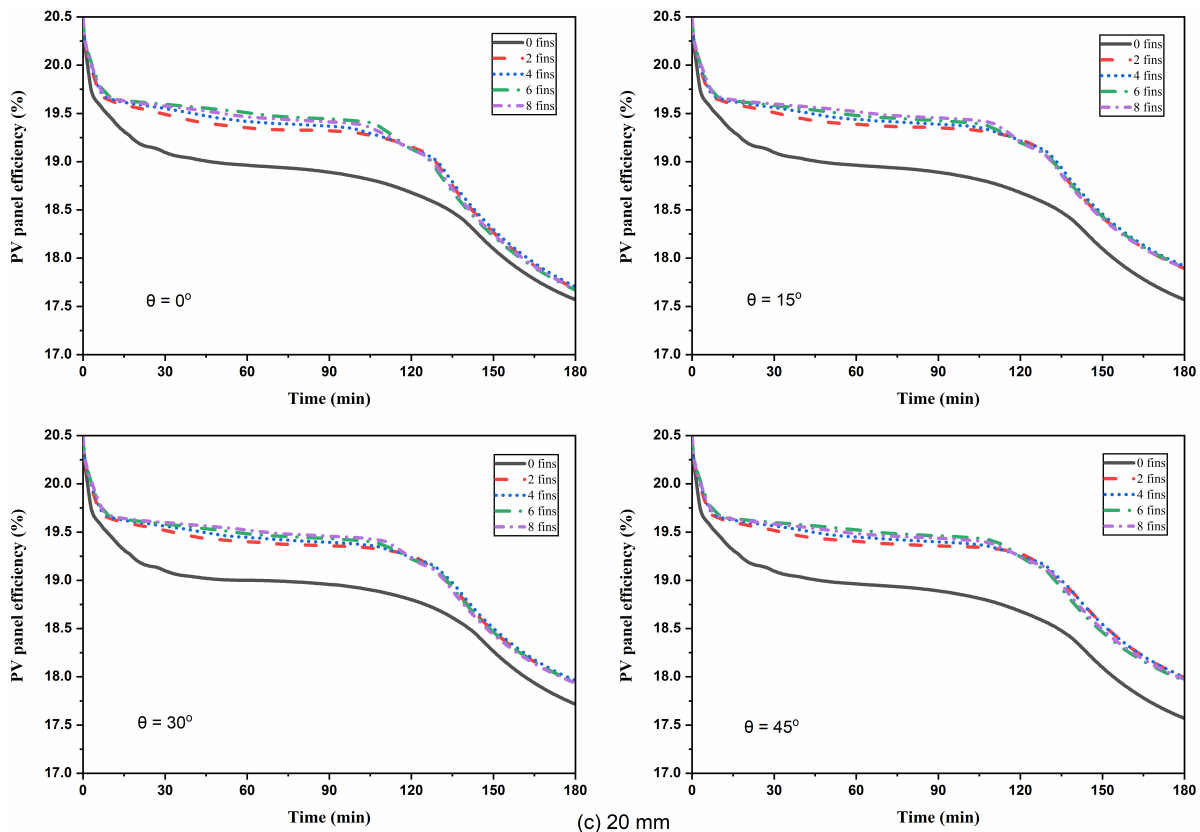
154
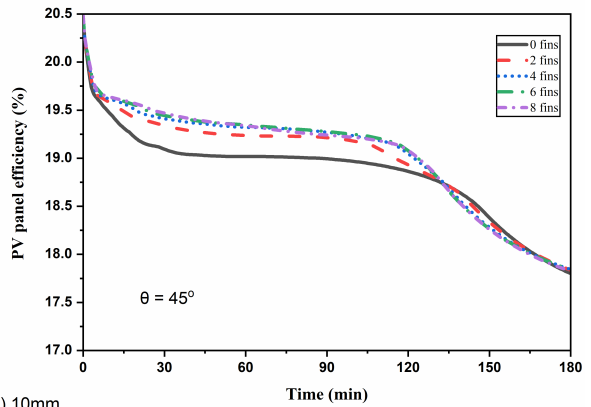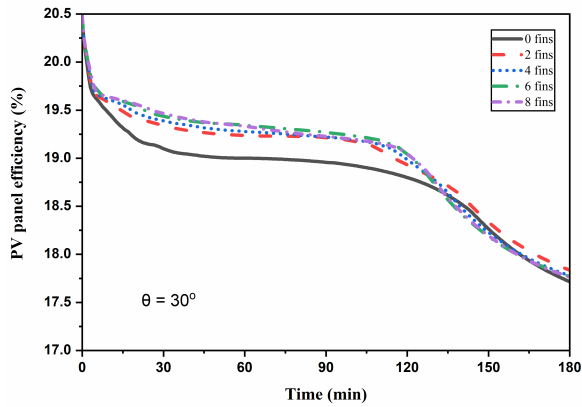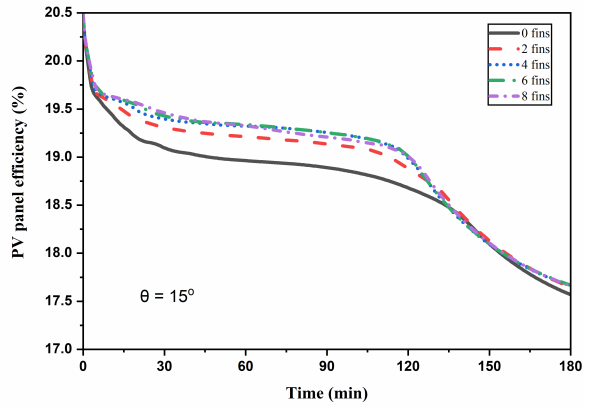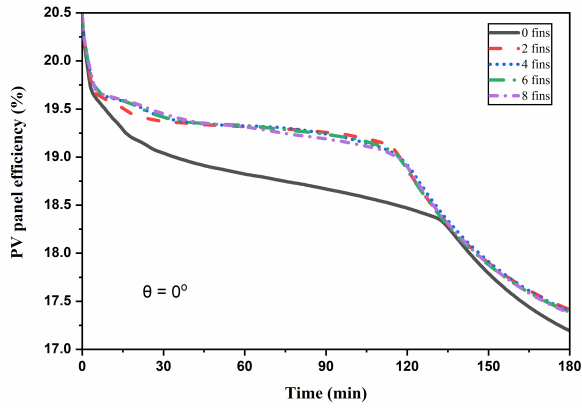
a) 10mm

b) 15 mm

**Figure 9.** Variation of electrical efficiency of the module with time for PV-PCM and finned PV-PCM systems with fin lengths (a) 10 mm (b) 15 mm and (c) 20 mm at different inclinations.
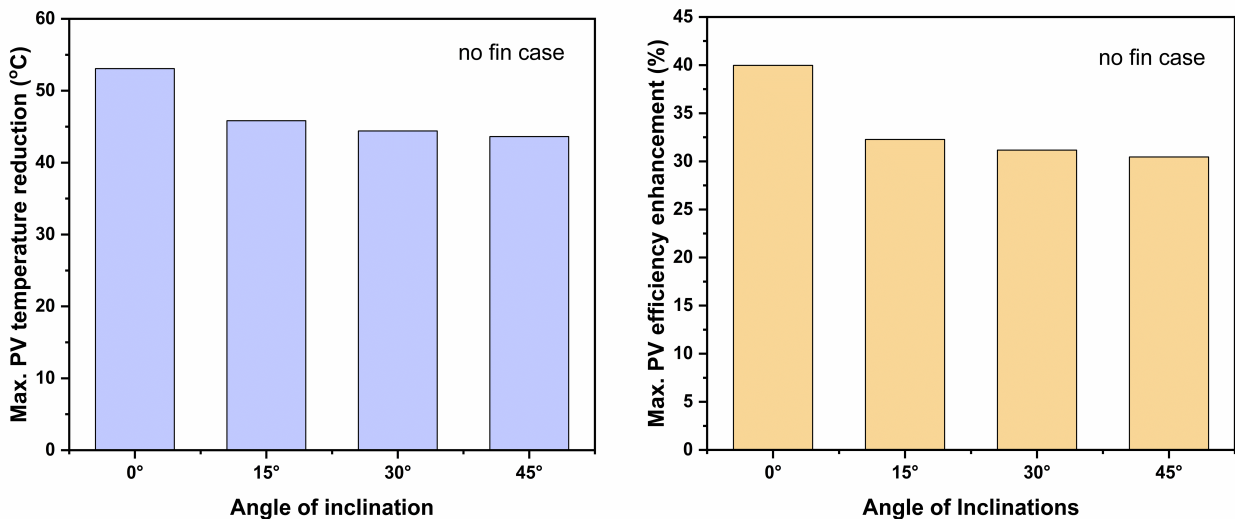


**Figure. 10** Comparison of (a) maximum reduction in PV temperature and (b) Maximum percentage increase in efficiency of PV-PCM systems of different orientations with PV-only cases.

Fig. 11 shows the highest PV temperature reduction for finned PV-PCM systems with different fin lengths and the number of fins at various orientations compared to the PV-only system. The inclusion of fins leads to the best results in the form of the highest temperature reduction of the module for horizontal systems due to the involvement of conduction heat transfer from the module to PCM in such systems. For horizontal systems, the conduction heat transfer rate is enhanced due to the inclusion of fins without any effect that reduces the rate of heat transfer. However, in the inclined systems, convection heat transfer mode is present when the PCM is in the liquid phase. Increased heat transfer area with the inclusion of the fins leads to a higher rate of heat transfer in inclined systems. But, higher surface area with finned systems will also enhance the fluid friction, which reduces the strength of convection currents. Hence, in the inclined systems, two competing opposite effects in the form of increased heat transfer rate and fluid friction are present, leading to a relatively lower effect compared to horizontal systems. As the figure indicates, for any inclination, with the

increase in fin length, the PV module temperature is further reduced, and consequently, electrical efficiency is improved. So when comparing the different fin lengths, systems with 20 mm fin length give the best results in terms of maximum PV temperature reduction and improving PV efficiency. Among the systems with 20 mm fin length, the performance statistics are relatively best when number of fins equals 6. It is also apparent that the effect of the inclusion of fins is greatest for horizontal systems with an inclination of 0° and diminishes as the inclination angle increases. The highest temperature reduction of 59.65 °C is observed for the PV-PCM system with 6 fins for fin length = 20 mm at an inclination angle 0°, and the lowest is observed for the system with 2 fins for 10 mm fin length at an inclination angle of 45°.
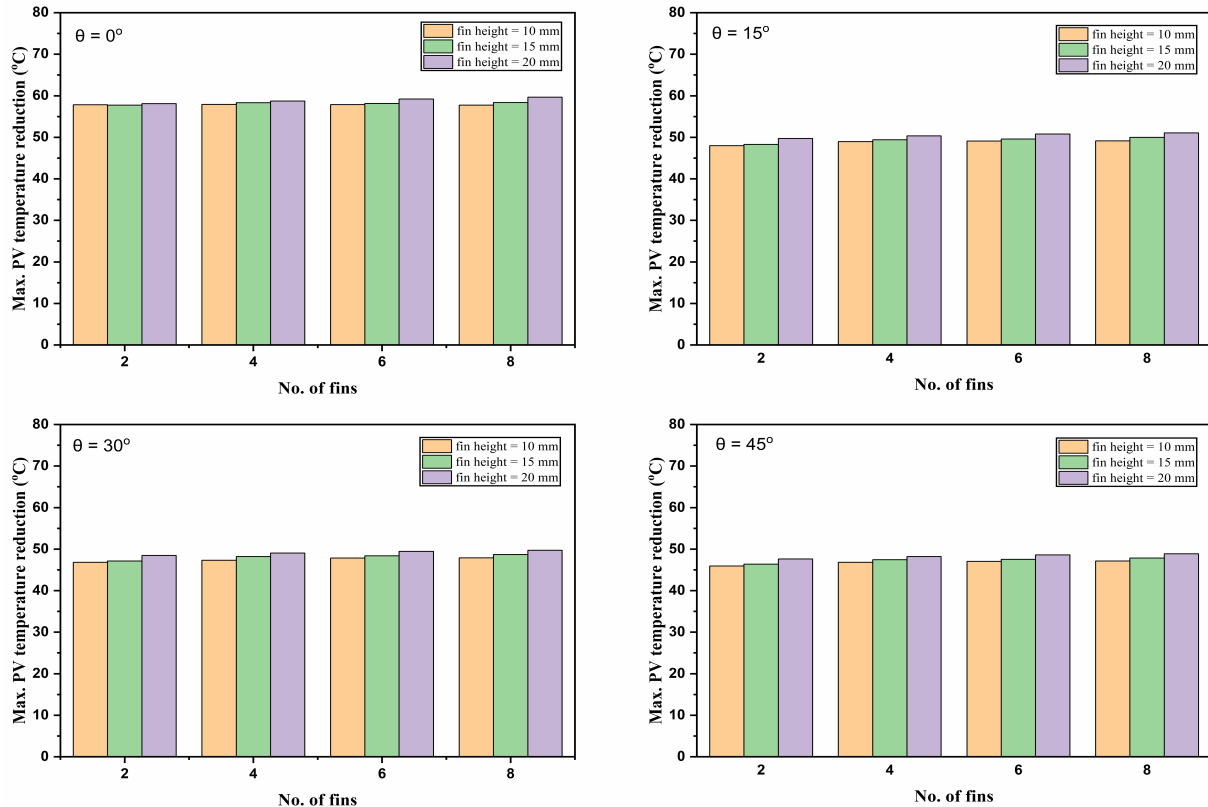


**Figure 11.** Comparison of maximum temperature reduction of finned PV-PCM with respect to multiple numbers of fins and inclinations for different fin lengths.

The comparison of maximum enhancement in electrical efficiency of the module for finned PV-PCM systems with different fin lengths and number of fins at various inclinations with PV-only systems is shown in Fig. 12. It is clear that efficiency levels increase with the increase in fin lengths, with a maximum obtained for 20 mm fin length (full length) configuration for a particular number of fins and inclination. The highest and lowest enhancement values of efficiency are obtained for systems with 0° and 45° orientations, respectively, indicating that the effect of fin inclusion is more prominent when the inclination is low. Maximum efficiency enhancement of 45.08% is obtained for the system with 6 fins at inclination 0° for fin length 20 mm and the least value of 32.07% obtained for 10 mm 2 finned PV-PCM systems at 45°. It is clear that the inclusion of fin is most effective when the inclination of the system is small.

As the PV efficiency values are highest for 20 mm fin length systems, the comparison of the maximum power output of PV module for different finned PV-PCM systems with fin lengths of 20 mm, including the unfinned system at different inclinations are shown in Fig. 13. There is a marked improvement in PV module power output for finned systems compared to unfinned one. The PV output levels increase with the increase in inclination angle for a particular number of fins. The PV power output is found to increase with the increase in number of fins for finned PV-PCM systems up to 6 fins, then decreases for the system with 8 fins. The maximum power output of 14.16 W is observed for the PV-PCM system with 6 fins at an inclination angle of 45°.

The time taken for the complete melting of PCM with respect to inclinations for different numbers of fins with 20 mm fin length is shown in Fig. 14. The figure shows that the melting is slower for unfinned systems compared to finned ones, indicating a lesser heat transfer rate inside PCM of unfinned systems. There is a considerable decrease in melting time with an increase in inclination as the heat transfer rate is higher to PCM in the systems at higher inclinations. This is due to the increased natural convection heat transfer rate within the melted PCM due to the existence of a

higher buoyant force. The reduction of PCM melting time with the increase in number of fins is because when the number of fins is higher, the surface area available for heat transfer within PCM is also higher.

The lowest melting time of PCM is obtained as 132 min for the system with 8 fins with an orientation of 45°, and the highest melting time is 148.7 min for the unfinned system with $\theta = 0$.
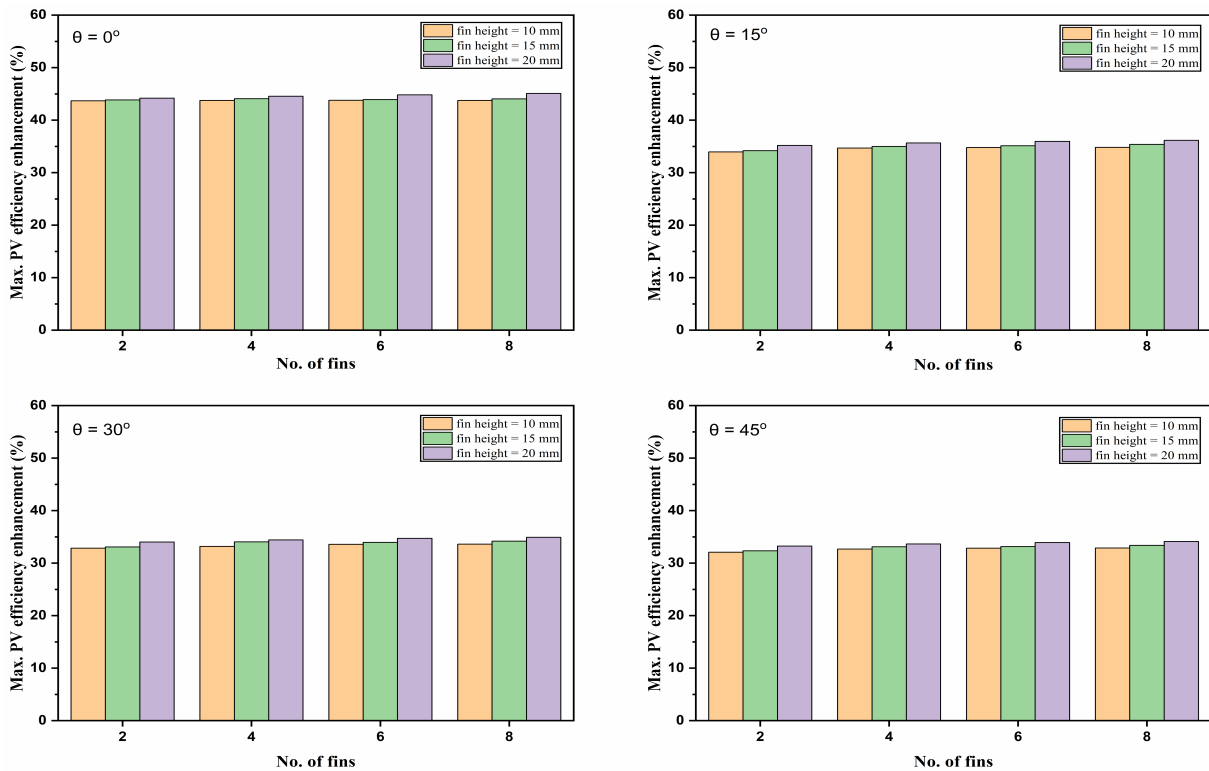


**Figure 12.** Comparison of maximum efficiency enhancement of finned PV-PCM systems with respect to multiple numbers of fins and fin lengths for different inclinations.

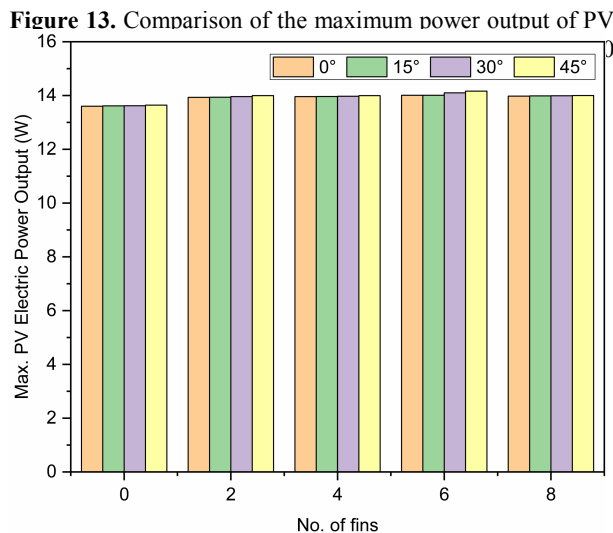**Figure 13.** Comparison of the maximum power output of PV



Fig. 15 (a)-(c) depicts the peak value of the average velocity of melted PCM for unfinned and finned PV-PCM systems with different fin lengths (half fin, three-quarter fin and full fin) at various inclinations. Peak average velocity indicates the strength of the convection current that has been created inside the melted PCM. Among the different finned PV-PCM systems considered in the present study, it is clear that the velocity values are generally lowest for full fin cases, indicating a reduction of convection currents inside the PCM. In the full fin case, the resistance to the flow of melted PCM increases as the flow channel's

length is reduced and fluid friction increases, which reduces the developed buoyancy force and consequent convection current inside the PCM chamber. The velocity magnitude appears to decrease with an increase in the number of fins as the convection channel length gets reduced and fluid friction increases further.
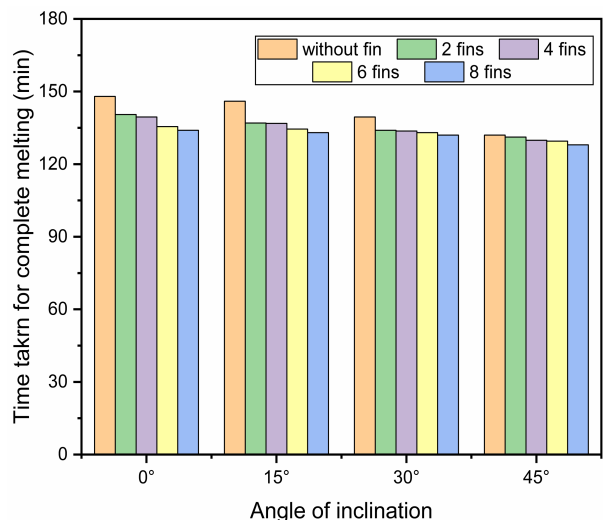


**Figure 14.** Comparison of melting time of PCM for all PV-PCM systems with 20 mm fin length at different inclinations.

Among all the systems with PCM, the lowest peak velocity magnitude is found in the unfinned PV-PCM system with the inclination of 0°, suggesting that convection heat transfer is insignificant and conduction is the primary heat transfer mode. As temperature differences inside the PCM rise, the peak velocity increases slightly with the number of fins for systems with 0° orientation. For inclined systems, because of the buoyancy force created within the melted PCM, the peak velocity increases as the angle of inclination increases for any fin length and number of fins. In the comparison of systems with full fin and unfinned cases, the highest magnitude of velocity is obtained as 0.61 mm/s for the unfinned PV-PCM system with the orientation of 45°. For three-quarter fin and half fin cases, the convection levels are higher than the full fin case as the flow of melted PCM can still occur through the space below the fin. The corresponding values are 0.893 mm/s for three quarter (15 mm) fin case with an inclination of 45° when the number of fins is two as well as 0.925 mm/s for half fin case (10 mm) with an inclination of 45° when the number of fins is 8.
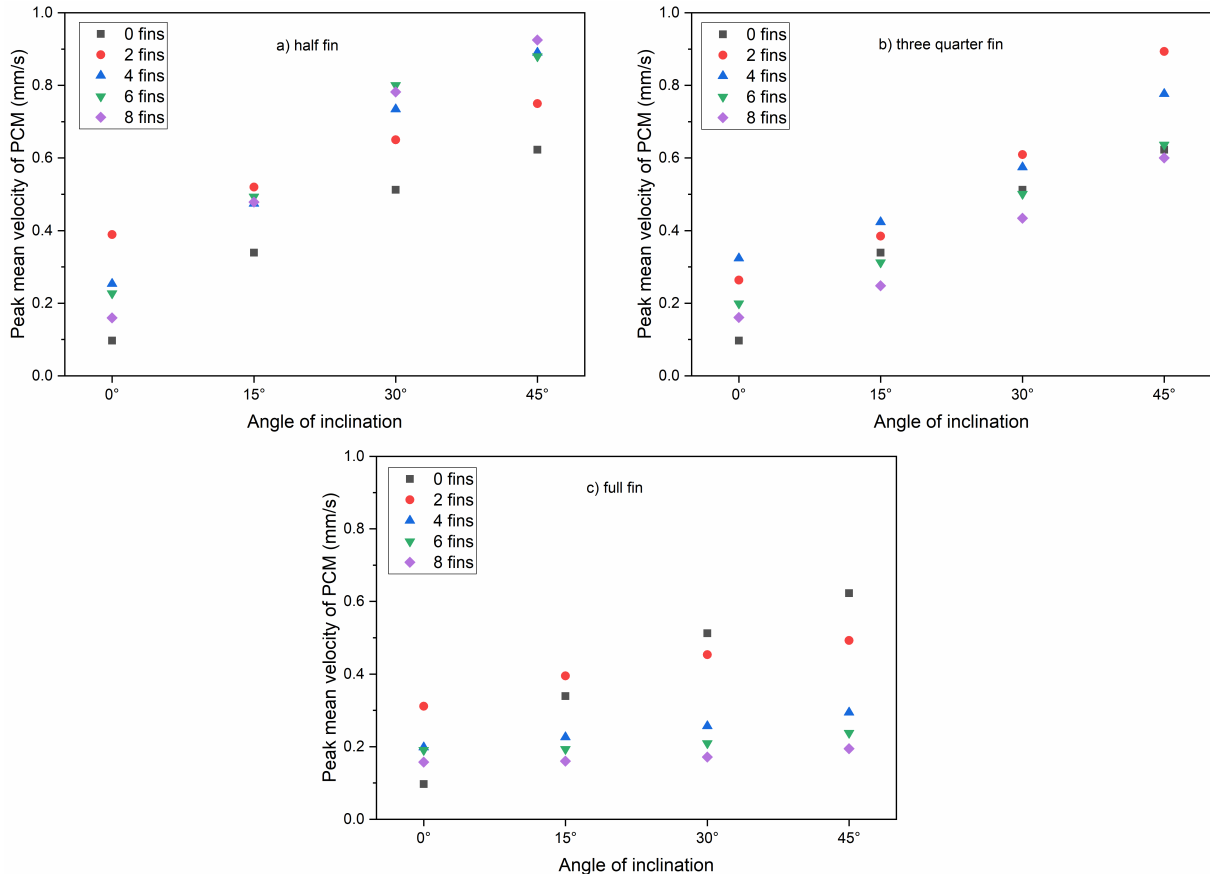


**Figure 15.** Comparison of peak magnitude of the velocity of melted PCM for finned PV-PCM systems at different inclinations: (a) half fin, (b) three-quarter fin, and (c) full fin.

## CONCLUSIONS

The performance augmentation of the PV module, when integrated with finned PCM (RT25HC) for different numbers of fins and fin lengths, is numerically investigated at different inclinations of the system using a three-dimensional model. It is found that both increases in the number of fins and inclination angle reduce the PV temperature and thereby enhance the electrical efficiency of the PV module. Different findings of the present investigations are summarized as follows:

- The average temperature of the PV module decreases with an increase in inclination and an increase in fin length. The PV efficiency follows the opposite trend in contrast to PV temperature; PV efficiency increases with the

inclination. The drop in the average temperature of the PV with the inclusion of PCM and fins is relatively highest for the finned PV-PCM system with 6 fins.

- For conventional PV-PCM systems (no fins), the maximum temperature reduction values compared to corresponding PV-only cases are 53.4°C and 43.63°C, respectively, for 0° and 45° orientations. The maximum efficiency enhancement for the corresponding orientations is 39.6% and 30.45%, respectively.

- The effectiveness of fin inclusion in the system tends to reduce with an increase in inclination.

- The effectiveness of increment in the number of fins is more prominent for full fin cases.
- The full-finned PV-PCM system with 6 fins gives a maximum PV temperature reduction of 59.65°C compared to the conventional PV-only system when the inclination is 0° among all the finned PV-PCM systems, and the corresponding maximum enhancement of efficiency is 45.1% compared to the PV-only system.
- The full-finned PV-PCM system with 6 fins and 45° inclination gives the highest instantaneous power output of 14.16 W.
- The melting rate of the PCM in the PV-PCM system is strongly influenced by inclination and number of fins, indicating the extent of the heat transfer rate within the PCM. Enhancement in melting rate with respect to increasing in inclination is due to increment in convective heat transfer rate, whereas with respect to number of fins, is due to increase in the rate of conduction heat transfer rate.
- The peak value of the average velocity of melted PCM increases with the inclination angle and decreases with the presence of fins. An increase in fin length also reduces the velocity values as it adversely affects the convection current inside melted PCM.

## REFERENCES

Abdulmunem, A.R., Mohd Samin, P., Abdul Rahman, H., Hussien, H.A., Izmi Mazali, I., Ghazali, H., 2021, Numerical and experimental analysis of the tilt angle's effects on the characteristics of the melting process of PCM-based as PV cell's backside heat sink, *Renew. Energy*, 173, 520–530.

Agrawal, B., Tiwari, G.N., 2010, Optimizing the energy and exergy of building integrated photovoltaic thermal (BIPVT) systems under cold climatic conditions, *Appl. Energy*, 87, 417–426.

Akshayveer, Kumar, A., Pratap Singh, A., Sreeram Kotha, R., Singh, O.P., 2021, Thermal energy storage design of a new bifacial PV/PCM system for enhanced thermo-electric performance. *Energy Convers. Management,* 250, 114912.

Ali, H.M., 2020, Recent advancements in PV cooling and efficiency enhancement integrating phase change materials based systems – A comprehensive review, *Sol. Energy*, 197, 163–198.

Azarpour, A., Suhaimi, S., Zahedi, G., Bahadori, A., 2013, A review on the drawbacks of renewable energy as a promising energy source of the future. *Arab. J. Sci. Eng*, 38, 317–328.

Balavinayagam, K., K S, U., Rohinikumar, B., 2021, Numerical investigations on phase change material-

based battery thermal management system. *J. Phys. Conf. Ser*, 2054, 012003.

Bilen, K., Erdoğan, İ., 2023, Effects of cooling on performance of photovoltaic/thermal (PV/T) solar panels: A comprehensive review. *Sol. Energy*, 262, 111829.

Biwole, P.H., Groulx, D., Souayfane, F., Chiu, T., 2018. Influence of fin size and distribution on solid-liquid phase change in a rectangular enclosure, *Int. J. Therm. Sci.*, 124, 433–446.

Brent, A.D., Voller, V.R., Reid, K.J., 1988, Enthalpy-porosity technique for modeling convection-diffusion phase change: Application to the melting of a pure metal, *Numer. Heat Transf.*, 13, 297–318.

Bria, A., Raillani, B., Chaatouf, D., Salhi, M., Amraqui, S., Mezrhab, A., 2023, Effect of PCM thickness on the performance of the finned PV/PCM system, *Mater. Today Proc.,* 72, 3617–3625.

Chibani, A., Merouani, S., Laidoudi, H., Dehane, A., Morakchi, M.R., Bendada, L., 2023, Analysis and optimization of concentrator photovoltaic system using a phase change material (RT 35HC) combined with variable metal fins, *J. Energy Storage*, 72.

Cuce, E., Bali, T., Sekucoglu, S.A., 2011, Effects of passive cooling on performance of silicon photovoltaic cells, *Int. J. Low-Carbon Technol.*, 6, 299–308.

Cuce, E., Cuce, P.M., 2014, Tilt Angle Optimization and Passive Cooling of Building-Integrated Photovoltaics (BIPVs) for Better Electrical Performance, *Arab. J. Sci. Eng.*, 39, 8199–8207.

Da, J., Li, M., Li, G., Wang, Y., Zhang, Y., 2023, Simulation and experiment of a photovoltaic—air source heat pump system with thermal energy storage for heating and domestic hot water supply, *Build. Simul.*

Duan, J., 2021, The PCM-porous system used to cool the inclined PV panel, *Renew. Energy*, 180, 1315–1332.

Dubey, S., Sarvaiya, J.N., Seshadri, B., 2013, Temperature dependent photovoltaic (PV) efficiency and its effect on PV production in the world - A review, *Energy Procedia*, 33, 311–321.

Emam, M., Ahmed, M., 2018, Cooling concentrator photovoltaic systems using various configurations of phase-change material heat sinks, *Energy Convers. Manag.*, 158, 298–314.

Fujii, T., Imura, H., 1972, Natural-convection heat transfer from a plate with arbitrary inclination, *Int. J. Heat Mass Transf.*, 15, 755–767.

Groulx, D., Biwole, P.H., Bhouri, M., 2020, Phase change heat transfer in a rectangular enclosure as a function of inclination and fin placement, *Int. J. Therm. Sci.*, 151, 106260.

Huang, M.J., Eames, P.C., Norton, B., Hewitt, N.J., 2011, Natural convection in an internally finned phase change material heat sink for the thermal management of photovoltaics, *Sol. Energy Mater. Sol. Cells*, 95, 1598–1603.

Hui Dai, Wei-Min Ma, 2002, A novelty Bayesian method for unsupervised learning of finite mixture models, *in: Proceedings of 2004 International Conference on Machine Learning and Cybernetics (IEEE Cat. No.04EX826). IEEE*, pp. 3574–3578.

Incropera, F., Dewitt, D., 1985, *Introduction to heat transfer*, John Wiley and Sons Inc, United States.

Johnston, E., Szabo, P.S.B., Bennett, N.S., 2021, Cooling silicon photovoltaic cells using finned heat sinks and the effect of inclination angle, *Therm. Sci. Eng. Prog.*, 23, 100902.

Kaldellis, J.K., Kapsali, M., Kavadias, K.A., 2014, Temperature and wind speed impact on the efficiency of PV installations, Experience obtained from outdoor measurements in Greece, *Renew. Energy*, 66, 612–624.

Kant, K., Shukla, A., Sharma, A., Biwole, P.H., 2016, Heat transfer studies of photovoltaic panel coupled with phase change material, *Sol. Energy*, 140, 151–161.

Kaplani, E., Kaplanis, S., 2014, Thermal modelling and experimental assessment of the dependence of PV module temperature on wind velocity and direction, module orientation and inclination, *Sol. Energy*, 107, 443–460.

Kazem, H.A., Al-Waeli, A.H.A., Chaichan, M.T., Sopian, K., Ahmed, A.A., Wan Nor Roslam, W.I., 2023, Enhancement of photovoltaic module performance using passive cooling (Fins): A comprehensive review, *Case Stud. Therm.*, Eng. 49, 103316.

Khanna, S., Newar, S., Sharma, V., Reddy, K.S., Mallick, T.K., 2019, Optimization of fins fitted phase change material equipped solar photovoltaic under various working circumstances, *Energy Convers. Manag.*, 180, 1185–1195.

Khanna, S., Reddy, K.S., Mallick, T.K., 2018, Optimization of finned solar photovoltaic phase change material (finned pv pcm) system, *Int. J. Therm. Sci.*, 130, 313–322.

Khanna, S., Reddy, K.S., Mallick, T.K., 2017, Performance analysis of tilted photovoltaic system integrated with phase change material under varying operating conditions, *Energy*, 133, 887–899.

Klemm, T., Hassabou, A., Abdallah, A., Andersen, O., 2017, Thermal energy storage with phase change materials to increase the efficiency of solar photovoltaic modules, *Energy Procedia*, 135, 193–202.

Kumar, K.S., Kumar, H.A., Gowtham, P., Kumar, S.H.S., Sudhan, R.H., 2020, Experimental analysis and increasing the energy efficiency of PV cell with nano-PCM (calcium carbonate, silicon carbide, copper), *Mater. Today Proc.*, 37, 1221–1225.

Mahdi, J.M., Mohammed, H.I., Talebizadehsardari, P., 2021, A new approach for employing multiple PCMs in the passive thermal management of photovoltaic modules, *Sol. Energy*, 222, 160–174.

Metwally, H., Mahmoud, N.A., Ezzat, M., Aboelsoud, W., 2021, Numerical investigation of photovoltaic hybrid cooling system performance using the thermoelectric generator and RT25 Phase change material, *J. Energy Storage*, 42, 103031.

Mohanraj, M., Gunasekar, N., Velmurugan, V., 2016, Comparison of energy performance of heat pumps using a photovoltaic – thermal evaporator with circular and triangular tube configurations, *Building Simulations*, 9, 27–41.

Nouira, M., Sammouda, H., 2018, Numerical study of an inclined photovoltaic system coupled with phase change material under various operating conditions, *Appl. Therm. Eng.*, 141, 958–975.

Park, J., Kim, T., Leigh, S.B., 2014, Application of a phase-change material to improve the electrical performance of vertical-building-added photovoltaics considering the annual weather conditions, *Sol. Energy*, 105, 561–574.

Poirier, D.R., 1987, Permeability for flow of interdendritic liquid in columnar-dendritic alloys, *Metall. Trans. B.*, 18, 245–255.

Sasidharan, U.K., Bandaru, R., 2022, Thermal management of photovoltaic panel with nano-enhanced phase change material at different inclinations, *Environ. Sci. Pollut. Res.*, 29, 34759–34775.

Savvakis, N., Dialyna, E., Tsoutsos, T., 2020, Investigation of the operational performance and efficiency of an alternative PV + PCM concept, *Sol. Energy*, 211, 1283–1300.

Sharma, S., Tahir, A., Reddy, K.S., Mallick, T.K., 2016, Performance enhancement of a Building-Integrated Concentrating Photovoltaic system using phase change material, *Sol. Energy Mater. Sol. Cells*, 149, 29–39.

161

Singh, P., Khanna, S., Becerra, V., Newar, S., Sharma, V., Mallick, T.K., Hutchinson, D., Radulovic, J., Khusainov, R., 2020, Power improvement of finned solar photovoltaic phase change material system, *Energy*, 193, 116735.

Unnikrishnan, Jayatej, M., B, R., 2023, Three-dimensional numerical analysis of performance of PV module integrated with PCM and internal pin fins of different shapes, *J. Therm. Anal. Calorim.*, 148, 9739–9760.

Variji, N., Siavashi, M., Tahmasbi, M., Bidabadi, M., 2022, Analysis of the effects of porous media parameters and inclination angle on the thermal storage and efficiency improvement of a photovoltaic-phase change material system, *J. Energy Storage*, 50, 104690.

Yıldız, Ç., Arıcı, M., Nižetić, S., Shahsavar, A., 2020, Numerical investigation of natural convection behavior of molten PCM in an enclosure having rectangular and tree-like branching fins, *Energy*, 207.

**Unnikrishnan K S** is currently a research scholar in the Dept. of Mechanical Engr. at the National Institute of Technology, Calicut, Kozhikode, India. He obtained his M.Tech. degree, specialising in thermal power engineering, from APJ Abdul Kalam Technological University, Kerala, in 2018. He received a B.Tech. degree in mechanical engineering from Mahatma Gandhi University, Kottayam. His current research interest focuses on the passive thermal management of PV, heat transfer, phase change material, and CFD.

**Sumanth Babu Pathipati** is currently an Associate Software Engineer at IQVIA Bengaluru, India. He completed his M Tech degree, specialising in energy engineering and management, in 2022 from the National Institute of Technology, Calicut, India. He earned his B.Tech. degree in Mechanical Engineering in 2019 from VRS Engineering College, Andhra Pradesh, India. His areas of interest include heat transfer, thermal management, and energy systems.

**Dr. Rohinikumar Bandaru** is currently an Asst. Prof. at the Dept. of Mech. Engr., National Inst. of Tech. Calicut, India. He obtained his PhD in Mech. Engr. from the National Institute of Technology, Calicut, India, in 2018. He has teaching experience spanning more than 20 years in the areas of thermodynamics, fluid mechanics, heat transfer, Fluid Flow and Heat Transfer in Energy Systems, Analytical Methods in Heat Transfer , Thermodynamic Property Relations and Exergy Analysis, Design and Analysis of Energy Systems and Computational Fluid Dynamics and Heat Transfer. His research interests include Fluid Flow and Heat Transfer; Experimental Investigations, Modeling, and Simulation of Solar Energy Systems; Thermal Management on Solar PV Panels; Lithium-ion battery thermal management; Thermal management of Fuel cell and Heat pipes as well as vapour chamber Modelling and refrigeration, and Air-Conditioning.

# THEORETICAL PERFORMANCE ASSESSMENT OF A PARABOLIC TROUGH HUMIDIFYING SOLAR COLLECTOR-BASED SOLAR STILL

**Harris J.N. WELEPE \*, Hüseyin GÜNERHAN \*\*, Levent BİLİR \*\*\***
\* Graduate School of Natural and Applied Sciences, Mech. Engr. Dept., Ege Uni., 35100-Bornova-Izmir,
hwelepe@gmail.com ; harrisharrismail@gmail.com, ORCID: 0000-0001-7431-9813
\*\* Department of Mechanical Engineering, Faculty of Engineering, Ege University, 35100-Bornova-Izmir
huseyingunerhan@gmail.com, ORCID: 0000-0003-4256-2418
\*\*\* Department of Energy Systems Engineering, Faculty of Engr., Yaşar University, 35230-Bornova-Izmir
levent.bilir@yasar.edu.tr, ORCID: 0000-0002-8227-6267

**Abstract:** In this paper, a parabolic trough humidifying solar collector-based solar still (PHSC-SS) is proposed. Its purpose is to apply some important performance improvement techniques to the flat plate humidifying solar collector-based solar still (flat plate HSC-SS), to significantly improve overall system performance. These included the use of parabolic trough solar concentrators and the design of humidifying solar collectors from evacuated tube collectors. The results reveal that, unlike flat plate HSC-SS, which must operate with a turbulent airflow regime to achieve optimum overall performance, PHSC-SS must operate with a laminar airflow regime and high inlet and outlet temperatures of air (at least 55 °C and less than 100 °C, at atmospheric pressure) in the heat collector element. For 900 W/m² of incident solar irradiance, 2 m² of solar collector area, and 0,00042 kg/s of air flow rate, the maximum energy efficiency, exergy efficiency and daily freshwater productivity of PHSC-SS were found to be 68,12%, 14,87% and 1,697 kg/h, respectively. Whereas for the same incident solar irradiance and solar collector area, and 0,1 kg/s of air flow rate, those of the flat plat HSC-SS were 72,9%, 1,12%, and between 1,07 – 2,923 kg/h (for inlet and outlet temperatures of air less than 30 °C, at atmospheric pressure), respectively. Although in some extreme cases freshwater productivity of flat plate HSC-SS can be higher than that of PHSC-SS, it should be noted that laminar airflow regime confers great advantages to PHSC-SS. These are higher air temperatures at condenser inlet (which ease water condensation process), no need of an auxiliary cooling device (needed in the flat plate HSC-SS), less mechanical vibrations of system, reduced condenser size, and less energy consumed by air blowers. Furthermore, the upper limit of the PHSC-SS is a PHSC-SS that operates without air flow, but rather by vaporization of water droplets at boiling point from absorber, followed by their suction to condenser, similarly to a flash evaporation.
**Keywords**: seawater desalination, parabolic trough humidifying solar collector, heat collector element, energy efficiency, exergy efficiency

## PARABOLİK OLUKLU NEMLENDİRİCİ GÜNEŞ KOLLEKTÖRÜ BAZLI GÜNEŞ ENERJİLİ DESALİNASYON SİSTEMİNİN TEORİK PERFORMANS DEĞERLENDİRİLMESİ

**Özet:** Bu makalede, parabolik oluklu nemlendirici güneş kolektörü bazlı güneş enerjili desalinasyon sistemi (PHSC-SS) önerilmektedir. Amacı, bazı önemli performans iyileştirme tekniklerini düz plaka nemlendirici güneş kolektörü bazlı desalinasyon sistemine (düz plaka HSC-SS) uygulamaktır. Genel sistem performansını önemli ölçüde iyileştirmek içindir. Bunlar arasında parabolik oluklu güneş yoğunlaştırıcılarının kullanımı ve nemlendirici güneş kolektörlerinin tahliye borulu kolektörlerden tasarlanması yer almaktadır. Sonuçlar, optimum genel performans elde etmek için türbülanslı bir hava akışı rejimiyle çalışması gereken düz plakalı HSC-SS'nin aksine, PHSC-SS'nin laminer bir hava akışı rejimiyle ve ısı kolektörü elemanında yüksek hava giriş ve çıkış sıcaklıklarıyla (atmosferik basınçta en az 55 °C ve 100 °C'den düşük) çalışması gerektiğini ortaya koymaktadır. 900 W/m² gelen güneş ışınımı, 2 m² güneş kolektörü alanı ve 0,00042 kg/s hava akış hızı için PHSC-SS'nin maksimum enerji verimi, ekserji verimi ve tatlı su üretkenliği sırasıyla %68,12, %14,87 ve 1.697 kg/saat olarak bulunmuştur. Aynı gelen güneş ışınımı, güneş kolektörü alanı, ve 0,1 kg/s hava akış hızı için düz plakalı HSC-SS'nin elde edilen değerleri sırasıyla %72,9, %1,12 ve atmosferik basınçta 30 °C'den düşük hava giriş ve çıkış sıcaklıkları için 1,07 - 2,923 kg/saat arasında olarak bulunmuştur. Bazı aşırı durumlarda düz plakalı HSC-SS'nin tatlı su verimliliği,

PHSC-SS'den daha yüksek olsa da, laminer hava akımı rejiminin PHSC-SS'ye büyük avantajlar sağladığı belirtilmelidir. Bunlar, kondenser girişindeki daha yüksek hava sıcaklıkları (suyun yoğuşma işlemi kolaylaştırması), yardımcı bir soğutma cihazına gerek olmaması (düz plakalı HSC-SS'te gereklidir), sistemin daha az mekanik titreşimi, kondenser boyutunun küçülmesi ve hava üfleyiciler tarafından daha az enerji tüketilmesidir. Ayrıca, PHSC-SS'nin üst sınırı, hava akışı olmadan çalışan bir PHSC-SS'dir. Bu sistem, kaynama noktasındaki su damlacıklarının absorberden buharlaştırılması ve ardından kondensere emilmesi ile çalışmaktadır. Bu, bir flaş buharlaşmaya benzemektedir.

**Anahtar Kelimler**: deniz suyu desalinasyonu, parabolik oluklu nemlendirici güneş kolektörü, ısı toplayıcı elemanı, enerji verimliliği, ekserji verimliliği

## NOMENCLATURE

$a$ : length of the collector cross-section area (m)
$A$ : area, projection area of parabolic trough refl. (m²)
$A_k$ : cross-sectional area of absorber (m²)
$A_{a,ext}$ : absorber outer area (m²)
$A_{a,int}$ : absorber inner area (m²)
$A_{e,ext}$ : glass envelope outer area (m²)
$A_{e,int}$ : glass envelope inner area (m²)
$c_p$ : specific heat at constant pressure (J/kg.K)
$c_v$ : specific heat at constant volume (J/kg.K)
$d$ : diameter (m)
$D_{AB}$ : mass diffusion coefficient of substance A into substance B (m²/s)
$D_{H_2O-air}$ : mass diffusion coefficient of water into air, especially liquid water from absorber surface into air passing through the collector (m²/s)
$\dot{E}$ : incident solar irradiance (W/m²)
$e_e$ : emissivity of glass cover or overall emissivity between the sky and the glass cover
$\dot{E}_{ex}$ : incident solar exergy (W)
$e_a$ : emissivity of absorber
$e_{ae}$ : overall emissivity between abs. and glass envelope
$f$ : Darcy friction factor
$h_f$ : specific enth. of liq. water sprayed into system (J/kg)
$h_{fg}$ : latent heat of water vaporization (J/kg)
$h_g$ : specific enthalpy of water vapor (J/kg)
$h_{g@T_e}$ : specific enth. of saturated water vapor at the glass cover temperature (J/kg)
$h_{g@T_a}$ : specific enthalpy of saturated water vapor at the absorber temperature (J/kg)
$h_{mass}$ : mass transfer coefficient (m/s)
$h_{wind}$ : convective heat transfer coefficient resulting from wind effect (W/m².K)
$h$ : enthalpy of moist air per unit mass of dry air (J/kg(dry air)), convective heat transfer coefficient (W/m².K)
$K(i)$: incident angle modifier
$k$ : thermal conductivity (W/m.K)
$L$ : length of heat collector element (m)
$Le$ : Lewis number
$M$ : molar mass, molar mass of moist air (kg/kmol)
$\dot{m}_f$ : mass flow rate of moist air (kg/s)
$\dot{m}$ : dry air mass flow rate passing through the system (kg/s)
$\dot{m}_{wa,Fick'slaw}$ : water evaporation rate from absorber or liquid water surface derived from Fick's law (kg/s)
$\dot{m}_{wa}$ : maximum water mass flow rate that can be evaporated into the system, (kg/s)
$n_b$ : number of brackets
$Nu$ : Nusselt number
$Nu_\infty$ : Nusselt number for a fully developed flow
$p$: partial pressure (Pa), perimeter
$P$ : total pressure (Pa), and (atm) in the expression of $D_{AB}$, 1 atm = 101325 Pa
$p_a$: partial pressure of dry air in moist air (Pa)
$Pe$: Peclet number
$Pr$: Prandlt number
$\dot{Q}$: heat transfer, total enthalpy, total enthalpy variation (W)
$R_a$: gas constant of dry air (J/kg.K)
$Re$: Reynolds number
$Sc$: Schmidt number
$Sh$: Sherwood number
$s_f$ : entropy of liquid water sprayed into system (J/kg.K)
$s_g$ : water vapor entropy (J/kg.K)
$T$ : temperature (K)
$y$ : proportion y of the water mass flow rate that reaches the abs. to the total sprayed water mass flow rate ($0 \leq y \leq 1$).

**Abbreviations**
ETC: evacuated tube collector
HCE: heat collector element
HDH: humidification – dehumidification
HSC-SS: humidifying solar collector-based solar still
ISD: interfacial solar desalination
MSF: multi-stage flash
PCM: phase change material
PHSC: parabolic humidifying solar collector
PHSC-SS: parabolic humidifying solar collector-based solar still
SAH/SWH-HDH: solar air and water heaters-based humidification – dehumidification
SAH: solar air heater
SAH-HDH: solar air heater-based humidification – dehumidification
SS: solar still
SWH: solar water heater
SWH-HDH: solar water heater-based humidification – dehumidification

**Subscripts**
0: dead state, ambient environment
1: state 1 of air, state of air at system inlet
2: state 2 of air, state of air at condenser inlet
a: absorber
abs: absorbed
amb: ambient environment
b: bracket
bb: base of bracket
ci: condenser inlet
co: condenser outlet
cond: conduction
conv: convection
e: glass envelope
evap: evaporation
ext: external
f: moist air, air flowing through the heat coll. element
g: gas in vacuum annulus (air in this study)
int: internal
opt: optical
r: reflector (parabolic trough reflector)
rad: radiation
s: sun
sat: saturated state
wa : liquid water sprayed into system

**Greek symbols**
$\alpha$ : absorptivity,
$\gamma$: product of effective optical efficiency terms
$\delta$: molecular diameter (m)
$\Gamma$: specific heat ratio
$\Delta T$ : difference between air temperature at heat collector element outlet and inlet (K or °C)
$\varepsilon$ : roughness of the inner wall of the collector (m)
$\eta_{ex}$ : exergy efficiency
$\eta$ : energy efficiency, optical efficiency
$\lambda$: mean free path (m)
$\mu$ : dynamic viscosity of moist air (kg/m.s)
$\nu$ : kinematic viscosity of moist air (m²/s)
$\rho$ : density, density of moist air (kg/m³)
$\rho_r$: clean mirror reflectivity
$\sigma$ : Stefan-Boltzmann constant (W/m².K⁴)
$\tau_e$ : transmissivity of glass envelope
$\varphi(i)$: collector geometrical end losses
$\psi$ : exergy of moist air per unit mass of dry air (J/kg(dry air))
$\psi_{wa}$ : exergy of liquid water per unit mass (J/kg)
$\omega$ : humidity ratio of moist air (kg(water) / kg(dry air))
$\widetilde{\omega}$ : molar ratio between water vapor concentration and dry air concentration in moist air (Mol(water) / Mol(dry air))

## INTRODUCTION

Direct solar desalination systems are among the major research on seawater desalination technologies for freshwater production. Although they are not yet used on an industrial scale because of their low productivity, they are of great interest for small-scale and low-cost freshwater production. They are characterized by the fact that seawater directly receives incident solar irradiance, heats up, and evaporates into air, unlike indirect desalination systems where it receives solar energy through heat exchangers.

Direct solar desalination systems can be classified into three technologies: solar stills (SS) (Abbaspour et al., 2022; Alatawi et al., 2022; Angappan et al., 2022; Elgendi et al., 2022; Kabeel et al., 2017; Kaushal & Varun, 2010; Muthu Manokar et al., 2014; Sampathkumar et al., 2010; Sharshir, Yang, et al., 2016), humidification–dehumidification (HDH) systems (Alnaimat et al., 2021; Chauhan et al., 2021; Kasaeian et al., 2019; M & Yadav, 2017; Rahimi-Ahar, Hatamipour, & Ahar, 2020; Santosh et al., 2019, 2022), and interfacial solar desalination systems (ISD) (Liang et al., 2021; Luo et al., 2021; Trinh et al., 2022; Wang et al., 2022). This paper is part of research for designing a solar still with improved overall performance. Solar stills have been widely developed and studied, and still attract interest because of the low cost of materials and easiness of system construction. The techniques that have been applied in earlier works to improve their performance can be summarized as follows (Welepe et al., 2022):

- modification of the shape of solar still (Durkaieswaran & Murugavel, 2015; Ghandourah et al., 2022; Kumar Chauhan & Kumar Shukla, 2022b; Mohammadi et al., 2020; Prasanna & Deshmukh, 2022; Sambare et al., 2022; Saravanakumar et al., 2022; Shanazari & Kalbasi, 2018; Siddula et al., 2022),
- heat transfer optimization by using evacuated tube collectors (ETC) (M. A. Essa et al., 2021; Shafii et al., 2016), corrugated absorber (H. Ahmed et al., 2022; Elshamy & El-Said, 2018), absorber coating (Chandrashekara & Yadav, 2017; Kumar Chauhan & Kumar Shukla, 2022a), fins on absorber (Dhivagar et al., 2022; Kabeel & Abdelgaied, 2017; Velmurugan et al., 2008; Yousef et al., 2019), porous absorber (A. F. Mohamed et al., 2019; Shah et al., 2022; Thakur et al., 2022; Yousef et al., 2019), nanofluids (Bait & Si–Ameur, 2018; Elango et al., 2015; Kabeel et al., 2014b, 2014a; Mahian et al., 2017; Meng et al., 2022; Nijmeh et al., 2005; Sharshir, Elkadeem, et al., 2020; Sharshir et al., 2017, 2019),
- the use of solar concentrators and auxiliary heat sources (Bahrami et al., 2019; Chandrashekara & Yadav, 2017; Elminshawy et al., 2015; Hashemi et al., 2020; Jafari Mosleh et al., 2015; Maliani et al., 2020; Nassar et al., 2007; Nayagam et al., 2022; Wu et al., 2017),

- water vapor mass transfer optimization from the evaporation surface to the condenser (Peng et al., 2022), and separation of condenser from evaporator to avoid water vapor condensation on glass cover, which decreases its transmissivity and therefore freshwater productivity (Al-Otoom & Al-Khalaileh, 2020; Elminshawy et al., 2015; Ibrahim & Dincer, 2015; Shoeibi, Kargarsharifabad, Rahbar, et al., 2022; Wu et al., 2017),
- preheating seawater and regulating its flow rate by using wicks (Abdelaziz et al., 2021; Abdullah et al., 2019; Abdullah, Omara, Essa, Alarjani, et al., 2021; Abdullah, Omara, Essa, Younes, et al., 2021; Dhindsa, 2021; F. A. Essa, Alawee, et al., 2021; F. A. Essa, Omara, et al., 2021; Fayaz et al., 2022; Jobrane et al., 2021, 2022; Modi, Maurya, et al., 2022; Modi, Patel, et al., 2022; Modi & Modi, 2019; Negi et al., 2022; Omara et al., 2013; Sharshir, El-Samadony, et al., 2016; Sharshir, Eltawil, et al., 2020; Younes, Abdullah, Essa, & Omara, 2021; Younes, Abdullah, Essa, Omara, et al., 2021; Zaheen Khan, 2022), water pumps (Abozoor et al., 2022; M. M. Z. Ahmed et al., 2022; Kumar et al., 2014), rotating belts (Al-Otoom & Al-Khalaileh, 2020; Saeed et al., 2022),
- glass cover cooling (Elashmawy, 2019; Kousik Suraparaju & Kumar Natarajan, 2022; Sharshir, El-Samadony, et al., 2016; Sharshir et al., 2017; Sharshir, Rozza, Joseph, et al., 2022; Sibagariang et al., 2022), s
- the use of heat storage materials such as latent heat storage or phase change material (PCM) and sensible heat storage (H. Ahmed et al., 2022; Al-harahsheh et al., 2018; Al-Harahsheh et al., 2022; Arunkumar & Kabeel, 2017; Chandrashekara & Yadav, 2017; Deshmukh & Thombre, 2017; Elashmawy & Ahmed, 2021; Jafari Mosleh & Ahmadi, 2019; Mohanraj et al., 2021; Poonia et al., 2022; Saeed et al., 2022; Shoeibi, Kargarsharifabad, Mirjalily, et al., 2022),
- breaking water surface tension by using cracked trays, air bubbles, water vaporizers, and foggers (Abed et al., 2021; Dumka & Mishra, 2020; El-Said et al., 2021; El-Said & Abdelaziz, 2020; F. A. Essa, Abdullah, et al., 2021; Fallahzadeh et al., 2020).

Many comprehensive reviews of these enhancement techniques have been conducted over time (Abbaspour et al., 2022; Alatawi et al., 2022; Angappan et al., 2022; Elgendi et al., 2022; Hussein et al., 2024; Kabeel et al., 2017; Kaushal & Varun, 2010; Mehta et al., 2024; Muthu Manokar et al., 2014; Omara, Ahmed, et al., 2024; Omara, Alawee, et al., 2024; Sampathkumar et al., 2010; Sharshir, Yang, et al., 2016). In general, most systems integrate two or more enhancement techniques (Welepe et al., 2022).

Abbaspour et al. (Abbaspour et al., 2024) investigated the efficacity of a vertical solar still (VSS), focusing on variables such as wick selection, condensate plate

wettability, and device dimensions. The research highlighted 5.1% performance enhancement with cotton wicks compared to gauze, and 34% increase in freshwater production with super hydrophilic plates over super hydrophobic ones. In addition, optimal VSS dimensions of 32 cm × 30 cm were identified. The authors declared that these findings underscore the potential for enhancing VSS efficiency, offering valuable insights for addressing global water scarcity and facilitating clean water access, with the maximum daily freshwater production rate reaching 1.250 kg per m² of solar receiver.

Mahala and Sharma (Mahala & Sharma, 2024) studied the combined impact of rectangular fins, gravels (G), and phase change material (PCM) on the efficiency of pyramid solar stills, comparing conventional solar stills (CSS) with modified ones (MSS). Experimental results, conducted in Uttar Pradesh, India, during May 2023, revealed significant improvements in daily productivity, energy, exergy efficiency, and economic and environmental parameters for MSS + G, CSS + G, and MSS, compared to CSS. Notably, MSS + G demonstrates 4.82 $L/m^2$ (84% increase) of daily freshwater productivity, 30.58% (81.1% increase) of maximum energy efficiency, 3.4% (273% increase) of maximum exergy efficiency, and a 0,02 $/L (29.2% reduction) of cost per liter of fresh water produced, alongside mitigating 19.14 tons of $CO_2$ emissions.
Saha et al. (Saha et al., 2024) experimentally studied a novel solar-energy-driven water purification system, by incorporating vacuum pressure and paraffin wax (PCM) as an energy storage material into a conventional double-slope solar still. The system was designed to enhance freshwater production in remote areas lacking grid electricity and underground water access. Experimental results demonstrated an increase of 63% in daily freshwater productivity i.e., from 5.46 $L/m^2$ to 7.03 $L/m^2$, along with 82% (28.72% enhancement) of maximum energy efficiency and 8.3% (22.43% enhancement) of maximum exergy efficiency for the modified system compared to the conventional one. These findings highlighted the potential of vacuum-pressure and PCM integration to enhance solar still performance, offering a cost-effective solution for freshwater production in resource-constrained areas.

Ziapour et al. (Ziapour et al., 2024) conducted a study on an innovative single-slope solar still desalination system with an enhanced modeling approach, aiming to address global desalination challenges. Through energy, exergy, and economic analyses, the system's performance is evaluated in cities such as Boushehr, Lisboa, Riyadh, and Tripoli. By utilizing flat reflectors and semi-transparent modules, the system achieved notable daily freshwater production values ranging from 11.15 kg/day to 15.58 kg/day across the cities. The analysis also revealed that despite promising outcomes, the system's reliance on weather conditions poses a limitation, suggesting the need for future

research to minimize this dependency and scale up production capacities.

Lauvandy et al. (Lauvandy et al., 2024) designed and studied a low-cost floating solar still prototype to address water scarcity issues in rural areas, particularly on Sumba Island, Indonesia. Constructed from accessible materials like PVC pipes, mica sheets, foam blocks, and towels, the solar still is easily replicable by local communities. Testing conducted in Bandung, Sumba, and Jatiluhur Dam during the dry season demonstrated the prototype's ability to produce significant amounts of fresh water, ranging from 0.590 kg/day to 1.165 kg/day. The authors concluded that despite its effectiveness, limitations such as reduced evaporation rates due to cover saturation and warmer temperatures hindering condensation are noted, and further optimization are needed for long-term reliability and durability.

Elashmawy et al. (Elashmawy et al., 2024) investigated a tubular solar still with two troughs to enhance evaporation and energy efficiency while reducing freshwater production costs. Conducted in Suez, Egypt, the two-trough device demonstrated a significant increase in freshwater productivity (36.1%) and energy efficiency (43.46%) compared to the single-trough device. Daily freshwater productivity for the two-trough and single-trough devices were 6.83 $L/m^2/day$ and 5.02 $L/m^2/day$, respectively, with energy efficiencies of 54.5% and 37.99%, respectively. Moreover, the two-trough configuration reduced water production costs by 22.3%, reaching $11.78/ton. Future research suggestions of this work include testing triple-trough configurations, investigating shadow effects, conducting deeper thermal analysis, and exploring solar concentrating techniques to further enhance tubular solar still performance.

Pandey and Naresh (Pandey & Naresh, 2024) performed experimental investigation on a modified pyramid solar still (MPSS) integrated with a pulsating heat pipe (PHP), aiming to enhance freshwater productivity, energy efficiency, and cost-effectiveness compared to conventional pyramid solar stills (CPSS). Experimental investigations conducted in Surat City, India, revealed that the MPSS consistently outperforms the CPSS. For instance, at a water depth of 2 cm, the MPSS achieved a daily freshwater productivity of approximately 4.10 $L/m^2/day$ compared to CPSS's productivity of 3.05 $L/m^2/day$, with 25.51% increase in energy efficiency compared to CPSS as well. Future research directions suggested by the authors include exploring advanced heat transfer mechanisms, integrating additional enhancements like fins and phase change materials, and employing computational fluid dynamics modeling for further optimization and validation.

Amin et al. (Amin et al., 2024) integrated metallic thermal transfer constituents and parabolic trough

collectors (PTC) into passive tubular solar still configurations, alongside beeswax phase change material (PCM), to produce fresh water. The developed model combines a heat exchanger (HE) and beeswax PCM. The empirical analysis revealed a significant enhancement, with 8.06 L/m²/day (66.18% increase) of freshwater productivity and a maximum energy efficiency of 76% (54 % average). Whereas the TSS without HE and PCM achieved a freshwater productivity and energy efficiency of 2.5 L/m²/day and 16.10%, respectively. Finally, the authors declared these outcomes underscored the effectiveness of the developed tubular solar distillation system in consistent and reliable freshwater generation, driven by strategic integration and operational synergy.

Luo et al. (Luo et al., 2024) investigated a desalination system based on a unidirectional heat transfer solar still, integrating efficient evaporation with waste heat recovery for high energy utilization. The design optimizes light transmission and condensation functions while integrating high-performance interfacial evaporation materials and minimizing heat loss through unidirectional heat transfer. Using a self-made hydrogel sponge, outdoor experiments demonstrated an evaporation rate of 6.0 kg/m²/h and a freshwater productivity of 4.5 kg/m²/h under an average sunlight intensity of 1.07 kW/m², with potential for further improvement. The authors stated that this study contributes valuable insights into optimizing interfacial evaporative solar stills, advancing solar desalination through system structure design and evaporation material development.

Somwanshi and Shrivastava (Somwanshi & Shrivastava, 2023) studied a closed loop inclined wick solar still (CLIWSS) with an additional heat storage reservoir to address freshwater scarcity in remote regions. The CLIWSS operates in a closed loop, continuously feeding warm water back into the still. A thermal model of the CLIWSS was developed and validated, showing enhanced freshwater productivity compared to a typical Inclined Wick Solar Still (IWSS). For Jodhpur, India, the CLIWSS achieved a maximum hourly freshwater productivity of 1.025 L/m²/h in May and 0.556 L/m²/h in December. The total daily freshwater productivity for summer and winter was 8.432 L/m² and 3.618 L/m², respectively, representing increases of 115% and 98% compared to conventional IWSS. The CLIWSS offered a competitive and cost-effective solution for solar desalination in India, particularly for remote and small communities, according to the authors. They also conducted a similar study on a closed loop inclined wick solar still augmented with an external bottom reflector (CLIWSSR) (Somwanshi & Shrivastav, 2024). The daily freshwater productivity of the CLIWSSR in a typical winter day in Raipur, Chhattisgarh, India was 6.106 kg/m², whereas the that of the CLIWSS in the same day was 5.047 kg/m², that is, an increase of 21%.

Ahmed et al. (H. Ahmed et al., 2022) designed and studied a solar still modified with a corrugated absorber plate and PCM. As a result, the freshwater productivity of the solar still with PCM was 4.5 L/day against 4.1 L/day for the solar still without PCM.

Sharshir et al. (Sharshir, Rozza, Joseph, et al., 2022) carried out experiments on a new trapezoidal pyramid solar still augmented with multi-thermal enhancers such as hang wicks, glass cover cooling, solar concentrators, and nanofluid (copper oxide, CuO). The results showed freshwater productivity, energy and exergy efficiencies of the system compared to those of the conventional solar still were improved by 147.3%, 144.2%, and 275.5%, respectively. They also conducted a similar study (Sharshir, Rozza, Elsharkawy, et al., 2022), with TiO₂-based nanofluid. Freshwater productivities obtained were 7 L/m²/day and 3.08 L/m²/day for the modified pyramid and traditional solar still, respectively, with daily energy efficiencies of 83.8% and 37.87%.

Tuly et al. (Tuly et al., 2022) investigated an active double slope solar still incorporating an internal sidewall reflector, hollow circular fins, and nanoparticle (Al₂O₃) mixed PCM. The maximum freshwater productivity and maximum energy efficiency achieved were 1.853 L/day and 21.56%, respectively. Moreover, they noticed significant improvements in freshwater productivity of 61.36% and 92%, respectively, in the modified solar still with pure PCM and that modified with nanofluid mixed PCM, compared to that of the conventional solar still.

Alqsair et al. (Alqsair et al., 2022) conducted a theoretical and experimental study on a drum solar still augmented with a parabolic solar concentrator, PCM, and nanoparticles coating. As a result, they obtained a system energy efficiency of 72%, and the maximum improvement in freshwater productivity noticed was 320% compared to that of the conventional solar still.

Despite these enhancement techniques, solar stills have the disadvantage of having excess water in evaporation chamber, i.e., the amount of water that receives solar energy at each instant is much higher than the evaporation rate. In fact, this increases the time needed to reach optimal evaporation temperatures and prevents optimal energy extraction from the solar absorber, leading to an increase in energy losses to the external environment and in exergy destroyed (Welepe et al., 2022).

To resolve this issue, Welepe et al. (Welepe et al., 2022) designed a new type of solar collector, named humidifying solar collector, in which the amount of water that receives solar energy at each instant equals the evaporation rate. Then, they studied the performance of a flat plate humidifying solar collector-based solar still. As a result, freshwater productivity, energy efficiency, and exergy efficiency reached 2.9 kg/h, 73%, and 1.6%, respectively, under

900 W/m$^2$ of incident solar irradiance. As a conclusion of their study, they stated important recommendations to improve overall system performance. These were the use of solar concentrators (parabolic trough, parabolic dish, Fresnel mirrors) to increase the solar irradiance received by the water to evaporate, and the design of humidifying solar collectors from ETC to decrease heat losses to the ambient environment.

This paper applies these recommendations or performance enhancement techniques by designing for the first time a parabolic trough humidifying solar collector-based solar still (PHSC-SS), with an ETC as heat collector element (HCE). Like in (Welepe et al., 2022), the performance parameters that will be investigated are energy and exergy efficiencies, dry air mass flow rate required, and the maximum water flow rate that can evaporate and saturate that air. The system operates in a closed air cycle to recover the energy contained in exhausted air from condenser. In this condition, freshwater productivity equals evaporated water flow rate.

Therefore, a theoretical investigation of the PHSC-SS performance is carried out in the following. Its thermodynamic model is developed and validated, its performance is analyzed, then a comparison between its freshwater productivity and those of some solar stills previously designed and studied in the literature is presented.

**METHODOLOGY AND SYSTEM DESCRIPTION**

The PHSC-SS has fundamentally the same operating principle as the flat plate HSC-SS. The difference is that the PHSC-SS uses a parabolic trough solar reflector and ETC as absorber for improved performance.

Hence, thin seawater droplets are sprayed uniformly on the absorber, then heat up, evaporate, and saturate the air passing through the HCE (Welepe et al., 2022). The resulting moist air is directed to the condenser to produce fresh water. Because the system operates in a closed air/open water loop as illustrated in Figure 1, and the sprayed water amount corresponds to the maximal value that can evaporate and saturate the incoming air flow rate, freshwater productivity equals the evaporated water flow rate, which in turn equals the sprayed water flow rate since there is no liquid water discharge from HCE.

Note that this control can be achieved by an external electronic circuit and sensors, which control the values of water and air flow rates circulating in the system, and then command water pumps and air blowers. These values are dynamically provided by the resolution of thermodynamic equations in section 3.

Energy and exergy equations will be solved in the Engineering Equations Solver (EES) software. Some thermodynamic and physical properties relations, therefore, will be skipped since they are included in the source code of this software.

Figure 1 presents the schematic diagram of the PHSC-SS, which includes its main components (PHSC, Condenser) and the circulation paths of air and water. The numbers 1 and 2 on this figure represent the state of air in the psychrometric chart (See Figure 5).
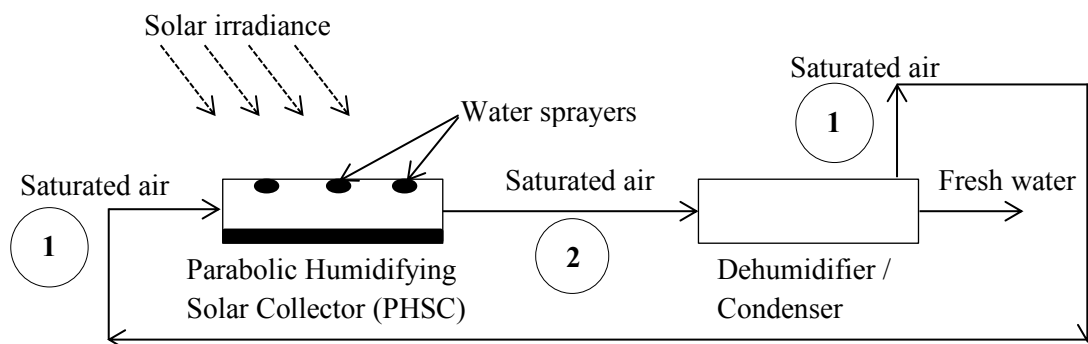


**Figure 1.** Schematic diagram of the PHSC-SS operating in closed air/open water loop. Adapted from (Welepe et al., 2022).

Figure 2 presents the longitudinal section view of the PHSC's HCE, with the heat and mass transfer mechanisms occurring inside and around it. This helps in establishing energy balance equations of Section 3.
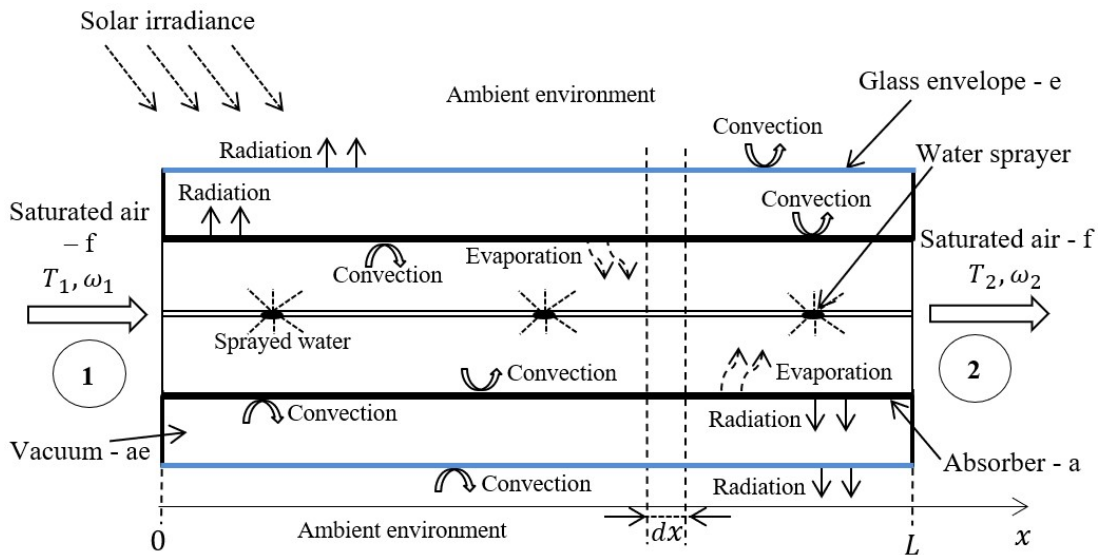
**Figure 2.** Longitudinal section view of the HCE of the PHSC: Heat and mass transfer mechanisms occurring inside and around it. Adapted from (Forristall, 2003; Padilla et al., 2011; Welepe et al., 2022; Yılmaz & Mwesigye, 2018).

Figure 3, like Figure 2, shows the heat and mass transfer mechanisms occurring inside and around the PHSC's HCE, but in a cross-sectional view, to enhance the representation of the system. Figure 4 depicts the thermal circuit of the PHSC's HCE. It is particularly useful in system thermodynamic analysis, as unlike Figures 2 and 3, it simplifies the representation of heat and mass transfer mechanisms, and therefore energy balance equations.
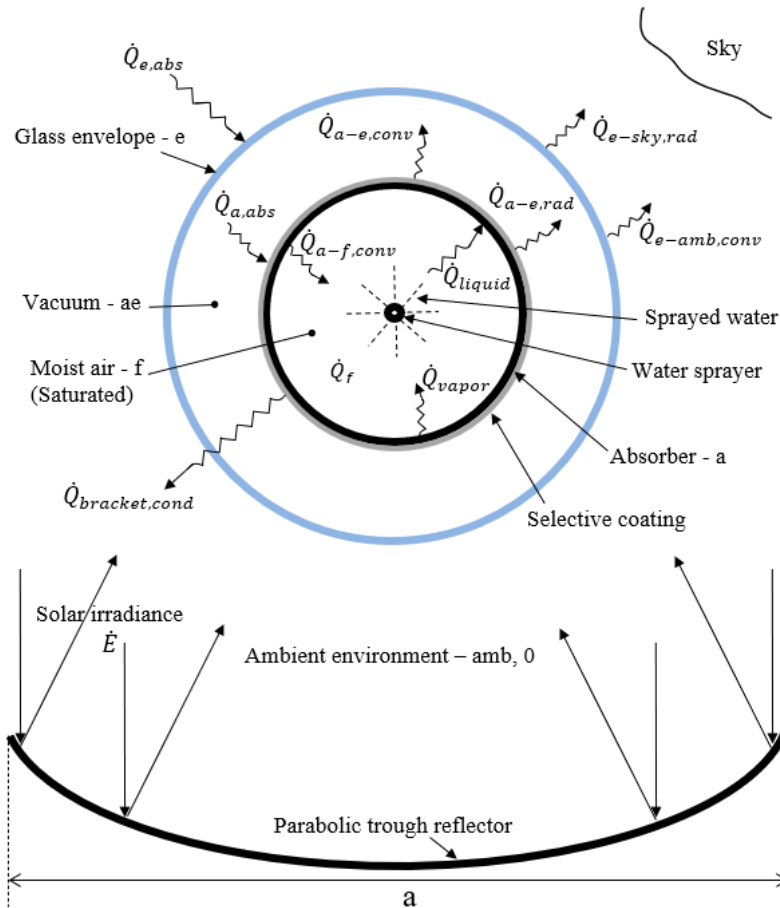


**Figure 3.** Cross-sectional view of the PHSC: Heat and mass transfer mechanisms occurring inside and around it. Adapted from (Forristall, 2003; Padilla et al., 2011; Yılmaz & Mwesigye, 2018).
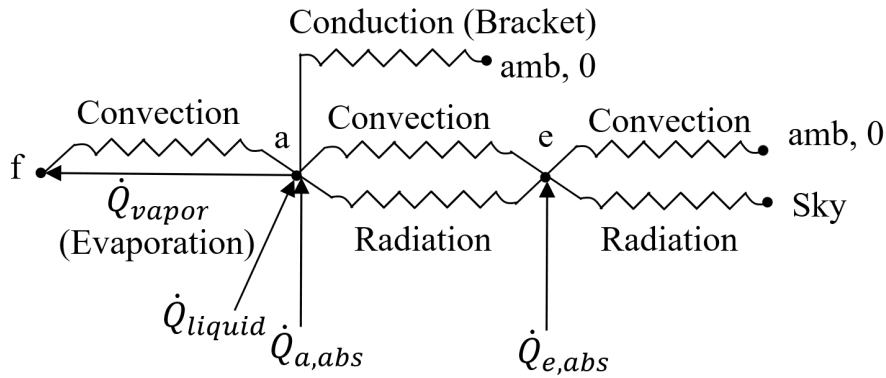
**Figure 4.** Thermal circuit of the PHSC. Adapted from (Forristall, 2003; Padilla et al., 2011).

As for Figure 5, it shows the psychrometric path followed by air in the PHSC-SS, operating in closed air/open water loop. In this operating scenario, air remains saturated and follows the path 1-2-1, state 1 being the desired initial state of air at the HCE inlet, and state 2 being the desired state of air at the HCE outlet.

Path 1-2: heating and humidification of air in the HCE.

Path 2-1: cooling and dehumidification of air in the condenser (direct contact condenser), with freshwater production by water vapor condensation.

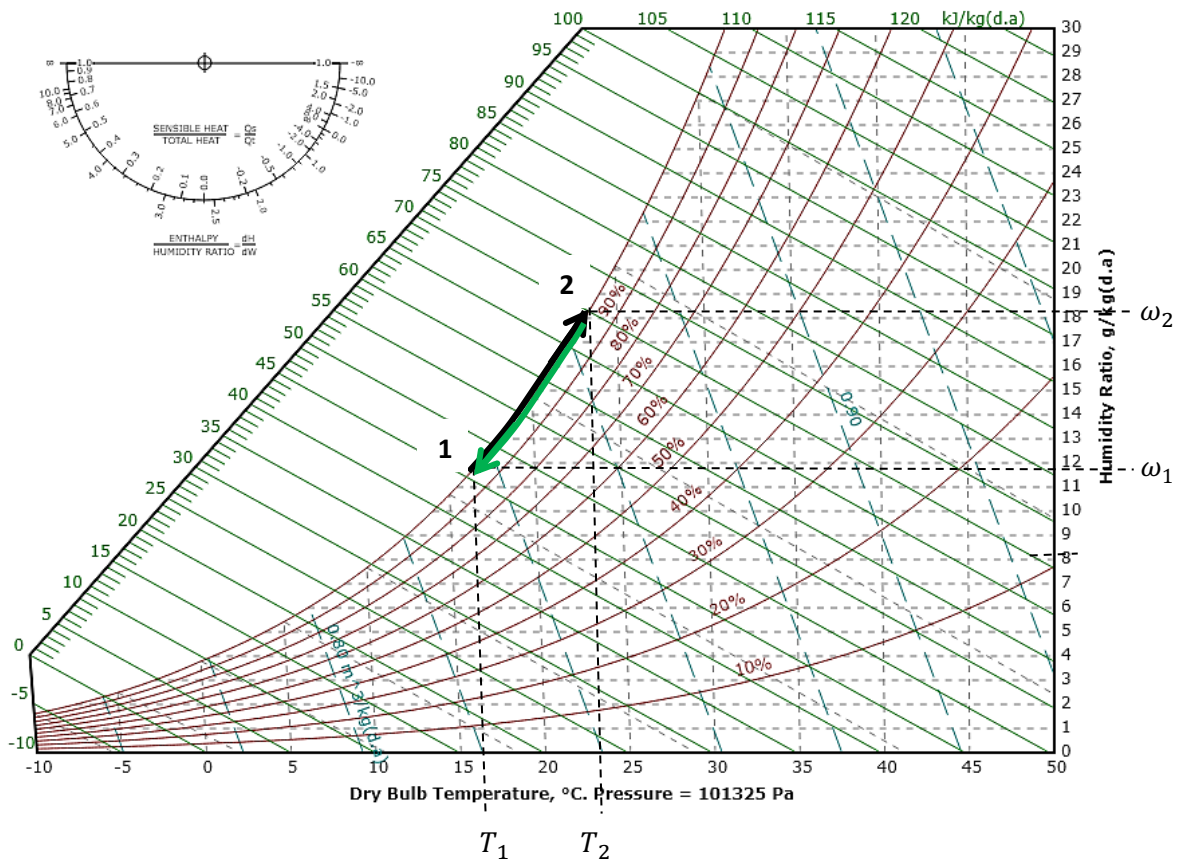To investigate the performance parameters of this system, its thermodynamic analysis must be carried out.



**Figure 5.** Air path in the PHSC-SS operating in closed air/open water loop on the psychrometric chart. Adapted from (FlyCarpet, 2021; Welepe et al., 2022).

## THERMODYNAMIC ANALYSIS

### Assumptions

The following assumptions are considered:
- According to Forristall (Forristall, 2003), for short parabolic solar collectors (less than 100 m in length) a 1D energy balance gives reasonable results.
- The pressure in the system is equal to atmospheric pressure. Since the system operates in a closed loop, and therefore, the internal pressure is controllable, especially under laminar air flow conditions.
- Thin water droplets sprayed into the HCE adhere to absorber surface, heat up to absorber temperature (since water depth in the HCE is negligible), and evaporate into the flowing air.
- No water droplet is carried away by the air stream, meaning that the proportion of the water mass flow rate that reaches the absorber to the total sprayed water mass flow rate equals 1.

### Energy analysis of the PHSC-SS

### Energy balance equations

- Energy balance equation of glass envelope

$$\dot{Q}_{e,abs} + \dot{Q}_{a-e,rad} + \dot{Q}_{a-e,conv} = \dot{Q}_{e-sky,rad} + \dot{Q}_{e-amb,conv}$$

- Energy balance equation of absorber

$$\dot{Q}_{a,abs} = \dot{Q}_{a-e,rad} + \dot{Q}_{a-e,conv} + \dot{Q}_{a-f,conv} + \dot{Q}_{a-f,evap} + \dot{Q}_{bracket,cond} \quad (2)$$

$$\dot{Q}_{a-f,evap} = \dot{Q}_{vapor} - \dot{Q}_{liquid} \quad (3)$$

- Energy balance equation of air flow in the PHSC

$$\dot{Q}_f = \dot{Q}_{a-f,conv} + \dot{Q}_{vapor} \quad (4)$$

### Expressions of heat transfer mechanisms

### Solar energy absorption

This heat transfer mechanism is expressed as follows(Padilla et al., 2011):

$$\dot{Q}_{e,abs} = \rho_r \gamma \alpha_e K(i)\varphi(i)A\dot{E}, \text{ with } A = aL \quad (5)$$

$$\dot{Q}_{a,abs} = \eta_{opt} K(i)\varphi(i)A\dot{E}, \text{ with } \eta_{opt} = \rho_r\gamma(\tau_e\alpha_a)_n \quad (6)$$

Duffie and Beckman (Duffie & Beckman, 2013) recommend the value $(\tau_e\alpha_a)_n = 1.01\tau_e\alpha_a$.

In this study, $K(i) = 1$ and $\varphi(i) = 1$ as assumed in (Padilla et al., 2011). The factor $\gamma$ is the product of effective optical efficiency terms as given below (Padilla et al., 2011):

$$\gamma = \prod_{i=1}^{6} \gamma_i \quad (7)$$

Indeed, these factors are optical imperfection factors. Their values are presented in Table 1.

**Table 1.** Effective optical efficiency terms (Forristall, 2003; Padilla et al., 2011).

| Factor and optical properties | | Symbol | Value |
|---|---|---|---|
| HCE shadowing | Luz black chrome | $\gamma_1$ | 0.974 |
| | Luz cermet | $\gamma_1$ | 0.971 |
| Twisting and tracking error | | $\gamma_2$ | 0.994 |
| Geometry accuracy of the collector mirrors | | $\gamma_3$ | 0.980 |
| Mirror clearness | | $\gamma_4$ | 0.950 |
| Dirt on HCE | | $\gamma_5$ | 0.980 |
| Miscellaneous factor | | $\gamma_6$ | 0.960 |
| Clean mirror reflectivity | | $\rho_r$ | 0.935 |

### Radiation

The below expressions are used (Yunus A. Çengel, 2011):

$$\dot{Q}_{a-e,rad} = e_{ae}A_{a,ext}\sigma(T_a^4 - T_e^4), \text{ with}$$
$$e_{ae} = \left(\frac{1}{e_a} + \left(\frac{1-e_e}{e_e}\right)\left(\frac{d_{a,ext}}{d_{e,int}}\right)\right)^{-1} \quad (8)$$

$$\dot{Q}_{e-sky,rad} = e_{es}A_{e,ext}\sigma(T_e^4 - T_{sky}^4), \text{ with}$$
$$e_{es} = e_e \quad (9)$$

$$T_{sky} = 0.0552 \times T_0^{1.5} \text{ for a cloudless sky} \quad (10)$$
(Evangelisti et al., 2019).

Many relations of sky temperature exist. But in general, it doesn't have a great effect in solar collector performance, unlike in radiative cooling as a passive cooling method where it has a significant effect (Duffie & Beckman, 2013). The radiative properties of different HCEs are given in Table 2.

**Table 2.** Radiative properties for different HCEs (Forristall, 2003).

| Selective coating | Envelope transmittance | Coating absorptance | Coating emittance | |
|---|---|---|---|---|
| | | | @ 100 °C | @ 400 °C |
| Luz black chrome | 0.935 | 0.94 | 0.11 | 0.27 |
| Luz cermet | 0.935 | 0.92 | 0.06 | 0.15 |
| Solel UVAC cermet a | 0.965 | 0.96 | 0.07 | 0.13 |
| Solel UVAC cermet b | 0.965 | 0.95 | 0.08 | 0.15 |
| Solel UVAC cermet avg (average values) | 0.965 | 0.955 | 0.075 | 0.14 |

In this work, the Solel UVAC cermet avg is considered as the HCE of the PHSC-SS, with coating emittance at 100 °C.

**Convection**

**Convection in annulus**

The annulus is filled with air under vacuum. The use of an evacuated annulus aims to minimize convective and conductive heat losses. Therefore, vacuum pressure must correspond to the free molecule regime or near free molecule conditions, i.e., approximately 0.0001 Torr (0.013 Pa) (Forristall, 2003; Padilla et al., 2011). In this case, convective heat transfer in the annulus is expressed as follows (Forristall, 2003; Padilla et al., 2011; Yılmaz & Mwesigye, 2018):

$$\dot{Q}_{a-e,conv} = h_{ae}A_{a,ext}(T_a - T_e) \tag{11}$$

$$h_{ae} = k_g/(A + B), \quad A = 0.5d_{a,ext}\ln(d_{e,int}/d_{a,ext}), \quad B = b\lambda\big((d_{e,int}/d_{a,ext}) + 1\big) \tag{12}$$

$$b = \left(\frac{2-\alpha}{\alpha}\right)\left(\frac{9\Gamma-5}{2(\Gamma+1)}\right), \quad \Gamma = c_p/c_v \tag{13}$$

$$\lambda = \frac{1.38\times10^{-23}\times T_{ae}}{\pi\sqrt{2}\delta^2 P} \qquad T_{ae} = (T_a + T_e)/2 \tag{14}$$

The coefficient $\alpha$ ranges from 0.01 to nearly 1. For most gas–solid interactions the value $\alpha = 1$ could be assumed in the absence of relevant information; and for air, $\delta = 3.66 \times 10^{-10}$ m (Padilla et al., 2011).

**Convection between the envelope and the ambient environment** (Forristall, 2003; Padilla et al., 2011)

$$\dot{Q}_{e-amb,conv} = h_{wind}A_{e,ext}(T_e - T_{amb}) \tag{15}$$

The expression of $h_{wind}$ depends on 'wind' and 'no wind' conditions (Forristall, 2003; Padilla et al., 2011). In this study the value 10 W/m².K is considered as an average value for free convection (Forristall, 2003; Padilla et al., 2011).

**Convection between absorber and air** (Yunus A. Çengel, 2011)

$$\dot{Q}_{a-f,conv} = h_{af}A_{a,int}(T_a - T_f), \text{ with} \atop A_{a,int} = \pi d_{a,int}L \tag{16}$$

$$h_{af} = kNu/d_{a,int} \tag{17}$$

Nusselt, Reynolds, and Prandtl numbers are needed in evaluating $h_{af}$.

$$Re = \dot{m}_f d_{a,int}/A_k\mu, \quad \dot{m}_f = \dot{m}(1 + \omega), \atop A_k = \pi d_{a,int}^2/4 \quad \text{(Yunus A. Çengel, 2011)} \tag{18}$$

The expressions of Nusselt number for short pipes are given as follows (Kakaç et al., 2012):

$$Nu = [3.66^3 + 1.61^3(PeD_h/L)]^{1/3}, \quad Pe = RePr, \text{ for laminar air flows } (Re < 2300) \tag{19}$$

$$Nu = Nu_\infty\big[1 + (D_h/L)^{2/3}\big], \text{ for turbulent air flows} \tag{20}$$

The expression of $Nu_\infty$ is (Kakaç et al., 2012; Yunus A. Çengel, 2011):

$$Nu_\infty = \frac{(f/8)(Re - 1000)Pr}{1 + 12.7(f/8)^{0.5}(Pr^{2/3} - 1)} \tag{21}$$

With $3 \times 10^3 < Re < 5 \times 10^6$ and $0.5 \leq Pr \leq 2000$ (Yunus A. Çengel, 2011). This relation can also be considered valid for $2300 < Re < 10^4$ (Kakaç et al., 2012).

The value of $f$ can be evaluated from (Yunus A. Çengel, 2011):

$$\frac{1}{\sqrt{f}} \cong -1.8\log\left[\frac{6.9}{Re} + \left(\frac{\varepsilon/D_h}{3.7}\right)^{1.11}\right] \tag{22}$$

**Conduction**

To be maintained at the focal point of parabolic reflectors, HCE is supported by support brackets. This contact leads to conductive heat loss to the ambient environment. To express it, each support bracket is considered as an infinite fin, whose perimeter is 0.2032 m, cross-sectional area is $1.613 \times 10^{-4}$ m², with a thermal conductivity of 48.0 W/m.K (plain carbon steel at 600 K) as described in (Forristall, 2003; Padilla et al., 2011). In this case the expression of $\dot{Q}_{bracket,cond}$ is given as (Forristall, 2003; Yunus A. Çengel, 2011):

$$\dot{Q}_{bracket,cond} = n_b\sqrt{h_b p_b k_b A_b}(T_{bb} - T_{amb}) \text{ with } T_{bb} = T_a - 10 \text{ (Forristall, 2003), } h_b = h_{wind} \tag{23}$$

To determine the number of support brackets, it should be considered that there is a support bracket at each end of every HCE, i.e., about every 4 m of HCE's length (Forristall, 2003).

**Evaporation and enthalpy variation of moist air**

These heat transfer mechanisms are expressed as follows (Yunus A. Çengel, 2011):

$$\dot{Q}_f = \dot{m}(h_2 - h_1) \tag{24}$$

$$\dot{Q}_{a-f,evap} = \dot{m}_{wa}\big(h_{g@T_a} - h_{f@T_{wa}}\big), \text{ with} \atop \dot{m}_{wa} = \dot{m}(\omega_2 - \omega_1) \tag{25}$$

$$\dot{Q}_{vapor} = \dot{m}_{wa}h_{g@T_a} \tag{26}$$

$$\dot{Q}_{liquid} = \dot{m}_{wa}h_{f@T_{wa}} \tag{27}$$

**System energy efficiency**

The expression of the energy efficiency of the HCE is:

$$\eta = \frac{\dot{m}h_2 - (\dot{m}h_1 + \dot{m}_{wa}h_{f@T_{wa}})}{A\dot{E}} = \frac{\dot{m}[h_2 - h_1 - (\omega_2 - \omega_1)h_{f@T_{wa}}]}{A\dot{E}}, \quad A = a \times L \tag{28}$$

**Exergy analysis of the PHSC-SS**

The expression of the exergy of moist air per unit mass of dry air is (Bejan, 2016):

$$\psi_i = (c_{p,a} + \omega_i c_{p,v})T_0\left(\frac{T_i}{T_0} - 1 - \ln\frac{T_i}{T_0}\right) \\ + (1 + \widetilde{\omega}_i)R_a T_0 \ln\frac{P_i}{P_0} \\ + R_a T_0\left(\widetilde{\omega}_i \ln\frac{\widetilde{\omega}_i}{\widetilde{\omega}_0}\right. \\ \left. + (1 + \widetilde{\omega}_i)\ln\frac{1 + \widetilde{\omega}_0}{1 + \widetilde{\omega}_i}\right) \tag{29}$$

$$\widetilde{\omega}_i = 1.608\omega_i, \quad \widetilde{\omega}_0 = 1.608\omega_0, \quad i \in \{1, 2\}$$

The dead state is that of the outside air and the pressure in the system is considered equal to atmospheric pressure (see paragraph 3.1. for assumptions), i.e., $P_i = P_0$.

On the other hand, the expression of exergy of liquid water per unit mass is (Bejan, 2016):

$$\psi_{wa} = h_f(T_{wa}, P_0) - h_g(T_0, p_{v0}) \\ - T_0\left(s_f(T_{wa}, P_0)\right. \\ \left. - s_g(T_0, p_{v0})\right) \tag{31}$$

The expression of the exergy rate from the sun is given as (Ge et al., 2014; Jafarkazemi & Ahmadifard, 2013; Kalogirou et al., 2016; Sadaghiyani et al., 2018):

$$\dot{E}_{ex} = A\dot{E}\left(1 - \frac{4}{3}\frac{T_0}{T_s} + \frac{1}{3}\left(\frac{T_0}{T_s}\right)^4\right) \tag{32}$$

The expression of the exergy efficiency of the HCE is (Bejan, 2016):

$$\eta_{ex,ps} = \frac{exergy\ rate\ obtained\ (output)}{sum\ of\ provided\ exergy\ rates\ (input)} \\ = \frac{\dot{m}\psi_2}{\dot{E}_{ex} + \dot{m}_{wa}\psi_{wa} + \dot{m}\psi_1} \tag{33}$$

**MODEL VALIDATION**

The operating principle of the flat plate HSC, as well as its thermodynamic analysis and model were detailed and validated in (Welepe et al., 2022). The same thermodynamic analysis was applied to the analysis of the PHSC. Moreover, all the specificities related to the HCE of PHSC, which have been modeled and validated in (Forristall, 2003; Padilla et al., 2011), have been scrupulously respected and their thermodynamic model applied. Consequently, it can be stated that the thermodynamic model of the PHSC used in this work is also valid and will provide reliable results. Nevertheless, it is still useful to check whether the current model follows the well-known thermodynamic law that depicts the evaporation of water from the absorber of HCE into air. That law is named Fick's law and leads the mass transfer by diffusion. In this study, it is about water diffusion into air. (30)

Although there are some simplification formulae of Fick's law, all derive from the following expressions (American Society of Heating Refrigerating and Air-Conditioning Engineers Inc. (ASHRAE), 2021; Lienhard IV & Lienhard V, 2020; Yunus A. Çengel, 2011):

$$h_{mass} = D_{AB}Sh/D_h \tag{34}$$

$Sh$ is derived from the relations of $Nu$ by substituting $Pr$ with $Sc$.

$$Sc = \nu_f/D_{AB} \tag{35}$$

$$D_{AB} = D_{H_2O-air} = 1.87 \times 10^{-10}\left(T_f^{2.072}/P\right) \tag{36}$$

$$\dot{m}_{wa,Fick's law} = h_{mass}\left(\rho_{wa,a} - \rho_{vapor,f}\right)A_{a,int} \tag{37}$$

$\rho_{wa,w}$ and $\rho_{v,f}$ are evaluated at saturation state (Welepe et al., 2022).

Figures 6, 7, and 8 present the comparison results of freshwater productivities obtained from the current model and Fick's law, for an incident solar irradiance of 900 W/m², 600 W/m², and 300 W/m², respectively.
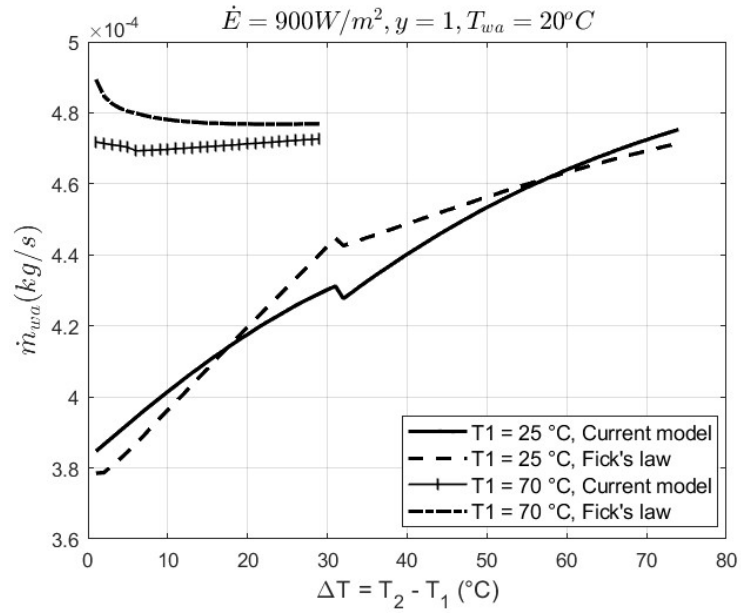
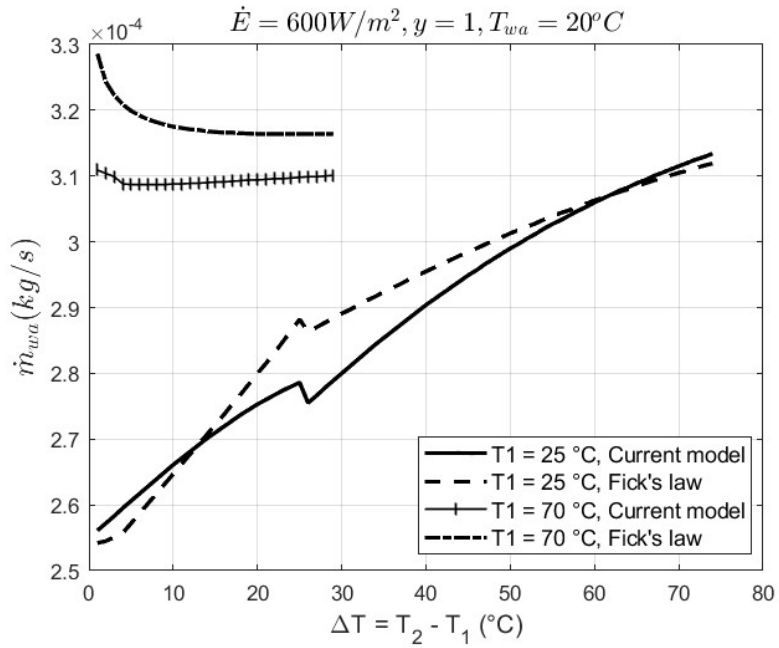**Figure 6.** Comparison of freshwater productivities obtained from the current model and Fick's law, for $\dot{E} = 900 \, W/m^2$.



**Figure 7.** Comparison of freshwater productivities obtained from the current model and Fick's law, for $\dot{E} = 600 \, W/m^2$.
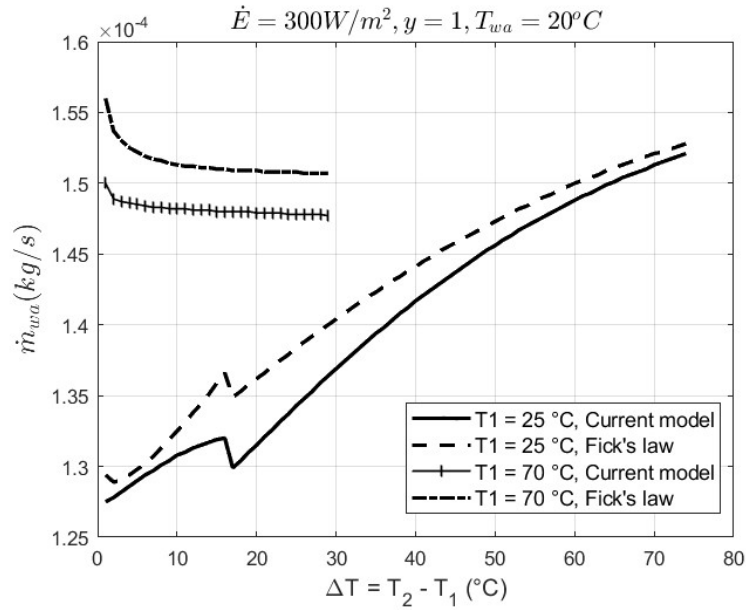
**Figure 8.** Comparison of freshwater productivities obtained from the current model and Fick's law, for $\dot{E} = 300\ W/m^2$.

In these figures, laminar and turbulent flow effects can be distinguished. Laminar and turbulent parts are separated by a jump or a sudden change of values (for instance, at $\Delta T \cong 31$ °C in Figure 6). Turbulent regime corresponds to the smallest $\Delta T$ values, i.e., before the jump, while laminar regime corresponds to largest $\Delta T$ values, i.e., after the jump. These figures show a good fit between the model of the HCE developed in this work and that of Fick's law. The discrepancies are acceptable for this study. This is justified by the fact that, although the study is theoretical, it is based on systems, models, and equations that have been studied and validated in earlier works [21,113,114].

**RESULTS AND DISCUSSION**

**Performance analysis of the PHSC**

**Curves of performance parameters**

The performance parameters investigated are energy and exergy efficiencies, the required dry air mass flow rate and the maximum water mass flow rate that can be evaporated, i.e., to be sprayed on absorber. Table 3 presents the dimensions of the PHSC, and other quantities needed to carry out the study.

The investigation is performed following three parameters which are the most important ones that can affect system performance. These are the incident solar irradiance (900 W/m$^2$, 600 W/m$^2$, 300 W/m$^2$), air temperature at the HCE inlet (25 °C, 40 °C, 55 °C, 70 °C), and air temperature variation between HCE inlet and outlet (1 to 74 °C, outlet temperature being less than 100 °C).

All equations were solved in EES software, and the curves of performance parameters were plotted in MATLAB software. Figures 9 – 14 present these curves.

**Table 3.** Dimensions of the PHSC and other quantities.

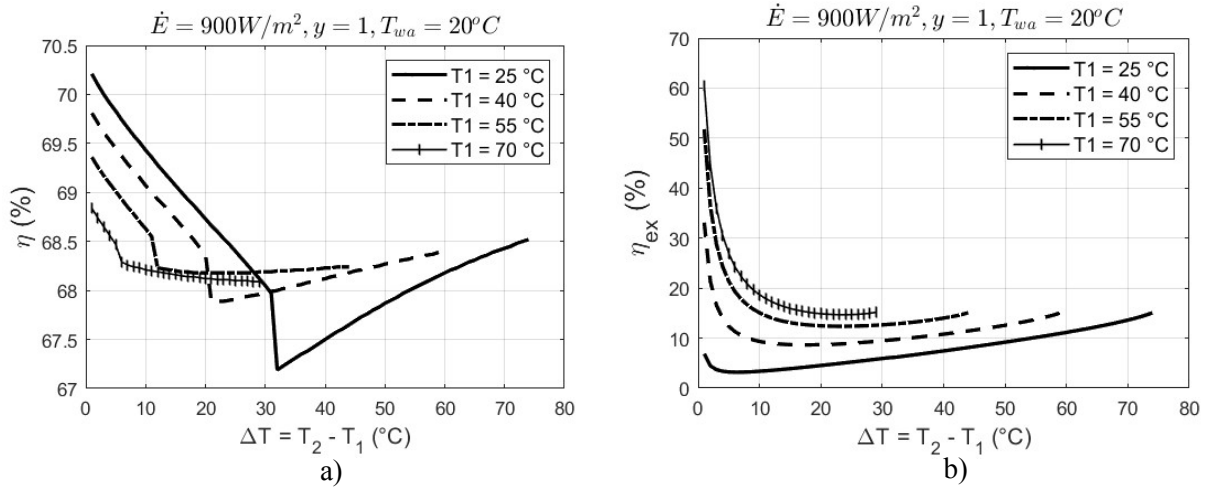| Quantity | Value (m) | Quantity | Value (m) | Quantity | Value |
|---|---|---|---|---|---|
| $d_{a,ext}$ | 0.097 | $d_{e,int}$ | 0.117 | $n_b$ | 2 |
| $d_{a,int}$ | 0.095 | $a$ | 1 | $T_{amb}$ | 25 °C |
| $d_{e,ext}$ | 0.121 | $L$ | 2 | $T_{wa}$ | 20 °C |

**Figure 9.** Performance of the PHSC for $\dot{E} = 900\ W/m^2$. a) Energy efficiency, b) Exergy efficiency.



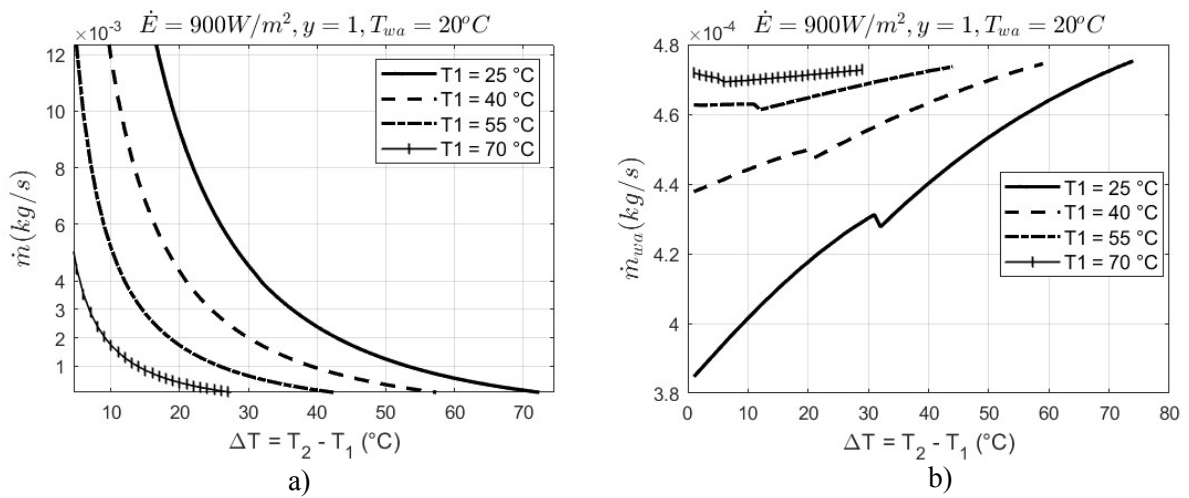**Figure 10.** Performance of the PHSC for $\dot{E} = 900\ W/m^2$. a) Required air mass flow rate, b) Water mass flow rate to be sprayed.



**Figure 11.** Performance of the PHSC for $\dot{E} = 600\ W/m^2$. a) Energy efficiency, b) Exergy efficiency.

176

**Figure 12.** Performance of the PHSC for $\dot{E} = 600\,W/m^2$. a) Required air mass flow rate, b) Water mass flow rate to be sprayed.
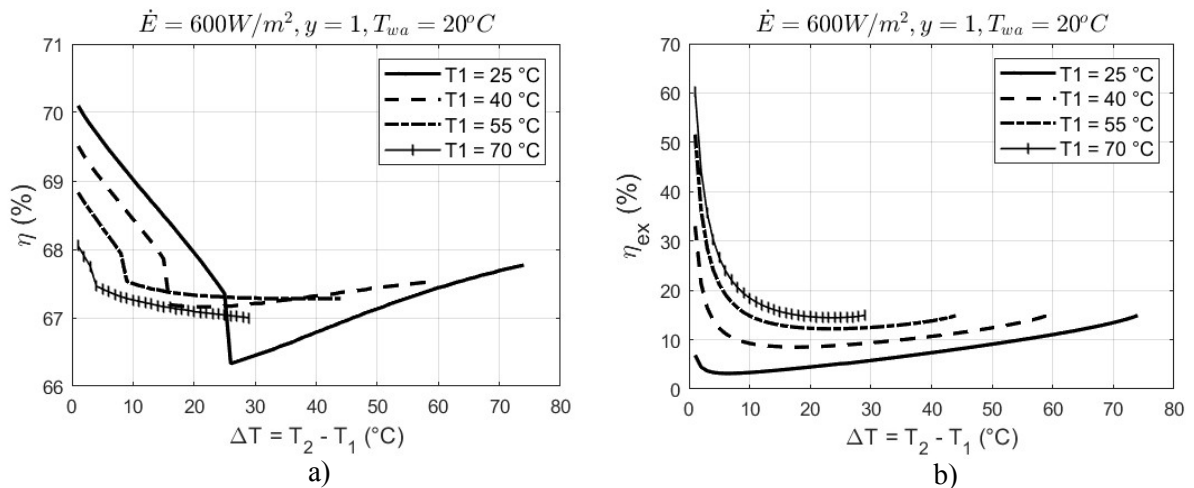


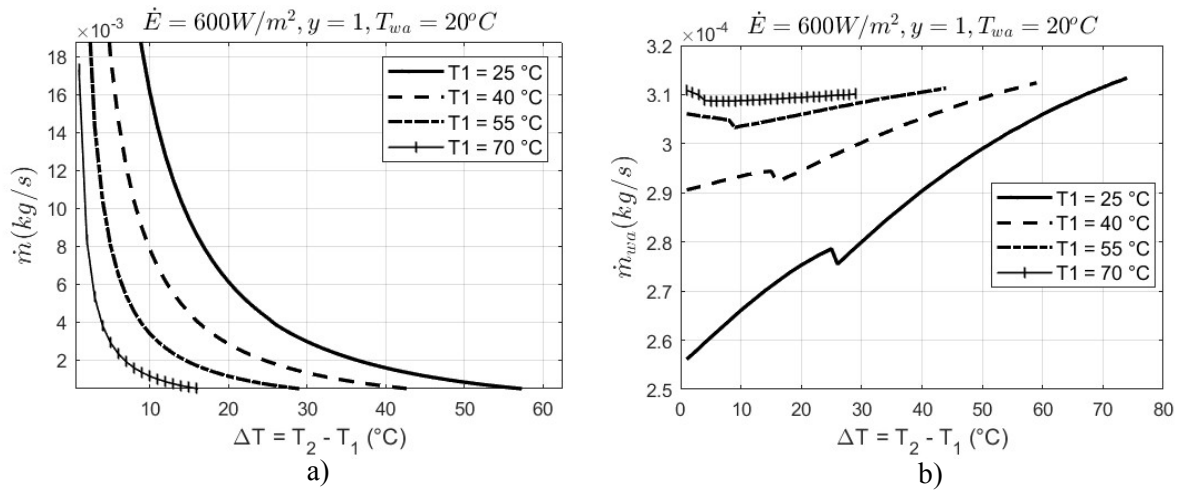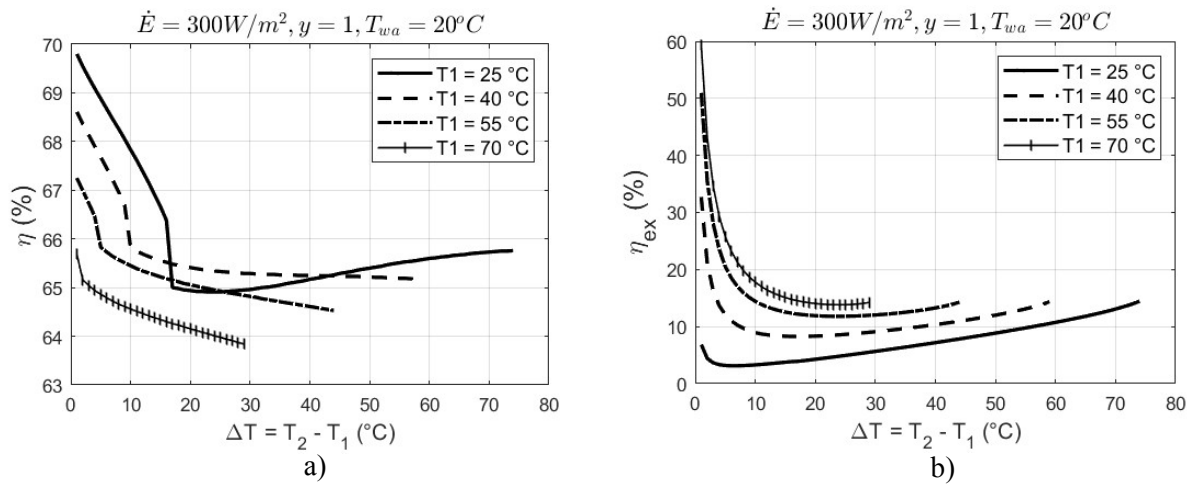**Figure 13.** Performance of the PHSC for $\dot{E} = 300\,W/m^2$. a) Energy efficiency, b) Exergy efficiency.
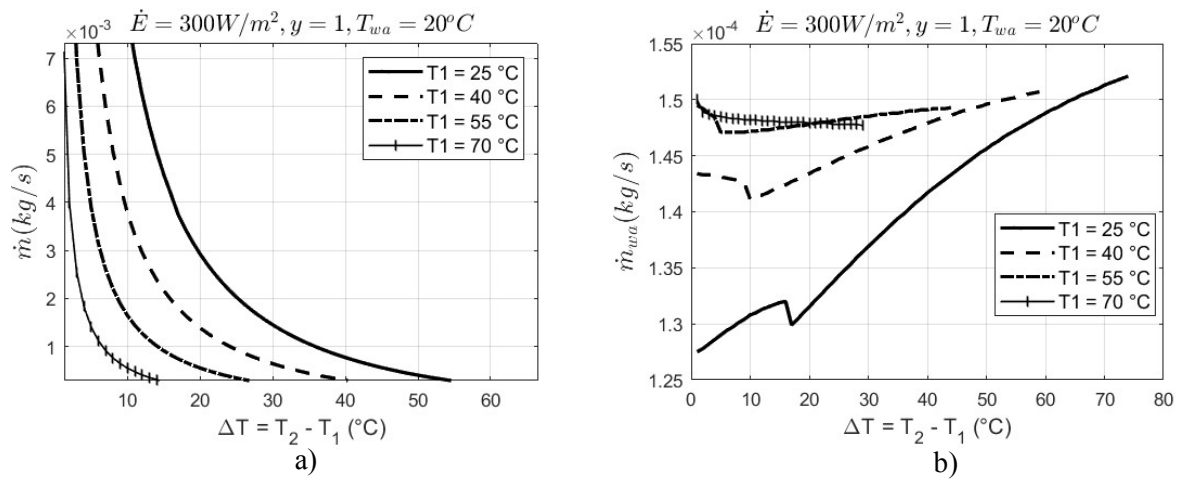


**Figure 14.** Performance of the PHSC for $\dot{E} = 300\,W/m^2$. a) Required air mass flow rate, b) Water mass flow rate to be sprayed.

From these curves, the effects of solar irradiance, airflow regime and air temperatures are noticeable and presented in the following sections.

**Effect of solar irradiance**

All performance parameters increase with solar irradiance. However, the increase in energy and exergy efficiencies is slight, i.e., a maximum difference of about 4% and 0.3% respectively, between $\dot{E} = 300\,W/m^2$ and $\dot{E} = 900\,W/m^2$.

177

Note that, these are efficiencies (percentages) not the values of useful energy and exergy which, on the other hand, significantly increase with solar irradiance. Whereas air and water mass flow rates almost triple from $\dot{E} = 300 \, W/m^2$ to $\dot{E} = 900 \, W/m^2$, i.e., almost by a proportionality ratio of solar irradiance.

This slight variation of energy and exergy efficiencies with solar irradiance is due to vacuum in the annulus of HCE, the use of low emissivity absorber and glass envelope, and water evaporation from absorber surface which minimizes absorber temperature. In fact, these efficiency enhancement techniques allow approaching the lowest levels of heat losses and exergy destroyed, i.e., system performance limit, whose percentages, therefore, remain practically constant with the variation of solar irradiance. Consequently, since air and water flow rates carry useful energy and exergy, there is a significant increase in their values with solar irradiance.

In contrast, for the flat plate HSC, all these performance parameters increase significantly with solar irradiance (Welepe et al., 2022).

**Effect of airflow regime**

The effects of laminar and turbulent airflow regimes can be observed on the curves of water mass flow rate to be sprayed and energy efficiency, i.e., Figures 10, 12, 14. Laminar and turbulent parts are separated by a jump or a sudden change of values. Turbulent regime corresponds to the smallest $\Delta T$ values, i.e., before the jump, while laminar regime corresponds to largest $\Delta T$ values, i.e., after the jump. The jump region corresponds to the transient regime. For example, for $T_1 = 25° \, C$, energy efficiency decreases with $\Delta T$ for turbulent airflow regime and increases for laminar airflow regime.

Furthermore, larger values of the water mass flow rate to be sprayed, which is equal to the evaporated water mass flow rate and the freshwater productivity, correspond to the smaller air mass flow rates, and therefore to a laminar air flow. This result is opposite to that of the flat plate HSC-SS studied in (Welepe et al., 2022). It is particularly important because it shows that the PHSC-SS does not need to operate with a turbulent airflow regime to produce higher amounts of fresh water, unlike the flat plate HSC-SS. A laminar regime is sufficient and necessary, allowing to process reduced air mass flow rates. Therefore, the condenser size of the PHSC-SS can be much smaller than that of the flat plate HSC-SS. In addition, smaller air mass flow rates reduce mechanical vibrations of the system and energy consumed by air blowers.

This analysis shows that the upper limit of freshwater productivity of the PHSC-SS is reached when air mass flow rate equals zero, i.e., with absorber temperature at least equal to water boiling point to cause direct evaporation of sprayed water droplets by ebullition. Thus, the upper limit of the PHSC-SS is a PHSC-SS operating without air flow, rather by ebullition and evaporation of water droplets from absorber, and suction of the resulting water vapor to condenser.

Thus, this system is similar to a flash evaporation-based desalination system like the multi-stage flash (MSF) system which is a well-known indirect solar water desalination technology. But, with the difference that in the upper limit of the PHSC-SS, water receives solar energy in the evaporation chamber (the HCE), whereas in the MSF system it receives heat in a heat exchanger before entering the evaporation chamber. This remark can justify why indirect solar desalination technologies so far offer higher freshwater productivity than that of direct solar desalination technologies.

**Effect of air temperatures**

For a given inlet temperature of air ($T_1$, temperature at HCE inlet), air and water mass flow rates decrease and increase, respectively, with its outlet temperature ($T_2$, temperature at HCE outlet). On the other hand, for a given outlet temperature of air, both increase with its inlet temperature. However, for high values of inlet temperature of air (from $T_1 = 55° \, C$) water mass flow rate slightly varies to become almost constant. But a small increase is still beneficial since it is the desired product. Therefore, an inlet air temperature more than 55 °C should be chosen.

This point shows that to obtain higher freshwater productivity, the system must operate with high values of inlet and outlet temperature of air. However, these temperatures must be less than the water boiling point, i.e., 100 °C at atmospheric pressure, to remain within the validity conditions of the system operating principle and its thermodynamic model.

**Combined effects of airflow regime and air temperatures**

For a given inlet temperature of air ($T_1$), its outlet temperature ($T_2$, corresponding to its temperature at the condenser inlet) for a turbulent airflow regime is less than that of the laminar airflow regime. As a result, with a turbulent airflow regime, condensation of water vapor will be more difficult, since heat extraction from air in condenser strongly depends on the temperature difference between air and cooling water. For instance, with a cooling water at 20°C in condenser, the heat transfer with a

saturated air at 70°C is higher than that with a saturated air at 40°C. That is, the condensation rate of water vapor from the saturated air at 40°C is less than that from the saturated air at 70°C.

Moreover, whatever the airflow regime, system energy and exergy efficiencies range from 64.9 to 70.2% and from 3.1 to 15.1%, respectively. Unlike the flat plate HSC-SS, whose energy efficiency ranged from 28 to 73%, and whose values of more than 64.9% (minimum value for the PHSC-SS) were only obtained with highly turbulent air flows (Welepe et al., 2022).

Note that although turbulent air flows induce better energy efficiency and freshwater productivity in the flat plate HSC-SS, they involve higher air flow rates than the laminar airflow regime, leading to more mechanical vibrations of the system, more energy consumed by air blower, and larger condenser.

Additionally, they imply low air temperatures at the HSC outlet (condenser inlet), which can make difficult the water condensation process. Unlike laminar air flows in PHSC, which lead to higher air temperatures at the HCE outlet and thus condenser inlet, as shown in Figures. 9a, 11a and 13a.

Furthermore, whatever the airflow regime, exergy efficiency of the flat plate HSC ranged from 0.62 to 1.6% (Welepe et al., 2022), i.e., significantly lower than that of the PHSC (3.1 to 15.1%).

Therefore, the PHSC-SS must operate with a laminar airflow regime and high inlet and outlet temperatures of air in HCE to achieve optimum overall performance. Moreover, with a laminar airflow regime, the assumption that no water droplet is carried away by the air stream is more plausible since air flow rates are low.

## COMPARISON BETWEEN THE FRESHWATER PRODUCTIVITY OF THE PHSC-SS AND THOSE OF SOME DIRECT SOLAR DESALINATION SYSTEMS IN THE LITERATURE

For a reliable result, the comparison is performed as described in (Welepe et al., 2022), i.e., for all systems, by using a proportionality ratio, freshwater productivity is estimated for the same total energy received chosen as base of calculations. This base of calculations considers incident solar energy and secondary heat sources employed for heating water and air. Omitted from the calculations is the mechanical energy generated by water pumps, air blowers, and other devices, as the pertinent values were not available in the scrutinized articles.

The base of calculations is the aggregate solar energy received per unit time by 2 m$^2$ of parabolic trough reflectors operating under 900 W/m$^2$ of solar irradiance, i.e., equivalent to 1800 W (Welepe et al., 2022). The result of calculations is summarized in Table 4. In that table, the terms SAH-HDH, SWH-HDH, and SAH/SWH-HDH mean solar air heater-based HDH solar desalination system, solar water heater-based HDH solar desalination system, and solar air and water heaters-based HDH solar desalination system, respectively (Welepe et al., 2022).

Freshwater productivity of the PHSC-SS is estimated for $\dot{E} = 900\ W/m^2$, $T_1 = 70\ °C$ and $\Delta T = 20\ °C$ (i.e., $T_2 = 90\ °C$). Since it operates in a closed-air loop, and there is no liquid water discharge from HCE, amounts of water sprayed, evaporated water and condensed water (fresh water) are equal. Therefore, its freshwater productivity in kg/s can be read from Figure 10b. Its value in kg/h is given in Table 4.

Note that, in Table 4, the unit of values in column "Average freshwater productivity (kg/m$^2$.h)" is kg/m$^2$.h. However, since in some articles that have been reviewed, the total area of solar absorber plus reflectors was not provided, the unit kg/h is used and mentioned near the corresponding values.

The freshwater productivity of PHSC-SS is higher than those of most previous direct solar desalination systems.

Among systems having higher freshwater productivity than the PHSC-SS, there are:
- HSC-SS, with Tci = 27°C and Tco = 20°C. Although in this operating condition the system has higher freshwater productivity, it should be noted that it operates with turbulent air flows or higher air flow rates (0.1 kg/s in the HSC-SS against 0.00042 kg/s in the PHSC-SS for optimal performance), which imply low air temperatures at condenser inlet which make difficult the water condensation process and impose the use of an auxiliary cooling device. Since the current condenser operates with ambient water. This also leads to more mechanical vibrations of system, increase condenser size, as well as energy consumed by air blowers.

**Table 4.** Comparison of freshwater productivities of the PHSC-SS and some direct solar desalination systems in the literature (Welepe et al., 2022).

| Authors | Type of system | Average incident solar irradiance (W/m$^2$) | Average total energy input (W) | Average freshwater productivity(kg/m$^2$.h) | Average freshwater productivity for a total energy input of 1800 W (kg/h) | Remarks |
|---|---|---|---|---|---|---|
| Ghandourah et al. (Ghandourah et al., 2022) | SS | 700 | 700 | 0.5 (kg/h) | 1.29 | Pyramid solar still with corrugated absorber plate. |
| Alqsair et al. (Alqsair et al., 2022) | SS | 750 | - | 0.954 | - | Use of parabolic solar concentrator, PCM, and nanoparticles coating. |
| Saeed et al. (Saeed et al., 2022) | SS | 750 | - | 0.915 | - | Use of corrugated drum and nano-based phase change material. |
| Tuly et al. (Tuly et al., 2022) | SS | 400 | 415 | 0.206 (kg/h) | 0.89 | Active double slope solar stills incorporating internal sidewall reflector, hollow circular fins, and nanoparticle mixed PCM. |
| Ahmed et al. (H. Ahmed et al., 2022) | SS | 480 | 507.36 | 0.19 (kg/h) | 0.674 | Utilization of a corrugated absorber plate and phase change material |
| Essa et al. (F. A. Essa, Abdullah, et al., 2021) | SS | 656.75 | - | 0.5 | 1.096 | Utilization of external mirrors to enhance solar energy absorption. |
| Essa et al. (M. A. Essa et al., 2021) | SS | 682.41 | - | 0.48 | 1.270 | Incorporation of an ETC with internal porous material functioning as fins, facilitating the heating of water. |
| Abed et al. (Abed et al., 2021) | SS | 592.5 | 959.11 | 0.4 | 0.461 | Integration of an external SWH along with four high-frequency ultrasonic vaporizers. |
| Al-Otoom and Al-Khalaileh (Al-Otoom & Al-Khalaileh, 2020) | SS | 852.4 | 1278.6 | 4.113 | 8.684 | Implementation of a rotating belt featuring black painted aluminum lips and a kaolin solution (hygroscopic solution) within the system. |
| Bahrami et al. (Bahrami et al., 2019) | SS | 900 | - | 0.93 | 0.930 | Deployment of a parabolic dish solar collector. Operates with boiling water. |
| Shafii et al. (Shafii et al., 2016) | SS | 890.88 | | 0.54 | 1.091 | Implementation of an ETC featuring stainless-steel wool embedded within the tube for water heating. |
| Elminshawy et al. (Elminshawy et al., 2015) | SS | 572.5 | 1687 | 2.75 | 2.939 | Integration of 1000 W electric water heaters, complemented by external mirrors. |
| Abdelaziz et al. (Abdelaziz et al., 2022) | SWH/ SAH-HDH | 775 | 3276 | 0.858 (kg/h) | 0.471 | Incorporation of an ETC as SWH, with high-frequency ultrasonic humidifier. |
| Alrbai et al. (Alrbai et al., 2022) | SWH-HDH | - | - | 3.85 (kg/h) | - | Deployment of an ETC as a SWH, coupled with a water fogger in both the humidifier and dehumidifier. |

| | | | | | |
|---|---|---|---|---|---|
| Mohamed et al. (A. S. A. Mohamed et al., 2021) | SWH-HDH | - | 5003 | 6.99 (kg/h) | 2.515 | Combination of ETC, insulated tank, auxiliary electric heater. |
| Rahimi-Ahar et al. (Rahimi-Ahar, Hatamipour, Ghalavand, et al., 2020) | SAH-HDH | 1123 | 3930.5 | 1.8 (kg/h) | 0.824 | Vacuum pump to decrease humidifier pressure, and promote water evaporation. Incorporation of an ETC as a SWH, paired with a flat plate solar collector. |
| Zubair et al. (Zubair et al., 2017) | SWH-HDH | - | - | 0.87 | - | ETC is utilized as SWH. |
| Deniz and Çınar (Deniz & Çınar, 2016) | SAH-HDH | 730.56 | 2483.9 | - | 0.439 | Flat plate SAH and flat plate SWH are used. |
| Sharshir et al. (Sharshir, Peng, et al., 2016) | SWH-HDH | 692.5 | 1385 | 1.091 | 2.836 | ETC is utilized as SWH |
| | SS | 692.5 | 775.6 | 0.464 | 1.207 | Hot brine exhausted from a HDH system is used. |
| | SS | 692.5 | 775.6 | 0.317 | 0.823 | A conventional solar still |
| | Hybrid SS-HDH | 692.5 | 2160.6 | 0.474 | 1.233 | ETC is utilized as SWH in the HDH system. Solar still is fed with hot brine exhausted from HDH system. |
| Welepe et al. (Welepe et al., 2022) Tci = 29 °C Tco = 25 °C | HSC-SS | 900 | 1800 | 0.535 | 1.07 | A smooth duct-shaped flat plate SAH/solar collector is used. Without fins, auxiliary heat sources, or solar concentrators. |
| Welepe et al. (Welepe et al., 2022) Tci = 27 °C Tco = 20 °C | | 900 | 1800 | 1.462 | 2.923 | |
| Present study | PHSC-SS | 900 | 1800 | 0.848 | 1.697 | Use of an ETC and parabolic trough reflectors, without fins and auxiliary heat sources. |

- The solar still designed by Al-Otoom and Al-Khalaileh (Al-Otoom & Al-Khalaileh, 2020). In this system, heat transfer is increased by fins, and by a rotating belt which brings mechanical energy not considered in the evaluation. This system also uses a duct-shaped flat plate solar collector like in the HSC-SS and thus should require much more air flow rates than the PHSC-SS, leading to the consequences evoked in the first point.
- SWH-HDH. These systems used an ETC as SWH. That is, solar energy is only concentrated in water with fewer energy losses. Thus, the outcome can be justified by the fact that the amount of evaporated water is commensurate with the energy received by liquid water. However, larger water and air quantities are pumped, that is, larger electrical and mechanical energies are required by circulation pumps and air blowers. In addition, these systems generally use higher number of HCE (more than one), plus a separate humidification chamber (humidifier) that make them more cumbersome. Whereas, only one HCE is used in the PHSC-SS, and also serves as the system's humidifier.

The greatest advantage that PHSC-SS has in front of those systems is that it operates with laminar air flows, i.e., with lower air flow rates. This leads to higher air temperatures at condenser inlet, which eases the water condensation process, decreases mechanical vibrations of system, and lowers condenser sizes and energy consumed by air blowers.

In addition, PHSC-SS can operate with high air temperatures at HCE inlet ($T_1 = 70 \,°C$ for instance). Indeed, since cooling water temperature must be lower

than air temperature at condenser outlet, i.e., HCE inlet, high air temperature at HCE inlet allows a wide range of cooling water temperatures in condenser. For instance, for $T_1 = 70\ °C$, temperature of cooling water in condenser must be less than 70 °C, while it must be less than 20 °C in HSC-SS since Tco = 20 °C, and equal to or less than the ambient temperature in most desalination systems.

Furthermore, for equal air temperatures at condenser inlet, equal cooling water temperatures in condenser, and equal air flow rates to be cooled, the water condensation process in PHSC-SS will require less cooling water quantity or flow rate than other desalination systems, and therefore less energy consumed by cooling water pump, since in PHSC-SS, air temperature at condenser outlet can be much higher than that of air at condenser outlet of other desalination systems, with optimal system performance.

Finally, since there is no water exhausted (brine) from the HCE, salt grains will crystallize on absorber surface and thus, negatively impact the performance of the PHSC-SS. Nevertheless, this can be resolved by a regular cleaning of the HCE, water-based cleaning particularly, which is part of system maintenance.

## CONCLUSION

The recommendations of the study carried out by Welepe et al. (Welepe et al., 2022) on the flat plate humidifying solar collector–based solar still (flat plate HSC-SS) suggested that using solar concentrators (parabolic trough, parabolic dish, Fresnel mirrors), and designing humidifying solar collectors from evacuated tube collectors, could be very interesting deals because these techniques are known to significantly improve overall system performance. Hence, the purpose of the present study was to implement these performance improvement techniques in a parabolic trough humidifying solar collector–based solar still (PHSC-SS), and its objective was to theoretically assess system performance. The main results obtained can be stated as follows:
- Unlike flat plate HSC-SS, which must operate with a turbulent airflow regime to achieve optimum overall performance, PHSC-SS must operate with a laminar airflow regime and high inlet and outlet temperatures of air from the heat collector element (HCE) to achieve optimum overall performance. In addition, laminar airflow regime implies higher air temperatures at condenser inlet, which ease the water condensation process (thus freshwater productivity), and lowers mechanical vibrations of system, condenser size, and energy consumed by air blowers as well.
- Vacuum in annulus, low emissivity absorber and glass envelope, and especially the newly introduced enhancement technique (water evaporation from absorber surface which minimizes absorber temperature) allowed approaching system performance limit, i.e., the

lowest levels of heat losses and exergy destroyed in the PHSC-SS, whose percentages, therefore, remain practically constant with the variation of solar irradiance. Consequently, since air and water flow rates carry useful energy and exergy, there is a significant increase in their values with solar irradiance.
- The upper limit of freshwater productivity of PHSC-SS is reached when air mass flow rate equals zero, i.e., with absorber temperature at least equal to water boiling point to cause direct evaporation of sprayed water droplets by ebullition. That is, the upper limit of the PHSC-SS is a PHSC-SS operating without air flow, by ebullition and evaporation of water droplets from absorber, and suction of the resulting water vapor to condenser. Thus, it is similar to a flash evaporation-based desalination system.

This last point introduces the future scope of this work. It would be interesting to design and study such a system, with attention to the effects of pressure variation on its performance, since decreasing pressure lowers water boiling point and therefore promotes water evaporation.

## DECLARATION OF COMPETING INTEREST

## DECLARATION OF GENERATIVE AI AND AI-ASSISTED TECHNOLOGIES IN THE WRITING PROCESS

## ACKNOWLEDGMENTS

## REFERENCES
Abbaspour, M., Esmaili, Q., & Ramiar, A. (2024). Improving vertical solar still performance for efficient Desalination: Investigating the influence of Wick, condensate plate and device dimensions. Solar Energy, 272, 112468.
https://doi.org/10.1016/j.solener.2024.112468

Abbaspour, M., Ramiar, A., & Esmaili, Q. (2022). Efficiency improvement of vertical solar stills – A review. Solar Energy, 235, 19–35.
https://doi.org/10.1016/j.solener.2022.02.027

Abdelaziz, G. B., Algazzar, A. M., El-Said, E. M. S., Elsaid, A. M., Sharshir, S. W., Kabeel, A. E., & El-Behery, S. M. (2021). Performance enhancement of tubular solar still using nano-enhanced energy storage material integrated with v-

corrugated aluminum basin, wick, and nanofluid. Journal of Energy Storage, 41, 102933. https://doi.org/10.1016/j.est.2021.102933

Abdelaziz, Gamal. B., Dahab, M. A., Omara, M. A., Sharshir, S. W., Elsaid, A. M., & El-Said, E. M. S. (2022). Humidification dehumidification saline water desalination system utilizing high frequency ultrasonic humidifier and solar heated air stream. Thermal Science and Engineering Progress, 27, 101144. https://doi.org/10.1016/j.tsep.2021.101144

Abdullah, A. S., Alarjani, A., Abou Al-sood, M. M., Omara, Z. M., Kabeel, A. E., & Essa, F. A. (2019). Rotating-wick solar still with mended evaporation technics: Experimental approach. Alexandria Engineering Journal, 58(4), 1449–1459. https://doi.org/10.1016/j.aej.2019.11.018

Abdullah, A. S., Omara, Z. M., Essa, F. A., Alarjani, A., Mansir, I. B., & Amro, M. I. (2021). Enhancing the solar still performance using reflectors and sliding-wick belt. Solar Energy, 214, 268–279. https://doi.org/10.1016/j.solener.2020.11.016

Abdullah, A. S., Omara, Z. M., Essa, F. A., Younes, M. M., Shanmugan, S., Abdelgaied, M., Amro, M. I., Kabeel, A. E., & Farouk, W. M. (2021). Improving the performance of trays solar still using wick corrugated absorber, nano-enhanced phase change material and photovoltaics-powered heaters. Journal of Energy Storage, 40, 102782. https://doi.org/10.1016/j.est.2021.102782

Abed, A. H., Hoshi, H. A., & Jabal, M. H. (2021). Experimental investigation of modified solar still coupled with high-frequency ultrasonic vaporizer and phase change material capsules. Case Studies in Thermal Engineering, 28, 101531. https://doi.org/10.1016/j.csite.2021.101531

Abozoor, M. K. S., Meraj, M., Azhar, M., Khan, M. E., Seraj, M., Ahsan, M., Ahmed, S. A., & Bani Hani, E. H. (2022). Energy and exergy analyses of active solar still integrated with evacuated flat plate collector for New Delhi. Groundwater for Sustainable Development, 19, 100833. https://doi.org/10.1016/j.gsd.2022.100833

Ahmed, H., Najib, A., Zaidi, A. A., Naseer, M. N., & Kim, B. (2022). Modeling, design optimization and field testing of a solar still with corrugated absorber plate and phase change material for Karachi weather conditions. Energy Reports, 8, 11530–11546. https://doi.org/10.1016/j.egyr.2022.08.276

Ahmed, M. M. Z., Alshammari, F., Alatawi, I., Alhadri, M., & Elashmawy, M. (2022). A novel solar desalination system integrating inclined and tubular solar still with parabolic concentrator. Applied Thermal Engineering, 213, 118665. https://doi.org/10.1016/j.applthermaleng.2022.118665

Alatawi, I., Khaliq, A., Ahmed Heniegal, A. M., Abdelaziz, G. B., & Elashmawy, M. (2022). Tubular solar stills: Recent developments and future. Solar Energy Materials and Solar Cells, 242, 111785. https://doi.org/10.1016/j.solmat.2022.111785

Al-Harahsheh, M., Abu-Arabi, M., Ahmad, M., & Mousa, H. (2022). Self-powered solar desalination using solar still enhanced by external solar collector and phase change material. Applied Thermal Engineering, 206, 118118. https://doi.org/10.1016/j.applthermaleng.2022.118118

Al-harahsheh, M., Abu-Arabi, M., Mousa, H., & Alzghoul, Z. (2018). Solar desalination using solar still enhanced by external solar collector and PCM. Applied Thermal Engineering, 128, 1030–1040. https://doi.org/10.1016/j.applthermaleng.2017.09.073

Alnaimat, F., Ziauddin, M., & Mathew, B. (2021). A review of recent advances in humidification and dehumidification desalination technologies using solar energy. Desalination, 499, 114860. https://doi.org/10.1016/j.desal.2020.114860

Al-Otoom, A., & Al-Khalaileh, A. T. (2020). Water desalination using solar continuous humidification–dehumidification process using hygroscopic solutions and rotating belt. Solar Energy, 197, 38–49. https://doi.org/10.1016/j.solener.2019.12.075

Alqsair, U. F., Abdullah, A. S., & Omara, Z. M. (2022). Enhancement the productivity of drum solar still utilizing parabolic solar concentrator, phase change material and nanoparticles' coating. Journal of Energy Storage, 55, 105477. https://doi.org/10.1016/j.est.2022.105477

Alrbai, M., Hayajneh, H., Arakza, F., Enizat, J., Al-Dahidi, S., Al-Ghussain, L., & Hassan, M. A. (2022). Techno-economic analysis of a solar-powered humidification-dehumidification desalination system under fogging effect. Sustainable Energy Technologies and Assessments, 53, 102752. https://doi.org/10.1016/j.seta.2022.102752

American Society of Heating Refrigerating and Air-Conditioning Engineers Inc. (ASHRAE). (2021). 2021 ASHRAE Handbook - Fundamentals. https://www.ashrae.org

Amin, M., Umar, H., Ginting, S. F., Amir, F., Rizal, T. A., Septiadi, W. N., & Mahlia, T. M. I. (2024). Enhancing solar distillation through beeswax-infused tubular solar still with a heat exchanger using parabolic trough collector. Journal of Energy Storage, 86, 111262. https://doi.org/10.1016/j.est.2024.111262

Angappan, G., Pandiaraj, S., Panchal, H., Kathiresan, T., Ather, D., Dutta, C., Subramaniam, M. K., Muthusamy, S., Kabeel, A. E., El-Shafay, A. S., & Sadasivuni, K. K. (2022). An extensive review of performance enhancement techniques for pyramid solar still for solar thermal applications. Desalination, 532, 115692. https://doi.org/10.1016/j.desal.2022.115692

Arunkumar, T., & Kabeel, A. E. (2017). Effect of phase change material on concentric circular tubular solar still-Integration meets enhancement. Desalination, 414, 46–50. https://doi.org/10.1016/j.desal.2017.03.035

Bahrami, M., Madadi Avargani, V., & Bonyadi, M. (2019). Comprehensive experimental and theoretical study of a novel still coupled to a solar dish concentrator. Applied Thermal Engineering, 151, 77–89. https://doi.org/10.1016/j.applthermaleng.2019.01.103

Bait, O., & Si–Ameur, M. (2018). Enhanced heat and mass transfer in solar stills using nanofluids: A review. Solar Energy, 170, 694–722. https://doi.org/10.1016/j.solener.2018.06.020

Bejan, A. (2016). Advanced Engineering Thermodynamics. Wiley. https://doi.org/10.1002/9781119245964

Chandrashekara, M., & Yadav, A. (2017). An experimental study of the effect of exfoliated graphite solar coating with a sensible heat storage and Scheffler dish for desalination. Applied Thermal Engineering, 123, 111–122. https://doi.org/10.1016/j.applthermaleng.2017.05.058

Chauhan, V. K., Shukla, S. K., Tirkey, J. V., & Singh Rathore, P. K. (2021). A comprehensive review of direct solar desalination techniques and its advancements. Journal of Cleaner Production, 284, 124719. https://doi.org/10.1016/j.jclepro.2020.124719

Deniz, E., & Çınar, S. (2016). Energy, exergy, economic and environmental (4E) analysis of a solar desalination system with humidification-dehumidification. Energy Conversion and Management, 126, 12–19. https://doi.org/10.1016/j.enconman.2016.07.064

Deshmukh, H. S., & Thombre, S. B. (2017). Solar distillation with single basin solar still using sensible heat storage materials. Desalination, 410, 91–98. https://doi.org/10.1016/j.desal.2017.01.030

Dhindsa, G. S. (2021). Performance enhancement of basin solar still using paraffin wax and floating wicks in the basin. Materials Today: Proceedings, 37, 3310–3316. https://doi.org/10.1016/j.matpr.2020.09.121

Dhivagar, R., El-Sapa, S., Alrubaie, A. J., Al-khaykan, A., Chamkha, A. J., Panchal, H., El-Sebaey, M. S., & sharma, K. (2022). A case study on thermal performance analysis of a solar still basin employing ceramic magnets. Case Studies in Thermal Engineering, 39, 102402. https://doi.org/10.1016/j.csite.2022.102402

Duffie, J. A., & Beckman, W. A. (2013). Solar Engineering of Thermal Processes (4th ed.). John Wiley & Sons, Inc. https://doi.org/10.1002/9781118671603

Dumka, P., & Mishra, D. R. (2020). Performance evaluation of single slope solar still augmented with the ultrasonic fogger. Energy, 190, 116398. https://doi.org/10.1016/j.energy.2019.116398

Durkaieswaran, P., & Murugavel, K. K. (2015). Various special designs of single basin passive solar still – A review. Renewable and Sustainable Energy Reviews, 49, 1048–1060. https://doi.org/10.1016/j.rser.2015.04.111

Elango, T., Kannan, A., & Kalidasa Murugavel, K. (2015). Performance study on single basin single slope solar still with different water nanofluids. Desalination, 360, 45–51. https://doi.org/10.1016/j.desal.2015.01.004

Elashmawy, M. (2019). Effect of surface cooling and tube thickness on the performance of a high temperature standalone tubular solar still. Applied Thermal Engineering, 156, 276–286. https://doi.org/10.1016/j.applthermaleng.2019.04.068

Elashmawy, M., & Ahmed, M. M. Z. (2021). Enhancing tubular solar still productivity using composite aluminum/copper/sand sensible energy storage tubes. Solar Energy Materials and Solar Cells, 221, 110882. https://doi.org/10.1016/j.solmat.2020.110882

Elashmawy, M., Nafey, A. S., Sharshir, S. W., Abdelaziz, G. B., & Ahmed, M. M. Z. (2024). Experimental investigation of developed tubular solar still using multi-evaporator design. Journal of Cleaner Production, 443, 141040. https://doi.org/10.1016/j.jclepro.2024.141040

Elgendi, M., Kabeel, A. E., & Essa, F. A. (2022). Improving the solar still productivity using thermoelectric materials: A review. Alexandria Engineering Journal. https://doi.org/10.1016/j.aej.2022.10.011

Elminshawy, N. A. S., Siddiqui, F. R., & Addas, M. F. (2015). Experimental and analytical study on productivity augmentation of a novel solar humidification–dehumidification (HDH) system. Desalination, 365, 36–45. https://doi.org/10.1016/j.desal.2015.02.019

El-Said, E. M. S., & Abdelaziz, G. B. (2020). Experimental investigation and economic assessment of a solar still performance using high-frequency ultrasound waves atomizer. Journal of Cleaner Production, 256, 120609. https://doi.org/10.1016/j.jclepro.2020.120609

El-Said, E. M. S., Dahab, M. A., Omara, M., & Abdelaziz, G. B. (2021). Solar desalination unit coupled with a novel humidifier. Renewable Energy, 180, 297–312. https://doi.org/10.1016/j.renene.2021.08.105

Elshamy, S. M., & El-Said, E. M. S. (2018). Comparative study based on thermal, exergetic and economic analyses of a tubular solar still with semi-circular corrugated absorber. Journal of Cleaner Production, 195, 328–339. https://doi.org/10.1016/j.jclepro.2018.05.243

Essa, F. A., Abdullah, A. S., Omara, Z. M., Kabeel, A. E., & Gamiel, Y. (2021). Experimental study on the performance of trays solar still with cracks and reflectors. Applied Thermal Engineering, 188, 116652. https://doi.org/10.1016/j.applthermaleng.2021.116652

Essa, F. A., Alawee, W. H., Mohammed, S. A., Dhahad, H. A., Abdullah, A. S., & Omara, Z. M. (2021). Experimental investigation of convex tubular solar still performance using wick and nanocomposites. Case Studies in Thermal Engineering, 27, 101368. https://doi.org/10.1016/j.csite.2021.101368

Essa, F. A., Omara, Z. M., Abdullah, A. S., Kabeel, A. E., & Abdelaziz, G. B. (2021). Enhancing the solar still performance via rotating wick belt and quantum dots nanofluid. Case Studies in Thermal Engineering, 27, 101222. https://doi.org/10.1016/j.csite.2021.101222

Essa, M. A., Ibrahim, M. M., & Mostafa, N. H. (2021). Experimental parametric passive solar desalination prototype analysis. Journal of Cleaner Production, 325, 129333. https://doi.org/10.1016/j.jclepro.2021.129333

Evangelisti, L., Guattari, C., & Asdrubali, F. (2019). On the sky temperature models and their influence on buildings energy performance: A critical review. Energy and Buildings, 183, 607–625. https://doi.org/10.1016/j.enbuild.2018.11.037

Fallahzadeh, R., Aref, L., Madadi Avargani, V., & Gholamiarjenaki, N. (2020). An experimental investigation on the performance of a new portable active bubble basin solar still. Applied Thermal Engineering, 181, 115918. https://doi.org/10.1016/j.applthermaleng.2020.115918

Fayaz, Z., Dhindsa, G. S., & Sokhal, G. S. (2022). Experimental study of solar still having variable slope tilted

wick in the basin to enhance its daily yield. Materials Today: Proceedings, 48, 1421–1426. https://doi.org/10.1016/j.matpr.2021.09.195

FlyCarpet. (2021, May 7). Free Online Interactive Psychrometric Chart. http://www.flycarpet.net/en/PsyOnline

Forristall, R. (2003). Heat Transfer Analysis and Modeling of a Parabolic Trough Solar Receiver Implemented in Engineering Equation Solver. https://www.nrel.gov/docs/fy04osti/34169.pdf

Ge, Z., Wang, H., Wang, H., Zhang, S., & Guan, X. (2014). Exergy Analysis of Flat Plate Solar Collectors. Entropy, 16(5), 2549–2567. https://doi.org/10.3390/e16052549

Ghandourah, E., Panchal, H., Fallatah, O., Ahmed, H. M., Moustafa, E. B., & Elsheikh, A. H. (2022). Performance enhancement and economic analysis of pyramid solar still with corrugated absorber plate and conventional solar still: A case study. Case Studies in Thermal Engineering, 35, 101966. https://doi.org/10.1016/j.csite.2022.101966

Hashemi, S. A., Kazemi, M., Taheri, A., Passandideh-Fard, M., & Sardarabadi, M. (2020). Experimental investigation and cost analysis on a nanofluid-based desalination system integrated with an automatic dual-axis sun tracker and Fresnel lens. Applied Thermal Engineering, 180, 115788. https://doi.org/10.1016/j.applthermaleng.2020.115788

Hussein, A. K., Rashid, F. L., Rasul, M. K., Basem, A., Younis, O., Homod, R. Z., El Hadi Attia, M., Al-Obaidi, M. A., Ben Hamida, M. B., Ali, B., & Abdulameer, S. F. (2024). A review of the application of hybrid nanofluids in solar still energy systems and guidelines for future prospects. Solar Energy, 272, 112485. https://doi.org/10.1016/j.solener.2024.112485

Ibrahim, A. G. M., & Dincer, I. (2015). A solar desalination system: Exergetic performance assessment. Energy Conversion and Management, 101, 379–392. https://doi.org/10.1016/j.enconman.2015.05.060

Jafari Mosleh, H., & Ahmadi, R. (2019). Linear parabolic trough solar power plant assisted with latent thermal energy storage system: A dynamic simulation. Applied Thermal Engineering, 161, 114204. https://doi.org/10.1016/j.applthermaleng.2019.114204

Jafari Mosleh, H., Jahangiri Mamouri, S., Shafii, M. B., & Hakim Sima, A. (2015). A new desalination system using a combination of heat pipe, evacuated tube and parabolic trough collector. Energy Conversion and Management, 99, 141–150. https://doi.org/10.1016/j.enconman.2015.04.028

Jafarkazemi, F., & Ahmadifard, E. (2013). Energetic and exergetic evaluation of flat plate solar collectors. Renewable Energy, 56, 55–63. https://doi.org/10.1016/j.renene.2012.10.031

Jobrane, M., Kopmeier, A., Kahn, A., Cauchie, H.-M., Kharroubi, A., & Penny, C. (2021). Internal and external improvements of wick type solar stills in different configurations for drinking water production– A review. Groundwater for Sustainable Development, 12, 100519. https://doi.org/10.1016/j.gsd.2020.100519

Jobrane, M., Kopmeier, A., Kahn, A., Cauchie, H.-M., Kharroubi, A., & Penny, C. (2022). Theoretical and experimental investigation on a novel design of wick type solar still for sustainable freshwater production. Applied Thermal Engineering, 200, 117648. https://doi.org/10.1016/j.applthermaleng.2021.117648

Kabeel, A. E., & Abdelgaied, M. (2017). Performance enhancement of modified solar still using multi-groups of two coaxial pipes in basin. Applied Thermal Engineering, 118, 23–32. https://doi.org/10.1016/j.applthermaleng.2017.02.090

Kabeel, A. E., Arunkumar, T., Denkenberger, D. C., & Sathyamurthy, R. (2017). Performance enhancement of solar still through efficient heat exchange mechanism – A review. Applied Thermal Engineering, 114, 815–836. https://doi.org/10.1016/j.applthermaleng.2016.12.044

Kabeel, A. E., Omara, Z. M., & Essa, F. A. (2014a). Enhancement of modified solar still integrated with external condenser using nanofluids: An experimental approach. Energy Conversion and Management, 78, 493–498. https://doi.org/10.1016/j.enconman.2013.11.013

Kabeel, A. E., Omara, Z. M., & Essa, F. A. (2014b). Improving the performance of solar still by using nanofluids and providing vacuum. Energy Conversion and Management, 86, 268–274. https://doi.org/10.1016/j.enconman.2014.05.050

Kakaç, S., Liu, H., & Pramuanjaroenkij, A. (2012). Heat Exchangers: Selection, Rating, and Thermal Design (3rd ed.). CRC Press. https://doi.org/10.1201/b11784

Kalogirou, S. A., Karellas, S., Badescu, V., & Braimakis, K. (2016). Exergy analysis on solar thermal systems: A better understanding of their sustainability. Renewable Energy, 85, 1328–1333. https://doi.org/10.1016/j.renene.2015.05.037

Kasaeian, A., Babaei, S., Jahanpanah, M., Sarrafha, H., Sulaiman Alsagri, A., Ghaffarian, S., & Yan, W.-M. (2019). Solar humidification-dehumidification desalination systems: A critical review. Energy Conversion and Management, 201, 112129. https://doi.org/10.1016/j.enconman.2019.112129

Kaushal, A., & Varun. (2010). Solar stills: A review. Renewable and Sustainable Energy Reviews, 14(1), 446–453. https://doi.org/10.1016/j.rser.2009.05.011

Kousik Suraparaju, S., & Kumar Natarajan, S. (2022). Effect of Natural Sisal Fibre on Enhancing the Condensation Rate of Solar Still for Sustainable Clean Water Production. Thermal Science and Engineering Progress, 101527. https://doi.org/10.1016/j.tsep.2022.101527

Kumar Chauhan, V., & Kumar Shukla, S. (2022a). Analytical and experimental study of performance of Pyrex glass Q-dot based passive solar still glass evaporator. Thermal Science and Engineering Progress, 34, 101387. https://doi.org/10.1016/j.tsep.2022.101387

Kumar Chauhan, V., & Kumar Shukla, S. (2022b). Experimental study of effect of glass cover tilt angle of solar still in winter season of India's composite climate. Thermal Science and Engineering Progress, 33, 101348. https://doi.org/10.1016/j.tsep.2022.101348

Kumar, S., Dubey, A., & Tiwari, G. N. (2014). A solar still augmented with an evacuated tube collector in forced mode. Desalination, 347, 15–24. https://doi.org/10.1016/j.desal.2014.05.019

Lauvandy, A. F., Raihananda, F. A., Estefan, M. J., Damanik, W. S., Mu'min, G. F., Juangsa, F. B., & Sambegoro, P. (2024). Application of a low-cost floating solar still in Indonesia. Energy for Sustainable Development, 79, 101410. https://doi.org/10.1016/j.esd.2024.101410

Liang, P., Liu, S., Ding, Y., Wen, X., Wang, K., Shao, C., Hong, X., & Liu, Y. (2021). A self-floating electrospun nanofiber mat for continuously high-efficiency solar desalination. Chemosphere, 280, 130719. https://doi.org/10.1016/j.chemosphere.2021.130719

Lienhard IV, J. H., & Lienhard V, J. H. (2020). A Heat Transfer Textbook (5th ed.). Phlogiston Pres. https://ahtt.mit.edu/wp-content/uploads/2020/08/AHTTv510.pdf

Luo, X., Jiao, L., Guo, Y., Bao, H., Zhao, C., & Gu, X. (2024). Ultrahigh freshwater production achieved by unidirectional heat transfer interfacial evaporation solar still integrated with waste heat recovery. Energy Conversion and Management, 304, 118226. https://doi.org/10.1016/j.enconman.2024.118226

Luo, X., Shi, J., Zhao, C., Luo, Z., Gu, X., & Bao, H. (2021). The energy efficiency of interfacial solar desalination. Applied Energy, 302, 117581. https://doi.org/10.1016/j.apenergy.2021.117581

M, C., & Yadav, A. (2017). Water desalination system using solar heat: A review. Renewable and Sustainable Energy Reviews, 67, 1308–1330. https://doi.org/10.1016/j.rser.2016.08.058

Mahala, T., & Sharma, N. (2024). Experimental investigations of a novel solar still with heat storage materials - energy, exergy, economic and environmental analyses. Desalination, 578, 117467. https://doi.org/10.1016/j.desal.2024.117467

Mahian, O., Kianifar, A., Heris, S. Z., Wen, D., Sahin, A. Z., & Wongwises, S. (2017). Nanofluids effects on the evaporation rate in a solar still equipped with a heat exchanger. Nano Energy, 36, 134–155. https://doi.org/10.1016/j.nanoen.2017.04.025

Maliani, O. D., Bekkaoui, A., Baali, E. H., Guissi, K., El Fellah, Y., & Errais, R. (2020). Investigation on novel design of solar still coupled with two axis solar tracking system. Applied Thermal Engineering, 172, 115144. https://doi.org/10.1016/j.applthermaleng.2020.115144

Mehta, P., Bhatt, N., Bassan, G., Said, Z., & ElCheikh, A. (2024). Exploring stepped solar still developments with a case study for potable water provision in salt farming regions. Sustainable Energy Technologies and Assessments, 64, 103700. https://doi.org/10.1016/j.seta.2024.103700

Meng, Z., Li, Z., Li, Y., Zhang, C., Wang, K., Yu, W., Wu, D., Zhu, H., & Li, W. (2022). Novel nanofluid based efficient solar vaporization systems with applications in desalination and wastewater treatment. Energy, 247, 123513. https://doi.org/10.1016/j.energy.2022.123513

Modi, K. V., Maurya, S. R., Parmar, J. H., Kalsariya, A. B., & Panasara, P. B. (2022). An experimental investigation of the effectiveness of partially and fully submerged metal hollow-fins and jute cloth wick-fins on the performance of a dual-basin single-slope solar still. Cleaner Engineering and Technology, 6, 100392. https://doi.org/10.1016/j.clet.2021.100392

Modi, K. V., & Modi, J. G. (2019). Performance of single-slope double-basin solar stills with small pile of wick materials. Applied Thermal Engineering, 149, 723–730. https://doi.org/10.1016/j.applthermaleng.2018.12.071

Modi, K. V., Patel, U. N., Patel, S. J., Patel, J. N., & Patel, S. R. (2022). Efficacy of partially and fully submerged circular cross-section metal hollow-fins and black cotton cloth wick-segments on a single-basin dual-slope solar still. Journal of Cleaner Production, 344, 131059. https://doi.org/10.1016/j.jclepro.2022.131059

Mohamed, A. F., Hegazi, A. A., Sultan, G. I., & El-Said, E. M. S. (2019). Augmented heat and mass transfer effect on performance of a solar still using porous absorber: Experimental investigation and exergetic analysis. Applied Thermal Engineering, 150, 1206–1215. https://doi.org/10.1016/j.applthermaleng.2019.01.070

Mohamed, A. S. A., Shahdy, A. G., & Salem Ahmed, M. (2021). Investigation on solar humidification dehumidification water desalination system using a closed-air cycle. Applied Thermal Engineering, 188, 116621. https://doi.org/10.1016/j.applthermaleng.2021.116621

Mohammadi, K., Taghvaei, H., & Rad, E. G. (2020). Experimental investigation of a double slope active solar still: Effect of a new heat exchanger design performance. Applied Thermal Engineering, 180, 115875. https://doi.org/10.1016/j.applthermaleng.2020.115875

Mohanraj, M., Karthick, L., & Dhivagar, R. (2021). Performance and economic analysis of a heat pump water heater assisted regenerative solar still using latent heat storage. Applied Thermal Engineering, 196, 117263. https://doi.org/10.1016/j.applthermaleng.2021.117263

Muthu Manokar, A., Kalidasa Murugavel, K., & Esakkimuthu, G. (2014). Different parameters affecting the rate of evaporation and condensation on passive solar still – A review. Renewable and Sustainable Energy Reviews, 38, 309–322. https://doi.org/10.1016/j.rser.2014.05.092

Nassar, Y. F., Yousif, S. A., & Salem, A. A. (2007). The second generation of the solar desalination systems. Desalination, 209(1–3), 177–181. https://doi.org/10.1016/j.desal.2007.04.039

Nayagam, V. S., Geetha, K., Vallikannu, R., Muthuvel, S. K., Ram, G. C., Gupta, P., Sudhakar, M., Mohanavel, V., & Sathyamurthy, R. (2022). Energy efficient tubular solar still for augmented yield using electrical heater. Energy Reports, 8, 959–964. https://doi.org/10.1016/j.egyr.2022.10.283

Negi, A., Dhindsa, G. S., & Sehgal, S. S. (2022). Experimental investigation on single basin tilted wick solar still integrated with flat plate collector. Materials Today:

Proceedings, 48, 1439–1446. https://doi.org/10.1016/j.matpr.2021.09.210

Nijmeh, S., Odeh, S., & Akash, B. (2005). Experimental and theoretical study of a single-basin solar sill in Jordan. International Communications in Heat and Mass Transfer, 32(3–4), 565–572. https://doi.org/10.1016/j.icheatmasstransfer.2004.06.006

Omara, Z. M., Ahmed, M. M. Z., Alawee, W. H., Shanmugan, S., & Elashmawy, M. (2024). A comprehensive review of nano-enhanced phase change materials on solar stills with scientometric analysis. Results in Engineering, 22, 102088. https://doi.org/10.1016/j.rineng.2024.102088

Omara, Z. M., Alawee, W. H., Basem, A., & Jawad Al-Bayati, A. D. (2024). Heat loss reduction techniques for walls in solar stills: A review. Results in Engineering, 22, 101996. https://doi.org/10.1016/j.rineng.2024.101996

Omara, Z. M., Eltawil, M. A., & ElNashar, E. A. (2013). A new hybrid desalination system using wicks/solar still and evacuated solar water heater. Desalination, 325, 56–64. https://doi.org/10.1016/j.desal.2013.06.024

Padilla, R. V., Demirkaya, G., Goswami, D. Y., Stefanakos, E., & Rahman, M. M. (2011). Heat transfer analysis of parabolic trough solar receiver. Applied Energy, 88(12), 5097–5110. https://doi.org/10.1016/j.apenergy.2011.07.012

Pandey, N., & Naresh, Y. (2024). A comprehensive 4E (energy, exergy, economic, environmental) analysis of novel pyramid solar still coupled with pulsating heat pipe: An experimental study. Renewable Energy, 225, 120227. https://doi.org/10.1016/j.renene.2024.120227

Peng, G., Xu, Z., Ji, J., Sun, S., & Yang, N. (2022). A study on the upper limit efficiency of solar still by optimizing the mass transfer. Applied Thermal Engineering, 213, 118664. https://doi.org/10.1016/j.applthermaleng.2022.118664

Poonia, S., Singh, A. K., & Jain, D. (2022). Performance evaluation of PCM based solar concentrator type desalination device. Materials Today: Proceedings. https://doi.org/10.1016/j.matpr.2022.02.637

Prasanna, Y. S., & Deshmukh, S. S. (2022). Energy, exergy and economic analysis of an air cavity appended passive solar still of different basin material at varying depth. Energy for Sustainable Development, 71, 13–26. https://doi.org/10.1016/j.esd.2022.09.008

Rahimi-Ahar, Z., Hatamipour, M. S., & Ahar, L. R. (2020). Air humidification-dehumidification process for desalination: A review. Progress in Energy and Combustion Science, 80, 100850. https://doi.org/10.1016/j.pecs.2020.100850

Rahimi-Ahar, Z., Hatamipour, M. S., Ghalavand, Y., & Palizvan, A. (2020). Comprehensive study on vacuum humidification-dehumidification (VHDH) desalination. Applied Thermal Engineering, 169, 114944. https://doi.org/10.1016/j.applthermaleng.2020.114944

Sadaghiyani, O., Boubakran, M., & Hassanzadeh, A. (2018). Energy and exergy analysis of parabolic trough collectors. International Journal of Heat and Technology, 36(1), 147–158. https://doi.org/10.18280/ijht.360120

Saeed, A. A., Alharthi, A. M., Aldosari, K. M., Abdullah, A. S., Essa, F. A., Alqsair, U. F., Aljaghtham, M., & Omara, Z. M. (2022). Improving the drum solar still performance using corrugated drum and nano-based phase change material. Journal of Energy Storage, 55, 105647. https://doi.org/10.1016/j.est.2022.105647

Saha, S., Sarker, M. R. I., Kader, M. A., Ahmed, M. M., Tuly, S. S., & Mustafi, N. N. (2024). Development of a vacuum double-slope solar still for enhanced freshwater productivity. Solar Energy, 270, 112385. https://doi.org/10.1016/j.solener.2024.112385

Sambare, R. K., Dewangan, S. K., Gupta, P. K., & Joshi, S. (2022). Energy, exergy and economic analyses of Tubular solar still with various transparent cover materials. Process Safety and Environmental Protection. https://doi.org/10.1016/j.psep.2022.10.064

Sampathkumar, K., Arjunan, T. V., Pitchandi, P., & Senthilkumar, P. (2010). Active solar distillation—A detailed review. Renewable and Sustainable Energy Reviews, 14(6), 1503–1526. https://doi.org/10.1016/j.rser.2010.01.023

Santosh, R., Arunkumar, T., Velraj, R., & Kumaresan, G. (2019). Technological advancements in solar energy driven humidification-dehumidification desalination systems - A review. Journal of Cleaner Production, 207, 826–845. https://doi.org/10.1016/j.jclepro.2018.09.247

Santosh, R., Lee, H.-S., & Kim, Y.-D. (2022). A comprehensive review on humidifiers and dehumidifiers in solar and low-grade waste heat powered humidification-dehumidification desalination systems. Journal of Cleaner Production, 347, 131300. https://doi.org/10.1016/j.jclepro.2022.131300

Saravanakumar, R., Venugopal, J., Udagani, C., Thiyagarajan, V., Kumar, S. K. N., Karnan, L., Kabeel, A. E., Madhu, B., & Sathyamurthy, R. (2022). A mini review on recent advancements in inclined solar still. Energy Reports, 8, 641–645. https://doi.org/10.1016/j.egyr.2022.09.174

Shafii, M. B., Jahangiri Mamouri, S., Lotfi, M. M., & Jafari Mosleh, H. (2016). A modified solar desalination system using evacuated tube collector. Desalination, 396, 30–38. https://doi.org/10.1016/j.desal.2016.05.030

Shah, R., Makwana, M., Makwana, N., & Desai, R. (2022). Perfromance analysis of black gravel solar still. Materials Today: Proceedings. https://doi.org/10.1016/j.matpr.2022.09.115

Shanazari, E., & Kalbasi, R. (2018). Improving performance of an inverted absorber multi-effect solar still by applying exergy analysis. Applied Thermal Engineering, 143, 1–10. https://doi.org/10.1016/j.applthermaleng.2018.07.021

Sharshir, S. W., Elkadeem, M. R., & Meng, A. (2020). Performance enhancement of pyramid solar distiller using nanofluid integrated with v-corrugated absorber and wick: An experimental study. Applied Thermal Engineering, 168, 114848. https://doi.org/10.1016/j.applthermaleng.2019.114848

Sharshir, S. W., El-Samadony, M. O. A., Peng, G., Yang, N., Essa, F. A., Hamed, M. H., & Kabeel, A. E. (2016).

Performance enhancement of wick solar still using rejected water from humidification-dehumidification unit and film cooling. Applied Thermal Engineering, 108, 1268–1278. https://doi.org/10.1016/j.applthermaleng.2016.07.179

Sharshir, S. W., Eltawil, M. A., Algazzar, A. M., Sathyamurthy, R., & Kandeal, A. W. (2020). Performance enhancement of stepped double slope solar still by using nanoparticles and linen wicks: Energy, exergy and economic analysis. Applied Thermal Engineering, 174, 115278. https://doi.org/10.1016/j.applthermaleng.2020.115278

Sharshir, S. W., Kandeal, A. W., Ismail, M., Abdelaziz, G. B., Kabeel, A. E., & Yang, N. (2019). Augmentation of a pyramid solar still performance using evacuated tubes and nanofluid: Experimental approach. Applied Thermal Engineering, 160, 113997. https://doi.org/10.1016/j.applthermaleng.2019.113997

Sharshir, S. W., Peng, G., Wu, L., Yang, N., Essa, F. A., Elsheikh, A. H., Mohamed, S. I. T., & Kabeel, A. E. (2017). Enhancing the solar still performance using nanofluids and glass cover cooling: Experimental study. Applied Thermal Engineering, 113, 684–693. https://doi.org/10.1016/j.applthermaleng.2016.11.085

Sharshir, S. W., Peng, G., Yang, N., El-Samadony, M. O. A., & Kabeel, A. E. (2016). A continuous desalination system using humidification – dehumidification and a solar still with an evacuated solar water heater. Applied Thermal Engineering, 104, 734–742. https://doi.org/10.1016/j.applthermaleng.2016.05.120

Sharshir, S. W., Rozza, M. A., Elsharkawy, M., Youns, M. M., Abou-Taleb, F., & Kabeel, A. E. (2022). Performance evaluation of a modified pyramid solar still employing wick, reflectors, glass cooling and TiO2 nanomaterial. Desalination, 539, 115939. https://doi.org/10.1016/j.desal.2022.115939

Sharshir, S. W., Rozza, M. A., Joseph, A., Kandeal, A. W., Tareemi, A. A., Abou-Taleb, F., & Kabeel, A. E. (2022). A new trapezoidal pyramid solar still design with multi thermal enhancers. Applied Thermal Engineering, 213, 118699. https://doi.org/10.1016/j.applthermaleng.2022.118699

Sharshir, S. W., Yang, N., Peng, G., & Kabeel, A. E. (2016). Factors affecting solar stills productivity and improvement techniques: A detailed review. Applied Thermal Engineering, 100, 267–284. https://doi.org/10.1016/j.applthermaleng.2015.11.041

Shoeibi, S., Kargarsharifabad, H., Mirjalily, S. A. A., & Muhammad, T. (2022). Solar district heating with solar desalination using energy storage material for domestic hot water and drinking water – Environmental and economic analysis. Sustainable Energy Technologies and Assessments, 49, 101713. https://doi.org/10.1016/j.seta.2021.101713

Shoeibi, S., Kargarsharifabad, H., Rahbar, N., Khosravi, G., & Sharifpur, M. (2022). An integrated solar desalination with evacuated tube heat pipe solar collector and new wind ventilator external condenser. Sustainable Energy Technologies and Assessments, 50, 101857. https://doi.org/10.1016/j.seta.2021.101857

Sibagariang, Y. P., Napitupulu, F. H., Kawai, H., & Ambarita, H. (2022). Investigation of the effect of a solar collector, nozzle, and water cooling on solar still double

slope. Case Studies in Thermal Engineering, 40, 102489. https://doi.org/10.1016/j.csite.2022.102489

Siddula, Sundeep., Stalin, N., Mahesha, C. R., Dattu, V. S. N. C. H., S, H., Singh, D. P., Mohanavel, V., & Sathyamurthy, R. (2022). Triangular and single slope solar stills: Performance and yield studies with different water mass. Energy Reports, 8, 480–488. https://doi.org/10.1016/j.egyr.2022.10.225

Somwanshi, A., & Shrivastav, R. (2024). Enhancement in the performance of closed loop inclined wick solar still by attaching external bottom reflector. Desalination and Water Treatment, 317, 100063. https://doi.org/10.1016/j.dwt.2024.100063

Somwanshi, A., & Shrivastava, R. (2023). Thermal analysis of a closed loop inclined wick solar still (CLIWSS) with an additional heat storage water reservoir. Solar Energy, 262, 111902. https://doi.org/10.1016/j.solener.2023.111902

Thakur, A. K., Sathyamurthy, R., Saidur, R., Velraj, R., Lynch, I., & Aslfattahi, N. (2022). Exploring the potential of MXene-based advanced solar-absorber in improving the performance and efficiency of a solar-desalination unit for brackish water purification. Desalination, 526, 115521. https://doi.org/10.1016/j.desal.2021.115521

Trinh, V.-H., Nguyen, N.-A., Omelianovych, O., Dao, V.-D., Yoon, I., Choi, H.-S., & Keidar, M. (2022). Sustainable desalination device capable of producing freshwater and electricity. Desalination, 535, 115820. https://doi.org/10.1016/j.desal.2022.115820

Tuly, S. S., Ayon, A. B. S., Hassan, R., Das, B. K., Khan, R. H., & Sarker, M. R. I. (2022). Performance investigation of active double slope solar stills incorporating internal sidewall reflector, hollow circular fins, and nanoparticle-mixed phase change material. Journal of Energy Storage, 55, 105660. https://doi.org/10.1016/j.est.2022.105660

U.S. Particle Accelerator School Education in Beam Physics and Accelerator Technology. (2015). Vacuum Science and Technology for Accelerator Vacuum Systems. USPAS - Vacuum Fundamentals. https://uspas.fnal.gov/materials/15ODU/Session1_Fundamentals.pdf

Velmurugan, V., Gopalakrishnan, M., Raghu, R., & Srithar, K. (2008). Single basin solar still with fin for enhancing productivity. Energy Conversion and Management, 49(10), 2602–2608. https://doi.org/10.1016/j.enconman.2008.05.010

Wang, Q., Wang, L., Song, S., Li, Y., Jia, F., Feng, T., & Hu, N. (2022). Flexible 2D@3D Janus evaporators for high-performance and continuous solar desalination. Desalination, 525, 115483. https://doi.org/10.1016/j.desal.2021.115483

Welepe, H. J. N., Günerhan, H., & Bilir, L. (2022). Humidifying solar collector for improving the performance of direct solar desalination systems: A theoretical approach. Applied Thermal Engineering, 216, 119043. https://doi.org/10.1016/j.applthermaleng.2022.119043

Wu, G., Zheng, H., Ma, X., Kutlu, C., & Su, Y. (2017). Experimental investigation of a multi-stage humidification-dehumidification desalination system heated directly by a cylindrical Fresnel lens solar concentrator. Energy

Conversion and Management, 143, 241–251. https://doi.org/10.1016/j.enconman.2017.04.011

Yılmaz, İ. H., & Mwesigye, A. (2018). Modeling, simulation and performance analysis of parabolic trough solar collectors: A comprehensive review. Applied Energy, 225, 135–174. https://doi.org/10.1016/j.apenergy.2018.05.014

Younes, M. M., Abdullah, A. S., Essa, F. A., & Omara, Z. M. (2021). Half barrel and corrugated wick solar stills – Comprehensive study. Journal of Energy Storage, 42, 103117. https://doi.org/10.1016/j.est.2021.103117

Younes, M. M., Abdullah, A. S., Essa, F. A., Omara, Z. M., & Amro, M. I. (2021). Enhancing the wick solar still performance using half barrel and corrugated absorbers. Process Safety and Environmental Protection, 150, 440–452. https://doi.org/10.1016/j.psep.2021.04.036

Yousef, M. S., Hassan, H., & Sekiguchi, H. (2019). Energy, exergy, economic and enviroeconomic (4E) analyses of solar distillation system using different absorbing materials. Applied Thermal Engineering, 150, 30–41. https://doi.org/10.1016/j.applthermaleng.2019.01.005

Yunus A. Çengel. (2011). Heat and Mass Transfer: A Practical Approach, 3rd Edition.

Zaheen Khan, M. (2022). Diffusion of single-effect vertical solar still fixed with inclined wick still: An experimental study. Fuel, 329, 125502. https://doi.org/10.1016/j.fuel.2022.125502

Ziapour, B. M., Afzal, S., Mahdian, J., & Reza Miroliaei, A. (2024). Enhancing solar still performance through innovative modeling, integration with reflectors, and semi-transparent solar cells: A 3E analysis and multi-objective optimization. Applied Thermal Engineering, 242, 122464. https://doi.org/10.1016/j.applthermaleng.2024.122464

Zubair, M. I., Al-Sulaiman, F. A., Antar, M. A., Al-Dini, S. A., & Ibrahim, N. I. (2017). Performance and cost assessment of solar driven humidification dehumidification desalination system. Energy Conversion and Management, 132, 28–39. https://doi.org/10.1016/j.enconman.2016.10.005

# EFFECTS OF PISTON COATING ON COMBUSTION STABILITY IN A CRDI DIESEL ENGINE RUN UNDER DUAL-FUEL MODE

**Ali ŞANLI** [*], **İlker Turgut YILMAZ** [**], **Ali ÖZ**[***]

* Maritime Higher Vocational School, Piri Reis University, 34940, Tuzla, İstanbul, Türkiye,
asanli@pirireis.edu.tr
**Department of Mechanical Engineering, Faculty of Technology, Marmara Uni., 34722, Maltepe, İstanbul, Türkiye,
ilker.yilmaz@marmara.edu.tr
*** Department of Automotive, Technical Sciences Vocational School, Burdur Mehmet Akif Ersoy Uni., Burdur,
alioz@mehmetakif.edu.tr

**Abstract:** Combustion stability in diesel engines is defined by cycle-to-cycle variations. In this study, effects of piston coating and engine load on cycle-to-cycle combustion behavior were investigated in a diesel engine operated on gaseous fuel mixture at different loads. Coated and uncoated piston tests under dual-fuel and single diesel modes were performed at three different loads including 50 Nm, 75 Nm, and 100 Nm at a constant speed of 1750 rpm. The piston bowls were coated by %8 yttria stabilized zirconia with the thickness of 0.4 mm. Dual-fuel mode is consisted of mixture of hydrogen enriched synthetic biogas, with the percentage of 80% $CH_4$, 10% $CO_2$, and 10% $H_2$. Main combustion parameters (cylinder pressure with crank angle, peak cylinder pressure ($CP_{max}$), peak pressure rise rate ($PRR_{max}$), indicated mean effective pressure (IMEP), CA10, CA50, CA90, and CA10-90 duration) were addressed in view of cyclic aspects. The results showed that the piston coating was comparatively more effective in reducing the coefficient of variation (COV) and standard deviation (SD) values of main combustion parameters, especially at low and medium loads. SD, frequency distribution, and COVs of $CP_{max}$ and IMEP were quite better at a medium test load of 75 Nm. The piston coating also reduced COV of CP with crank angle under all tests. As increasing the engine load, cyclic samples of $CP_{max}$ and $PRR_{max}$ enhanced and advanced for both diesel and dual-fuel modes. By the piston coating and engine loads, Cyclic CA10 and CA50 variations were slightly affected whereas cyclic CA90 were tremendously changed. Therefore, CA10-90 period was importantly affected by piston coating and load. The highest relationship among the main combustion parameters was between $CP_{max}$ and $PRR_{max}$ for both piston cases. In dual-fuel mode, a strong relationship emerged between IMEP and $CP_{max}$ at low load.

**Keywords:** Piston bowl coating, cycle-to-cycle variations, Common Rail Direct Injection (CRDI) diesel engine, biogas.

## ÇİFT YAKITLA ÇALIŞTIRILAN BİR OHDE DIZEL MOTORDA YANMA KARARLILIĞI ÜZERİNE PİSTON KAPLAMANIN ETKİLERİ

**Özet:** Dizel motorlarda yanma kararlılığı çevrimden çevrime değişimlerle belirlenir. Bu çalışmada, farklı yükler altında gaz karışımlarıyla çalıştırılan bir dizel motorda çevrimden çevrime yanma davranışları üzerine piston kaplamanın ve motor yükünün etkileri araştırılmıştır. 1750 d/d'lık sabit bir devirde, çift-yakıt ve dizel çalışma şartlarında kaplamalı ve kaplamasız piston testleri 50, 75 ve 100 Nm'lik üç motor yükü altında yapılmıştır. Piston çanağı 0.4 mm kalınlıkta yttria stabilize zirkonya ile kaplanmıştır. Çift-yakıt modu %80 $CH_4$, %10 $CO_2$ ve %10 $H_2$ karışımdan oluşan hidrojenle zenginleştirilmiş sentetik biyogazdır. Ana yanma parametreleri (krank açısına göre silindir basıncı, pik silindir basıncı ($P_{maks}$), pik basınç artış oranı ($BAO_{maks}$), ortalama indike basınç (OIB), KA10, KA50, KA90 ve KA10-90 süresi) çevrimsel açıdan ele alınmıştır. Sonuçlar göstermektedir ki; piston kaplama ana yanma parametrelerinin çevrimsel değişim katsayısı (ÇDK) ve standart sapma (SS) değerlerini azaltmada, özellikle düşük ve orta yüklerde oldukça etkindir. SS, frekans dağılımı ve $CP_{maks}$ ile OIB için ÇDK değerleri 75 Nm'lik orta yükte oldukça iyidir. Ayrıca, tüm yüklerde piston kaplama krank açısına göre silindir basıncının ÇDK değerlerini de azaltmıştır. Motor yükü artarken, dizel ve çift-yakıt çalışmalarında $P_{maks}$ ve $BAO_{maks}$ için çevrimsel değerler artış göstermiş ve daha erken oluşmuştur. Piston kaplama ve motor yüküyle, KA10 ve KA50 parametrelerinin çevrimsel değişimleri küçük mertebelerde iken KA90 parametresinin çevrimsel değişimleri önemli orandadır. Sonuçta, KA10-90 süresi piston kaplama ve motor yüküyle birlikte önemli oranda değişmiştir. Ana yanma parametreleri arasındaki en büyük ilişki her iki piston için $P_{maks}$ ve $BAO_{maks}$ arasında olmuştur. Çift-yakıt modunda, düşük yükte OIB ve Pmaks arasında güçlü bir ilişki ortaya çıkmıştır.

**Anahtar kelimeler**: Piston çanağı kaplama, çevrimsel değişimler, Ortak-hat direkt enjeksiyon (OHDE) dizel motor, biyogaz.

## NOMENCLATURE

| | |
|---|---|
| $\bar{x}$ | Mean value |
| *SD* | Standard deviation |
| *COV* | Coefficient of variance |
| CRDI | Common rail direct injection |
| $PRR_{max}$ | Maximum pressure rise rate [bar/°CA] |
| $CP_{max}$ | Maximum cylinder pressure [bar] |
| IMEP | Indicated mean effective pressure [bar] |
| CA10 | Crank angle when 10% of CHR emerged |
| CA50 | Crank angle when 50% of CHR emerged |
| CA90 | Crank angle when 90% of CHR emerged |
| CA10-90 | Combustion duration [°CA] |
| R | Correlation coefficient |
| n | Cycle number |
| $CH_4$ | Methane |
| $H_2$ | Hydrogen |
| ESR | Energy substitution rate |
| LHV | Lower heating value [kJ/kg] |
| $\dot{m}$ | Mass flow rate [kg/h] |
| YSZ | Yttria stabilized zirconia |
| TBC | Thermal barrier coating |

## INTRODUCTION

Internal combustion engines (ICEs) are frequently used for power producing, transportation, industrial applications, shipping propulsion, generators, and vehicles. Compression ignition (CI) engines are further preferred than spark ignition engines due to high efficiency, lower fuel consumption, and carbon-related emissions. About two-third of energy produced in ICEs is lost through coolant and exhaust systems. If heat loss through cooling is reduced, not only thermal efficiency can be increased, but also emissions can be reduced, and fuel economy improved (Hazar et al., 2016; Assanis et al., 1991).

Thermal barrier coating (TBC) of some engine components makes this possible by reducing the heat transfer from combustion chamber. Plasma spray method shows simple operation and high preparation efficiency, therefore used in most TBC applications. In ICE applications, TBC is applied to engine components such as pistons, valves, cylinder heads and exhaust manifolds that are exposed to high-temperature combustion gases in ICEs. Coated engine parts become more resistant to wear, friction, heating, corrosion, and oxidation. TBC system usually consist of two layers: bond and main coat materials. The first is the bond layer, which protects the substrate against oxidation and corrosion and also ensures compatibility between the ceramic layer and the substrate. The latter, with low thermal conductivity, greatly reduces heat losses to surrounding sources. TBC helped to extend the life of components in aircraft engines and stationary gas turbines by reducing the metal temperature (Schulz et al., 2003). The high combustion temperature resulting from the thermal insulation of ICE components can result in relatively higher thermal efficiency and lower fuel consumption (Taymaz, 2007; Selvam et al., 2018). Thanks to the thermal insulation of the exhaust manifold, the heat carried by the exhaust gases can also be used to further drive the turbocharger turbine, which increases volumetric efficiency and improves engine performance (Godiganur, 2021). Reducing carbon dioxide ($CO_2$) and hydrocarbon (HC) emissions, and improvement in aftertreatment performance by accelerating the catalyst light-off time can be possible with the thermal insulation of combustion chamber parts. Coating the walls of the combustion chamber with materials with lower thermal conductivity has been practiced since the 80s, but the results have not always been satisfactory (Vittal et al., 1999). It is needed to durable engine parts to resist higher temperatures caused by TBC. On the other hand, the increase in $NO_x$ emissions is high due to such high combustion temperatures in the TBC engine (Hazar, 2010; Reddy et al., 2021; Aydın, 2013). It is possible to reduce $NO_x$ emissions by using the internal exhaust gas recirculation (Shabir et al., 2014) or alternative fuels (Özer et al., 2021). All of them has partly prevented TBC technology from becoming widespread.

Numerous materials such as yttria stabilized zirconia (YSZ), silicon carbide, titanium, mullite, anodized alumina, magnesium silicate, molybdenum can be used for insulating the parts of combustion chamber in ICEs. Research groups in academic environment are still studying to obtain reasonable results by means of coating the engine parts. The effects of piston coating with different thicknesses of YSZ on the performance of different CI engines were investigated (Selvam et al., 2014; Sivakumar and Kumar, 2014; Goud et al., 2015). Coating process was done by the plasma spray method, and the used material had acceptable properties in view of lower thermal conductivity, higher thermal expansion coefficient, stable phase structure, and high Poission's ratio at elevated temperatures. Better thermal efficiency, lower fuel consumption, and lower HC and CO emissions were obtained in the engine with coated piston compared to the standard engine. Temperature on the coated piston was higher than that on the uncoated piston, and thickness of the coating material on the piston was highly important in view of temperature and thermal stress distribution (Cerit and Coban, 2014). Hejwowski and Weronski (2002) performed an experimental and simulation study in a naturally aspirated CI engine used different coating materials on the piston crown, which were $ZrO_2$, $Al_2O_3$, and $TiO_2$. Engine power and torque respectively enhanced almost 8% and 6%, and brake specific fuel consumption (bsfc) decreased about 15-20% by the coated piston. Simulation findings demonstrated that the optimum thickness of the coating material on piston was below 0.5 mm, and the coating material with aluminum-titania had the strongest corrosion resistance. Ramasamy et al. (2021) compared the coating materials on the piston of a CI engine fueled with diesel and biodiesel. They emerged that the YSZ material gave better results concerning the engine performance, whereas $Al_2O_3.SiO_2$ material showed lower emissions of NO, $CO_2$, and CO for each fuel type. Similarly, Ali et al.

(2018) performed a numerical comparative study on the effects of different ceramic materials (YSZ and $TiO_2$) applied on the piston surface on the performance of dual-fuel engine. YSZ revealed promising results compared to $TiO_2$, which had higher indicated thermal efficiency, lower bsfc, and higher exhaust gas temperature. Aydın et al. (2015) carried out performance, emission and combustion investigations in biomass fueled CI engine whose piston and valves were coated with $ZrO_2$, MgO, and $Al_2O_3$ materials. TBC improved bsfc and thermal efficiency results. $NO_x$ emissions partially elevated but HC, CO, and smoke emissions reduced with TBC application. Cylinder pressure relatively enhanced for the engine with coating parts. Civiniz et al. (2008) reported a 2% increase in engine power, and 1.5-2.5% increase in engine torque, and 4.5-9% reduction in bsfc by coating the piston, cylinder head, and valves of the test engine. The $NO_x$ emissions enhanced by 10%, and the smoke emission decreased by about 18% with the TBC application. Experimental results with the piston coating application can sometimes reveal contrary results to the expected ones; for instance, lower indicated thermal efficiency and higher soot values could be observed at partial loads (Caputo et al., 2019), higher bsfc values (Serrano et al. 2015), and lower $NO_x$ emissions (Ramu et al. 2009; Lawrence et al. 2011).

Cyclic variations directly influence the engine performance, emissions, combustion stability and engine noise. Drivability viewpoint of the vehicles with a multi cylinder engine might be closely related to cyclic combustion variability. Residuals from previous cycle, variations of air/fuel ratio, ignition delay, fuel type, and fluctuations in pressure, timing, and duration of fuel injection are usually responsible to the cycle-to-cycle variabilities. In the literature, there are several studies on alternative fuels in diesel engines (Şanlı, 2023; Kyrtatos et al. 2016; Pera et al., 2013, Wang et al., 2015; Zhong et al., 2003; Adomeit et al., 2007; Barton et al., 1970; Gupta et al., 2019). The overall conclusion from the studies is that cycle-to-cycle combustion variations are very important as they limit the load and power range in dual-fuel mode.

In most of the published papers, performance and emission analysis of the engine running on alternative fuels have been performed. Effects of TBC on combustion stability of the diesel engines working with the alternative fuels are seen unclear therefore it is needed more detailed investigations. This study was carried out to gain an in-depth understanding of the combustion behavior of a dual-fuel diesel engine with the coated piston bowls. The study is novel and fills the gap in the literature on cycle-to-cycle variations of the piston-coated dual-fuel diesel engines. Comprehensive cyclic combustion results are presented and discussed in this study for the coated and uncoated pistons under diesel and dual-fuel modes at different loads for the CRDI diesel engine.

## EXPERIMENTAL METHOD

### Test Equipment

Experiments were performed in a four-cylinder, Renault K9K, CRDI diesel engine to investigate cyclic variability under gaseous fuel operation. Diesel fuel having euro-diesel norms was used in the tests. Engine exhaust gas recirculation valve was canceled to avoid the partial effects of the exhaust gases. Before the tests, the engine was idled for a while to reach a stable regime. For the investigation, test conditions at which the engine was mostly operated under normal driving conditions were selected. The tests were performed at three loads, covering 50, 75, and 100 Nm torques. Engine speed was kept constant at 1750 rpm. The engine properties are given in Table 1, and Fig. 1 presents test bench layout. An eddy-current dynamometer, measurement capable of 150 kW rated power and 8000 rpm maximum rotational speed, was used to adjust the load and speed variations of the test engine. K-type thermocouples measured temperature variations at critical points of the engine, such as inlet and outlet cooling water, lubrication oil, exhaust gas outlet and fuel inlet. Measurement of the air mass flow rate was done by New Flow air flow meter. Instantaneous cylinder pressure data were collected by Optrand glow plug type cylinder pressure sensor. 200 sequential pressure data were used for the investigation. A shaft encoder with a resolution of 1° detected the crank angle degree. Instantaneous fuel pressure was metered by Kistler model fuel pressure device and its data were amplified by a Kistler charge amplifier. Amplified pressure signal was passed on National Instrument data card and send into a computer for combustion analysis. An on-board diagnostic device (OBD) was connected to the engine electronic control unit in order to show numeric data from the chosen engine sensors.

**Table 1.** Engine specifications

| Main properties | Four-stroke, turbocharger, CRDI fuel injection system |
|---|---|
| Number of cylinders | 4 |
| Bore - Stroke | 76 mm - 80.5 mm |
| Compression ratio | 18.25:1 |
| Total stroke volume | 1.461 liter |
| Injector type | With 5 nozzle holes, Selenoid controlling by Delphi management system |
| Maximal torque (@1750 rpm) | 160 Nm |
| Maximal power (@4000 rpm) | 48 kW |

.
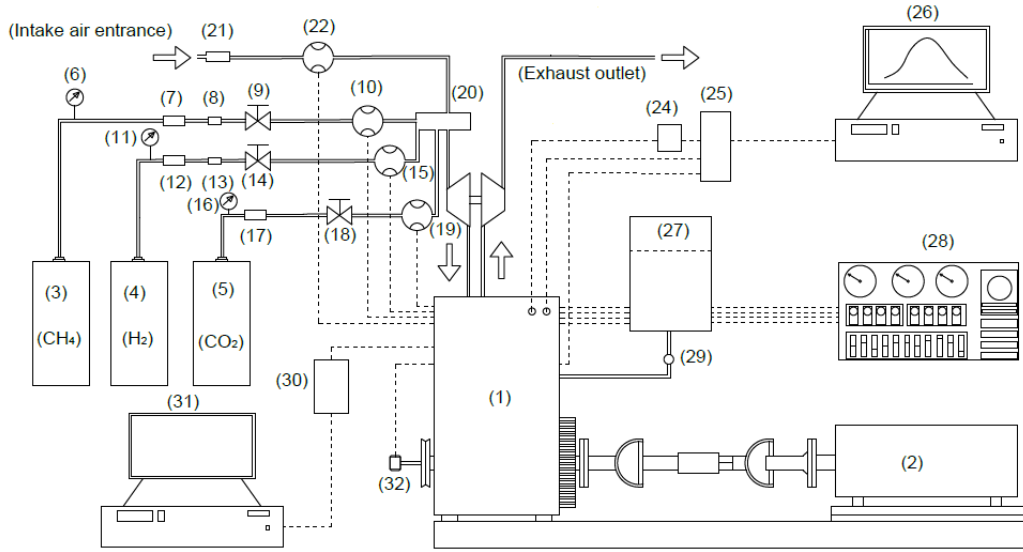
1.Test engine, 2.Eddy-current dynamometer, 3.CH4 tube, 4. H2 tube, 5. CO2 tube, 6-11-16.Manometers, 7-12-17. Pressure regulators, 8-13.Flame arresters, 9-14-18.Control valves, 10-15-19. Gas flow meters, 20.Mixing chamber, 21.Air filter, 22. Air flow meter, 23. Exhaust , 24.Charge amplifier, 25. Data card, 26. PC for combustion and emissions data, 27.Diesel tank, 28.Dynamometer control, 29. Burette, 30. On board diagnostics card, 31. PC for OBD interface, 32. Crank shaft encoder.

**Fig. 1.** Test bench.

The gaseous fuels were supplied with 50-liter bottles and connected to the test system via appropriate tools. They were sent to a mixing room mounted on the intake line, and after the turbocharging process, the mixture of air-gaseous fuels was sent to the engine cylinders. The mixture was ignited by the conventional diesel (pilot fuel). Energy amount of the pilot diesel fuel was varied depending on the test conditions and adjusted in approximately 20% of the total energy amount. Flame arresters on CH4 and H2 gas lines were utilized to prevent back flow of the sparked gaseous fuel and a possible explosion. CH4, CO2, and H2 flow rates were determined by Sierra model gas flow meters. In tests, entire metering values were displayed on the dynamometer control panel and OBD connected computer. Uncertainty of the used equipment is given in Table 2. After the standard engine tests, the standard pistons were replaced with YSZ-coated pistons. A similar test procedure was followed for the engine with the coated pistons.

In this study, the engine pistons were coated by YSZ and Ni-Al bond coat by plasma spray method. The coated and standard pistons can be seen in Fig. 2. 0.4 mm thicken YSZ surface ceramic coating (8%) and 0.1 mm thicken nickel-aluminum (Ni-Al) bond were applied to the piston bowl, respectively.
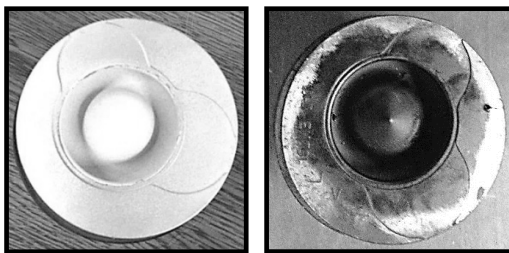


**Fig. 2.** Coated and standard pistons.

**Calculation Method of Cycle-To-Cycle Analysis**

Energy substitution rate (ESR) of each fuel was calculated by Eq. (1) presented below (Bouguessa et al., 2020),

$$ESR_{fuel} = \frac{\dot{m}_{fuel}LHV_{fuel}}{\dot{m}_d LHV_d + \dot{m}_{CH}+LHV_{CH4}+\dot{m}_{H2}LHV_{H2}} \tag{1}$$

where, $\dot{m}$ and $LHV$ symbolize mass flow rate (kg/h) and lower heating value (kJ/kg) of the test fuels, respectively. ESR value of each fuel for the test cases are given in Table. 3. Combustion stability is defined by means of SD and COV. SD for examined combustion characteristic can be calculated from Eq. (2)

$$SD = \sqrt{\frac{\sum_{i=1}^{n}(X_i - \bar{X})^2}{n-1}} \tag{2}$$

where $\bar{X}$ and $X_i$ express mean value and parameter value at cycle number $i$ of a combustion parameter, respectively. $n$ represents number of the cycles, which is 200 in this study.

$COV$ calculation of the combustion parameters is shown in Eq. (3), as follows:

$$COV = \frac{SD}{\bar{X}}100\% = \frac{\sqrt{\frac{\sum_{i=1}^{n}(X_i - \bar{X})^2}{n-1}}}{\bar{X}}100\% \tag{3}$$

In this paper, relationships among CP_max, PRR_max, and IMEP parameters were addressed. Correlation coefficient $R$ reveals numerical relationship between two combustion findings, referred as X and Y, and is computed from Eq. (4) (Şanlı et al. 2020),

$$R(X,Y) = \frac{\frac{1}{n}[\sum_{i=1}^{n}(X_i-\bar{X})(Y_i-\bar{Y})]}{SD_{(X)}SD_{(Y)}} \qquad (4)$$

**Table 2.** Properties of the test apparatus.

| Parameter | Unit | Measurement range | Accuracy |
|---|---|---|---|
| Fuel line pressure | bar | 0 ~ 3000 | 0.5 % |
| Cylinder pressure | bar | 0 ~ 200 | 1% |
| $CH_4$ flow rate | l/min | max. 200 | 1% |
| $H_2$ flow rate | l/min | max. 200 | 1% |
| Air flow rate | $m^3/h$ | max. 1200 | 1% |

**Table 3.** Energy substitution rates of dual-fuel diesel modes under different loads and pistons.

| Load (Nm) | Standard piston | | | Coated piston | | |
|---|---|---|---|---|---|---|
| | Diesel (%) | $CH_4$ (%) | $H_2$ (%) | Diesel (%) | $CH_4$ (%) | $H_2$ (%) |
| 50 | 23 | 74.6 | 2.4 | 19.8 | 77.5 | 2.7 |
| 75 | 22 | 75.5 | 2.5 | 21 | 76.2 | 2.8 |
| 100 | 23 | 74.6 | 2.4 | 20 | 77.4 | 2.6 |

## RESULTS AND DISCUSSION

### Cyclic Cylinder Pressure Variations

Under the dual-fuel and single diesel operations, cyclic cylinder pressure traces versus crank angle for the 200 sequential cycles are shown in Fig. 3 and Fig. 4 for YSZ coated piston and standard piston operations. It is observed from the figures that the cylinder pressure fluctuations for all cases are generally stable. The coated piston significantly affected magnitude of the cylinder pressure. This is clearly recognized in Fig. 5. Moreover, SD and COV of CP at each crank angle are presented in Fig.5. First of all, trend of COV of CP well agrees with published literature (Liu et al., 2022). Trend of COV of CP emerged that the coated piston at 100 Nm caused to strength pressure oscillations under dual-fuel modes, and peak COV of CP was reduced with the piston coating as well as lower COV values of 3%, suggesting the combustion stability was smoother in case of the coated piston. Fig. 6 is presented for a detailed examination of the cycle-to-cycle variations of $CP_{max}$. Additionally, average, SD, COV values, and frequency distribution of $CP_{max}$ are indicated in the Fig.6. Compared to the standard piston, the average value of the $CP_{max}$ for the coated piston under dual-fuel mode increased from 86.83 bar to 95.65 bar at 50 Nm, from 101.48 bar to 125.18 bar at 75 Nm, and from 133.26 bar to 137.02 bar at 100 Nm load. Apparent elevation of $CP_{max}$ was valid for the coated piston under the single diesel operation. This can be attributed to less heat loss to the cylinder walls and higher cylinder gas temperature caused from the piston coating (Yao et al., 2018). SD reflects the deviation from the mean value. Its minimum value is generally preferred for any variable. Generally, a lower SD value was found with coated piston at tested engine loads. COV presents the degree of dispersion of data samples around the mean. COV of $CP_{max}$ was mostly lower with the coated piston operations. It varies similarly to the SD of $CP_{max}$.
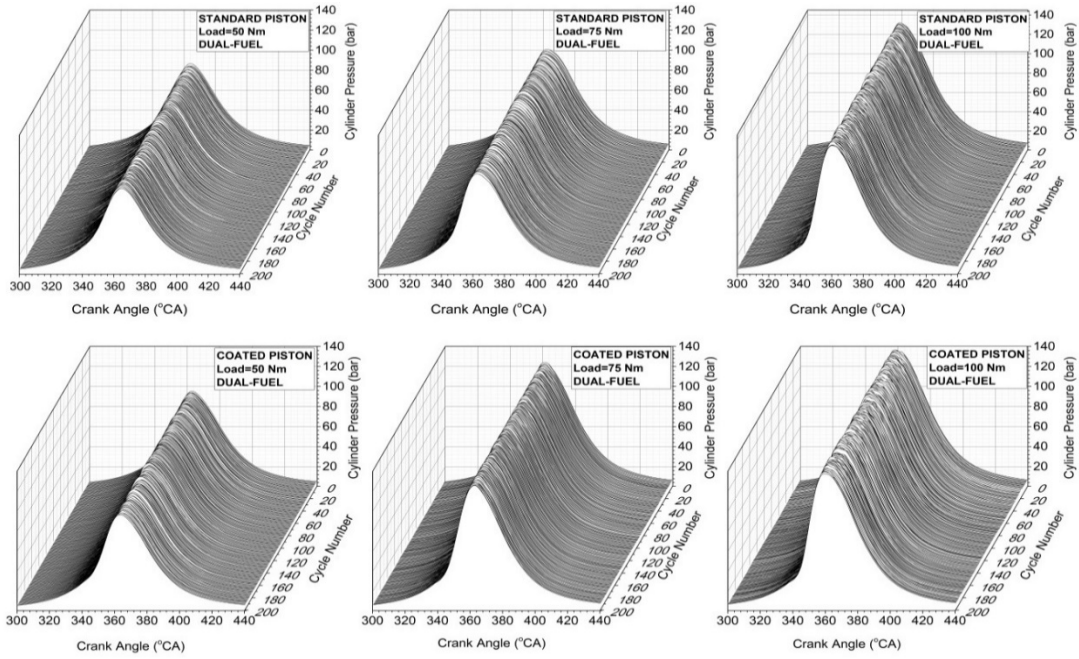


**Fig. 3.** Cyclic cylinder pressure curves with crank angle for standard piston and coated piston at different loads under single diesel mode.

**Fig. 4.** Cyclic cylinder pressure curves with crank angle for standard piston and coated piston at different loads under dual-fuel mode.
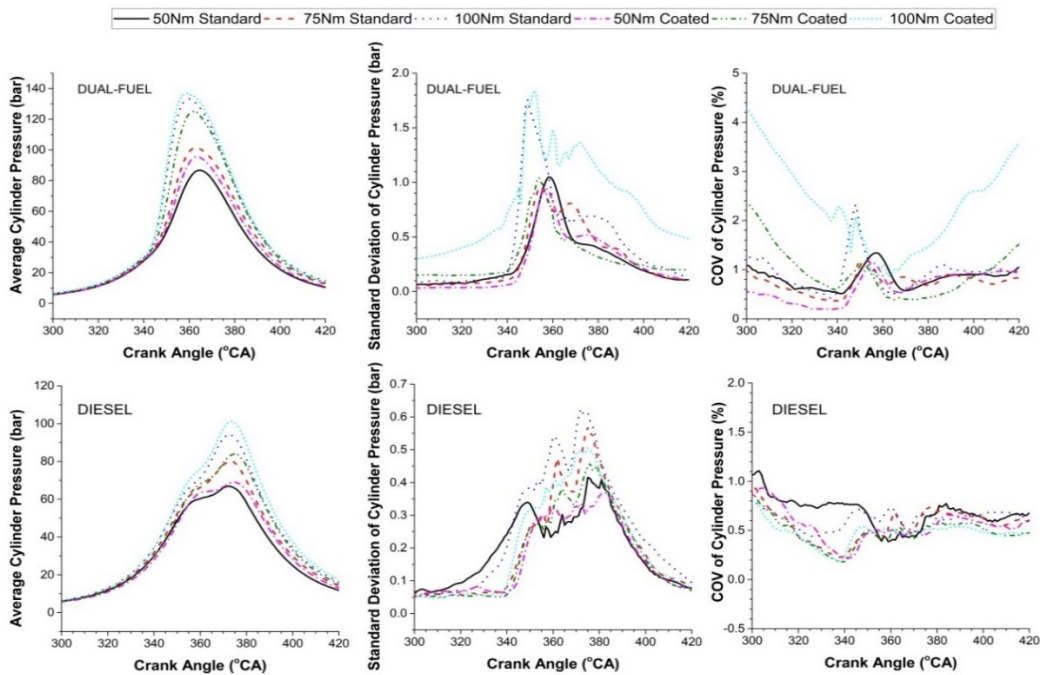


**Fig. 5.** Average, SD, and COV of cylinder pressure with crank angle for coated and standard piston engine at different engine loads under diesel and dual-fuel mode.

Frequency distribution reflects the repeatability for the same value of any parameter. A larger number of frequency distributions means more repeatability for the same value during multi-cycles. It can be clearly seen that the maximum frequency of $CP_{max}$ occurs at 50 Nm load in diesel mode and 75 Nm load in dual-fuel mode, regardless of whether the pistons are coated or uncoated. It was observed that under 100 Nm load, the frequency distribution of $CP_{max}$ was wider, i.e. more $CP_{max}$ values occurred, so a larger variety of $CP_{max}$ values emerged.
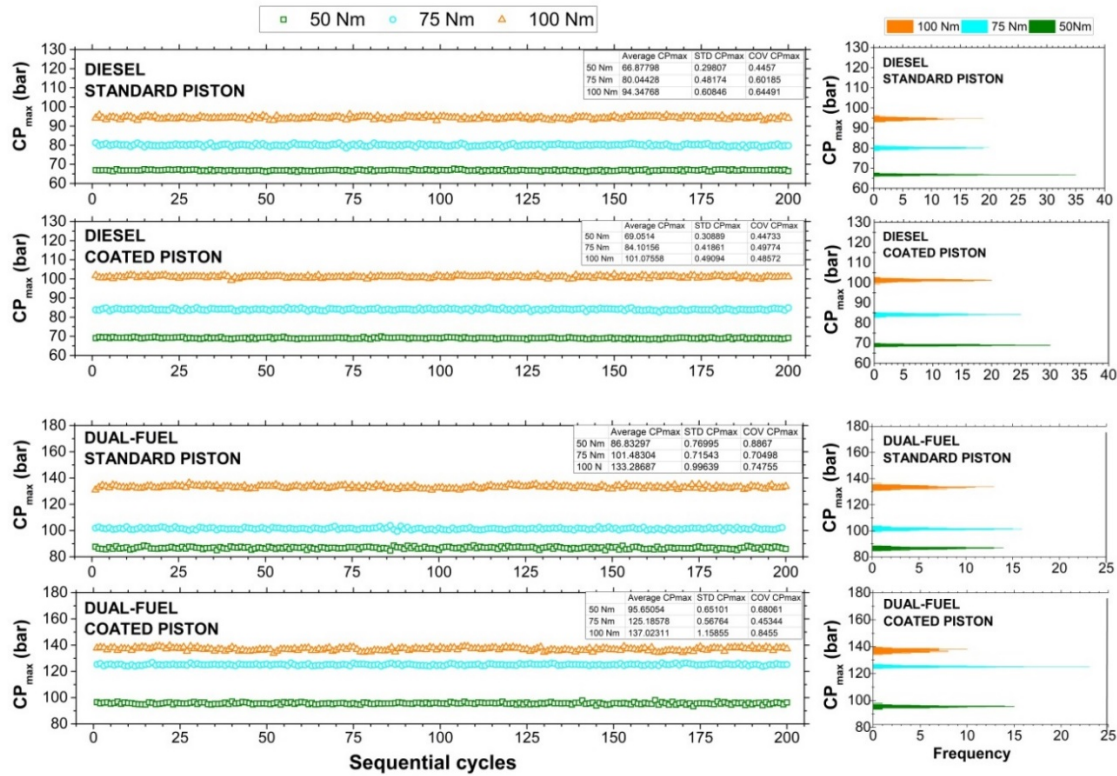
**Fig. 6.** Cyclic $CP_{max}$ and frequency variations for standard and coated pistons at various fuel and load cases.

$CP_{max}$ values and their crank angle (CA) locations are presented in Fig. 7 for all test conditions. As the load was increased the cyclic $CP_{max}$ locations notably advanced under dual-fuel mode; whereas it slightly advanced under single diesel mode. It can be hence said that $CP_{max}$ locations are more sensitive to load changing in operation with the gaseous fuels. In the case of coated piston, earlier $CP_{max}$ positions were observed in dual-fuel mode and later $CP_{max}$ positions were observed in single diesel mode. The piston bowl coating keeps the heat energy of fuel in combustion chamber thus increasing the temperature of the burning gases in cylinders (Yao et al.,

2018). The ignition points occur earlier in the piston bowl, especially with the gaseous fuel operations. Turbocharged diesel engines run with extremely lean air/fuel mixture at idle. Increased load means more fuel entering the cylinders; as a result, the combustion temperature increases. Especially, dual-fuel mode presents homogeneously operation all over the cylinders and is easily ignited by the pre-injection of the diesel fuel. The pre-injection timing is strongly dependent on the engine operating characteristics, especially the load variation, which is considered as a root cause of earlier $CP_{max}$ locations (Wang et al., 2021).
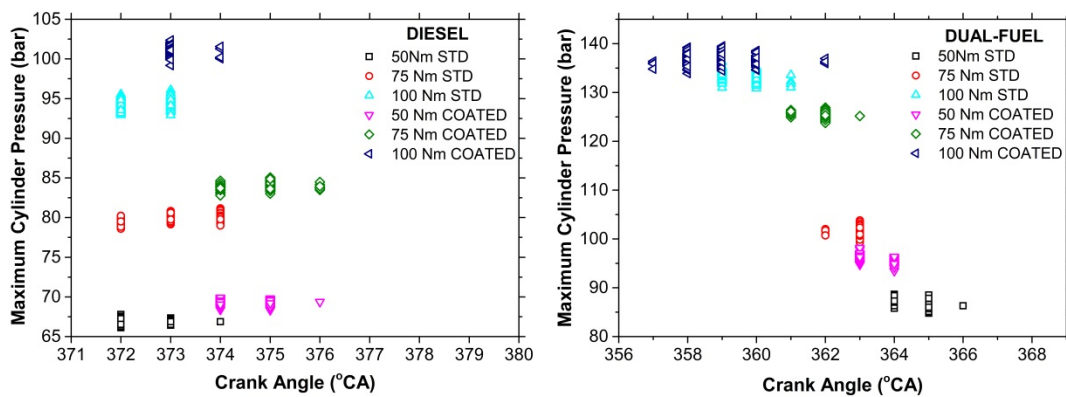


**Fig. 7.** $CP_{max}$ and corresponding CAs at different cases.

### Cyclic Pressure Rise Rate Variations

Pressure rise rate (PRR) is a meaningful tool for evaluating the knock during the burning phase. Cyclic

variations of the PRR during 200 cycles are seen in Fig. 8 for different cases. As increasing the engine load, it can be clearly observed that cyclic $PRR_{max}$ values elevate for each test case. Average $PRR_{max}$ was detected as 3.91,

5.69, and 9.59 bar/°CA at 50 Nm, 75 Nm and 100 Nm loads respectively for the standard piston operation of dual-fuel mode, while 5.01, 7.99, and 10.6 bar/°CA at 50 Nm, 75 Nm and 100 Nm loads respectively for the coated piston operation in dual-fuel mode. Remarkable $PRR_{max}$ increase was not detected for single diesel mode. From these observations, it can be concluded that the coating piston significantly affected the cyclic $PRR_{max}$ values. At high load of 100 Nm and piston coating caused to the severe diesel knock with the high average value of 10.6 bar/°CA. Some cycles led to higher $PRR_{max}$ values at 100 Nm under dual-fuel coated piston mode. The highest $PRR_{max}$ value happened in 65. cycle with a value of 12.15 bar/°CA at the stated test case.

Frequency distribution of $PRR_{max}$ showed that the dual-fuel mode led to extremely lessen the repeatability of $PRR_{max}$ values. The highest value of $PRR_{max}$ frequency in single diesel mode was 63 at 50 Nm under uncoated piston and 59 times at 75 Nm under coated piston. The highest frequency value of $PRR_{max}$ in dual-fuel mode was 17 at 75 Nm under uncoated piston and 16 at 75 Nm under coated piston. On the other hand, the load

increasing was resulted in more $PRR_{max}$ values and therefore less $PRR_{max}$ frequency. Higher temperatures and severe pressure oscillations caused by the increase in the amount of fuel delivered into the cylinders and ignition cores due to increasing the engine load can be among possible reasons for the higher frequency of $PRR_{max}$ values. Similarly, the coating of piston bowl mostly led to an increase in frequency distribution of $PRR_{max}$; in other words, the repeatability of the same values increased. Sometimes, this may be associated with the SD variations. In all tests, COV of $PRR_{max}$ values were lower than 3%. This means that the stable running was continued during the tests. When the engine was operated with the coated piston, remarkable decrease in COV of $PRR_{max}$ was seen, especially in dual-fuel mode. For example, when the engine's standard pistons were replaced with the coated ones, COV of $PRR_{max}$ at 75 Nm load dropped from 2.18 bar/°CA to 1.90 bar/°CA in dual-fuel mode. Moreover, the lowest COV of $PRR_{max}$ values was obtained at 75 Nm. This indicates that the test engine operates the best at that load in view of the cyclic variations.
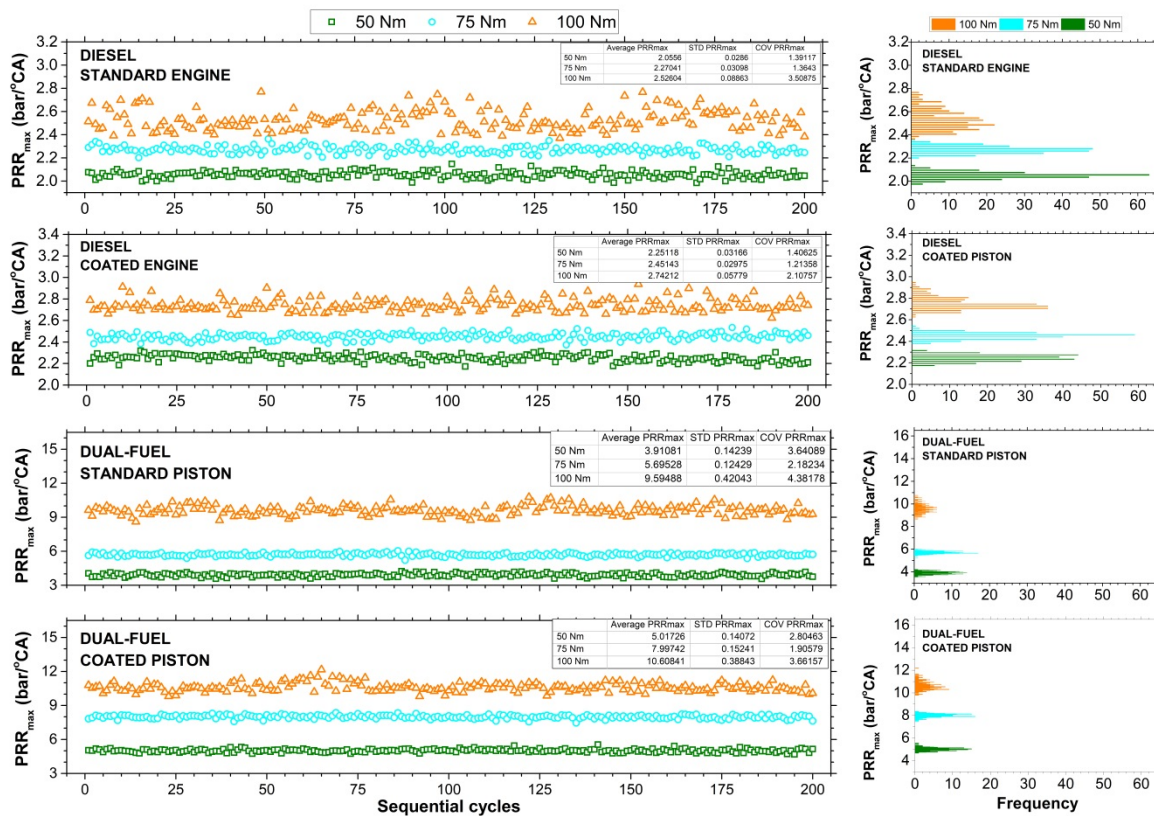


**Fig. 8.** Cyclic $PRR_{max}$ and frequency variations for standard and coated pistons at various fuel and load cases.

$PRR_{max}$ values and its corresponding crank angle positions for 200 experimental samples are illustrated in Fig. 9 for different cases of the fuels, loads and coatings. Mostly, a similar trend to the $CP_{max}$ outcomes was observed under the diesel and dual-fuel modes. As the engine load was enhanced, advanced CA locations and higher values of $PRR_{max}$ were noticed. Compared to 50 Nm and 75 Nm loads, there were seen two CA groups of

$PRR_{max}$ locations for the conventional diesel operation at 100 Nm regardless of the coated or uncoated piston cases. This is due to the pre-injection and main injection phases of the common-rail fuel-injection system (Şanlı and Yılmaz, 2022). As changing the injection amount and timing with the engine load, first peak and second peak are more noticeable under sole diesel operations. On the other hand, the bowl coating caused to earlier CAs of

PRR$_{max}$ at a given load. Increased temperatures and cylinder pressure oscillations with the engine load and the piston coating appear to promote severe diesel knocking. Besides, when the engine was operated in dual-fuel mode, PRR$_{max}$ locations were notably retarded, in the range of 2-9 $^o$CA at 50 Nm, 1-7 $^o$CA at 75 Nm, and 2-6 $^o$CA at 100 Nm. This can be ascribed to the dynamic injection timing variations, which is one of the superior specifications of the common-rail engine management system.
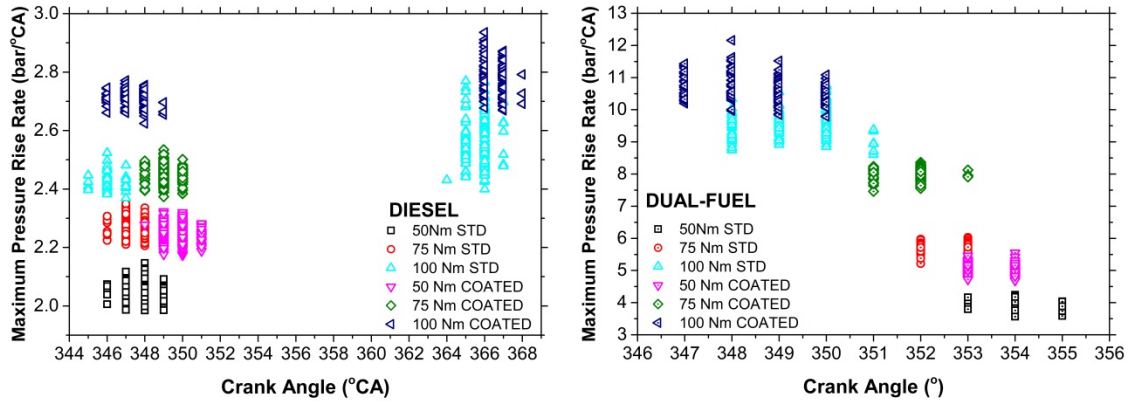


**Fig. 9.** Crank angle and PRR$_{max}$ for coated and standard piston cases at different loads.

## Cyclic IMEP Variations

IMEP reflects average cycle efficiency obtained by the indicator diagram. Sequential IMEP variations and frequency distribution for different test cases are illustrated in Fig. 10. It can be clearly observed that the cyclic IMEP values increase as the engine load increases. However, under dual-fuel mode and coated piston case of 100 Nm, the cyclic IMEP values were not enhanced more and remained similar to those of medium load.

Average values were 8.76 bar and 8.74 bar for the respective loads of 75 Nm and 100 Nm in that test condition. Combined effects of the coated piston and high load under dual-fuel mode caused severe diesel knock as observed earlier in Figs. 8 and 9, and this apparently limited IMEP boost with enhanced load. In the published paper, Ramu and Saravanan (2009) reported lower IMEP values of TBC engine with fuel additive compared to uncoated engine. They emphasized that to be caused by lower power production during combustion process in TBC engine.
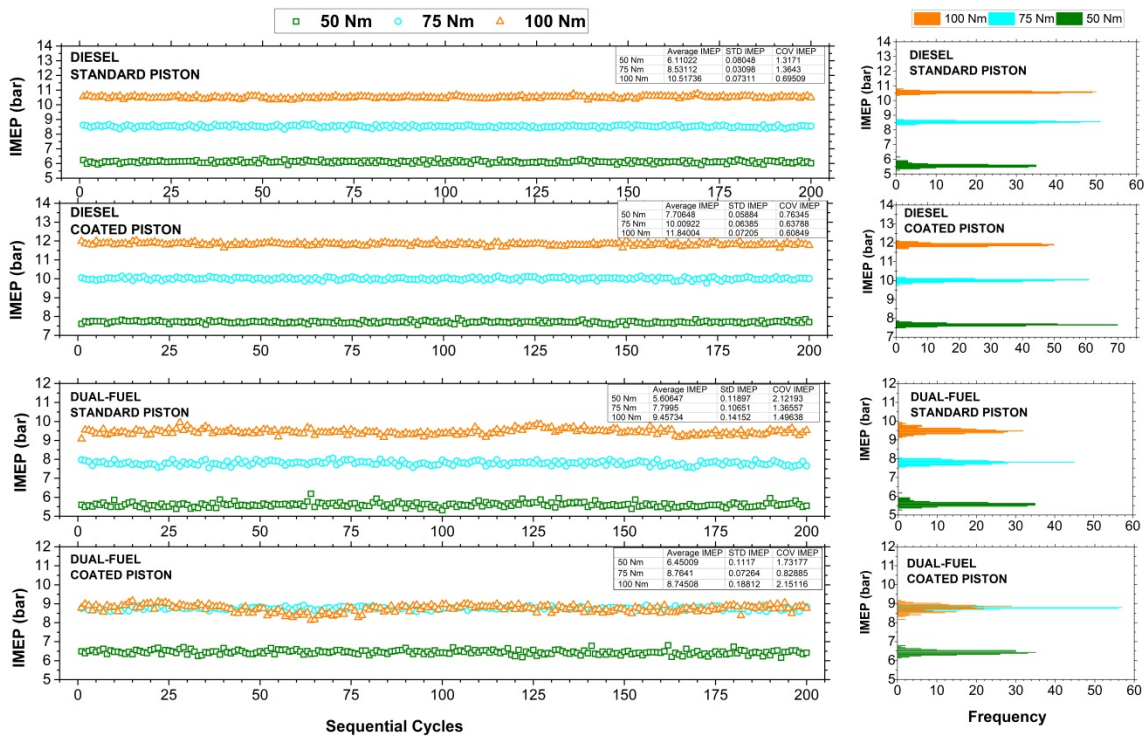


**Fig. 10.** Cyclic IMEP variations for standard piston and coated piston at various loads.

## Cyclic CA10, CA50, CA90, and CA10-90 Variations

CA positions detected by corresponding cumulative heat release (CHR) findings are frequently used in combustion studies. The positions of CA10, CA50, and CA90 are important findings accounting for determining of the combustion phases. CA10, CA50, and CA90 are CA positions corresponding to 10%, 50% and 90% of the energy released by the combustion of each fuel respectively (Şanlı et al. 2020). They depend on engine design, fuel type, and load conditions. The positions of CAs during the combustion can be affected by several parameters such as intake conditions, injection characteristics, and ignition delay period. CA10-90 term describes the period from 10% to 90% of the burned fuel mass. Longer CA10-90 period clearly refers to slower combustion period, suggesting that more heat loss, inefficient combustion, lower thermal efficiency and power output, and more HC formation. In Figs. 11 and 12, CA10, CA50, CA90, and CA10-90 variations from one cycle to another are exhibited for all test cases. Cyclic CA10 and CA50 results at all tests showed modest differences. However, cyclic CA90 results exhibited larger oscillations during the sequential cycles. Cyclic CA10-90 variations therefore showed extreme fluctuations, indicating that the combustion duration in a cycle is greatly dependent on post-burning phase (Liu et al., 2022). It is perceived from the Figs. 11 and 12 that as the engine load was enhanced, cyclic CA90 and CA10-90 variations notably decreased in diesel fuel mode whereas increased in dual-fuel mode. At the end of the diffusion combustion, combined effects of the residual gases from the previous cycle and the unburned fuel in crevice regions play a critical role in cyclic fluctuations of CA90 and CA10-90 parameters. Furthermore, the cycle-to-cycle variation of the intake air pressure can be critical for the formation of CA points during the combustion phase. This is obviously proved in Fig. 13 for several subsequent cycles (cycle number from 147 to 151) in dual-fuel coated piston mode under 100 Nm load. In 148.-150. cycles, it was noticeable that the intake air was taken into the cylinders with relatively lower intake pressure compared to 147. and 151. cycles. During the post-combustion period, as seen in CHR graphic at right-hand below, it was detected later CA90 points in 148.-150. cycles. In the meantime, fuel line pressure graphic for the specified cycles, at left-hand above in Fig. 13, showed that the CA points were influenced by the injection pressure. It is obvious that similar injection pressure traces in 148. and 149. cycles yielded similar HRR and CHR profiles whereas no similar cylinder pressure profiles. Therefore, combined effects of the fuel injection pressure and the intake air pressure are proved to be quite effective in cycle-to-cycle combustion variations in this study. Moreover, it is clear from the Fig. 13 that as passing from CA10 to CA90, the crank interval between the CAs drastically enlarged. Additionally, when the coated piston was applied to the engine, it was observed cyclic improvement for CA90 and CA10-90 for each fuel mode. This is possibly due to improvement in the post-burning phenomenon and a reduction in the amount of the unburned gases in operation with the coated piston. In dual-fuel operation, combustion changes from a constant pressure process to a constant volume process. Overall, cyclic variations of examined CAs and CA10-90 period showed quite smooth variations compared to those in spark ignition engines in published literature (Liu et al., 2022; Chen et al., 2021).
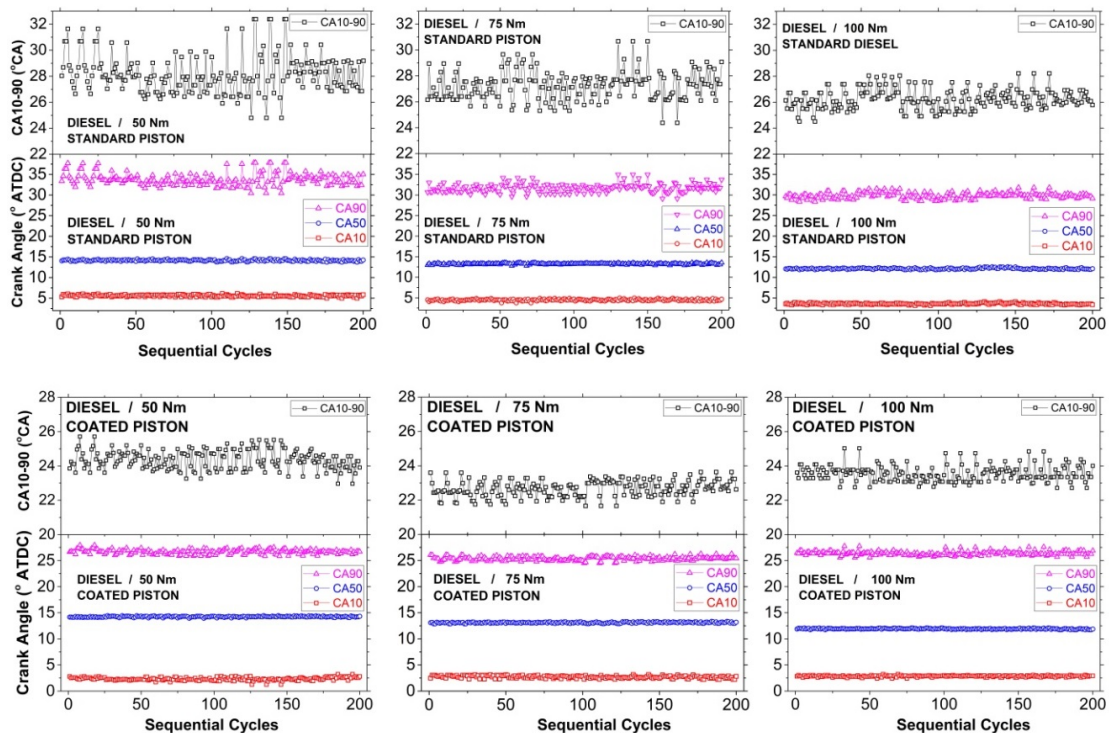


**Fig. 11.** Cyclic CA10, CA50, CA90, and CA10-90 variations under different loads for diesel mode
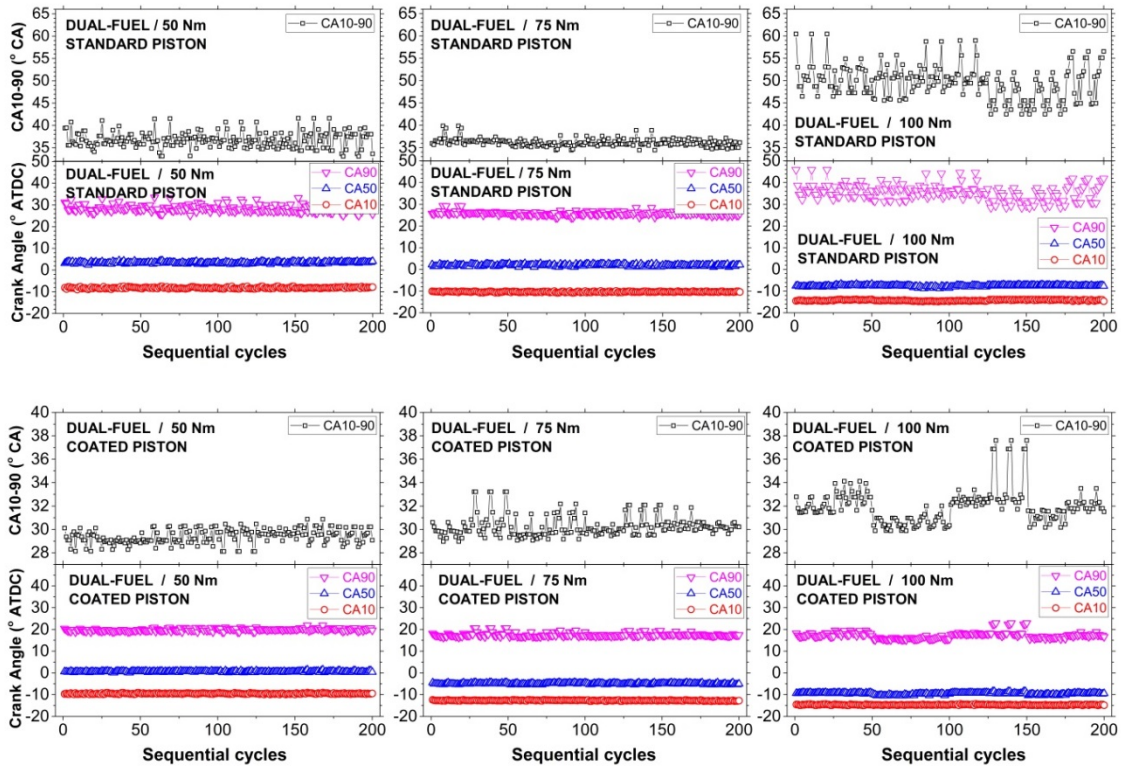
**Fig. 12.** Cyclic CA10, CA50, CA90, and CA10-90 variations under different loads for dual-fuel mode.
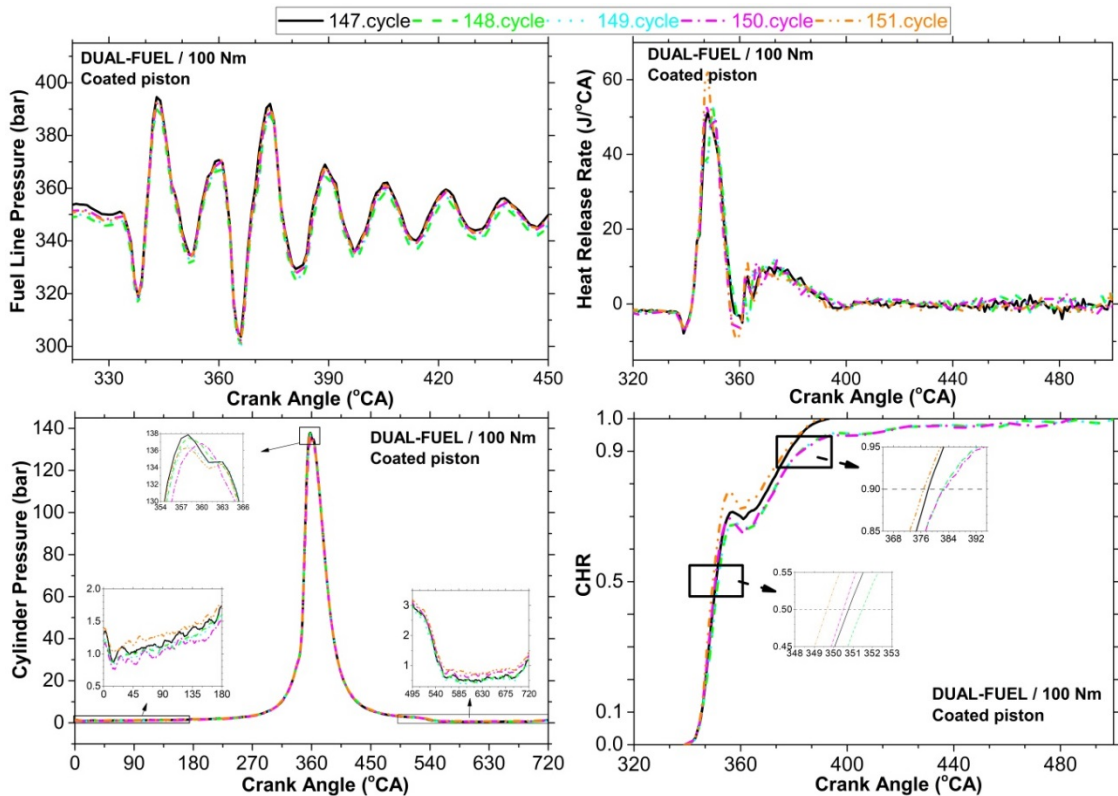


**Fig. 13.** Cyclic variations in fuel line pressure, heat release rate, cylinder pressure, and CHR for several subsequent cycles.

Corresponding average values of CA10, CA50, CA90 and CA10-90 are presented in Fig. 14a for all test cases. With increasing engine load, average CA10, CA50, and CA90 positions were often advanced and average CA10-90 duration increased that is an expected phenomenon since more fuel is injected in the cylinders with load and needed to more time to burn. On the other hand, it was observed that the piston coating reduced CA10-90

duration. Piston coating leads to higher combustion temperature in the cylinders which in turn encourages flame propagation speed; as a result, time period between CA10 and CA90 is diminished (Venu and Appavu, 2019). Concerning the SD findings of CAs and CA10-90, it could be seen in Fig. 14b that the coated piston was recognizable to lead lower SD, meaning that minimal

deviance from the mean value occurred. In case of the single diesel mode with the standard piston operation the highest SD value was obtained with CA90 and CA10-90 duration at 100 Nm as the deviance from the mean value for the CA90 and CA10-90 parameters was highly larger, as clearly seen in Fig. 13.
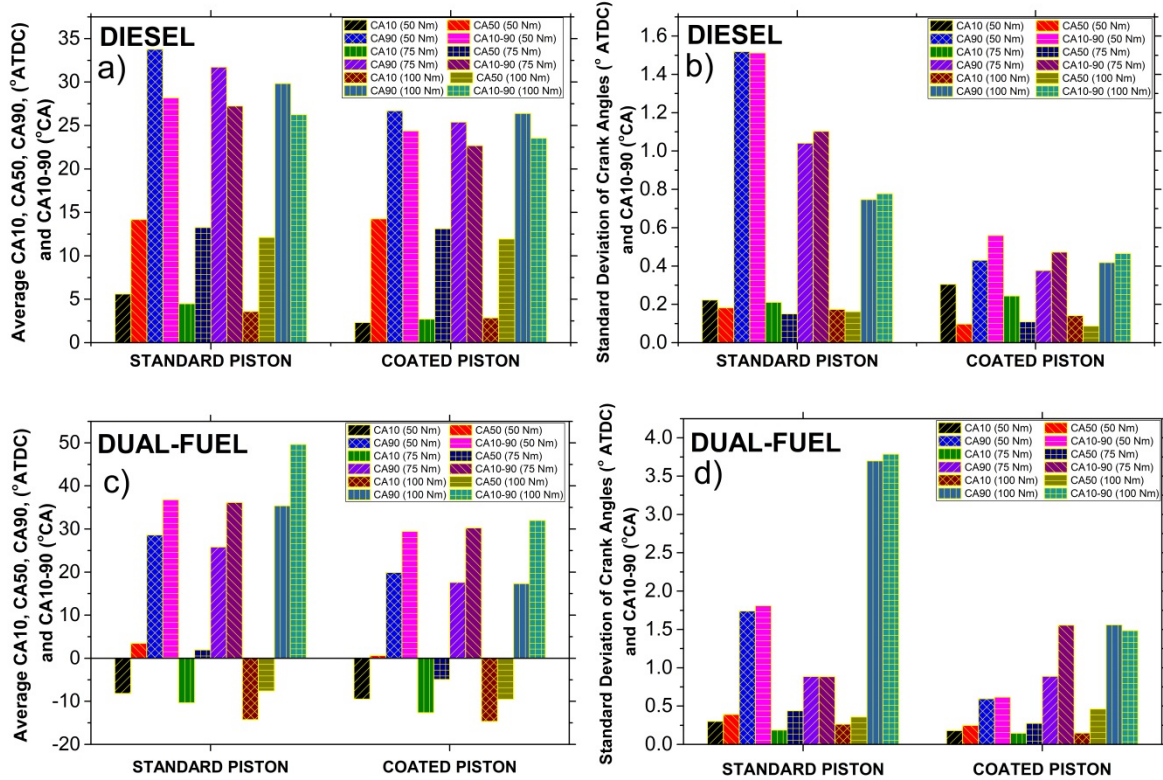


**Fig. 14.** Average values (a) and SD values (b) of CA10, CA50, CA90 and CA10-90 durations.

**Relationship Between Main Combustion Parameters**

In Fig.15, it can be seen the relation on fundamental burning parameters covering $CP_{max}$, $PRR_{max}$, and IMEP under all the test cases. The highest correlation coefficients were found between $CP_{max}$ and $PRR_{max}$ as R=0.84 and R=0.82 at 50 Nm for dual-fuel operations and R=0.73 and R=0.61 at 100 Nm for diesel operations under the standard and coated pistons, respectively. This represents a strong relation for the mentioned parameters and operating conditions (Şanlı and Yılmaz, 2022). In contrast, the lowest correlation coefficients were found between IMEP and $PRR_{max}$ as 0.02 at 100 Nm for standard piston operation and 0.09 at 75 Nm for coated piston operation under dual-fuel modes, and 0.07 and 0.15 at 75 Nm for standard piston under diesel

operations. Except for them, there were not seen higher correlation coefficients but there were mostly weak linear relationships between IMEP and $PRR_{max}$. As for the correlation between IMEP and $CP_{max}$, it was found a linear relationship for all dual-fuel modes between IMEP and $CP_{max}$ since the obtained values were in order of R=0.43-0.79. Whereas there were weak linear relationships for single diesel operations, except for the condition of 75 Nm load with the standard piston. Meanwhile, it was generally found poor relationships between each other for the parameters of CA10, CA50, CA90, and CA10-90 at diesel and dual-fuel modes. Also, their relationships with main combustion parameters ($CP_{max}$, $PRR_{max}$, and IMEP) were with lower correlation coefficient, suggesting a weak relationship.
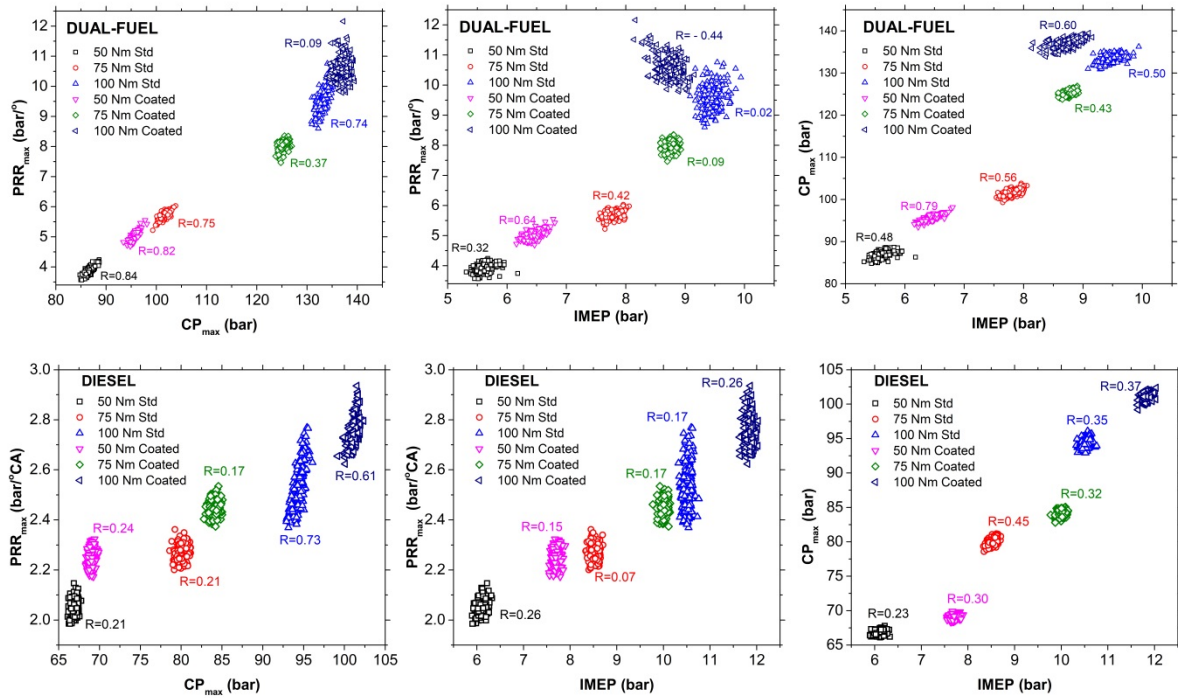
**Fig. 15.** Correlations between the parameters of $CP_{max}$, $PRR_{max}$, and IMEP for dual-fuel operations.

## CONCLUSIONS

An experimental study was carried out on the combustion stability of a CRDI automotive diesel engine in which the piston bowls were coated with YSZ at different loads. The study was performed to reveal cyclic variations of main combustion parameters in operation with the gaseous fuels at different loads. Following conclusions were achieved from the study.

- 
- 

Compared to operation with uncoated piston engine, average $CP_{max}$ and $PRR_{max}$ enhanced with coated piston engine for all cycles. As increasing the load, cyclic $CP_{max}$ and $PRR_{max}$ were remarkably advanced and enhanced. Peak value of COV of CP with crank angle decreased under the coated piston engine. At high load of 100 Nm under dual-fuel mode, severe knock indication emerged with coated piston operation, which could be possible reason for higher SD traces of cylinder pressure with the crank angle.

IMEP improvement was limited at high load of 100 Nm under coated piston operating due to knock existence. Frequency distribution of cylinder pressure and IMEP showed that the best running was achieved at medium load of 75 Nm. Accordingly, COV and SD results were mostly the best at 75 Nm load for both diesel and gaseous fuel operations under the piston coating.

Cyclic CA10 and CA50 variations were in acceptable range during the cycles. However, CA90 and CA10-90 duration further fluctuated from cycle to cycle. As increasing the engine load, CA90 and CA10-90 fluctuations remarkably reduced in diesel mode but elevated in dual-fuel mode. Furthermore, coating piston

reduced cyclic fluctuations of CA90 and CA10-90. In the cyclic discrepancies of CA90 and CA10-90 during sequential cycles, fuel injection pressure and intake air pressure were the critical factors and played an important role.

SD of CA10, CA50, CA90, and CA10-90 was reduced by the coated piston under diesel and dual-fuel modes.

Relationship between main combustion characteristics varied with given operation cases. Correlation coefficient between IMEP-$CP_{max}$ parameters was always higher than 0.4, meaning that there was a linear relationship and in acceptable range for all operation cases. The highest correlation coefficient was found between $PRR_{max}$ and $CP_{max}$ parameters, which are 0.84 and 0.82 corresponding to low load of 50 Nm load under dual-fuel mode with coated and uncoated pistons, respectively.

In the future studies, it is recommended that a more comprehensive study is conducted with another alternative fuels, such as natural gas, biogas, biodiesel, higher alcohols. Furthermore, tested engine parameters can be expanded with more range of loads, speeds, and fuel fractions.

## REFERENCES

Adomeit P., Lang O., Pishinger S., Aymanns R., Graf M., Stapf G., 2007, Analysis of cyclic fluctuations of charge motion and mixture formation in a DISI engine in stratified operation, *SAE Technical Paper,* 2007-01-1412.

Ali H.L., Li F., Wang Z., Shuai S., 2018, Effect of ceramic coated pistons on the performance of a compressed natural gas engine, *IOP conference series: Materials Science and Engineering*, 417, 012021.

Assanis D., Wiese K., Schwarz E., Bryzik W., 1991, The effects of ceramic coatings on diesel engine performance and exhaust emissions, *SAE Technical Paper,* 910460.

Aydin H., 2013, Combined effects of thermal barrier coating and blending with diesel fuel on usability of vegetable oils in diesel engines, *Applied Thermal Engineering*, 2013;51(1-2):623-9.

Aydın S., Sayin C., Aydin H., 2015, Investigation of the usability of biodiesel obtained from residual frying oil in a diesel engine with thermal barrier coating, *Applied Thermal Engineering*, 80, 212-9.

Barton R., Kenemuth D., Lestz S., Meyer W, 1970, Cycle-by-cycle variations of a spark ignition engine- A statistical analysis, *SAE Technical Paper,* 700488.

Bouguessa R., Tarabet L., Loubar K., Bilmrabet T., Tazerout M., 2020, Experimental investigation on biogas enrichment with hydrogen for improving the combustion in diesel engine operating under dual fuel mode, *International Journal of Hydrogen Energy*, 45(15), 9052 – 63.

Caputo S., Millo F., Boccardo G., Piano A., Cifali G., Pesce F.C., 2019, Numerical and experimental investigation of a piston thermal barrier coating for an automotive diesel engine application. *Applied Thermal Engineering*, 162, 114233.

Cerit M. and Coban M., 2014, Temperature and thermal stress analyses of a ceramic-coated aluminum alloy piston used in a diesel engine, *International Journal of Thermal Sciences*, 77, 11-8.

Chen Z., He J., Chen H., Geng L., Zhang P., 2021, Experimental study on cycle-to-cycle variations in natural gas/methanol bi-fueled engine under excess air/fuel ratio at 1.6, *Energy*, 224, 120233.

Civiniz M., Hasimoğlu C., Şahin F., Salman M.S., 2008, Impact of thermal barrier coating application on the performance and emissions of a turbocharged diesel engine, *Proc IMechE Part D: J Automobile Engineering*, 222(12), 2447-55.

Godiganur V.S., Nayaka S., Kumar G.N., 2021, Thermal barrier coating for diesel engine application – A review. *Materials Today: Proceedings,* 45,133-7.

Goud G.B., Singh C.T.D.K., 2015, Investigation of CI diesel engine emission control and performance parameters using biodiesel with YSZ coated piston crown. *International Journal of Engineering and Technology*, 2(3), 467-74.

Gupta S.K. and Mittal M., 2019, Effect of compression ratio on the performance and emission characteristics, and cycle-to-cycle combustion variations of a spark-ignition engine fueled with bio-methane surrogate, *Applied Thermal Engineering*, 148, 1440-53.

Hazar H., 2010, Cotton methyl ester usage in a diesel engine equipped with insulated combustion chamber, *Applied Energy*, 87,134-40.

Hazar H., Ozturk U., Gül H., 2016, Characterization and effect of using peanut seed oil methyl ester as a fuel in a low heat rejection diesel engine, *Energy&Fuels,* 30(10), 8425-31.

Heywowski T., Weronski A., The effect of thermal barrier coatings on diesel engine performance, *Vacuum,* 65, 427-32.

Kyrtatos P., Brücker C., Bouchoulos K., 2016, Cycle-to-cycle variations in diesel engines, *Applied Energy,* 171, 120-32.

Lawrence P., Mathews P.K., Deepanraj B., 2011, Experimental investigation on performance and emission characteristics of low heat rejection diesel engine with ethanol as fuel, *American Journal of Applied Sciences*, 8(4), 348-54.

Liu J.J., Ding S.F., Ding S.L., Gao J.S., Song E.Z., Yang F.Y., 2022, Effects of gas injection timing on combustion instability for a spark ignition natural gas engine under low load, *Applied Thermal Engineering,* 206, 118144.

Özer S., Vural E., Özel S., 2021, Effects of fusel oil use in a thermal coated engine, *Fuel*, 306, 121716.

Pera C., Chevillard S., Reveillon J.,2013, Effects of residual burnt gas heterogeneity on early flame propagation and on cyclic variability in spark-ignited engines, *Combustion and Flame*, 160(6), 1020-32.

Ramasamy N., Kalam M.A., Varman M., Teoh Y.H., 2021, Comparative studies of piston crown coating with YSZ and $AL_2O_3.SiO_2$ on engine out responses using conventional diesel and palm oil biodiesel, *Coatings,* 11(8), 885.

Ramu P., Saravanan C.G.,2009, Effect of ZrO2-Al2O3 and SiC coating on diesel engine to study the combustion and emission characteristics, *SAE Technical Paper,* 2009-01-1435.

Ramu P., Saravanan C.G., 2009, Investigation of combustion and emission characteristics of a diesel engine with oxygenated fuels and thermal barrier coating, *Energy&Fuels*, 23(2), 653-6.

Reddy G.V., Krupakaran R.L., Tarigonda H., Reddy A.R., Rasu N.G., 2021, Energy balance and emission analysis on diesel engine using different thermal barrier

coated pistons. *Materials Today: Proceedings,* 43(1), 646-54.

Schulz U., Leyens C., Fritscher K., Peters M., Saruhan-Brings B., Lavigne O., Dorvaux J.M., Poulain M., Mevrel R., Caliez M., 2003, Some recent trends in research and technology of advanced thermal barrier coatings. *Aero Science and Technology,* 7, 73-80.

Selvam M., Shanmugan S., Palani S., 2018, Performance analysis of IC engine with ceramic-coated piston. *Environmental Science and Pollution Research*, 25, 35210-20.

Serrano J.R., Arnau F.J., Martin J., Hernandez M., Lombard B., 2015, Analysis of engine walls thermal insulation: Performance and Emissions, *SAE Technical Paper*, 2015-01-1660.

Shabir M.F., Prasath B.R., Tamilporai P., 2014, Analysis of combustion performance and emission of extended cycle and iEGR for low heat rejection turbocharged direct injection diesel engines, *Thermal Science*, 18(1), 129-42.

Sivakumar G. and Kumar S.S., 2014, Investigation on effect of Yttria Stabilized Zirconia coated piston crown on performance and emission characteristics of a diesel engine, *Alexandria Engineering Journal,* 53(4), 787-94.

Şanlı A., Yılmaz I.T., Gümüş M., 2019, Experimental evaluation of performance and combustion characteristics in a hydrogen-methane port fueled diesel engine at different compression ratios. *Energy&Fuels*, 34, 2272-83.

Şanlı A., Yılmaz I.T., 2022, Cycle-to-cycle combustion analysis in hydrogen fumigated common-rail diesel engine. *Fuel*, 320, 123887.

Şanlı A., 2023, Experimental study of combustion and cyclic variations in a CRDI engine fueled with heptanol/iso-propanol/butanol and diesel blends. *Energy*, 269, 126800.

Taymaz I., 2007, The effect of thermal barrier coatings on diesel engine performance. *Surface and Coatings Technology*, 201(9-11), 5249-52.

Venu H. and Appavu P., 2019, Analysis on a thermal barrier coated (TBC) piston in a single cylinder diesel engine powered by Jatropha biodiesel-diesel blends, *SN Applied Science*, 1,1669.

Vittal M., Borek J.A., Marks D.A., Boehman A.L., Okrent D.A., Bentz A.P., 1999, The effects of thermal barrier coatings on diesel engine emissions, *J. Eng Gas Turbines Power,* 121(2), 218-25.

Wang Y., Xiao F., Zhao Y., Li D., Lei X., 2015, Study on cycle-by-cycle variations in a diesel engine with dimethyl ether as port premixing fuel, *Applied Energy*, 143, 58-70.

Wang Y., Ma T., Liu L., Yao M., 2021, Numerical investigation of the effect of thermal barrier coating on combustion and emissions in a diesel engine, *Applied Thermal Engineering*, 2021, 186, 116497.

Yao M., Ma T., Wang H., Zheng Z., Liu H., Zhang Y. A., 2018, Theoretical study on the effects of thermal barrier coating on diesel engine combustion and emission characteristics, *Energy*, 162, 744-52.

Zhong L., Singh I.P., Han J., Lai M-C., Henein N.A., Bryzik W., 2003, Effect of cycle-to-cycle variation in the injection pressure in a common rail diesel injection system on engine performance. *SAE Technical Paper*, 2003-01-0699.

# GENERALIZED THERMAL OPTIMIZATION METHOD FOR THE PLATE-FIN HEAT SINKS OF HIGH LUMEN LIGHT EMITTING DIODE ARRAYS

**Haluk KUNDAKÇIOĞLU\*, Nazlı DÖNMEZER\*\***

\*Boğaziçi University, Mechanical Engineering Department, 34342 Bebek, İstanbul, 0000-0002-5239-9995
\*\*Boğaziçi Uni., Mechanical Eng. Dept. 34342 Bebek, İstanbul, 0000-0003-0359-5567
nazli.donmezer@bogazici.edu.tr

**Abstract**: The performance of high-lumen light-emitting diode (LED) arrays is strongly affected by high temperatures. For better performance, the design of better thermal management techniques is required. In this work, an analytical thermal optimization algorithm for the passive heat sinks of high-lumen LED arrays is presented. With the aid of this algorithm, a broader range of heat sink geometry alternatives can be explored for the identification of the optimal heat sink design. This task is challenging using experimental or numerical techniques. The results demonstrate that the algorithm yields design with a reduction of more than 30% in base temperatures compared to previous heat sink design studies when minimum mass and maximum total efficiency constraints are applied. For devices with high powers, small chip spacing, and space limitations in the horizontal axis where base temperatures cannot be further reduced using these constraints, minimum temperature optimization can result in up to a 17% reduction in base temperatures. This reduction in base temperatures significantly improves the junction temperatures and the overall lighting quality of the LEDs.
**Keywords**: Heat sink design, Optimization, High-lumen LED array

## YÜKSEK LÜMENLİ IŞIK YAYAN DİYOT DİZİLERİNİN PLAKALI ISI EMİCİLERİ İÇİN GENELLEŞTİRİLMİŞ TERMAL OPTİMİZASYON YÖNTEMİ

**Özet**: Yüksek lümenli ışık yayan diyot (LED) dizilerinin performansı, yüksek sıcaklıklardan büyük ölçüde etkilenir. Bu yapıların yüksek performansı için geliştirilmiş termal yönetim tekniklerinin tasarımı gereklidir. Bu çalışmada, yüksek lümenli LED dizilerinin pasif soğutucuları için analitik bir termal optimizasyon algoritması sunulmaktadır. Bu algoritmanın yardımıyla, optimum ısı emici tasarımının belirlenmesi için daha geniş bir yelpazedeki ısı emici geometri alternatifleri araştırılabilir. Kullanılan analitik yaklaşım optimizasyon için kullanımı zor olan deneysel veya sayısal tekniklere alternatif sunmaktadır. Sonuçlar, minimum kütle ve maksimum toplam verimlilik kısıtlamaları ile elde edilen taban sıcaklıklarında önceki ısı emici tasarım çalışmalarına göre %30'dan fazla bir azalma göstermektedir. Yüksek güce, küçük çip aralığına ve bu kısıtlamalar kullanılarak taban sıcaklıklarının daha fazla düşürülemeyeceği yatay eksende alan sınırlamalarına sahip cihazlar için minimum sıcaklık kısıtlaması ile gerçekleştirilen optimizasyon, taban sıcaklıklarında %17'ye kadar bir azalmaya neden olabilir. Taban sıcaklıklarındaki bu azalma, bağlantı sıcaklıklarını ve LED'lerin genel aydınlatma kalitesini önemli ölçüde artırır.
**Anahtar Kelimeler**: Isı emici tasarımı, Optimizasyon, Yüksek lümenli LED dizisi

## INTRODUCTION

Light-emitting diodes (LEDs) have been used for several years in automotive, building, and street lighting applications. Due to their advantages such as low energy consumption, efficiency, and lifetime, they have been preferred more than other technologies such as incandescent light, fluorescent, and halogen lamps (Karlicek et al., 2017). Although LEDs have these advantages, the thermal problems of this technology still exist. LED structures produce heat and light by using electrical energy. About 80% - 90% of the total electrical energy is converted into heat (Ye et al., 2011). This often causes a single LED chip to generate 100-125 W/cm² heat flux (Wang et al., 2015). Generated heat leads to high chip temperatures. In high-lumen LED array systems used for

high-performance applications such as outdoor and industrial lighting, hundreds of LED chips are used together. Since these chips are placed on a printed circuit board (PCB) as illustrated in Figure 1, higher temperatures can be seen because of the number of LED chips and the thermal crosstalk between them (Rammohan et al., 2021).

High chip temperatures negatively affect the chip's efficiency, light output, performance, and lifetime. To solve the thermal problems of the LED arrays, different thermal management techniques such as thermoelectric coolers (TECs) (Li et al., 2011), heat pipes (Delendik et al., 2021; Lu et al., 2011), liquid cooling methods (Deng
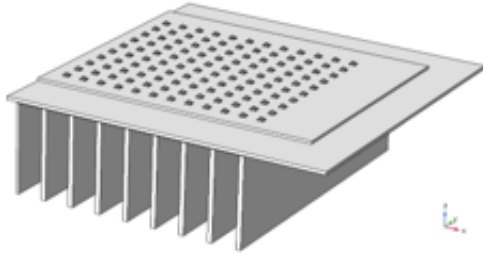
**Figure 1.** High-lumen LED array structure.

and Liu, 2010), and finned heat sinks (Hsu et al., 2020; Ye et al., 2011) have been suggested in the literature. (TECs) (Li et al., 2011), heat pipes (Delendik et al., 2021; Lu et al., 2011), liquid cooling methods (Deng and Liu, 2010), and finned heat sinks (Hsu et al., 2020; Ye et al., 2011) have been suggested in the literature. Among these methods, passive thermal management via finned heat sinks is preferred the most since no extra parts such as fans and/or pumps as well as cooling liquids are required (Feng et al., 2018). Although there are heat sinks with various fin cross-section geometries (triangular, pin, etc.), plate-fin heat sinks, shown in Figure 2, are the most frequently used type due to their relatively simple fabrication and easy maintenance.
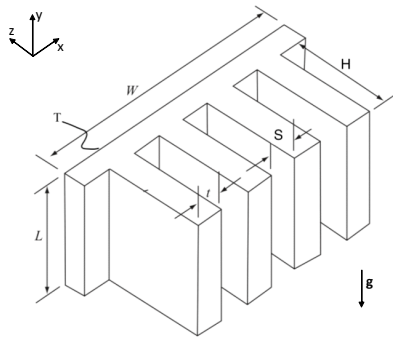


**Figure 2.** Fin structure.

Design and optimization of plate-fin heat sinks have been known for a long time. Countless analytical (Bar-Cohen et al., 2003; Bar-Cohen and Jelinek, 1985; Elenbaas, 1948), numerical (Ben Abdelmlek et al., 2021, 2017; Goshayeshi et al., 2011), parametric (Patel and Matawala, 2019; Walunj et al., 2013) and experimental (Abdelmlek et al., 2015; Yüncü and Anbar, 1998) work have been performed in the past for this purpose. However, most of the previous studies performed optimization using a fixed base temperature and area. For high-lumen LED arrays the heat load instead of base temperature is fixed and the base area can be varied with the different arrangements of the array elements. There are a limited number of optimization studies performed without using fixed base temperature (Hsieh and Li, 2015; Liu, 2012; Tang et al., 2015). However, the LED array powers used in these studies are relatively low and the effect of the LED configuration on optimization is not studied. Moreover, these studies involve finite element simulations with high mesh requirements due to the geometrical nature of fin elements. Therefore, previous methodologies are not

sufficient to design optimized heat sinks for high-lumen LED arrays. There is a need for a fast and reliable generalized heat sink optimization algorithm for the passive thermal management of high-lumen LED arrays.

In this study, we display a generalized optimization method that allows variable base temperatures and areas. Using this algorithm, a wider group of alternatives is searched, and more suitable heat sinks for high-lumen LED arrays are achieved. The results are analyzed to observe the positive effects of more flexible design variables on the optimization performed. This task is challenging using experimental or numerical techniques. Although this study is dedicated to plate-fin heat sinks used for passive thermal management, the methodology can be modified or extended for the analysis of heat sinks with different topologies used in both passive and active thermal management.

## METHOD

In this section, the details of the numerical algorithm used in the generalized optimization technique are provided. The algorithm depends on empirical natural convection correlations gathered from the literature. The calculations are performed for each configuration in MATLAB. Pure aluminum with thermal conductivity, density, and the specific heat of $k_{fin}$=197 W/m·K, $\rho_{fin}$ = 2700 kg/m3, and $c_p$ =910 J/kg·K, respectively is chosen as the heat sink material (Incropera et al., 2007a). The input parameters are the total number of LED chips ($N_{chips}$) and the desired heat dissipation ($\dot{Q}_{desired}$). The numerical optimization technique presented here starts with the above input variables and aims to obtain the best LED array arrangement, fin number, fin spacing, and base temperature under different constraints. The methodology is explained below in two parts: a) Database Creation and b) Structure Selection.

### Database Creation

The steps of database creation summarized in Figure 4 are explained in this section.

1. The first step of the optimization is to enter the input variables: $N_{chips}$ and $\dot{Q}_{desired}$. The desired heat dissipation can be taken as 75% of the total power consumed by the LED array since only a certain amount of power is dissipated as heat.

2. Then set $N_x$ (number of chips in -x direction) and calculate $N_y$. Calculate the width ($W$) and length ($L$) of the heat sink based on the given arrangement, spacings, and size of the chips in

the array using the geometrical variables in Figure 3.

$$W = c_x \times N_x + d_x \times (N_x - 1) \qquad (1)$$

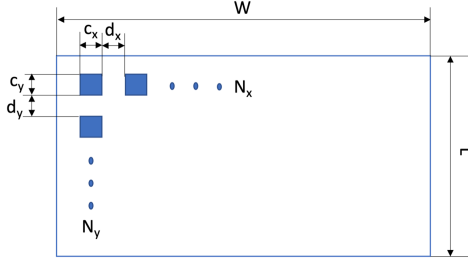$$L = c_y \times N_y + d_y \times (N_y - 1) \qquad (2)$$



**Figure 3.** LED array configuration.

3. Next set the base temperature of the fins to $T_{base}$. Then obtain the material properties (thermal conductivity ($k_{air}$), dynamic viscosity ($\mu_{air}$), and Prandtl number ($Pr$)) of the cooling fluid (in this case air) at the film temperature $\left(T_{film} = \frac{T_{base} + T_\infty}{2}\right)$, where $T_\infty = 300K$.

4. To find the heat transfer coefficient ($h_{wall}$) of the vertical walls between the fins, Rayleigh number ($Ra_L$) is calculated(Elenbaas, 1942):

$$Ra_L = \frac{g\beta\theta_b L^3}{\alpha v} \qquad (3)$$

where g is the gravitational constant, $\beta$ is the thermal expansion coefficient, $\theta_b = (T_{base} - T_\infty)$ is the temperature difference between the ambient and the base, $L$ is the length of the fin, $\alpha$ is the thermal diffusivity and $v$ is the kinematic viscosity of the air at film temperature.

5. The convection coefficient of the vertical fin wall shown is calculated (Incropera et al., 2007b):

$$h_{wall} = \begin{cases} \frac{0.59 Ra_z^{0.25} k_{air}}{L} , 10^4 < Ra_L < 10^9 \\ \frac{0.1 Ra_z^{1/3} k_{air}}{L} , 10^9 < Ra_L < 10^{13} \end{cases} \qquad (4)$$

6. The optimum spacing between the fins, $S$ is calculated using the relations of Bar-Cohen and Rohsenow (Bar-Cohen and Rohsenow, 1984):

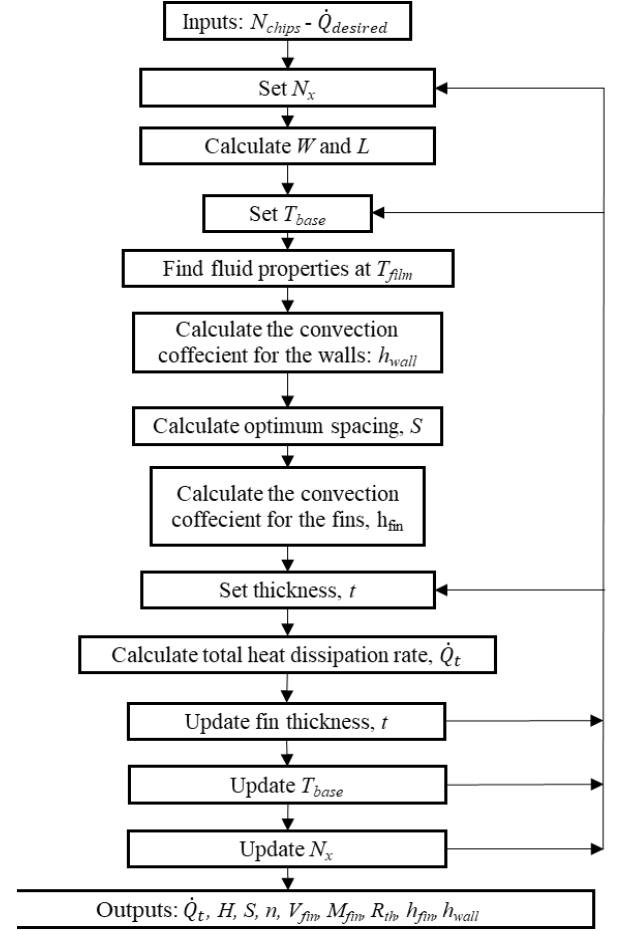$$S = 2.714 Ra_L^{-0.25} L \qquad (5)$$



**Figure 4.** Optimization Algorithm.

7. To find the convection heat transfer coefficient on fin surfaces: $h_{fin}$, natural convection correlations obtained by Elenbaas (Elenbaas, 1942) are used. To do this first the Rayleigh number based on optimum spacing is calculated (Lee, 2010):

$$Ra_S = \frac{g\beta\theta_b S^3}{\alpha v} \qquad (6)$$

Then Elenbaas number (El) is calculated with $Ra_S$, $S_{opt}$, and L with below equation (Kraus, et al., 2001):

$$El = Ra_S \frac{S}{L} \qquad (7)$$

Nusselt number, $Nu$ is calculated (Kraus, et al., 2001):

$$Nu = \left(\frac{576}{El^2} + \frac{2.873}{El^{0.5}}\right)^{-0.5} \qquad (8)$$

Finally, the heat transfer coefficient of the fin is obtained from the $Nu$ number and the optimum

spacing.

$$h_{fin} = \frac{Nu \times k_{air}}{S} \qquad (9)$$

8. Next to perform the optimization with varying fin thickness, set a fin thickness, $t$.

9. Assuming the heat loss at the fin tip is negligible, the heat transfer rate from a single fin with an adiabatic tip ($\dot{q}_f$) is calculated using (Kraus, et al., 2001):

$$\dot{q}_f = \sqrt{2h_{fin}k_{fin}t}\,\theta_b L tanh(mH) \qquad (10)$$

where $m$ is the performance factor and $H$ is the height of the fin:

$$m = \left(\frac{2h_{fin}}{k_{fin}t}\right)^{0.5} \qquad (11)$$

To get the maximum heat transfer rate, the following fin height formula is used (Kraus, et al., 2001):

$$H(t) = \frac{1.4192\left(\frac{k_{fin}t}{2h_{wall}}\right)^{0.5}}{\left[1 - 1.125\left(\frac{k_{fin}t}{2h_{wall}}\right)^{0.5}\frac{h_{wall}}{k_{fin}}\right]} \qquad (12)$$

Later, the total heat transfer rate from the walls of heat sink is calculated as (Kraus, et al., 2001):

$$\dot{q}_w = h_{wall}LS_{opt}\theta_b \qquad (13)$$

The total heat transfer rate is the sum of the heat transfer from the walls and fin surfaces (Kraus, et al., 2001).

$$\dot{Q}_t = nL\theta_b\left[\sqrt{2h_{fin}k_{fin}t}\,tanh(mH) + h_{wall}\left(\frac{W}{n} - t\right)\right]$$
$$(14)$$

where $n$ is the number of the fins allowed for given $S$, $t$, and $W$.

$$n = \frac{W}{S+t} \qquad (15)$$

Finally, the total thermal resistance, fin volume and mass of the heat sink are calculated.

$$R_{th} = \theta_b / \dot{Q}_t \qquad (16)$$

$$V_{fin} = L \times H \times t \times n \qquad (17)$$

$$M_{fin} = V_{fin} * \rho_{fin} \qquad (18)$$

where $\rho_{fin}$ is the fin density.

10. Change thickness and repeat steps 8 and 9 until all desired thickness values are analyzed.

11. Change $T_{base}$ and repeat steps 3 to 10 until all desired base temperature values are analyzed.

12. Change $N_x$ and repeat steps 2 to 11 until $N_x=N_{chips}$.

At the end of these steps, a database given in Table 1 is obtained. $\dot{Q}_t, H, S, n, V_{fin}, M_{fin}, R_{th}, h_{fin}, h_{wall}$ values for each thickness and temperature are stored in the database.

**Table 1.** Optimization outputs for a given base temperature and fin thickness.

| | Temperature (K) | | | |
|---|---|---|---|---|
| **Thickness (mm)** | **300 K** | **300.1 K** | **...** | **350 K** |
| 1 mm | $\dot{Q}_t, H, S, n,$ $V_{fin}, M_{fin},$ $R_{th}, h_{fin}, h_{wall}$ | ... | ... | ... |
| 1.1 mm | ... | ... | ... | ... |
| ... | ... | ... | ... | ... |
| 20 mm | ... | ... | ... | $\dot{Q}_t, H, S, n,$ $V_{fin}, M_{fin},$ $R_{th}, h_{fin}, h_{wall}$ |

**Structure Selection**

After creating the database, it is filtered to find the configurations with a total heat removal rate equal to the desired heat dissipation rate $\dot{Q}_t = \dot{Q}_{desired}$. Then, the data is analyzed to find the optimum structure. As shown in Figure 5 optimization can be performed with varying motives. These are explained next.
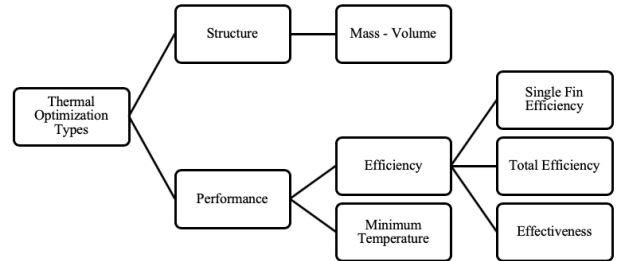


**Figure 5.** Optimization Types.

Minimum Fin Mass ($M_{fin}$): This type of optimization is generally chosen for low-cost (Feng et al., 2018) and lightweight applications. The cost of the heat sink can be reduced by decreasing the total material used. The configuration with the smallest mass is chosen.

Total Efficiency ($\eta_{tot}$):

$$\eta_{tot} = \frac{Q}{Q_{max}} \qquad (19)$$

where, $\dot{Q}_{max} = \theta_b h_{fin} n(2(L + tH + LS)$ is another selection criterion. The filtered database is analyzed to obtain the configuration with the highest $\eta_{tot}$.

Maximum Single Fin Efficiency ($\eta_{fin}$): Single fin efficiency is the ratio of the heat transfer from a single fin to the maximum possible heat transfer from the fin (Ghajar et al., 1986):

$$\eta_{fin} = \frac{\tanh{(mH)}}{mH} \qquad (20)$$

The data is analyzed to obtain the configuration with the highest $\eta_{fin}$ to reduce the number of the fins.

Minimum base temperature ($T_{base}$): Minimum base temperature is obtained where the thermal resistance, given by Eq. (16) is smallest. The data is analyzed to obtain the configuration with the minimum thermal resistance that will give the minimum base temperature.

The optimization performed using the above steps assumes there are no geometric limitations. However, in real applications there may be some restrictions, mostly coming from fabrication limitations, such as the maximum/minimum fin thickness, fin length, or the ratio of the fin height to fin thickness. If any of these restrictions exist, then additional data filtering is needed at the beginning of structure selection. Here data that does not comply with the given limitations can be removed.

**RESULTS**

The above methodology is applied to optimize the heat sink of a high lumen LED array composed of $N_{chips}$=240 LED chips (Cree X-Lamp XP-E). The total heat generated by the chips are calculated as $\dot{Q}_{desired}$=192 W (with a single chip generating 0.8W heat). The chip dimensions and spacings are $c_x = c_y = 3.45$ mm and $d_x = d_y = 2$ mm, respectively. Using the numerical optimization algorithm described above, optimization is performed for different chip layout configurations. Table 2 summarizes these layout configurations and the resulting base area dimensions.

Table 2. Different chip layout configurations.

| Configurations | $N_x$ | $N_y$ | W (mm) | L (mm) |
|---|---|---|---|---|
| 1 | 48 | 5 | 269.6 | 29.25 |
| 2 | 24 | 10 | 138.8 | 56.5 |
| 3 | 16 | 15 | 95.2 | 83.75 |
| 4 | 12 | 20 | 73.4 | 111 |
| 5 | 10 | 24 | 62.5 | 132.8 |

The effect of optimization type on the base temperature of LED arrays with different layout configurations is plotted in Figure 6. When the number of chips along the $y$-direction ($N_y$) decreases, the fin length $L$ decreases, and the fin width $W$ increases. As a result of this, optimum spacing, $S$ decreases, and the number of fins ($n$) as well as the convection coefficient at the fin surfaces ($h_{fin}$) increases. Thus, the heated air can leave the structure quickly and the base temperatures are reduced. However, very high masses are observed for these types of configurations.
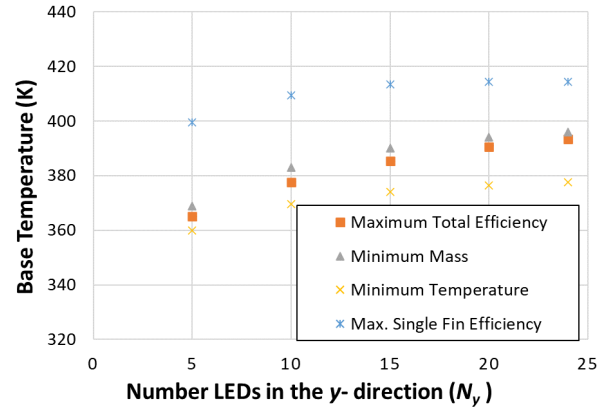


**Figure 6.** Base temperature vs. number of LED chips in y-direction when different optimization criteria are used.

When the number of chips along the $y$-direction increases, the heated air cannot leave the structure quickly, fin convection coefficients decrease, and the base temperature increases. However, the increase in base temperatures slows down when $N_y$ exceeds 15. Given the tendency for vertically oriented LED arrays to experience elevated temperatures, opting for minimum temperature optimization can offer substantial advantages in terms of temperature management. Such configuration may yield a reduction in a temperature rise of up to 17%, albeit accompanied by a three-to-four-fold increase in mass. In general, total efficiency is a safe optimization type for all configurations since it provides a design with a reasonable base temperature and fin mass.

Later, the 2nd configuration with $N_x$=24 is chosen to have a closer look at the effects of the optimization constraints on the optimized structure. The results are summarized in Table 3. In Table 3, maximum fin height and temperatures are observed when the single fin efficiency optimization type is chosen. Although the total number of fins is low, they weigh more than 10 times the fins in other optimization types making the heat sink extremely heavy. Therefore, single-fin efficiency optimization is not recommended while designing heat sinks for high-lumen LED arrays. Minimum fin heights are observed when the minimum mass optimization type is chosen. However, the base temperatures are still higher than the ones obtained from two other optimizations. Although the minimum base temperature optimization type has the lowest temperature, it results in a heat sink design with a higher mass and length than the one obtained for maximum efficiency optimization. For this configuration, and in general, the maximum efficiency optimization type provides a reasonable mass value and a base temperature. There are a limited number of optimization studies performed without using fixed base temperature (Hsieh and Li, 2015; Liu, 2012; Tang et al., 2015).

The above results are obtained when the heat generation is kept constant at $\dot{Q}_{desired}$= 192 W. However, LED arrays can have varying heat generation values. To understand the effect of this on the optimization, the following heat generation values are used $\dot{Q}_{desired}$= 48 W,

96 W, 192 W, 216W, and 240 W. Number of chips ($N_{chips}$ = 240), layout ($N_x$=24 and $N_y$=10), and spacings ($d_x = d_y$ = 2 mm) are kept constant. The effect of optimization type on base temperature for different LED powers is plotted in Figure 7.

According to Figure 7 optimization type does not have a strong effect on the base temperature and can be chosen freely at low powers. The difference increases at higher powers. Single-fin efficiency and minimum mass constraints should be avoided, and minimum temperature or maximum total efficiency constraints should be preferred when designing heat sinks for LED arrays at higher powers where temperatures are closer to design limitations.
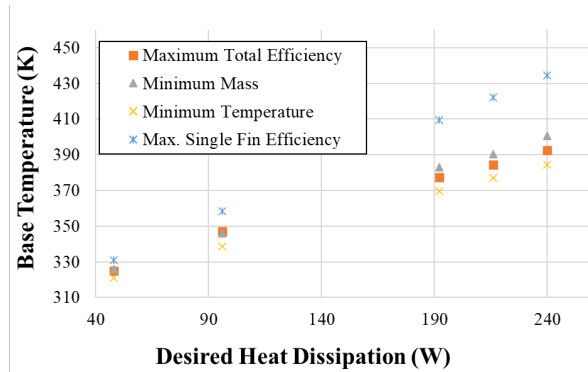


**Figure 7.** Base temperature vs. desired heat dissipation when different optimization criteria are used. Number of chips ($N_{chips}$ = 240), layout ($N_x$=24 and $N_y$=10), and spacings ($d_x = d_y = 2$ mm) are kept constant.

Finally, to observe the effect of chip spacing on base temperatures chip spacing values are varied as $d_x = d_y$= 1, 2, 3, 4, and 5 mm. The total amount of desired heat dissipation ($\dot{Q}_{desired}$= 192 W), number of chips ($N_{chips}$ = 240), and the layout ($N_x$=24 and $N_y$=10) are kept constant. The effect of optimization type on base temperatures for different LED spacings is plotted in Figure 8. According to Figure 8, the choice of the optimization type does not have a strong effect on base temperature when chips are spread out to a wider area. For larger spacing configurations, the contribution of the base of the heat sink to convection is increased, thus the effect of the fins on heat transfer is reduced. This situation leads to lower base temperatures and reduces the significance of the choice of optimization type. However, if the spacings are small then the base temperature values may exceed the

maximum junction temperatures of the LED chips present in their datasheets. If the spacings are small, then the minimum temperature optimization type can be chosen despite its other disadvantages to reduce thermal risks.
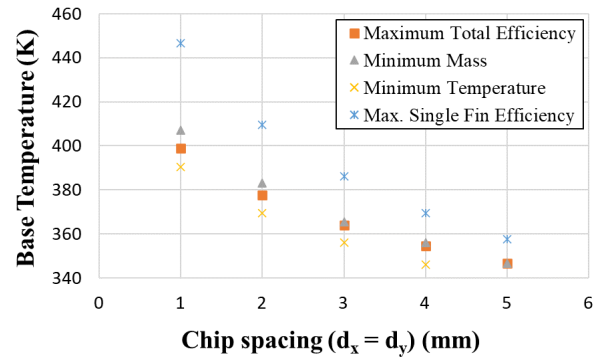


**Figure 8.** Base temperature vs. distance between LED chips when different optimization criteria are used. The total amount of desired heat dissipation ($\dot{Q}_{desired}$= 192 W), number of chips ($N_{chips}$ = 240), and the layout ($N_x$=24 and $N_y$=10) are kept constant.

The base temperatures presented for the initial structure in Table 3 are compared with the base temperatures of previous analytical studies which typically begin the optimization using a fixed base temperature (Bar-Cohen et al., 2003) calculated from the maximum allowed junction temperature in LED datasheets. With the maximum total efficiency and minimum mass constraints of the proposed methodology, a reduction of more than 30% in base temperatures is achieved. Additionally, when a minimum temperature constraint is chosen, a further 5% reduction in base temperatures can be achieved. Although this option has a high mass disadvantage for devices with closely packed, vertically arranged, high-power chips where base temperatures cannot be further reduced using other constraints, the minimum temperature constraint is a viable option, resulting in a 17% reduction in base temperatures. Similar improvements have been reported in the literature but for smaller devices using lengthy numerical calculations (Ben Abdelmlek et al., 2021, 2017).

**CONCLUSION**

In high-lumen LED array systems extremely high temperatures are observed due to the large amount of heat

**Table 3.** Optimization results of the initial structure.

| Optimization Type | H (mm) | t (mm) | S (mm) | $T_{base}$ (K) | n | $R_{th}$ (K/W) | $\eta_{fin}$ (%) | $\eta_{tot}$ (%) | $M_{fin}$ (kg) | $\varepsilon_{fin}$ | $h_{fin}$ (W/m²K) | $h_{wall}$ (W/m²K) |
|---|---|---|---|---|---|---|---|---|---|---|---|---|
| Maximum $\eta_{tot}$ | 163 | 1.30 | 5.16 | 378 | 22 | 0.42 | 38.9 | 65.3 | 0.75 | 202 | 7.37 | 9.01 |
| Minimum Mass | 148 | 1.00 | 5.13 | 383 | 24 | 0.44 | 34.2 | 65.1 | 0.53 | 229 | 7.48 | 9.17 |
| Minimum $T_{base}$ | 268 | 3.20 | 5.23 | 370 | 17 | 0.37 | 56.4 | 62.2 | 2.22 | 125 | 7.20 | 8.82 |
| Maximum $\eta_{fin}$ | 580 | 16.0 | 5.00 | 410 | 7 | 0.59 | 84.8 | 39.4 | 9.29 | 40.0 | 7.92 | 9.71 |

generation and the thermal crosstalk between the chips. To reduce the thermal problems of the LED arrays, proper heat sink design should be performed. In this study, we display a computationally effective analytical optimization method that allows the exploration of a wider group of base temperature and area alternatives. The proposed scheme only requires two input variables: the number of chips and the desired heat dissipation to create a database. The database is analyzed using a numerical technique to find the most suitable chip layout and heat sink geometry. The algorithm is tested on an LED chip array to discuss the heat sink base temperatures achieved by this algorithm using different optimization constraints in different scenarios. The results are summarized as follows:

- With the maximum total efficiency and minimum mass constraints of the proposed methodology, a reduction of more than 30% in base temperatures is achieved compared to previous heat sink design studies. These previous studies typically begin with optimization using a fixed base temperature calculated from the maximum allowed junction temperature in LED datasheets.
- When a minimum temperature constraint is chosen a further 5% reduction in base temperatures can be achieved, however, the heat sink mass is significantly increased.
- For devices with closely packed, vertically arranged, high-power chips where base temperatures cannot be further reduced using other constraints, minimum temperature constraint results in a 17% reduction in base temperatures. In scenarios where mass is not a constraint, minimum temperature optimization should be prioritized for such LED arrays to ensure the lowest achievable temperature.
- Maximum single-fin efficiency should not be a constraint in any optimization study since it leads to heat sink designs with extremely high mass and base temperatures.

The reduction in base temperatures will cause a similar decrease in junction temperatures and strongly affect the lighting quality of the devices. Although this study is dedicated to plate-fin heat sink optimization for passive thermal management, the methodology can be modified or extended to analyze passive and active heat sinks with different topologies.

## ACKNOWLEDGMENTS

## AUTHORS

**Haluk Kundakçıoğlu**

B.Sc. Yıldız Teknik Üniversitesi, Mechanical Engineering, 2016
M.Sc. Boğaziçi Üniversitesi, Mechanical Engineering, 2020

**Nazlı Dönmezer**

B.Sc. METU, Mechanical Engineering, 2007
M.Sc. METU, Mechanical Engineering, 2009
Ph.D. Georgia Institute of Technology, Mechanical Engineering, 2014

## NOMENCLATURE

| | |
|---|---|
| $\alpha$ | Thermal diffusivity of air [m²/s] |
| $\beta$ | Thermal expansion coefficient of air [1/m] |
| $\upsilon$ | Kinematic viscosity of air [m²/s] |
| $k_{air}$ | Thermal conductivity of air [W/m·K] |
| $k_{fin}$ | Thermal conductivity of fin material [W/m·K] |
| El | Elenbaas Number $\left[Ra_S \frac{S}{L}\right]$ |
| $g$ | Gravitational constant [m/s²] |
| H | Fin height [mm] |
| $L$ | Fin length [mm] |
| $W$ | Base plate width [mm] |
| $T$ | Fin thickness [mm] |
| $P$ | Fin perimeter [mm] |
| $S$ | Optimum fin spacing [mm] |
| $A$ | Fin base area [mm²] |
| $M_{fin}$ | Fin mass [kg] |
| $V_{fin}$ | Fin volume [m³] |
| $Ra_s$ | Rayleigh number based on fin spacing $\left[\frac{g\beta\theta_b S^3}{\alpha\upsilon}\right]$ |
| $Ra_L$ | Rayleigh number for vertical plates $\left[\frac{g\beta\theta_b L^3}{\alpha\upsilon}\right]$ |
| $\theta_b$ | Ambient air and base temperature difference [K] |
| Nu | Nusselt number $\left[\frac{h_{fin}S}{k_{air}}\right]$ |
| $h_{fin}$ | Fin convection coefficient [W/m²K] |
| $h_{wall}$ | Wall convection coefficient [W/m²K] |
| $m$ | Performance factor $\left[\sqrt{\frac{2h_{fin}}{k_{fin}t}}\right]$ |
| $R_{th}$ | Thermal Resistance [K/W] |
| $\dot{q}_f$ | Heat transfer rate from a single fin [W] |
| $\dot{Q}_t$ | Total heat transfer rate [W] |
| $\dot{Q}_{desired}$ | Desired heat dissipation rate [W] |

# REFERENCES

Abdelmlek, K. Ben, Araoud, Z., Charrada, K., Canale, L., Zissis, G., 2015. Experimental study of orientation effects on natural convection around new/old LED package, in: 3ème Conférence Internationale Des Energies Renouvelables.

Bar-Cohen, A., Iyengar, M., Kraus, A.D., 2003. Design of optimum plate-fin natural convective heat sinks. J. Electron. Packag. Trans. ASME. https://doi.org/10.1115/1.1568361

Bar-Cohen, A., Jelinek, M., 1985. Optimum arrays of longitudinal, rectangular fins in corrective heat transfer. Heat Transf. Eng. https://doi.org/10.1080/01457638508939633

Bar-Cohen, A., Rohsenow, W.W., 1984. Thermally optimum spacing of vertical, natural convection cooled, parallel plates. J. Heat Transfer 106. https://doi.org/10.1115/1.3246622

Ben Abdelmlek, K., Araoud, Z., Canale, L., Charrada, K., Zissis, G., 2021. Optimal substrate design for thermal management of high power multi-chip LEDs module. Optik (Stuttg). 242, 167179. https://doi.org/https://doi.org/10.1016/j.ijleo.2021.167179

Ben Abdelmlek, K., Araoud, Z., Charrada, K., Zissis, G., 2017. Optimization of the thermal distribution of multi-chip LED package. Appl. Therm. Eng. 126, 653–660. https://doi.org/10.1016/J.APPLTHERMALENG.2017.07.136

Delendik, K., Kolyago, N., Voitik, O., 2021. Design and investigation of cooling system for high-power LED luminaire. Comput. Math. with Appl. 83, 84–94. https://doi.org/10.1016/J.CAMWA.2020.01.026

Deng, Y., Liu, J., 2010. A liquid metal cooling system for the thermal management of high power LEDs. Int. Commun. Heat Mass Transf. https://doi.org/10.1016/j.icheatmasstransfer.2010.04.011

Elenbaas, W., 1948. The dissipation of heat by free convection from vertical and horizontal cylinders. J. Appl. Phys. https://doi.org/10.1063/1.1715035

Elenbaas, W., 1942. Heat dissipation of parallel plates by free convection. Physica 9, 1–28. https://doi.org/10.1016/S0031-8914(42)90053-3

Feng, S., Shi, M., Yan, H., Sun, S., Li, F., Lu, T.J., 2018. Natural convection in a cross-fin heat sink. Appl. Therm. Eng. 132, 30–37. https://doi.org/10.1016/j.applthermaleng.2017.12.049

Ghajar, Cengel, Y.A., Afshin, J., 1986. Heat and Mass Transfer: Fundamentals & Applications, Genetics. https://doi.org/10.1017/CBO9780511676420.004

Goshayeshi, H.R., Fahiminia, M., Naserian, M.M., 2011. Numerical modeling of natural convection on various configurationof rectangular fin arrays on vertical base plates. World Acad. Sci. Eng. Technol. https://doi.org/10.5281/zenodo.1055852

Hsieh, C.C., Li, Y.H., 2015. The study for saving energy and optimization of led street light heat sink design. Adv. Mater. Sci. Eng. https://doi.org/10.1155/2015/418214

Hsu, C.-N., Chen, C.-C., Chang, C.-H., Wang, C.-C., 2020. Using Graphene-powder-based Thermal Interface Material for High Lumen LED Array Chip: An Experimental Study of Heat Dissipation. Sensors \& Mater. 32.

Incropera, F.P., DeWitt, D.P., Bergman, T.L., Lavine, A.S., 2007a. Fundamentals of Heat and Mass Transfer 6th Edition, Fundamentals of Heat and Mass Transfer 6th Edition. https://doi.org/10.1016/j.applthermaleng.2011.03.022

Incropera, F.P., DeWitt, D.P., Bergman, T.L., Lavine, A.S., 2007b. Fundamentals of Heat and Mass Transfer, Water. https://doi.org/10.1016/j.applthermaleng.2011.03.022

Karlicek, R., Sun, C.C., Zissis, G., Ma, R., 2017. Handbook of Advanced Lighting Technology, Handbook of Advanced Lighting Technology. https://doi.org/10.1007/978-3-319-00176-0

Kraus, A., Aziz, A., Welty, J., Sekulic, D., 2001. Extended Surface Heat Transfer. Appl. Mech. Rev. https://doi.org/10.1115/1.1399680

Lee, H.S., 2010. Thermal Design: Heat Sinks, Thermoelectrics, Heat Pipes, Compact Heat Exchangers, and Solar Cells, Thermal Design: Heat Sinks, Thermoelectrics, Heat Pipes, Compact Heat Exchangers, and Solar Cells. https://doi.org/10.1002/9780470949979

Li, J., Ma, B., Wang, R., Han, L., 2011. Study on a cooling system based on thermoelectric cooler for thermal management of high-power LEDs. Microelectron. Reliab. https://doi.org/10.1016/j.microrel.2011.05.006

Liu, Y.B., 2012. On thermal structure optimization of a power LED lighting, in: Procedia Engineering. https://doi.org/10.1016/j.proeng.2012.01.387

Lu, X., Hua, T.-C., Wang, Y., 2011. Thermal analysis of high power LED package with heat pipe heat sink. Microelectronics J. https://doi.org/10.1016/j.mejo.2011.08.009

Patel, H., Matawala, V.K., 2019. Performance Evaluation and parametric optimization of a Heat Sink for Cooling of Electronic Devices with Entropy Generation Minimization. Eur. J. Sustain. Dev. Res. https://doi.org/10.29333/ejosdr/5896

Rammohan, R., Kumar, R., Chandramohan, V.P., 2021. Experimental analysis on estimating junction temperature and service life of high power LED array. Microelectron. Reliab. 120, 114121. https://doi.org/10.1016/J.MICROREL.2021.114121

Tang, H., Li, D., Pan, M., Yang, T., Yuan, C., Fan, X., 2015. Thermal analysis and optimization design of LED streetlight module, in: 2013 10th China International Forum on Solid State Lighting, ChinaSSL 2013. https://doi.org/10.1109/SSLCHINA.2013.7177346

Walunj, A., Daund, V., Palande, D.D., 2013. Parametric Analysis of Plate-Fin Heat Sink Over Heat Transfer. Int. J. Res. Advent Technol. 1.

Wang, J., Zhao, X.J., Cai, Y.X., Zhang, C., Bao, W.W., 2015. Experimental study on the thermal management of high-power LED headlight cooling device integrated with thermoelectric cooler package. Energy Convers. Manag. https://doi.org/10.1016/j.enconman.2015.05.040

Ye, H., Sau, K., Van Zeijl, H., Gielen, A.W.J., Zhang, G., 2011. A review of passive thermal management of LED module. J. Semicond. https://doi.org/10.1088/1674-4926/32/1/014008

Yüncü, H., Anbar, G., 1998. An experimental investigation on performance of rectangular fins on a horizontal base in free convection heat transfer. Heat Mass Transf. und Stoffuebertragung. https://doi.org/10.1007/s002310050222

# PEA GRAINS IN DRYING: UNRAVELING THE KINETICS OF HOT-AIR DRYING AND EXPLORING MATHEMATICAL MODELS FOR MOISTURE DIFFUSION

**İbrahim DOYMAZ *, Nil ACARALI ***

\* Yildiz Technical University, Department of Chemical Engineering, 34220 Esenler, Istanbul, Türkiye
doymaz@yildiz.edu.tr, ORCID: 0000-0002-4429-6443
\*\* Yildiz Technical University, Department of Chemical Engineering, 34220 Esenler, Istanbul, Türkiye
nbaran@yildiz.edu.tr, ORCID: 0000-0003-4618-1540 (Corresponding author)

**Abstract:** Pea drying studies were assessed to learn more about the kinetics and properties of drying in a hot-air dryer. Research was done on impact of temperatures and pre-treatments on drying behaviours. The drying rate graphs demonstrated that the entire drying procedure took place when rates were declining. To properly understand the experimental data, four mathematical models (Henderson & Pabis, Page, Wang & Singh, and Aghbashlo et al.) were used. The Page model was discovered to be the ideal one to depict peas' curves of drying. The identification of the Page model as the most suitable for depicting pea drying curves underscored the applicability in modeling drying behaviors in similar agricultural products. With Fick's second law of diffusion, effective moisture diffusivity ($D_{eff}$) sorted from $2.45 \times 10^{-10}$ to $6.55 \times 10^{-10}$ m²/s at given temperature. $D_{eff}$ was expressed as a function of temperature with an Arrhenius type equation. For samples from Potas, Blanch, and Control codes, the activation energy for moisture diffusion was computed as 21.48, 22.82, and 22.32 kJ/mol, respectively. The computation of activation energy for moisture diffusion for different samples offered practical information for optimizing drying processes under various conditions. The results showed the importance of pea drying kinetics and practical implications for industry on drying efficiency and product quality.
**Keywords:** Drying kinetics, pea, effective moisture diffusivity, Page model

## BEZELYE TANELERİNİN KURUTULMASI: SICAK HAVA KURUTMA KİNETİĞİNİN ÇÖZÜMLENMESİ VE NEM DİFÜZYONU İÇİN MATEMATİKSEL MODELLERİN İNCELENMESİ

**Özet:** Sıcak hava kurutucusunda kurutmanın kinetiği ve özellikleri hakkında daha fazla bilgi edinmek için bezelye kurutma çalışmaları değerlendirilmiştir. Sıcaklıkların ve ön işlemlerin kurutma davranışları üzerindeki etkisi üzerine araştırma yapılmıştır. Kurutma hızı grafikleri, kurutma prosedürünün tamamının hızlar düşerken gerçekleştiğini göstermiştir. Deneysel verileri doğru bir şekilde anlamak için dört matematiksel model (Henderson & Pabis, Page, Wang & Singh, ve Aghbashlo vd.) kullanılmıştır. Page modelinin, bezelyelerin kuruma eğrilerini tasvir etmek için ideal model olduğu keşfedilmiştir. Page modelinin bezelye kuruma eğrilerini tasvir etmek için en uygun model olarak tanımlanması, benzer tarım ürünlerinde kuruma davranışlarının modellenmesinde uygulanabilirliğin altını çizmiştir. Fick'in ikinci difüzyon yasasına göre, efektif nem difüzivitesi ($D_{eff}$), belirli sıcaklıkta $2.45 \times 10^{-10}$ to $6.55 \times 10^{-10}$ m²/s arasında sıralanmıştır. $D_{eff}$, Arrhenius tipi bir denklemle sıcaklığın bir fonksiyonu olarak ifade edilmiştir. Potas, Blanch ve Kontrol kodlarından alınan numuneler için nem difüzyonuna yönelik aktivasyon enerjisi sırasıyla 21.48, 22.82 ve 22.32 kJ/mol olarak hesaplanmıştır. Farklı numuneler için nem difüzyonuna yönelik aktivasyon enerjisinin hesaplanması, çeşitli koşullar altında kurutma proseslerinin optimize edilmesi için pratik bilgiler sunmuştur. Sonuçlar, bezelye kurutma kinetiğinin önemini ve endüstri için kurutma verimliliği ve ürün kalitesi üzerindeki pratik sonuçlarını göstermiştir.
**Anahtar Kelimeler:** Kurutma kinetiği, bezelye, efektif nem difüzivitesi, Page modeli

## INTRODUCTION

Due to great amount of high fiber content, protein, vitamins, minerals, and other nutrients, low fat and absence of cholesterol, the pea (Pisum sativum L.) is one of the most widely farmed edible legumes in the world (An et al., 2010). Turkey has produced 107344 tons of peas in 2018 on an area of 10917 acres (FAO, 2020). Peas must be preserved in some way, such as canning, freezing, or cold storage, because they are both seasonal and perishable, making them unavailable for immediate use. An alternative method of preserving peas is drying

technique. Because they have a longer shelf life, they are more palatable and easier to transport and handle. Thus, dried peas become more and more popular (Pardeshi et al., 2009).

In the food industry, drying is a conventional or industrial preservation technique. To minimize the growth of bacteria, enzymatic processes, and other biochemical activities, it is frequently utilized to reduce the moisture content and water activity of food (Doymaz, 2011; Li et al., 2016). Drying is an intricate and unsteady thermal process. It is essential from an engineering perspective to maintain control over the variables of this complex process. Numerous mathematical models are employed to control the drying process or to improve new or existing drying systems (Demirpolat et al., 2022). According to Doymaz (2013), the models can be divided into various categories. Recent mathematical modeling studies and experimental research on the drying properties of peas have been conducted (Pardeshi et al., 2009; Jadhav et al., 2010; Pandey et al., 2019; Taşova, 2019; Kaveh et al., 2021; Skulinová et al., 2011). Due to waxy layer covering the pea's surface, drying of peas requires a long time. However, by applying a specific chemical pre-treatment that increases the moisture diffusivity of the waxy layer, the drying method's effectiveness can be improved (Brar et al., 2020). Additionally, they provide a high-quality dried product and speed up drying by loosening tissue structure. Some of the most common and widely used as pre-treatments are citric acid, sodium chloride etc. In the literature, there have been several research for drying peas using chemical pre-treating (Burande et al., 2008; Jadhav et al., 2010; Doymaz and Kocayigit, 2011). One pre-treatment technique used to halt several physiological processes before drying fruits and vegetables is blanching. Enzymes that cause undesirable reactions, like enzymatic browning and oxidation during processing and storage, are revealed when the enzymes are inactivated. Additionally, drying time is shortened. Additionally, the elimination of intercellular air from tissues, which softens the tissue and causes the retention of carotene and ascorbic acid, are factors that affect storage (Jadhav et al., 2010).

The major goals of this study are to find out how green pea drying, and rehydration behaviors are impacted by drying temperature and pre-treatments. Other objectives of this study include computing activation energy and the effective moisture diffusivity of green peas, as well as fitting experimental results to four mathematical models. By assessing how different temperatures and pre-treatments influence the drying process, the research shed light on optimizing drying conditions for peas, which can have implications for industrial drying processes. Among the four mathematical models, the study identifies the Page model as the most suitable for depicting the drying curves of peas. This finding provides valuable guidance in selecting the appropriate model for modeling and predicting drying behavior in similar subjects. By applying Fick's second law of diffusion, the study estimates the effective moisture diffusivity at different temperatures.

The study calculates the activation energy for moisture diffusion for samples from different treatments (Potas, Blanch, and Control codes). Additionally, this study advances the understanding of pea drying kinetics and properties offering valuable insights and methodologies that can be applied in the optimization of drying processes not only for peas but also for other agricultural products. The findings contribute to the broader literature on drying kinetics, modeling, and process optimization in the field of food engineering and agricultural sciences. While previous research may have examined drying processes in general on other crops, this study delves into the intricacies of pea drying including the impact of temperature variations and pre-treatments on drying behaviors. The utilization of multiple mathematical models and the identification of the Page model as the most suitable for depicting pea drying curves contribute novel insights to the literature. Overall, the unique focus on peas, coupled with the comprehensive approach to analyzing drying kinetics and properties, distinguishes this study from existing literature in the field of agricultural drying.

## MATERIAL AND METHODS

### Sample Preparation

In Istanbul, Turkey, fresh green peas (Pisum sativum) are bought at a neighboring market. After a visual inspection, the dry, immature, and fractured pods are manually removed. Hand-shelled pea pods are used. Average diameter for peas is 1.0±0.1 cm. Before drying, the pea samples are split into three sample lots. 4% potassium carbonate (Potas code) (Sigma-Aldrich, ACS reagent 99.0%) is added to an aqueous solution that is used to soak one batch of pea samples for three minutes. The second batch of pea samples is placed in boiling water for three minutes (Blanch code). The other lot (Control code) is left untreated. The initial moisture content of peas is assessed utilizing a standard approach (AOAC 1990), which involve vacuum drying them during 24 hours at 70°C over a desiccant consisting of magnesium sulfate. To get a reliable average, this is done as three times. The samples' original moisture content is determined to be 72.70% on a wet basis (2.663 kg water/kg dry matter). Standard deviation is found as approximately 0.0082%.

### Drying Procedure

The cabinet dryer (APV & PASILAC, UK) is used to dry the pea samples (Figure 1). To create steady-state conditions, the dryer is started around 30 minutes before experimental part. At constant air speeds of 2 m/s and air temperatures of 50, 60, 70, and 80°C, the drying experiments are carried out. A Testo 440 vane probe anemometer (Lutron, AM-4201, Taiwan) is used to measure air velocity. The surfaces of the samples are crossed by horizontal airflow. The sample, which weighed roughly 50 g, is then put in the dryer. The weight loss of the peas is monitored with a digital scale (model

BB3000, Mettler-Toledo AG, Grefensee, Switzerland) for a measuring range of 0-3000 g and a reading precision of 0.1 g. When samples have a moisture level of roughly 0.17 kg water/kg dry matter (d.b), drying is completed. The dry peas' low-density polyethylene bags are then chilled and heat-sealed. Two-way analysis of variance is carried out to examine drying data with a 0.05 level of significance.
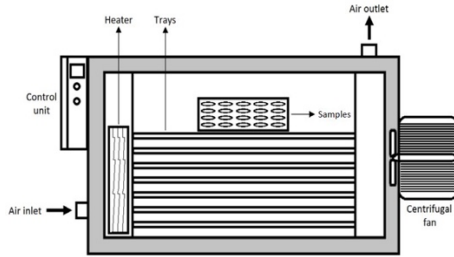


**Figure 1.** Experimental set up

## Determination of Drying Parameters

The following formula (Eq. 1) is used to determine the experimental moisture content of pea pod waste over a specified period:

$$M = \frac{W_t - W_d}{W_d} \qquad (1)$$

where $W_t$ is the mass at time t (in kg), $W_d$ is the mass at which a solid is bone-dry (also in kg), and M is the moisture content at that time (in kg water/kg dry matter). Following equation (Eq. 2) is utilized to calculate the moisture ratio (MR) for green peas:

$$MR = \frac{M_t - M_e}{M_0 - M_e} \qquad (2)$$

where t is the drying time in minute unit and $M_t$, $M_e$ and $M_0$, are the moisture contents at any time, equilibrium moisture content (kg water/kg dry matter) and starting moisture content, respectively. $M_e$ can be equal to zero without a substantial $M_0$ since $M_e$ values are relatively modest in comparison to $M_0$ (Pandey et al., 2019). Consequently, MR can be condensed to (Eq. 3):

$$MR = \frac{M_t}{M_0} \qquad (3)$$

Eq. (4) is used to compute the drying rate (DR):

$$DR = \frac{M_{t1} - M_{t2}}{t_2 - t_1} \qquad (4)$$

where $M_{t1}$ and $M_{t2}$ are the moisture contents (d.b) at those times, and $t_1$ and $t_2$ are the drying times (min).

## Mathematical Modelling

Four drying models, which are often used to simulate drying curves, are employed to fit the data from the drying of peas (Table 1). Statistica 8.0.550 (StatSoft Inc., Tulsa, OK, USA) are used to analyze the data. A non-linear

regression method based on the Levenberg-Marquardt method is used to estimate model parameters. The coefficient of determination ($R^2$) and root mean square error (RMSE) are utilized to define how well each model fit the experimental data. The following formulas are used to determine these parameters (Eq. 5, Eq. 6):

$$R^2 = 1 - \frac{\sum_{i=1}^{N}(MR_{pre,i} - MR_{exp,i})^2}{\sum_{i=1}^{N}(\overline{MR_{pre}} - MR_{exp,i})^2} \qquad (5)$$

$$RMSE = \left[\frac{1}{2}\sum_{i=1}^{N}(MR_{pre,i} - MR_{exp,i})^2\right]^{\frac{1}{2}} \qquad (6)$$

where $MR_{exp,i}$ and $MR_{pre,i}$, respectively, are the observed and predicted dimensionless moisture ratios, and N is the total observation number, z is the total number constant, and z is the total constant number. Higher $R^2$ and lower RMSE values demonstrate a better fit of the experimental data to the model (Pandey et al., 2019; Zhu, 2018).

**Table 1.** The drying models utilized to determine the drying curves

| Model name | Model [1] |
|---|---|
| Henderson & Pabis | $MR = a \exp(-kt)$ |
| Page | $MR = \exp(-kt^n)$ |
| Wang & Singh | $MR = 1 + at + bt^2$ |
| Aghbashlo et al. | $MR = \exp\left(-\frac{k_1 t}{1 + k_2 t}\right)$ |

[1] *Empirical constants and coefficients in drying models are a, b, k, $k_1$, $k_2$, and n.*

## Determination of Effective Moisture Diffusivity

The following equation, which is a mass-diffusion equation in a period of falling rate, illustrates Fick's second law of diffusion:

$$\frac{\partial MR}{\partial t} = D_{eff} \nabla^2 . MR \qquad (7)$$

For unstable state diffusion in spherical coordinates, Fick's second rule (Eq. 7) can be analytically solved under the following circumstances, according to Crank (1975): Low shrinkage, consistent effective diffusivity, diffusion-based moisture migration, and drying process temperature:

$$MR = \frac{6}{\pi^2} \sum_{n=1}^{\infty} \frac{1}{n^2} \exp\left(-n^2 \pi^2 \frac{D_{eff} t}{r^2}\right) \qquad (8)$$

For lengthy drying intervals, Eq. (8) can be simplified even further by only using the first component in the series. As a result, Eq. (9) is given as follows in a logarithmic form:

$$ln(MR) = ln\left(\frac{6}{\pi^2}\right) - \left(\pi^2 \frac{D_{eff} t}{r^2}\right) \qquad (9)$$

Plotting the experimental drying data as ln (MR) vs time

(min) reveals the effective moisture diffusivity. A plot of ln MR versus time using Eq. (9), which has the following slope (Eq. 10):

$$Slope = \frac{\pi^2 D_{eff}}{r^2} \qquad (10)$$

## Computation of Activation Energy

It is believed that an Arrhenius-style equation can adequately capture the link between effective moisture diffusivity and air temperature (Eq. 11):

$$D_{eff} = D_0 exp \left(- \frac{E_a}{R(T+273.15)}\right) \qquad (11)$$

Here, T is the temperature in degrees Celsius, $E_a$ is the activation energy in kilojoules per mole, R is the universal gas constant in kilojoules per mole per kilogram, and $D_0$ is the preexponential factor in $m^2/s$. The slope and intercept of the plot of ln ($D_{eff}$) vs 1/(T+273.15) can be used to compute both kinetic parameters ($E_a$ and $D_0$).

## Rehydration Experiments

The samples are dried at various temperatures before being rehydrated at 20°C. Dried samples weighing 1.5 g of sample is put into glass beakers with distilled water in a ratio of 1:160 (w/w). After 300 minutes, the samples are taken out and weighed with an electronic digital scale (Precisa, model XB220A, Precisa Instruments AG, Dietikon, Switzerland) with a sensitivity of 0.001 g. According to Eq. (12), the rehydration capacity (RC) is determined.

$$RC = \frac{W_1}{W_2} \qquad (12)$$

In this case, $W_1$ is the weight before rehydration, and $W_2$ is the weight after.

## RESULTS AND DISCUSSION

### Drying Curves

Figure 2 illustrates how drying peas' drying curves are affected by temperature. For vegetables of a similar type, the drying curves are typical. The moisture content decreases over the course of drying in every case study, and at higher air temperatures, it does so more quickly.

As the temperature increases, the moisture content decreases. At 50, 60, 70, and 80°C, the drying times necessary to estimate the end moisture content of the peas are 465, 405, 285 and 240 min for control samples, respectively. From 50 to 80°C, the samples' average drying rates increase by 1.937 times.

At higher temperatures, the increased heat absorption causes a greater driving force for mass transfer, a faster drying rate, and subsequently, a shorter drying time. Similar results are obtained, which support previous

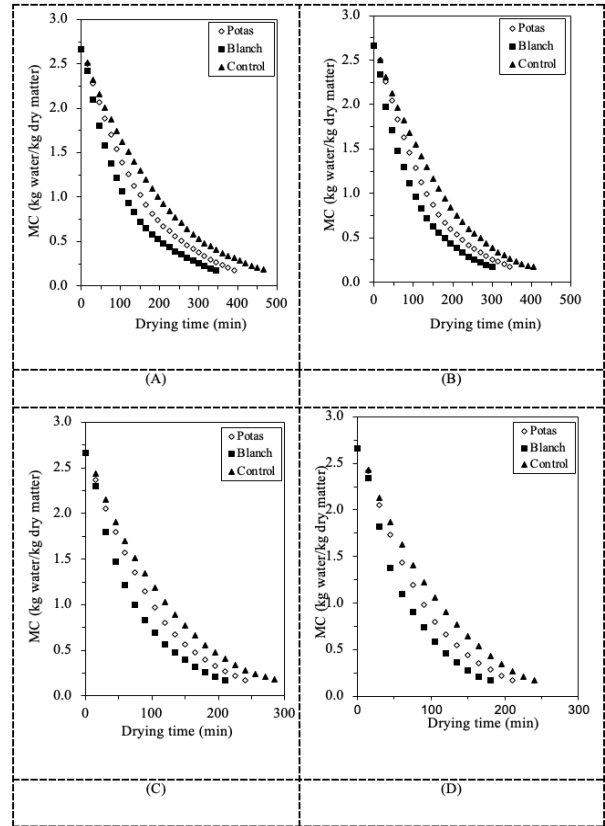findings about peas (Doymaz and Kocayigit, 2011; Taskin et al., 2016; Pandey et al., 2019).



**Figure 2.** Pea drying curves at various temperatures, with and without pre-treatments (A: 50°C, B: 60°C, C: 70°C, D: 80°C)

### Impact of Pre-Treatment Solution

Findings in Figure 2 show that pre-treatment is a key factor that influences drying time. In comparison to the other Potas and Control samples, the samples that are immersed in hot water before drying takes less time. In comparison to control samples, which requires 465 min for drying at 50°C to obtain a final water content of 0.17 kg water/kg dry matter, peas pre-treated with hot water blanching (Blanch code) and potassium carbonate solution (Potas code) take 345 and 390 min, respectively, to reach this water content. For samples of Blanch and Potas codes, the difference in drying periods is roughly 25.81% and 16.13%, respectively. These findings demonstrate that the pre-treatment solution increases the permeability of pea cell membranes, increasing water diffusivity. Similar patterns are seen while drying at 60, 70, and 80°C. Previous investigations on pea drying (Simal et al., 1996; Burande et al., 2008; Doymaz and Kocayigit 2011; Pandey et al., 2019) have documented the observed pre-treatment features.

### Drying Rate

Figure 3 depicts the pea drying rate curves. In certain instances, a constant-rate period is not seen. The warming-up and falling-rate periods can be seen as two distinct periods in Figure 3, respectively. The existence of falling-

rate drying behavior, according to Darvishi (2017), shows that the internal barrier to mass and heat transport is always increasing. The drying rate and moisture content are seen to be decreasing over time in Figure 3. Additionally, as the temperature rises, the rate of drying accelerates. When the peas' moisture content drops during the drying process, the drying rates gradually fall from their initial levels. The outcomes are in line with the findings of several authors who have observed the drying of different products (Pardeshi et al., 2009; Ponkham et al., 2012).
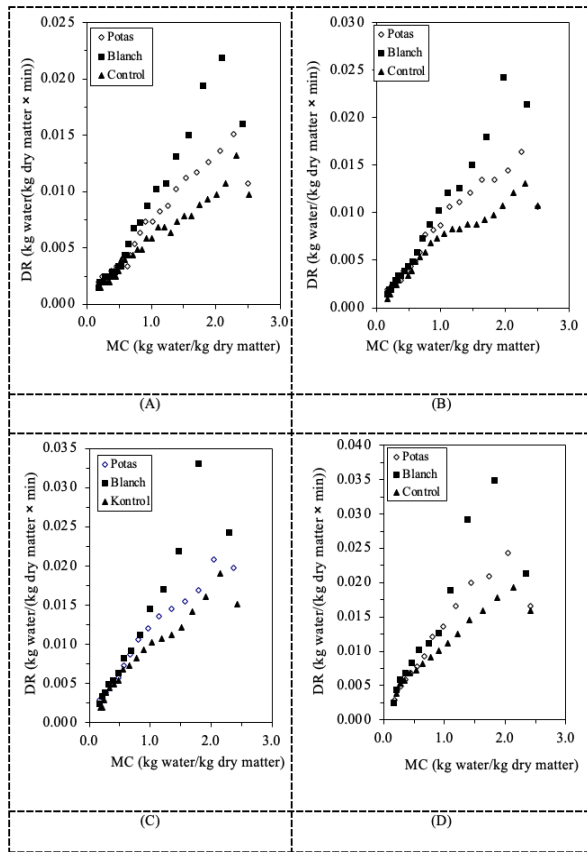


**Figure 3.** Moisture content vs drying rate for A: 50°C, B: 60°C, C: 70°C, D: 80°C

## Assessment of Models

Four drying models are utilized to fit the moisture content data from the MR that is gathered at various temperatures (Table 1). The Page model, one of the thin-layer drying models, accurately predicts the kinetics of pea drying at all drying temperatures and coefficients different from other models (Table 2).

The model with the highest $R^2$ and lowest RMSE values is deemed to be the best. Table 3 displays the outcomes of the statistical calculation. Each model has an $R^2$ value greater than 0.98.

The models are given if the average $R^2$ values determined by applying the models are ranked highest to lowest: Page > Wang & Singh > Henderson & Pabis > Aghbashlo et al. The models are listed as follows if the average RMSE values are ranked from lowest to highest: Aghbashlo et al., Page, Wang & Singh, Henderson & Pabis, and others. This assessment led to the Page model being determined as the best representative model. In that situation, the data points on the plots have a common focal point that is a 45° straight line. Additional proof that the program can accurately predict how peas will dry is provided by this pattern by comparing predicted and experimental values (Figure 4). Different studies have reported similar findings in the literature (Senadeera et al., 2003; Yang et al., 2018).
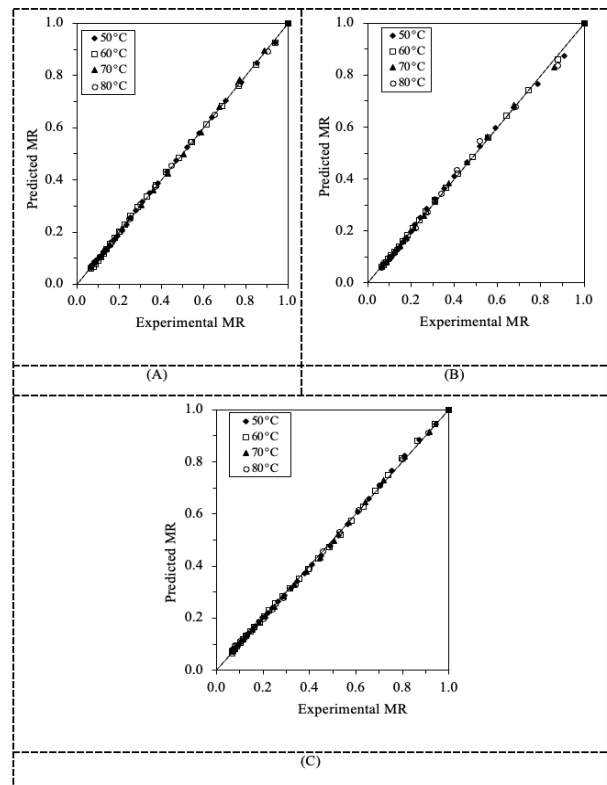


**Figure 4.** Comparison of experimental and predicted moisture ratio values using Page model (A: Potas, B: Blanch, C: Control)

**Table 2.** Coefficients of pea drying models at various temperatures

| T (°C) | Code | Models | Coefficient-1 | Coefficient-2 |
|---|---|---|---|---|
| 50 | Potas | Henderson & Pabis | a=1.033200 | k=0.006620 |
| | | Page | k=0.004176 | n=1.082660 |
| | | Wang & Singh | a=-0.005090 | b=0.000007 |
| | | Aghbashlo et al. | $k_1$=0.005899 | $k_2$=-0.00039 |
| | Blanch | Henderson & Pabis | a=1.000601 | k=0.008403 |
| | | Page | k=0.009833 | n=0.967951 |
| | | Wang & Singh | a=-0.006542 | b=0.000012 |
| | | Aghbashlo et al. | $k_1$=0.008919 | $k_2$=0.000390 |
| | Control | Henderson & Pabis | a=1.032609 | k=0.005307 |
| | | Page | k=0.002836 | n=1.110415 |
| | | Wang & Singh | a=-0.004064 | b=0.000005 |
| | | Aghbashlo et al. | $k_1$=0.004502 | $k_2$=-0.000502 |
| 60 | Potas | Henderson & Pabis | a=1.051832 | k=0.007665 |
| | | Page | k=0.003482 | n=1.146526 |
| | | Wang & Singh | a=-0.005745 | b=0.000009 |
| | | Aghbashlo et al. | $k_1$=0.006343 | $k_2$=-0.000732 |
| | Blanch | Henderson & Pabis | a=0.996229 | k=0.009503 |
| | | Page | k=0.010834 | n=0.973517 |
| | | Wang & Singh | a=-0.007415 | b=0.000015 |
| | | Aghbashlo et al. | $k_1$=0.009938 | $k_2$=0.000296 |
| | Control | Henderson & Pabis | a=1.049279 | k=0.006171 |
| | | Page | k=0.002333 | n=1.176208 |
| | | Wang & Singh | a=-0.004584 | b=0.000006 |
| | | Aghbashlo et al. | $k_1$=0.004832 | $k_2$=-0.000829 |
| 70 | Potas | Henderson & Pabis | a=1.036354 | k=0.010211 |
| | | Page | k=0.004958 | n=1.145214 |
| | | Wang & Singh | a=-0.007735 | b=0.000016 |
| | | Aghbashlo et al. | $k_1$=0.008367 | $k_2$=-0.001173 |
| | Blanch | Henderson & Pabis | a=1.012128 | k=0.013032 |
| | | Page | k=0.011851 | n=1.018354 |
| | | Wang & Singh | a=-0.010088 | b=0.000028 |
| | | Aghbashlo et al. | $k_1$=0.012774 | $k_2$=-0.000071 |
| | Control | Henderson & Pabis | a=1.041003 | k=0.008612 |
| | | Page | k=0.003878 | n=1.154493 |
| | | Wang & Singh | a=-0.006461 | b=0.000011 |
| | | Aghbashlo et al. | $k_1$=0.006914 | $k_2$=-0.001073 |
| 80 | Potas | Henderson & Pabis | a=1.055277 | k=0.011777 |
| | | Page | k=0.004456 | n=1.199866 |
| | | Wang & Singh | a=-0.008735 | b=0.000021 |
| | | Aghbashlo et al. | $k_1$=0.009166 | $k_2$=-0.001585 |
| | Blanch | Henderson & Pabis | a=1.037488 | k=0.014843 |
| | | Page | k=0.008894 | n=1.108724 |
| | | Wang & Singh | a=-0.011211 | b=0.000034 |
| | | Aghbashlo et al. | $k_1$=0.013020 | $k_2$=-0.000982 |
| | Control | Henderson & Pabis | a=1.050422 | k=0.009713 |
| | | Page | k=0.003541 | n=1.201108 |
| | | Wang & Singh | a=-0.007152 | b=0.000014 |
| | | Aghbashlo et al. | $k_1$=0.007366 | $k_2$=-0.001519 |

**Table 3.** Predicted statistical data from various models

| Coefficient | T (°C) | Code | Models | | | |
|---|---|---|---|---|---|---|
| | | | Henderson & Pabis | Page | Wang & Singh | Aghbashlo et al. |
| $R^2$ | 50 | Potas | 0.9989 | 0.9996 | 0.9959 | 0.9989 |
| | | Blanch | 0.9978 | 0.9982 | 0.9818 | 0.9988 |
| | | Control | 0.9972 | 0.9995 | 0.9983 | 0.9998 |
| | 60 | Potas | 0.9969 | 0.9994 | 0.9978 | 0.9977 |
| | | Blanch | 0.9993 | 0.9995 | 0.9846 | 0.9997 |
| | | Control | 0.9940 | 0.9993 | 0.9996 | 0.9995 |
| | 70 | Potas | 0.9958 | 0.9996 | 0.9991 | 0.9997 |
| | | Blanch | 0.9988 | 0.9987 | 0.9897 | 0.9987 |
| | | Control | 0.9950 | 0.9993 | 0.9992 | 0.9997 |
| | 80 | Potas | 0.9940 | 0.9996 | 0.9981 | 0.9979 |
| | | Blanch | 0.9958 | 0.9970 | 0.9928 | 0.9956 |
| | | Control | 0.9924 | 0.9991 | 0.9994 | 0.9996 |
| **Average $R^2$** | | | **0.9963** | **0.9990** | **0.9946** | **0.9988** |
| | | | | | | |
| RMSE | 50 | Potas | 0.0326 | 0.0247 | 0.0803 | 0.0353 |
| | | Blanch | 0.0557 | 0.0432 | 0.1532 | 0.0297 |
| | | Control | 0.0734 | 0.0275 | 0.0528 | 0.0168 |
| | 60 | Potas | 0.0605 | 0.0285 | 0.0565 | 0.0563 |
| | | Blanch | 0.0298 | 0.0181 | 0.1330 | 0.0120 |
| | | Control | 0.1022 | 0.0290 | 0.0236 | 0.0257 |
| | 70 | Potas | 0.0669 | 0.0160 | 0.0282 | 0.0161 |
| | | Blanch | 0.0231 | 0.0235 | 0.0949 | 0.0197 |
| | | Control | 0.0781 | 0.0284 | 0.0275 | 0.0142 |
| | 80 | Potas | 0.0751 | 0.0142 | 0.0390 | 0.0396 |
| | | Blanch | 0.0475 | 0.0384 | 0.0759 | 0.0417 |
| | | Control | 0.0896 | 0.0293 | 0.0237 | 0.0145 |
| **Average RMSE** | | | **0.0612** | **0.0267** | **0.0657** | **0.0268** |

**Effective Moisture Diffusivity**

$D_{eff}$ values at various temperatures range from $2.45 \times 10^{-10}$ to $6.55 \times 10^{-10}$ m²/s are shown in Figure 5. It is evident that as air temperature rises, $D_{eff}$ values rise significantly as well. Drying at 80°C results in the highest $D_{eff}$ value, while drying at 50°C results in the lowest value. Higher drying temperatures will ultimately result in more heating energy and more active water molecules, which means higher moisture diffusivity. Pre-treated samples have greater effective diffusion coefficient values than untreated samples (Control code). Therefore, it can be said that the pretreatment solutions alter the sample's structure to speed up drying. Samples that have been pre-treated with hot water and subsequently dried are where the substance with the highest effective diffusion coefficient is discovered. According to Zogzas et al. (1996), the range of $D_{eff}$ values for drying food items is often between $10^{-12}$ and $10^{-8}$ m²/s. The $D_{eff}$ values are close to those for peas published in literature: $3.52 \times 10^{-11}$-$5.66 \times 10^{-10}$ m²/s (Tao et al., 2018); $3.95 \times 10^{-10}$-$6.23 \times 10^{-10}$ m²/s (Pardeshi et al., 2009); $4.05 \times 10^{-11}$-$1.51 \times 10^{-10}$ m²/s (Jadhav et al., 2010); $8.05 \times 10^{-11}$-$1.97 \times 10^{-10}$ m²/s (Doymaz and Kocayigit, 2011). The differences between the results

can be explained by effect of type, pre-treatment solution, composition of peas and proposed model used for calculation.
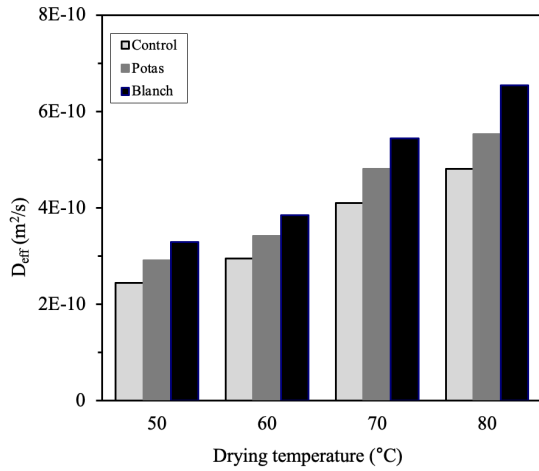


**Figure 5.** Effective moisture diffusivity versus temperature

## Activation Energy

The activation energy represents the energy threshold necessary to initiate the drying process by surpassing the barrier. Since ln ($D_{eff}$) plotted as a function of $1/(T+273.15)$ generates a line with a slope equal to (-$E_a/R$), it is simple to calculate $E_a$ (Figure 6). The pre-treated and control samples' $D_{eff}$ are affected by temperature in Eqs. (13), (14) and (15), with the following coefficients:

Potas:
$$D_{eff} = 8.492 \times 10^{-7} exp\left(-\frac{2584.5}{(T+273.15)}\right)(R^2 = 0.9719) \quad (13)$$

Blanch:
$$D_{eff} = 1.564 \times 10^{-6} exp\left(-\frac{2745.8}{(T+273.15)}\right)(R^2 = 0.9751) \quad (14)$$

Control:
$$D_{eff} = 9.817 \times 10^{-7} exp\left(-\frac{2685.7}{(T+273.15)}\right)(R^2 = 0.9836) \quad (15)$$

For the Potas, blanch, and Control code samples, the activation energies are 21.48, 22.82, and 22.32 kJ/mol, respectively. According to Zogzas et al. (1996), the activation energy levels for elements associate to food generally sequence from 12.7 to 110 kJ/mol. A considerable amount of agreement exists between the activation energy estimations reported in this experiment and the activation energy predicts for drying peas in published studies: 28.40 kJ/mol (Simal et al., 1996); 22.48 kJ/mol (Pardeshi et al., 2009); 25.45-28.40 kJ/mol (Honarvar et al., 2011); 22.01-30.99 kJ/mol (Doymaz and Kocayigit, 2011); and 29.76-30.23 kJ/mol (Tao et al., 2018).
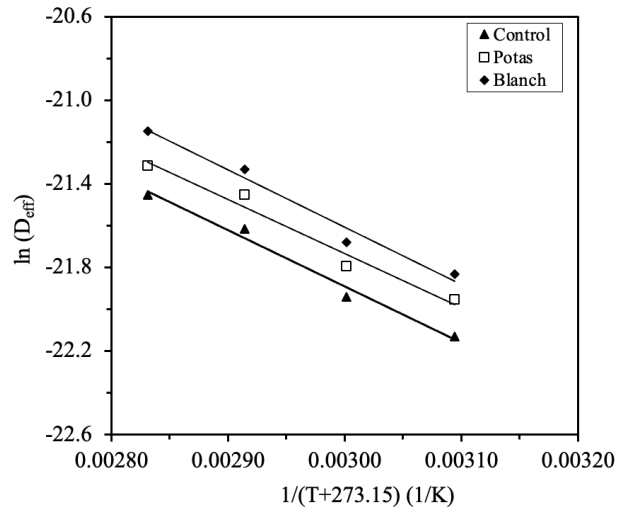


**Figure 6.** Arrhenius-type relationship between effective moisture diffusivity and temperature

## Rehydration Capacity

Rehydration capacity (RC) is a commonly used dry product quality measure. According to Karacabey et al. (2016), rehydration values give information on the physical and chemical modifications to a dried sample's composition that are brought on by drying and other treatments utilized before dehydration. Rehydration capacity diminishes as drying temperature rises, as shown in Figure 7, with greater RC values at 50°C. Additionally, following drying at the same temperatures, the RC values of samples that has been pre-treated with potassium carbonate solution are higher than those that have been blanched with hot water and control samples. It can be claimed that during the drying process, the samples suffer only minor physical damage from the potassium carbonate solution. As a result, it is possible to say that the capacity for rehydration has improved. Kaur and Bawa (2002), and Burande et al. (2008) obtain comparable results.
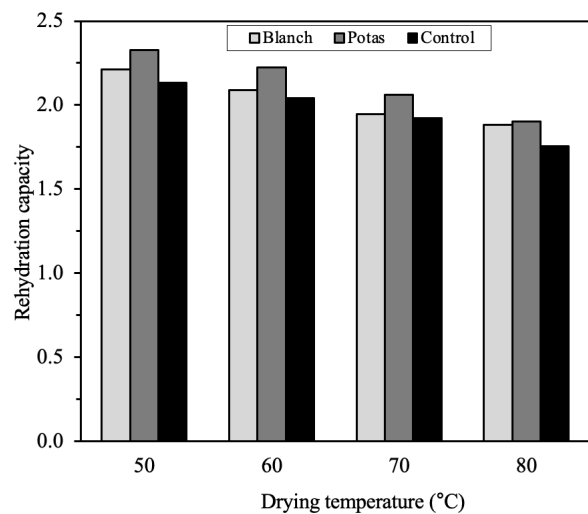


**Figure 7.** Effect of pre-treatment and air-drying temperature on rehydration capacity of peas

## CONCLUSIONS

At various temperatures, the hot-air dryer is used to test the green pea's drying qualities. Peas dry during the periods of rising and falling rates for each infrared power. Temperature and pre-treatments have a big impact on drying speed. Drying time is decreased by pre-treatment and an increase in temperature. The Page model produces the best findings and is most compatible with the experimental data from the pea drying trials when compared to the other three thin-layer drying models. For temperature investigation in range of 50-80°C, the $D_{eff}$ values range from $2.45 \times 10^{-10}$ to $6.55 \times 10^{-10}$ $m^2/s$. The effective moisture diffusivity rises as the temperature increases. Drying at 80°C shows in the highest $D_{eff}$ value, while drying at 50°C results in the lowest value. Each model from experiments has an $R^2$ value greater than 0.98. For samples of Blanch and Potas codes, the difference in drying periods is nearly 25.81% and 16.13%, respectively. Using an Arrhenius type equation, the activation energies for the Potas, Control, and Blanch samples are identified as 21.48, 22.82, and 22.32 kJ/mol, respectively.

## Author contributions
**İ.D:** Conceptualization, Methodology, Writing–review & editing.
**N.A:** Investigation, Writing–review & editing.

## Declarations
**Conflicts of interest:** The author declares there is no conflicts to declare.

## Ethics approval
This article does not contain any studies with human or animal subjects.

## REFERENCES

An, D., Arntfield, S. D., Beta, T. and Cenkowski, S., 2010, Hydration Properties of Different Varieties of Canadian Field Peas (Pisum Sativum) from Different Locations, *Food Res. Int*., 43, 520-525, doi.org/10.1016/j.foodres.2009.09.034

AOAC., 1990, Official Method of Analysis, 15th edn, Association of Official Analytical Chemists, Arlington, VA.

Brar, H. S., Kaur, P., Subramanian, J., Nair, G. R. and Singh, A., 2020, Effect of Chemical Pretreatment on Drying Kinetics and Physiochemical Characteristics of Yellow European Plums. *Int. J. Fruit Sci*., 20(Sup. 2), 252-279, doi.org/10.1080/15538362.2020.1717403

Burande, R. R., Kumbhar, B. K., Ghosh, P. K. and Jayas, D. S., 2008, Optimization of Fluidized Bed Drying Process of Green Peas Using Response Surface Methodology. *Dry. Technol*., 26, 920-930, dx.doi.org/10.1080/07373930802142739

Crank, J., 1975, The Mathematics of Diffusion. London: Oxford University Press.

Darvishi, H., 2017, Quality, Performance Analysis, Mass Transfer Parameters and Modeling of Drying Kinetics of Soybean. *Brazilian J. Chem.Eng*., 34, 143-148, doi.org/10.1590/0104-6632.20170341s20150509

Demirpolat, A. B., Aydoğmuş, E. and Arslanoğlu, H., 2022, Drying Behavior for Ocimum Basilicum Lamiaceae with the New System: Exergy Analysis and RSM Modeling. *Biomass Convers. Biorefinery*., 12, 515–526, doi.org/10.1007/s13399-021-02010-x

Doymaz, I., 2011, Drying of Pomegranate Arils and Selection of a Suitable Drying Model. *Food Biophys*., 6, 461-467, dx.doi.org/10.1007/s11483-011-9226-z

Doymaz, I. and Kocayigit, F., 2011, Drying and Rehydration Behaviors of Convection Drying of Green Peas. *Dry. Technol*., 29, 1273-1282, dx.doi.org/10.1080/07373937.2011.591713

Doymaz, I., 2013, Experimental Study on Drying of Pear Slices in a Convective Dryer. *Int. J. Food Sci., Technol*., 48, 1909-1915, dx.doi.org/10.1111/ijfs.12170

FAO, Food and Agricultural Organization Statistica Database (2020). Available at: http://faostat3.fao.org/download/Q/QC/E (Accessed March 04, 2020).

Honarvar, B., Mowla, D. and Safekori, A. A., 2011, Physical Properties of Green Pea in an Inert Medium FBD Dryer Assisted by IR Heating. *Iranian J. Chem. Chem. Eng*., 30(1), 107-118.

Jadhav, D. B., Visavale, G. L., Sutar, N., Annapure, U. S. and Thorat, B. N., 2010, Studies on Solar Cabinet Drying of Green Peas (Pisum Sativum). *Dry. Technol*., 28, 600-607, doi.org/10.1080/073733931003788064

Karacabey, E., Baltacioglu, C., Cevik, M. and Kalkan, H., 2016, Optimization of Microwave-Assisted Drying of Jerusalem Artichokes (Helianthus Tuberosus L.) by Response Surface Methodology and Genetic Algorithm. *Italian J. Food Sci*., 28, 121-130, dx.doi.org/10.14674/1120-1770/ijfs.v466

Kaur, H. and Bawa, A. S., 2002, Studies on Fluidized Bed Drying of Peas. *J. Food Sci. Technol*., 39, 272–275.

Kaveh, M., Abbaspour-Gilandeh, Y. and Nowacka, M., 2021, Comparison of Different Drying Techniques and Their Carbon Emissions in Green Peas. *Chem. Eng. Process.: Process Intensif*., 160, 108274, doi.org/10.1016/j.cep.2020.108274

Li, W., Yuan, L., Xiao, X. and Yang, X., 2016, Dehydration of Kiwifruit (Actinidia Deliciosa) Slices Using Heat Pipe Combined with Impingement Technology. *Int. J. Food Eng.*, 12, 265-276, doi.org/10.1515/ijfe-2015-0165

Pandey, O. P., Mishra, B. K. and Misra, A., 2019, Comparative Study of Green Peas Using with Blanching & Without Blanching Techniques. *Inf. Proces. Agric.*, 6, 285-296, doi.org/10.1016/j.inpa.2018.10.002

Pardeshi, I. L., Arora, S. and Borker, P. A., 2009, Thin-layer Drying of Green Peas and Selection of a Suitable Thin-Layer Drying Model. *Dry. Technol.*, 27, 288-295, dx.doi.org/10.1080/07373930802606451

Ponkham, K., Meeso, N., Soponronnarit, S. and Siriamornpun, S., 2012, Modeling of Combined Far-Infrared Radiation and Air Drying of a Ring Shaped-Pineapple with/without Shrinkage. *Food Bioprod. Proces.*, 90, 155-164, doi.org/10.1016/j.fbp.2011.02.008

Senadeera, W., Bhandari, B. R., Young, G. and Wijesinghe, B., 2003, Influence of Shapes of Selected Vegetable Materials on Drying Kinetics During Fluidized Bed Drying. *J. Food Eng.*, 58, 277-283, doi.org/10.1016/S0260-8774(02)00386-2

Simal, S., Mulet, A., Tarrazo, J. and Rossello, C., 1996, Drying Models for Green Peas. *Food Chem.*, 55, 121-128, doi.org/10.1016/0308-8146(95)00074-7

Skulinová, M., Kadlec, P., Kaasová, J., Dostálová, J., Zátopková, M., Hosnedl, V. and Hrachovinová, J., 2011, Microwave Treatment and Drying of Germinated Pea. *Czech J. Food Sci.*, 20(1), 23–30, doi.org/10.17221/3505-cjfs

Tao, Z., Yang, Z., Yu, F. and Yang, Z., 2018, Effect of Ultrasound on Heat Pump Drying Characteristics of Pea Seeds. *Int. J. Food Eng.*, 14(11-12), 20180204, doi.org/10.1515/ijfe-2018-0204

Taskin, O., Izli, N. and Vardar, A., 2016, Analysis on Photovoltaic Energy-Assisted Drying of Green Peas. *Int. J. Photoenerg.*, 3814262, doi.org/10.1155/2016/3814262

Taşova, M., 2019, Effect on the Effective Diffusion and Activation Energy Values of Pea (Pisum sativum L.) Grains of Drying Temperature. *ISVOS Journal*, 3(1), 8–13.

Yang, Z., Li, X., Tao, Z., Luo, N. and Yu, F., 2018, Ultrasound Assisted Heat Pump Drying of Pea Seed. *Dry. Technol.*, 36, 1958-1969, dx.doi.org/10.1080/07373937.2018.1430041

Zhu, A., 2018, The Convective Hot Air Drying of Lactuca Sative Slices. *Int. J. Green Energ.*, 15, 201-207, dx.doi.org/10.1080/15435075.2018.1434523

Zogzas, N. P., Maroulis, Z. B. and Marinos-Kouris, D., 1996, Moisture Diffusivity Data Compilation in Foodstuffs. *Dry. Technol.*, 14, 2225-2253, doi.org/10.1080/07373939608917205

# EXPLORING THE IMPACT OF GEOMETRIC PARAMETERS ON HEAT TRANSFER AND FLUID FLOW CHARACTERISTICS IN CROSS-TRIANGULAR GROOVED CHANNELS: A COMPUTATIONAL STUDY

**Yeliz ALNAK**
Sivas Cumhuriyet University, Technology Fac., Manufacturing Eng. Dept., 58140, Sivas, Türkiye
ytas@cumhuriyet.edu.tr, ORCID: 0000-0003-4383-3806

**Abstract:** In this study, the impact of geometric parameters of rectangular baffles with varying location angles and heights is investigated on the heat transfer and fluid flow characteristics of cross-triangular grooved channels. Computational methods are employed to explore these effects, utilizing the Ansys-Fluent program to solve the Navier-Stokes and energy equations, incorporating the k-ε turbulence model for numerical simulations. The inlet temperature of the air, serving as the working fluid, is set at 293 K, while the wall surface temperature of the lower triangular grooved channel remains fixed at 373 K. Rectangular baffles are tested with angles of 30°, 60°, and 90°, and heights of 0.25H, 0.5H, and 0.75H, respectively. The numerical results show good agreement with a 3.53% deviation compared to existing empirical data in the literature. The obtained findings are presented in terms of mean Nusselt ($Nu_m$) number, fluid temperature, and Performance Evaluation Criterion (PEC) number variations taking into consideration of pressure drop for each rectangular baffle angle and height. Additionally, contour distributions of temperature and velocity are evaluated for different Reynolds numbers (Re) and arrangements of rectangular baffles. It has been determined that the Nu number value increases by 197.56% at a 90° angle and 0.75H height, compared to the 0.25H baffle height at Re=6000. Furthermore, at Re=1000, the PEC number is 84.50% higher with a baffle height of 0.25H and a baffle angle of 30° compared to the condition with a 90° angle.
**Keywords:** Cross-triangular grooved channels, rectangular baffles, Heat transfer, Computational fluid dynamics, Navier-Stokes equations

## ÇAPRAZ ÜÇGEN YİVLİ KANALLARDA GEOMETRİK PARAMETRELERİN ISI TRANSFERİ VE AKIŞKAN AKIŞ ÖZELLİKLERİ ÜZERİNDEKİ ETKİSİNİN ARAŞTIRILMASI: HESAPLAMALI BİR ÇALIŞMA

**Özet:** Bu çalışmada, konum açıları ve yükseklikleri değişen dikdörtgen engellerin geometrik parametrelerinin çapraz üçgen oluklu kanalların ısı transferi ve akışkan akışı özellikleri üzerindeki etkisi araştırılmaktadır. Bu etkileri keşfetmek için hesaplamalı yöntemler kullanılmış olup; Ansys-Fluent programı kullanılarak Navier-Stokes ve enerji denklemleri çözülmüş, sayısal simülasyonlar için k-ε türbülans modeli dahil edilmiştir. Çalışma akışkanı olarak kullanılan havanın giriş sıcaklığı 293 K iken, üçgen oluklu alt kanalın duvar yüzey sıcaklığı sabit 373 K olarak belirlenmiştir. Dikdörtgen engeller sırasıyla 30°, 60° ve 90° açılarında ve 0,25H, 0,5H ve 0.75H yüksekliklerinde test edilmiştir. Sayısal sonuçlar, literatürde mevcut olan deneysel verilere göre %3,53 sapma ile iyi bir uyum göstermektedir. Elde edilen bulgular, her bir dikdörtgen engel açısı ve yüksekliği için ortalama Nusselt ($Nu_m$) sayısı, akışkan sıcaklığı ve basınç düşüşünü dikkate alan Performans Değerlendirme Kriteri (PEC) sayısı değişimleri açısından sunulmaktadır. Ayrıca, farklı Reynolds sayıları (Re) ve dikdörtgen engellerin düzenlemeleri için sıcaklık ve hız konturu dağılımları değerlendirilmektedir. Re=6000'de 0,25H engel yüksekliğine göre Nu sayısı değerinin 90° açı ve 0,75H yükseklikte %197,56 arttığı belirlenmiştir. Ayrıca, Re=1000'de, 0,25H engel yüksekliği ve 30° açısında, 90° açıdaki durumla karşılaştırıldığında PEC sayısı %84,50 daha yüksektir.
**Anahtar Kelimeler:** Çapraz-üçgen oluklu kanallar, Dikdörtgen engeller, ısı transferi, Hesaplamalı akışkanlar dinamiği, Navier-Stokes denklemleri

## INTRODUCTION

Heat exchangers play a crucial role in transferring heat from a hot fluid to a cold fluid, finding extensive applications across various industries including heating and cooling systems, chemical manufacturing, oil refining, electrical power generation, and other engineering sectors. Among the different types of heat exchangers, plate heat exchangers are particularly popular due to their compact design, cost-effectiveness, simplicity, and high efficiency. These heat exchangers are continuously evolving and improving, adapting to meet the increasing demands of diverse industries (Liang et. al., 2019 ).

The parallel plate channel structure represents one of the most common and straightforward configurations of plate heat exchangers. However, its performance is relatively low, prompting many researchers to seek improvements. Scott and Lobato (2003) and Zhang (2005) have made strides in enhancing heat and mass transfer in plate heat exchangers by refining a cross-grooved sinusoidal and triangular channel structure. Their approach involves combining numerous corrugated layers within a plate heat exchanger to create flow channels, with adjacent channels angled specifically to form flow ducts and facilitate fluid separation. This arrangement results in a cross-grooved plate with robust mechanical endurance. Aslan et al. (2023) experimentally and numerically evaluated the friction factor, convection heat transfer and field compliance factor properties of pipe bundles with smooth and offset rows. The Reynolds number was changed from 989 to 6352 and the Pr number was kept at 0.70. It was found that offset orders lead to a larger Nu number and friction factor values compared to smooth arrangement. Notably, at low Reynolds numbers, internal flow becomes turbulent due to the widening feature upon contact in grooved ducts, leading to a notably high coefficient of heat transfer (Zang., 2016).

Researchers have conducted extensive experimental and theoretical investigations aimed at improving the heat transfer performance of cross-grooved channels. Liu and Niu and Niu (2015) examined the impact of aspect ratio and apex angle on the thermal-hydraulic performance of a cross-grooved duct, highlighting the significant influence of the apex angle on the duct's properties. Krishnan et al. (2021) empirically evaluated the effects of corrugation pattern, corrugation angle, plate length, and depth-to-pitch ratio on the thermal-hydraulic performance of grooved flow ducts, emphasizing the importance of groove angle and depth-to-pitch ratio on heat transfer and pressure drop. Saha et al. (2020) investigated the cross-grooved performance of plate heat exchangers across corrugation angle ranges, observing an increase in pressure drop per unit length with an increase in corrugation angle. Guo-Guo-Yan et al. (2005) conducted numerical and experimental analyses on sinusoidal cross-grooved heat exchangers, concluding that a steady-state laminar model is suitable for a specified Reynolds number range, with a slight deviation between computational and empirical results. Zhang et al. (2014, 2005, 2005) studied heat and mass transfer, as well as fluid flow, in cross-grooved triangular ducts for membrane-based exchangers, deriving correlation equations for friction factors, Sherwood numbers, and Reynolds numbers. Li et al. (2015) investigated heat and mass transfer enhancements in cross-grooved membrane exchanger ducts by varying apex angles, finding that larger apex angles resulted in higher Nusselt and Sherwood numbers. Muley and Manglik (1999) analyzed the thermal-hydraulic characteristics of grooved-plate channels with different plate configurations, reporting significantly higher heat transfer compared to flat-plate ducts under equivalent pumping power conditions, considering Reynolds number, chevron angle, and surface area enlargement factor. Zimmerer et al. (2002) studied the wavelength, groove shape, and inclination angle of heat exchangers for local heat and mass transfer and pressure losses. Ajeel et al. (2019) investigated the thermal and hydraulic properties of trapezoidal-grooved ducts using $SiO_2$-water nanofluid, observing substantial enhancements in Nusselt number with an increase in height-to-width ratio. In another study, Ajeel et al. (2019) explored heat transfer enhancement in grooved channels of semi-circle, trapezoidal, and straight shapes using alumina oxide-water nanofluid, finding the highest enhancement in trapezoidal grooved ducts. Furthermore, Ajeel et al. (2019) empirically evaluated semi-circle-grooved and trapezoidal-grooved ducts using $SiO_2$-water nanofluid, demonstrating significant improvements in heat transfer rate and pressure drop compared to straight channels.

Baffles serve as effective means to augment heat transfer area, alter the primary flow direction, and enhance flow irregularity and heat transfer. However, there have been relatively few studies utilizing baffles. Li and Gao (2017) examined heat transfer characteristics in cross-grooved triangular ducts employing delta-shaped baffles. They observed a significant increase in pressure drop and a 2.1 to 4.3 times increase in Nusselt number when the baffle height equaled the trough height. Saim et al. (2013) conducted numerical investigations on heat transfer and turbulent flow along ducts with inclined baffles, noting improved friction factor and heat transfer with inclined baffles. Alnak (2020) numerically studied heat transfer, pressure drop, and thermohydraulic performance of cross-grooved triangular ducts with rectangular baffles at different settlement angles. Results showed a 52.8% higher mean Nusselt number for ducts with a 90° angle

baffle compared to those with a 60° angle baffle at Re=6000. Feng et al. (2022) numerically analyzed the impact of trapezoidal baffles on flow and heat transfer properties of cross-grooved triangular ducts. They found Nusselt and friction factors of ducts with trapezoidal baffles to be 1.7 and 3.5 times higher, respectively, than those without baffles, leading to a 30% increase in Performance Evaluation Criterion (PEC) value. Li et al. (2022) investigated the influence of baffle position and apex angle on heat and flow characteristics of cross-corrugated triangular ducts. They introduced trapezoidal baffles to enhance heat transfer, finding that the PEC value for ducts with a specific baffle position at a 120° apex angle could be lower than that without baffles. Liang et al. (2019) conducted computational work using an SST k-ε model to examine six different baffle configurations' effects on temperature patterns and distribution in cross-grooved triangular ducts. They found that compared to ducts without baffles, Nusselt numbers increased by 1.5 to 1.6 times for certain baffle configurations, resulting in a 13% increase in heat transfer efficiency under the same fan power.

The corrugated channels used in the study are employed in the design of plate heat exchangers, which are frequently exerted in heat transfer applications and are formed by combining many thin metal plates. In the reviewed literature, the heat transfer and flow characteristics of baffle setups, spacing, and apex angles in corrugation troughs of cross-grooved channels have been extensively studied. In this study, unlike the studies in the literature, the effects of rectangular baffle angles and heights at the top section of cross-triangular grooved ducts were investigated regarding heat transfer, flow structure, and performance evaluation criterion (PEC) number taking into consideration of pressure drop. Rectangular baffles were positioned at the upper section of the grooved duct at varying angles and heights. Computational research utilized the Ansys-Fluent software program with the k-ε turbulence model to solve steady, three-dimensional equations of energy and Navier-Stokes. The inlet air temperature was set at 293 K, and the fixed surface temperature of the lower triangular grooved ducts was 373 K. Parameters such as Reynolds number and baffle placement angles and heights were varied. The Reynolds number range investigated was 1000-6000, with baffle placement angles of 30°, 60°, and 90°, and heights of 0.25H, 0.5H, and 0.75H. However, in the case of a baffle height of 0.75H when using an angle of 30º, the baffle protrudes from the duct, so the baffle height of 0.75H could not have been analyzed at 30º. Computational results were compared with empirical and computational findings from existing literature, showing agreement. Outcome variables included fluid velocity, temperature, mean Nusselt number (Nu), and performance evaluation

criterion (PEC) number along the midpoint of the upper grooved duct section. Additionally, fluid exit temperature variations were assessed for each baffle angle and height, compared to the non-baffle case. Contour distributions of fluid velocity, temperature along the cross-grooved triangular duct were evaluated for various baffle angles and heights at Reynolds numbers of 1000 and 6000.

## COMPUTATIONAL METHOD

In this study, numerical solutions for flow and heat transfer were conducted using a 3D, steady-state turbulence model based on the k-ε model within the Ansys-Fluent program. The investigation focused on a cross-triangular grooved triangular channel with various angle and height configurations of rectangular baffles. Convergence criteria were set at 10^-6 and 10^-7 for the energy and momentum equations, respectively. The heat transfer and flow structure analysis for the cross-triangular grooved triangular duct with rectangular baffle placement angles and heights involved solving partial differential equations derived from conservation equations of time-averaged mass, momentum, and energy for turbulent flow. Besides, since irregular flow fluctuations will occur in the channel due to the presence of baffles and grooves in the study, the study was modeled as turbulent, and the k-ε model was used as the turbulence model. However, accurate modeling of turbulence is essential in heat transfer simulations. Direct numerical simulation of turbulent flows is very difficult and time consuming. There are various turbulence models used in numerical modeling. Besides, among turbulence models, the k-ε turbulence model, which is a semi-empirical model, is widely used due to its economy and acceptable accuracy in many flow events. In one of the studies on impinging jets, Wang and Mujumdar (2005) tested several k-ε turbulence models with low Re numbers for turbulent jets. They found that the models were able to determine the general shape of the Nu number distribution and that the models applied better in heated areas for large jet-to-plate distances. In their study, they determined that the k-ε turbulence model showed a good performance in determining the heat transfer properties of impinging jets when compared to standard high Re number models. In addition, compared to other turbulence models (Yıldızeli et. al., 2023), they determined that the k-ε turbulence model is suitable because it reduces kinetic energy production and approaches the required result in the heated zone. Accordingly, taking into account the results obtained from studies in the literature (Karabulut., 2023, Karabulut., 2023, Karabulut and Alnak., 2023), the standard k-ε turbulence model was used in the numerical calculations in this study.

These analyses were carried out under steady-state conditions with no body forces present (Flunet., 2003, Karabulut and Alnak., 2020):

Continuity equation

$$\frac{\partial \bar{u}}{\partial x} + \frac{\partial \bar{v}}{\partial y} + \frac{\partial \bar{w}}{\partial z} = 0 \tag{1}$$

Momentum equation:

x momentum equation:

$$\left[ \bar{u}\frac{\partial \bar{u}}{\partial x} + \frac{\partial \overline{(u')^2}}{\partial x} \right] + \left[ \bar{v}\frac{\partial \bar{u}}{\partial y} + \frac{\partial \overline{(u'v')}}{\partial y} \right] + \left[ \bar{w}\frac{\partial \bar{u}}{\partial z} + \frac{\partial \overline{u'w'}}{\partial z} \right] = -\frac{1}{\rho}\frac{\partial \bar{p}}{\partial x} + \nu \left( \frac{\partial^2 \bar{u}}{\partial x^2} + \frac{\partial^2 \bar{u}}{\partial y^2} + \frac{\partial^2 \bar{u}}{\partial z^2} \right) \tag{2.1}$$

y momentum equation:

$$\left[ \bar{u}\frac{\partial \bar{v}}{\partial x} + \frac{\partial \overline{(v')^2}}{\partial x} \right] + \left[ \bar{v}\frac{\partial \bar{v}}{\partial y} + \frac{\partial \overline{(v'v')}}{\partial y} \right] + \left[ \bar{w}\frac{\partial \bar{v}}{\partial z} + \frac{\partial \overline{v'w'}}{\partial z} \right] = -\frac{1}{\rho}\frac{\partial \bar{p}}{\partial y} + \nu \left( \frac{\partial^2 \bar{v}}{\partial x^2} + \frac{\partial^2 \bar{v}}{\partial y^2} + \frac{\partial^2 \bar{v}}{\partial z^2} \right) \tag{2.2}$$

z momentum equation:

$$\left[ \bar{u}\frac{\partial \bar{w}}{\partial x} + \frac{\partial \overline{(w')^2}}{\partial x} \right] + \left[ \bar{v}\frac{\partial \bar{w}}{\partial y} + \frac{\partial \overline{(w'v')}}{\partial y} \right] + \left[ \bar{w}\frac{\partial \bar{w}}{\partial z} + \frac{\partial \overline{w'w'}}{\partial z} \right] = -\frac{1}{\rho}\frac{\partial \bar{p}}{\partial z} + \nu \left( \frac{\partial^2 \bar{w}}{\partial x^2} + \frac{\partial^2 \bar{w}}{\partial y^2} + \frac{\partial^2 \bar{w}}{\partial z^2} \right) \tag{2.3}$$

Energy equation:

$$\left[ \bar{u}\frac{\partial \bar{T}}{\partial x} + \bar{v}\frac{\partial \bar{T}}{\partial y} + \bar{w}\frac{\partial \bar{T}}{\partial z} \right] + \frac{\partial \overline{(u'T')}}{\partial x} + \frac{\partial \overline{(v'T')}}{\partial y} + \frac{\partial \overline{(w'T')}}{\partial z} = \left( \frac{k}{\rho c_p} \right) \left( \frac{\partial^2 \bar{T}}{\partial x^2} + \frac{\partial^2 \bar{T}}{\partial y^2} + \frac{\partial^2 \bar{T}}{\partial z^2} \right) \tag{3}$$

Turbulence kinetic energy equation:

$$\frac{\partial (\rho u k')}{\partial x} + \frac{\partial (\rho v k')}{\partial y} + \frac{\partial (\rho w k')}{\partial z} = \frac{\partial}{\partial x}\left( \frac{\mu_t}{\sigma_k}\frac{\partial k'}{\partial x} \right) + \frac{\partial}{\partial y}\left( \frac{\mu_t}{\sigma_k}\frac{\partial k'}{\partial y} \right) + \frac{\partial}{\partial z}\left( \frac{\mu_t}{\sigma_k}\frac{\partial k'}{\partial z} \right) + \mu_t \phi - \rho \varepsilon \tag{4}$$

Turbulence viscosity:

$$\mu_t = C_{\mu'} \rho \frac{k'^2}{\varepsilon} \tag{5}$$

At the turbulence model of k-ε in the study employed by Karabulut (2019), when ε displays distribution of turbulence, k′ and φ present terms of turbulence kinetic energy and dissipation of viscous, respectively.

Turbulence kinetic energy:

$$k' = \frac{1}{2}\left( \overline{u'^2} + \overline{v'^2} + \overline{w'^2} \right) \tag{6}$$

Viscous dissipation term:

$$\phi = 2\mu \left[ \left( \frac{\partial u}{\partial x} \right)^2 + \left( \frac{\partial v}{\partial y} \right)^2 + \left( \frac{\partial w}{\partial z} \right)^2 \right] + \mu \left[ \left( \frac{\partial v}{\partial x} + \frac{\partial u}{\partial y} \right)^2 + \left( \frac{\partial w}{\partial y} + \frac{\partial v}{\partial z} \right)^2 + \left( \frac{\partial u}{\partial z} + \frac{\partial w}{\partial x} \right)^2 \right] \tag{7}$$

Turbulence kinetic energy disappearance equation:

$$\frac{\partial (\rho u \varepsilon)}{\partial x} + \frac{\partial (\rho v \varepsilon)}{\partial y} + \frac{\partial (\rho w \varepsilon)}{\partial z} = \frac{\partial}{\partial x}\left( \frac{\mu_t}{\sigma_\varepsilon}\frac{\partial \varepsilon}{\partial x} \right) + \frac{\partial}{\partial y}\left( \frac{\mu_t}{\sigma_\varepsilon}\frac{\partial \varepsilon}{\partial y} \right) + \frac{\partial}{\partial z}\left( \frac{\mu_t}{\sigma_\varepsilon}\frac{\partial \varepsilon}{\partial z} \right) + C_{1\varepsilon}\mu_t \frac{\varepsilon}{k'}\phi - C_{2\varepsilon}\rho \frac{\varepsilon^2}{k'} \tag{8}$$

$C_\mu$, $C_{1\varepsilon}$, $C_{2\varepsilon}$, $\sigma_k$ and $\sigma_\varepsilon$ which are model firms are the typical values of default employed in the standard turbulence model of k-ε (Flunet., 2003). The values of these firms were obtained by numerous iterations of data fitting for many turbulent flows.

Re number is computed by the equation given below (Lin and Gao., 2017, Karabulut and Alnak., 2020, Karabulut, 2019).

$$\text{Re} = \frac{V_\infty D_h}{\nu} \tag{9}$$

$D_h$ is the jet inlet hydraulic diameter (Lin and Gao., 2017, Karabulut and Alnak., 2020, Karabulut, 2019).

$$D_h = \frac{4A_c}{P} \tag{10}$$

In this equation, $A_c$ and P are the jet inlet cross-sectional area and perimeter lengths, respectively.

The Nu number is defined to be a ratio of the convection heat transfer rate to the conduction heat transfer rate (Welty et. al., 2014).

$$-k\left( \frac{\partial T}{\partial n} \right)_s = h \Delta T_{lm} \text{ and } Nu = \frac{hL}{k} \tag{11}$$

Here, h is the local heat transfer coefficient on the surface and n is the perpendicular direction to the surface and the local Nu number is calculated as above.

The logarithmic temperature difference between the wall surface of the triangular corrugations and fluid is computed by Liu and Niu (2015).

$$\Delta T_{lm} = \frac{(T_i - T_o)}{ln\left( \frac{T_w - T_i}{T_w - T_o} \right)} \tag{12}$$

where $T_i$, $T_o$ and $T_w$ are the inlet and outlet temperatures of the fluid and the wall surface temperature of the triangular corrugations, respectively.

Mean heat transfer coefficient (Welty et. al., 2014).

$$h_m = \frac{1}{L} \int_0^L h \, dx \qquad (13)$$

Mean Nu number (Welty et. al., 2014).

$$Nu_m = \frac{h_m L}{k} \qquad (14)$$

Pressure drop is calculated with Liu and Niu (2015).

$$\Delta p = \frac{f \rho L}{2 D_h} u_m^2 \qquad (15)$$

Where $\Delta p$ is the drop of pressure of the cross-triangular grooved triangular duct between the entry and exit, f is the factor of friction and L is the duct long.

PEC (Performance Evaluation Criterion) number (Akbarzadeh et. al., 2017)

$$PEC = \frac{Nu_{\text{ channel with baffles}} / Nu_{\text{channel without baffles}}}{(\Delta p_{\text{ channel with baffles}} / \Delta p_{\text{channel without baffles}})} \qquad (16)$$

The dimensionless variable is described as

$$z^* = \frac{z}{L} \qquad (17)$$

where z displays the local duct long.

## GEOMETRIC DESIGN

Figure 1A illustrates a perspective view of the cross-triangular corrugated duct with rectangular baffles, while Figure 1B shows a channel view depicting boundary conditions and dimensions of the cross-corrugated channel. The dimensions of the triangular cross-grooved duct are specified as follows: length (L) = 70.71 mm, width (W) = 8.165 mm, height of the duct (H) = 7.071 mm, and distance between two rectangular baffles (d) = 8.165 mm. Rectangular baffles are utilized at heights of 0.25H, 0.5H, and 0.75H. The entry velocity range of the air varies from 2.1436 m/s (Re=1000) to 12.8616 m/s (Re=6000). A constant height of 4.0825 mm is maintained for the triangular corrugations. Figure 2 displays the tetrahedral mesh structure for the cross-triangular grooved triangular duct. Based on the duct dimensions reported in the literature, ten rectangular baffles and triangular grooved troughs are present in the lower part of the duct.

This study is conducted under the following assumptions:

a) The flow domain for the cross-triangular grooved triangular duct is three-dimensional (3D), steady, and turbulent.
b) The working fluid used is air, considered to be incompressible.
c) The thermal properties of the air are assumed to be constant throughout the analysis.
d) There is no heat generation within the air flow or on the surfaces of the rectangular baffles.

## ASSESSMENT OF THE RESULTS

To assess the influence of grid refinement on the Nusselt number (Nu) of the surfaces within the cross-grooved duct, grid independence tests were conducted for the non-baffled duct across various Reynolds numbers (Re) including 1000, 2000, 3000, and 4000. The results are presented in Table 1. Upon examination of Table 1, it can be observed that 611,037 grid elements are sufficient for achieving grid independence for the non-baffled grooved duct

Tab. 1. Independence of grid test results considering the $Nu_m$ for the grooved duct non-baffle

| Mesh Num. | Re=1000 -$Nu_m$ | Re=2000 - $Nu_m$ | Re=3000 - $Nu_m$ | Re=6000 - $Nu_m$ |
|---|---|---|---|---|
| 450571 | 6.7850 | 11.285 | 14.985 | 23.9356 |
| 860452 | 6.874 | 11.299 | 14.9898 | 23.9402 |
| **970002** | **6.875** | **11.3** | **14.99** | **23.94** |
| 1152004 | 6.8754 | 11.304 | 14.9954 | 23.9403 |

Figures 3a and 3b illustrate the Nusselt number (Nu) values obtained from empirical studies by Scott and Lobato (2003) and computational studies by Liu and Niu (2015), Zhang (2005), Zhang (2005), and Li and Gao (2017). These figures compare the Nu values for apex angles of 60° and 90° in cross-corrugated ducts without baffles, respectively, with the computational results from this study. In Figure 3a, comparisons are made between the computational data from Zhang (2005), Zhang (2005), and Li and Gao (2017), which used the k-ε turbulence model, and the results from this study for a grooved channel with an apex angle of 60° and no baffles. Figure 3b, on the other hand, compares the experimental results from Scott and Lobato (2003) and numerical results from Liu and Niu (2015), Li and Gao (2017), and this study, all of which utilized various turbulence models, for a corrugated duct with an apex angle of 90° without baffles. The maximum deviation observed in this study for Nu is 4.8% compared to numerical results for the 60° apex angle (Figure 3a). However, the differences between the numerical results of this study and the values of the experimental data are within 3.53% for an apex angle of 90° (Figure 3b). The utilization of the k-ε turbulence model demonstrates satisfactory agreement between numerical and experimental results, thus providing a reliable basis for comparative analyses across various rectangular baffle angles and heights.
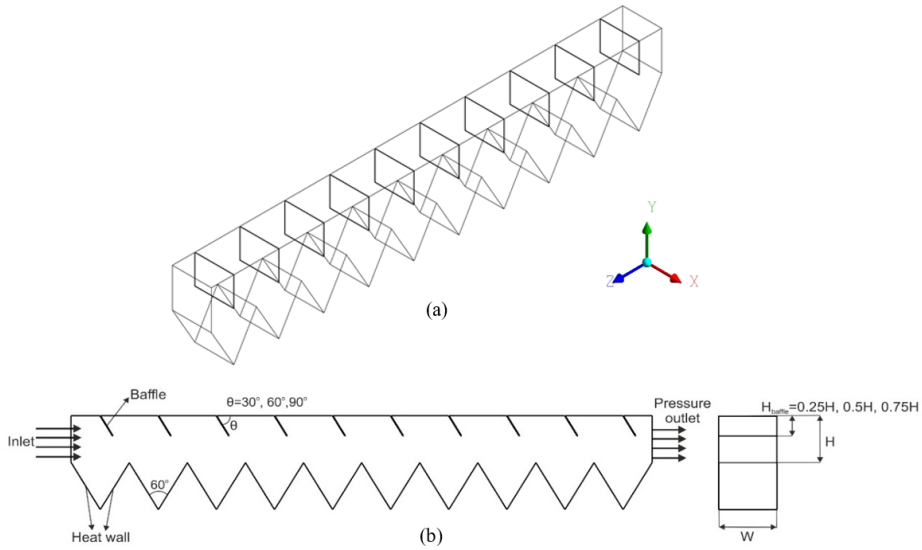
(a)



(b)

**Fig. 1.** (a) Cross-triangular corrugated triangular duct perspective view with baffle
(b) duct view with dimensions and boundary conditions



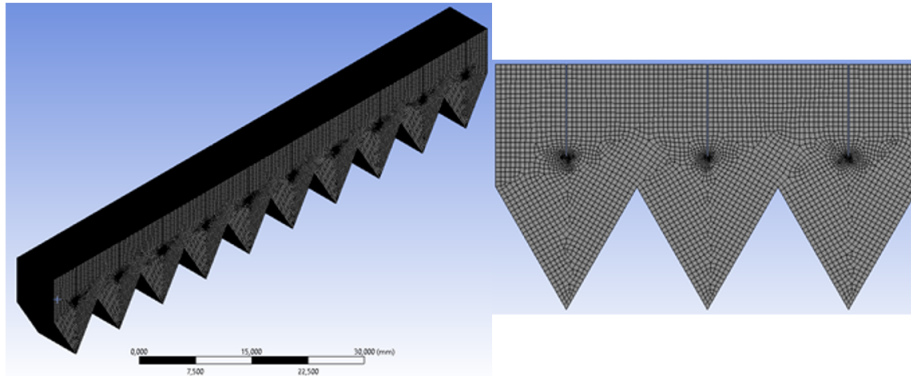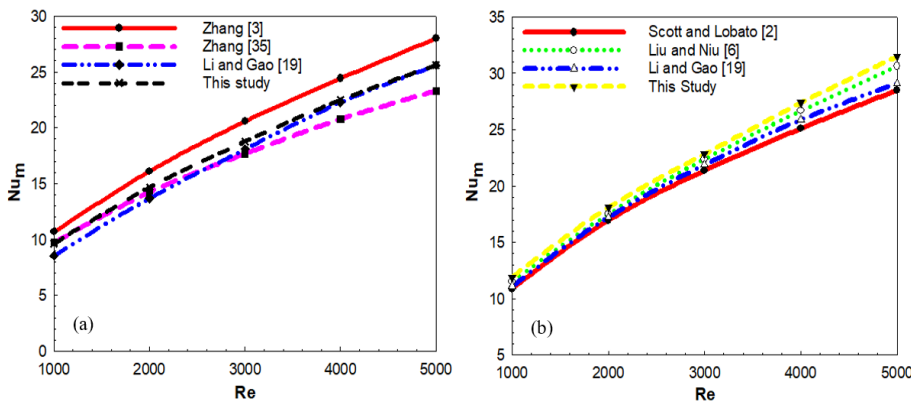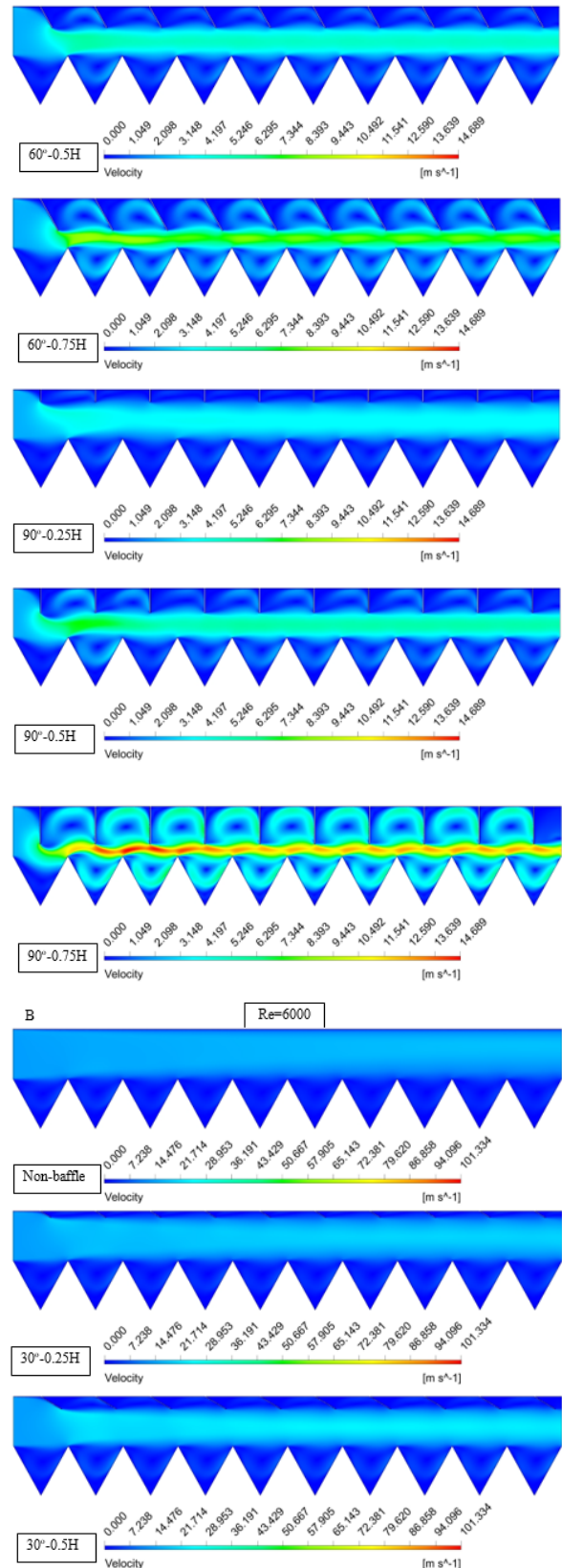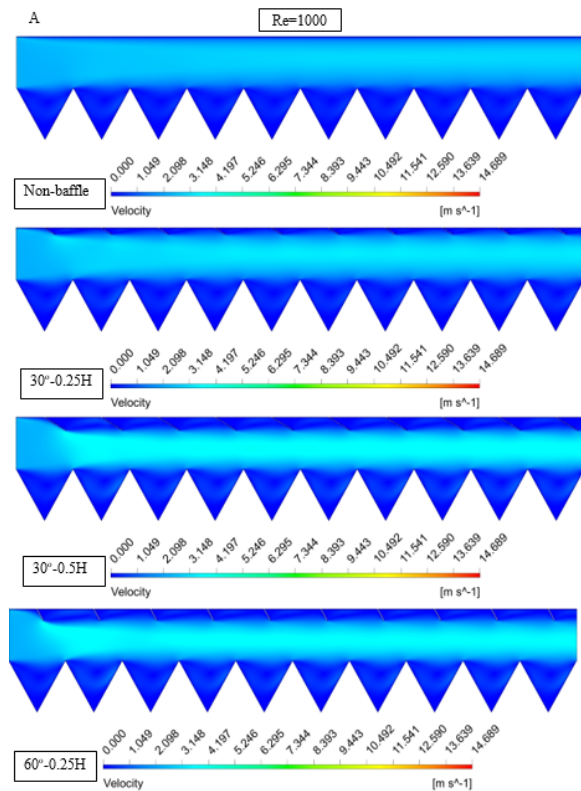**Fig. 2.** Cross-triangular corrugated triangular duct mesh structure



(a)

(b)

**Fig. 3.** Mean Nu number ($Nu_m$) comparing results of the computational and empirical with the outcomes of this work for the apex angles of (a) 60º (b) 90º

**Fig. 4.** Velocity contour distributions of triangular corrugated rectangular ducts non-baffle and with discrete angles and heights of baffles A-Re=1000 B-Re=6000

Figures 4A and 4B illustrate the velocity contour distributions of rectangular channels with triangular corrugations, both without baffles and with baffles featuring angles of 30°, 60°, and 90°, as well as heights of 0.25H, 0.5H, and 0.75H. In the absence of baffles, the fluid velocity is notably low throughout the channel, including within the triangular corrugations. However, upon the introduction of baffles at the upper section of the rectangular channel, the fluid begins to be directed towards the triangular corrugations. This orientation towards the corrugations becomes more prominent with increasing baffle angle. Additionally,

increasing the baffle height enhances both the direction of flow and turbulence within the fluid and corrugations. As observed in the contour distributions, higher fluid velocities are evident, particularly at baffle angles of 60° and 90°, when using 0.75H height baffles within the duct. At this baffle height (0.75H), under the 90° angled condition, the fluid velocity increases substantially, leading to a jet flow-like scenario due to cross-sectional narrowing in the channel. With the Re number increased to 6000, higher fluid velocity values are observed within the triangular corrugations, as the fluid activity within the duct becomes more pronounced. This increase in Re number results in heightened fluid movement and flow dynamics within the duct.
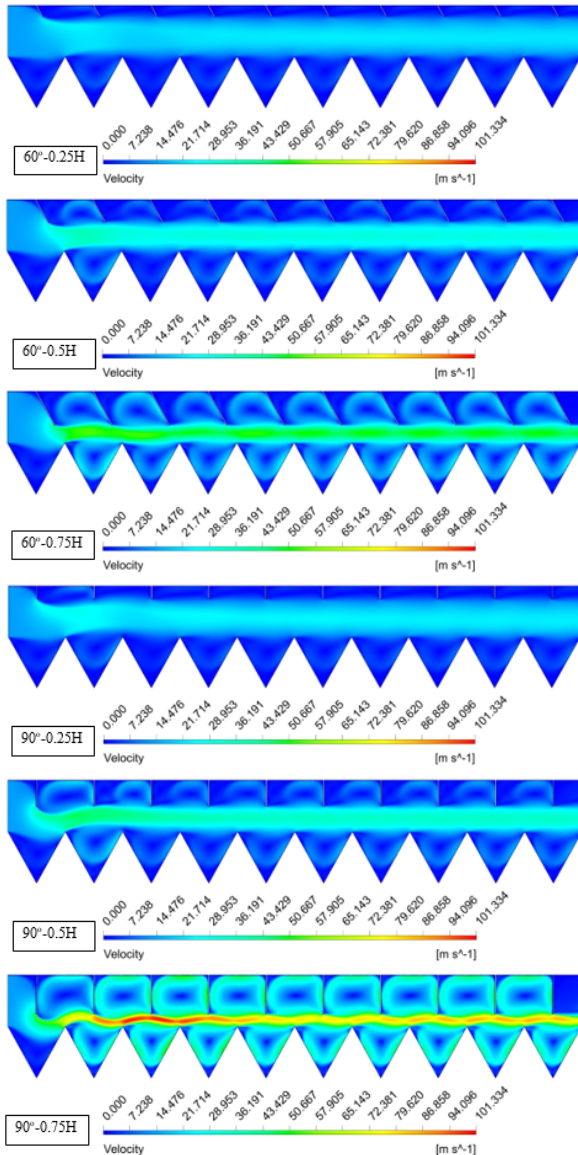


233

**Fig. 4.** Velocity contour distributions of triangular corrugated rectangular ducts
non-baffle and with discrete angles and heights of baffles A-Re=1000 B-Re=6000

Figures 5A and 5B depict the temperature contour distributions of rectangular ducts with triangular corrugations, both without baffles and with baffle angles of 30°, 60°, and 90°, as well as heights of 0.25H, 0.5H, and 0.75H, at Reynolds numbers (Re) of 1000 and 6000, respectively. In the absence of baffles, temperatures are notably high throughout the channels and within the triangular corrugations, indicating a need for cooling. At the peaks of the triangular corrugations, temperatures reach their highest values. Upon the addition of baffles to the channels, the fluid is directed towards these corrugations, facilitating cooling and reducing their temperature. Consequently, towards the end of the duct, the fluid within the channel and between the baffles experiences heating, leading to increased temperatures. With increasing baffle angle and height, the orientation towards the corrugations improves, enhancing heat transfer. This effect is

particularly pronounced at a height of 0.75H for Re=6000 and at baffle angles of 60° and 90°, where the reduction in temperature is most evident. Overall, using baffles enhances heat transfer efficiency and reduces temperature within the duct



234

90°-0.75H

B                                Re=6000



Non-baffle



30°-0.25H



30°-0.5H



60°-0.25H



60°-0.5H



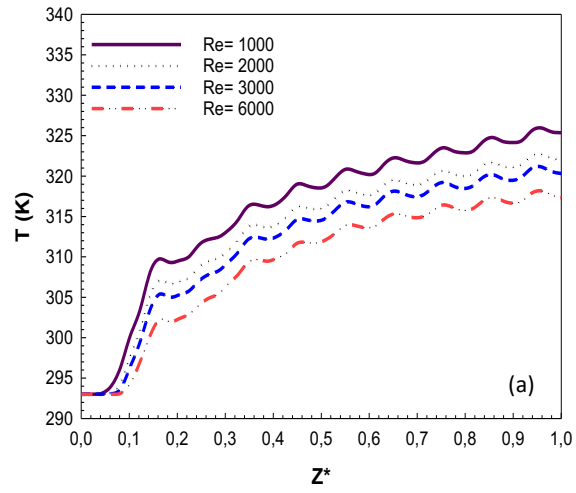60°-0.75H



90°-0.25H



90°-0.5H



90°-0.75H
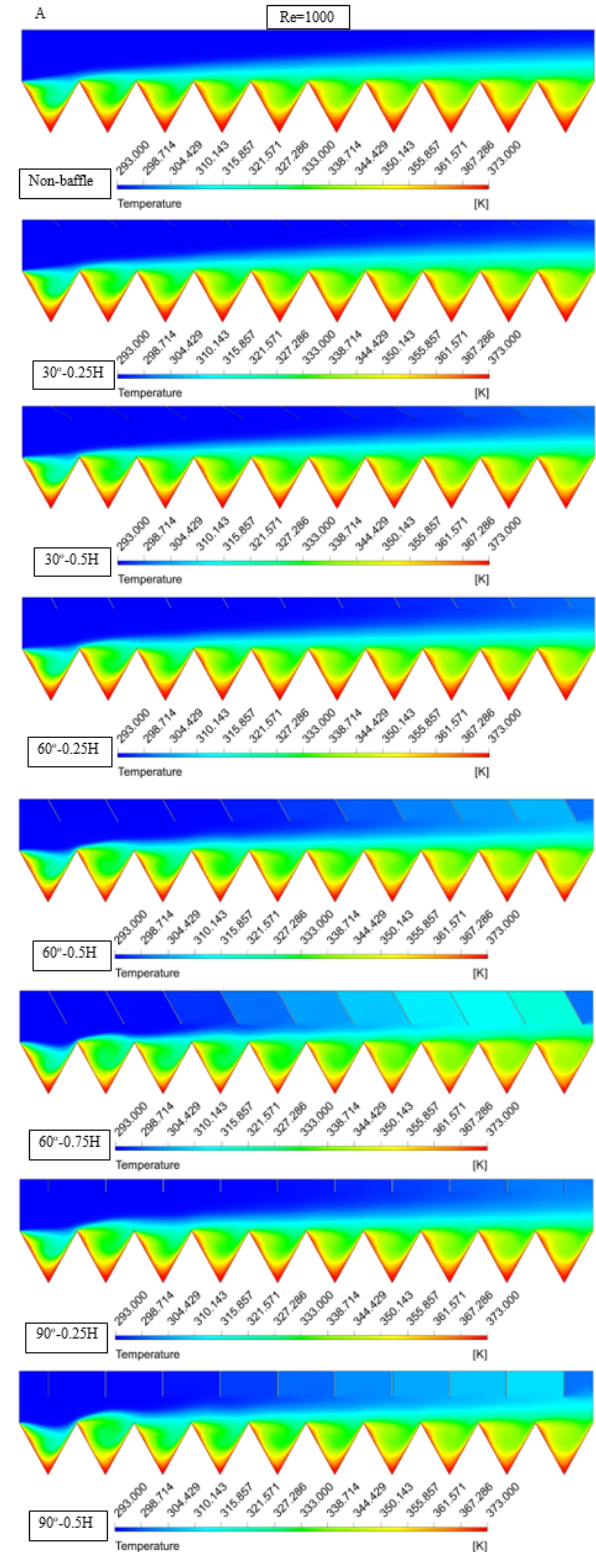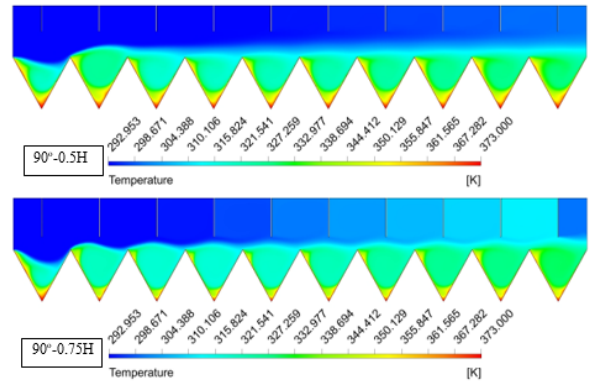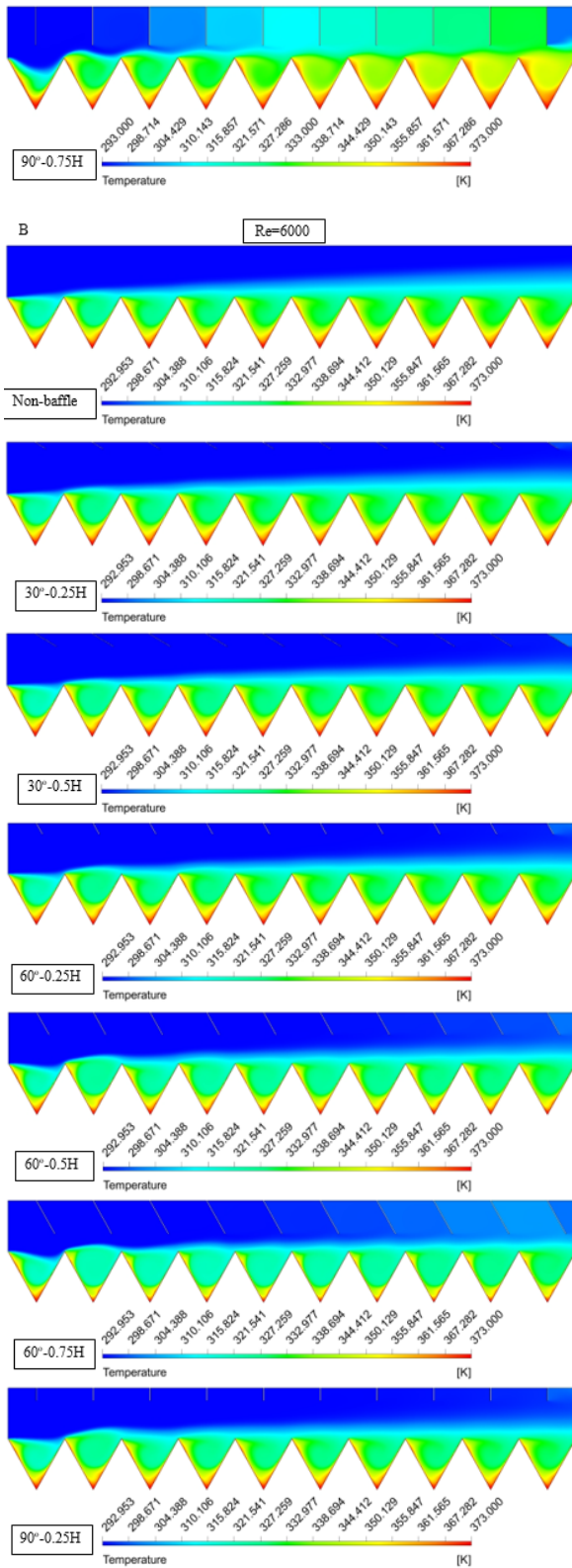
**Fig. 5.** Contour distributions of temperature of triangular grooved rectangular ducts
non-baffle and with discrete angles and heights of baffles A-Re=1000 B-Re=6000

Figure 6 illustrates the temperature variations along the rectangular channels with triangular corrugations, categorized by Reynolds numbers, and different baffle angles and heights. In the case of non-baffles (Figure 6a), temperatures of the fluids decrease as the Reynolds number increases, indicating enhanced cooling efficiency with higher fluid velocities. However, when baffles are introduced, temperature variations become more complex. Figures 6b to 6i represent the temperature variations for different baffle configurations, including various baffle angles and heights. It is observed that temperature values tend to increase with higher baffle angles and heights. This is because the baffles direct the flow towards the triangular corrugations, resulting in increased heat transfer and thus higher temperatures. Interestingly, fluctuations in temperature, particularly at the duct entrances, are observed depending on the angle and height setups of the baffles. However, in the channel arrangement with a 90° angle and 0.75H baffle height, temperatures reach their highest values more periodically and regularly compared to other channels. This suggests that this particular baffle configuration may offer more efficient and consistent heat transfer performance.
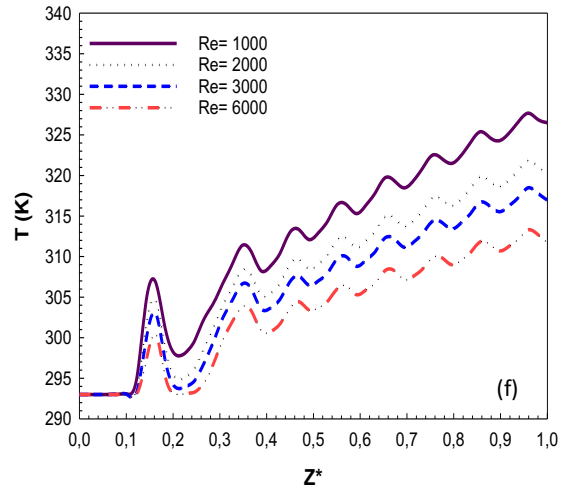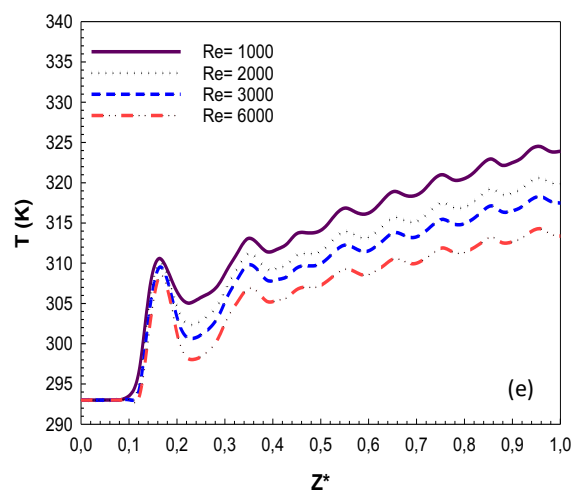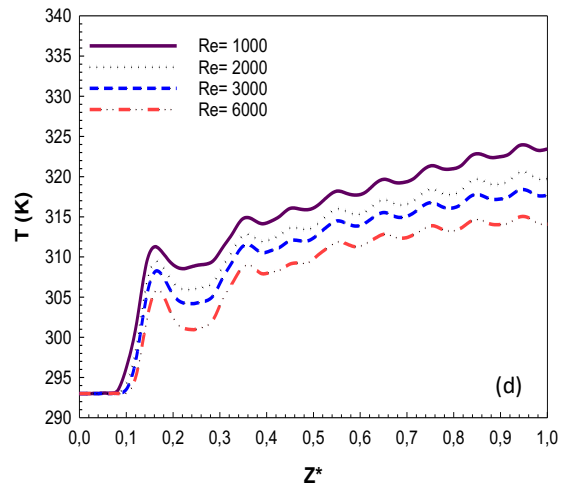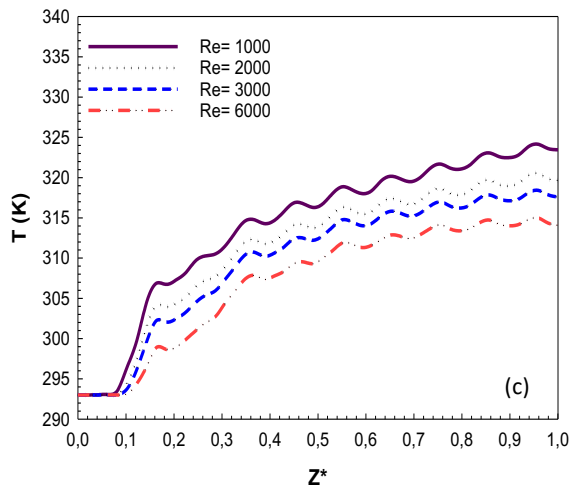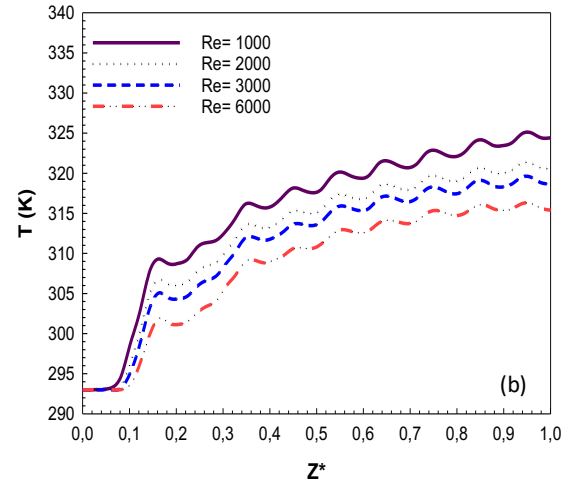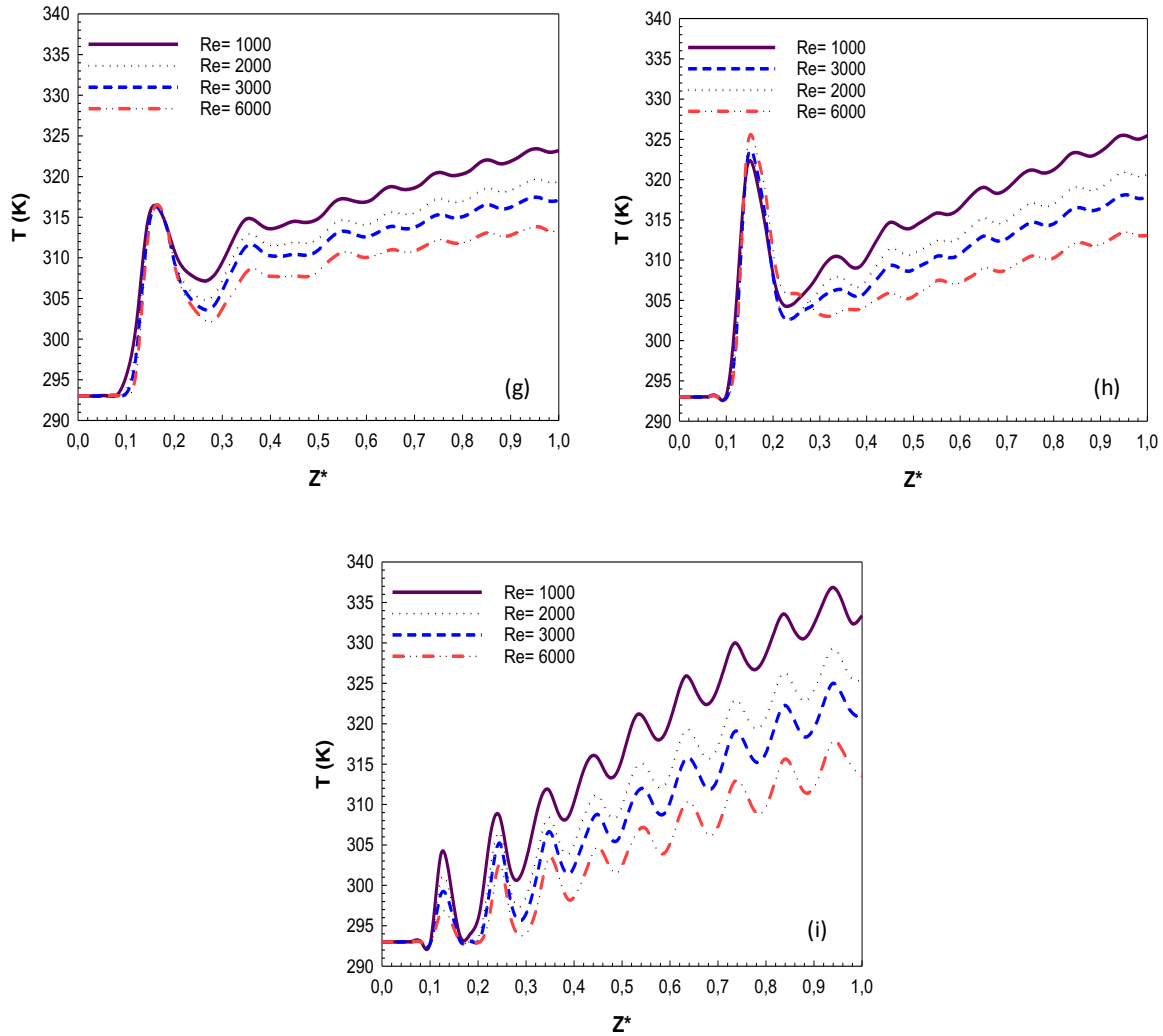
**Fig. 6.** Fluid temperature value variations of triangular corrugated rectangular ducts for the non-baffle duct (a) and ducts with discrete baffle angles and heights (b) 30°-0.25H (c) 30°-0.5H (d) 60°-0.25H (e) 60°-0.5H (f) 60°-0.75H (g) 90°-0.25H (h) 90°-0.5H (i) 90°-0.75H

Figure 7 displays the variations in mean Nusselt number (Num) versus different Reynolds numbers (Re) for rectangular channels with triangular corrugations, both without baffles and with rectangular baffles featuring angles of 30°, 60°, and 90°, as well as heights of (a) 0.25H, (b) 0.5H, and (c) 0.75H, respectively. Observations from the figure reveal that Nu values increase with higher heat transfer rates, corresponding to the increase in Reynolds number. This trend is consistent across all baffle configurations. Interestingly, the maximum Nu value is consistently achieved for all baffle heights at a baffle angle of 90°.

This indicates that the fluid flow experiences more intense vortex movements due to turbulence created within the fluid at this particular baffle angle value. Moreover, the highest Nu value is observed at a baffle angle of 90° and a baffle height of 0.75H. Specifically, at this configuration, the Nu value increases by 197.56% at Re=6000 compared to the Nu value at a baffle height of 0.25H for the same Reynolds number. This substantial increase in Nu highlights the significant enhancement in heat transfer efficiency achieved by employing the 90° angle and 0.75H baffle height configuration.
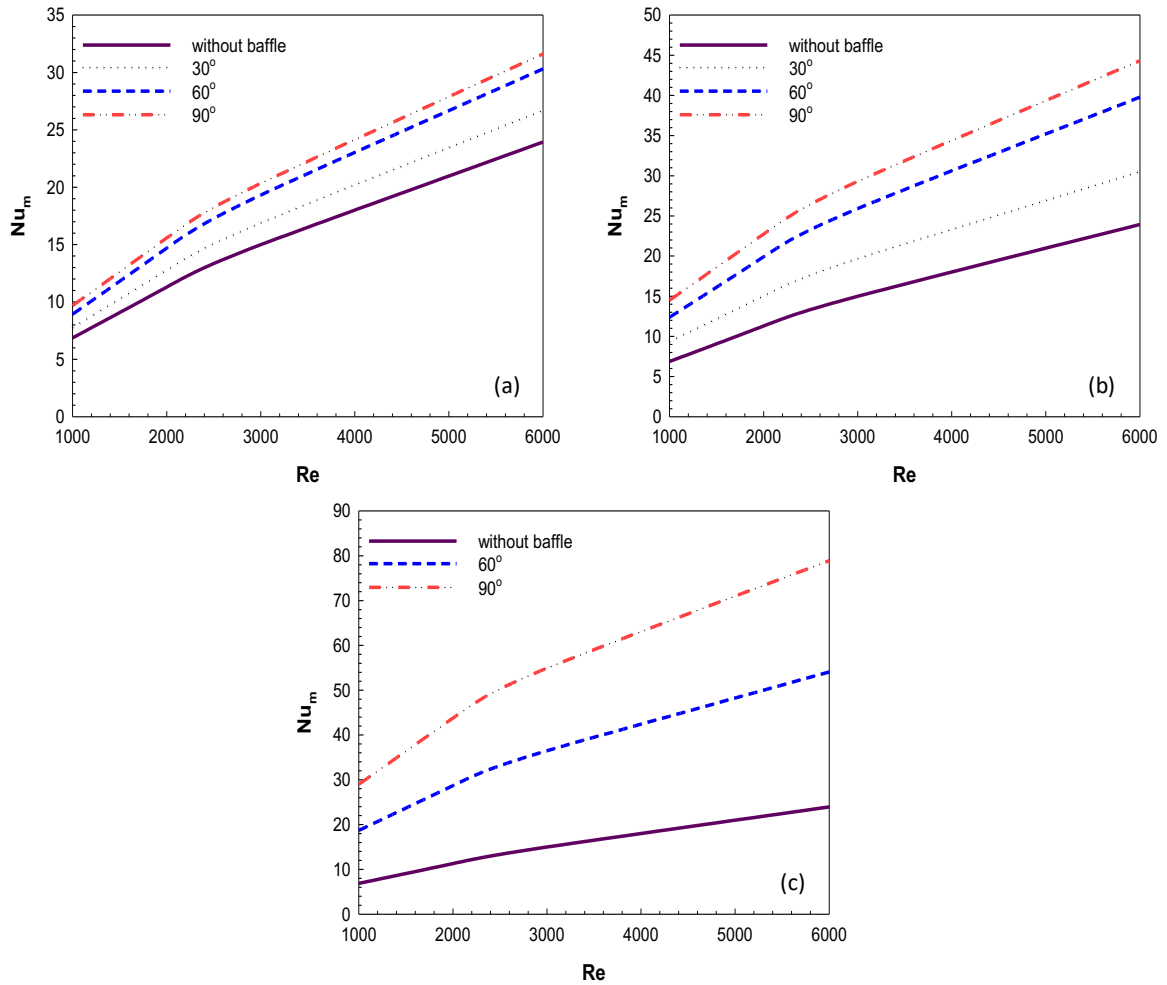
**Fig. 7.** Mean Nu number ($Nu_m$) variations of triangular corrugated rectangular ducts for the non-baffle and with baffle-angled for the baffle height of (a) 0.25H (b) 0.5H (c) 0.75H

In Figure 8, temperature variations of the fluid at the outlet of the rectangular channel with triangular corrugations are depicted, considering different baffle angles (30°, 60°, and 90°) and height arrangements of (a) 0.25H, (b) 0.5H, and (c) 0.75H, respectively. Observations from the figure reveal that the temperature values of the fluid at the exit of the duct decrease with increasing Reynolds number. This decrease is attributed to the enhanced heat transfer efficiency associated with higher fluid velocities.

Moreover, temperature values increase as the baffle angle and height are increased. This increase in temperature is due to the improved heat transfer achieved by directing the flow towards the triangular corrugations through the use of baffles. Comparing with the non-baffled situation, the highest temperature values are obtained for the duct with a 90° baffle angle and 0.75H height. This configuration enhances heat transfer efficiency to the extent that it results in the highest temperature values at the duct outlet.
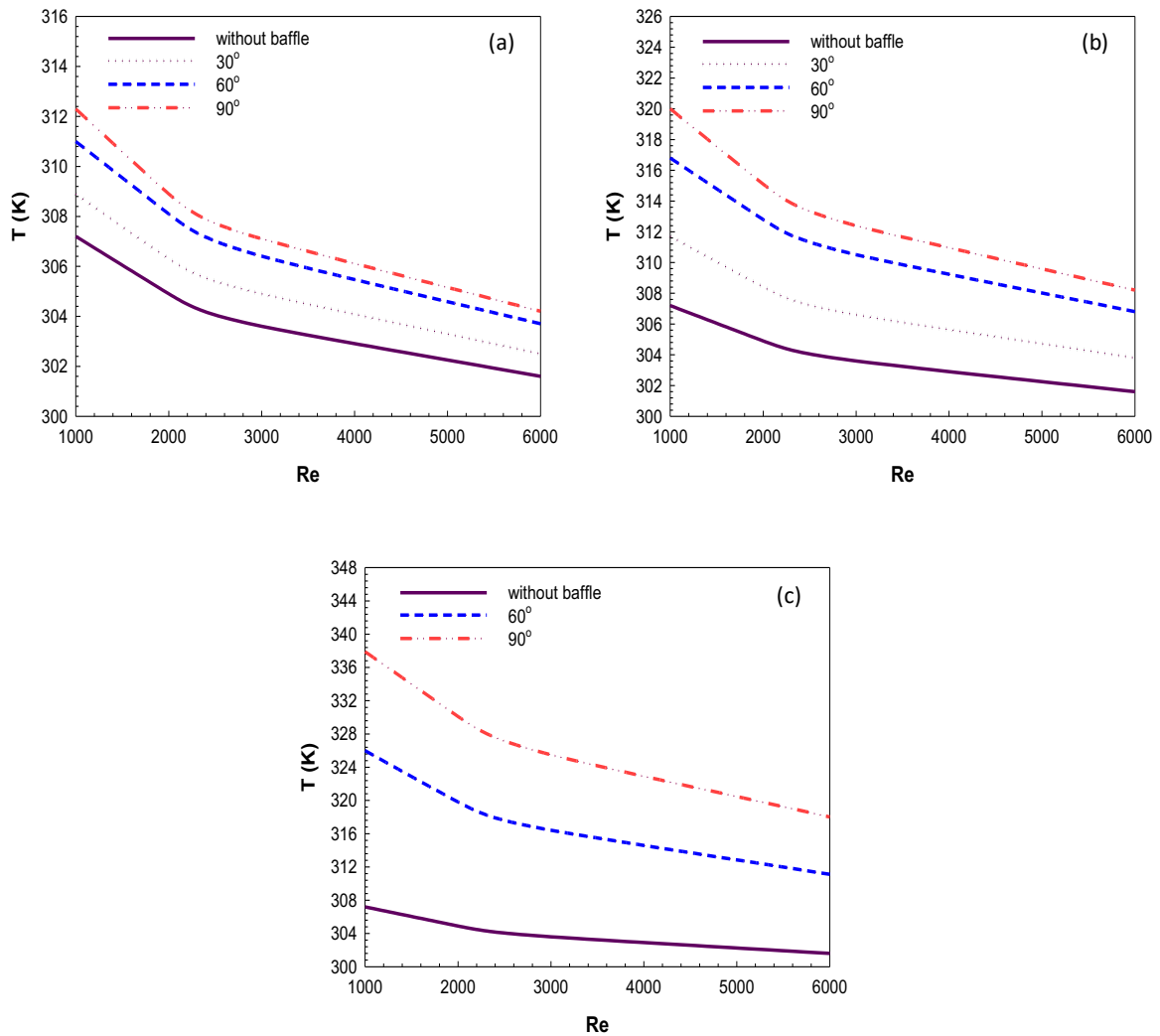
**Fig. 8.** Fluid outlet temperature variations of triangular corrugated rectangular ducts for the non-baffle and with baffle-angled for the baffle height of (a) 0.25H (b) 0.5H (c) 0.75H

In Figure 9, variations of the Performance Evaluation Criterion (PEC) for rectangular channels with triangular corrugations are depicted as a function of Reynolds number (Re), considering different baffle angles (30°, 60°, and 90°) and heights of (a) 0.25H, (b) 0.5H, and (c) 0.75H, respectively. PEC is a thermal-hydraulic performance factor, representing the ratio of the mean Nusselt number (Nu) enhancement to the increase in pressure drop (Δp) in the baffled state compared to the non-baffled state. Observations from the figure indicate that the PEC number decreases with increasing baffle angle, height, and Reynolds number. This decrease occurs because the enhancement in pressure drop (Δp) outweighs the increase in Nu, resulting in a lower PEC value. For example, at Re=1000, the PEC number is 84.50% higher at a baffle height of 0.25H and a baffle angle of 30° compared to the 90° angled condition. This suggests that the 30°

baffle angle configuration at a height of 0.25H offers better thermal-hydraulic performance, as it achieves a higher PEC number due to a more favourable effect between Nu improvement and pressure drop increase. Although the PEC value decreases with the increase in the baffle height and angle, the fact that relatively higher PEC number values are obtained at low height and angle values shows that the investigated geometries have potential to be used in heat transfer applications in order to use energy more efficiently and economically, considering the increase in heat transfer performance achieved. Similar results were obtained in the studies in the literature (Li and Gao (2017), Feng et al. (2022) and Liang et al. (2019)), and with the addition of baffles to the channels, a significant pressure drop and friction factor increase were observed despite the increase in the Nu number.
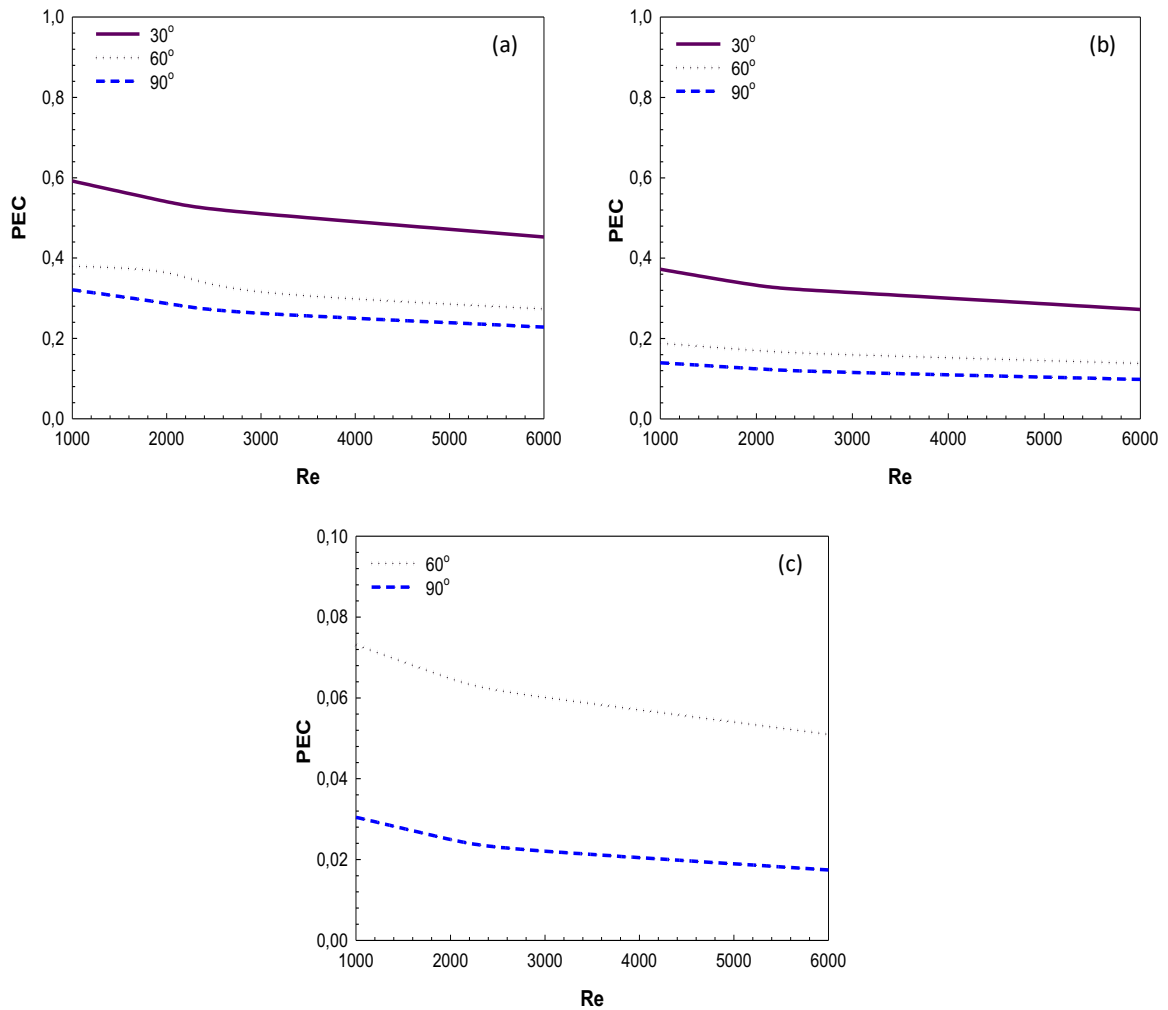
**Fig. 9.** Performance Evaluation Criterion (PEC) number variations of triangular corrugated rectangular ducts for the without baffle and with baffle-angled for the baffle height of (a) 0.25H (b) 0.5H (c) 0.75H

## CONCLUSIONS

This study comprehensively investigates the effects of various rectangular baffle angles and heights in rectangular channels with triangular corrugations on several parameters including heat transfer (Num), fluid outlet temperature, and the performance evaluation criterion (PEC) taking into consideration of pressure drop. The findings are summarized as follows:

Introduction of baffles into the rectangular channel redirects the fluid flow towards the triangular corrugations, increasing the flow velocity and turbulence within the fluid and corrugations. Particularly, at higher baffle angles and heights, such as 60° and 90° with a 0.75H height, the fluid velocity increases significantly, resembling a jet flow-like situation.

Baffles intensify turbulence within the duct, enhancing heat transfer. This increase in turbulence intensity is particularly pronounced at the baffle tips and corrugation tops, and it penetrates deeper into the corrugations and baffle spaces with higher baffle angles and heights.

Temperature decreases along the channel with increasing Reynolds number but increases with higher baffle angles and heights. However, temperature fluctuations, especially at duct entrances, are observed based on the baffle angle and height configurations. Channels with a 90° baffle angle and 0.75H height exhibit more periodic and regular temperature peaks.

Mean Nusselt number (Num) increases with higher Reynolds numbers, with the maximum Num achieved at a baffle angle of 90°. The highest Num value is observed at a 90° angle and 0.75H baffle height, with a 197.56% increase compared to a 0.25H baffle height at Re=6000.

Outlet temperature increases with higher heat transfer improvement resulting from increased baffle angle and height. The highest temperature values are obtained for channels with a 90° baffle angle and 0.75H height, particularly in non-baffled situations.

240

Performance Evaluation Criterion (PEC) decreases with increasing baffle angle, height, and Reynolds number due to the greater increase in pressure drop compared to the increase in Num. Specifically, for Re=1000, PEC is 84.50% higher at a 0.25H baffle height and 30° baffle angle compared to a 90° angle condition.

Overall, this study provides valuable insights into the thermal-hydraulic performance of rectangular channels with triangular corrugations and demonstrates the significant impact of baffle angle and height configurations on various performance parameters.

## NOMENCLATURE

| | |
|---|---|
| $A_c$ | Jet inlet cross section, [m$^2$] |
| $H$ | Channel height, [m] |
| $L$ | Channel lenght, [m] |
| $W$ | Channel width, [m] |
| $D_h$ | Hydraulic diameter of the channel, [m] |
| $h$ | Local convective heat transfer coefficient, [Wm$^{-2}$K$^{-1}$] |
| $k$ | Thermal conductivity, [Wm$^{-1}$K$^{-1}$] |
| $V$ | Fluid velocity in the channel entry, [ms$^{-1}$] |
| $c_p$ | Specific heat capacity of the fluid, [Jkg$^{-1}$K$^{-1}$] |
| $P$ | Jet inlet cross section perimeter length,[m] |
| $p$ | Pressure, [Nm$^{-2}$] |
| $T$ | Temperature, [K] |
| $u, v, w$ | Velocity components of x,y,z directions, [ms$^{-1}$] |
| $u', v', w'$ | Fluctuating velocity components in x,y,z directions, [ms$^{-1}$] |
| $\overline{u}, \overline{v}, \overline{w}$ | Mean velocities in coordinates, [ms$^{-1}$] |
| $Re$ | Reynolds number [=V$_\infty$D$_h$/v] |
| $Nu$ | Local Nusselt number [=hL/k] |

### Greek Symbols

| | |
|---|---|
| $\mu$ | Dynamic viscosity, [kgs$^{-1}$m$^{-1}$] |
| $\mu_t$ | Turbulent viscosity, [kgs$^{-1}$m$^{-1}$] |
| $\upsilon$ | Kinematic viscosity, [m$^2$s$^{-1}$] |
| $\rho$ | Density, kgm$^{-3}$ |
| $\phi$ | Viscous dissipation term, [m$^2$s$^{-3}$] |
| $k'$ | Turbulance kinetic energy, [m$^2$s$^{-2}$] |
| $\varepsilon$ | Turbulent dissipation rate, [m$^2$s$^{-3}$] |
| $\varphi$ | Rectangular baffle angle, [°] |

### Subscripts

| | |
|---|---|
| s | Surface |
| Sm | Surface mean |
| ∞ | Fluid |
| m | Mean |

## REFERENCES

Ajeel R.K., Salim W.S.-I.W., Hasnan K. Influences of geometrical parameters on the heat transfer characteristics through symmetry trapezoidal-corrugated channel using SiO₂-water nanofluid, Int. Comm. Heat Mass Transf. 101, 1–9, 2019.

Ajeel R.K., Salim W.S.-I.W., Hasnan K. Experimental and numerical investigations of convection heat transfer in corrugated channels using alumina nanofluid under a turbulent flow regime, Chem. Eng. Res. Des. 148, 202-217, 2019.

Ajeel R.K., Salim W.S.-I.W., Hasnan K. An experimental investigation of thermal-hydraulic performance of silica nanofluid in corrugated channels, Ad. Powder Technol. 30, 2262–2275, 2019.

Alnak D.E. Thermohydraulic performance study of different square baffle angles in cross-corrugated channel, Journal of Energy Storage, 28, 101295, 2020.

Aslan, E., Taymaz, I., Cakır, K., Eker Kahvecı, E. Numerical and experimental investigation of tube bundle heat exchanger arrangement effect on heat transfer performance in turbulent flows, J. of Thermal Science and Technology 43 (2), 175-190, 2023.

Akbarzadeh, M., Rashidi, S., Esfahani, J. A. Influences of corrugation profiles on entropy generation, heat transfer, pressure drop, and performance in a wavy channel, Appl. Therm. Eng. 1 (2017) 278–291.

Feng C.N., Liang C.H., Li Z.X. Friction factor and heat transfer evaluation of cross-corrugated triangular flow channels with trapezoidal baffles, Energy&Buildings, 257, 111816, 2022.

FLUENT User's Guide, Fluent Inc. Lebanon, Netherland, 2003.

Guo-Yan Z., Shan-Tung T., Hu-Gen M. Numerical and experimental study on the heat transfer and pressure drop of compact cross-corrugated recuperators, J. Heat Transf. 136, 071801, 2014.

Karabulut, K. Investigation of heat transfer improvements of graphene oxide-water and diamond-water nanofluids in cross-flow-impinging jet flow channels having fin, J. of Thermal Science and Technology 43 (1), 11-30, 2023.

Karabulut K. Heat transfer increment study taking into consideration fin lengths for CuO-water nanofluid in cross flow-impinging jet flow channels, Thermal Science, 27 (6A), 4345-4360, (2023).

Karabulut, K., Alnak, Y. A study on microchip cooling performance increment by using air jet impingement with one and double rows. Proceedings of the Institution of Mechanical Engineers, Part E: Journal of Process Mechanical Engineering, 0 (0), 2023.

Karabulut, K., Alnak, D.E. Study of cooling of the varied designed warmed surfaces with an air jet impingement, Pamukkale Univ. J. Eng. Sci. 26 (1), 88-98, 2020.

Karabulut, K. Heat transfer improvement study of electronic component surfaces using air jet impingement, J. Comput. Electron 18, 1259-1271, 2019.

Krishnan E.N., Ramin H., Guruabalan A., Simonson C.J. Experimental investigation on thermo-hydraulic performance of triangular cross-corrugated flow passages, Int. Commun. Heat Mass Tran. 122, 105160, 2021.

Liang C.H., Feng C.N., Lei T.Y., Li Z.X. Numerical studies on the effect of the baffle on the heat transfer and flow in cross-corrugated triangular ducts, IOP Conf. Series: Earth and Environmental Science, 238, 012086, 2019.

Liu X.P., Niu J.L. Effects of geometrical parameters on the thermohydraulic characteristics of periodic cross-corrugated channels, Int. J. Heat Mass Tran. 84, 542–549, 2015.

Li Z.X., Zhong T.S., Niu J.L., Xiao F., Zhang L.Z. Conjugate heat and mass transfer in a total heat exchanger with cross-corrugated triangular ducts and one-step made asymmetric membranes, Int. J. Heat Mass Tran. 84, 390–400, 2015.

Li Z-X., Sun S-Q., Wang C., Liang C.H., Zeng S., Zhong T., Hu W-P., Feng C-N. The effect of trapezoidal baffles on heat and flow characteristics of a cross-corrugated triangular duct, Case Studies in Thermal Engineering 33, 101903, 2022.

Li Z., Gao Y. Numerical study of turbulent flow and heat transfer in cross-corrugated triangular ducts with delta-shaped baffles, Int. J. Heat Mass Transf. 108, 658–670, 2017.

Liang C.H., Feng C.N., Lei T.Y., Li Z.X. Numerical studies on the effect of baffle on the heat transfer and flow in cross-corrugated triangular ducts, IOP Conf. Series: Earth and Environmental Science, 238, 012086, 2019.

Muley A., Manglik R.M. Experimental study of turbulent flow heat transfer and pressure drop in a plate heat exchanger with Chevron plates, ASME J. Heat Transfer, 121, 110–117, 1999.

Saha S.K., Khan A.H. Numerical study on the effect of corrugation angle on thermal performance of cross corrugated plate heat exchangers, Therm. Sci. Eng. Prog. 20, 100711, 2020.

Saim R., Bouchenafa R., Benzenine H., Oztöp H.F., Al-Salem K., Abboudi S. A computational work on turbulent flow and heat transfer in a channel fitted with inclined baffles, Heat Mass Trans 49, 761–774, 2013.

Scott K., Lobato J. Mass transport in cross-corrugated membranes and influence of $TiO_2$ for separation processes, Industrial&Engineering Chemistry Research, 42 (22), 5697-5701, 2003.

Wang S.J., Mujumdar A.S. A Comparative study of five low Reynolds number k-ε models for impingement heat transfer, Applied Thermal Engineering, 25, 31-44, 2005.

Welty, J., Rorrer, G.L., Foster, D.G. revised 6th edition, Fundamentals of Momentum, Heat, and Mass Transfer 768 Wiley, United States, 2014 ISBN: 978-1-118-94746-3.

Yıldızeli, A., Cadırcı, S. Numerical investigation of plate cooling using multiple impinging jets in different alignments, J. of Thermal Science and Technology 43 (1), 1-10, 2023.

Zhang L. Numerical study of periodically fully developed flow and heat transfer in cross-corrugated triangular channels in transitional flow regime, Numerical Heat Transfer Part A: Applications, 48 (4), 387-405, 2005.

Zhang L.Z. A reliability-based optimization of membrane-type total heat exchangers under uncertain design parameters, Energy, 101, 390-401, 2016.

Zhang L.Z. Turbulent three-dimensional air flow and heat transfer in a cross-corrugated triangular duct, J. Heat Tran. 127, 1151–1158, 2005.

Zhang L.Z. Numerical study of periodically fully developed flow and heat transfer in cross-corrugated triangular channels in transitional flow regime, Numer. Heat Tran. 48, 387–405, 2005.

Zhang L.Z., Chen Z.Y. Convective heat transfer in cross-corrugated triangular ducts under uniform heat flux boundary conditions, Int. J. Heat Mass Tran. 54, 597–605, 2011.

Zhang, L.Z. Convective mass transport in cross-corrugated membrane exchangers, Journal of Membrane Science 260, 75–83, 2005.

Zimmerer C., Gshwind P., Gaiser G., Kottke V. Comparison of heat and mass transfer in different heat exchanger geometries with corrugated walls, Exp. Therm. Fluid Sci. 26, 269–273, 2002.

**Statements&Declarations**

**Competing Interests and Funding**

The author has no relevant financial or non-financial interests to disclose.

**Author Contribution**

The author contributed to the study's conception and design. Material preparation, data collection and analysis were performed by Yeliz ALNAK. The first draft of the manuscript was written by Yeliz ALNAK and the author commented on previous versions of the manuscript. The author read and approved the final manuscript.

**Data Availability**

The data that support the findings of this study are available from the corresponding author upon reasonable request.

**Author information**

Yeliz Alnak received her bachelor's degree from Ataturk University of machine engineering, Erzurum, Turkiye, in 2003. She is her master's degrees from Sivas Cumhuriyet University, machine engineering, Sivas, Turkiye, in 2007. She is her Ph.D. from Firat University, in machine train-ing, Elazığ, Turkiye, in 2020. She is a doctoral faculty member at Sivas Cumhuriyet University Faculty of Technology. Her research interests including energy, CFD, Ansys, fluid flow.

# ISI KÖPRÜLERİNDE HİGROTERMAL PERFORMANSIN VE ISI KAYIPLARININ İNCELENMESİ

**Filiz UMAROĞULLARI\*, Esma MIHLAYANLAR\*\*, Melek SEYİT\*\*\***
Trakya Üniversitesi, Mimarlık Fakültesi, Mimarlık Bölümü, Edirne
filizu@trakya.edu.tr, ORCID: 0000-0002-9503-1816*
emihlayanlar@trakya.edu.tr, ORCID: 0000-0002-0020-2839**
melekseyit@trakya.edu.tr, ORCID: 0000-0003-1916-7508***

**Özet:** Enerji verimliliğinde önemli bir potansiyele sahip olan binalarda enerji kaybının en büyük kısmı bina kabuğundan gerçekleşmektedir. Günümüzde; farklı kalınlık ve özellikteki çeşitli katmanlardan oluşan bina kabuğunda, ısı kaybının azaltılmasında, ısı köprülerinden kaçınmaya yönelik uygulamalar en temel yaklaşımlardan biridir. Diğer bileşenlere oranla ısı iletiminin daha fazla olduğu ve nem problemlerinin öncelikle karşılaşıldığı alanlar olan ısı köprülerinin bina enerji performansının değerlendirilmesinde önemi büyüktür. Günümüzde yaygın olarak uygulanan betonarme karkas yapım sisteminde çeşitli nedenlerle çok sayıda ısı köprüsü meydana gelmektedir. Köşe noktalarında meydana gelen ısı köprüleri binanın ortalama ısı geçirgenliğini önemli ölçüde etkiler. Aynı zamanda yoğuşma ve küf oluşumunun da yaygın görüldüğü bölgelerdir. Bu bölgelerin yalıtım durumu da ısıl ve higrotermal performansı etkilemektedir. Tasarım aşamasında bina kabuğunun higrotermal performansı hesaplanarak gerekli önlemler alınmalıdır. Bu amaçla çeşitli benzetim araçları kullanılmaktadır. Böylece tasarım aşamasında bina kabuğunun enerji, konfor ve sağlık koşullarını sağlaması mümkün olabilecektir. Bu çalışmada ısı köprülerindeki ısı kayıpları ve higrotermal performans araştırılmıştır. Mevcut bir konut yapısının köşe noktasında meydana gelen ısı köprüleri, yalıtımsız, kısmi yalıtımlı ve dışardan yalıtımlı olma durumlarına göre değerlendirilmiştir. Çalışma kapsamında Quick Field 6.3 ve Wufi 2D-4.3 programları aracılığıyla yapılan analizlerden ısı köprülerinin kısmi yalıtılması durumunda kesintisiz dışarıdan yalıtımlı olma durumuna göre %37 daha fazla ısı kaybı meydana geldiği görülmüştür. Aynı zamanda higrotermal performans açısından da kesintisiz dışardan yalıtımlı durumda yoğuşma riski görülmemektedir.
**Anahtar kelimeler:** Isı köprüsü, ısı kaybı, yoğuşma, higrotermal performans, ısı yalıtımı

# INVESTIGATION OF THERMAL BRIDGE EFFECT ON HEAT LOSSES AND HYGROTHERMAL PERFORMANCE

**Abstract:** The largest energy loss in buildings, which have a significant potential for energy efficiency, occurs in the building envelope. At present, one of the most basic approaches to reducing heat loss in the building envelope, which consists of various layers of different thicknesses and properties, is to avoid thermal bridges. Thermal bridges are areas where heat conduction is higher than other components of the building and where moisture problems are primarily encountered and are of great importance in the evaluation of building energy performance. In today's widely applied reinforced concrete frame construction system, many thermal bridges occur for various reasons. Thermal bridges occurring at the corner points of the building significantly affect the average thermal transmittance of the building. These areas are also the areas where condensation and mould formation are common. The insulation status of these regions affects the thermal and hygrothermal performance. Necessary measures should be taken by calculating the hygrothermal performance of the building envelope during the design phase. Various simulation tools are used for this purpose. In this way, the building envelope can provide energy, comfort, and health conditions during the design phase. In this study, heat losses and hygrothermal performance of thermal bridges are investigated. The thermal bridges occurring at the corner point of an existing residential building were evaluated according to the conditions of uninsulated, partially insulated and externally insulated. Analyses within the scope of the study were carried out with Quick Field 6.3 and Wufi 2D-4.3 programs. In the analyses, it is seen that 37% more heat loss occurs in the case of partial insulation of thermal bridges than in the case of continuous external insulation. Likewise, in terms of hygrothermal performance, there is no condensation risk in the case of continuous external insulation.
**Keywords:** Thermal bridge, heat loss, condensation, hygrothermal performance, thermal insulation

# 1. GİRİŞ (INTRODUCTION)

Nüfus artışı, enerji kıtlığı, iklim değişikliği etkileri ve sera gazı emisyonlarının artması küresel endişeleri de zamanla artırmaktadır. Enerji kullanımı bağlamında inşaat sektörü en fazla enerji tüketen sektörlerden biridir. Binalar, küresel olarak birincil enerji tüketiminin yaklaşık üçte birini tüketmekte olup toplam enerji kaynaklı sera gazı emisyonlarının da üçte birinden sorumludur (IEA, 2013). Artan bina stokuna karşı enerji kayıplarının ve olumsuz çevresel etkilerinin azaltılmasında bina enerji verimliliği ön plana çıkmaktadır. Uluslararası ölçekte topluluklar ve ülkeler bazında bina enerji verimliliği ve karbonsuzlaşmaya yönelik yıllara bağlı hedefler belirlenmektedir. Avrupa Birliği Konseyi iklim değişikliği ile mücadeleyi güçlendirmek amacıyla 1 Ocak 2021 tarihinden itibaren tüm yeni binaların yaklaşık Sıfır Enerjili /Zero Energy Buildings (nZEB) olmasını, 2030 yılında emisyonlardaki %40 azaltım hedefini de %50-55 oranına çıkarılmasını hedeflemiştir. 2050 yılına kadar iklim açısından karbon nötr bir AB'ye ulaşma hedefine onay verilmiştir (European Comission, 2020). AB'ye üye bütün ülkelerde, AB Bina Enerji Performansı Direktifi (EPBD) kabul edilerek uygulanmaktadır (Garay vd, 2014). Buna bağlı olarak bina enerji kodları belirlenmiştir. Binalarda enerji verimliliğini belirleyen çeşitli faktörler bulunmaktadır. Bina kabuğu ve bina kabuğunun ısıl performansı göz önünde bulundurulması gereken önemli faktörlerdendir (Goggins vd, 2016). Bu bağlamda, bina kabuğundaki ısı köprülerinin önemi artmıştır. Isı köprüleri, daha yüksek ısıl iletkenliğe sahip bina kabuğunun bir parçasını temsil etmekte ve onu çevreleyen elemanlardan daha yüksek ısı kayıplarına neden olmaktadır. Isı köprüleri, yapı bileşeninin bünyesinde çevresine göre daha az ısıl dirence sahip olan bölgelerdir. Isı, bu bölgelerdeki bileşenler üzerinden düşük sıcaklığa doğru ilerleyerek ısı kaybeden bir köprü oluşturmaktadır. Dolayısıyla bina kabuğunun ısıl performansını değerlendirirken bu ek ısı kayıplarını hesaba katmak önemlidir (O'Grady, 2018).

Isı köprüsü normalden daha fazla ısı iletiminin gerçekleştiği sınırlı alanlardır. Isı iletimi, sıcaklığın yüksek olduğu bölgeden düşük olduğu bölgeye ilerler ve vektörel bir büyüklüktür. Isı köprülerinin grafiksel gösteriminde ısı geçişlerinin yönünü anlayabilmek için ısı izoterm eğrileri kullanılmaktadır. Isının aktığı doğrultuyu ısı akısı vektörü gösterir ve ısı akısı vektörleri bir vektörel alan oluşturur. Isı akısı vektörleri izoterm eğrilerine dik doğrultudadır. Isı köprüsünün oluştuğu durumlarda; ısı akısının, açık şekilde dikliği ve sabit sıcaklık eğrilerinin (izoterm eğrilerinin) paralellikleri bozulmaktadır.

Bina kabuğunda oluşabilecek ısı köprüleri, kabuğun ısıl direnci üzerinde etkilidir. Isı köprülerinin soğuk (IEA, 2013; Evola vd, 2011) ya da sıcak (Bergero and Chiari, 2018; De Angelis and Serra, 2014; Martins vd, 2016; Zhao vd, 2022) iklim şartlarında enerji tüketimi üzerindeki etkisi önemlidir ve özellikle mimari

kısıtlamalar nedeniyle dış yalıtımın uygulanmadığı veya birçok çıkmanın bulunduğu tasarımlarda karşımıza çıkmaktadır (Erhorn-kluttig vd, 2009).

Bir yapıda ısı köprüsü oluşumuna neden olan detaylar; kiriş, kolon (Martin, Campos-Celador, Escudero vd, 2012), hatıl, balkon çıkmaları (Ge vd, 2013; Aghasizadeh vd, 2022), duvar (Aguilar vd, 2014; Ascione vd, 2013; Dumitrescu vd, 2017; Kotti vd, 2017; Marincioni vd, 2015; Viot vd, 2015) döşeme (Garay vd, 2014; Ascione vd, 2013; Kotti vd, 2017; Fantucci vd, 2017; Martin, Escudero, Erkoreka vd, 2012; El Saied vd,, 2022), kapı-pencere doğramaları (Asdrubali vd, 2012; Ahrab ve Akbari, 2013; Theodosiou, 2019; Terentjevas vd, 2021), çatı elemanları (Martin, Escudero, Erkoreka vd, 2012; Ahrab ve Akbari, 2013; Ascione vd, 2012) ve cephe kaplama elemanları (Theodosiou vd, 2017, Theodosiou vd, 2019) gibi elemanlar ve birleşim noktaları çeşitli çalışmalarda araştırılmıştır.

Binalarda ısı köprüsü çeşitli nedenlerden kaynaklanabilmektedir. Isı köprüsünün oluşma nedenleri (BS EN ISO 10211, 2007);

* Bina kabuğunun belli bir kısmının ya da tamamının farklı ısıl iletkenliklere sahip malzemelerden oluşması,
* Bina kabuğunun kalınlığındaki bir değişiklik,
* Binanın ya da yapı elemanlarının geometrisindeki farklılıklar (bina formu, köşe noktaları, balkon gibi çıkmalar),
* Duvar-zemin-tavan gibi bağlantı noktalarında dış ve iç yüzey büyüklüklerinde farklılıklar (ısıtma radyatörlerinin konumlandırıldığı duvarlar),
* Akışkan akımından kaynaklanan ısı köprüleri (mekân içinden geçen tesisat boruları) olarak sıralanabilir (BS EN ISO 10211, 2007).

Tablo 1'de binalarda; geometri, strüktür ve malzeme değişiminden kaynaklanan ısı köprüleri şematik olarak gösterilmektedir.

Genel olarak yapı bileşenleri veya yapı formunun değiştiği herhangi bir birleşme noktasında meydana gelen ısı köprüleri ile ısı köprüsü oluşmayan bölgeler karşılaştırıldığında;
a) Isı akış hızındaki değişiklik,
b) İç yüzey sıcaklığındaki değişiklik gibi iki temel sonuç ortaya çıkar (BS EN ISO 10211, 2007).

Isı köprüleri, etki etme şekillerine göre doğrusal ve noktasal olarak gruplandırılır. Yapının uzunluğuna göre genişliği dar olan ve yapının genişliği boyunca devam edenler "doğrusal ısı köprüleri" dir. Doğrusal ısı köprüleri, üç ortogonal eksenden biri boyunca düzgün bir kesite sahiptir (Prata vd, 2018).

**Tablo 1.** Binalarda geometri, strüktür ve malzeme değişiminden kaynaklanan ısı köprüleri
(Thermal bridges caused by geometry, structure and material changes in buildings)

| Isı köprüsü oluşum sebepleri | | | |
|---|---|---|---|
| Geometri farklılığı | Strüktür + Malzeme farklılığı | Strüktür + malzeme + Geometri farklılığı | |



Etkisi bir noktadaki ısıl geçirgenlik ile temsil edilen sınırlandırılmış olanlar "noktasal ısı köprüleri" dir (BS EN ISO 10211, 2007). Bağıl olarak küçük boyutlu, yapının kalınlığı boyunca uzamayan, yapı yüzeylerine dik olarak konumlanan birleşim elemanları çevresindeki ısı köprüleridir.

Isı köprüleri, sıcaklık dağılımını etkileyerek dağılımın bölgesel olarak bozulmasına neden olur. Ayrıca ısı geçirgenlik direncini azaltarak yüzey sıcaklıklarının düşmesine neden olduğu için elemanın yüzey sıcaklığı ile ortam sıcaklığı arasındaki farkın artmasına neden olur. Yapı kabuğunun ısı geçirgenliğine bağlı olarak yüzey sıcaklıkları önemli ölçüde değişir (Erhorn-kluttig vd, 2009). Bu fark yaz ve kış koşullarından etkilenir.

Soğuk iklimlerde binalardaki ısı köprüleri önemli bir sorundur. Çünkü bu alanlarda sadece ısı kayıpları değil, aynı zamanda yoğuşma ve küf gelişimi de söz konusudur. İç yüzey sıcaklıklarında ortaya çıkan azalma sonucu su buharı faz değiştirerek sıvılaşmakta ve küflenme ortaya çıkmaktadır. Donma-çözülme etkileri sonucunda yapı elemanının bünyesindeki gerilmeler artarak yüzeylerde kabarma ve dökülmeler görülmekte hatta aşırı gerilmeler zorlanmalara ve çatlaklara neden olabilmektedir. Ayrıca yoğuşma sırasında su ile dolan boşlukların ısıl iletkenlik özellikleri de artmaktadır. Elektriklenme sonucu yüzeylerde tozlanma oluşmaktadır. Bunun yanı sıra donatılı elemanlarda görülen ısı köprülerinde, korozyon gibi kimyasal paslanmalar da söz konusudur. Bu durum yapı malzemelerinin deformasyonuna, yapı hasarlarına ve iç hava kalitesinin bozulmasına yol açacaktır (Evola vd, 2011; Erhorn-kluttig vd, 2009). Dolayısıyla yapı sağlığı üzerinde de önemli bir etkiye sahip olan ısı köprüleri, enerji korunumunu, iç ortam kalitesini ve kullanıcı sağlığını da etkilemektedir. Isı köprülerinin iyileştirilmesi ekonomik açıdan yarar sağlamakla birlikte karbondioksit emisyonlarının azaltılması gibi enerji verimliliği ve çevresel faydalar da sağlamaktadır (Evola vd, 2011).

Isı köprülerinin enerji tüketimi üzerindeki etkisinin azaltılmasında bina kabuğunun sürekli bir şekilde yalıtılması büyük önem taşır (Erhorn-kluttig vd, 2009).

Bina kabuğunda yapı elemanlarından (duvar, döşeme, pencere, çatı vb.) farklı oranlarda ısı kayıpları gerçekleşmektedir. Isı köprülerinden kaynaklanan ısı kayıpları %20-50 arasında değişen büyük bir orana sahiptir (Theodosiou vd, 2019). Şekil 1'de yalıtımsız bir binada gerçekleşen ısı kayıpları gösterilmiştir. Binaların ısı kayıplarına karşı korumanın en etkili yolu, uygun ve kesintisiz ısı yalıtımının yapılmasıyla sağlanabilmektedir. Literatürde yapı kabuğunda yalıtımın yeri ve kalınlığının belirlenmesinde pek çok çalışma bulunmaktadır. Özel (2022), duvar yönüne bağlı olarak tuğla duvar gövdesi üzerinde optimum yalıtım kalınlığını ısıtma ve soğutma yükleri üzerinden değerlendirmektedir (Özel, 2022). Çağlayan (2022), Türkiye'nin 81 ili için yıllık enerji tüketimi ve maliyet analizi ile optimum yalıtım kalınlıklarını belirlemeye yönelik çalışmada hem tuğla duvar hem de aynı kalınlıkta betonarme bileşen için hesaplamalar yapmıştır (Çağlayan vd, 2022).
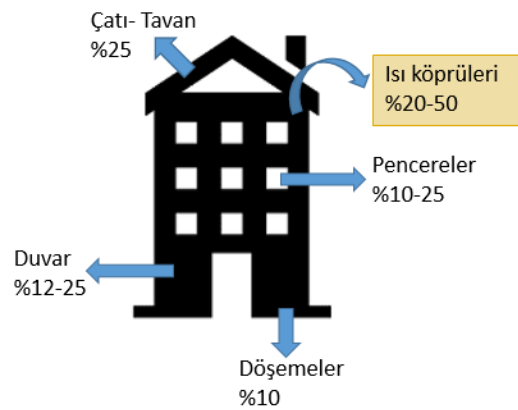


**Şekil 1.** Yalıtımsız bir binada ısı kayıpları
(Heat losses in uninsulated building)

Isı kayıplarının yüksek olduğu ısı köprüsü bölgelerinin analizlerinde ısı transferi iki boyutludan tek boyuta indirgenerek hesaplanmaktadır. Isı iletimi hesaplamalarında nümerik yaklaşımlar önerilmektedir (El Saied vd, 2022; Asdrubali vd, 2012; Terentjevas, 2021; Al-Sanea ve Zedan, 2012). Yapı bileşenlerinin ısıl davranışını değerlendirirken, ısıl geçirgenliğin deneysel

olarak belirlenmesinde genellikle sıcak kutu (hot box) test) yöntemi (IEA, 2013; ISO 8990, 1994; Asdrubali ve Baldinel, 2011; Asdrubali vd, 2012; Fang vd, 2006) termal görüntülemelerle analiz edilmesinde kızılötesi termografi cihazları (IEA, 2013; O'Grady vd, 2018) ve sayısal olarak hesaplanmasında bir dizi hesaplamalar ve algoritmalar (Zalewski vd, 2010) kullanılmaktadır.

Çalışmalarda ısı köprülerinin etki alanları sabit rejim (Garay vd, 2014; Martin, Campos-Celador, Escudero vd, 2012; Aguilar vd, 2014; Aghasizadeh vd, 2022; Capozzoli vd, 2013) ve dinamik rejim (Martin, Campos-Celador, Escudero vd, 2012; Al-Sanea ve Zedan, 2012; BrumĂ vd, 2015; Quinten ve Feldheim, 2016) şartlarından birine göre ya da her ikisine (Martin, Campos-Celador, Escudero vd, 2012) göre ele alınarak değerlendirilmektedir. Yapılan incelemelerde QUICK FIELD (Karacavus ve Can, 2008), ANSYS (CFX, FLUENT) (O'Grady vd, 2018; Martins vd, 2016; Martin, Campos-Celador, Escudero vd, 2012; Aghasizadeh vd, 2022; Ascione vd, 2012; Theodosiou vd, 2017), THERM (De Angelis ve Serra, 2014; Kotti vd, 2018; El Saied vd, 2022; Terentjevas vd, 2021; Romero vd, 2021), MATLAB (Aguilar vd, 2014; Martin, Escudero, Erkoreka vd, 2012), ANOVA-FAST (Capozzoli, Gorrino, Corrado vd, 2013; Capozzoli, Gorrino, Corrado, Grinzato vd, 2013), WUFİ (Ge ve Baba, 2015; Antretter vd, 2013) gibi yazılım araçları ve benzetim ile elde edilen sonuçların sayısal modeller yardımıyla hesaplandığı görülmektedir.

Genellikle betonarme (Garay vd, 2014; Evola vd, 2011; Martin, Campos-Celador, Escudero vd, 2012; Real vd, 2016) başta olmak üzere ahşap (Martin, Campos-Celador, Escudero vd, 2012; Viot vd, 2015; Prata vd, 2018), çelik (De Angelis ve Serra, 2014; Martins vd, 2016; Fukuyo, 2003; Schöck Ltd., 2015) ve alüminyum (Theodosiou vd, 2019) yapı elemanları ve bileşenleri ile ilgili ısı kayıpları birçok yönden ele alınmaktadır. Yapılan çalışmalar arasında, yapı elemanına uygulanan yalıtım durumuna göre oluşacak ısı köprüsü ile ilgili ölçümler (Prata vd, 2018), dış duvar elemanı için yalıtım tabakasının kalınlığının artırılması (Martin, Campos-Celador, Escudero vd, 2012) ile yalıtımın ısı köprüsü üzerindeki etkisi incelenmektedir. Ayrıca araştırmacılar yalıtımlı yüksek binaların gerçek ısı kaybının tanımlanmasını ve ısı köprülerinin iyileştirilmesini değerlendiren araçlar geliştirmektedir (Asdrubali vd, 2012).

Türkiye'de genellikle gelişmiş geleneksel yapım sistemlerinden betonarme sistemler tercih edilmektedir. Bu doğrultuda yapılan akademik çalışmalarda da ısı köprüleri ve çevresindeki bölgelerde sıcaklık ve ısı akısı dağılımı incelenmiştir. Yalıtım sistemlerinin sayısal değerler üzerindeki etkisi ele alınmıştır. Uluslararası yayınlarda ise ısı köprülerinde sıcaklık ve ısı akısı dağılımlarının hesaplanması ile ilgili geliştirilen yaklaşımlar ve uygulama sonuçları karşılaştırılmaktadır.

Türkiye'de mevcut veya yeni binalarda enerjinin etkin kullanımının yanı sıra çevre korunumunu da hedefleyen yasal düzenlemeler aşağıda ısı köprüsü ile ilgili standartlar ile verilmektedir.

TS 825 (Binalarda Isı Yalıtım Kuralları) standardı binalarda yıllık ısıtma enerjisi tüketiminin sınırlandırılmasına yöneliktir. Bu standartla birlikte yeni yapılacak binalara yönelik çeşitli tasarım seçenekleri için önerilen hesap metodu ve değerleri uygulanarak, uygun enerji performansını sağlayacak yalıtım kalınlıkları belirlenir. Standarda göre ısı kaybı hesabında ısı köprülerinden iletilen ısı kaybı da değerlendirilmektedir (TS 825, 2013).

AB'nin 2002/91/EC sayılı "Binaların Enerji Performansı Direktifi" doğrultusunda hazırlanan Binalarda Enerji Performans Yönetmeliği (BEPY) ile binaların birincil enerji ve karbondioksit ($CO_2$) emisyonunun sınırlandırılması hedeflenir. Yönetmelik ile sera gazı emisyonlarının sınırlandırılması, ısıtma ve soğutma sistemlerinin kontrolü, bina performansının arttırılması ile uygulama esasları ve çevre korunumu amaçlanır. Dış iklim şartları, iç mekân gereksinimlerini, yerel şartlar ve maliyet faktörü de dikkate alınarak, bir binanın bütün enerji kullanımlarını değerlendirmeyi sağlayacak hesaplama kuralları belirlenir (BEPY, 2010).

Ayrıca 2010'da BEPY kapsamında binalara Enerji Kimlik Belgesi (EKB)'nin hazırlanması amacıyla ulusal hesaplama yöntemi olarak Bina Enerji Performansı Yazılımı (BEP-TR) geliştirilmiştir. Enerji Verimliliği Kanunu'na göre, tüm binaların Enerji Kimlik Belgesi almaları zorunludur. Bu belge düzenlenirken EN 15217 standardı dikkate alınır. BEP-TR ulusal yazılımıyla binanın azami yıllık enerji ihtiyacı belirlenmektedir. Binanın fonksiyonuna, bulunduğu iklim bölgesine, mimari tasarımına ve yürürlükteki zorunlu standartlara göre ısıtma, soğutma, havalandırma, sıcak su ve aydınlatma enerji tüketimi hesaplanır.

TS EN ISO 10211 (Bina yapılarında ısıl köprüler- Isı akışları ve yüzey sıcaklıkları- Ayrıntılı hesaplama yöntemleri) standardı; binalardaki 2 ve 3 boyutlu geometrik ısıl köprülerdeki ısı akışları ve yüzey sıcaklıklarının ayrıntılı hesaplama yöntemlerini açıklamaktadır. Standartta bir binadaki toplam ısı kayıplarının tespitinde ısı akışları ve yüzey buğulanma riskinin tayini için asgari yüzey sıcaklıkların sayısal olarak hesaplanmasında gerekli esaslar belirtilmektedir (TS EN ISO 10211, 2017).

TS EN ISO 14683 (Bina inşaatı-Isıl köprüler-Lineer ısıl geçirgenlik-Basitleştirilmiş metot ve hatasız değerler) standardı; yapı elemanlarında oluşan doğrusal ısıl köprüleri yoluyla ısı akışlarının belirlenmesi için basitleştirilmiş yöntemleri ele almaktadır. Isı köprüsü kataloglarına ve manuel hesaplama yöntemlerine ilişkin şartlar belirtilerek doğrusal ısı geçişleri için varsayılan değerler verilmektedir (TS EN ISO 14683, 2017).

Bu çalışmanın amacı öncelikli olarak ısı köprülerindeki ısı kayıpları ve higrotermal performansın analiz edilmesidir. Literatürde ısıl ve higrotermal performansı birlikte ele alan az sayıda çalışma bulunmaktadır. Türkiye'de yaygın olarak kullanılan betonarme iskelet sistemdeki ısı köprüsü etkilerinin farklı benzetim araçları ile örnek bina üzerinde analizlerin yapılması çalışmanın özgünlüğü açısından önemlidir. Bu amaçla yapı elemanı bazında köşe noktasında bulunan betonarme kolon kesiti farklı yalıtım durumlarına göre iki boyutlu ısı köprüsü etkisi açısından incelenmiştir. Ayrıca çalışma kapsamında örnek binanın yıllık enerji performansı da değerlendirilmiştir. Çalışma metodolojisinde problem tanımı (ısı köprüsü etkileri ve problemleri) ve yöntem (örnek binaya ait veriler ve kullanılan sayısal modeller) açıklanmıştır. Elde edilen bulgular tablo ve grafiklerle analiz edilerek yorumlanmıştır.

## 2. MATERYAL VE METOT (MATERIAL AND METHOD)

Isı köprülerinin oluşum nedenleri, ısı ve nem performansı üzerindeki olumsuz etkileri çalışmanın ana problemini ortaya koymaktadır. Bu doğrultuda Türkiye'deki yapım koşulları açısından yaygın olarak kullanılan betonarme bina tipolojisi örnek olarak seçilmiştir. Örnek binaya ait özellikler tablo ve şekille özetlenmiştir. Isıl ve higrotermal performans; yatay kesitte köşe noktasında bulunan betonarme kolon kesiti, farklı yalıtım durumlarına göre Quickfield ve WUFI programlarıyla belirlenmiştir. Ayrıca binanın toplam enerji performansı BEP-TR programı kullanılarak değerlendirilmiştir. Elde edilen veriler değerlendirilerek ısı köprüsü problemlerinin azaltılmasına yönelik öneriler sunulmuştur. Çalışma kapsamında izlenen yol Şekil 2'de gösterilmektedir.
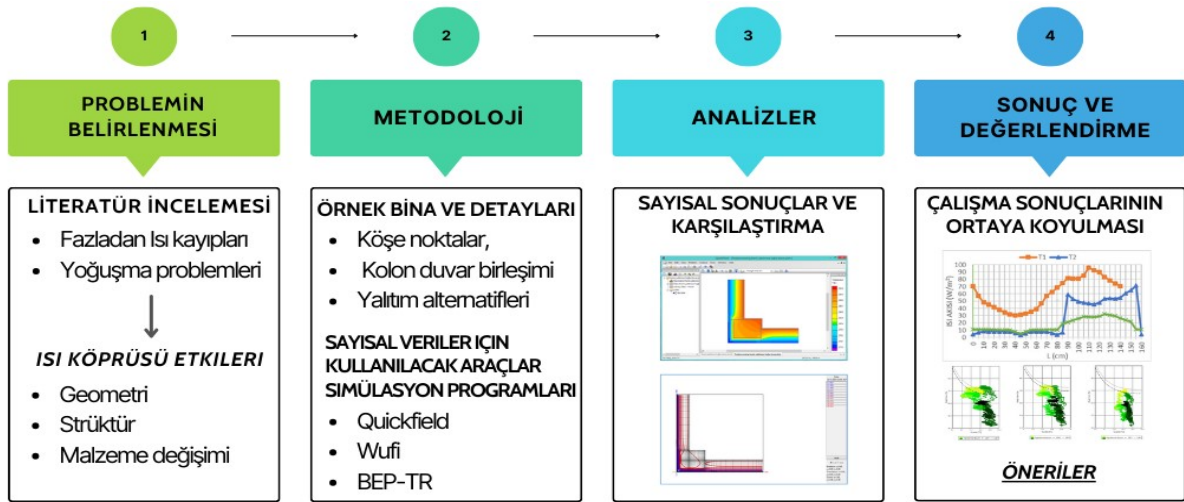


**Şekil 2.** Çalışmanın metodolojisi (Methodology of this study)

**Tablo 2.** Örnek bina ile ilgili bilgiler (Information about the case building)



| *Kat adedi* | Bodrum+Zemin+3 Normal Kat | *Bağımsız Bölüm Sayısı* | 8 (Her katta 2 daire) ~~var)~~ |
| --- | --- | --- | --- |
| *Taban Alanı* | 196 m² | *Toplam Alan* | 1100 m² |
| *Dış cephe toplam yüzey alanı (bitişik cephe hariç)* | 625,8 m² | *Dış cephedeki toplam betonarme alanı* | 104,55 m² |
| *Çatı* | Ahşap, kırma, oturtma çatı | *Taşıyıcı sistem* | Betonarme iskelet |
| *Duvar dolgu malz.* | 19 cm tuğla | *Isı yalıtımı* | 5 cm yalıtım levhası |
| *Isıtma sistemi* | Merkezi ısıtma (kömür/katı yakıt) | *Arsa Durumu* | Bir kenarı bitişik nizam |

249

Çalışmada Türkiye'de 2. Derece Gün Bölgesinde yer alan Edirne/Uzunköprü İlçesindeki 2017 tarihli bir apartman yapısı örnek bina olarak seçilmiştir. Apartman binası betonarme iskelet sistem; bodrum+zemin ve 3 normal kata sahiptir. 196m² taban alanına sahip 8 bağımsız bölümden oluşan konutta merkezi ısıtma sistemi kullanılmaktadır. Tablo 2'de bina hakkında bilgiler yer almaktadır.

## 2.1. Problem Tanımı *(Problem Definition)*

Çalışmada sabit rejim şartları altında hesap yapan Quikfield programında girdi olarak TS 825 Standardında belirlenen en soğuk ay olan Ocak ayı değerleri kullanılmıştır. Aylık ortalama iç sıcaklık değeri 20 ºC=293 Kelvin iken dış sıcaklık 0 ºC=273 Kelvin olarak kabul edilmiştir (Şekil 3). Periyodik rejim koşullarında hesap yapan Wufi programında ise Edirne'nin bir yıllık saatlik iklim verileri kullanılmıştır.
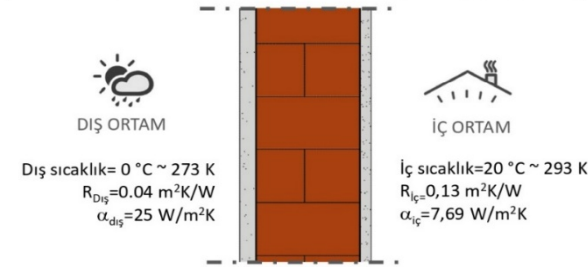


**Şekil 3.** Kabul koşulları (Accepted values)

Türkiye'de inşaat sektöründe yaygın olarak betonarme iskelet sistem kullanılmaktadır. Bu sistemde, betonarme kolon, kirişler, hatıllar, lentolar, döşeme alınları vb. yapı elemanları, tuğla ve gazbeton gibi farklı malzemelerle kurgulanan duvarlardan daha yüksek ısı iletkenliğine sahiptir ve ısı köprülerinin oluşumu kaçınılmazdır.

Bu çalışmada, Türkiye'de betonarmenin geniş kullanımı ile karakterize edilmiş sıklıkla karşılaşılan ısı köprülerine atıfta bulunarak elde edilen verilerin doğruluğu incelenmektedir. Bu amaçla mevcut bir konut yapısının köşe noktasında oluşabilecek ısı köprüsü üzerindeki etkiler, kendi içinde yalıtım uygulaması durumuna göre 3 farklı konfigürasyonla iki boyutta (2D) ele alınmıştır. Bu çerçevede yatay düzlemde duvar-kolon köşe birleşimleri için tuğla duvar malzemeli ve betonarme kolonlu bir köşe noktası incelenmiştir. Seçilen örnek için tamamen yalıtımsız (*Tip 1*), kolon dıştan kısmi yalıtımlı (*Tip 2*) ve dıştan sürekli yalıtımlı (*Tip 3*) konfigürasyonları program yardımıyla analiz edilmiştir. Sıcaklık değerlerinin yanı sıra ısı akısı özellikleri de araştırılmıştır. Isı köprüsü analizi için yatay kesitte binanın köşe noktasında konumlanan 30x40 cm boyutundaki betonarme kolondan itibaren her iki doğrultudaki eleman uzunluğu 1 m alınmıştır. Simüle edilen konfigürasyonlar ile ilgili genel bilgiler ve kullanılan yapı malzemelerinin TS 825 Standardına göre ısıl özellikleri (TS 825, 2013) Tablo 3'te verilmiştir. Konfigürasyonların U değerleri (ısıl geçirgenlik katsayısı) TS 825'e uygun olarak hesaplanmıştır. TS 825'te 2. Bölge için duvarlarda izin verilen maksimum U değeri 0,60 W/m²K tavsiye edilmektedir. Yalıtımsız durumda (U=1,54 W/m²K) bu sınır değer aşılmaktadır. Yalıtımlı durumda ise U değeri 0,52 W/m²K ile sınır değerin altındadır.

**Tablo 3.** Örnek binadaki dış duvarlara ait değişkenler (Variables of the external walls in the case building

| Yalıtım Durumu | *Tip 1* *Yalıtımsız* | *Tip 2* *Kolon kısmi yalıtımlı* | *Tip 3* *Sürekli/kesintisiz yalıtımlı* |
|---|---|---|---|
| (Tuğla duvar 19 cm) |  |  |  |
| Düğüm noktası | 188 | 208 | 224 |

| *Katmanlar* | Tabaka Kalınlığı, d (m) | Su buharı difüzyon direnci, μ | Yoğunluk, δ (kg/m³) | Isıl iletkenlik katsayısı, λ (W/mK) | Isıl iletkenlik Direnci, R (m².K/W) |
|---|---|---|---|---|---|
| Yüzeysel ısıl iletim katsayısı (İç) $\alpha_i$ | - | - | - | - | 0,13 |
| İç sıva (alçı harcı) | 0,02 | 10 | 1400 | 0,7 | 0,028 |
| Donatılı normal beton (TS 500) | 0,30 x 0,40 | 100 | 2400 | 2,5 | 0,12 |
| Yatay Delikli Tuğla (TS EN 771-1) | 0,19 | 10 | 1000 | 0,45 | 0,42 |
| Expanded polistren köpük-EPS (TS 11989 EN 13164) | 0,05 | 50 | 16 | 0,04 | 1,25 |
| Yalıtım Sıvası | 0,008 | 10 | 200 | 0,3 | 0,026 |
| Dış sıva (çimento harcı) | 0,3 | 15 | 1800 | 1 | 0,03 |
| Yüzeysel ısıl iletim katsayısı (Dış) $\alpha_d$ | - | - | - | - | 0,04 |
| Lejant | SIVA | TUĞLA | BETONARME | YALITIM LEVHASI | |

## 2.2. Yöntem *(Method)*

Yapı elemanlarındaki ısı geçişi gerçek durumda üç boyutlu olarak meydana gelmekte ve karmaşık hesap metotları içermektedir. Ancak hesaplamaların daha pratik olarak yapılabilmesi için tek ve iki boyutlu hesaplama metotları yaygın olarak kullanılmaktadır. Bu çalışma kapsamında ısı köprüsü etkisi kolon ve çevresi ile sınırlandırılarak iki boyutlu ısı geçişi iki farklı benzetim aracı ile modellenmiştir. Analizler için Quick Field 6.3 ve Wufi 2D-4.3 paket programları kullanılmıştır. Quick Field Programı; manyetik parçalar, elektrostatik çözümler, ısı transferi, stres analizleri ve elektrik devreleri gibi konularda birçok çalışmaya altlık oluşturmaktadır. Program sonlu eleman analizleri metodunu (Finite Element Method - FEM) kullanmaktadır.

Bu çalışmada, özellikle ısı transferi analizleri yardımıyla iki boyutlu ısı iletimi çözümü yapılmıştır. Bu çerçevede ısı köprüsü detayları için belirlenen kalınlık ve ebatlardaki elemanlar programda oluşturularak malzeme özellikleri ve ısıl iletkenlik değerleri girilmiştir. Kesişim noktalarında belirli düğüm noktaları (nodes) belirlendikten sonra program otomatik olarak elemanları 'mesh' denilen üçgensel alanlara bölmektedir. Benzetim sonucunda eleman içerisindeki sıcaklık ve ısı dağılımları görülebilmektedir. İstenilen noktalar için özel ölçümler alınabilmekte ve seçili alanlardaki ısı akısı ve sıcaklıkla ilgili büyüklükler grafiklere aktarabilmektedir (Quick Field, 2017). Şekil 4'te ise Quick Field 6.3 versiyonu ara yüzü hakkında bilgi verilmektedir.
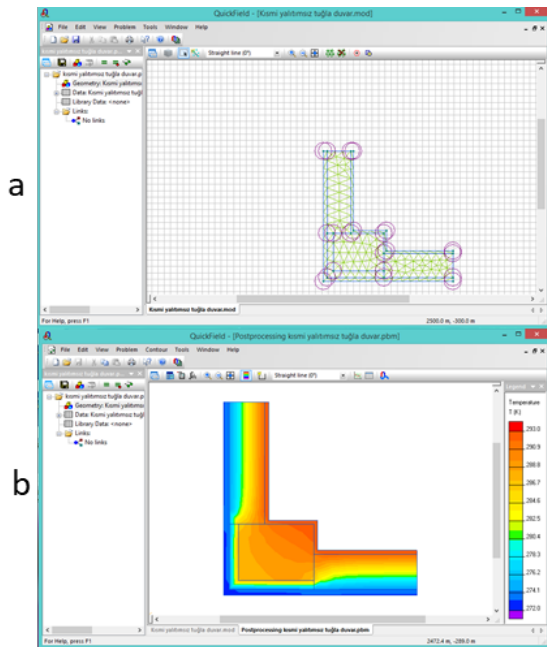


**Şekil 4.** Quick Field 6.3 programının ara yüzünde a) Düğüm noktaları ve ağ yapısı b) İzotermal görünüm (Interface of the Quick Field 6.3 program a) Nodes and meshes b) Isothermal view)

Wufi 2D programı bina bileşenlerinin iki boyutlu kesitinde zamana bağlı olarak ısı ve nem performansını hesaplamaktadır. Sonlu elemanlar yöntemi ile çalışmaktadır ve seçilen geometri için bir ağ modeli tanımlanması gerekmektedir. Bu ağ modeli; hesaplamaların hassasiyeti ve hesaplama süresi açısından sık, normal ve seyrek değerlerde seçilebilmektedir. Program hesaplamalarda EN 15026 (Yapı bileşenlerinin ve yapı elemanlarının higrotermal performansı) standardını esas almaktadır. Bu yöntemle geometrik ve yapısal ısı köprülerinin etkileri de hesaplanabilir. Isı köprülerinin hesaplanmasında ISO 10211 standardına göre hesap yapılmaktadır. Aynı zamanda ilk inşaat nemi, bileşenlerin kuruma zamanı, yoğuşma riskini belirlemek amacıyla da kullanılmaktadır.

Çalışma kapsamında ele alınan köşe noktası geometrisi için yeterli hassasiyeti sağlayacak normal değerde ağ aralıkları seçilmiştir. Çok katmanlı yapı bileşeninde; malzeme özellikleri, başlangıç koşulları, iklim verileri girdi olarak tanımlanmaktadır. Şekil 5'te Wufi 2D-4.3 versiyonu arayüzü görülmektedir.
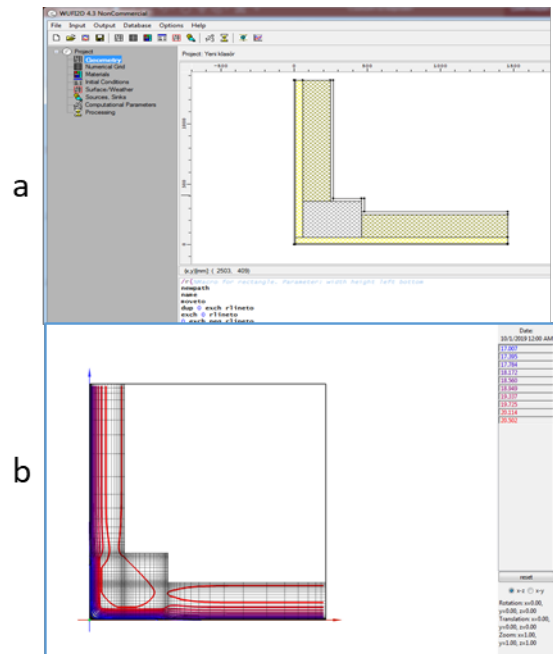


**Şekil 5.** Wufi 2D-4.3 Programının ara yüzünde a) Bileşen geometrisinin oluşturulması b) İzotermal görünüm (Interface of the Wufi 2D-4.3 Program a) Constructing the component geometry b) Isothermal view )

## 3. BULGULAR VE DEĞERLENDİRME (Findings and Evaluation)

Örnek binada seçilen detay (köşe) noktasında *Tip 1, 2 ve 3* konfigürasyonları için sıcaklık, ısı akısı, bağıl nem ve yoğuşma analizleri yapılmıştır. Isı köprüsü için Quick Field programında elde edilen sıcaklık ve ısı akısı değerleri ile WUFI programında elde edilen sıcaklığa bağlı bağıl nem değerleri Tablo 4'te verilmiştir. Bu konfigürasyonlar arasında en düşük sıcaklık ve en yüksek ısı akısı dağılımının yalıtımsız durumda olduğu görülmektedir. Kısmi yalıtımlı durumda yalıtımsız duruma göre iyileşme görülmesine rağmen homojen

olmayan sıcaklık ve ısı akısı dağılımları özellikle duvar kolon birleşim noktalarında dikkati çekmektedir. Dışardan kesintisiz yalıtımlı durumda sıcaklık ve ısı akısının dengeli ve ısı kaybının diğer durumlara göre büyük oranda azaldığı görülmektedir.

**Tablo 4.** Örnek binada köşe birleşiminde oluşan ısı köprüsü için 3 farklı durumda sıcaklık, ısı akısı ve bağıl nem analizleri (Temperature, heat flux and relative humidity analyzes in 3 different status for the thermal bridge formed at the corner junction in the case building)

| Tipler | Quick Field 6.3 | | Wufi 2D-4.3 | |
|---|---|---|---|---|
| | *Sıcaklık* | *Isı Akısı* | *Sıcaklık* | *Bağıl Nem* |
| Yalıtımsız Tuğla Duvar (Tip 1) |  |  |  |  |
| Kısmi Yalıtımlı Tuğla Duvar ( Tip 2) |  |  |  |  |
| Kesintisiz Yalıtımlı Tuğla Duvar (Tip 3) |  |  |  |  |

Yatay düzlemde köşe birleşimde yer alan taşıyıcı kolonda dıştan içe belirli bir istikamet doğrultusunda elde edilen veriler değerlendirilmiştir. 40/30 boyutundaki kolonun etrafındaki 5 cm'lik yalıtımın dış hattı üzerinde belirli aralıklarda ölçülen sıcaklık ve ısı akısı değerleri grafiğe aktarılmıştır.

Şekil 6'daki veriler incelendiğinde özellikle yalıtımsız durum *Tip 1*'de en düşük sıcaklıklar meydana gelmektedir. Aynı zamanda yalıtımsız durumda eleman kesitinde sıcaklık farkı daha yüksektir. Taşıyıcı eleman içerisinde en düşük sıcaklık farkları ise *Tip 2* ve *Tip 3* konfigürasyonlarında görülmektedir.

Aynı eleman içinde sıcaklık farklarının az olması, ısıl gerilmelerden kaynaklanan hasarların oluşumunu engeller. Bu sayede enerji tüketimine ve korunumuna da katkı sağlanır. Oluşan sıcaklık farkları, elemanın bünyesinde gerilmeler meydana getirerek taşıyıcı elemanın mukavemetinin düşmesine de sebep olur. Özellikle kış koşullarında iç ortam sıcaklıkları beklenen seviyelere ulaşamamakta, ısıl konfor koşulları sağlanamamaktadır. İç mekân ile dış mekân arasındaki sıcak farkının en yüksek olduğu dönemlerde kesit içerisindeki nem miktarı da artmaktadır. Su buharı, katmanlı yapı kabuğunda nem geçişine direnç gösteren bir bileşenle karşı karşıya geldiğinde ise yoğuşma oluşmaktadır. Bu durum yüzeylerin nemlenmesine ve rutubet-küf oluşumuna neden olarak hem kullanıcı hem de yapı sağlığını olumsuz etkilemektedir. Ayrıca donatılı betonarme elemanlarda demir donatılar, korozyona uğrayarak zamanla özelliklerini kaybedebilmekte ve binanın statiğini tehdit etmektedir.
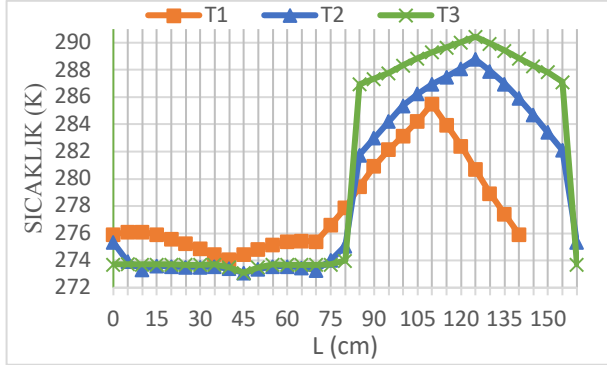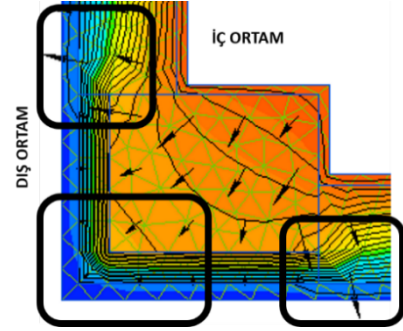
**Şekil 6.** Konfigürasyonlara göre kolon çevresi sıcaklık değerleri (Temperature values of around the column according to the configurations)

Çalışma doğrultusunda **Tip 3**'ün uygulanması durumunda yapı elemanı kesitinde **Tip 2**'den ort. 1-1,5 °C; **Tip 1**'den ise ort. 2,5-3 °C daha yüksek sıcaklıklar elde edilmiştir. **Tip 2**'de kolonun dışarıdan yalıtılmasına rağmen, istenen faydanın tam sağlanamadığı gözlenmektedir. Çünkü kolon korunsa da kolon-duvar birleşimlerinde ısıl iletkenlik farkı bulunan diğer elemanlar dış etkenlere maruz kalmakta ve bu olumsuzluklar kolon sıcaklıklarını da etkilemektedir. Dış iklim koşullarına açık olan duvar bileşeninden direkt ya da endirekt olarak suyun kesit içine girmesi engellenememektedir. Zamanla nemlilik oranı artan duvar bileşeninin, ısı yalıtım özelliği bozularak performansı önemli ölçüde azalacaktır. Eleman kesitinde oluşan ısıl gerilmeler Şekil 7'de vektör yönleri ve izoterm eğrileri ile ifade edilmeye çalışılmıştır.

Simüle edilen konfigürasyonlardaki ısı akısı dağılımı Şekil 8'de verilmiştir. Yalıtımsız durumda (**Tip 1**) yapı elemanı kesitinde meydana gelebilecek ısı kayıpları **Tip 2**'ye göre %55, **Tip 3**'e göre ise %72 daha fazladır. **Tip 3** konfigürasyonu ısı kayıpları açısından **Tip 2**'e göre %37 daha avantajlıdır. Benzer şekilde sürekli yalıtımlı

durumda eleman kesitindeki ısı dağılımları daha dengelidir. Yalıtımsız durumdaki elemanın kesitindeki yüksek ısı farkları, elemanının ısıl performansını olumsuz etkileyeceği göz ardı edilmemelidir.



**Şekil 7.** Kısmi yalıtılmış Tip 2 için elemanda gerçekleşen ısı kaybı ve ısıl gerilmeler (Heat loss and thermal stresses in the structural element for partially filled insulated Type 2)
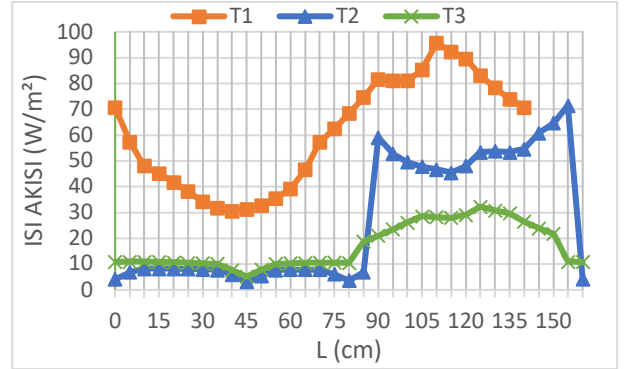


**Şekil 8.** Konfigürasyonlara göre kolon çevresi ısı akısı değerleri
(Heat flux values of the column according to the configurations)
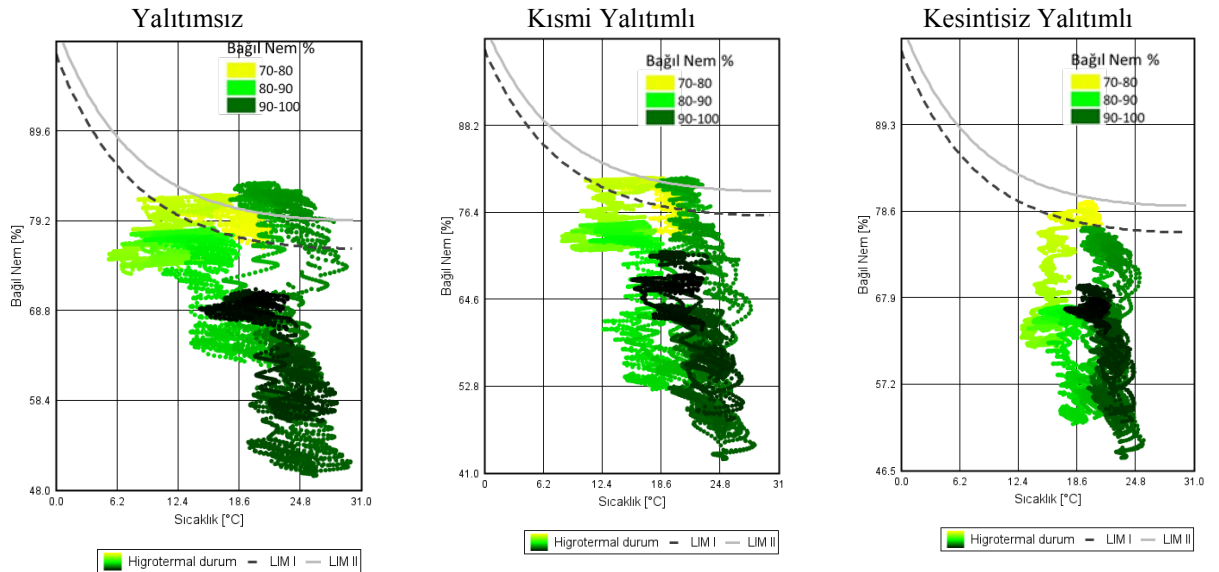


**Şekil 9.** Isı köprülerindeki yoğuşma durumu (Condensation in the thermal bridges)

253

WUFI programından elde edilen ve Şekil 9'da gösterilen yoğuşma grafiklerinde limit 1 suda ayrışamayan malzemelerin, limit 2 ise suda ayrışabilen malzemelerin sınır değerlerini ifade etmektedir. Görüldüğü gibi dışarıdan kesintisiz yalıtımlı durumda yoğuşma riski oluşmazken kısmi yalıtımlı durumda yoğuşma riski yüksektir. Yoğuşma durumunda yapı kabuğu performansını sağlayamayacak ve bileşenler bozulma etkileri ile karşı karşıya kalacaktır. Aynı zamanda bu durum iç ortam konfor koşullarını da olumsuz etkileyerek yapı sağlığının bozulmasına neden olacaktır.

Çalışma kapsamında ele alınan örnek binanın yapı kabuğu *Tip 3* senaryosu ile eşleşmektedir. BEP-TR programına bina özelliklerinin girilmesiyle binaya ait enerji tüketim sınıfı belirlenmiştir. Binaya ait enerji kimlik belgesinde yapının ihtiyaç duyduğu yıllık ısıtma, soğutma, sıcak su ve havalandırma için gerekli tüketim miktarları ve sera gazı emisyonu hakkında bilgiler yer almaktadır. Yapıya ait enerji kimlik belgesine göre yapı, kullanım alanı başına düşen toplam 310,44 kWh/m$^2$ enerji tüketimi ile enerji performans sınıfı 'C' sınıfı olarak belirlenmiştir. Yıllık $CO_2$ emisyonu yaklaşık 143 kg eşd. $CO_2$/m$^2$.yıl ile yine 'C' sınıfı olarak hesaplanmıştır. Yapıda yenilenebilir enerji kaynakları kullanılmamaktadır. Şekil 10'da yıllık nihai ısıtma, soğutma, havalandırma, sıcak su ve aydınlatma enerji tüketim miktarları ve sınıfları yer almaktadır.
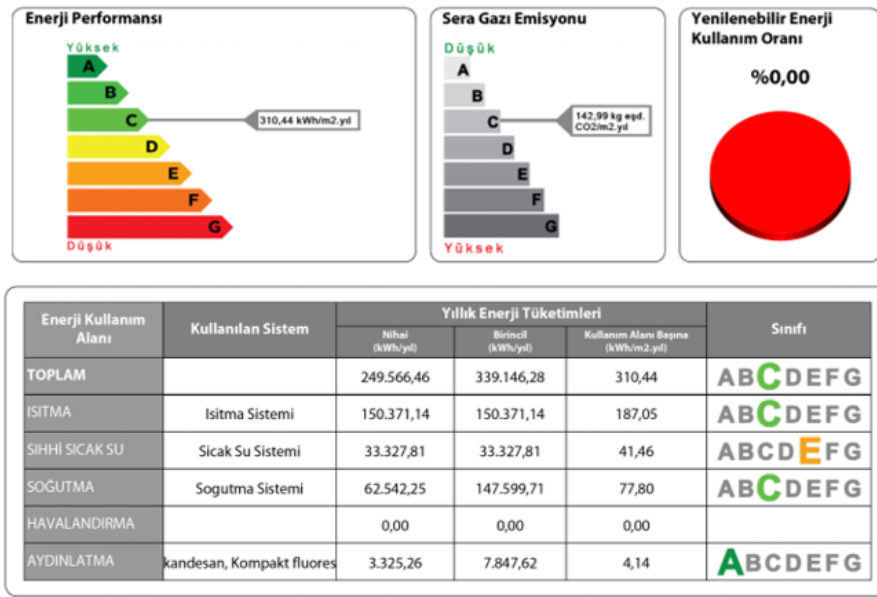


**Şekil 10.** Örnek binanın yıllık enerji ihtiyacı, enerji performans ve sera gazı emisyon sınıfları
(Annual energy demand, energy performance and greenhouse gas emission degrees in the case building)

Binaya uygulanan sınır yalıtım değeri ile enerji tüketim sınıfı C olarak belirlenmiştir. Enerji tüketiminin azaltılması ve enerji tüketim sınıfının iyileştirilmesi için yalıtım kalınlıklarının arttırılması, yenilenebilir enerji kaynaklarının kullanılması ve uygulama detaylarının iyileştirilerek binanın renovasyonu faydalı olacaktır.

## 4. SONUÇLAR (Conclusions)

Çalışmada çok katlı bir konut örneğinde yatay düzlemde ısı köprüsü oluşumu, elemanın geometrisi ve malzeme değişimine göre ele alınmıştır. Tuğla duvar-betonarme kolon birleşiminde, yalıtım durumuna göre 3 farklı konfigürasyon belirlenerek ısı köprüsü analizi yapılmıştır. Yapılan analizde, farklı konfigürasyonlar ayrı ayrı değerlendirilmiştir. Bir tarafı bitişik nizamlı olan binada diğer üç cephedeki betonarme kolon-kiriş yüzey alanı, toplam dış yüzey alanının %20'si kadardır. Zemin katta betonarme (kolon, perde, kiriş) dış cephede yer alırken 1, 2 ve 3. normal katlarda konsollar bulunmasından dolayı betonarme elemanlar iç yüzeyde kalmaktadır.

Benzetim sonuçları analiz edildiğinde yalıtımsız durum *Tip 1*'de, ısı yalıtımı yapılmamış elemanların yüzeylerinden yüksek ısı kayıpları meydana gelmektedir. Kolon ve kirişlerin dışarıdan yalıtıldığı *Tip 2* ve *Tip 3*'te, eleman kesiti sıcak tarafta kalmaktadır. Ancak *Tip 2*'de ısı köprülerinin dışarıdan yalıtılması ile bu kısımlar korunmakta fakat duvar kesitleri dış koşullarla direkt temas etmektedir. *Tip 3*'te yapı elemanı içerisinde daha az sıcaklık değişimi görülmektedir. Yapı elemanın ortalama kesit sıcaklığına göre *Tip 3*, *Tip 2*'den ort. 1-1,5 °C; *Tip 1*'den ise ort. 2,5-3 °C daha yüksek sıcaklıklara sahiptir. Yapı elemanı kesitinde meydana gelebilecek ısı kayıpları *Tip 1*'de *Tip 2*'ye göre %55, *Tip 3*'e göre ise %72 daha fazladır. *Tip 3*'deki ısı kayıpları *Tip 2*'den %37 daha azdır. Literatürdeki çalışmalara bakıldığında bina kabuğundaki yapı elemanları üzerinde kesintisiz yalıtımın olumlu etkileri (enerji tüketimi, ısı ve nem performansı açısından) görülmektedir (Martin, Campos-Celador, Escudero vd, 2012; Asdrubali vd, 2012; Capozzoli vd, 2013; Umaroğulları vd, 2011).

Hallik vd. farklı iki örnek bina kabuğunda ısı köprülerini ISO 10211'e göre karşılaştırmakta ve bina tipine bağlı olarak ısı kayıplarının %35 ila %76 oranında azaldığını öne sürmektedir (Hallik ve Kalamees, 2021). Evola vd., ısı kaybının %30'unun ısı köprülerinden kaynaklandığını belirtmektedir (Evola vd, 2011). Ayrıca dışarıdan yalıtımın içeriden yalıtıma göre ısı köprüsü etkisini %53-65 oranında azaltabileceği belirtilmektedir (El Saied vd, 2022). Deneysel ve benzetim yöntemleriyle elde edilen benzer bulgular çalışma metodunu doğrular niteliktedir.

Çalışmada ele alınan örnek yapıya ait mevcut enerji kimlik belgesindeki veriler *Tip 3*'ün avantajlarını doğrulamaktadır. Yapının enerji performans sınıfının 'C' çıkmasında, yalıtımın etkisi büyüktür. Enerji korunumu açısından dış yalıtımın varlığı, yıllık tüketilen ısıtma ve soğutma enerjisi açısından tasarruf sağlamaktadır. Enerji sınıfının artırılabilmesi için ek önlemlerin alınması gerekmektedir. Hem enerji korunumu hem de yapı sağlığı açısından yalıtım kesintiye uğratılmamalı ve uygulamada ısı köprüsüne neden olabilecek hatalardan kaçınılmalıdır. Bina kabuğunda ısı köprüsüne neden olabilecek karmaşık geometrilerden kaçınılmalıdır. Fosil kaynaklardan elde edilen olumsuz çevresel etkileri azaltmak için yenilenebilir enerji kaynakları ya da atık vb. kaynaklardan yararlanılmalıdır.

Binanın enerji performans sınıfının yükseltilebilmesi için tasarım aşamasında bina benzetim yöntemlerinden faydalanılmalıdır. Bu amaçla duvar bileşen türü, yalıtım malzemesi türü, kalınlığı ve yeri (ısı ve nem performansı), yapı kabuğu sızdırmazlığı dikkate alınmalıdır. Enerji verimli tasarım için pasif tasarımlara öncelik verilmeli, bina sistemlerinin verimlilikleri arttırılmalı, enerji talebinin azaltılabileceği malzeme ve ekipman dahil edilerek bina enerji ihtiyacı yenilenebilir enerji kaynaklarından sağlanmalıdır. Ayrıca ülkemizde bina performansının iyileştirilmesine yönelik enerji verimliliği yaptırımlarının gözden geçirilmesi, Enerji Kimlik Belgesi C sınıfı koşulunun iyileştirilmesi de alınabilecek önlemler arasındadır.

## KAYNAKLAR (References)

IEA (International Energy Agency), 2013, Transition to Sustainable Buildings-Strategies and Opportunities to 2050. Transition to Sustainable Buildings. https://doi.org/10.1787/9789264202955-en

European Comission, 2020. (https://energy.ec.europa.eu/topics/energy-efficiency/energy-efficient-buildings/nearly-zero-energy-buildings_en#zero-emission-buildings).

Garay, R., Uriarte, A. and Apraiz, I., 2014, Performance assessment of thermal bridge elements into a full scale experimental study of a building façade. Energy and Buildings, 85, 579–591. https://doi.org/10.1016/J.ENBUILD.2014.09.024

Goggins, J., Moran, P., Armstrong, A. and Hajdukiewicz, M., 2016, Lifecycle environmental and economic performance of nearly zero energy buildings (NZEB) in Ireland, Energy Build. Vol:116, pp. 622–637.

O'Grady, M., Lechowska, A. A. and Harte, A. M., 2018, Application of infrared thermography technique to the thermal assessment of multiple thermal bridges and Windows, Energy and Buildings, 168, 347–362.

Evola, G., Margani, G. and Marletta, L. 2011, Energy and cost evaluation of thermal bridge correction in Mediterranean climate. Energy and Buildings, 43(9), 2385–2393. https://doi.org/10.1016/j.enbuild.2011.05.028.

Bergero, S. and Chiari, A., 2018, The influence of thermal bridge calculation method on the building energy need: A case study. Energy Procedia, 148(Ati), 1042–1049.

De Angelis, E. and Serra, E., 2014, Light steel-frame walls: Thermal insulation performances and thermal bridges. Energy Procedia, 45, 362–371.

Martins, C., Santos, P. and Da Silva, L. S., 2016, Lightweight steel-framed thermal bridges mitigation strategies: A parametric study. Journal of Building Physics, 39(4), 342–372.

Zhao, K., Jiang, Z., Huang, Y., Sun, Z., Wang, L., Gao, W. and GE, J., 2022, The method of reducing heat loss from thermal bridges in residential buildings with internal insulation in China's hot summer and cold winter zone. Journal of Building Engineering, 62, 105421.

Erhorn-kluttig, H., Erhorn, H., Citterio, M., Cocco, M., Orshoven, V. and Tilmans, A., 2009, Thermal Bridges in the EPBD context, 30th AIVC Conference "Trends in High Performance Buildings", Berlin/Germany, October 1-2.

Martin, K., Campos-Celador, A., Escudero, C., Gómez, I. and Sala, J. M., 2012, Analysis of a thermal bridge in a guarded hot box testing facility. Energy and Buildings, 50, 139–149.

Ge, H., McClung, V. R. and Zhang, S., 2013, Impact of balcony thermal bridges on the overall thermal performance of multi-unit residential buildings: A case study. Energy and Buildings, 60, 163–173.

Aghasizadeh, S., Kari, B.M, Fayaz, R., 2022, "Thermal performance of balcony thermal bridge solutions in reinforced concrete and steel frame structures", Journal of Building Engineering, Volume 48, 1 May, 103984.

Aguilar, F., Solano, J. P. and Vicente, P. G., 2014, Transient modeling of high-inertial thermal bridges in buildings using the equivalent thermal wall method. Applied Thermal Engineering, 67(1–2), 370–377.

Ascione, F., Bianco, N., De Masi, R. F., De'Rossi, F. and Vanoli, G. P., 2013, Simplified state space representation for evaluating thermal bridges in building: Modelling, application and validation of a methodology. Applied Thermal Engineering, 61(2), 344–354.

Dumitrescu, L., Baran, I. and Pescaru, R. A., 2017, The Influence of Thermal Bridges in the Process of Buildings Thermal Rehabilitation. Procedia Engineering, 181, 682–689.

Kotti, S., Teli, D. and James, P. A. B., 2017, Quantifying Thermal Bridge Effects and Assessing Retrofit Solutions in a Greek Residential Building. Procedia Environmental Sciences, 38, 306–313.

Marincioni, V., May, N. and Altamirano-Medina, H., 2015, Parametric study on the impact of thermal bridges on the heat loss of internally insulated buildings. Energy Procedia, 78, 889–894.

Viot, H., Sempey, A., Pauly, M. and Mora, L., 2015, Comparison of different methods for calculating thermal bridges: Application to wood-frame buildings. Building and Environment, 93(P2), 339–348.

Fantucci, S., Isaia, F., Serra, V. and Dutto, M., 2017, Insulating coat to prevent mold growth in thermal bridges. Energy Procedia, 134, 414–422.

Martin, K., Escudero, C., Erkoreka, A., Flores, I. and Sala, J. M., 2012, Equivalent wall method for dynamic characterisation of thermal bridges. Energy and Buildings, 55, 704–714.

El Saied, A., Maalouf, C., Bejat, T. and Wurtz, E., 2022, Slab-on-grade thermal bridges: A thermal behavior and solution review, Energy and Buildings, Volume 257, 111770.

Asdrubali, F., Baldinelli, G. and Bianchi, F., 2012, A quantitative methodology to evaluate thermal bridges in buildings. Applied Energy, 97, 365–373.

Ahrab, M. A. M. and Akbari, H., 2013, Hygrothermal behaviour of flat cool and standard roofs on residential and commercial buildings in North America. Building and Environment, 60, 1–11.

Theodosiou, T., Tsikaloudaki, K., Tsoka, S. and Chastas, P. 2019, Thermal bridging problems on advanced cladding systems and smart building facades. Journal of Cleaner Production, 214, 62–69.

Terentjevas, J., Šadauskaitė, M., Šadauskienė, J., Ramanauskas, J., Buska, A. and Fokaides, P. A. 2021, Numerical investigation of buildings point thermal bridges observed on window-thermal insulation interface, Case Studies in Construction Materials, Volume 15.

Ascione, F., Bianco, N., De Rossi, F., Turni, G. and Vanoli, G. P., 2012, Different methods for the modelling of thermal bridges into energy simulation programs: Comparisons of accuracy for flat heterogeneous roofs in Italian climates. Applied Energy, 97, 405–418.

Theodosiou, T., Tsikaloudaki, K. and Bikas, D., 2017, Analysis of the Thermal Bridging Effect on Ventilated Facades. Procedia Environmental Sciences, 38, 397–404.

BS EN ISO 10211, 2007, Thermal bridges in building construction- Heat flows and surface temperatures- Detailed calculations, 3(1), 54.

Prata, J., Simões, N. and Tadeu, A., 2018, Heat transfer measurements of a linear thermal bridge in a wooden building corner. Energy and Buildings, 158, 194–208.

Özel, M., 2022, Determination of indoor design temperature, thermal characteristics and insulation thickness under hot climate conditions. Isı Bilimi ve Tekniği Dergisi, 42, 1, 49-64.

Çağlayan S., Ozorhon, B. and Kurnaz, L. 2022, Nationwide mapping of optimum wall insulation thicknesses: a stochastic approach. Isı Bilimi ve Tekniği Dergisi, 42, 2, 169-202.

ISO 8990, 1994, Thermal insulation- Determination of steady-state thermal transmission properties- Calibrated and guarded hot box.

Asdrubali, F. and Baldinelli, G., 2011, Thermal transmittance measurements with the hot box method: calibration, experimental procedures, and uncertainty analysis of three different approaches, Energy Build. Vol:43, pp.1618–1626.

Fang, Y., Eames, P.C., Norton, B. and Hyde, T.J. 2006, Experimental validation of a numerical model for heat transfer in vaccum glazing, Sol. Energy. Vol:80, pp.564–577.

Zalewski, L., Lassue, S., Rousse, D. and Boukhalfa, K., 2010, Experimental and numerical characterization of thermal bridges in prefabricated building walls. Energy Conversion and Management, 51(12), 2869–2877.

Capozzoli, A., Gorrino, A. and Corrado, V., 2013, A building thermal bridges sensitivity analysis. Applied Energy, 107, 229–243.

Al-Sanea, S. A. and Zedan, M. F., 2012, Effect of thermal bridges on transmission loads and thermal resistance of building walls under dynamic conditions. Applied Energy, 98, 584–593.

BrumĂ, B., Moga, L. and Moga, I., 2015, Aspects Regarding Dynamic Calculation of Plan Building Elements Having Thermal Bridges. Energy Procedia, 85(November 2015), 77–84.

Quinten, J. and Feldheim, V., 2016, Dynamic modelling of multidimensional thermal bridges in building envelopes: Review of existing methods, application and new mixed method. Energy and Buildings, 110, 284–293.

Karacavus, B. and Can, A., 2008, Experimental investigation of a solar energy heating system under the climatic conditions of Edirne. Renewable Energy, 33(9), 2084–2096.

Romero, M. J., Aguilar, F. and Vicente, P. G., 2021, Analysis of design improvements for thermal bridges formed by double-brick façades and intermediate slabs for nZEB residential buildings in Spain, Journal of Building Engineering, Volume 44, 103270.

Capozzoli, A., Gorrino, A., Corrado, V., Grinzato, E., Vavilov, V., Kauppinen, T., Fukuyo, K., 2013, Energy and cost evaluation of thermal bridge correction in Mediterranean climate. Energy and Buildings, 107(9), 2385–2393.

Ge, H. and Baba. F., 2015, Dynamic effect of thermal bridges on the energy performance of a low-rise residential building". Energy and Buildings Volume 105, Pages 106-118.

Antretter, F., Dring, J. R. and Pazold, M., 2013, Coupling of Dynamic Thermal Bridge and Whole-Building Simulation, Thermal Performance of the Exterior Envelopes of Whole Buildings XII International Conference, Buildings XII.

Real, S., Gomes, M.G., Rodrigues, A.M. and Bogas, J.A., 2016, Contribution of structural lightweight aggregate concrete to the reduction of thermal bridging effect in buildings, Construction and Building Materials. Vol: 121, pp.460–470.

Fukuyo, K., 2003, Heat flow visualization for thermal bridge problems. International Journal of Refrigeration, 26(5), 614–617.

Schöck Ltd., 2015, Thermal Bridging Guide. Schöck Ltd, Oxford, (June). Retrieved from https://www.schoeck.co.uk/view/5993/Thermal_Bridging_Guide_Schoeck_Isokorb_%5B5993%5D.pdf

TS 825, 2013, Binalarda Isı Yalıtım Kuralları, Türk Standartları Enstitüsü, Ankara.

BEPY, 2010, Binalarda Enerji Performansı Yönetmeliği, Bayındırlık ve İskân Bakanlığı, Aralık.

TS EN ISO 10211, 2017, Bina yapılarında ısıl köprüler- Isı akışları ve yüzey sıcaklıkları- Ayrıntılı hesaplama yöntemleri, Türk Standartları Enstitüsü, Ankara.

TS EN ISO 14683, 2017, Bina inşaatı-Isıl köprüler-Lineer ısıl geçirgenlik-Basitleştirilmiş metot ve hatasız değerler, Türk Standartları Enstitüsü, Ankara.

Quick Field, 2017, Quick Field ™ Finite Element Analysis System Version 6.3 User's Guide, Tera Analysis Ltd. / http://quickfield.com (Son erişim tarihi:16.05.2023)

Umaroğulları, F., Zorer Gedik, G. and Mıhlayanlar, E., 2011, Condensation Control of Insulated and Uninsulated Concrete Walls in the Periodic Regime: The Case of Edirne. Megaron, 6(1): 13-20.

Hallik, J. and Kalamees, T., 2021, The effect of flanking element length in thermal bridge calculation and possible simplifications to account for combined thermal bridges in well insulated building envelopes, Energy & Buildings 252, 111397, 1-10.

**Filiz UMAROĞULLARI,** Trakya Üniversitesi Mimarlık Fakültesi Mimarlık Bölümü'nde 2020 yılından beri Doçent olarak görev yapmaktadır. Lisansüstü eğitimini Trakya Üniversitesi Fen Bilimleri Enstitüsü Mimarlık Anabilim dalında tamamlamış olup 2011 yılında doktora derecesini almıştır. Çalışma alanları yapı fiziği, fiziksel çevre kontrolü ve binalarda enerji verimliliğidir.

**Esma MIHLAYANLAR,** Manisa/Kula'da doğdu. 1988 yılında Trakya Üniversitesi Mühendislik Mimarlık Fakültesi Mimarlık Bölümünü kazandı. 1993 yılında Trakya Üniversitesi Mühendislik Mimarlık Fakültesi Mimarlık Bölümü Yapı Bilgisi Anabilim Dalı'na Araştırma Görevlisi olarak girdi. 2024 yılından itibaren Trakya Üniversitesi Mimarlık Fakültesi Mimarlık Bölümünde Profesör olarak görevine devam etmektedir. Mesleki ilgi alanları yapı ve yapım teknolojileri / sistemleri, yapı fiziği ve malzemesi konularıdır. Özellikle enerji verimli sürdürülebilir binalar, enerji korunumu, bina renovasyonu ve fiziksel çevre kontrolü konularıyla ilgili olarak çalışmaktadır.

**Melek SEYİT,** Trakya Üniversitesi Mimarlık Fakültesi Mimarlık Bölümü'nde Araştırma görevlisi olarak görev yapmaktadır. Yüksek Lisans eğitimini 2014 yılında Trakya Üniversitesi Fen Bilimleri Enstitüsü Mimarlık Anabilim Dalında tamamlamış doktora eğitimini ise 2023 yılında tamamlayarak doktora derecesini almıştır. Çalışma alanları yapı ve yapım teknolojileri, inşa edilebilirlik, fiziksel çevre kontrolüdür.

# ISI BİLİMİ VE TEKNİĞİ DERGİSİ İÇİN MAKALE HAZIRLAMA ESASLARI

Isı Bilimi ve Tekniği Dergisi'nde, ısı bilimi alanındaki özgün teorik ve deneysel çalışmaların sonuçlarının sunulduğu makaleler ve yeterli sayıda makaleyi tarayarak hazırlanmış olan literatür özeti makaleler yayınlanmaktadır. Makaleler, Türkçe veya İngilizce olarak kabul edilmektedir. Makaleler ilk sunumda serbest formatta hazırlanabilir. Ancak yayın için kabul edilmiş olan makaleler dergimizin basım formatına tam uygun olarak yazarlar tarfından hazırlanmalıdır. Aşağıda, ilk sunuş ve basıma hazır formatta makale hazırlamak için uyulması gereken esaslar detaylı olarak açıklanmıştır.

## İLK SUNUŞ FORMATI

İlk sunuşta, makale A4 boyutundaki kağıda tek sütun düzeninde, 1.5 satır aralıklı ve sayfa kenarlarından 25'er mm boşluk bırakılarak yazılmalıdır. Yazı boyutu 11 punto olmalı ve **Times New Roman** karakter kullanılmalıdır. Şekiller, tablolar ve fotograflar makale içinde **olmaları gereken yerlere** yerleştirilmelidir. Makale, elektronik olarak editörün e-posta adresine gönderilmelidir.

## BASIMA HAZIR MAKALE FORMATI

Hakem değerlendirmelerinden sonra, yayın için kabul edilmiş olan makaleler, dergimizin basım formatına tam uygun olarak yazarlar tarafından hazırlanmalıdır. Makaleler yazarların hazırladığı haliyle basıldığı için, yazarların makalelerini basım için hazır formatta hazırlarken burada belirtilen esasları titizlikle takip etmeleri çok önemlidir. Aşağıda, basıma hazır formatta makale hazırlamak için uyulması gereken esaslar detaylı olarak açıklanmıştır.

### Genel Esaslar

Makaleler genel olarak şu başlıklar altında düzenlenmelidir: Makale başlığı (title), yazar(lar)ın ad(lar)ı, yazar(lar)ın adres(ler)i, özet (abstract), anahtar kelimeler (keywords), semboller, giriş, materyal ve metod, araştırma sonuçları, tartışma ve sonuçlar, teşekkür, kaynaklar, yazarların fotoğrafları ve kısa özgeçmişleri ve ekler. Yazılar bilgisayarda tek satır aralıklı olarak, 10 punto Times New Roman karakteri kullanılarak Microsoft Office Word ile iki sütun düzeninde yazılmalıdır. Sayfalar, üst kenardan 25 mm, sol kenardan 23 mm, sağ ve alt kenarlardan 20 mm boşluk bırakılarak düzenlenmelidir. İki sutun arasındaki boşluk 7 mm olmalıdır. Paragraf başları, sütunun sol kenarına yaslanmalı ve paragraflar arasında bir satır boşluk olmalıdır.

Birinci seviye başlıklar büyük harflerle kalın olarak, ikinci seviye başlıklar bold ve kelimelerin ilk harfleri büyük harf olarak ve üçüncü seviye başlıklar sadece ilk harfi büyük olarak yazılır. Bütün başlıklar sutunun sol kenarı ile aynı hizadan başlamalıdır ve takip eden paragrafla başlık arasında bir satır boşluk olmalıdır. Şekiller, tablolar, fotoğraflar v.b. metin içinde ilk atıf yapılan yerden hemen sonra uygun şekilde yerleştirilmelidir. İlk ana bölüm başlığı, Özetten (Abstract'tan) sonra iki satır boşluk bırakılarak birinci sutuna yazılır.

### Başlık, Yazarların Adresi, Özet, Abstract ve Anahtar Kelimeler

Yazılar Türkçe veya Ingilizce olarak hazırlanabilir. Her iki durumda da makale özeti, başlığı ve anahtar kelimeler her iki dilde de yazılmalıdır. Eğer makale Türkçe olarak kaleme alınmışsa, Türkçe başlık ve özet önce, İngilizce başlık ve Özet (Abstract) sonra yazılır. Eğer makale İngilizce olarak kaleme alınmışsa önce İngilizce başlık ve özet (abstract) sonra Türkçe başlık ve özet yazılır. Başlık, sayfanın üst kenarından 50 mm aşağıdan başlar ve kalın olarak 12 punto büyüklüğünde, büyük harflerle bütün sayfayı ortalayacak şekilde yazılır. Yazar(lar)ın adı, adresi ve elektronik posta adresi başlıktan sonra bir satır boşluk bırakılarak yazılmalıdır. Yazarların adı küçük, soyadı büyük harflerle yazılmalı ve bold olmalıdır. Yazarların adresinden sonra üç satır boşluk bırakılarak, Özet ve Abstract 10 punto büyüklüğünde bütün sayfa genişliğinde yazılır. Özet ve Abstractan sonra anahtar kelimeler (Keywords) yazılır.

### Birimler

Yazılarda SI birim sistemi kullanılmalıdır.

### Denklemler

Denklemler, 10 punto karakter boyutu ile bir sütuna (8 cm) sığacak şekilde düzenlenmelidir. Veriliş sırasına göre yazı alanının sağ kenarına yaslanacak şekilde parantez içinde numaralanmalıdır. Metin içinde, denklemlere **'Eş. (numara)'** şeklinde atıfta bulunulmalıdır.

### Şekiller

Şekiller 8 cm (bir sütun) veya 16 cm (iki sütun) genişliğinde olmalıdır ve makale içerisinde olmaları gereken yerlere bilgisayar ortamında sutunu (veya bütün sayfa genişliğini) ortalayacak şekilde yerleştirilmelidir. Şekil numaraları (sıra ile) ve isimleri şekil **altına, 9 punto büyüklüğünde** yazılmalıdır.

### Tablolar

Tablolar 8 cm (bir sütun) veya 16 cm (iki sütun) genişliğinde olmalıdır. Makale içerisinde olmaları gereken yerlere bilgisayar ortamında sutunu (veya bütün sayfa genişliğini) ortalayacak şekilde yerleştirilmelidir. Tablo numaraları (sıra ile) ve isimleri tablo **üstüne, 9 punto büyüklüğünde** yazılmalıdır.

### Fotograflar

Fotograflar, siyah/beyaz ve 8 cm (bir sütun) veya 16 cm (iki sütun) genişliğinde olmalıdır. Fotograflar digitize edilerek, makale içinde bulunmaları gereken yerlere bilgisayar ortamında sutunu (veya bütün sayfa genişliğini) ortalayacak şekilde yerleştirilmelidir ve şekil gibi numaralandırılmalı ve adlandırılmalıdır.

### Yazar(lar)ın Fotograf ve Kısa Özgeçmişleri

Yazarların fotografları digitize edilerek, makalenin en sonuna özgeçmişleri ile birlikte uygun bir şekilde yerleştirilmelidir.

### SEMBOLLER

Makale içinde kullanılan bütün semboller alfabetik sırada Özetten sonra liste halinde tek sütun düzeninde yazılmalıdır. Boyutlu büyüklükler birimleri ile birlikte ve boyutsuz sayılar (Re, Nu, vb.) tanımları ile birlikte verilmelidir.

### KAYNAKLAR

Kaynaklar metin sonunda, ilk yazarın soyadına göre alfabetik sırada listelenmelidir. Kaynaklara, yazı içinde, yazar(lar)ın soyad(lar)ı ve yayın yılı belirtilerek atıfta bulunulmalıdır. Bir ve iki yazarlı kaynaklara, her iki yazarın soyadları ve yayın yılı belirtilerek (Bejan, 1988; Türkoğlu ve Farouk, 1993), ikiden çok yazarlı kaynaklara ise birinci yazarın soyadı ve "vd." eki ve yayın yılı ile atıfta bulunulmalıdır (Ataer vd, 1995). Aşağıda makale, kitap ve bildirilerin kaynaklar listesine yazım formatı için örnekler verilmiştir.

Ataer Ö. E., Ileri A. and Göğüş, Y. A., 1995, Transient Behaviour of Finned-Tube Cross-Flow Heat Exchangers, *Int. J. Refrigeration,* 18, 153-160.

Bejan A., 1998, *Advanced Engineering Thermodynamics* (First Ed.), Wiley, New York.

Türkoğlu H. and Farouk B., 1993, Modeling of Interfacial Transport Processes in a Direct-Contact Condenser for Metal Recovery, *Proc. of 73rd Steel Making Conference*, Detroit, 571-578.

Türkoğlu H., 1990, *Transport Processes in Gas-Injected Liquid Baths*, Ph.D. Thesis, Drexel University, Philadelphia, PA, USA.

İnternet, 2004, Türkiye İstatistik Kurumu, *Atıksu İstatistikleri*, http://www.tuik.gov.tr/HaberBulteni.

### DİĞER HUSUSLAR

Hakem değerlendirmesinden sonra kabul edilen makaleler, yukarıda açıklandığı şekilde dizilerek basıma hazırlandıktan sonra, bir elektronik kopyası editöre gönderilmelidir. Makalenin basıma hazır kopyası ile birlikte, "Telif Hakkı Devri Formu" da doldurularak göderilmelidir. Telif Hakkı Devir Formu'na ve bu yazım klavuzuna www.tibtd.org.tr adresinden ulaşılabilir.

FOTOĞRAFINIZ

**TÜRK ISI BİLİMİ VE TEKNİĞİ DERNEĞİ**
**ÜYELİK BAŞVURU FORMU**

A. Adınız Soyadınız :

Ünvanınız :

Doğum yeri : : Doğum tarihi: / / 19 T.C. Kimlik No:

İş Adresiniz :

Ev adresiniz :

Telefonunuz : İş Ev Cep

E-posta :

B. *Derneğe ☐Asil üye ☐Fahri üye olmak istiyorum.

1. Sizi tanıyan dernek üyesi (Üyelik için) :

2. Mezun olduğunuz
   <u>Yüksek Okullar</u>    <u>Yıl</u>   <u>Branşınız</u>   <u>Ünvanınız</u>

3. İlgilendiğiniz konular :

2015 yılı aidatı olarak toplam 25 YTL (Yirmibeş Milyon TL) derneğin

  İş Bankası Maltepe Şubesi Hesap No: 42120867567
  IBAN: TR08 0006 4000 0014 2120 8675 67

 hesabına yatırılmıştır.

Tarih : İmza :

* Asil üye olmak için beş yıllık deneyim gereklidir.
  Fahri üyelik için yüksekokul mezunu olma şartı yoktur.

Türk Isı Bilimi ve Tekniği Derneği
Gazi Üniversitesi
Mühendislik Fakültesi
Makina Mühendisliği Bölümü
06570 Maltepe/ ANKARA

# İÇİNDEKİLER / CONTENTS